frontiers | Research Topics

Ocular biomechanics in health and pathophysiology

Edited by
Matthew A. Reilly, Jonathan Vande Geest
and J. Crawford Downs

Published in
Frontiers in Bioengineering and Biotechnology

ISSN 1664-8714
ISBN 978-2-8325-5039-7
DOI 10.3389/978-2-8325-5039-7

About Frontiers

Frontiers is more than just an open access publisher of scholarly articles: it is a pioneering approach to the world of academia, radically improving the way scholarly research is managed. The grand vision of Frontiers is a world where all people have an equal opportunity to seek, share and generate knowledge. Frontiers provides immediate and permanent online open access to all its publications, but this alone is not enough to realize our grand goals.

Frontiers journal series

The Frontiers journal series is a multi-tier and interdisciplinary set of open-access, online journals, promising a paradigm shift from the current review, selection and dissemination processes in academic publishing. All Frontiers journals are driven by researchers for researchers; therefore, they constitute a service to the scholarly community. At the same time, the *Frontiers journal series* operates on a revolutionary invention, the tiered publishing system, initially addressing specific communities of scholars, and gradually climbing up to broader public understanding, thus serving the interests of the lay society, too.

Dedication to quality

Each Frontiers article is a landmark of the highest quality, thanks to genuinely collaborative interactions between authors and review editors, who include some of the world's best academicians. Research must be certified by peers before entering a stream of knowledge that may eventually reach the public - and shape society; therefore, Frontiers only applies the most rigorous and unbiased reviews. Frontiers revolutionizes research publishing by freely delivering the most outstanding research, evaluated with no bias from both the academic and social point of view. By applying the most advanced information technologies, Frontiers is catapulting scholarly publishing into a new generation.

What are Frontiers Research Topics?

Frontiers Research Topics are very popular trademarks of the *Frontiers journals series*: they are collections of at least ten articles, all centered on a particular subject. With their unique mix of varied contributions from Original Research to Review Articles, Frontiers Research Topics unify the most influential researchers, the latest key findings and historical advances in a hot research area.

Find out more on how to host your own Frontiers Research Topic or contribute to one as an author by contacting the Frontiers editorial office: frontiersin.org/about/contact

Ocular biomechanics in health and pathophysiology

Topic editors

Matthew A. Reilly — The Ohio State University, United States

Jonathan Vande Geest — University of Pittsburgh, United States

J. Crawford Downs — University of Alabama at Birmingham, United States

Citation

Reilly, M. A., Geest, J. V., Downs, J. C., eds. (2024). *Ocular biomechanics in health and pathophysiology*. Lausanne: Frontiers Media SA.

doi: 10.3389/978-2-8325-5039-7

Table of contents

05 Orbital fat swelling: A biomechanical theory and supporting model for spaceflight-associated neuro-ocular syndrome (SANS)
Matthew A. Reilly, Steven E. Katz and Cynthia J. Roberts

15 The lens capsule significantly affects the viscoelastic properties of the lens as quantified by optical coherence elastography
Taye Mekonnen, Christian Zevallos-Delgado, Hongqiu Zhang, Manmohan Singh, Salavat R. Aglyamov and Kirill V. Larin

24 Quantifying the morphology of eyeballs with posterior staphyloma with Zernike polynomials
Hua Rong, Lin Liu, Yuling Liu, Wanzeng Fu, He Xu, Danyang Yu, Di Wu, Bei Du, Xuejun Zhang, Bin Zhang and Ruihua Wei

33 Corneal optical density: Structural basis, measurements, influencing factors, and roles in refractive surgery
Ye He, Bo-Sheng Ma, Jun-Hao Zeng and Dai-Jin Ma

43 Classification of Vogt-Koyanagi-Harada disease using feature selection and classification based on wide-field swept-source optical coherence tomography angiography
Peng Xiao, Ke Ma, Xiaoyuan Ye, Gengyuan Wang, Zhengyu Duan, Yuancong Huang, Zhongzhou Luo, Xiaoqing Hu, Wei Chi and Jin Yuan

56 The role of corneal biomechanics in visual field progression of primary open-angle glaucoma with ocular normotension or hypertension: a prospective longitude study
Yahui Wei, Yu Cai, Chenying Bao, Yanfei Zhu and Yingzi Pan

63 Comparison of bilateral differential characteristics of corneal biomechanics between keratoconus and normal eyes
Yiyong Xian, Yu Zhao, Ling Sun, Xiaoyu Zhang, Lan Ding, Zesheng Liu, Yuan Li, Yanlan Ding, Lin Jiang, Xingtao Zhou and Yang Shen

73 Assessment of age-related change of the ocular support system
Ahmed Makarem, Ahmed Abass, Fangjun Bao and Ahmed Elsheikh

82 Screening of sensitive *in vivo* characteristics for early keratoconus diagnosis: a multicenter study
Xuan Chen, Huazheng Cao, Yan Huo, Jiaxin Song, Haohan Zou, Jing Li, Jie Hou and Yan Wang

90 Effect of central corneal curvature on corneal material stiffness parameter acquired by dynamic corneal responses
Zhe Chu, Qi Ren, Wenjie Su, Wei Cui and Jie Wu

96 Numerical study of critical straight, frown, and chevron incisions in small incision cataract surgery
Yang Han and Nan Qi

104 Patient-specific air puff-induced loading using machine learning
Nada A. Desouky, Mahmoud M. Saafan, Mohamed H. Mansour and Osama M. Maklad

117 Machine learning analysis with the comprehensive index of corneal tomographic and biomechanical parameters in detecting pediatric subclinical keratoconus
Shengwei Ren, Kaili Yang, Liyan Xu, Qi Fan, Yuwei Gu, Chenjiu Pang and Dongqing Zhao

126 Ocular pulse amplitude (OPA) in canine *ADAMTS10*-open-angle glaucoma (*ADAMTS10*-OAG)
Vanessa A. Raphtis, Dhruv Sharma, Sichao Wang, Jae Y. Kim, Amanda L. Jacobson, Christine D. Harman and András M. Komáromy

137 Analysis of morphological and quantitative changes in pathological myopia and perioperative changes in posterior scleral reinforcement using three-dimensional magnet resonance imaging
Lin Liu, Hua Rong, Di Wu, He Xu, Qing He, Bei Du, Xuejun Zhang and Ruihua Wei

146 Implantation of a capsular tension ring during cataract surgery attenuates predicted remodeling of the post-surgical lens capsule along the visual axis
Kurt A. Ameku, Caleb C. Berggren and Ryan M. Pedrigi

158 Effect of corneal cross-linking on biomechanical changes following transepithelial photorefractive keratectomy and femtosecond laser-assisted LASIK
Wen Chen, FangJun Bao, Cynthia J. Roberts, Jia Zhang, Chong Wang, XueFei Li, JunJie Wang, Anas Ziad Masoud Abu Said, Kevin Nguelemo Mayopa, YaNi Chen, XiaoBo Zheng, Ashkan Eliasy, Ahmed Elsheikh and ShiHao Chen

171 Assessing REALTER simulator: analysis of ocular movements in simulated low-vision conditions with extended reality technology
Mattia Barbieri, Giulia A. Albanese, Andrea Merello, Marco Crepaldi, Walter Setti, Monica Gori, Andrea Canessa, Silvio P. Sabatini, Valentina Facchini and Giulio Sandini

frontiers | Frontiers in Bioengineering and Biotechnology

TYPE Hypothesis and Theory
PUBLISHED 09 February 2023
DOI 10.3389/fbioe.2023.1095948

OPEN ACCESS

EDITED BY
Fuyou Liang,
Shanghai Jiao Tong University, China

REVIEWED BY
Xiaofei Wang,
Beihang University, China
Rouzbeh Amini,
Northeastern University, United States

*CORRESPONDENCE
Matthew A. Reilly,
reilly.196@osu.edu

SPECIALTY SECTION
This article was submitted to Biomechanics, a section of the journal Frontiers in Bioengineering and Biotechnology

RECEIVED 11 November 2022
ACCEPTED 30 January 2023
PUBLISHED 09 February 2023

CITATION
Reilly MA, Katz SE and Roberts CJ (2023), Orbital fat swelling: A biomechanical theory and supporting model for spaceflight-associated neuro-ocular syndrome (SANS).
Front. Bioeng. Biotechnol. 11:1095948.
doi: 10.3389/fbioe.2023.1095948

Orbital fat swelling: A biomechanical theory and supporting model for spaceflight-associated neuro-ocular syndrome (SANS)

Matthew A. Reilly[1,2]*, Steven E. Katz[3] and Cynthia J. Roberts[1,2]

[1]Department of Biomedical Engineering, The Ohio State University, Columbus, OH, United States, [2]Department of Ophthalmology and Visual Sciences, The Ohio State University, Columbus, OH, United States, [3]Ohio Neuro-Ophthalmology, Orbital Disease & Oculoplastics, Columbus, OH, United States

Spaceflight-Associated Neuro-ocular Syndrome (SANS) is a descriptor of several ocular and visual signs and symptoms which commonly afflicts those exposed to microgravity. We propose a new theory for the driving force leading to the development of Spaceflight-Associated Neuro-ocular Syndrome which is described *via* a finite element model of the eye and orbit. Our simulations suggest that the anteriorly directed force produced by orbital fat swelling is a unifying explanatory mechanism for Spaceflight-Associated Neuro-ocular Syndrome, as well as producing a larger effect than that generated by elevation in intracranial pressure. Hallmarks of this new theory include broad flattening of the posterior globe, loss of tension in the peripapillary choroid, decreased axial length, consistent with findings in astronauts. A geometric sensitivity study suggests several anatomical dimensions may be protective against Spaceflight-Associated Neuro-ocular Syndrome.

KEYWORDS

microgravity, biomechanics, spaceflight-associated neuro-ocular syndrome (SANS), orbital fat, cephalad fluid shift

Introduction

Spaceflight-Associated Neuro-ocular Syndrome (SANS) is a common condition affecting individuals exposed to microgravity with severity partially dependent on length of time in microgravity. While its features vary, the most common ocular findings include optic disc edema, cotton wool spots, horizontal choroidal folds, globe flattening, shortening of axial length, and hyperopic shift (Brunstetter, 2018). To date, these symptoms and signs have been considered independently since the same set of findings were not consistently evaluated with each mission. For example, up to 29% of astronauts were reported to experience globe flattening (Stenger et al., 2017), but this requires an imaging study to evaluate, which was not consistently performed at pre and post-flight time points. Initially, elevated intracranial pressure (ICP) was thought to play a major role in optic nerve head edema (Stenger et al., 2017), and the syndrome was called Visual Impairment due to Intracranial Pressure (VIIP). However, it has since been recognized that ICP elevation alone is insufficient and other factors would likely be involved to generate the induced optic disc edema and retinal changes that were observed (Brunstetter, 2018). It has also been suggested that a chronic low increase in ICP occurs, accompanied by a lack of the normal terrestrial loading and unloading cycle associated with a change in position from supine to standing, which is absent in a microgravity environment (Stenger et al., 2017).

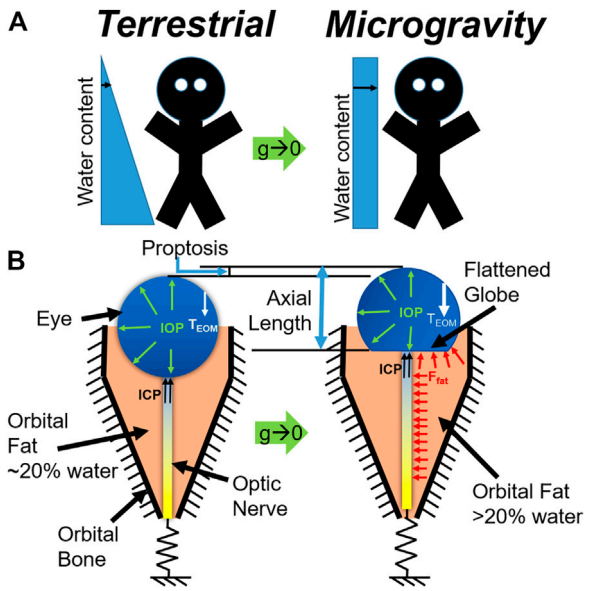

FIGURE 1
(A) Schematic representation of the microgravity-induced fluid shift and **(B)** corresponding changes in the eye and orbit (below). Model C is represented at left, while Model D is represented at right.

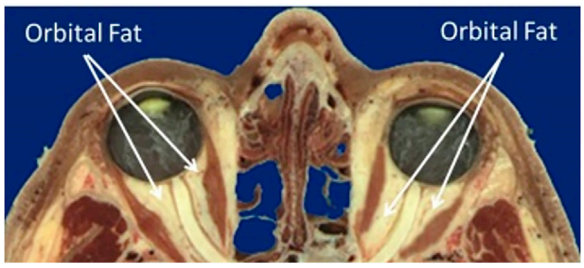

FIGURE 2
Sagittal section of the orbit and contents (Ackerman, 1998).

Therefore, in recognition that other mechanisms may play an important role, the syndrome was renamed SANS.

We present a mechanistic biomechanical theory, shown schematically in Figure 1, which unifies the ocular findings associated with SANS. It is proposed that during exposure to microgravity, the terrestrial hydrostatic pressure profile is absent, leading to a cephalad fluid shift. This increase in liquid volume would necessarily increase the volume of orbital contents and, therefore, apply an additional load on the globe (Louf et al., 2019). This additional load does not depend on hydrostatic potential but on water content. Another way to conceive of this is to consider the mechanical energy balance where the work done on the eye and orbit due to expanding orbital content volume is the integral of pressure over change in volume. Since the orbital bone is rigid relative to the eye, this work must be done on the eye itself. Thus, even if there is no change in orbital pressure, the amount of work done can be sufficient to deform the eye. This energy method is used in finite element analysis (Szabo and Babuska, 1991) to compute the equilibrium state of the orbital contents and eye and led us to our conclusion. We also note that there are several key differences between the terrestrial (supine) case and microgravity. In particular, the hydrostatic pressure gradient is never re-established during microgravity, implying that there may be some chronic component necessary for the equilibrium water distribution to shift so far in the superior direction.

Figure 2 shows the anatomy of the bony orbit (Ackerman, 1998) which is shaped like a cone, gradually narrowing toward the apex. The retrobulbar space is filled with soft tissues including the optic nerve, ocular blood vessels, extraocular muscles, and adipose tissue or fat. The pressure exerted on the orbital structures is increased, including the bones defining the boundary of the orbit, the blood vessels entering the optic canal and tracking along the optic nerve, and the posterior surface of the globe involving the outer sclera, inner choroid, and retina. Therefore, the purpose of the current study is to computationally simulate the impact of increased orbital pressure on the ocular structures with finite element modeling and compare the predicted results to the ocular signs that have been reported with extended exposure to microgravity.

Methods

Theoretical basis

An axial force balance on the eye was first undertaken to define the system and estimate the relative contributions of each potential source to the axial motion of the eye. Specifically, these included contributions from intracranial pressure (F_{ICP}), fat swelling (F_{fat}), extraocular muscle tension (F_{EOM}), and optic nerve stretching (F_{ON}), giving the net force balance

$$\uparrow^{+}_{anterior} \sum F_z = F_{ICP} + F_{fat} - F_{EOM} - F_{ON} = 0. \quad (1)$$

The homeostatic, terrestrial contributions from each source were estimated from literature sources and clinical experience as follows:

- F_{EOM} ~ 1–4 mN in the posterior direction [passive contribution only; (Guo et al., 2016)]
- F_{ON} ~ 0 for small displacements due to slack in the nerve; and
- F_{ICP} ~ 0–1.75 mN [0–20 cmH_2O, representing intracranial hypotension to borderline hypertension (Swyden et al., 2021)]

Based on this analysis, we are left to conclude that Eq. 1 can be reduced to

$$F_{EOM} \approx F_{fat} + F_{ICP}, \quad (2)$$

Indicating that EOM tension must increase by some amount unknown *a priori* and depend on the balance of volumetric swelling forces and must be estimated computationally. The model also has a boundary condition representing F_{ON} for completeness since these effects may come into play at larger deformations or during eye movements.

Model construction

Based on the force balance, an axisymmetric geometric model (Figure 3) was constructed in COMSOL Multiphysics v5.6

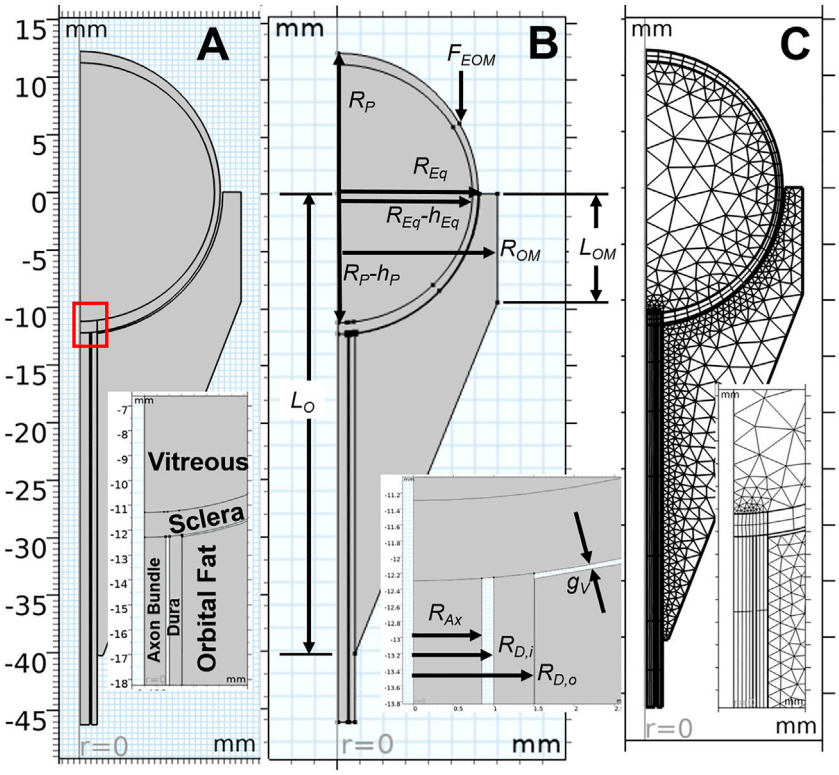

FIGURE 3
Key aspects of the computational model are shown, with inset images detailing the optic nerve head region. An axisymmetric representation of ocular and orbital anatomy is given in **(A)**, while **(B)** shows parameterization of the geometry. Note that all parameter values for the base model are given in Table 1. The finite element meshes used to solve the Baseline Model are shown in **(C)**.

TABLE 1 Geometric parameters used for the baseline model.

Symbol	Description	Value	Source
R_{Eq}	Equatorial radius	12.36 mm	Figure 2
R_P	Polar radius	12.36 mm	Figure 2
h_{Eq}	Equatorial thickness	0.5 mm	
h_P	Polar thickness	1.0 mm	
R_{OM}	Orbit margin radius	13.95 mm	Figure 2
L_{OM}	Orbit margin length	9.51 mm	Figure 2
L_O	Total length of orbit	40.26 mm	Figure 2
R_A	Radius of axon bundle	0.85 mm	Lagrèze et al. (2009)
$R_{D,i}$	Inner radius of dura	1.0 mm	Figure 2
$R_{D,o}$	Outer radius of dura	1.515 mm	Lagrèze et al. (2009), Figure 2
g_v	Gap to allow for vitreous swelling	133–217 μm	From simulation

(COMSOL, Inc., Burlington, MA) using nominal dimensions for the eye and orbit, based on the histological sections in Figure 2 (Ackerman, 1998). A baseline model intended to represent a normal human eye and orbit, in terms of anatomy and material properties was created and used as a basis for modeling predictions (Figure 3A). This model, referred to as the "Baseline Model," was used as a starting point for all sensitivity analyses performed. This geometry was parametrized as shown in Figure 3B, while Table 1 gives the parameter values for the Baseline Model. An ICP of 10 mmHg (13.6 cmH_2O) was chosen for the Baseline Model as it corresponds to the middle of normal ICP [6.5–19.5 cmH_2O (Swyden et al., 2021)].

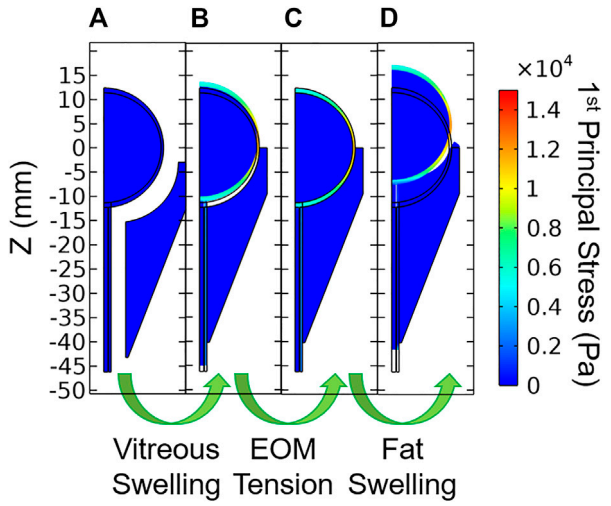

FIGURE 4
Stages of model loading. **(A)** The zero-stress state is determined iteratively, then vitreous swelling is used to produce **(B)** the residually-stressed state of the eye. Extraocular muscle tension is then incremented which gives **(C)** the *in vivo* terrestrial geometry. Finally, orbital fat swelling is simulated to produce **(D)** the predicted ocular dimensions in microgravity.

The living eye is loaded with intraocular pressure (*IOP*), intracranial pressure (*ICP*), tension from the extraocular muscles (F_{EOM}), and the contact force generated by the swelling fat (F_{fat}). All tissues were modeled using an incompressible, isotropic, neo-Hookean hyperelastic material model. Assumed values for elastic moduli are given the table below.

Each model was solved using a sequence of three steps (Figure 4). Model A modeled the zero-stress state of the eye and optic nerve in the presence of vitreous swelling and ICP while the orbit, fat, and all other external forces were absent. Model A was found using a coordinate search algorithm by varying the geometry of the zero-stress eye (i.e., the polar and equatorial elliptical radii) and the vitreous hygroscopic strain such that the resulting eye corresponded to the target geometry and IOP. Loading of Model A with vitreous swelling gives the residual stress state of the eye, Model B. Model B was then taken as the initial condition of the eye and optic nerve when simulating fat swelling as follows. Model B was set within the orbit and orbital fat, then the extraocular muscle tension was gradually added to find Model C—the terrestrial (homeostatic) state of the eye and orbit. Finally, orbital fat swelling and ICP were incremented to study the response of the eye and optic nerve, giving Model D as a final output. Results described below are for Model D relative to Model C rather than the intermediate models; it therefore represents the changes which might occur due to the hypothesized swelling of the orbital contents arising from the microgravity-induced fluid shift.

Fat swelling was modeled using a hygroscopic swelling model in which the hygroscopic volume ratio J_H was varied as a modeling parameter. This was achieved in COMSOL by using the hygroscopic swelling model, where the hygroscopic strain $\varepsilon_H = \beta(C_W - C_{W,0})$, with β as the coefficient of hygroscopic swelling of the fat-water mixture (equivalent to the inverse of density, or about 0.001 m^3/kg for water), $C_{W,0}$ as the baseline (terrestrial) water content, and C_W as the current water content. Thus, $J_H = (1 + \varepsilon_H)^3$. Values of J_H were studied to indicate how much fat swelling would be required to induce the ocular findings associated with SANS.

The IOP was also generated using a hygroscopic swelling model to mimic the physiological process which maintains IOP (i.e., the eye has more fluid in it than it does in its zero-stress state). In this case, the dimensions of the zero-stress geometry were estimated, swelling in the vitreous simulated, and the difference between the model predictions and target ellipse radii and target IOP were calculated using convex objective functions. COMSOL's Optimization Module was used to determine the zero-stress geometry, the amount of "swelling" required to achieve IOP. Once this optimization was complete, the orbit and fat were constructed and assumed to be in contact with the eye and ON prior to simulating fat swelling.

Boundary conditions

This residually loaded state was then inserted into the model containing the fat, F_{EOM}, and ICP to find the terrestrial baseline geometry and stresses. The lateral and posterior boundaries of the orbital fat were held fixed to simulate attachment to the orbital bone. Intracranial pressure was applied to the exterior surface of the sclera over a segment representing the sub-arachnoid space with a radial distance of 270 μm [estimated from Figure 1 of (Lagrèze et al., 2009)].

Contact boundaries were established between the orbital fat and the sclera. This allowed sliding to occur at the sclera-fat interface, as would be expected *in vivo* as the eye must easily rotate during routine visual tasks.

Boundary conditions were applied as indicated in the free body diagrams shown in Figure 1B. The nerve is constrained using a spring boundary condition: the tension in the nerve increases with forward translation of the eye. Thus, tension could arise in the nerve if (A) significant proptosis occurred and/or (B) normal eye movements resulted in removal of slack. Demer (Demer, 2016) measured ON length in relation to orbit length, finding an increasing trend [Figure 11 of (Demer, 2016)]. To infer slack from these measurements, one would also need to know the axial length of the eye, allowing the slack to be approximated as

$$ON\ slack = ON\ length - orbit\ length - \frac{1}{2}(axial\ length).$$

Taking the values for orbit length and axial length from Table 1, along with the regression equation from the referenced figure, gives a value for ON slack of 8.4 mm. We therefore chose a threshold slack of 6 mm as a conservative estimate of ON slack. This threshold was never exceeded during any simulations, so the optic nerve remained slack at all times.

The extraocular muscle tension was applied as a point source to the peripheral anterior globe. This tension was modeled as an analytical function representing the force required to achieve passive stretching of a single rectus muscle multiplied by the number of rectus muscles (i.e., four) [Eq. 10 of (Guo et al., 2016)]:

$$F_{EOM} = 4M\left(-0.29w + 4.79e^{\frac{w}{4.57}} - 3.01\right), \quad (3)$$

where w is the anterior displacement of the EOM insertion point in mm to give F_{EOM} in mN and M is a multiplier used to increment the loading as described below. Generally, M was incremented from 0–1 to simulate the passive muscle tension. Since the active forces in the muscle are unknown, an additional study was undertaken in which M was incremented from 0–2.25 to simulate additional EOM tension

TABLE 2 Changes in ocular anatomy due to orbital fat swelling.

Spaceflight-associated water in orbital fat (kg/m^3)	Orbital fat volume ratio (dimensionless)	Proptosis (mm)	Change in axial length (μm)	Change in peripapillary arc length (μm)	Change in posterior ROC (mm)
0.000	1.000	0.00	0.00	0.00	0.00
0.010	1.030	0.59	−7.29	−0.78	0.02
0.015	1.046	0.91	−9.56	−1.11	0.03
0.020	1.061	1.24	−11.81	−1.42	0.04
0.025	1.077	1.57	−14.16	−1.74	0.06
0.030	1.093	1.91	−16.66	−2.06	0.07
0.035	1.109	2.25	−19.33	−2.40	0.08
0.040	1.125	2.59	−22.20	−2.76	0.09
0.045	1.141	2.93	−25.26	−3.13	0.10
0.050	1.158	3.28	−28.58	−3.54	0.11
0.055	1.174	3.62	−32.12	−3.96	0.13
0.060	1.191	3.97	−35.94	−4.41	0.14
0.065	1.208	4.31	−40.03	−4.89	0.15
0.070	1.225	4.66	−44.41	−5.39	0.17

arising from active contributions. This simplifying approach was adopted since neither the active nor passive contributions are known for SANS, and an M value of 2.25 resulted in a net doubling of F_{EOM}.

Simulations

The balance of forces was computed numerically using finite element analysis in COMSOL Multiphysics (Figure 3) to investigate the effect of an increase in retrobulbar fat water content on the eye. All simulations included geometric non-linearity. Following the aforementioned procedure for determining the terrestrial state of the eye, the ICP and J_H were systematically varied to simulate the effects of a microgravity-induced fluid shift on the eye and orbital tissues.

Changes to axial length and posterior radius of curvature (ROC) were calculated as a proxy for globe flattening. ROC was estimated by fitting a circle to the deformed scleral surface within a 4 mm radius of the axis of symmetry using the Pratt method (Pratt, 1987). Change in choroidal arc length was used to imply the formation of choroidal folds: shortening indicates a decrease in tension and the possibility of wrinkling (Ligarò and Barsotti, 2008; Barsotti and Ligarò, 2014). The peripapillary arc length is the arc length along the inner boundary of the sclera spanning the posterior-most quarter of the eye's circumference in the zero-stress state. While this definition is somewhat arbitrary, we found that the results were robust when other definitions were considered (e.g., 1/8 or 1/2 rather than 1/4).

An additional series of simulations was conducted to determine whether and to what extent measurable anatomical variations may influence the risk of SANS based on a change in the water content of the orbital fat with exposure to microgravity. The varied parameters were polar radius R_p (where axial length = $2R_p$), equatorial radius R_{eq}, orbit depth L_0, radius of the orbit margin R_{OM}, and depth of orbit margin L_{OM} as shown in Figure 3B.

Results

Model verification

Iterative mesh refinement indicated that the solution was largely independent of mesh density using quartic Lagrangian shape functions, even with a coarse mesh. The mesh density used for the reported simulations (Figure 3C) was therefore selected on the basis that it offered improved stability for the non-linear solver for the variety of studies conducted.

Baseline model predictions

The predicted deformations corresponding to 0%–7% increase in retrobulbar content volume are given in Table 2 and shown in Figure 5. Decreasing axial length and increasing posterior ROC correspond to physical signs of globe flattening. Decreased peripapillary arc length indicates compression of, or reduced tension in, the choroid which could result in choroidal folds. In addition, the model predicted low levels of proptosis. Although subtle proptosis has not been reported with SANS, it could be easily missed on clinical exam.

Sensitivity analysis

Sensitivity studies were performed to evaluate the model's sensitivity to modeling assumptions. First, the boundary conditions were investigated. Since a single representative ICP value selected for the Baseline Model was selected from numerous literature values, a thorough sensitivity analysis was performed to compare the relative contributions of ICP and fat swelling to ocular

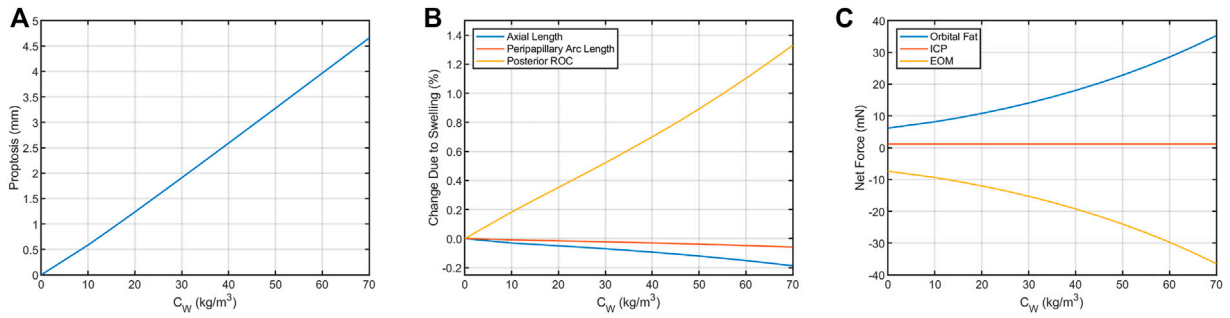

FIGURE 5
Resultant axial loads predicted for each term in Eq. 2 for the Baseline Model. In the terrestrial state (hygroscopic strain = 0), tension in the extraocular muscles (EOM) keeps the eye seated in the orbit by pulling in the posterior direction. This tension is balanced by the net axial load arising from intracranial pressure (ICP, assumed to be 13.6 cmH_2O) and compression of the orbital fat. This results in **(A)** proptosis and **(B)** decreases in axial length and peripapillary arc length along with increased posterior ROC. **(C)** These biometric changes are the result of changes in the balance of forces between the eye, fat, and extraocular muscles. The contribution from ICP increases from 1.17 to 1.75 mN if ICP increases from 13.6 cmH_2O to 20 cmH_2O, representing a possible increase from normal to borderline intracranial hypertension (Swyden et al., 2021).

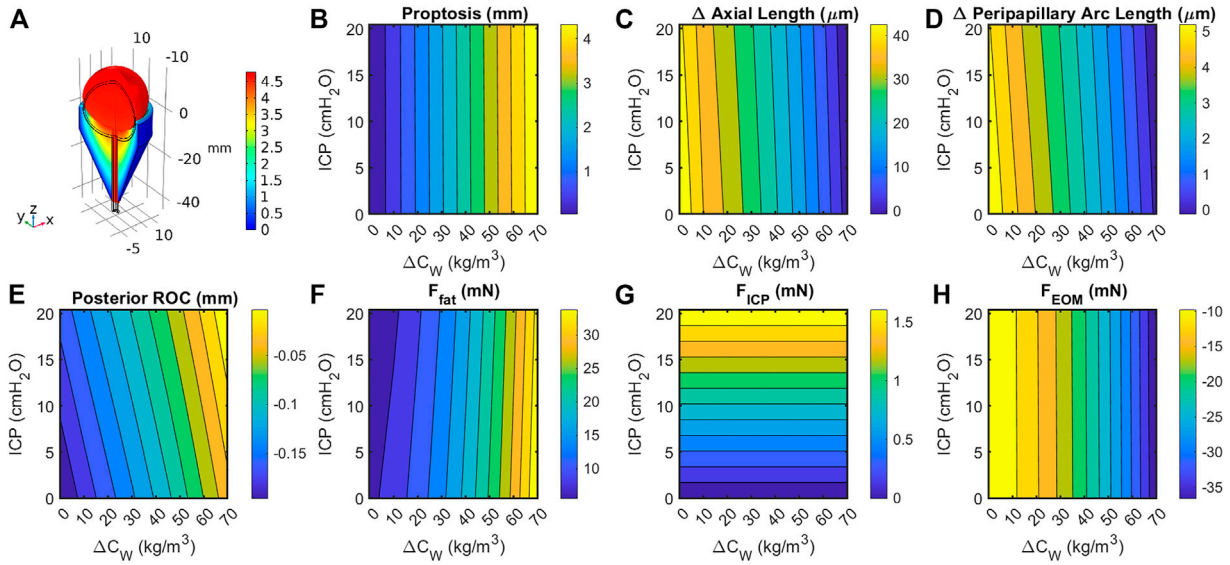

FIGURE 6
(A) Cutaway section showing eye, optic orbit, and optic nerve following a 15% increase in retrobulbar fat volume. Black lines indicate geometry prior to swelling. Coloration indicates total change in volume due to elastic and hygroscopic effects. Fat swelling, but not ICP, had a large effect on change in **(B)** axial length; **(C)** posterior radius of curvature within 4 mm of axis; **(D)** peripapillary arc length decreases, suggesting decreased tension and possibly choroidal folding; and **(E)** proptosis of the anterior pole. Contributions to the axial force balance (Eq. 2) from **(F)** fat swelling, **(G)** intracranial pressure, and **(H)** extraocular muscle tension are largely one-dimensional, though the fat force is slightly dependent on both intracranial pressure and fat volume ratio.

deformation (Figure 6). Axial length, posterior ROC, peripapillary choroidal arc length, and proptosis depend very weakly on ICP but strongly on orbital fat swelling. Applying IOP using a hygroscopic swelling model in the vitreous gave results which were nearly identical (i.e., within 1%) to those applying a pressure boundary condition to simulate IOP. Initial simulations modeled the boundary between the eye and ON with the orbital fat as a tied boundary, as opposed to the more realistic frictionless contact boundary. This caused much larger ocular deformations but gave qualitatively similar results in all cases. Approximately doubling F_{EOM} to simulate active tension in the EOM decreased proptosis by 7% while resulting in a 63% larger drop in axial, 33% more decline in peripapillary arc length, and increased radius of curvature by 8%. This was achieved by setting $M = 2.25$ in Eq. 1, thereby increasing the maximum EOM force from 25.3 to 53.8 mN for the same extent of swelling.

Next, the elastic moduli E of the sclera, vitreous, and fat were varied over a broad range. Varying E_{fat} from 0.7–1.5 kPa and $E_{vitreous}$ from 6.5–25 Pa had no effect on any modeling predictions over the entire range of E_{sclera} considered (0.25–5 MPa) as expected, since their incompressibility dominates their mechanical response. The fat and vitreous have a very low shear modulus all materials were modeled as incompressible and linearly elastic with the properties given in Table 3. Relative to bulk modulus, implying that they will effectively behave as

TABLE 3 Tissue properties used for baseline model.

Tissue	Elastic modulus	Source
Ocular coats	1.5 MPa	Nguyen et al. (2018)
Vitreous humor	6.5 Pa	Tram and Swindle-Reilly (2018)
Orbital fat	700 Pa	Yoo et al. (2011)
Orbital bone	Infinite (rigid)	—

incompressible fluids under the conditions studied: they change shape very easily but do not appreciably change volume due to loading. However, the response of the eye depended strongly on E_{sclera} over this range, with all SANS signs increased in magnitude in less stiff eyes (Figure 7).

Finally, sensitivity to orbital anatomy and ocular anatomical dimensions were examined (Figure 8). The model predicted orbit depth (L_O) to be the most important feature of orbit anatomy, with a 10% increase resulting in ~25% changes in the predicted responses. Increasing the eye's equatorial diameter by 10% had a similar effect on globe flattening (i.e., change in axial length and posterior radius of curvature). Orbital depth varies considerably between individuals. Fat swelling-induced changes could therefore depend significantly on an individual's orbital anatomy.

The terrestrial force balance (Eq. 2) for the Baseline Model indicates that $F_{EOM} \approx 7.36\,mN$, $F_{ICP} \approx 1.17\,mN$, and $F_{fat} \approx 5.6\,mN$. Increasing ICP to 20 cmH_2O–the lower limit of borderline intracranial hypertension (Swyden et al., 2021)—only increased $F_{ICP} \approx 1.75\,mN$, while 7% swelling could increase $F_{fat} \approx 36.3\,mN$. Thus, even a pathological increase in ICP would be unlikely to contribute to a biomechanical mechanism of SANS.

Discussion

As orbital fat water content increased, the model predicted a small amount of forward motion of the eye (proptosis), a shortening of axial length which is associated with globe flattening, and negative choroidal strain that would be associated with induced choroidal folds. The change in axial length, globe flattening, and choroidal folds are consistent with ocular findings in astronauts that have been reported and are illustrated in Figure 6. Up to 29% of astronauts have experienced globe flattening [Figure 9; (Brunstetter, 2018)], as well as a reported hyperopic shift. A hyperopic shift result from shortening of axial length. Choroidal folds occur in 21% of astronauts during long duration space flight [Figures 9D, E; (Brunstetter, 2018)]. It can resolve or reduce post-flight, but persistence up to 12 years has been measured [Figure 9E; (Brunstetter, 2018)]. The model predicts that as the globe flattens under the increased pressure exerted by the swelling orbital fat, the arc length of the impacted section of the globe shortens [Figure 6; (Gogola et al., 2018)]. If the scleral arc length shortens enough, the choroidal membrane it supports wrinkles, as illustrated in the analogous case of thin films in Figures 9F, G (Diaby et al., 2006; Holmes, 2015).

Proptosis has not been previously reported in astronauts. However, it has likely never been adequately evaluated or quantified since it is not obvious due the relatively small magnitude in the presence of facial swelling. In thyroid-associated orbitopathy (TAO) (Kaichi et al., 2016) and Rosai-Dorfman disease with proptosis (Singh et al., 2018), an increase in volume of the orbital contents results in proptosis. Proptosis during thyroid eye disease has been found to exceed 2 mm in a significant proportion of patients (Dorkhan et al., 2006). Thus, it is reasonable to expect subtle proptosis may occur in a microgravity environment due to cephalad fluid shift. A benefit of this numerical model is that it suggests a testable hypothesis that would add supporting evidence if found in astronauts. In addition, optic disc edema has been reported in thyroid eye disease which resolves with decompression surgery (Kleinberg and Bilyk, 2016), similar to astronauts. Patients with active TED have experienced a hyperopic shift as their orbital pressure increases, also similar to astronaut experience and

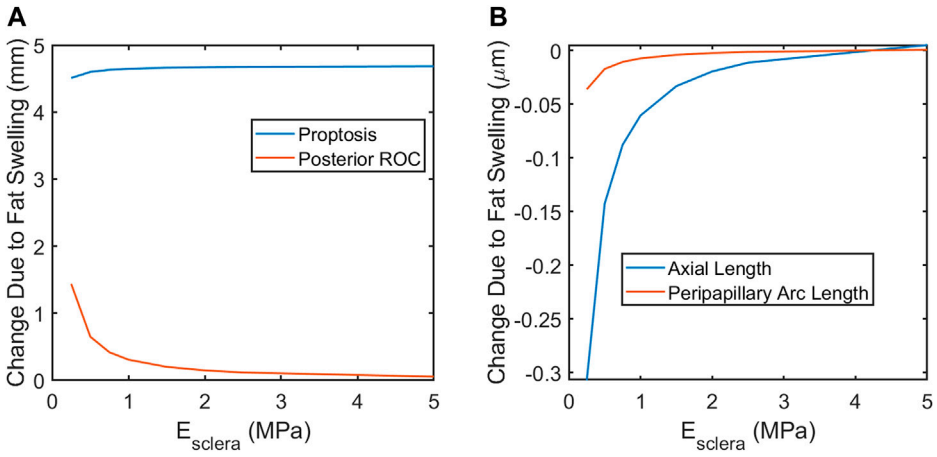

FIGURE 7
A softer sclera may result in increased magnitude of SANS-associated changes. **(A)** proptosis is relatively independent of the scleral elastic modulus. Globe flattening, as indicated by increased posterior ROC **(A)** and decreased axial length **(B)**. Severity of choroidal folding, as indicated by decreased peripapillary arc length, would be higher in softer eyes.

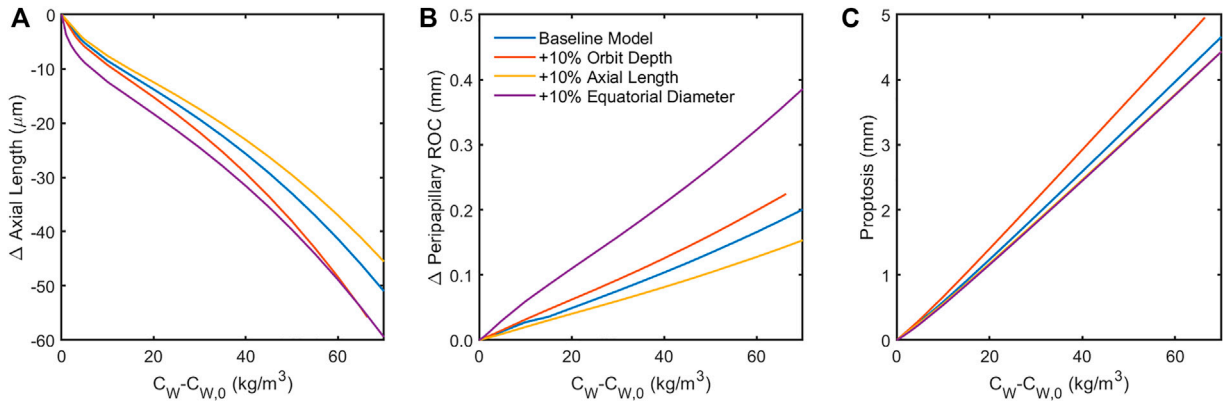

FIGURE 8
Sensitivity of the model to 10% increase in anatomical dimensions. Increasing the orbit depth had the largest effect of all orbital dimensions, while increasing the equatorial diameter of the globe had the largest effect of all ocular dimensions. Both of these parameters had the effect of increasing the force of fat swelling on the globe's posterior by placing more fat behind the eye (orbit depth) or confining the space around the eye available for anterior displacement of the swelling fat (equatorial diameter). Increased axial length appears to offer some protection from globe flattening **(A,B)**. Note that the results in **(C)** for changes in axial length and equatorial diameter are indistinguishable, suggesting that proptosis is diminished when the eye is larger owing to displacement of orbital fat volume.

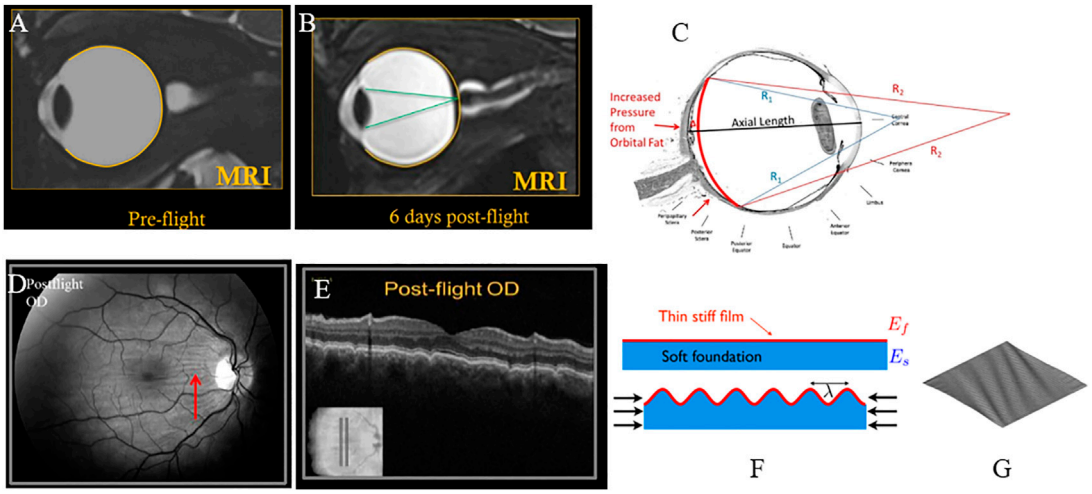

FIGURE 9
(A) Pre-flight MRI of astronaut; **(B)** Post-flight MRI with globe flattening and shortened axial length leading to hyperopic shift with focus of light behind the retina (Brunstetter, 2018). **(C)** Arclength of the sclera shortens with globe flattening, as illustrated by the red curve [adapted from (Gogola et al., 2018)]. **(D)** Choroidal folds in an astronaut measured post-flight; **(E)** corresponding cross-sectional OCT image showing undulations or waviness (Gogola et al., 2018). **(F)** Schematic illustration of wrinkling of a thin film with forces that shorten the foundation (Holmes, 2015). **(G)** Plot of a thin membrane subject to shear forces, generating wrinkles (Diaby et al., 2006). All figures **(A–E)** reused under CC BY-NC-ND license. **(F)** is reused with written permission of the author. **(G)** reused under CC BY license from HAL Open Science.

predicted by our model. In addition, flattening of the posterior globe is reported in TED due to increased volume of orbital contents (Chandrasekaran et al., 2006).

Elevated intracranial pressure has been considered as a possible risk factor for SANS (e.g., Feola et al., 2016; Raykin et al., 2017). The present model suggests that, while ICP elevation could play a role, its biomechanical effects directly contributing to SANS pathology is likely limited. This does not rule out ICP elevation as a potential mechanobiological contributor to SANS that the present model cannot predict.

One key result of this study is the identification of possible anatomical risk factors which might increase sensitivity of astronauts to SANS. In particular the depth of the orbit can have a very large effect on all SANS signs, with larger orbital depth leading to greater shortening in axial length, greater globe flattening leading to increased risk of choroidal folds, and greater proptosis. In contradistinction, longer axial length may be protective against specific aspects of SANS, including less globe flattening.

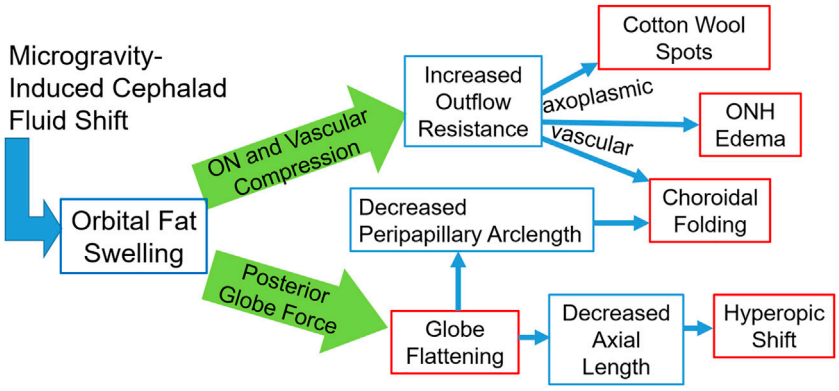

FIGURE 10
A schematic representation of the fat-swelling theory of SANS. Orbital fat swelling would necessarily lead to increased radial compression of the optic nerve and orbital vasculature, thereby increasing both axoplasmic and vascular resistance. These changes would present as cotton wool spots, ONH edema, and choroidal folding (in conjunction with globe flattening). Fat swelling will also cause a distributed loading applied to the globe's posterior surface, resulting in decreased axial length and/or proptosis. Globe flattening would likely contribute to the formation of choroidal folding as well as a hyperopic shift. Red boxes indicate the signs and symptoms comprising SANS, while blue boxes indicate the hypothesized biomechanical linkages between the cephalad fluid shift and SANS.

Although not directly modeled, it is expected that with orbital congestion, the low-pressure venous outflow through the ophthalmic vein may be compromised. This would be expected to result in a mild chronic increase in venous pressure. A comprehensive schematic of the proposed effects of orbital congestion is given in Figure 10. The posterior globe force arm has been supported by the results of the presented biomechanical simulations. The optic nerve and vascular compression arm is hypothesized to account for the remaining ocular findings, such that orbital congestion is a unifying mechanism underlying most reported signs and symptoms of SANS.

One significant limitation of this model is its sensitivity to the relationship between anterior motion of the globe and resulting EOM tension. The EOM tension in the present form of the model is taken from the passive contribution to stretching a fully relaxed rectus muscle. In reality, some unknown active contribution to the EOM tension would be present under most circumstances. Our computational investigation shows that incorporation of this muscle activation decreases proptosis and enhances globe flattening. Without a more detailed knowledge of EOM activation, this model can still place constraints on the upper and lower limits by considering the two extreme cases where the muscle is purely passive (as in the Baseline Model) and the muscle is rigid (i.e., it prevents all anterior translation of the globe). The true case must then lie somewhere between.

Choroidal folding presumably results from a loss of tension in the direction perpendicular to wrinkling. This is a geometric phenomenon and would therefore be driven by globe flattening: as the principal radii of curvature change, tension in an inflated membrane (e.g., the choroid) can be lost (Burd et al., 2017). Once tension is removed, these folds may be permanent (Cassidy and Sanders, 1999).

Finally, the model suggests the importance of scleral stiffness and various anatomical markers in predicting susceptibility to SANS. In particular, lower scleral stiffness, shorter axial length, greater equatorial diameter, and greater orbital depth all increase susceptibility to globe flattening and the subsequent hyperopic shift and choroidal folds as orbital fat swells. Recent studies have indicated the possibility of extracting the biomechanical properties of the sclera *in vivo* from air-puff tonometry data (Nguyen et al., 2020). Therefore, scleral stiffness and axial length are readily measured with existing ophthalmic clinical devices, while equatorial diameter, orbital depth, and baseline posterior globe curvature could be quantified with an MRI.

The primary limitations of this model are due to its axisymmetry, crude anatomical representation, the use of simple material models, and lack of active contributions to EOM tension. For example, since this is an axisymmetric model, it cannot predict the directionality of choroidal wrinkles, but suggests the mechanical mechanism driving them: wrinkles in the horizontal direction suggest a loss of tension in the superior-inferior direction. Still, none of these factors is likely to alter the underlying mechanism of SANS presented in this study.

If this model is to be adapted to predict SANS susceptibility in astronauts, future studies should include expanding this model to three dimensions. Inclusion of subject-specific anatomical measurements and biomechanical properties, especially of the sclera, would allow screening for risk or prophylactic treatment. Pre-flight MRI data could supply the requisite anatomical information.

Conclusion

This biomechanical theory for orbital fat swelling-induced SANS can explain all reported signs of SANS using a single mechanism. The other hallmark prediction of this theory–proptosis–has not been reported but this may be a result of its subtlety in concert with facial swelling due to the microgravity-induced headward fluid shift. Measurements of ocular position (i.e., proptosis) and shape, as well as orbital fat volume and water content before, during, and immediately after spaceflight would offer a powerful validation of this theory. In addition, an understanding of the mechanism would allow development of effective countermeasures. Greater understanding of individual characteristics (i.e., orbital depth, axial length, scleral stiffness) associated with susceptibility to SANS is paramount.

Data availability statement

The original contributions presented in the study are included in the article/Supplementary Material, further inquiries can be directed to the corresponding author.

Author contributions

MR and CR conceived and designed the study. SK provided clinical input during model development. MR performed all simulations and drafted the manuscript. CR and SK wrote sections of the manuscript. All authors contributed to manuscript revision, read, and approved the submitted version.

Conflict of interest

The authors declare that the research was conducted in the absence of any commercial or financial relationships that could be construed as a potential conflict of interest.

Publisher's note

All claims expressed in this article are solely those of the authors and do not necessarily represent those of their affiliated organizations, or those of the publisher, the editors and the reviewers. Any product that may be evaluated in this article, or claim that may be made by its manufacturer, is not guaranteed or endorsed by the publisher.

References

Ackerman, M. J. (1998). The visible human project: A resource for anatomical visualization. *Stud. Health Technol. Inf.* 52, 1030–1032. doi:10.1109/ITAB.1997.649392

Barsotti, R., and Ligarò, S. S. (2014). Static response of elastic inflated wrinkled membranes. *Comput. Mech.* 53 (5), 1001–1013. doi:10.1007/s00466-013-0945-5

Brunstetter, T. (2018). Spaceflight associated neuro-ocular syndrome (SANS): Current clinical insight & questions of interest. *Eye Brain* 12, 105. doi:10.2147/EB.S234076

Burd, H. J., Montenegro, G. A., Panilla Cortés, L., Barraquer, R. I., and Michael, R. (2017). Equatorial wrinkles in the human lens capsule. *Exp. Eye Res.* 159, 77–86. doi:10.1016/j.exer.2017.02.004

Cassidy, L. M., and Sanders, M. D. (1999). Choroidal folds and papilloedema. *Br. J. Ophthalmol.* 83 (10), 1139–1143. doi:10.1136/bjo.83.10.1139

Chandrasekaran, S., Petsoglou, C., Billson, F. A., Selva, D., and Ghabrial, R. (2006). Refractive change in thyroid eye disease (a neglected clinical sign). *Br. J. Ophthalmol.* 90 (3), 307–309. doi:10.1136/bjo.2005.078295

Demer, J. L. (2016). Optic nerve sheath as a novel mechanical load on the globe in ocular duction. *Invest. Ophthalmol. Vis. Sci.* 57 (4), 1826–1838. doi:10.1167/iovs.15-18718

Diaby, A., Le Van, A., and Wielgosz, C. (2006). Buckling and wrinkling of prestressed membranes. *Finite Elem. Analysis Des.* 42 (11), 992–1001. doi:10.1016/j.finel.2006.03.003

Dorkhan, M., Lantz, M., Frid, A., Groop, L., and Hallengren, B. (2006). Treatment with a thiazolidinedione increases eye protrusion in a subgroup of patients with type 2 diabetes. *Clin. Endocrinol.* 65 (1), 35–39. doi:10.1111/j.1365-2265.2006.02542.x

Feola, A. J., Myers, J. G., Raykin, J., Mulugeta, L., Nelson, E. S., Samuels, B. C., et al. (2016). Finite element modeling of factors influencing optic nerve head deformation due to intracranial pressure. *Invest. Ophthalmol. Vis. Sci.* 57 (4), 1901–1911. doi:10.1167/iovs.15-17573

Gogola, A., Jan, N-J., Brazile, B., Lam, P., Lathrop, K. L., Chan, K. C., et al. (2018). Spatial patterns and age-related changes of the collagen crimp in the human cornea and sclera. *Investigative Ophthalmol. Vis. Sci.* 59 (7), 2987–2998. doi:10.1167/iovs.17-23474

Guo, H., Gao, Z., and Chen, W. (2016). Contractile force of human extraocular muscle: A theoretical analysis. *Appl. Bionics Biomech.* 2016, 1–8. doi:10.1155/2016/4091824

Holmes, D. P. (2015). Elastic instabilities for form and function, buckling: Wrinkling, folding, and snapping. *Short. Course.* Available at: https://shellbuckling.com/papers/Sapienza2015_Buckling.pdf.

Kaichi, Y., Tanitame, K., Itakura, H., Ohno, H., Yoneda, M., Takahashi, Y., et al. (2016). Orbital fat volumetry and water fraction measurements using T2-weighted FSE-IDEAL imaging in patients with thyroid-associated orbitopathy. *Am. J. Neuroradiol.* 37, 2123–2128. doi:10.3174/ajnr.a4859

Kleinberg, T. T., and Bilyk, J. R. (2016). Evolution of disc edema in thyroid-related compressive optic neuropathy. *Ophthalmic Plastic Reconstr. Surg.* 32 (4), e100. doi:10.1097/iop.0000000000000606

Lagrèze, W. A., Gaggl, M., Weigel, M., Schulte-Mönting, J., Bühler, A., Bach, M., et al. (2009). Retrobulbar optic nerve diameter measured by high-speed magnetic resonance imaging as a biomarker for axonal loss in glaucomatous optic atrophy. *Invest. Ophthalmol. Vis. Sci.* 50 (9), 4223–4228. doi:10.1167/iovs.08-2683

Ligarò, S. S., and Barsotti, R. (2008). Equilibrium shapes of inflated inextensible membranes. *Int. J. Solids Struct.* 45 (21), 5584–5598. doi:10.1016/j.ijsolstr.2008.06.008

Louf, J-F., Lu, N., O'Connell, M., Cho, H. J., Bhattacharjee, T., and Datta, S. (2019). Under pressure: Mechanics of swelling hydrogels under confinement. *Sci. Adv.* 2019, 01. doi:10.1126/sciadv.abd2711

Nguyen, B. A., Reilly, M. A., and Roberts, C. J. (2020). Biomechanical contribution of the sclera to dynamic corneal response in air-puff induced deformation in human donor eyes. *Exp. Eye Res.* 191, 107904. doi:10.1016/j.exer.2019.107904

Nguyen, B. A., Roberts, C. J., and Reilly, M. A. (2018). Biomechanical impact of the sclera on corneal deformation response to an air-puff: A finite-element study. *Front. Bioeng. Biotechnol.* 6, 210. doi:10.3389/fbioe.2018.00210

Pratt, V. (1987). Direct least-squares fitting of algebraic surfaces. *SIGGRAPH Comput. Graph* 21 (4), 145–152. doi:10.1145/37402.37420

Raykin, J., Forte, T. E., Wang, R., Feola, A., Samuels, B. C., Myers, J. G., et al. (2017). Characterization of the mechanical behavior of the optic nerve sheath and its role in spaceflight-induced ophthalmic changes. *Biomech. Model Mechanobiol.* 16 (1), 33–43. doi:10.1007/s10237-016-0800-7

Singh, P., Kapoor, S., Sen, S., and Bajaj, M. S. (2018). Cataract surgery in a case of Rosai-Dorfman disease with proptosis. *J. Cataract. Refract Surg.* 44 (11), 1398–1399. doi:10.1016/j.jcrs.2018.07.050

Stenger, M. B., Tarver, W. J., Burunstetter, T., Gibson, C. R., Laurie, S. S., Lee, S. M. C., et al. (2017). *Risk of spaceflight associated neuro-ocular syndrome (SANS)*. Houston, Texas: Lyndon B. Johnson Space Center.

Swyden, S., Carter, C., and Shah, S. U. (2021). *Intracranial hypotension. StatPearls. Treasure*. Island (FL): StatPearls Publishing.

Szabo, B., and Babuska, I. (1991). *Finite element analysis*. Hoboken: John Wiley & Sons.

Tram, N. K., and Swindle-Reilly, K. E. (2018). Rheological properties and age-related changes of the human vitreous humor. *Front. Bioeng. Biotechnol.* 6, 199. doi:10.3389/fbioe.2018.00199

Yoo, L., Gupta, V., Lee, C., Kavehpore, P., and Demer, J. L. (2011). Viscoelastic properties of bovine orbital connective tissue and fat: Constitutive models. *Biomech. Model Mechanobiol.* 10 (6), 901–914. doi:10.1007/s10237-010-0281-z

frontiers | Frontiers in Bioengineering and Biotechnology

TYPE Original Research
PUBLISHED 09 March 2023
DOI 10.3389/fbioe.2023.1134086

OPEN ACCESS

EDITED BY
Matthew A Reilly,
The Ohio State University, United States

REVIEWED BY
Pavel Shilyagin,
Institute of Applied Physics (RAS), Russia
Yilong Zhang,
University of Dundee, United Kingdom

*CORRESPONDENCE
Kirill V. Larin,
klarin@uh.edu

SPECIALTY SECTION
This article was submitted to Biomechanics, a section of the journal Frontiers in Bioengineering and Biotechnology

RECEIVED 29 December 2022
ACCEPTED 21 February 2023
PUBLISHED 09 March 2023

CITATION
Mekonnen T, Zevallos-Delgado C, Zhang H, Singh M, Aglyamov SR and Larin KV (2023), The lens capsule significantly affects the viscoelastic properties of the lens as quantified by optical coherence elastography. *Front. Bioeng. Biotechnol.* 11:1134086. doi: 10.3389/fbioe.2023.1134086

The lens capsule significantly affects the viscoelastic properties of the lens as quantified by optical coherence elastography

Taye Mekonnen[1], Christian Zevallos-Delgado[1], Hongqiu Zhang[1], Manmohan Singh[1], Salavat R. Aglyamov[2] and Kirill V. Larin[1]*

[1]Department of Biomedical Engineering, University of Houston, Houston, TX, United States, [2]Department of Mechanical Engineering, University of Houston, Houston, TX, United States

The crystalline lens is a transparent, biconvex structure that has its curvature and refractive power modulated to focus light onto the retina. This intrinsic morphological adjustment of the lens to fulfill changing visual demands is achieved by the coordinated interaction between the lens and its suspension system, which includes the lens capsule. Thus, characterizing the influence of the lens capsule on the whole lens's biomechanical properties is important for understanding the physiological process of accommodation and early diagnosis and treatment of lenticular diseases. In this study, we assessed the viscoelastic properties of the lens using phase-sensitive optical coherence elastography (PhS-OCE) coupled with acoustic radiation force (ARF) excitation. The elastic wave propagation induced by ARF excitation, which was focused on the surface of the lens, was tracked with phase-sensitive optical coherence tomography. Experiments were conducted on eight freshly excised porcine lenses before and after the capsular bag was dissected away. Results showed that the group velocity of the surface elastic wave, V, in the lens with the capsule intact ($V = 2.55 \pm 0.23\,m/s$) was significantly higher ($p < 0.001$) than after the capsule was removed ($V = 1.19 \pm 0.25\,m/s$). Similarly, the viscoelastic assessment using a model that utilizes the dispersion of a surface wave showed that both Young's modulus, E, and shear viscosity coefficient, η, of the encapsulated lens ($E = 8.14 \pm 1.10\,kPa, \eta = 0.89 \pm 0.093\,Pa \cdot s$) were significantly higher than that of the decapsulated lens ($E = 3.10 \pm 0.43\,kPa, \eta = 0.28 \pm 0.021\,Pa \cdot s$). These findings, together with the geometrical change upon removal of the capsule, indicate that the capsule plays a critical role in determining the viscoelastic properties of the crystalline lens.

KEYWORDS

lens capsule, viscoelastic properties, lens biomechanical properties, acoustic radiation force, optical coherence elastography (OCE)

1 Introduction

The primary function of the lens of the eye, along with the cornea, is to focus light onto the retina. Unlike the cornea, the lens has a dynamically modulated curvature and refractive power to produce sharp images of objects at variable distances during a process called accommodation. The mechanism of accommodation is a complex phenomenon, and various theories (Wang and Pierscionek, 2019) were put forward to explain the underlying

physiological process. For example, according to Helmholtz's widely accepted accommodation theory, the lens and its capsule are elastic, and the change in shape and power of the lens involves the capsule transferring the tension produced by the contraction and relaxation of the zonule and ciliary muscles to the lens (von Helmholtz and Southall, 1924; Wang and Pierscionek, 2019). The applied tension deforms the lens, changing the lens curvature, which effectively determines the focal distance of the lens. This intrinsic morphological adjustment of the lens to fulfill changing visual demands has prompted numerous studies on the mechanical properties of the lens and its suspension system, which includes the capsular bag, ciliary muscles, zonules, and choroids (Beers and Van Der Heijde, 1994; Pedrigi et al., 2007; Weeber and van der Heijde, 2007; Ronci et al., 2011; Sharma et al., 2011). In particular, the role of the lens capsule in the accommodative function as well as in cataract surgery, is associated with its biomechanical properties (Huang et al., 2021). The progressive change in capsular mechanical strength due to aging alters the dynamic interaction between the capsule and lens and could lead to changes in the accommodation process. In cataract surgery, a procedure that involves removing the lens content through an opening in the anterior capsule and replacing it with an artificial intraocular lens (IOL), the post-surgical capsular remodeling could have significant biomechanical consequences on not only the capsular matrix but also the lens substance (Berggren et al., 2021). Some other pathological conditions, such as the thinning, rupture, and exfoliation of the anterior lens capsule, could also affect the normal functions of the lens (Irvine, 1940; Liu et al., 2021). Hence, information about the mechanical modulation of the lens with and without the anterior capsular bag is essential to better understand the physiological process of accommodation and to design optimal cataract surgery (Rich and Reilly, 2022).

Over the last few years, the biomechanical properties of the lens have been examined using spinning tests (Burd et al., 2011; Wilde et al., 2012; Reilly et al., 2016), indentation (Weeber et al., 2007; Reilly and Ravi, 2009), Brillouin microscopy (Scarcelli et al., 2011; Ambekar et al., 2020), atomic force microscopy (AFM) (Ziebarth et al., 2011; Avetisov et al., 2021), acoustic techniques (Yoon et al., 2012; 2013; Park et al., 2017), mechanical compression (Won et al., 2015; Cheng et al., 2016), and optical coherence elastography (OCE) (Wu et al., 2015; Wu et al., 2018; Li et al., 2019; Zhang et al., 2019; Ambekar et al., 2020; Chen et al., 2022; Zhang et al., 2022). Using these methods, the lenticular biomechanical properties were assessed as a function of various parameters, including intraocular pressure (Park et al., 2017; Wu et al., 2018) and age and age-related diseases (Scarcelli et al., 2011; Wu et al., 2015; Cheng et al., 2019; Avetisov et al., 2021). On the other hand, typical methods of characterizing capsular biomechanical properties include inflation (Heistand et al., 2005; Avetisov et al., 2020) and uniaxial tensile (Wollensak and Spoerl, 2004) tests on sample fragments. Yet, knowledge of the role of the lens capsule in determining the biomechanical properties of the whole lens is scarce. A microindentation-based mechanical test conducted by applying dynamic displacement waveforms to the lens anterior pole indicated that the lens stiffness decreased significantly after the capsule was removed (Reilly and Ravi, 2009). Despite the significance of the results of this study in providing insight into the potential influence of capsular bag on the mechanical properties of the lens, the method requires cutting the lens to allow assessment of internal stiffness variations, which may disturb the lens structural integrity. In another study, results from spinning tests by Wilde et al. showed that the deformation in the encapsulated lens is less than that in the decapsulated lens for younger subjects and *vice versa* for older subjects (Wilde et al., 2012). This method involves imaging the outline of a lens while it is rotating around its optical axis (typically at 1000 RPM) and quantifying the deformation amplitude induced by centripetal forces. The spinning lens test is advantageous as the lens is subject to minor mechanical disturbances during measurement, but internal stiffness variations cannot be determined directly but rather inferred from axisymmetric finite element (FE) inverse analysis using a neo-Hookean model (Burd et al., 2011). Reilly et al. implemented the inverse FE method to perform mechanical analysis of both the lens and its capsule from a compression test (Reilly and Cleaver, 2017). This method is promising in enabling the assessement of lenses with different shapes, sizes, and mechanical properties, but the assumed model neglects viscous effects and known spatial variations of lenticular biomechanical properties.

In this study, we present a quantitative analysis comparing the viscoelastic properties of porcine lenses with and without a capsule using dynamic wave-based optical coherence elastography (OCE) (Singh et al., 2022; Zvietcovich and Larin, 2022). Here, OCE utilized phase-sensitive optical coherence tomography (PhS-OCT) (Sticker et al., 2001) coupled with an acoustic radiation force (ARF) transducer for non-invasive assessment of tissue mechanical properties at microscale spatial resolution. A microscale and localized tissue displacement induced by focused ARF excitation propagated as an elastic wave and was tracked using a high-resolution PhS-OCT system. The high deformation sensitivity of OCE is important to avoid inducing irreversible hysteresis, which may lead to plastic deformation in some indentation and compression methods. Moreover, small displacements are necessary for clinical applications to ensure adherence to safety limits. Using *ex vivo* porcine lenses, we analyzed the surface elastic wave speed, Young's modulus, and shear viscosity of the crystalline lens with and without the capsule to shed light on the influence of the capsule on the whole lens biomechanical properties.

2 Materials and methods

2.1 Porcine samples

Experiments were conducted on eight freshly excised porcine lenses *ex vivo*, both before and after the lens capsule was removed. The whole eye-globes were shipped overnight on ice (Sioux-Preme Packing Co., Sioux Center, IA), and all procedures were performed within 48 h of enucleation. The lenses were mounted on a custom holder.

2.2 Optical coherence elastography

The OCE system shown in Figure 1A was comprised of a 3.5 MHz ultrasound transducer of focal length ~19 mm (V382-SU, Olympus Corp., Japan) coupled with a PhS-OCT system that employed a broadband superluminescent diode (S840-B-I-20; Superlum Diodes Ltd., Carrigtwohill, Ireland) operating at 840 nm center wavelength with FWHM of 49 nm as a light source. The axial resolution of the system was ~9 μm in the air, while the displacement stability and

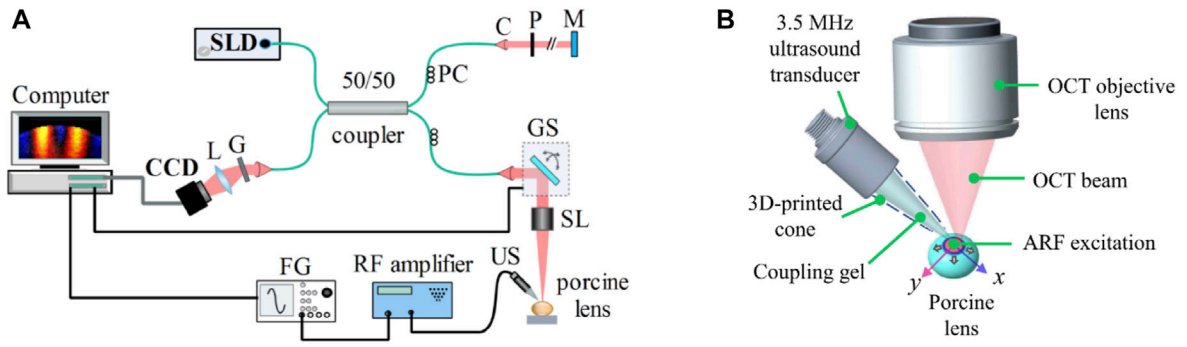

FIGURE 1
(A) Schematic of the experimental setup comprising a phase sensitive spectral domain OCT system for imaging and acoustic radiation force system for excitation. C: collimator, CCD: charge-coupled device (line scan camera), FG: function generator, G: grating, GS: 2D galvo scanner, L: lens, M: reference mirror, P: pinhole, PC: polarization controller, SL: scan lens, SLD: superluminescent diode, US: ultrasound transducer. **(B)** Ultrasound transducer producing acoustic radiation force excitation at the apex of the lens. Propagating elastic waves were imaged and analyzed along the orthogonal *x* and *y* axes.

transverse resolution were 0.28 nm and ~8 μm, respectively. The transducer driving signal, a continuous 3.5 MHz sinusoidal signal modulated by a square pulse of short duration (i.e., 0.5 ms), was generated by a function generator (DG4162, RIGOL Tech, Beijing, China) followed by amplification using an RF power amplifier (1040L, Electronics & Innovation, Ltd., Rochester, NY, United States). The excitation, which was coupled to the lens using ultrasound gel (McKesson Ultrasound Gel Pink, Richmond, VA), was focused roughly on the apex of the anterior surface of the lens, as shown in Figure 1B. M-B mode scans (Wang and Larin, 2014) were performed along orthogonal axes, which are marked as x and y in Figure 1B, intersecting at the excitation point. Each M-mode scan contained 1000 A-lines and was repeated at 251 lateral points (B-scan), covering scan lengths of 7.67 mm and 7.72 mm on the two orthogonal axes. Measurements were conducted at an A-line rate of 25 kHz.

2.3 Data processing

The acquired OCE data was processed using MATLAB® R2021a (Mathworks, Inc., Natick, MA, United States). First, the axial phase shift was computed from the temporal A-scans, followed by producing the spatiotemporal map of the elastic wave propagation. Then, the elastic wave group velocity was computed from the spatiotemporal phase map using the ratio of propagation distance to corresponding time (i.e., the slope in the spatiotemporal image) (Zvietcovich and Larin, 2022). This procedure was repeated for the subsurface layers of the lens, and a depth-wise averaging over a thickness of ~0.4 mm was performed to obtain the mean elastic wave speed for each lens.

2.4 Viscoelastic quantification

Group velocity alone may not fully describe the biomechanical properties of lossy media such as tissues (Parker et al., 2018; Zvietcovich and Larin, 2022). Hence, quantifying the viscoelastic properties of the lens (Zhang et al., 2022) would more accurately describe the capsular influence on lenticular biomechanical properties. Elastic waves induced by short-duration ARF pulse, such as the one in this study, are composed of multiple frequencies, and thus, dispersion curves (i.e., phase velocity as a function of frequency) can be produced by spectrally decomposing the elastic wave propagation obtained from OCE measurement data. To this end, a 2D discrete fast Fourier transform (FFT) was applied to the spatiotemporal displacement map to obtain the wavenumber (k) *versus* frequency (f) magnitude map (Han et al., 2016; Kijanka and Urban, 2021). Then, the phase velocity-frequency map was produced using the relation $c_p = f/k$. Subsequently, the surface wave dispersion curve was obtained by selecting the maximum intensity for each frequency. To assess the viscoelastic properties of the lens, we applied a rheological Kelvin-Voigt (KV) model in which the complex shear modulus is given by $\mu_D = \mu + i\eta\omega$, where $\omega = 2\pi f$ is the angular frequency of vibration and; μ and η are the shear elasticity and shear viscosity moduli, respectively. Given the limited penetration depth of the elastic wave and the free space-tissue boundary for an isolated lens, the detected elastic wave was modeled as a surface wave (Rayleigh wave) (Nenadic et al., 2011; Zhang, 2016). Assuming the lens is a nearly incompressible material, the lens shear wave velocity, c_s, and Rayleigh wave velocity, c_R, are related by $c_R/c_s = 0.95$. Here, the Rayleigh wave model was used to estimate the viscoelastic properties because the mean thickness (T) of the lens at the measurement regions, i.e., near the apex of the lens ($T_{encapsulated}$ = 4.9 mm; $T_{decaspulated}$ = 4.1 mm), was determined to be greater than the wavelength of the induced elastic wave ($\lambda_{encapsulated}$ = ~3.6 mm; $\lambda_{decapsulated}$ = ~1.7 mm) at the center frequency of excitation of 706 Hz**.** Therefore, solving a one-dimensional Helmholtz equation, the phase velocity of the elastic wave, c_p, utilizing the KV model can be computed as (Jin et al., 2020; Liu et al., 2020):

$$c_p(\omega) = 0.95\sqrt{\left(\frac{2\left(\mu^2+\omega^2\eta^2\right)}{\rho\left(\mu+\sqrt{\left(\mu^2+\omega^2\eta^2\right)}\right)}\right)} \quad (1)$$

where $\rho = 1183\,kg/m^3$ was the lens density (Vilupuru and Glasser, 2001). The shear modulus parameters, i.e., μ and η, were determined by fitting the viscoelastic wave Equation 1 to the OCE-measured

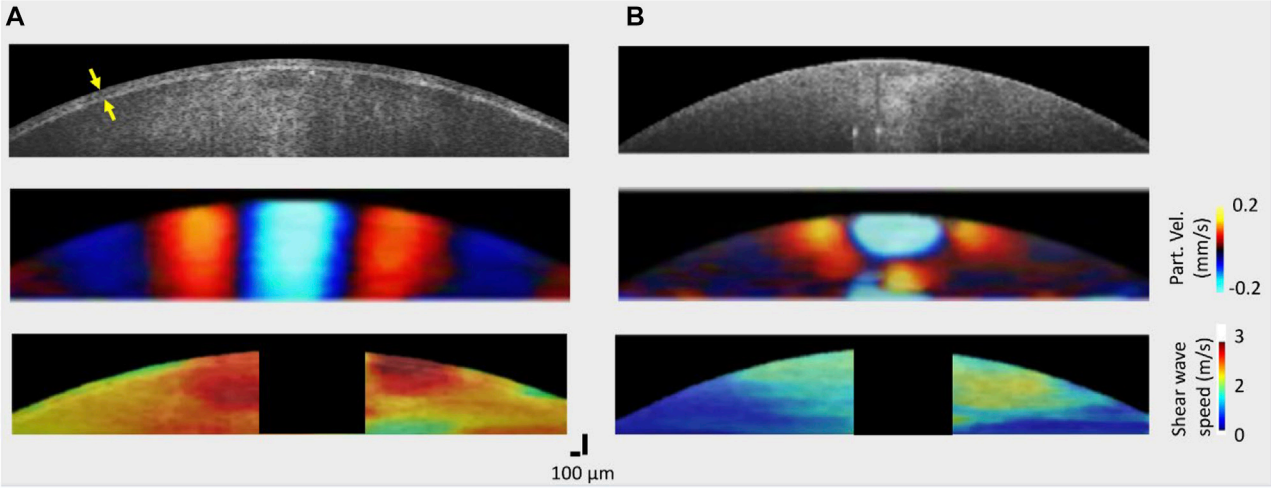

FIGURE 2
OCT structural images and elastic wave propagation characteristics of a typical porcine lens **(A)** with the capsule intact and **(B)** after the capsule was removed. Top: OCT structural images acquired before (left) and after removal (right) of the capsule; middle: wave propagation snapshots indicating instantaneous particle velocity in an encapsulated (left) and decapsulated (right) lens; bottom: spatial shear wave speed map in the encapsulated (left) and decapsulated (right) lens. The capsule layer is indicated by the yellow arrow in the top left structural image. For all samples, the excitation location was roughly at the apex.

surface wave dispersion curve using the iterative Levenberg-Marquardt error optimization algorithm. Assuming an isotropic and homogenous lens, the elastic (Young's) modulus, E, was computed from the shear modulus using $E = 2\mu(1 + \nu)$, with the Poisson's ratio, $\nu = 0.499$.

Furthermore, we assessed the wave amplitude attenuation characteristics using the intensity map in the spatial-frequency domain. The intensity map was produced by applying a 1D FFT on the spatiotemporal map of the wave field. In the spatial-frequency domain, for each lateral position, x, the wave amplitude profile was fitted to the exponential decay function for cylindrical wave ($C_o/\sqrt{x} \cdot e^{-\alpha x}$) to estimate the attenuation coefficient, α, at the center frequency of excitation, where C_0 is a constant (Zvietcovich and Larin, 2022).

2.5 Lenticular morphology

To investigate the relationship between lens morphology and its biomechanical properties, we quantified the lens geometry using a swept source OCT system that was able to capture the whole lens. The system operated at a center wavelength of 1310 nm, bandwidth of 100 nm, imaging depth of over 7 mm (in air), and a sweep rate of 100 kHz. A 3D scan of the whole lens was acquired using this system, and volumetric images were reconstructed using a custom MATLAB® R2021a (Mathworks, Inc., Natick, MA, United States) program. From the volumetric images of the whole lens, geometric parameters such as the equatorial diameter and the sagittal (apical) thickness were quantified (Wang and Pierscionek, 2019). To obtain more accurate geometric parameters, image distortions caused by refraction and the scanning mechanism (non-telecentric) were corrected using the lens refractive index (n_l = 1.49) and a 3D non-telecentric scan correction method (Zhao et al., 2010), respectively. Results were statistically analyzed using a t-test to assess the significance of variation before and after the removal of the capsule. Also, the repeatability of the experiment was assessed using ANOVA single-factor analysis.

3 Results

3.1 Elastic wave group velocity

Figure 2 shows the structural images and elastic wave speed characteristics in a typical porcine lens before (left) and after (right) removal of the capsule. In (Figure 2A, top), the capsule with a mean thickness of 58 ± 7 µm can be resolved (as shown by the yellow arrows) in the structural image. Furthermore, the motion snapshot of wave propagation at 2 ms after excitation shows a difference in the wavelength between the encapsulated and decapsulated lens (Figures 2A, B middle): longer in the encapsulated lens than the decapsulated lens. As can be observed from the middle images of Figures 2A, B, the elastic wave propagates further laterally in the encapsulated lens while the wave attenuates faster for the decapsulated lens. The wave attenuation characteristics are presented in the subsequent discussion. Moreover, the bottom row in Figures 2A, B depicts shear wave group speed maps. The wave speed maps indicate that the lens is stiffer with the capsule intact (average speed = 2.55 ± 0.23 m/s) than after the removal of the capsule (average speed = 1.19 ± 0.25 m/s). While there is likely regional variation in the stiffness of the lens, the significant difference in wave speed between nearer and farther regions from the excitation point shown in Figure 2B (bottom) might just be due to the rapid wave attenuation, and low signal to noise ratio in farther regions.

Figure 3 shows a box-whisker plot of the mean elastic wave speed in the lens for the two measurement conditions: with and without the capsule. The top and bottom boundaries of the box are the 25th and 75th percentiles, respectively, while the mean is shown

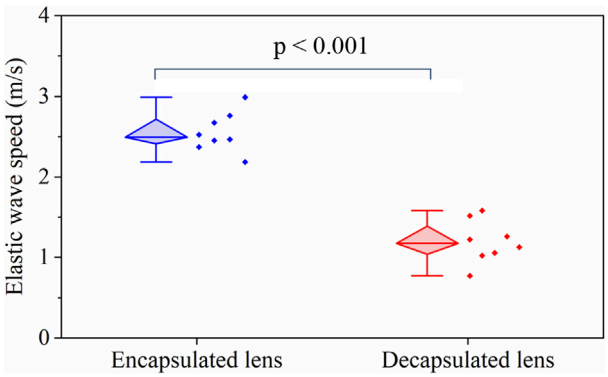

FIGURE 3
A box-whisker plot and measured data set distribution of the elastic group wave speed in the porcine lens before and after removal of capsule for N = 8 porcine lenses. The horizontal bar in the diamond box corresponds to the median of the data.

by the horizontal bar inside the diamond box. The distribution of the mean wave speed for the two groups is shown by the scatter plots in Figure 3. The mean wave speed with the capsule intact (2.55 ± 0.23 m/s) is approximately twice the value after the capsule was dissected away (1.19 ± 0.25 m/s). Statistical testing by a one-way ANOVA showed no significant intra-group difference in the wave speed for both the capsulated (F (7,26) = 0.58, p = 0.75) and decapsulated (F (7,16) = 0.32, p = 0.92) states, highlighting the repeatability of the experiment. The inter-group statistical analysis using a student t-test showed that the wave speed was significantly higher with the capsule intact than after dissecting it away (p < 0.001).

3.2 Lenticular viscoelasticity

Figure 4A shows a dispersion curve (i.e., phase velocity as a function of frequency) obtained from an OCE measurement and the Rayleigh surface wave curve fitted to the data. For the selected frequency range, it appears that the rate of change of velocity with frequency is greater for the encapsulated lens. Figure 4B depicts a summary of the viscoelastic properties of the encapsulated and decapsulated lens estimated using the phase velocity dispersion curve fitted to the Rayleigh surface wave model. The Young's modulus, E, and shear viscosity coefficient, η, decreased from E = 8.14 ± 1.10 kPa and η = 0.89 ± 0.09 Pa·s in the encapsulated lens to E = 3.10 ± 0.43 kPa and η = 0.28 ± 0.02 Pa·s in the decapsulated lens. The mean Young's modulus and viscosity coefficient of the decapsulated lens were both significantly lower than that of the encapsulated lens (p < 0.001).

In addition to the change in elastic wave velocity (i.e., dispersion) with frequency, characterizing the amplitude reduction (i.e., attenuation) as the elastic wave propagates through the medium, would provide further insight into the viscoelastic properties of the lens, as we have shown in the cornea previously (Li et al., 2014). Here, we quantified the amplitude attenuation of the elastic wave propagated across the lens in the lateral direction using the wave intensity map in the spatial-frequency domain, as shown in Figure 5A, which was produced by applying a 1D FFT on the spatiotemporal displacement map. Comparing the top and bottom intensity maps in Figure 5A, the wave amplitude dissipates more rapidly in the decapsulated lens than in the encapsulated lens, where ~80% of wave amplitude attenuated at 1.39 mm and 0.68 mm of propagation, respectively. This difference can be observed in the normalized spatial distribution profile of the peak intensity shown in Figure 5B. From the exponential decay fitting, the attenuation coefficient of the surface wave in the decapsulated lens was found to be roughly twice that of the encapsulated one (ratio = 1.21/0.46 = 2.63) at a center frequency of 706 Hz.

3.3 Lenticular morphology

A summary of the lens equatorial diameter and sagittal thickness, quantified using OCT images, is shown in

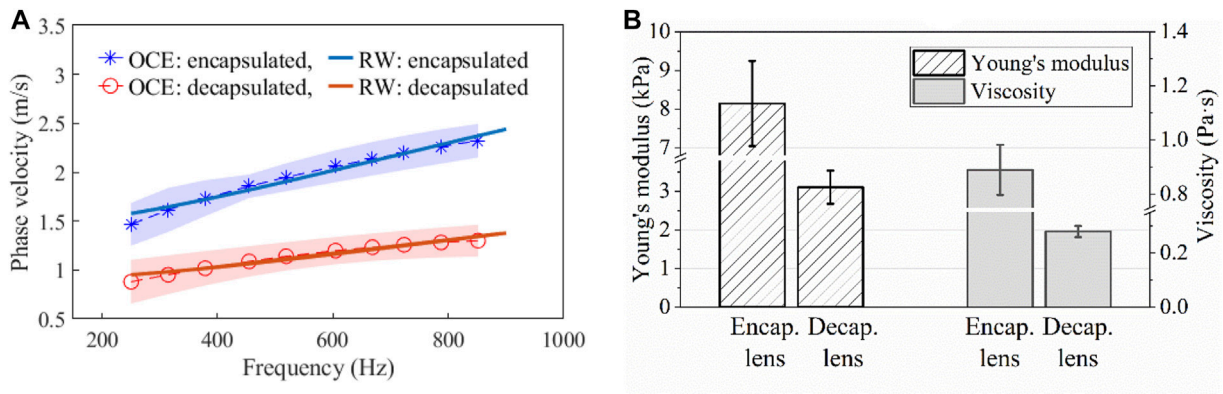

FIGURE 4
(A) Typical elastic wave dispersion curves in the porcine lens before and after capsule removal fitted with Rayleigh wave dispersion equation. The shaded region indicates the error band (standard deviation) of the OCE results. **(B)** Estimated Young's modulus and viscosity coefficient using Rayleigh wave dispersion equation for encapsulated and decapsulated lens. N = 8 porcine eye lenses.

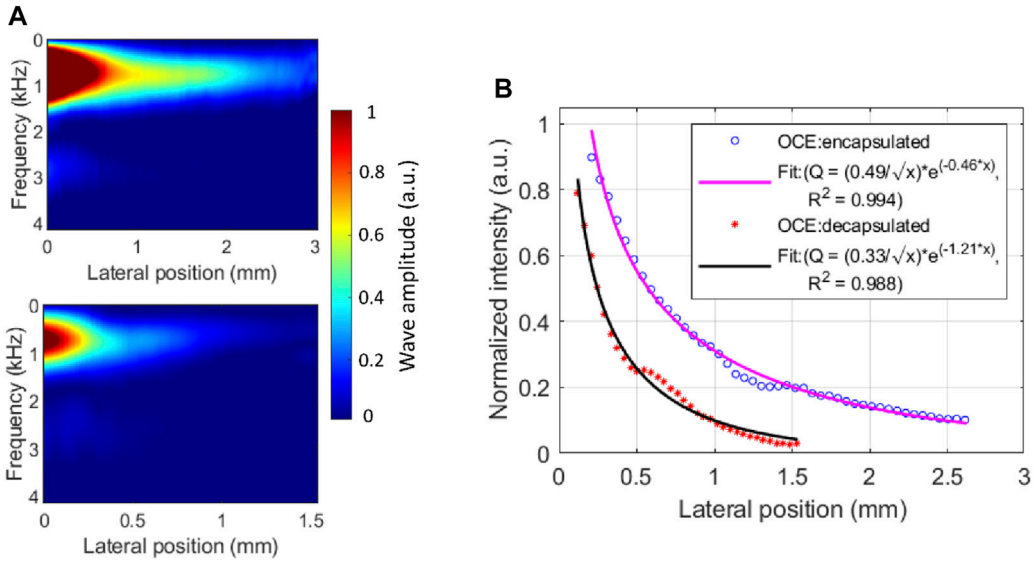

FIGURE 5
Elastic wave attenuation characteristics in a typical porcine eye lens. **(A)** The energy distribution map of laterally propagating elastic wave in encapsulated (top) and decapsulated (bottom) lens. **(B)** The normalized spatial distribution curve of the peak intensity and the exponential fitting before and after capsule removal. The peak intensity occurred at a center frequency of ~706 Hz. At the center frequency, the mean attenuation coefficient is higher in the decapsulated lens ($\alpha = 1.21 mm^{-1}$) than in the encapsulated lens ($\alpha = 0.46\, mm^{-1}$).

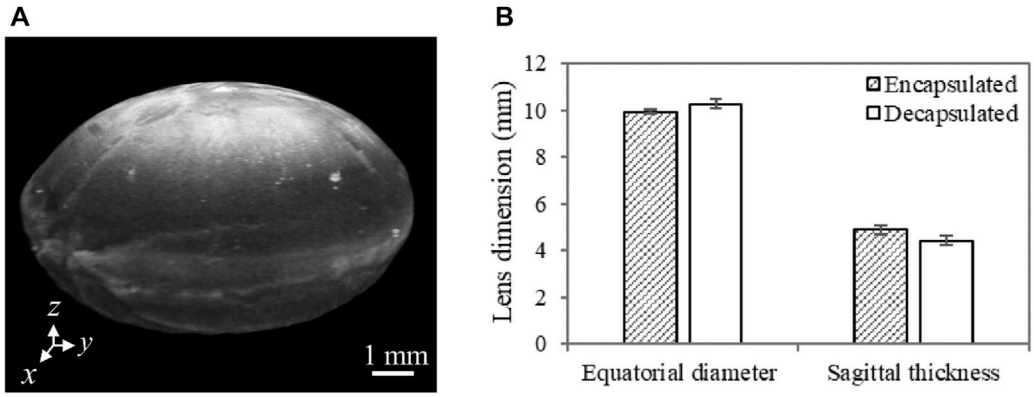

FIGURE 6
(A) A representative 3D OCT image of a dissected porcine lens. The anterior region is facing up (i.e., along the *z*-axis). Lens sagittal thickness represents the maximum thickness along the anterior-posterior direction (along the *z*-axis), while the equatorial diameter stands for the maximum thickness along the *x*-axis or the *y*-axis. **(B)** Porcine lens geometric features characterized by the sagittal thickness and equatorial diameter with and without the capsule. For each sample, multiple cross-sectional images (n = 4) extracted from 3D OCT images were used to quantify the mean geometric features. N = 3 for each group of lenses.

Figure 6B. The results indicate that the lens sagittal thickness is slightly lower while the equatorial diameter is slightly higher after capsule removal. Despite the observed consistency in this trend among all samples, the difference in both geometric features between encapsulated and decapsulated lenses was not statistically significant. However, it is worth noting that the decrease in the sagittal thickness (470 ± 19 μm) was greater than the thickness of the removed capsule (58 ± 10 μm). The increase in equatorial diameter and the decrease in axial/sagittal thickness with the removal of the capsule lead to an increase in the radius of curvature of the lens.

4 Discussion

This study aimed to investigate the viscoelastic properties of the porcine lens using ARF-based OCE, and, specifically, to assess the influence of the capsular bag on the biomechanical properties of the

lens. A comparison of elastic wave speeds demonstrates that the lens was significantly stiffer with the capsule intact than after the capsule was dissected away ($p < 0.001$), as shown in Figure 3. The viscoelastic properties of the lens quantified using the dispersion of a Rayleigh wave also showed a similar trend of significantly greater Young's modulus and shear viscosity coefficient in encapsulated lenses compared to their decapsulated counterparts ($p < 0.001$), which is plotted in Figure 4B. Furthermore, the shorter wave propagation distance observed in the decapsulated lenses correlated with a greater magnitude of attenuation coefficient, as plotted in Figure 5A. The wave attenuation coefficient of the decapsulated lenses was roughly twice that of the encapsulated lenses at the measured center frequency, indicating a higher rate of exponential decay in wave amplitude in the decapsulated lens as a function of propagation distance from the excitation position. These results suggest that the lens capsule plays a significant role in determining the mechanical properties of the lens.

The intra-sample correlation assessment of group wave speed using one-way ANOVA indicated the repeatability of the measurements both with ($F(7,26) = 0.58$, $p = 0.75$) and without ($F(7,16) = 0.32$, $p = 0.92$) capsule. For the encapsulated lens, the estimated Young's modulus was 8.14 ± 1.10 kPa and is in good agreement with previous OCE studies conducted on the porcine lens (Zhang et al., 2019; Ambekar et al., 2020; Chen et al., 2022). Despite the difference in the loading frequencies, the change in the viscoelastic properties with the removal of the capsule showed a similar trend to prior studies (Reilly and Ravi, 2009). The encapsulated lens appears to be significantly stiffer and has a higher shear viscosity ($p < 0.001$) relative to the isolated lens matrix, reinforcing the notion that the lens exhibits viscoelastic properties (Schachar et al., 2007). The elastic wave attenuation coefficient and the frequency-dependent phase velocity presented in this study could be important for the mechanical modeling of a lens with and without a capsule during personalized refractive procedures.

From the morphological point of view, the decrease in the sagittal thickness as well as the increase in the equatorial diameter with the removal of the capsule (Figure 6), suggests that the lens relaxes by remodeling its internal structure and does not retain its original shape after the capsule is removed. Thus, the capsule prevents the lens from flowing away, or that the lens is in a compressed (accommodated) state while the capsule is intact. Furthermore, the volume of the crystalline lens, as determined using the discrete integration method described by Marussich et al., showed no significant change ($p > 0.05$) after capsule removal, indicating that the change in morphology is potentially due to the redistribution of the internal tissue structure (Marussich et al., 2015). This morphological change coincides with the decrease in the elastic and viscous moduli, signifying that the capsule plays an important role in maintaining the morphology of the lens. In essence, with its low elasticity a dominant feature, the lens could assume an unwanted shape (e.g., the tendency of flattening or bulging anteriorly/posteriorly) when capsular integrity is compromised (e.g., due to disease or aging) or in the absence of (weakened) capsular support. Normally, alterations in the organization of constituent collagen IV and laminin meshwork and a reduction in the percentage of collagen IV with age could cause a change in capsular structural integrity (Rich and Reilly, 2022). Capsular support may also be compromised due to complications in extracapsular cataract extraction or phacoemulsification procedure (Por and Lavin, 2005).

While this study successfully demonstrated the mechanical interaction between the lens and its capsule, there are a few limitations that could be addressed in future research. First, porcine eyes lack the ability to accommodate and hence, may not be an appropriate model for human eyes. However, the results of the current study can be relevant in assessing the biomechanical properties of eyes with accommodative dysfunction, such as aged human or presbyopic eyes. Second, lens stiffness was characterized based on the propagation of the elastic wave in the selected area, which was at the anterior apex of the lens, mainly due to the low internal optical scattering of the lens substance. Third, it was not possible to discern the stiffness of the thin capsule from the results of the current study, mainly due to the relatively long wavelength of the induced elastic wave.

5 Conclusion

The current study highlights the influence of the capsule on the biomechanical properties of the lens as well as demonstrates the capability of the non-contact OCE system to provide a quantitative assessment of lens stiffness as a function of the capsule. Our study suggests that the measurement of the lens and its capsule stiffness as a unit may not reflect only the crystalline lens stiffness, which appears to be significantly influenced by the capsule. Future studies may consider quantifying the spatial anisotropy in the viscoelastic properties of the lens to provide a comprehensive assessment of the significance of the capsule in determining the structural integrity and function of the lens. Furthermore, higher excitation frequencies may assist in increasing elastic contrast and hence, discerning regional variations in lens stiffness, e.g., resolving elasticity gradient in the cortex and nucleus as well as the thin capsular layer.

Data availability statement

The raw data supporting the conclusions of this article will be made available by the authors, without undue reservation.

Author contributions

TM: experimental design and data acquisition, manuscript writing and data analysis; CZ-D: experimental design and data acquisition; HZ: experimental design; MS: optical system construction and programming, SA and KL: study conceptualization; all authors contributed to the manuscript revision and editing.

Funding

This work was supported by the NIH grant R01EY030063 and Core grant P30EY07551.

Conflict of interest

MS and KVL have a financial interest in ElastEye LLC., which is not directly related to this work.

The remaining authors declare that the research was conducted in the absence of any commercial or financial relationships that could be construed as a potential conflict of interest.

Publisher's note

References

Ambekar, Y. S., Singh, M., Zhang, J., Nair, A., Aglyamov, S. R., Scarcelli, G., et al. (2020). Multimodal quantitative optical elastography of the crystalline lens with optical coherence elastography and Brillouin microscopy. *Biomed. Opt. Express* 11 (4), 2041–2051. doi:10.1364/BOE.387361

Avetisov, K. S., Bakhchieva, N. A., Avetisov, S. E., Novikov, I. A., Frolova, A. A., Akovantseva, A. A., et al. (2020). Biomechanical properties of the lens capsule: A review. *J. Mech. Behav. Biomed. Mater* 103, 103600. doi:10.1016/j.jmbbm.2019.103600

Avetisov, K. S., Bakhchieva, N. A., Avetisov, S. E., Novikov, I. A., Shitikova, A. V., Frolova, A. A., et al. (2021). Assessment of age-related changes in lens capsule biomechanics using atomic force microscopy. *Vestn. Oftalmol.* 137 (1), 28–34. doi:10.17116/oftalma202113701128

Beers, A. P., and Van Der Heijde, G. L. (1994). *In vivo* determination of the biomechanical properties of the component elements of the accommodation mechanism. *Vis. Res.* 34 (21), 2897–2905. doi:10.1016/0042-6989(94)90058-2

Berggren, C. C., Ameku, K. A., and Pedrigi, R. M. (2021). Altered stress field of the human lens capsule after cataract surgery. *J. Biomech.* 115, 110127. doi:10.1016/j.jbiomech.2020.110127

Burd, H. J., Wilde, G. S., and Judge, S. J. (2011). An improved spinning lens test to determine the stiffness of the human lens. *Exp. Eye Res.* 92 (1), 28–39. doi:10.1016/j.exer.2010.10.010

Chen, Y., Ye, S., Wang, Q., Shen, M., Lu, F., Qu, J., et al. (2022). *In situ* assessment of lens elasticity with noncontact optical coherence elastography. *Biomed. Opt. Express* 13 (12), 6671–6681. doi:10.1364/BOE.475306

Cheng, C., Gokhin, D. S., Nowak, R. B., and Fowler, V. M. (2016). Sequential application of glass coverslips to assess the compressive stiffness of the mouse lens: Strain and morphometric analyses. *J. Vis. Exp.* e53986 (111), 53986. doi:10.3791/53986

Cheng, C., Parreno, J., Nowak, R. B., Biswas, S. K., Wang, K., Hoshino, M., et al. (2019). Age-related changes in eye lens biomechanics, morphology, refractive index and transparency. *Aging (Albany NY)* 11 (24), 12497–12531. doi:10.18632/aging.102584

Han, Z., Singh, M., Aglyamov, S. R., Liu, C. H., Nair, A., Raghunathan, R., et al. (2016). Quantifying tissue viscoelasticity using optical coherence elastography and the Rayleigh wave model. *J. Biomed. Opt.* 21 (9), 090504. doi:10.1117/1.JBO.21.9.090504

Heistand, M. R., Pedrigi, R. M., Delange, S. L., Dziezyc, J., and Humphrey, J. D. (2005). Multiaxial mechanical behavior of the porcine anterior lens capsule. *Biomech. Model Mechanobiol.* 4 (2-3), 168–177. doi:10.1007/s10237-005-0073-z

Huang, D., Xu, C., Guo, R., Ji, J., and Liu, W. (2021). Anterior lens capsule: Biomechanical properties and biomedical engineering perspectives. *Acta Ophthalmol.* 99 (3), e302–e309. doi:10.1111/aos.14600

Irvine, R. (1940). Exfoliation of the lens capsule (glaucoma capsularis): Forty cases of exfoliation. *Arch. Ophthalmol.* 23 (1), 138–160. doi:10.1001/archopht.1940.00860130150012

Jin, Z., Zhou, Y., Shen, M., Wang, Y., Lu, F., and Zhu, D. (2020). Assessment of corneal viscoelasticity using elastic wave optical coherence elastography. *J. Biophot.* 13 (1), e201960074. doi:10.1002/jbio.201960074

Kijanka, P., and Urban, M. W. (2021). Dispersion curve calculation in viscoelastic tissue-mimicking materials using non-parametric, parametric, and high-resolution methods. *Ultrasonics* 109, 106257. doi:10.1016/j.ultras.2020.106257

Li, J., Han, Z., Singh, M., Twa, M. D., and Larin, K. V. (2014). Differentiating untreated and cross-linked porcine corneas of the same measured stiffness with optical coherence elastography. *J. Biomed. Opt.* 19 (11), 110502. doi:10.1117/1.JBO.19.11.110502

Li, Y., Zhu, J., Chen, J. J., Yu, J., Jin, Z., Miao, Y., et al. (2019). Simultaneously imaging and quantifying *in vivo* mechanical properties of crystalline lens and cornea using optical coherence elastography with acoustic radiation force excitation. *Apl. Photonics* 4 (10), 106104. doi:10.1063/1.5118258

Liu, H. C., Kijanka, P., and Urban, M. W. (2020). Acoustic radiation force optical coherence elastography for evaluating mechanical properties of soft condensed matters and its biological applications. *J. Biophot.* 13 (3), e201960134. doi:10.1002/jbio.201960134

Liu, W., Huang, D., Guo, R., and Ji, J. (2021). Pathological changes of the anterior lens capsule. *J. Ophthalmol.* 2021, 1–5. doi:10.1155/2021/9951032

Marussich, L., Manns, F., Nankivil, D., Maceo Heilman, B., Yao, Y., Arrieta-Quintero, E., et al. (2015). Measurement of crystalline lens volume during accommodation in a lens stretcher. *Invest. Ophthalmol. Vis. Sci.* 56 (8), 4239–4248. doi:10.1167/iovs.15-17050

Nenadic, I. Z., Urban, M. W., Aristizabal, S., Mitchell, S. A., Humphrey, T. C., and Greenleaf, J. F. (2011). On Lamb and Rayleigh wave convergence in viscoelastic tissues. *Phys. Med. Biol.* 56 (20), 6723–6738. doi:10.1088/0031-9155/56/20/014

Park, S., Yoon, H., Larin, K. V., Emelianov, S. Y., and Aglyamov, S. R. (2017). The impact of intraocular pressure on elastic wave velocity estimates in the crystalline lens. *Phys. Med. Biol.* 62 (3), N45–N57. doi:10.1088/1361-6560/aa54ef

Parker, K. J., Ormachea, J., and Hah, Z. (2018). Group versus phase velocity of shear waves in soft tissues. *Ultrason. Imaging* 40 (6), 343–356. doi:10.1177/0161734618796217

Pedrigi, R. M., David, G., Dziezyc, J., and Humphrey, J. D. (2007). Regional mechanical properties and stress analysis of the human anterior lens capsule. *Vis. Res.* 47 (13), 1781–1789. doi:10.1016/j.visres.2007.03.014

Por, Y. M., and Lavin, M. J. (2005). Techniques of intraocular lens suspension in the absence of capsular/zonular support. *Surv. Ophthalmol.* 50 (5), 429–462. doi:10.1016/j.survophthal.2005.06.010

Reilly, M. A., and Cleaver, A. (2017). Inverse elastographic method for analyzing the ocular lens compression test. *J. Innovative Opt. Health Sci.* 10 (6), 1742009. doi:10.1142/S1793545817420093

Reilly, M. A., Martius, P., Kumar, S., Burd, H. J., and Stachs, O. (2016). The mechanical response of the porcine lens to a spinning test. *Z Med. Phys.* 26 (2), 127–135. doi:10.1016/j.zemedi.2015.12.009

Reilly, M., and Ravi, N. (2009). Microindentation of the young porcine ocular lens. *J. Biomech. Eng.* 131 (4), 044502. doi:10.1115/1.3072891

Rich, W., and Reilly, M. A. (2022). A review of lens biomechanical contributions to presbyopia. *Curr. Eye Res.* 48, 182–194. doi:10.1080/02713683.2022.2088797

Ronci, M., Sharma, S., Chataway, T., Burdon, K. P., Martin, S., Craig, J. E., et al. (2011). MALDI-MS-imaging of whole human lens capsule. *J. Proteome Res.* 10 (8), 3522–3529. doi:10.1021/pr200148k

Scarcelli, G., Kim, P., and Yun, S. H. (2011). *In vivo* measurement of age-related stiffening in the crystalline lens by Brillouin optical microscopy. *Biophys. J.* 101 (6), 1539–1545. doi:10.1016/j.bpj.2011.08.008

Schachar, R. A., Chan, R. W., and Fu, M. (2007). Viscoelastic shear properties of the fresh porcine lens. *Br. J. Ophthalmol.* 91 (3), 366–368. doi:10.1136/bjo.2006.105965

Sharma, P. K., Busscher, H. J., Terwee, T., Koopmans, S. A., and van Kooten, T. G. (2011). A comparative study on the viscoelastic properties of human and animal lenses. *Exp. Eye Res.* 93 (5), 681–688. doi:10.1016/j.exer.2011.08.009

Singh, M., Zvietcovich, F., and Larin, K. V. (2022). Introduction to optical coherence elastography: Tutorial. *J. Opt. Soc. Am. A Opt. Image Sci. Vis.* 39 (3), 418–430. doi:10.1364/JOSAA.444808

Sticker, M., Hitzenberger, C. K., Leitgeb, R., and Fercher, A. F. (2001). Quantitative differential phase measurement and imaging in transparent and turbid media by optical coherence tomography. *Opt. Lett.* 26 (8), 518–520. doi:10.1364/ol.26.000518

Vilupuru, A. S., and Glasser, A. (2001). Optical and biometric relationships of the isolated pig crystalline lens. *Ophthalmic Physiol. Opt.* 21 (4), 296–311. doi:10.1046/j.1475-1313.2001.00593.x

von Helmholtz, H., and Southall, J. P. C. (1924). "Mechanism of accommodation," in *Helmholtz's treatise on physiological optics, Vol. 1 (Trans. from the 3rd German*. Editor J. P. C. Southall (Rochester, NY, US: Optical Society of America), 143–172.

Wang, K., and Pierscionek, B. K. (2019). Biomechanics of the human lens and accommodative system: Functional relevance to physiological states. *Prog. Retin Eye Res.* 71, 114–131. doi:10.1016/j.preteyeres.2018.11.004

Wang, S., and Larin, K. V. (2014). Shear wave imaging optical coherence tomography (SWI-OCT) for ocular tissue biomechanics. *Opt. Lett.* 39 (1), 41–44. doi:10.1364/OL.39.000041

Weeber, H. A., Eckert, G., Pechhold, W., and van der Heijde, R. G. (2007). Stiffness gradient in the crystalline lens. *Graefes Arch. Clin. Exp. Ophthalmol.* 245 (9), 1357–1366. doi:10.1007/s00417-007-0537-1

Weeber, H. A., and van der Heijde, R. G. (2007). On the relationship between lens stiffness and accommodative amplitude. *Exp. Eye Res.* 85 (5), 602–607. doi:10.1016/j.exer.2007.07.012

Wilde, G. S., Burd, H. J., and Judge, S. J. (2012). Shear modulus data for the human lens determined from a spinning lens test. *Exp. Eye Res.* 97 (1), 36–48. doi:10.1016/j.exer.2012.01.011

Wollensak, G., and Spoerl, E. (2004). Influence of indocyanine green staining on the biomechanical properties of porcine anterior lens capsule. *Curr. Eye Res.* 29 (6), 413–417. doi:10.1080/02713680490522498

Won, G. J., Fudge, D. S., and Choh, V. (2015). The effects of actomyosin disruptors on the mechanical integrity of the avian crystalline lens. *Mol. Vis.* 21, 98–109.

Wu, C., Aglyamov, S. R., Han, Z., Singh, M., Liu, C. H., and Larin, K. V. (2018). Assessing the biomechanical properties of the porcine crystalline lens as a function of intraocular pressure with optical coherence elastography. *Biomed. Opt. Express* 9 (12), 6455–6466. doi:10.1364/BOE.9.006455

Wu, C., Han, Z., Wang, S., Li, J., Singh, M., Liu, C. H., et al. (2015). Assessing age-related changes in the biomechanical properties of rabbit lens using a coaligned ultrasound and optical coherence elastography system. *Invest. Ophthalmol. Vis. Sci.* 56 (2), 1292–1300. doi:10.1167/iovs.14-15654

Yoon, S., Aglyamov, S., Karpiouk, A., and Emelianov, S. (2012). A high pulse repetition frequency ultrasound system for the *ex vivo* measurement of mechanical properties of crystalline lenses with laser-induced microbubbles interrogated by acoustic radiation force. *Phys. Med. Biol.* 57 (15), 4871–4884. doi:10.1088/0031-9155/57/15/4871

Yoon, S., Aglyamov, S., Karpiouk, A., and Emelianov, S. (2013). The mechanical properties of *ex vivo* bovine and porcine crystalline lenses: Age-related changes and location-dependent variations. *Ultrasound Med. Biol.* 39 (6), 1120–1127. doi:10.1016/j.ultrasmedbio.2012.12.010

Zhang, H., Singh, M., Zvietcovich, F., Larin, K., and Aglyamov, S. (2022). Age-related changes in the viscoelasticity of rabbit lens characterised by surface wave dispersion analysis. *Quantum Electron* 52 (1), 42–47. doi:10.1070/Qel17964

Zhang, H., Wu, C., Singh, M., Nair, A., Aglyamov, S., and Larin, K. (2019). Optical coherence elastography of cold cataract in porcine lens. *J. Biomed. Opt.* 24 (3), 1–7. doi:10.1117/1.JBO.24.3.036004

Zhang, X. (2016). Identification of the Rayleigh surface waves for estimation of viscoelasticity using the surface wave elastography technique. *J. Acoust. Soc. Am.* 140 (5), 3619–3622. doi:10.1121/1.4966673

Zhao, M., Kuo, A. N., and Izatt, J. A. (2010). 3D refraction correction and extraction of clinical parameters from spectral domain optical coherence tomography of the cornea. *Opt. Express* 18 (9), 8923–8936. doi:10.1364/oe.18.008923

Ziebarth, N. M., Arrieta, E., Feuer, W. J., Moy, V. T., Manns, F., and Parel, J. M. (2011). Primate lens capsule elasticity assessed using Atomic Force Microscopy. *Exp. Eye Res.* 92 (6), 490–494. doi:10.1016/j.exer.2011.03.008

Zvietcovich, F., and Larin, K. V. (2022). Wave-based optical coherence elastography: The 10-year perspective. *Prog. Biomed. Eng. (Bristol)* 4 (1), 012007. doi:10.1088/2516-1091/ac4512

frontiers | Frontiers in Bioengineering and Biotechnology

TYPE Original Research
PUBLISHED 09 March 2023
DOI 10.3389/fbioe.2023.1126543

OPEN ACCESS

EDITED BY
Matthew A. Reilly,
The Ohio State University, United States

REVIEWED BY
Kaihui Nan,
Wenzhou Medical University, China
Zhili Zheng,
Broad Institute, United States

*CORRESPONDENCE
Bin Zhang,
bz52@nova.edu
Ruihua Wei,
rwei@tmu.edu.cn

SPECIALTY SECTION
This article was submitted to Biomechanics, a section of the journal Frontiers in Bioengineering and Biotechnology

RECEIVED 18 December 2022
ACCEPTED 27 February 2023
PUBLISHED 09 March 2023

CITATION
Rong H, Liu L, Liu Y, Fu W, Xu H, Yu D, Wu D, Du B, Zhang X, Zhang B and Wei R (2023), Quantifying the morphology of eyeballs with posterior staphyloma with Zernike polynomials.
Front. Bioeng. Biotechnol. 11:1126543.
doi: 10.3389/fbioe.2023.1126543

Quantifying the morphology of eyeballs with posterior staphyloma with Zernike polynomials

Hua Rong[1], Lin Liu[1], Yuling Liu[1], Wanzeng Fu[2], He Xu[3], Danyang Yu[1], Di Wu[1], Bei Du[1], Xuejun Zhang[3], Bin Zhang[4]* and Ruihua Wei[1]*

[1]Tianjin International Joint Research and Development Centre of Ophthalmology and Vision Science, Eye Institute and School of Optometry, Tianjin Medical University Eye Hospital, Tianjin, China, [2]Qcraft Inc., Beijing, China, [3]Department of Radiology, Second Hospital of Tianjin Medical University, Tianjin, China, [4]College of Optometry, Nova Southeastern University, Davie, FL, United States

Purpose: To quantify the morphology of eyeballs with posterior staphyloma (PS) with Zernike decomposition and to explore the association between Zernike coefficients with existing PS classification.

Methods: Fifty-three eyes with high myopia (HM, ≤-6.00D) and 30 with PS were included. PS was classified with traditional methods based on OCT findings. Eyeballs' morphology was obtained with 3D MRI, from which the height map of the posterior surface was extracted. Zernike decomposition was performed to derive the coefficients of the 1st-27th items, which were compared between HM and PS eyes with the Mann-Whitney-U test. Receiver operating characteristics (ROC) analysis was used to test the effectiveness of using Zernike coefficients to discriminate PS from HM.

Results: Compared to HM eyeballs, PS eyeballs had significantly increased vertical and horizontal tilt, oblique astigmatism, defocus, vertical and horizontal coma, and higher order aberrations (HOA) (all Ps < 0.05). HOA was the most effective in PS classification with an area under the ROC curve (AUROC) value of 0.977. Among the 30 PS, 19 were the wide macular type with large defocus and negative spherical aberration; 4 were the narrow macular type with positive spherical aberration; 3 were inferior PS with greater vertical tilt, and 4were peripapillary PS with larger horizontal tilt.

Conclusion: PS eyes have significantly increased Zernike coefficients, and HOA is the most effective parameter to differentiate PS from HM. The geometrical meaning of the Zernike components showed great accordance with PS classification.

KEYWORDS

posterior staphyloma, 3D MRI, high myopia, Zernike polynomials, eyeball morphology

1 Introduction

Posterior staphyloma (PS) is a common complication of pathological myopia, which manifests as partial protrusion of the back of the eyeball. Retinal changes, such as retinoschisis and retinal detachment, are often observed in patients and lead to irreversible vision impairment and reduced life quality (Avila et al., 1984; Ohno-Matsui and Tokoro, 1996; Hayashi et al., 2010). As the worldwide prevalence of high myopia increases year by year, it is

critical to detect PS and evaluate its severity in a timely manner (Holden et al., 2016). In the early days, the detection and classification of PS mainly depended on findings under ophthalmoscopy or imaging technology, such as optical coherence tomography or B-scan ultrasound. Curtin classified PS into ten different types based on ophthalmoscopic appearance (Curtin, 1977). Shinohara et al. characterized the PS from OCT with choroid thinning toward the staphyloma margin, inward protrusion of the sclera, and scleral reversion in the post-marginal region (Shinohara et al., 2017). These findings are often local and do not reveal much about the overall shape of the eyeball.

Three-dimensional MRI (3D MRI) can display the morphology of the eye in its entirety (Moriyama et al., 2012; Shinohara et al., 2013; Nagra et al., 2014; Wang et al., 2016). Spaide et al. described PS as a protrusion in the posterior fundus area, and its radius of curvature is smaller than that of the adjacent eye wall (Spaide, 2014). Ohno-Matsui et al. used a combination of 3D MRI and ultra-widefield fundus imaging to classify PS into six different types based on the size, shape, and location of the staphylomas (Ohno-Matsui, 2014). However, these defining signs heavily rely on human subjective judgments, including whether the curvature changes and where the choroid begins to thin. More recent studies started classifying staphyloma based on quantitative analysis of 3D MRI images. Moriyama divided staphylomas into 18 categories based on parameters derived from the 3D MRI images (Moriyama et al., 2012). Lim fitted the largest section of MRI images into an ellipse and calculated the ratio between long and short axes to quantify the asphericity (Lim et al., 2019). Ishii et al. used MRI images and Fourier transform to analyze the shape of the eyeball (Ishii et al., 2011). But these studies only utilized certain arbitrarily chosen sections. As more studies were completed, Ohno-Matsui et al., 2017 suggested that there may be more variations in the shape of staphylomas than previously thought. Therefore, it is desirable to have a method that can incorporate all the information about the eye shape.

Zernike polynomials consist of a series of polynomials orthogonal to each other (Schwiegerling and Greivenkamp, 1997; Lakshminarayanan and Fleck, 2011), which are a set of basis vectors that can describe any curved surface in the unit circle. Different terms represent specific geometric meanings, and each term's coefficients can represent the surface shape's component (Tango, 1977; Wang and Silva, 1980). In ophthalmology, Zernike polynomials have been used to describe corneal shape changes in keratoconus (Wacker et al., 2015; Shugyo et al., 2021). We believe that the same principles could be applied to the posterior surface of the eyeball. In this study, 3D MRI images of eyeballs with or without PS were collected, and the height maps of the posterior surface were extracted. The height maps were further decomposed into Zernike components, such as tilt, defocus, coma, astigmatism, and HOAs. We first compared the difference in Zernike coefficients between the eyeballs with and without PS. Moreover, the relationship between Zernike coefficients and existing types of PS was analyzed.

2 Methods

2.1 Patients

This prospective study included 45 participants recruited at Tianjin Medical University Eye Hospital between October 2020 and May 2022. The subjects were divided into two groups, the HM group and the PS group, respectively. HM was defined as spherical equivalent (SE)≤-6.00D, the eyeball was regular spherical or ellipsoid under 3D MRI, and there was no posterior scleral staphyloma. OCT and fundus photo examination showed no fundus lesions. A PS was defined by an outward bowing of the sclera on the OCT images, with the curvature radius of the staphyloma being smaller than the curvature radius of the surrounding sclera (Figure 1A) and with retinal atrophy evident on fundus photography (Figure 1B). There was no restriction on axial length, as staphyloma may still occur even with a short axial length (Moriyama et al., 2011; Wang et al., 2016). The diagnosis of HM or PS was made by two investigators independently, who agreed with all diagnoses made (Xu et al., 2019). The exclusion criteria were: scleral buckling, ocular trauma that could affect the eyeball shape, claustrophobia, presence of a pacemaker or intraocular metal foreign body, and systemic disease. Written informed consent was obtained from all participants. All study procedures adhered to the tenets of the Declaration of Helsinki and were approved by the ethics committee of Tianjin Medical University Eye Hospital (NO. 2020KY-04).

2.2 Measurements

All participants had comprehensive ocular examinations, including best-corrected visual acuity (BCVA), refractive error measurements with an auto refractometer (ARK-730; Nidek, Nagoya, Japan) without cycloplegia, axial length measurements using Lenstar LS-900 (Haag-Streit AG, Berne, Switzerland), detailed ophthalmoscopic examinations, fundus images (Optos, PLC, Dunfermline, Scotland), and OCT (VG200, SVision Imaging, Henan, China). The BCVA was measured with a chart of Landolt rings set at a distance of 5 m. For statistical analyses, the decimal BCVAs were converted to the logarithm of minimal angle of resolution (logMAR) units. The Discovery MR750 3.0T scanner (GE Healthcare, Milwaukee, WI, United States), an 8-channel phased head coil, was used for 3D MRI imaging. Axial position images were acquired using a fast-recovery-fast-spin-echo acceleration sequence (3D FRFSE-XL).

2.3 MRI image analysis

In this study, we utilized Python3.7.9 to preprocess DICOM files of MRI images in this study. MRI images with obvious artifacts or poor quality were excluded from processing. The "breadth-first algorithm" was used to search for the boundary of the vitreous body. A search starts from an arbitrary point within the vitreous body, moving from center towards the periphery. If the contrast difference between the next point and the previous point is less than the threshold, the next point is included in the vitreous matrix; otherwise, the search is stopped. Finally, all points contained in the vitreous bodies in a slice are included in the matrix. The contrast threshold between the vitreous body and surrounding tissue was set to 1800, which allows for automatic differentiation between the two through experimentation. We determine the physical distance in every

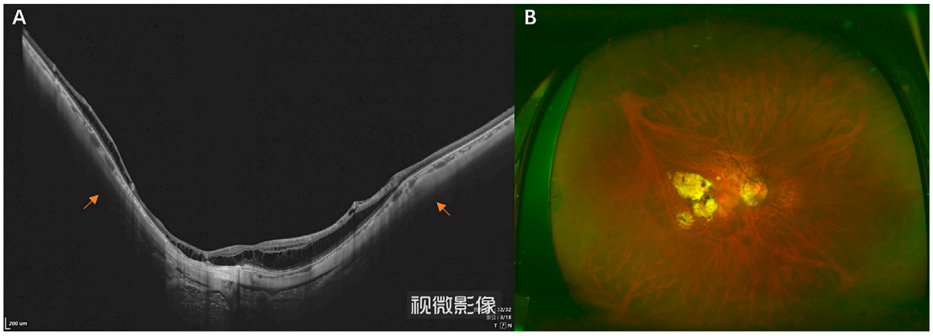

FIGURE 1
OCT **(A)** and wide-field fundus image **(B)** of an eyeball with PS. The yellow arrow indicates the choroid's thinning and the scleral curvature change.

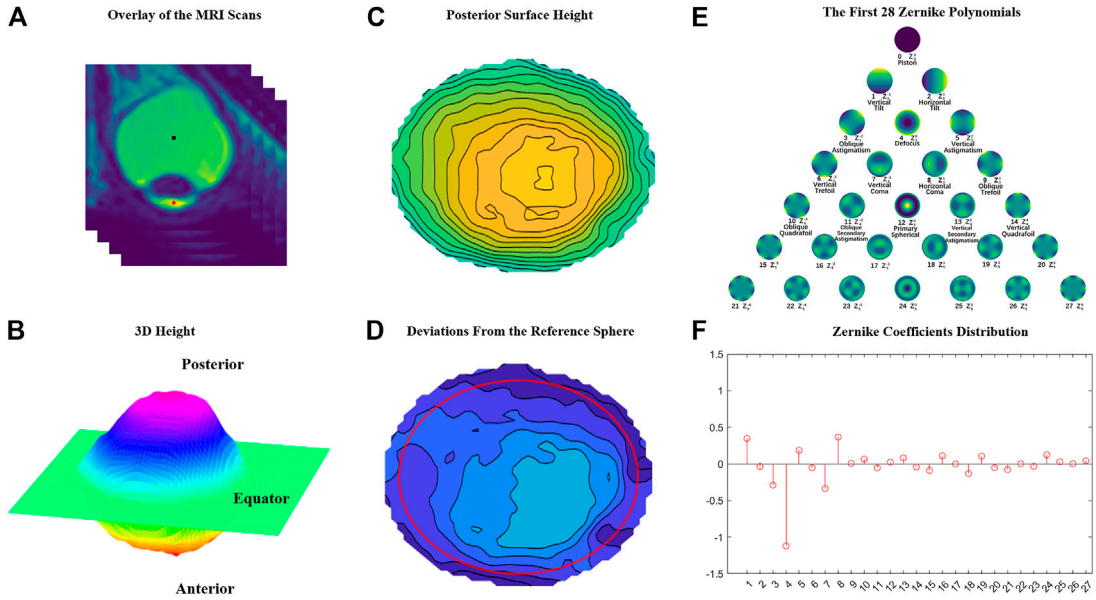

FIGURE 2
The Zernike coefficient analysis process of the posterior surface of the eyeball. **(A)** A stack of 2D MRI images is superimposed into a 3D image. **(B)** The posterior surface of a height map is extracted. **(C)** The posterior surface height map. **(D)** The residual height map after a standard sphere with a radius of 12.5 mm is subtracted from the original height map. **(E)** The first 28 Zernike polynomials derived from a residual height map. **(F)** Zernike analysis is performed on the height matrix within a radius of 11 mm (the red circle in Figure 2D).

direction for each pixel based on the field of view and layer spacing of the MRI. The distance between each pixel in the same fault is 0.703 mm, and the layer spacing is 0.5 mm. In each slice, after the boundary of the vitreous chamber was extracted, the slices were stacked over in sequence, and the 3D boundary of the entire vitreous body could be extracted into a matrix (Figure 2A). The geometric center VC of the vitreous body (VC, the black point in Figure 2A) and the geometric center of the cornea (CC, the red point in Figure 2A) were also calculated. Using Rodrigues formula, we first determined the rotation matrix that can align the vector VC_to_CC with the vertical-downward direction. Then the entire eyeball is rotated with such a matrix. The libraries used in the process are pandas, numpy, math, matplotlib, mpl_toolkits, pydicom, and os from the Python ecosystem. The eyeball was divided into the front and back parts by the equator plane, which perpendicular to the axis of the VC_to_CC with the largest cross-sectional area (Figure 2B). The height of a point on the back surface was defined as its distance, parallel to the direction of the VC_to_CC vector, to the equator surface. A surface height map was derived after all points' heights were calculated (Figure 2C). The surface height map was drawn using the mpl_toolkits.mplot3d.Axes3D.plot_surface function from a Python third-party library. To show how an eyeball's shape deviated from a perfect sphere, a residual height map was derived by subtracting the original height map with a perfect sphere with a radius of 12.5 mm (Figure 2D) which

TABLE 1 Characteristics of the study groups.

Mean ± SD	PS	HM	P
No. patients (eyes)	18 (30)	27 (53)	—
Men	8 (13)	12 (24)	—
Women	10 (17)	15 (29)	—
Age (y)	57.76 ± 12.09	48.24 ± 10.29	<0.01*
SE (D)	−13.90 ± 2.64	−8.50 ± 1.16	<0.01*
AL (mm)	29.74 ± 1.75	27.20 ± 0.76	<0.01*
BCVA (LogMAR)	0.66 ± 0.38	0.00 ± 0.02	<0.01*

*Means significant differences between the two groups using the Mann-Whitney U test.

corresponded to the median radius of the coronal plane sections of the eyeballs. Zernike analysis was performed only within the central 11 mm radius (Red circle in Figure 2D). Figure 2E is the geometric meaning of 0–28th Zernike coefficients. The coefficients of the 1st to the 27th components are shown in Figure 2F.

2.4 Classification of PS

We classified PS according to the classification method proposed by Ohno-Matsui (Ohno-Matsui et al., 2017), which can divide PS into six categories, namely, wide macular PS, narrow macular PS, peripapillary PS, nasal PS, inferior PS, and other types of PS.

2.5 Statistical analysis

The normality of data was assessed using the Kolmogorov–Smirnov test. The mean and standard deviation were calculated for SE, AL. Median and quartile were calculated for tilt, defocus, coma, astigmatism, and HOAs (6th-27th) root-mean-square (RMS) for each group. Because some Zernike terms exhibited inconsistent normality among the two groups, the two groups were compared using the non-parametric Mann-Whitney U test. Differences were considered statistically significant when the *p*-value was less than 0.05. The receiver operating characteristic (ROC) curves were built for HOAs-RMS, defocus, and coma in the classification of PS. The area under the ROC curve (AUROC) was calculated, and the cutoff value with the highest Youden indices (Youden index = sensitivity + specificity - 1) was determined. All statistical calculations were performed in IBM SPSS Statistics, version 26.0 (IBM Corp, Armonk, NY)

3 Results

3.1 Basic information

A total of 27 patients with 53 eyes in the HM group and 18 patients with 30 eyes in the PS group were included in this study. The basic information about the patients is summarized in Table 1.

3.2 Zernike components

An example of the HM eyeball (Figure 3A) and an example of the PS eyeball (Figure 3B). Compared to the HM eyeball, the posterior side of the PS eyeball was bulging out. The median and quartile values from the population data were summarized in Table 2 and illustrated in Figure 4. Mann-Whitney test results showed that vertical and horizontal tilt, oblique astigmatism, defocus, vertical and horizontal coma, and HOAs-RMS in the PS group were significantly greater than those in the HM group, and there was no significant difference in vertical astigmatism.

3.3 Receiver operating characteristics analysis

ROC analysis was performed to see if individual Zernike coefficients could distinguish PS eyeballs from HM eyeballs. The ROC curve shows how true and false positive rate change as the criterion changes. Two completely separated populations without any overlap would push the curve to the top-left corner (0% false positive and 100% true positive) and lead to the largest AUC. Outliers from each population would increase the false positive rate and move the curve away from the top-left corner, thus creating a smaller AUC. In this study, the ROC curve was automatically generated by the SPSS software, and the AUC value was provided too. Among all parameters, HOAs-RMS has the greatest classification power with an AUROC value of 0.977. The cut-off value of 0.0686 for total ocular HOAs-RMS provided the highest Youden indices with 90% sensitivity and 98% specificity (Figure 5A). The second best parameter was the defocus, with an AUROC value of 0.864. Others are summarized in Table 3. The joint distribution of HOAs-RMS and defocus, the two parameters with the largest AUROC, illustrate the difference between HM and PS even better (Figure 5B).

3.4 PS classification and Zernike coefficients

In this study, we identified 19 wide macular PS (63.3%), four narrow macular PS (13.3%) eyes, three inferior PS (10%), and four peripapillary PS (13.3%). There were no nasal PS and other PS types. To illustrate the association between Zernike coefficients and the types of PS, examples of the four types of PS found in this study are shown in Figure 6, respectively.

4 Discussion

This study used Zernike polynomials to describe the eyeball's posterior surface shape. The advantage of this method is that it can fully use 3D MRI information. The shape of the posterior surface of the eyeball can be reconstructed with less than 30 coefficients, and each parameter has good interpretability. This study showed that the most recognizable change in PS eyeballs was the increase of HOAs-RMS.

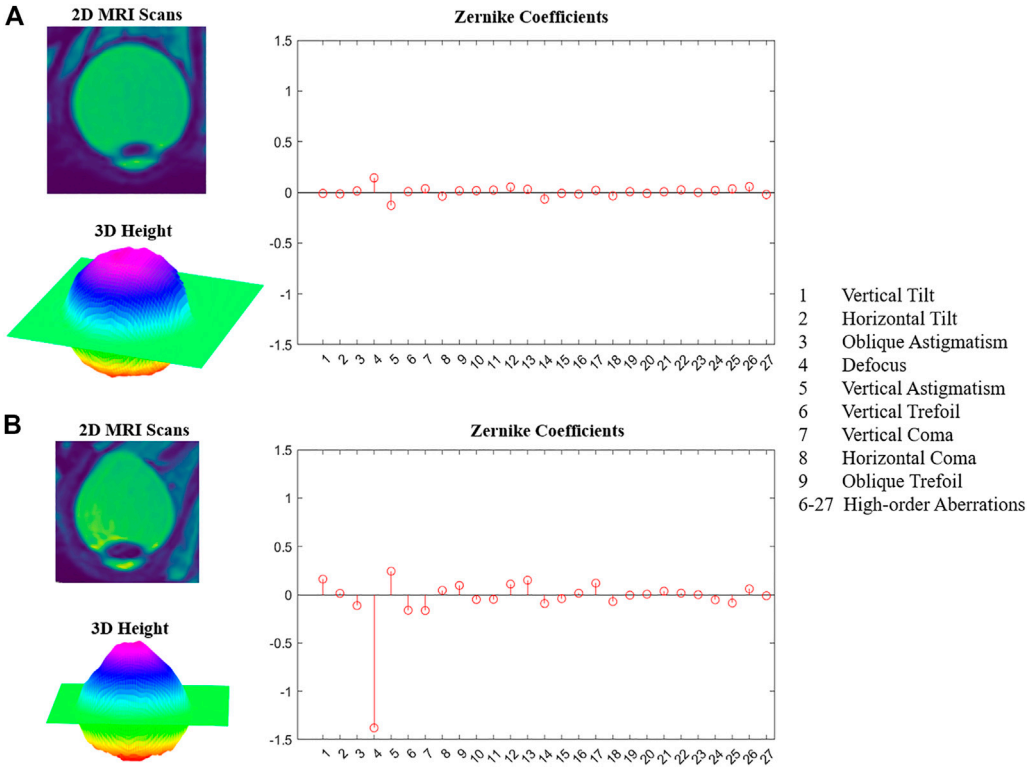

FIGURE 3
Examples of HM and PS. **(A)** HM eyeball 2D MRI image, 3D posterior surface height map, Zernike coefficients. **(B)** PS eye ball 2D MRI image, 3D posterior surface height map, Zernike coefficients.

TABLE 2 Zernike coefficients and HOAs-RMS of HM and PS.

Zernike coefficients	HM	PS	Adj. P
Vertical Tilt	0.157 (0.056,0.241)	0.297 (0.124,0.698)	<0.01
Horizontal Tilt	0.126 (0.06,0.199)	0.435 (0.109,0.786)	<0.001
Oblique astigmatism	0.051 (0.019,0.127)	0.124 (0.063,0.285)	<0.001
Defocus	0.051 (-0.120,0.229)	0.654 (0.438,1.044)	<0.001
Vertical astigmatism	0.146 (0.073,0.220)	0.181 (0.073,0.251)	0.992
Vertical Coma	0.042 (0.022,0.083)	0.190 (0.072,0.256)	<0.001
Horizontal Coma	0.041 (0.026,0.073)	0.153 (0.062,0.223)	<0.001
HOAs-RMS	0.044 (0.036,0.054)	0.107 (0.076,0.120)	<0.001

4.1 Asymmetry

Previous studies have shown that eyeballs with PS are more likely to have asymmetrical shapes (Moriyama et al., 2012; Ohno-Matsui et al., 2012). Ohno-Matsui et al. showed that the eyeballs asymmetry was significantly greater in the eyeballs with PS than in the eye without PS(Ohno-Matsui et al., 2012). Moriyama showed that PS is more likely to be located underside of the nose, which could explain the increase in oblique astigmatism in the PS group (Moriyama et al., 2012). In this study, the tilt, coma, and oblique astigmatism were significantly increased in the PS group compared with HM. These coefficients represent the degree of asymmetry in the particular meridian of the eyeball (Tango, 1977). Previous studies have shown a higher probability of fundus lesions and visual field defects in asymmetric eyeballs (Moriyama et al., 2012; Ohno-Matsui et al., 2012). Therefore, the ability to quantitatively describe the asymmetry of the eyeball has values for the clinical prediction of fundus damage. Tilt represents the inclination along the X or *Y*-axis, coma represents the asymmetry of the local height, and astigmatism means the asymmetry in the difference between the height of an axis and its orthogonal direction (Tango, 1977). Zernike analysis can distinguish the asymmetry caused by the three components, which is impossible with previous description methods.

4.2 Defocus and HOAs- root-mean-square

In this study, the defocus in the PS group was significantly greater than that in the HM group. Geometrically, defocus represents the overall prominence of the eyeball. The larger the defocus, the closer the eyeball was to an elongated ellipsoid (Wang and Silva, 1980). A greater defocus value indicates in PS that the overall trend of the eyeball of PS is steeper than that of

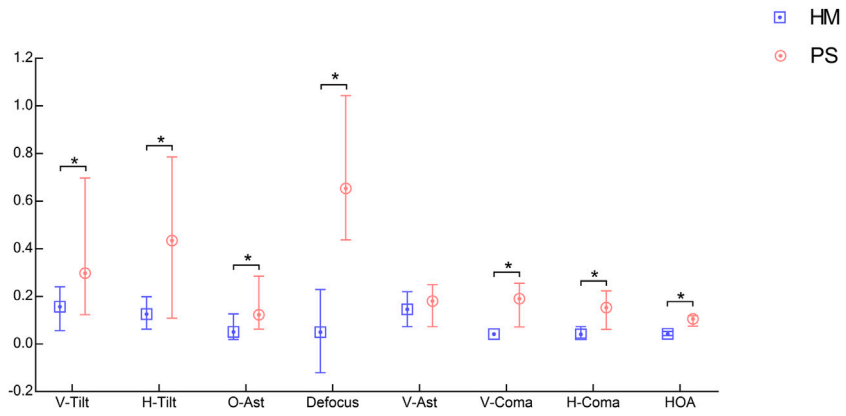

FIGURE 4
The median and quartiles values of Zernike coefficients for HM (blue) and PS (red) eyeballs.

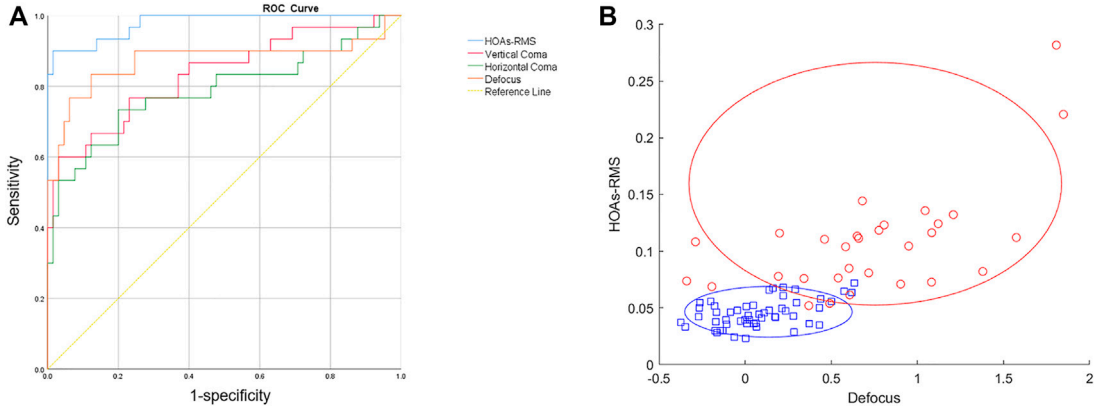

FIGURE 5
Zernike coefficients and PS classification. **(A)** ROC curves of different Zernike coefficients for PS classification. **(B)** Joint distribution of HOA and Defocus. Red: PS group. Blue: HM group.

TABLE 3 ROC analysis.

	AUROC	P	Sensitivity	Specificity	Cutoff	Youden index
HOAs-RMS	0.977	<0.001	0.90	0.98	0.0686	0.88
Defocus	0.864	<0.001	0.77	0.92	0.4500	0.69
VComa	0.827	<0.001	0.60	0.96	0.1463	0.56
HComa	0.791	<0.001	0.73	0.81	0.3312	0.54

the posterior surface of the eyeball of HM. In this study, ROC analysis showed that defocus was one of the key differences between PS and HM. Moriyama et al. showed that eyes with a steeper posterior surface had an increased probability of developing retinopathy (Moriyama et al., 2012; Wakazono et al., 2016), which further demonstrates the value of using the concept of defocus in evaluating eye shape.

As the HM eyeball still keep the spherical shape (Pope et al., 2017), Zernike decomposition revealed mainly low-order aberrations with few high-order aberration components. Posterior scleral PS are different in size, location, and shape (Ohno-Matsui et al., 2016). As the irregularity increases, low-order coefficients are insufficient to describe the eyeball shape fully. Therefore, in eyeballs with PS, HOAs-RMS should be more prominent. Our findings

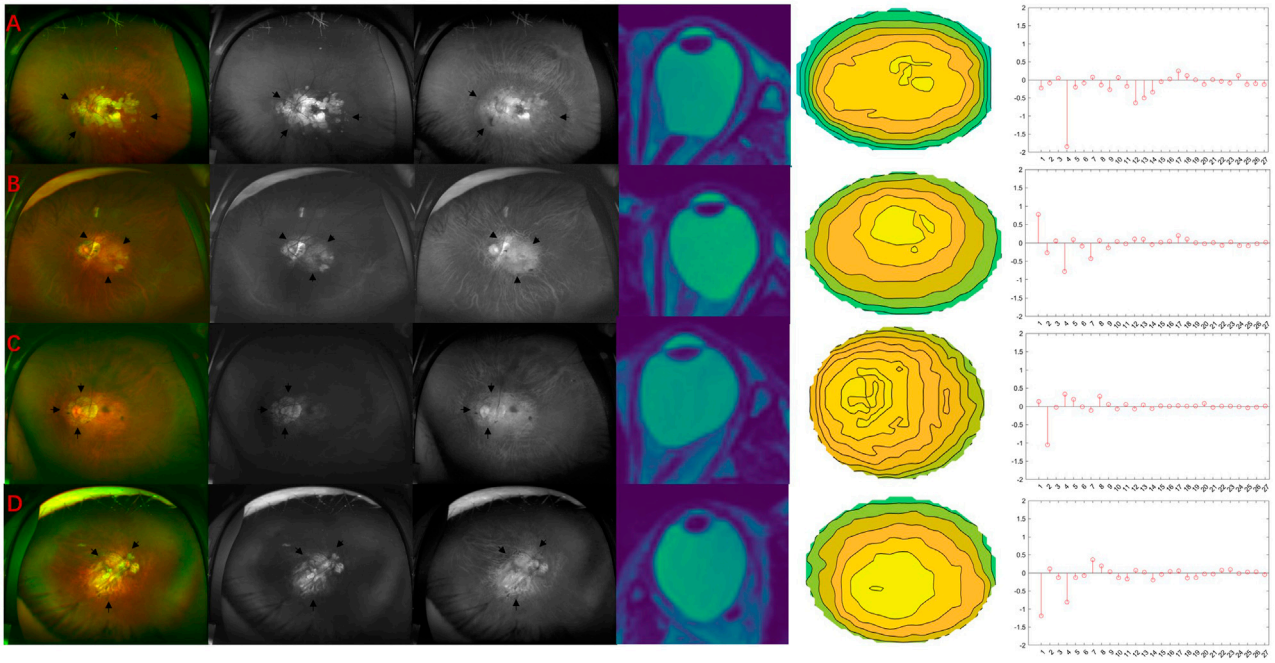

FIGURE 6
Four different types of PS. Black arrows indicate the borders of the staphyloma. **(A)** Wide macular PS. The nasal edge of macular PS exists more nasally beyond the nasal edge of the optic disc. 2D MRI tomographic image shows that the eyeball's posterior part is blunt. The height map of the posterior part of the eyeball shows spare contour lines in the central part. Note spherical aberration (12th) is negative, indicating that the local bulge in the center is not apparent. **(B)** Narrow macular PS. The macular PS's nasal edge is along the optic disc's nasal edge. 2D MRI tomographic images show sharp bulges at the back of the eyeball. The height map of the back of the eyeball shows dense contour lines in the central part. Note the spherical aberration (12th) is positive, indicating that the central part is prominently raised. **(C)** Peripapillary PS. Areas of marked retinal atrophy are seen around the optic disc. The 2D MRI tomographic image shows that the eyeball protruded significantly in the direction of the optic nerve. The height map of the back of the eyeball shows denser contour lines on the left (nasal side). Note the larger horizontal Tilt (2nd term). **(D)** Inferior PS. 2D MRI tomographic image shows that the posterior pole of the eyeball is prominent, and there is no significant horizontal tilt. The contour map of the back of the eyeball shows that the prominent position is lower. Note the large vertical tilt (1st term).

confirmed that conjecture. The values of the 6th-27th HOAs-RMS increased significantly in eyeballs with PS compared to eyeballs with HM. The combination of HOAs-RMS and defocus can distinguish PS from HM even better.

4.3 PS classifications

Different types of PS can cause retinal lesions in different parts, resulting in varying degrees of vision or visual field loss (Ohno-Matsui, 2014; Verkicharla et al., 2015; An et al., 2021; Lee et al., 2021). Many researchers have tried to propose a classification method for PS. Curtin divided PS into ten categories in 1977 (Curtin, 1977). On this basis, Ohno-Matsui divided PS into six categories, which is the most commonly used PS classification method (Ohno-Matsui et al., 2017). This study observed the proportion of different types of PS and the distribution difference of Zernike coefficients. The proportion of PS classification is basically consistent with previous research (Nagaoka et al., 2011; Ohno-Matsui et al., 2017). Wide macular PS accounted for the largest proportion, reaching 63.3%. The Zernike coefficients distribution of wide macular PS is characterized by large defocus. This is due to the wide macular PS eyeball showing a broad protrusion at the back, such as in Figure 6A. Although the posterior part of the eyeball is convex overall, the posterior pole is blunt. Compared with a perfectly spherical surface, the central part is relatively concaved. Therefore, the spherical term, which indicates the central local bulge is negative. In contrast, the narrow macular PS showed a greatly increased spherical term, such as in Figure 6B. This is because of the narrow central protrusion at the posterior pole. The eyeball of the peripapillary PS mainly showed a significant increase in horizontal tilt, which represented a tilt of the nose, while the optic nerve was located on the nasal side. The vertical tilt of the inferior PS was significantly reduced, which represented an increase in the inferior tilt. These results show the consistency between the Zernike coefficients and the actual eyeball geometry. In previous studies, eyeballs with an irregular or difficult-to-describe shape were defined as other classes, including double-edged staphyloma, etc (Ohno-Matsui et al., 2017). This also reflects that the traditional method has difficulty describing eyeballs in detail. Zernike analysis has the advantage of describing complex eyeball shapes in more detail and helps in the future automatic objective classification of PS.

5 Limitations

Firstly, the number of PS patients included in this study is relatively small. Therefore, we did not find the nasal PS and

other PS. Secondly, although the eyeball shape was quantitatively described in this study, the relationship with the degree of fundus damage in patients was not examined. In future studies, these should be achieved.

6 Conclusion

The Zernike polynomial can describe the morphology of the posterior eyeball well. The defocus, tilt, oblique astigmatism, coma, and HOAs-RMS of PS all had significant changes compared with HM. HOAs-RMS had the best effect in distinguishing PS from HM. In various types of PS, the changes in Zernike coefficients matched well with the morphological changes.

Data availability statement

The raw data supporting the conclusion of this article will be made available by the authors, without undue reservation.

Ethics statement

The studies involving human participants were reviewed and approved by the ethics committee of Tianjin Medical University Eye Hospital (NO. 2020KY-04). The patients/participants provided their written informed consent to participate in this study.

Author contributions

HR: Data analysis and interpretation and manuscript drafting. WF and BD: Data analysis. LL and YL: Manuscript revision. HX, DY, WD, and XZ: Data acquisition. BZ and RW: Study design.

Funding

This study was supported by grants from the Tianjin Health Science and Technology Project (No. TJWJ2021ZD006) and Tianjin Binhai New District Health Commission science and technology project (No. 2019BWKY022). The funding organization had no role in the design or conduct of this research.

Conflict of interest

Author WF is employed by QCraft Inc.

The remaining authors declare that the research was conducted in the absence of any commercial or financial relationships that could be construed as a potential conflict of interest.

Publisher's note

References

An, G., Dai, F., Wang, R., Liu, Z., Guo, J., Pan, M., et al. (2021). Association between the types of posterior staphyloma and their risk factors in pathological myopia. *Transl. Vis. Sci. Technol.* 10, 5. doi:10.1167/tvst.10.4.5

Avila, M. P., Weiter, J. J., Jalkh, A. E., Trempe, C. L., Pruett, R. C., and Schepens, C. L. (1984). Natural history of choroidal neovascularization in degenerative myopia. *Ophthalmology* 91, 1573–1581. doi:10.1016/s0161-6420(84)34116-1

Curtin, B. J. (1977). The posterior staphyloma of pathologic myopia. *Trans. Am. Ophthalmol. Soc.* 75, 67–86.

Hayashi, K., Ohno-Matsui, K., Shimada, N., Moriyama, M., Kojima, A., Hayashi, W., et al. (2010). Long-term pattern of progression of myopic maculopathy: A natural history study. *Ophthalmology* 117, 1595–1611. doi:10.1016/j.ophtha.2009.11.003

Holden, B. A., Fricke, T. R., Wilson, D. A., Jong, M., Naidoo, K. S., Sankaridurg, P., et al. (2016). Global prevalence of myopia and high myopia and temporal trends from 2000 through 2050. *Ophthalmology* 123, 1036–1042. doi:10.1016/j.ophtha.2016.01.006

Ishii, K., Iwata, H., and Oshika, T. (2011). Quantitative evaluation of changes in eyeball shape in emmetropization and myopic changes based on elliptic Fourier descriptors. *Invest. Ophthalmol. Vis. Sci.* 52, 8585–8591. doi:10.1167/iovs.11-7221

Lakshminarayanan, V., and Fleck, A. (2011). Zernike polynomials: A guide. *J. Mod. Opt.* 58, 545–561. doi:10.1080/09500340.2011.554896

Lee, K. M., Park, S. W., Kim, M., Oh, S., and Kim, S. H. (2021). Relationship between three-dimensional magnetic resonance imaging eyeball shape and optic nerve head morphology. *Ophthalmology* 128, 532–544. doi:10.1016/j.ophtha.2020.08.034

Lim, L. S., Matsumura, S., Htoon, H. M., Tian, J., Lim, S. B., Sensaki, S., et al. (2019). MRI of posterior eye shape and its associations with myopia and ethnicity. *Br. J. Ophthalmol.* 104, 1239–1245. doi:10.1136/bjophthalmol-2019-315020

Moriyama, M., Ohno-Matsui, K., Hayashi, K., Shimada, N., Yoshida, T., Tokoro, T., et al. (2011). Topographic analyses of shape of eyes with pathologic myopia by high-resolution three-dimensional magnetic resonance imaging. *Ophthalmology* 118, 1626–1637. doi:10.1016/j.ophtha.2011.01.018

Moriyama, M., Ohno-Matsui, K., Modegi, T., Kondo, J., Takahashi, Y., Tomita, M., et al. (2012). Quantitative analyses of high-resolution 3D MR images of highly myopic eyes to determine their shapes. *Invest. Ophthalmol. Vis. Sci.* 53, 4510–4518. doi:10.1167/iovs.12-9426

Nagaoka, N., Ohno-Matsui, K., Saka, N., Tokoro, T., and Mochizuki, M. (2011). Clinical characteristics of patients with congenital high myopia. *Jpn. J. Ophthalmol.* 55, 7–10. doi:10.1007/s10384-010-0896-8

Nagra, M., Gilmartin, B., and Logan, N. S. (2014). Estimation of ocular volume from axial length. *Br. J. Ophthalmol.* 98, 1697–1701. doi:10.1136/bjophthalmol-2013-304652

Ohno-Matsui, K., Akiba, M., Modegi, T., Tomita, M., Ishibashi, T., Tokoro, T., et al. (2012). Association between shape of sclera and myopic retinochoroidal lesions in patients with pathologic myopia. *Invest. Ophthalmol. Vis. Sci.* 53, 6046–6061. doi:10.1167/iovs.12-10161

Ohno-Matsui, K., Alkabes, M., Salinas, C., Mateo, C., Moriyama, M., Cao, K., et al. (2017). Features of posterior staphylomas analyzed in wide-field fundus images in patients with unilateral and bilateral pathologic myopia. *Retina* 37, 477–486. doi:10.1097/iae.0000000000001327

Ohno-Matsui, K., Lai, T. Y., Lai, C. C., and Cheung, C. M. (2016). Updates of pathologic myopia. *Prog. Retin Eye Res.* 52, 156–187. doi:10.1016/j.preteyeres.2015.12.001

Ohno-Matsui, K. (2014). Proposed classification of posterior staphylomas based on analyses of eye shape by three-dimensional magnetic resonance imaging and wide-field fundus imaging. *Ophthalmology* 121, 1798–1809. doi:10.1016/j.ophtha.2014.03.035

Ohno-Matsui, K., and Tokoro, T. (1996). The progression of lacquer cracks in pathologic myopia. *Retina* 16, 29–37. doi:10.1097/00006982-199616010-00006

Pope, J. M., Verkicharla, P. K., Sepehrband, F., Suheimat, M., Schmid, K. L., and Atchison, D. A. (2017). Three-dimensional MRI study of the relationship between eye dimensions, retinal shape and myopia. *Biomed. Opt. Express* 8, 2386–2395. doi:10.1364/boe.8.002386

Schwiegerling, J., and Greivenkamp, J. E. (1997). Using corneal height maps and polynomial decomposition to determine corneal aberrations. *Optom. Vis. Sci.* 74, 906–916. doi:10.1097/00006324-199711000-00024

Shinohara, K., Moriyama, M., Shimada, N., Nagaoka, N., Ishibashi, T., Tokoro, T., et al. (2013). Analyses of shape of eyes and structure of optic nerves in eyes with tilted disc syndrome by swept-source optical coherence tomography and three-dimensional magnetic resonance imaging. *Eye (Lond)* 27, 1233–1242. doi:10.1038/eye.2013.202

Shinohara, K., Shimada, N., Moriyama, M., Yoshida, T., Jonas, J. B., Yoshimura, N., et al. (2017). Posterior staphylomas in pathologic myopia imaged by widefield optical coherence tomography. *Invest. Ophthalmol. Vis. Sci.* 58, 3750–3758. doi:10.1167/iovs.17-22319

Shugyo, A., Koh, S., Inoue, R., Ambrosio, R., Jr., Miki, A., Maeda, N., et al. (2021). Optical quality in keratoconus is associated with corneal Biomechanics. *Cornea* 40, 1276–1281. doi:10.1097/ICO.0000000000002631

Spaide, R. F. (2014). *Pathologic myopia*. New York, NY: Springer, 167–176.

Tango, W. J. (1977). The circle polynomials of Zernike and their application in optics. *Appl. Phys.* 13, 327–332. doi:10.1007/bf00882606

Verkicharla, P. K., Ohno-Matsui, K., and Saw, S. M. (2015). Current and predicted demographics of high myopia and an update of its associated pathological changes. *Ophthalmic Physiol. Opt.* 35, 465–475. doi:10.1111/opo.12238

Wacker, K., McLaren, J. W., Amin, S. R., Baratz, K. H., and Patel, S. V. (2015). Corneal high-order aberrations and backscatter in fuchs' endothelial corneal dystrophy. *Ophthalmology* 122, 1645–1652. doi:10.1016/j.ophtha.2015.05.005

Wakazono, T., Yamashiro, K., Miyake, M., Nakanishi, H., Oishi, A., Ooto, S., et al. (2016). Association between eye shape and myopic traction maculopathy in high myopia. *Ophthalmology* 123, 919–921. doi:10.1016/j.ophtha.2015.10.031

Wang, J. Y., and Silva, D. E. (1980). Wave-front interpretation with Zernike polynomials. *Appl. Opt.* 19, 1510–1518. doi:10.1364/ao.19.001510

Wang, N. K., Wu, Y. M., Wang, J. P., Liu, L., Yeung, L., Chen, Y. P., et al. (2016). Clinical characteristics of posterior staphylomas in myopic eyes with axial length shorter than 26.5 millimeters. *Am. J. Ophthalmol.* 162, 180–190. doi:10.1016/j.ajo.2015.11.016

Xu, X., Fang, Y., Yokoi, T., Shinohara, K., Hirakata, A., Iwata, T., et al. (2019). Posterior staphylomas in eyes with retinitis pigmentosa without high myopia. *Retina* 39, 1299–1304. doi:10.1097/iae.0000000000002180

frontiers | Frontiers in Bioengineering and Biotechnology

TYPE Review
PUBLISHED 06 April 2023
DOI 10.3389/fbioe.2023.1144455

OPEN ACCESS

EDITED BY
J. Crawford Downs,
University of Alabama at Birmingham,
United States

REVIEWED BY
David Sánchez Porras,
University of Granada, Spain
Tu Hu,
Central South University, China

*CORRESPONDENCE
Dai-Jin Ma,
eyemdj@163.com

SPECIALTY SECTION
This article was submitted to Biomechanics, a section of the journal Frontiers in Bioengineering and Biotechnology

RECEIVED 14 January 2023
ACCEPTED 29 March 2023
PUBLISHED 06 April 2023

CITATION
He Y, Ma B-S, Zeng J-H and Ma D-J (2023), Corneal optical density: Structural basis, measurements, influencing factors, and roles in refractive surgery. *Front. Bioeng. Biotechnol.* 11:1144455. doi: 10.3389/fbioe.2023.1144455

Corneal optical density: Structural basis, measurements, influencing factors, and roles in refractive surgery

Ye He[1], Bo-Sheng Ma[2], Jun-Hao Zeng[3] and Dai-Jin Ma[1]*

[1]Changsha Aier Eye Hospital, Changsha, China, [2]Department of Ophthalmology, The Second Xiangya Hospital, Central South University, Changsha, China, [3]Xiangya School of Medicine, Central South University, Changsha, China

The cornea is the main refractive medium of the human eye, and its clarity is critical to visual acuity. Corneal optical density (COD) is an important index to describe corneal transparency. Intact corneal epithelial and endothelial cells, regular arrangement of collagen fibers in the stroma, and normal substance metabolism are all integral for the cornea to maintain its transparency. In the last two decades, the Pentacam Scheimpflug imaging system has emerged as a breakthrough for the measurement of COD (also called corneal densitometry). It has been found that a wide variety of factors such as age, refractive status, and corneal diseases can affect COD. Different corneal refractive surgery methods also change COD in different corneal regions and layers and affect visual acuity following the surgery. Thus, COD has gradually become a significant indicator to evaluate corneal health, one on which the attention of clinicians has been increasingly focused.

KEYWORDS

corneal optical density, corneal densitometry, pentacam scheimpflug imaging system, FS-LASIK, SMILE

1 Introduction

Visual acuity relies on proper transition and focusing of light through the cornea and other tissues before reaching the retina (Brown et al., 2020; Price et al., 2021). Located at the front of the eye, the cornea accounts for two-thirds of the total refraction therein. As such, its optical clarity critically affects the refraction of light and overall optical outcomes of the eye (Patel and Tutchenko, 2019; Mohan et al., 2022). The optical clarity of the cornea depends on its unique structure and biological characteristics, which include intact corneal epithelial and endothelial cells, regular arrangement of collagen fibers in the stroma, and normal substance metabolism (Onochie et al., 2019; Zhang et al., 2019; Mohan et al., 2022).

The measurement of corneal optical clarity began in the 1990s with concerns about the appearance of haze in the cornea following refractive surgery (Andrade et al., 1990). Because early measuring instruments possessed poor sensitivity and image acquisition, the measurement of the optical clarity of the cornea relied mainly on qualitative analysis, which was highly affected by the subjective experience of the clinician (Doughty and Jonuscheit, 2019). The Pentacam Scheimpflug imaging system solves this problem. Through a rotating Scheimpflug camera, the system is capable of assessing corneal optical densitometry (COD) to objectively and quantitatively evaluate the corneal optical clarity (Lou et al., 2022). The range of COD is defined as 0-100. When COD is 0, light can pass through the cornea uninhibited. When COD is 100, light cannot pass through the cornea at all (Takacs et al., 2011).

Recent studies based on Pentacam Scheimpflug imaging system have found that COD can be affected by edema or inflammation, both of which cause structural or biological changes in the cornea in various corneal diseases such as infectious keratitis and keratoconus (Lopes et al., 2014; Orucoglu et al., 2014; Sorcha et al., 2014). Different corneal refractive surgery methods also have distinct effects on COD, and changes in COD after surgery have a certain correlation with visual quality (Lazaridis et al., 2017; Wei et al., 2020; Hou et al., 2022). COD also gradually increases with advancing age in healthy elderly people (Hillenaar et al., 2011). In recent decades, COD has gradually become an important optical index to assess corneal health both in healthy people and in patients with corneal diseases.

2 Corneal structure and optical clarity

The cornea is ecial tissue located at the front of the eye with a convex meniscus shape and high transparency. Its equivalent refractive force is about 43 D, accounting for more than two-thirds of the eye's refraction (Otri et al., 2012; Patel and Tutchenko, 2019). The cornea is an avascular tissue with a complex composition and regular arrangement, and its structure is the key to maintaining its optical clarity (Yu et al., 2022).

2.1 Corneal epithelium

The corneal epithelium supports the tear film, protects underlying structures, and maintains the cornea's transparency (Lavker et al., 2020). The process of oxygen transport and metabolism of the corneal epithelium are vital to corneal clarity. Vicente *et al.* reported that, when the cornea suffered from hypoxia and hypercapnia due to long-term contact lens wearing, the corneal epithelial cells may suffer from acidosis and a subsequent decrease in corneal transparency (Moreno et al., 2022). Molecules such as superoxide dismutase (SOD), glutathione peroxidase (GPX), and catalase (CAT) have been reported to be associated with the normal antioxidant function of corneal epithelial cells (Chen et al., 2009).

2.2 Bowman's layer

Bowman's layer is an 8-12 μm thick layer formed by non-cellular aggregates that help the cornea maintain its shape (Cankaya et al., 2018). In healthy adults, COD was indicated to be negatively correlated with the thickness of Bowman's layer (Pekel et al., 2018). Following femtosecond laser-assisted LASIK, areas of focal disruption of the Bowman's layer were observed to correspond with areas of interface haze, suggesting that decreased corneal transparency is associated with damage to the Bowman's layer (Vaddavalli Pravin et al., 2012).

2.3 Corneal stroma

The corneal stroma is one of the most precisely arranged and transparent tissues in the cornea (Espana and Birk, 2020). The normal arrangement of collagen fibers in the stroma and the stability of stromal cells are critical to corneal clarity. Collagen type I is the primary collagen in the corneal stroma (Song et al.,

TABLE 1 Measurement methods of corneal optical clarity.

Methods	Types	Technical principle	Advantages	Disadvantage	Refs
Slit-lamp microscope	Qualitative	Evaluating corneal transparency by haze grading	Simple and practicable in use	Measurement is related to the experience and subjectivity of clinicians, and cannot objectively reflect the degree of corneal clarity	Anumanthan et al. (2017)
Ultrasound biomicroscope (UBM)	Qualitative	B-mode ultrasound	UBM can be used to observe the location, size, and range of corneal haze	Only moderate and above moderate haze can be measured	Kendall et al. (2015)
In vivo confocal microscopy	Qualitative	Confocal microscopy	Each sublayer of the cornea can be observed and analyzed by different light intensities	Usually needs to contact the cornea; potentially causes slight shape changes in the cornea, leading to potential measurement errors	McLaren et al. (2016)
Orbscan topography	Qualitative	Placido disc technique combined with the slit scan technique	Can visually display the anterior and posterior corneal surface height, corneal curvature, corneal astigmatism, and corneal thickness	Accuracy is significantly lower than ultrasonic pachymetry	Altan-Yaycioglu et al. (2007)
Optical coherence tomography (OCT)	Qualitative	Based on near-infrared light waves to image microstructures of the cornea	Has a higher resolution and faster speed than that of UBM	Penetrating power is weak and, when corneal opacity is high, is prone to measurement bias	Mori et al. (2009)
Pentacam Scheimpflug imaging system	Quantitative	Based on the Scheimpflug principle, in which the camera and light source speedily rotate and scan the eye	Boasts high resolution, accurate positioning, repeatable measurements, easy operation, non-contact, and quantitative analysis of corneal optical density	Good cooperation of subjects is required to avoid measurement bias	Garzón et al. (2017)

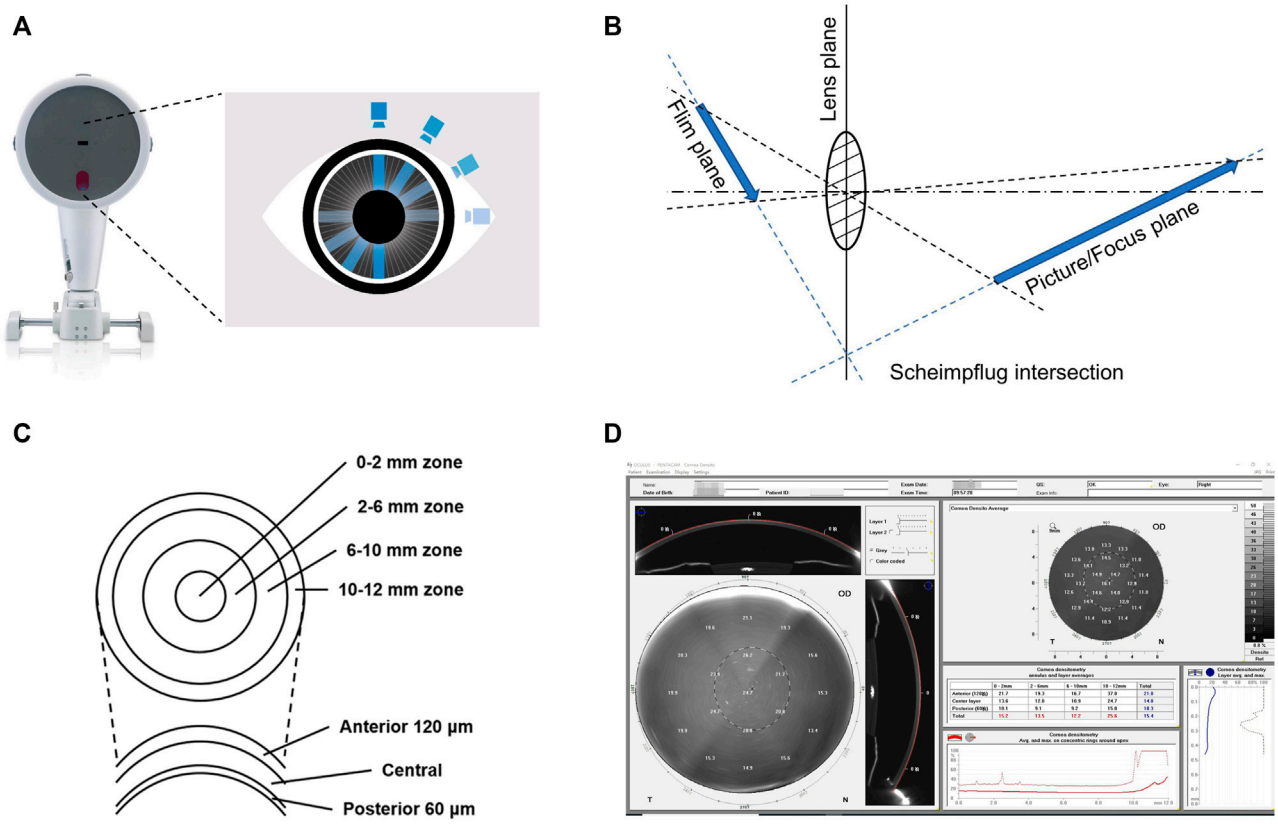

FIGURE 1
Measurement of corneal optical density by the Pentacam Scheimpflug imaging system. **(A)** Schematic representation of the rotation of the Scheimpflug camera of the Pentacam Scheimpflug imaging system. **(B)** Schematic representation of the Scheimpflug principle. Its main feature is that the plane of the film, the lens, and the picture/focus plane cut each other in a Scheimpflug intersection. Thus, the focused region is increased, and the sharpness of the image is improved. **(C)** Schematic representation of the corneal zones and layers defined by the Pentacam Scheimpflug imaging system. **(D)** Example of the software panel of the corneal optical densitometry in the Pentacam Scheimpflug imaging system. Displayed as a grayscale coded map, the average COD in different corneal zones and layers can be individually assessed and automatically displayed in the table chart.

2021). After corneal refractive surgery, collagen type III will appear (Abdelkader, 2013; Abdelkader, 2016). Compared with collagen type I, collagen type III is thicker in diameter and irregularly arranged (Gandhi and Jain, 2015). The appearance of a large number of collagen type III fibers induces structural changes in the stroma and consequently leads to a decrease in corneal transparency (Gibson et al., 2013).

Following injury of the corneal stroma, the repair process begins with the activation of cytokines to remove damaged cells. Corneal epithelial cells secrete cytokines that induce stromal cells to transform into activated stromal fibroblasts (SFs) (Kowtharapu et al., 2018). SFs have low crystalline contents that lead to a decrease in corneal transparency. In addition, SFs are able to synthesize large-diameter collagen fibers and abnormal extracellular matrix, leading to a higher refractive index and the appearance of corneal haze (Wang et al., 2003). Ha *et al.* have indicated the correlation between corneal haze and COD, and the therapeutic effect of mitomycin C on corneal haze (Ha et al., 2010). Mitomycin C has an antiproliferative effect on corneal SFs that prevent the decrease of corneal transparency (Carlos De Oliveira and Wilson, 2020).

2.4 Descemet's membrane

Descemet's membrane is a dense, thick, relatively transparent, and acellular basement membrane that separates the posterior stroma from the endothelial layer (de Oliveira and Wilson, 2020). Descemet's membrane originates from the secretion of endothelial cells at different stages of development and gradually thickens (Eghrari et al., 2015). It plays an important role in the maintenance of corneal transparency as a critical regulatory structure. Together with the endothelium, it is involved in the trafficking of substances, such as transforming growth factor beta (TGFβ) and platelet-derived growth factor (PDGF), that regulate stromal fibrosis and edema and may therefore influence COD (Medeiros et al., 2018).

2.5 Corneal endothelium

The corneal endothelium is located on the posterior corneal surface and lacks self-renewal capacity (Kumar et al., 2022). It keeps the corneal stroma in a relatively dehydrated state *via* transporting fluid from the corneal stroma to the aqueous humor, which is critical to corneal

TABLE 2 Influencing factors of corneal optical density in healthy people and patients with corneal diseases.

Factors	Impact	Descriptions of its impact on corneal optical density	Refs
Ages	Positive	Corneal optical density is significantly correlated with age and corneal thickness; corneal optical density increases with age in the healthy population	Cankaya et al. (2018)
	Non-relative	Corneal optical density is not correlated with age in Chinese patients with myopia	Wei et al. (2020)
Gender	Non-relative	There were no significant differences in corneal optical density between males and females	Sorcha et al. (2014)
	Relative	Females have a higher total corneal optical density than that of men	Garzón et al. (2017)
Regions	Relative	The average value of total corneal optical density in studies from different countries are distinct	Otri et al. (2012), Patel and Tutchenko (2019)
Soft contact lens wear	Positive	Corneal optical density of soft contact lens wearers was significantly higher than that of healthy participants	Ozek et al. (2021)
Orthokeratology lens wear	Positive	Long-term orthokeratology treatment could significantly increase the corneal optical density in young orthokeratology lens wearer	Zhao et al. (2022)
Keratoconus	Positive	Cornea optical density readings of patients with keratoconus were higher than those of the healthy population and correlated with the severity of keratoconus	Shen et al. (2019)
Infectious keratitis	Positive	After pathogenic bacteria invade the cornea, it will lead to a decrease in corneal transparency and a increase in corneal optical density	Orucoglu et al. (2014)
Corneal transplantation	Positive	Corneal optical density in eyes treated by various keratoplasty was significantly higher than that of the normal controls	Koh et al. (2012)
PRK	Positive	The postoperative corneal optical density was significantly higher than that before the surgery	Poyales et al. (2017)
LASIK	Non-relative	After 1 year of LASIK, the corneal optical density did not change significantly	Fares et al. (2012)
	Positive	Corneal optical density of patients with epithelial ingrowth after LASIK is significantly increased	Tian (2018)
FS-LASIK	Positive	Corneal optical density was found only in the peripheral zone (10-to-12 mm annulus) at 1 month after FS-LASIK.	Poyales et al. (2017)
	Negative	A long-term prospective study on FS-LASIK indicated that corneal optical density significantly decreased at 5 years post-surgery compared with the baseline	Wei et al. (2020)
SMILE	Non-relative	At 6-12 months after surgery, the corneal optical density of patients has no significant change from baseline after SMILE.	Wei et al. (2020)
	Negative	Corneal optical density significantly decreased in 3 months and 3 years after SMILE.	Han et al. (2017)

transparency (Sie et al., 2020). Tekin *et al.* indicated that COD was significantly correlated with cell density and percentage of hexagonal cells in healthy corneas (Tekin et al., 2017). However, Dorota *et al.* came to a different conclusion in patients with the pseudoexfoliation syndrome (PEX), which is characterized by the excessive production of granular amyloid-like protein fibers in the anterior segment (Tomczyk-Socha et al., 2022). Increased COD was observed in the corneal epithelium in the PEX group, whereas it was not associated with endothelial cell density (Urbaniak et al., 2018). This is possibly caused by the formation of a fibrous layer that is loosely attached to Descemet's membrane in advanced stages of PEX, and it may increase the COD of the corneal endothelium.

3 Measurement methods of the corneal optical density

Due to concerns about corneal haze after refractive surgery, the measurement of corneal optical clarity began in the 1990s (Andrade et al., 1990). In the early stages, the measurement of the optical clarity of the cornea was mainly qualitative analysis using such instruments as the slit-lamp microscope, ultrasound biomicroscope, and optical coherence tomograph (Table 1). Quantitative evaluation of the corneal optical clarity began with the emergence of Pentacam Scheimpflug imaging system (Lou et al., 2022).

3.1 Qualitative measurements of corneal optical clarity

3.1.1 Slit-lamp microscope

The slit-lamp microscope is one of the most widely used instruments in ophthalmic diagnosis. It can be used to observe the corneal haze to evaluate the optical clarity of the cornea (Anumanthan et al., 2017). According to the Fantes scale, the level of haze is graded as: grade 0, completely clear; grade 1, haze can be easily found under the slit-lamp microscope, but it does not affect the observation of iris details; grade 2: haze mildly affects the observation of iris details; grade

3: haze moderately affects the observation of iris and lens; grade 4: the cornea is so cloudy that the iris is totally obscured (Fantes et al., 1990). Although this grading method is simple to use, the grading is often dependent on the experience and subjectivity of clinicians. As such, it cannot objectively quantify the degree of haze. In order to quantify the levels of haze, Hollingsworth *et al.* devised a grading scale to demonstrate alterations in corneal morphology in keratoconus using *in vivo* confocal microscopy (Hollingsworth et al., 2005).

3.1.2 Ultrasound biomicroscopy (UBM)

UBM is able to objectively image the anterior segment of the eye at microscopic resolution (Pavlin et al., 1992). It can accurately determine the size, location, and range of corneal lesions, and it has been widely used in diseases related to changes in corneal clarity, including keratoconus, corneal dystrophy, and corneal scar (Silverman, 2009; Kendall et al., 2015). After photorefractive keratectomy, UBM examination is carried out to document and follow the haze phenomenon (Nagy et al., 1996). However, UBM is only able to assess moderate and above-moderate haze; subtle haze is not observable with UBM (Nagy et al., 1996).

3.1.3 In vivo confocal microscopy

In vivo confocal microscopy was first used for the non-invasive assessment of corneal injury and disease at the cellular level by Cavanagh in the 1990s (Cavanagh et al., 1993). *In vivo* confocal microscopy provides multidimensional high-resolution images of the corneal structure at each layer *in vivo*, which reduces the false results caused by specimen processing (Bilgihan et al., 2019). According to the observation of corneal haze, *in vivo* confocal microscopy can determine the structures that contribute to corneal haze at a high spatial resolution (McLaren et al., 2016). In comparison with the Pentacam Scheimpflug camera, *in vivo* confocal microscopy is more suitable for measuring backscatter in the corneas with the highest degree of haze (McLaren et al., 2016). However, the microscope usually needs to contact the cornea; thus the instrument will cause slight shape changes of the cornea in measuring corneal transparency, leading to potential measurement errors. Additionally, while the accuracy of confocal microscopy is high in the central cornea. It is relatively poor in the peripheral cornea (Takacs et al., 2011).

3.1.4 Orbscan topography

Orbscan topographer is a hybrid slit-scanning and Placido disc corneal topographer that can visually display the anterior and posterior corneal surface height, corneal curvature, corneal astigmatism, and complete corneal thickness (Fam et al., 2005; Karimian et al., 2011). It was demonstrated that Orbscan readings were inversely correlated to haze grade (Fakhry et al., 2002; Altan-Yaycioglu et al., 2007). However, its accuracy was significantly lower than ultrasonic pachymetry, suggesting that Orbscan topography alone is insufficient for measuring corneal haze (Altan-Yaycioglu et al., 2007). Moreover, Orbscan topography is a qualitative analysis and thus cannot quantitatively describe the clarity of the cornea.

3.1.5 Optical coherence tomography (OCT)

OCT is a high-resolution optical imaging technique that utilizes near-infrared light waves to image the microstructures of different tissue types (Yang et al., 2022). It was first applied for *in vivo* measurements of the human retinal structure by Swanson et al. (1993). Rahul *et al.* used OCT to assess corneal opacity and found that it could simulate the effect of phototherapeutic keratectomy performed for the removal of corneal opacity (Mori et al., 2009). OCT has a higher resolution and faster speed than that of UBM. However, UBM can better penetrate opaque or cloudy tissues, thereby improving the observation of the ciliary body, posterior iris structures, and anterior chamber in the case of corneal opacity, scarring, and edema (Ursea and Silverman, 2010).

3.2 Measurement of the corneal optical density with Pentacam Scheimpflug imaging system

The emergence of the Pentacam Scheimpflug imaging system represents a breakthrough in the evaluation of COD, which is an important quantitative index to evaluate corneal transparency.

3.2.1 Principles of Pentacam Scheimpflug imaging system

The system is based on the Scheimpflug principle (Figure 1A, B), in which the rapidly rotating Scheimpflug camera and light source scan the eye, obtaining 50 Scheimpflug images in less than 2 seconds (Efron, 2019). At the same time, using a second pupil camera, eye movements are detected and automatically corrected (Huang et al., 2014; Cavas-Martínez et al., 2016). Pentacam Scheimpflug imaging system measures COD in standardized gray units (GSU) on a scale of 0-100 to quantify corneal transparency at different zones and depths within the cornea (Hsieh et al., 2021).

3.2.2 Method of measuring corneal optical density

During the examination, the patient remains in a standardized dim-light condition for 5-10 min and is subjected to the test in the natural state of the pupil (Pakbin et al., 2022). The patient, who is seated with their chin fixed on a mandibular brace, is asked to stare at a fixed target in the center of the Pentacam blue stripe without blinking or moving their eyes. The examiner selects the measurement mode (usually 25 segments/second) for automatic scanning and acquires data for 2 seconds (Gao et al., 2016). Pentacam Scheimpflug imaging system divides the corneal area into four concentric zones and three layers with different depths (Figure 1C, D) (Li et al., 2021).

4 Factors influencing COD in healthy people and patients with corneal diseases

With Pentacam Scheimpflug imaging system, researchers have found that COD varies significantly between healthy people and patients with corneal diseases, as well as between people of different ages and regions (Table 2). Based on emerging evidence, COD has gradually become one significant indicator of corneal health.

4.1 Age and gender

COD was found to increase with age in healthy Caucasians from Belgium (Sorcha et al., 2014). In healthy Spanish participants,

change in COD was also positively associated with age in all layers of the cornea (the anterior, central, and posterior layers) (Garzón et al., 2017). However, regarding the concentric zones of the cornea, the change of COD was correlated with age only in the 6-10 mm annulus. In healthy Turkish participants, Ali *et al.* demonstrated a significant positive correlation between total COD and age (Cankaya et al., 2018). With *in vivo* confocal microscopy, Toine *et al.* also found that backscatter in the anterior stroma was significantly increased in healthy participants aged 50 years or older in the Netherlands (Hillenaar et al., 2011). However, Wei *et al.* indicated that COD was not statistically correlated with age in Chinese patients with myopia (Wei et al., 2020). The correlation between COD and age may be caused by the reduction of endothelial cells, which are critical to corneal clarity (Gipson, 2013).

Regarding gender, some studies demonstrate that the CODs of males and females are not significantly different from one another (Sorcha et al., 2014; Cankaya et al., 2018). However, a Spanish study has indicated that women tend to have slightly higher COD (16.60 ± 1.83 GSU) than men (16.22 ± 1.54 GSU) (Garzón et al., 2017). The influence of gender on COD still needs to be further confirmed.

4.2 Regional differences

The average values of total COD in studies from different countries are also distinct. A study from the UK showed that the average COD in healthy subjects (64 eyes) was 12.3 ± 2.4 GSU (Otri et al., 2012). A Japanese study (36 eyes) indicated that the average value of total COD in healthy Japanese was 16.4 ± 1.7 GSU (Ozek et al., 2021). A study based on healthy Caucasians from Belgium (794 eyes) indicated that the average COD of the 12 mm-diameter zone was 19.74 ± 3.89 GSU (Sorcha et al., 2014). In Spanish healthy participants (338 eyes), the average COD of the total zones was 16.46 ± 1.85 GSU (Garzón et al., 2017). These distinct results suggest that there may be regional differences in COD. This issue will be addressed by a large-scale international study in the future.

4.3 Soft contact lens wear

Soft contact lens wear may cause poor tear film dynamics, inflammatory events, and potential contact lens disease, leading to anatomical and physiological changes in the cornea (Kaido et al., 2020; Mickles et al., 2021; Wang and Jacobs, 2022). A study based on soft contact lens wearers demonstrated that the COD of anterior 0-6 mm annular zones was significantly higher than that of healthy participants; however, the CODs of the 6-12 mm zone in the two groups had no significant differences (Ozek et al., 2021). This change could be due to poor tear function and inflammatory events in the anterior 0-6 mm zone of the cornea, where the soft contact lens interacts with the cornea (Muhafiz et al., 2019).

4.4 Orthokeratology lens wear

A number of studies indicated that orthokeratology lens wear could slow the progression of myopia in school-aged children (Hiraoka, 2022). With Pentacam Scheimpflug imaging system, Zhao *et al.* indicated that long-term orthokeratology treatment (about 2 years) could significantly increase the COD of the 0-10 mm diameter area of the cornea in young orthokeratology lens wearers (10.43 ± 2.03 years old) (Zhao et al., 2022). Moreover, COD changes were associated with the fitting mode during the first year, and the COD did not significantly reduce after 1 month of discontinuation (Zhao et al., 2022). This is basically consistent with the effect of orthokeratology lenses, which flatten the central area and steepen the mid-peripheral area in the cornea (Alharbi and Swarbrick, 2003).

4.5 Keratoconus

In recent years, COD has gradually become an indicator of corneal health in ophthalmic diagnosis. Lopes *et al.* found that COD was significantly increased in Brazilian patients with keratoconus in comparison with healthy subjects and was positively correlated with the severity of keratoconus (Lopes et al., 2014). A study based on Chinese subjects also reached a similar conclusion (Shen et al., 2019). Additionally, the authors demonstrated that COD values for the anterior layers (0-6 mm), central layers (0-6 mm), posterior layer (2-6 mm), and total layers (0-6 mm) were significantly associated with the stiffness parameter-applanation time 1, which is an important index of corneal rigidity (Shen et al., 2019). Moreover, it was found that the COD of Down syndrome patients with keratoconus showed a significant increase in the middle thickness layer in the 6 mm zone compared to that of Down syndrome patients whose corneas were steeper and thinner than normal (Asgari et al., 2020). Myriam and Ali *et al.* also indicated that, due to the excessive collagen fibers proliferation, the COD of the stromal layer was significantly increased in keratoconus patients after corneal collagen cross-linking (Kim et al., 2016; Böhm et al., 2019; Mahdavi Fard et al., 2019).

4.6 Infectious keratitis

In infectious keratitis, corneal ulcers will occur after invasion of viruses, bacteria, and other pathogenic factors into the cornea (Cabrera-Aguas et al., 2022). Faik *et al.* reported that archipelago keratitis led to a significant increase in COD (Orucoglu et al., 2014). Following treatments with antiviral or antibacterial drugs, the infiltrates were able to be reduced within 5 weeks. The initial changes were unable to be observed *via* slit-lamp microscopy, but measurement of the COD allowed the evaluation of therapeutic improvement in corneal clarity, which was decreased from 96.5 to 38.6 GSU (Orucoglu et al., 2014). In bacterial keratitis, COD of the inflamed area was significantly increased. Even after 1 month, when the corneal wound was almost healed, COD was still higher than that of the adjacent normal corneal area (Otri et al., 2012). Therefore, measuring COD with Pentacam Scheimpflug imaging system may serve as a powerful tool to assess the severity of infectious keratitis and the efficacy of drugs therefor.

4.7 Corneal transplantation (keratoplasty)

Corneal transplantation is widely used following corneal damage (Català et al., 2022). Complications such as acute

rejection and/or corneal infection are the main causes of corneal transplant failure (Armitage et al., 2019). Salvatore *et al.* found that, following Bowman's layer transplantation, the transparency of the cornea decreased, mostly in the central and Bowman's layer transplantation posterior layers where the graft had been placed (Luceri et al., 2016). Moreover, a study based on various selective lamellar keratoplasty procedures demonstrated that COD in eyes treated by different keratoplasties was significantly higher than that of normal controls (Koh et al., 2012). These studies suggest that the measurement of COD could provide a basis for clinical diagnosis after corneal transplantation.

5 Roles of the corneal optical density after refractive surgery

With the improvement of corneal refractive surgery, most patients can obtain better visual acuity after surgery (Ang et al., 2021). However, due to the degree of laser ablation, corneal haze, poor wound repairing, and other reasons, there is still a small percentage of patients who do not experience the expected outcomes (Jahadi Hosseini et al., 2016; Chang et al., 2022). Corneal transparency and corneal optical density may be affected by damage to the cornea and affect the visual acuity after corneal refractive surgery (Savini et al., 2016; Charpentier et al., 2021).

5.1 Photorefractive keratectomy (PRK)

Corneal haze is a major complication following PRK, one that causes decreased visual acuity, refractive regression, and alterations in the quality of vision (Charpentier et al., 2021). Many studies have indicated that COD after PRK is significantly higher than before surgery (Cennamo et al., 2011; Takacs et al., 2011; Poyales et al., 2017). Increased ablation depth during surgery causes more serious corneal damage and a higher COD (Charpentier et al., 2021). At 3 months post-surgery, a decreased level of haze was associated with a reduction in COD (Boulze-Pankert et al., 2016). In order to evaluate the long-term effect of PRK on corneal densitometry, a recent study was carried out based on myopic patient who had photorefractive keratectomy more than 22 years (Montorio et al., 2020). The authors demonstrated that the COD of the anterior layer in the central zone of the cornea was significantly increased in eyes that had been operated on with greater ablation depth in comparison with unoperated eyes (Montorio et al., 2020). However, there was no significant difference in the CODs of eyes operated on with lower ablation depth and unoperated eyes (Montorio et al., 2020).

5.2 Laser-assisted in situ keratomileusis (LASIK)

In the past decade, LASIK has been a popular ophthalmologic surgy to correct myopia (Liu et al., 2021). Usama *et al.* reported that LASIK had good visual outcomes and did not significantly alter COD 1 year after LASIK (Fares et al., 2012). This result indicates that LASIK has less effect on corneal transparency than does PRK (Gadde et al., 2020). Some scholars have found that the COD of patients with epithelial ingrowth after LASIK is significantly increased, suggesting that COD could be used as an objective measurement of the level and progression of epithelial ingrowth following LASIK (Adran et al., 2017; Tian, 2018).

5.3 Femtosecond LASIK (FS-LASIK)

Following FS-LASIK, Poyales *et al.* reported that significant changes in COD were found only in the peripheral zone (10-to-12 mm annulus) at 1 month after surgery (Poyales et al., 2017). Giacomo *et al.* reported that the COD of myopic patients increased in the 0-10 mm region of the anterior cornea after FS-LASIK, but this situation gradually reversed within 6 months (Savini et al., 2016). However, the changes in COD were still significant in the annular zone ranging from 6 to 10 mm, where the flap edge was located (Savini et al., 2016). The anterior layer and middle layer within the range of 6-10 mm usually mark the edge of the corneal flap. When the basement membrane is damaged, fibrosis will be repaired, potentially resulting in a drop in corneal clarity (Stramer et al., 2003). A long-term prospective study on patients 5 years after FS-LASIK demonstrated that the COD at all corneal zones significantly decreased in comparison with the baseline, indicating that the clarity of the cornea could continue to improve over a long period following FS-LASIK (Wei et al., 2020).

5.4 Small incision lenticule extraction (SMILE)

It is not needed to make a corneal flap in SMILE; this permits a smaller incision and thus less damage to the cornea (Jiang et al., 2022). Apostolos *et al.* reported that the total COD at the annular zone of 0-6 mm showed no significant change 3 months after SMILE in comparison with preoperative values (Lazaridis et al., 2017). In addition, the total COD at the annular zone of 0-6 mm showed a weak negative association with lenticular thickness after SMILE (Lazaridis et al., 2017). Another study based on SMILE also indicated a negative correlation between the COD and corneal thickness, showing a significant reduction in postoperative COD 3 months after SMILE (Alio del Barrio et al., 2021). Because the number of keratocytes and collagen fibrils is associated with the corneal optical property, the reduction in COD may be a result of the decrease of overlying stroma that reduces backscatter components (Li et al., 2013; Lazaridis et al., 2017). Furthermore, animal study has shown that SMILE has a low level of postoperative inflammation and keratinocyte reaction after the surgery (Dong et al., 2014).

Some studies have compared the changes of COD after FS-LASIK and SMILE. Wei et al. reported that the change in COD of the anterior and central layers in SMILE was significantly smaller than that in FS-LASIK at 5 years post-surgery (Wei et al., 2020). Hou et al. indicated that, at 12 months post-surgery, patients who underwent SMILE had lower corneal density in all areas than those who underwent FS-LASIK (Hou et al., 2022). However, Shajari et al. came to a different conclusion; they followed up on changes in COD 1 year after SMILE or FS-LASIK and found no significant difference in COD between the two groups (Shajari et al., 2018).

To sum up, COD has been a significant index to evaluate corneal recovery after refractive surgery.

6 Conclusion

Corneal clarity plays a key role in visual acuity. To date, COD as measured by Pentacam Scheimpflug imaging system is the most widely used quantitative index for the evaluation of corneal clarity. Age, regional differences, contact lens wear, and corneal diseases can affect COD. COD increases in different regions of the cornea after surface refractive surgery such as PRK and LASIK. The increase of COD after SMILE and FS-LASIK may be closely related to postoperative corneal edema, corneal stromal fiber hyperplasia, and corneal inflammation. In addition, the change of COD in SMILE was smaller than that of FS-LASIK. The different postoperative COD changes between SMILE and FS-LASIK may be related to the distinct level of inflammatory reaction after the two surgeries. In sum, COD is an important indicator to evaluate the severity of corneal diseases and corneal injury and recovery after corneal refractive surgery.

Author contributions

D-JM was the major contributor to the design of the study. YH was the major contributor to manuscript writing, and figure creation. B-SM and J-HZ assisted in the data collection and analysis. All authors have read and approved the final manuscript.

Funding

Financial support was provided by the Scientific Research Fund of Aier Eye Hospital Group (AF2109D14).

Conflict of interest

The authors declare that the research was conducted in the absence of any commercial or financial relationships that could be construed as a potential conflict of interest.

The reviewer TH declared a shared parent affiliation with the authors BM and JZ to the handling editor at the time of review.

Publisher's note

References

Abdelkader, A. (2013). Corneal biomechanical properties and their correlates with healing process after descemetic versus pre-descemetic lamellar keratoplasty. *Eur. J. Ophthalmol.* 23, 652–657. doi:10.5301/ejo.5000279

Abdelkader, A. (2016). Effect of fibrin glue on corneal lamellar healing and how it correlates to biomechanical properties: Biomechanical wavefront analysis and confocal study. *Eye Vis. (Lond)* 3, 15. doi:10.1186/s40662-016-0046-6

Adran, D., Vaillancourt, L., Harissi-Dagher, M., Kruh, J. N., Syed, Z. A., Robinson, S., et al. (2017). Corneal densitometry as a tool to measure epithelial ingrowth after laser *in situ* keratomileusis. *Cornea* 36, 406–410. doi:10.1097/ico.0000000000001114

Alharbi, A., and Swarbrick, H. A. (2003). The effects of overnight orthokeratology lens wear on corneal thickness. *Invest. Ophthalmol. Vis. Sci.* 44, 2518–2523. doi:10.1167/iovs.02-0680

Alio Del Barrio, J. L., Parafita-Fernandez, A., Canto-Cerdan, M., Alio, J. L., and Teus, M. (2021). Evolution of corneal thickness and optical density after laser *in situ* keratomileusis versus small incision lenticule extraction for myopia correction. *Br. J. Ophthalmol.* 105, 1656–1660. doi:10.1136/bjophthalmol-2020-316601

Altan-Yaycioglu, R., Pelit, A., and Akova, Y. A. (2007). Comparison of ultrasonic pachymetry with orbscan in corneal haze. *Graefe's Archive Clin. Exp. Ophthalmol.* 245, 1759–1763. doi:10.1007/s00417-007-0578-5

Andrade, H. A., Mcdonald, M. B., Liu, J. C., Abdelmegeed, M., Varnell, R., and Sunderland, G. (1990). Evaluation of an opacity lensometer for determining corneal clarity following excimer laser photoablation. *Refract Corneal Surg.* 6, 346–351. doi:10.3928/1081-597x-19900901-10

Ang, M., Gatinel, D., Reinstein, D. Z., Mertens, E., Alió Del Barrio, J. L., and Alió, J. L. (2021). Refractive surgery beyond 2020. *Eye* 35, 362–382. doi:10.1038/s41433-020-1096-5

Anumanthan, G., Sharma, A., Waggoner, M., Hamm Chuck, W., Gupta, S., Hesemann Nathan, P., et al. (2017). Efficacy and safety comparison between suberoylanilide hydroxamic acid and mitomycin C in reducing the risk of corneal haze after PRK treatment *in vivo*. *J. Refract. Surg.* 33, 834–839. doi:10.3928/1081597x-20170921-02

Armitage, W. J., Goodchild, C., Griffin, M. D., Gunn, D. J., Hjortdal, J., Lohan, P., et al. (2019). High-risk corneal transplantation: Recent developments and future possibilities. *Transplantation* 103, 2468–2478. doi:10.1097/tp.0000000000002938

Asgari, S., Aghamirsalim, M., Mehravaran, S., and Hashemi, H. (2020). Effect of Down syndrome and keratoconus on corneal density and volume: A triple comparative study. *Sci. Rep.* 10, 9098. doi:10.1038/s41598-020-66108-4

Bilgihan, K., Yesilirmak, N., Altay, Y., Tefon, A. B., Ozdemir, H. B., Ozdogan, S., et al. (2019). Evaluation of long-term corneal morphology after photorefractive keratectomy by *in vivo* confocal microscopy and specular microscopy; 20-year follow-up. *Eye Contact Lens* 45, 360–364. doi:10.1097/icl.0000000000000585

Böhm, M., Shajari, M., Remy, M., and Kohnen, T. (2019). Corneal densitometry after accelerated corneal collagen cross-linking in progressive keratoconus. *Int. Ophthalmol.* 39, 765–775. doi:10.1007/s10792-018-0876-4

Boulze-Pankert, M., Dariel, R., and Hoffart, L. (2016). Corneal scheimpflug densitometry following photorefractive keratectomy in myopic eyes. *J. Refract. Surg.* 32, 788–791. doi:10.3928/1081597x-20160720-02

Brown, C. E., Waring, G. O. I. V., and Rocha, K. M. (2020). Redefining vision assessment. *Curr. Opin. Ophthalmol.* 31, 225–233. doi:10.1097/icu.0000000000000664

Cabrera-Aguas, M., Khoo, P., and Watson, S. L. (2022). Infectious keratitis: A review. *Clin. Exp. Ophthalmol.* 50, 543–562. doi:10.1111/ceo.14113

Cankaya, A. B., Tekin, K., Kiziltoprak, H., Karahan, S., and Yilmazbas, P. (2018). Assessment of corneal backward light scattering in the healthy cornea and factors affecting corneal transparency. *Jpn. J. Ophthalmol.* 62, 335–341. doi:10.1007/s10384-018-0584-7

Carlos De Oliveira, R., and Wilson, S. E. (2020). Biological effects of mitomycin C on late corneal haze stromal fibrosis following PRK. *Exp. Eye Res.* 200, 108218. doi:10.1016/j.exer.2020.108218

Català, P., Thuret, G., Skottman, H., Mehta, J. S., Parekh, M., Ní Dhubhghaill, S., et al. (2022). Approaches for corneal endothelium regenerative medicine. *Prog. Retin. Eye Res.* 87, 100987. doi:10.1016/j.preteyeres.2021.100987

Cavanagh, H. D., Petroll, W. M., Alizadeh, H., He, Y. G., Mcculley, J. P., and Jester, J. V. (1993). Clinical and diagnostic use of *in vivo* confocal microscopy in patients with corneal disease. *Ophthalmology* 100, 1444–1454. doi:10.1016/s0161-6420(93)31457-0

Cavas-Martínez, F., De La Cruz Sánchez, E., Nieto Martínez, J., Fernández Cañavate, F. J., and Fernández-Pacheco, D. G. (2016). Corneal topography in keratoconus: State of the art. *Eye Vis.* 3, 5. doi:10.1186/s40662-016-0036-8

Cennamo, G., Forte, R., Aufiero, B., and La Rana, A. (2011). Computerized Scheimpflug densitometry as a measure of corneal optical density after excimer laser refractive surgery in myopic eyes. *J. Cataract. Refract Surg.* 37, 1502–1506. doi:10.1016/j.jcrs.2011.03.037

Chang, J.-Y., Lin, P.-Y., Hsu, C.-C., and Liu, C. J.-L. (2022). Comparison of clinical outcomes of LASIK, Trans-PRK, and SMILE for correction of myopia. *J. Chin. Med. Assoc.* 85, 145–151. doi:10.1097/jcma.0000000000000674

Charpentier, S., Keilani, C., Maréchal, M., Friang, C., De Faria, A., Froussart-Maille, F., et al. (2021). Corneal haze post photorefractive keratectomy. *J. Fr. Ophtalmol.* 44, 1425–1438. doi:10.1016/j.jfo.2021.05.006

Chen, Y., Mehta, G., and Vasiliou, V. (2009). Antioxidant defenses in the ocular surface. *Ocul. Surf.* 7, 176–185. doi:10.1016/s1542-0124(12)70185-4

De Oliveira, R. C., and Wilson, S. E. (2020). Descemet's membrane development, structure, function and regeneration. *Exp. Eye Res.* 197, 108090. doi:10.1016/j.exer.2020.108090

Dong, Z., Zhou, X., Wu, J., Zhang, Z., Li, T., Zhou, Z., et al. (2014). Small incision lenticule extraction (SMILE) and femtosecond laser LASIK: Comparison of corneal wound healing and inflammation. *Br. J. Ophthalmol.* 98, 263–269. doi:10.1136/bjophthalmol-2013-303415

Doughty, M. J., and Jonuscheit, S. (2019). Corneal structure, transparency, thickness and optical density (densitometry), especially as relevant to contact lens wear-a review. *Cont. Lens Anterior Eye* 42, 238–245. doi:10.1016/j.clae.2018.11.014

Efron, N. (2019). "Anterior eye examination," in *Contact lens complications*. Editor N. Efron Fourth Edition (Philadelphia: Elsevier), 3–23.

Eghrari, A. O., Riazuddin, S. A., and Gottsch, J. D. (2015). "Chapter two - overview of the cornea: Structure, function, and development," in *Progress in molecular biology and translational science*. Editors J. F. Hejtmancik and J. M. Nickerson (Academic Press), 7–23.

Espana, E. M., and Birk, D. E. (2020). Composition, structure and function of the corneal stroma. *Exp. Eye Res.* 198, 108137. doi:10.1016/j.exer.2020.108137

Fakhry, M. A., Artola, A., Belda, J. I., Ayala, J. M., and Alió, J. L. (2002). Comparison of corneal pachymetry using ultrasound and Orbscan II. *J. Cataract Refract. Surg.* 28, 248–252. doi:10.1016/s0886-3350(01)01277-9

Fam, H.-B., Lim, K.-L., and Reinstein, D. Z. (2005). Orbscan global pachymetry: Analysis of repeated measures. *Optometry Vis. Sci.* 82, 1047–1053. doi:10.1097/01.opx.0000192348.37026.09

Fantes, F. E., Hanna, K. D., Waring, G. O., 3rd, Pouliquen, Y., Thompson, K. P., and Savoldelli, M. (1990). Wound healing after excimer laser keratomileusis (photorefractive keratectomy) in monkeys. *Arch. Ophthalmol.* 108, 665–675. doi:10.1001/archopht.1990.01070070051034

Fares, U., Otri, A. M., Al-Aqaba, M. A., Faraj, L., and Dua, H. S. (2012). Wavefront-optimized excimer laser *in situ* keratomileusis for myopia and myopic astigmatism: Refractive outcomes and corneal densitometry. *J. Cataract. Refract Surg.* 38, 2131–2138. doi:10.1016/j.jcrs.2012.07.041

Gadde, A. K., Srirampur, A., Katta, K. R., Mansoori, T., and Armah, S. M. (2020). Comparison of single-step transepithelial photorefractive keratectomy and conventional photorefractive keratectomy in low to high myopic eyes. *Indian J. Ophthalmol.* 68, 755–761. doi:10.4103/ijo.ijo_1126_19

Gandhi, S., and Jain, S. (2015). "The anatomy and physiology of cornea," in *Keratoprostheses and artificial corneas: Fundamentals and surgical applications* (Berlin, Heidelberg: Springer Berlin Heidelberg).

Gao, F., Lin, T., and Pan, Y. (2016). Effects of diabetic keratopathy on corneal optical density, central corneal thickness, and corneal endothelial cell counts. *Exp. Ther. Med.* 12, 1705–1710. doi:10.3892/etm.2016.3511

Garzón, N., Poyales, F., Illarramendi, I., Mendicute, J., Jáñez, Ó, Caro, P., et al. (2017). Corneal densitometry and its correlation with age, pachymetry, corneal curvature, and refraction. *Int. Ophthalmol.* 37, 1263–1268. doi:10.1007/s10792-016-0397-y

Gibson, D. J., Tuli, S. S., and Schultz, G. S. (2013). The progression of haze formation in rabbit corneas following phototherapeutic keratectomy. *Invest. Ophthalmol. Vis. Sci.* 54, 4776–4781. doi:10.1167/iovs.13-11976

Gipson, I. K. (2013). Age-related changes and diseases of the ocular surface and cornea. *Invest. Ophthalmol. Vis. Sci.* 54, 48–53. doi:10.1167/iovs.13-12840

Ha, B. J., Kim, T. I., Choi, S. I., Stulting, R. D., Lee, D. H., Cho, H. S., et al. (2010). Mitomycin C does not inhibit exacerbation of granular corneal dystrophy type II induced by refractive surface ablation. *Cornea* 29, 490–496. doi:10.1097/ico.0b013e3181c3258a

Han, T., Zhao, J., Shen, Y., Chen, Y., Tian, M., and Zhou, X. (2017). A three-year observation of corneal backscatter after small incision lenticule extraction (SMILE). *J. Refract Surg.* 33, 377–382. doi:10.3928/1081597x-20170420-01

Hillenaar, T., Cals, R. H., Eilers, P. H., Wubbels, R. J., Van Cleynenbreugel, H., and Remeijer, L. (2011). Normative database for corneal backscatter analysis by *in vivo* confocal microscopy. *Invest. Ophthalmol. Vis. Sci.* 52, 7274–7281. doi:10.1167/iovs.11-7747

Hiraoka, T. (2022). Myopia control with orthokeratology: A review. *Eye Contact Lens* 48, 100–104. doi:10.1097/icl.0000000000000867

Hollingsworth, J. G., Efron, N., and Tullo, A. B. (2005). *In vivo* corneal confocal microscopy in keratoconus. *Ophthalmic Physiol. Opt.* 25, 254–260. doi:10.1111/j.1475-1313.2005.00278.x

Hou, C., Li, J., Li, J., Peng, H., and Wang, Q. (2022). *In vivo* confocal microscopy of sub-basal corneal nerves and corneal densitometry after three kinds of refractive procedures for high myopia. *Int. Ophthalmol.* 43, 925–935. doi:10.1007/s10792-022-02494-0

Hsieh, T. H., Yu, H. J., Yang, I. H., Ho, R. W., Hsiao, Y. T., Fang, P. C., et al. (2021). Simultaneously monitoring whole corneal injury with corneal optical density and thickness in patients undergoing cataract surgery. *Diagn. (Basel)* 11, 1639. doi:10.3390/diagnostics11091639

Huang, J., Ding, X., Savini, G., Jiang, Z., Pan, C., Hua, Y., et al. (2014). Central and midperipheral corneal thickness measured with Scheimpflug imaging and optical coherence tomography. *PLoS One* 9, e98316. doi:10.1371/journal.pone.0098316

Jahadi Hosseini, S. H., Abtahi, S. M., and Khalili, M. R. (2016). Comparison of higher order aberrations after wavefront-guided LASIK and PRK: One year follow-up results. *J. Ophthalmic Vis. Res.* 11, 350–357. doi:10.4103/2008-322x.194069

Jiang, X., Wang, Y., Yuan, H., Li, Y., Wang, H., An, Z., et al. (2022). Influences of SMILE and FS-LASIK on corneal sub-basal nerves: A systematic review and network meta-analysis. *J. Refract. Surg.* 38, 277–284. doi:10.3928/1081597x-20220127-01

Kaido, M., Kawashima, M., Ishida, R., and Tsubota, K. (2020). Tear film dynamics of soft contact lens-induced dry eye. *Curr. Eye Res.* 45, 782–788. doi:10.1080/02713683.2019.1700530

Karimian, F., Feizi, S., Doozandeh, A., Faramarzi, A., and Yaseri, M. (2011). Comparison of corneal tomography measurements using Galilei, Orbscan II, and Placido disk-based topographer systems. *J. Refract Surg.* 27, 502–508. doi:10.3928/1081597x-20101210-02

Kendall, C. J., Prager, T. C., Cheng, H., Gombos, D., Tang, R. A., and Schiffman, J. S. (2015). Diagnostic ophthalmic ultrasound for radiologists. *Neuroimaging Clin. N. Am.* 25, 327–365. doi:10.1016/j.nic.2015.05.001

Kim, B. Z., Jordan, C. A., Mcghee, C. N., and Patel, D. V. (2016). Natural history of corneal haze after corneal collagen crosslinking in keratoconus using Scheimpflug analysis. *J. Cataract. Refract Surg.* 42, 1053–1059. doi:10.1016/j.jcrs.2016.04.019

Koh, S., Maeda, N., Nakagawa, T., and Nishida, K. (2012). Quality of vision in eyes after selective lamellar keratoplasty. *Cornea* 31, S45–S49. doi:10.1097/ico.0b013e318269c9cd

Kowtharapu, B. S., Murín, R., Jünemann, A. G. M., and Stachs, O. (2018). Role of corneal stromal cells on epithelial cell function during wound healing. *Int. J. Mol. Sci.* 19, 464. doi:10.3390/ijms19020464

Kumar, A., Yun, H., Funderburgh, M. L., and Du, Y. (2022). Regenerative therapy for the cornea. *Prog. Retin. Eye Res.* 87, 101011. doi:10.1016/j.preteyeres.2021.101011

Lavker, R. M., Kaplan, N., Wang, J., and Peng, H. (2020). Corneal epithelial biology: Lessons stemming from old to new. *Exp. Eye Res.* 198, 108094. doi:10.1016/j.exer.2020.108094

Lazaridis, A., Droutsas, K., Sekundo, W., Petrak, M., and Schulze, S. (2017). Corneal clarity and visual outcomes after small-incision lenticule extraction and comparison to femtosecond laser-assisted *in situ* keratomileusis. *J. Ophthalmol.* 2017, 1–9. doi:10.1155/2017/5646390

Li, M., Niu, L., Qin, B., Zhou, Z., Ni, K., Le, Q., et al. (2013). Confocal comparison of corneal reinnervation after small incision lenticule extraction (SMILE) and femtosecond laser *in situ* keratomileusis (FS-LASIK). *PLoS One* 8, e81435. doi:10.1371/journal.pone.0081435

Li, S., Siggel, R., Guo, Y., Loreck, N., Rokohl, A. C., Kurschat, C., et al. (2021). Corneal densitometry: A potential indicator for early diagnosis of fabry disease. *Graefe's Archive Clin. Exp. Ophthalmol.* 259, 941–948. doi:10.1007/s00417-020-05027-6

Liu, M., Shi, W., Liu, X., Li, N., Chen, T., and Gao, H. (2021). Postoperative corneal biomechanics and influencing factors during femtosecond-assisted laser *in situ* keratomileusis (FS-LASIK) and laser-assisted subepithelial keratomileusis (LASEK) for high myopia. *Lasers Med. Sci.* 36, 1709–1717. doi:10.1007/s10103-021-03320-2

Lopes, B., Ramos, I., and Ambrósio, R., Jr. (2014). Corneal densitometry in keratoconus. *Cornea* 33, 1282–1286. doi:10.1097/ico.0000000000000266

Lou, W., Du, W., Jin, H., and Hu, Y. (2022). Comparison of anterior corneal aberrations measured by Scheimpflug and Placido Disc System for myopes. *BMC Ophthalmol.* 22, 512. doi:10.1186/s12886-022-02753-9

Luceri, S., Parker, J., Dapena, I., Baydoun, L., Oellerich, S., Van Dijk, K., et al. (2016). Corneal densitometry and higher order aberrations after bowman layer transplantation: 1-Year results. *Cornea* 35, 959–966. doi:10.1097/ico.0000000000000860

Mahdavi Fard, A., Daei Sorkhabi, R., Khazaei, M., and Nader, N. D. (2019). The effects of collagen cross-linking on corneal density: A comparison between accelerated and conventional methods. *Int. Ophthalmol.* 39, 1559–1566. doi:10.1007/s10792-018-0961-8

Mclaren, J. W., Wacker, K., Kane, K. M., and Patel, S. V. (2016). Measuring corneal haze by using scheimpflug photography and confocal microscopy. *Investigative Ophthalmol. Vis. Sci.* 57, 227–235. doi:10.1167/iovs.15-17657

Medeiros, C. S., Marino, G. K., Santhiago, M. R., and Wilson, S. E. (2018). The corneal basement membranes and stromal fibrosis. *Investigative Ophthalmol. Vis. Sci.* 59, 4044–4053. doi:10.1167/iovs.18-24428

Mickles, C. V., Kinoshita, B. T., Lam, D., Wagner, H., Zimmerman, A. B., Sorbara, L., et al. (2021). The contact Lens risk survey to assess risk of soft contact lens-related

inflammatory events. *Contact Lens Anterior Eye* 44, 35–41. doi:10.1016/j.clae.2020.11.013

Mohan, R. R., Kempuraj, D., D'souza, S., and Ghosh, A. (2022). Corneal stromal repair and regeneration. *Prog. Retin Eye Res.* 91, 101090. doi:10.1016/j.preteyeres.2022.101090

Montorio, D., Cennamo, G., Menna, F., Donna, P., Napolitano, P., Breve, M. A., et al. (2020). Evaluation of corneal structures in myopic eyes more than twenty-two years after photorefractive keratectomy. *J. Biophot.* 13, e202000138. doi:10.1002/jbio.202000138

Moreno, V. C., Aguilella-Arzo, M., Del Castillo, R. M., Espinós, F. J., and Del Castillo, L. F. (2022). A refined model on flow and oxygen consumption in the human cornea depending on the oxygen tension at the interface cornea/post lens tear film during contact lens wear. *J. Optom.* 15, 160–174. doi:10.1016/j.optom.2020.12.002

Mori, H., Miura, M., Iwasaki, T., Goto, H., Sakurai, Y., Watanabe, Y., et al. (2009). Three-dimensional optical coherence tomography-guided phototherapeutic keratectomy for granular corneal dystrophy. *Cornea* 28, 944–947. doi:10.1097/ico.0b013e31819670c2

Muhafiz, E., Bayhan, H. A., Sahin, S., Göçmen, A. Y., Aslan Bayhan, S., and Gürdal, C. (2019). Evaluation of the ocular surface in different contact lens replacement schedules. *Cornea* 38, 587–594. doi:10.1097/ico.0000000000001870

Nagy, Z. Z., Németh, J., Süveges, I., and Csákány, B. (1996). Examination of subepithelial scar formation after photorefractive keratectomy with the ultrasound biomicroscope. *Klin. Monbl Augenheilkd* 209, 283–285.

Onochie, O. E., Zollinger, A., Rich, C. B., Smith, M., and Trinkaus-Randall, V. (2019). Epithelial cells exert differential traction stress in response to substrate stiffness. *Exp. Eye Res.* 181, 25–37. doi:10.1016/j.exer.2019.01.014

Orucoglu, F., Talaz, S., Aksu, A., and Muftuoglu, O. (2014). Corneal densitometry evaluation in archipelago keratitis. *Int. Ophthalmol.* 34, 99–102. doi:10.1007/s10792-013-9736-4

Otri, A. M., Fares, U., Al-Aqaba, M. A., and Dua, H. S. (2012). Corneal densitometry as an indicator of corneal health. *Ophthalmology* 119, 501–508. doi:10.1016/j.ophtha.2011.08.024

Ozek, D., Karaca, E. E., Kazanci, B., and Evren Kemer, O. (2021). Evaluation of corneal densitometry and endothelial layer in soft contact lens users. *Optometry Vis. Sci.* 98, 592–596. doi:10.1097/opx.0000000000001707

Pakbin, M., Khabazkhoob, M., Pakravan, M., Fotouhi, A., Jafarzadehpur, E., Aghamirsalim, M., et al. (2022). Repeatability of corneal densitometry measurements using a scheimpflug camera in healthy normal corneas. *J. Curr. Ophthalmol.* 34, 50–55. doi:10.4103/joco.joco_173_21

Patel, S., and Tutchenko, L. (2019). The refractive index of the human cornea: A review. *Contact Lens Anterior Eye* 42, 575–580. doi:10.1016/j.clae.2019.04.018

Pavlin, C. J., Mcwhae, J. A., Mcgowan, H. D., and Foster, F. S. (1992). Ultrasound biomicroscopy of anterior segment tumors. *Ophthalmology* 99, 1220–1228. doi:10.1016/s0161-6420(92)31820-2

Pekel, G., zbakış, F., Bahar, A., Pekel, E., and etin, E. N. (2018). Correlations of corneal optical densitometry, endothelial hexagonality percentage, and epithelium thickness. *Curr. Eye Res.* 43, 170–174. doi:10.1080/02713683.2017.1387271

Poyales, F., Garzón, N., Mendicute, J., Illarramendi, I., Caro, P., Jáñez, O., et al. (2017). Corneal densitometry after photorefractive keratectomy, laser-assisted *in situ* keratomileusis, and small-incision lenticule extraction. *Eye (Lond)* 31, 1647–1654. doi:10.1038/eye.2017.107

Price, M. O., Mehta, J. S., Jurkunas, U. V., and Price, F. W. (2021). Corneal endothelial dysfunction: Evolving understanding and treatment options. *Prog. Retin. Eye Res.* 82, 100904. doi:10.1016/j.preteyeres.2020.100904

Savini, G., Huang, J., Lombardo, M., Serrao, S., Schiano-Lomoriello, D., Venanzio, S., et al. (2016). Objective monitoring of corneal backward light scattering after femtosecond laser-assisted LASIK. *J. Refract Surg.* 32, 20–25. doi:10.3928/1081597x-20151207-08

Shajari, M., Wanner, E., Rusev, V., Mir Mohi Sefat, S., Mayer, W. J., Kohnen, T., et al. (2018). Corneal densitometry after femtosecond laser-assisted *in situ* keratomileusis (Fs-LASIK) and small incision lenticule extraction (SMILE). *Curr. Eye Res.* 43, 605–610. doi:10.1080/02713683.2018.1431288

Shen, Y., Han, T., Jhanji, V., Shang, J., Zhao, J., Li, M., et al. (2019). Correlation between corneal topographic, densitometry, and biomechanical parameters in keratoconus eyes. *Transl. Vis. Sci. Technol.* 8, 12. doi:10.1167/tvst.8.3.12

Sie, N. M., Yam, G. H.-F., Soh, Y. Q., Lovatt, M., Dhaliwal, D., Kocaba, V., et al. (2020). Regenerative capacity of the corneal transition zone for endothelial cell therapy. *Stem Cell Res. Ther.* 11, 523. doi:10.1186/s13287-020-02046-2

Silverman, R. H. (2009). High-resolution ultrasound imaging of the eye - a review. *Clin. Exp. Ophthalmol.* 37, 54–67. doi:10.1111/j.1442-9071.2008.01892.x

Song, Y., Overmass, M., Fan, J., Hodge, C., Sutton, G., Lovicu, F. J., et al. (2021). Application of collagen I and IV in bioengineering transparent ocular tissues. *Front. Surg.* 8, 639500. doi:10.3389/fsurg.2021.639500

Sorcha, N. D., Rozema, J. J., Jongenelen, S., Ruiz Hidalgo, I., Zakaria, N., and Tassignon, M. J. (2014). Normative values for corneal densitometry analysis by Scheimpflug optical assessment. *Invest. Ophthalmol. Vis. Sci.* 55, 162–168. doi:10.1167/iovs.13-13236

Stramer, B. M., Zieske, J. D., Jung, J. C., Austin, J. S., and Fini, M. E. (2003). Molecular mechanisms controlling the fibrotic repair phenotype in cornea: Implications for surgical outcomes. *Invest. Ophthalmol. Vis. Sci.* 44, 4237–4246. doi:10.1167/iovs.02-1188

Swanson, E. A., Izatt, J. A., Hee, M. R., Huang, D., Lin, C. P., Schuman, J. S., et al. (1993). *In vivo* retinal imaging by optical coherence tomography. *Opt. Lett.* 18, 1864–1866. doi:10.1364/ol.18.001864

Takacs, A. I., Mihaltz, K., and Nagy, Z. Z. (2011). Corneal density with the Pentacam after photorefractive keratectomy. *J. Refract Surg.* 27, 269–277. doi:10.3928/1081597x-20100618-02

Tekin, K., Sekeroglu, M. A., Kiziltoprak, H., and Yilmazbas, P. (2017). Corneal densitometry in healthy corneas and its correlation with endothelial morphometry. *Cornea* 36, 1336–1342. doi:10.1097/ico.0000000000001363

Tian, M. (2018). Management of recalcitrant epithelial ingrowth after laser *in situ* keratomileusis: A case report. *Med. Baltim.* 97, e13024. doi:10.1097/md.0000000000013024

Tomczyk-Socha, M., Tomczak, W., and Turno-Kręcicka, A. (2022). The importance of MicroRNA expression in pseudoexfoliation syndrome. *Int. J. Mol. Sci.* 23, 13234. doi:10.3390/ijms232113234

Urbaniak, D., Seredyka-Burduk, M., Błoch, W., Malukiewicz, G., and Kałużny, B. J. (2018). Scheimpflug camera measurement of optical density of the corneal epithelium, stroma, and endothelium in patients with pseudoexfoliation syndrome. *Med. Sci. Monit.* 24, 5826–5831. doi:10.12659/msm.908738

Ursea, R., and Silverman, R. H. (2010). Anterior-segment imaging for assessment of glaucoma. *Expert Rev. Ophthalmol.* 5, 59–74. doi:10.1586/eop.09.61

Vaddavalli Pravin, K., Hurmeric, V., Wang, J., and Yoo Sonia, H. (2012). Corneal haze following disruption of epithelial basement membrane on ultra-high-resolution OCT following femtosecond LASIK. *J. Refract. Surg.* 28, 72–74. doi:10.3928/1081597x-20111202-01

Wang, J., Fonn, D., Simpson, T. L., Sorbara, L., Kort, R., and Jones, L. (2003). Topographical thickness of the epithelium and total cornea after overnight wear of reverse-geometry rigid contact lenses for myopia reduction. *Invest. Ophthalmol. Vis. Sci.* 44, 4742–4746. doi:10.1167/iovs.03-0239

Wang, X., and Jacobs, D. S. (2022). Contact lenses for ocular surface disease. *Eye Contact Lens* 48, 115–118. doi:10.1097/icl.0000000000000879

Wei, R., Li, M., Yang, W., Shen, Y., Zhao, Y., Fu, D., et al. (2020). Corneal densitometry after small incision lenticule extraction (SMILE) and femtosecond laser-assisted LASIK (FS-LASIK): 5-Year prospective comparative study. *Front. Med. (Lausanne)* 7, 521078. doi:10.3389/fmed.2020.521078

Yang, L., Chen, Y., Ling, S., Wang, J., Wang, G., Zhang, B., et al. (2022). Research progress on the application of optical coherence tomography in the field of oncology. *Front. Oncol.* 12, 953934. doi:10.3389/fonc.2022.953934

Yu, F.-S. X., Lee, P. S. Y., Yang, L., Gao, N., Zhang, Y., Ljubimov, A. V., et al. (2022). The impact of sensory neuropathy and inflammation on epithelial wound healing in diabetic corneas. *Prog. Retin. Eye Res.* 89, 101039. doi:10.1016/j.preteyeres.2021.101039

Zhang, J., Patel, D. V., and Mcghee, C. N. J. (2019). The rapid transformation of transplantation for corneal endothelial diseases: An evolution from penetrating to lamellar to cellular transplants. *Asia-Pacific J. Ophthalmol.* 8, 441–447. doi:10.1097/apo.0000000000000265

Zhao, L., Jing, L., Li, J., and Du, X. (2022). Changes in corneal densitometry after long-term orthokeratology for myopia and short-term discontinuation. *PLoS ONE* 17, e0263121. doi:10.1371/journal.pone.0263121

frontiers | Frontiers in Bioengineering and Biotechnology

TYPE Original Research
PUBLISHED 02 May 2023
DOI 10.3389/fbioe.2023.1086347

OPEN ACCESS

EDITED BY
Matthew A. Reilly,
The Ohio State University, United States

REVIEWED BY
Bo Lei,
Henan Provincial People's Hospital, China
Chan Zhao,
Peking Union Medical College Hospital (CAMS), China

*CORRESPONDENCE
Peng Xiao,
xiaopengaddis@hotmail.com
Jin Yuan,
yuanjincornea@126.com

†These authors have contributed equally to this work and share the first authorship

RECEIVED 01 November 2022
ACCEPTED 20 April 2023
PUBLISHED 02 May 2023

CITATION
Xiao P, Ma K, Ye X, Wang G, Duan Z, Huang Y, Luo Z, Hu X, Chi W and Yuan J (2023), Classification of Vogt-Koyanagi-Harada disease using feature selection and classification based on wide-field swept-source optical coherence tomography angiography.
Front. Bioeng. Biotechnol. 11:1086347.
doi: 10.3389/fbioe.2023.1086347

Classification of Vogt-Koyanagi-Harada disease using feature selection and classification based on wide-field swept-source optical coherence tomography angiography

Peng Xiao†*, Ke Ma†, Xiaoyuan Ye, Gengyuan Wang, Zhengyu Duan, Yuancong Huang, Zhongzhou Luo, Xiaoqing Hu, Wei Chi and Jin Yuan*

State Key Laboratory of Ophthalmology, Zhongshan Ophthalmic Center, Sun Yat-sen University, Guangzhou, China

Background: Vogt-Koyanagi-Harada (VKH) disease is a common and easily blinded uveitis entity, with choroid being the main involved site. Classification of VKH disease and its different stages is crucial because they differ in clinical manifestations and therapeutic interventions. Wide-field swept-source optical coherence tomography angiography (WSS-OCTA) provides the advantages of non-invasiveness, large-field-of-view, high resolution, and ease of measuring and calculating choroid, offering the potential feasibility of simplified VKH classification assessment based on WSS-OCTA.

Methods: 15 healthy controls (HC), 13 acute-phase and 17 convalescent-phase VKH patients were included, undertaken WSS-OCTA examination with a scanning field of 15 × 9 mm^2. 20 WSS-OCTA parameters were then extracted from WSS-OCTA images. To classify HC and VKH patients in acute and convalescent phases, two 2-class VKH datasets (HC and VKH) and two 3-class VKH datasets (HC, acute-phase VKH, and convalescent-phase VKH) were established by the WSS-OCTA parameters alone or in combination with best-corrected visual acuity (logMAR BCVA) and intraocular pressure (IOP), respectively. A new feature selection and classification method that combines an equilibrium optimizer and a support vector machine (called SVM-EO) was adopted to select classification-sensitive parameters among the massive datasets and to achieve outstanding classification performance. The interpretability of the VKH classification models was demonstrated based on SHapley Additive exPlanations (SHAP).

Results: Based on pure WSS-OCTA parameters, we achieved classification accuracies of 91.61% ± 12.17% and 86.69% ± 8.30% for 2- and 3-class VKH classification tasks. By combining the WSS-OCTA parameters and logMAR BCVA, we achieved better classification performance of 98.82% ± 2.63% and 96.16% ± 5.88%, respectively. Through SHAP analysis, we found that logMAR BCVA and vascular perfusion density (VPD) calculated from the whole field of view region in the choriocapillaris (whole FOV CC-VPD) were the most important features for VKH classification in our models.

Conclusion: We achieved excellent VKH classification performance based on a non-invasive WSS-OCTA examination, which provides the possibility for future clinical VKH classification with high sensitivity and specificity.

KEYWORDS

Vogt-Koyanagi-Harada (VKH), wide-field swept-source optical coherence tomography (WSS-OCTA), feature selection and classification, equilibrium optimizer (EO), support vector machine (SVM)

1 Introduction

Vogt-Koyanagi-Harada (VKH) disease is a T-cell-mediated multisystem autoimmune disease targeting melanocyte-containing organs (Ei Ei Lin Oo et al., 2020). The incidence of VKH varies among populations worldwide with a common occurrence in Hispanics (mestizos), Asians, Native Americans, Middle Easterners, and Asian Indians (Read et al., 2001). It causes not only ocular manifestations such as bilateral granulomatous panuveitis, chorioretinitis, and exudative retinal detachment (Ei Ei Lin Oo et al., 2020), but also multiple extraocular manifestations, including the central nervous system, auditory, and cutaneous abnormalities (O'Keefe and Rao, 2017). According to the multimodal ocular vascular imaging approach, VKH is clinically manifested in four phases, specifically prodromal, acute, convalescent, and chronic recurrent phases (Luo et al., 2021). The prodromal phase starts rapidly, often with cold symptoms, and develops into the acute phase quickly. Early diagnosis, timely initiation of treatment, and appropriate and adequate therapy are key to optimal VKH management, while delayed diagnosis and initiation of appropriate therapy may lead to an increased risk of disease chronicity, complications, and visual impairment (Ei Ei Lin Oo et al., 2020). For example, the acute phase, if not adequately treated, can progress to the chronic recurrent stage (Agarwal et al., 2020). In contrast, with appropriate treatment such as corticosteroids, the disease will transition to the convalescent phase after several weeks to months. Because of the different treatment regimens and dosages in the acute and convalescent phases, it is important to accurately identify and classify VKH, especially in these two phases, so that patients with VKH can be given the proper and suitable treatment to recover and avoid chronic symptoms.

At present, the classification of VKH mainly focuses on clinical manifestations, supplemented by auxiliary examinations such as fluorescein angiography (FA), indocyanine green angiography (ICGA), and optical coherence tomography (OCT) (Li et al., 2021). The FA and ICGA have long been used as validation tools for the classification and evaluation of VKH, however, both are time-consuming, invasive, and non-quantitative, and also have potential dye-related risks (Qian et al., 2021). The enhanced depth imaging OCT (EDI-OCT) and swept-source OCT (SS-OCT) are non-invasive, more affordable techniques for assessing choroidal thickness and morphology (Urzua et al., 2020). Moreover, it has been shown that SS-OCT is superior to EDI-OCT, providing higher resolution and more measurable images and accurate qualitative and quantitative assessment of retinal and choroidal changes (Chee et al., 2017). The SS-OCT angiography (SS-OCTA) provides not only the advantages of SS-OCT such as non-invasive and high resolution but also the advantages of tissue penetration, visualizing and quantitatively measuring the retinal and choroidal vascular system with high repeatability and reproducibility, making it increasingly important and widely used in the field of uveitis (Liang et al., 2021). Several studies have used SS-OCTA to demonstrate choroidal retinal microvascular changes in VKH disease (Karaca et al., 2020; Liang et al., 2020; Fan et al., 2021). Compared with SS-OCTA, wide-field SS-OCTA (WSS-OCTA) can obtain a larger field of view and extract more vascular features, and thus is gradually being applied in VKH studies (Qian et al., 2021; Ye et al., 2021). However, to the best of our knowledge, there is no classification study or criteria for VKH based on the WSS-OCTA.

In addition, WSS-OCTA can extract many features, such as up to 20 features in our previous work (Ye et al., 2021), which help to analyze microvascular alterations in VKH patients. However, for VKH classification, high-dimensional features like these may contain not only relevant features but also irrelevant and redundant features, which can reduce VKH classification performance. Feature selection is one of the effective ways to reduce dimensionality, which helps to reduce the risk of overfitting, improve the generalization ability of the model and save computational effort because only a fewer features are calculated (Shilaskar and Ghatol, 2013). On the other hand, machine learning methods, such as support vector machines (SVM), logistic regression (LR), random forests (RF), K-nearest neighbors (KNN), and decision trees (DT), are widely used for classification and prediction of ophthalmic diseases, such as myopia and keratitis (Tang et al., 2020; Herber et al., 2021), glaucoma, uveitis, cataract, and age-related macular degeneration (Lin et al., 2020; Standardization of Uveitis Nomenclature SUN Working Group, 2021b; Ting et al., 2021), and recently also for VKH classification (Standardization of Uveitis Nomenclature SUN Working Group, 2021a; Chang et al., 2021), because of their good classification performance in small datasets. These classifiers are often trained with hyperparameters, which need to be optimized to obtain the best classification performance. Therefore, considering these two aspects, this paper attempts to achieve accurate VKH classification based on a small number of WSS-OCTA features by simultaneously performing the selection of numerous WSS-OCTA features, hyperparameter optimization of the classifier, and VKH classification. In short, this paper aims to investigate a simplified and accurate VKH classification method based on WSS-OCTA unimodal imaging. To achieve this, this paper proposes a new feature selection and

Classification method by combining an equilibrium optimizer (EO), a metaheuristic algorithm with strong search power (Faramarzi et al., 2020), and an SVM, named SVM-EO, to build accurate two-class (healthy control and VKH) and three-class (healthy control, acute-phase, and convalescent-phase VKH) VKH classification models. To verify the feasibility and validity

TABLE 1 The detailed information of the patients included (Ye et al., 2021).

	Healthy controls	Acute-phase VKH	Convalescent phase VKH	*p*-value
Number of eyes/patients	30/15	20/13	30/17	
Age (years)	34 (26–58)	34 (27–53)	36 (29–43)	0.971[a]
Sex (male/female)	5/10	8/5	9/8	0.302[b]

Notes: Patients' ages are presented as Median (P25-P75).
[a]Kruskal–Wallis test.
[b]Chi-square test.

of the method, two feature combination schemes were tested in this paper, namely, pure WSS-OCTA features and combined two basic clinical characteristics and WSS-OCTA features.

2 Methods

2.1 Subjects

This single-center study was conducted at the Zhongshan Eye Center in China and in accordance with the Declaration of Helsinki, and all participants signed informed consents. Table 1 gives a detailed information of the patients included, which was reported in our previous publication (Ye et al., 2021). The classification of VKH disease was made by experienced ophthalmologists in strict accordance with the revised classification criteria (RDC) developed by the First International Workshop on Vogt-Koyanagi-Harada (VKH) disease (Read et al., 2001). The acute VKH group and the convalescent VKH group were divided according to disease progression. For example, inclusion criteria for the acute VKH group were patients who were initially diagnosed or treated with systemic corticosteroids for less than 2 weeks and excluded severe exudative retinal detachment, severe anterior chamber inflammation, or vitreous opacities, whereas patients with convalescent VKH were those who had been treated with systemic corticosteroids for more than 3 months and did not have acute fundus inflammation. The healthy controls were included in the absence of ocular or systemic disease and matched for age and number of cases to the VKH group. In addition, some ophthalmic examinations were performed for all participants, including the logarithm of the minimum angle of resolution of best corrected visual acuity (BCVA) measured with a Snellen chart (logMAR BCVA), bilateral intraocular pressure (IOP), slit lamp microscopy, indirect fundus ophthalmoscopy, and FA examinations.

2.2 WSS-OCTA image acquisition and feature extraction

All WSS-OCTA images were acquired by an experienced technician using the PLEX Elite 9000 device (Carl Zeiss Meditec Inc., Dublin, CA, UNITED STATES OF AMERICA) with a central wavelength of 1,060 nm and a speed of 100,000 A-scans per second to perform a 15 × 9 mm^2 scan centered on the fovea of each eye. The PLEX Elite 9000 device has an active eye-tracking system with its auto-focus function to minimize the effects of eye aberrations when taking images. Poor quality WSS-OCTA images with a lot of motion artifacts or incorrect segmentation were excluded. All WSS-OCTA images were automatically segmented using the built-in software to generate superficial vascular plexus (SVP), deep vascular plexus (DVP), and choriocapillaris (CC), as shown in Figure 1 for an example. Then, four kinds of features were extracted from three slabs, namely, foveal avascular zone (FAZ), vascular perfusion density (VPD), vascular length density (VLD), and flow void (FV) across regions and layers parameters. The FAZ features included the area of the FAZ (AFAZ) and the acyclicity index (AI, the ratio of the FAZ perimeter to the perimeter of a circle of equal area) (Karaca et al., 2020) in SVP. To calculate the VPD, the ratio of vascular area to the total region of interest (ROI) (Triolo et al., 2017), 7 ROIs were selected, including the macular region in SVP, DVP, and CC, the peripapillary region in SVP, and the whole field of view (FOV) region in SVP, DVP, and CC, and thus a total of 7 VPD features were calculated, namely, macular SVP-VPD, macular DVP-VPD, macular CC-VPD, peripapillary SVP-VPD, whole FOV SVP-VPD, whole FOV DVP-VPD, and whole FOV CC-VPD. VLD is the length of vessels per unit area (Uji et al., 2017), allowing for a more sensitive classification of small blood vessels and capillaries. Similarly, 5 ROIs were first selected, namely, the macular region in SVP and DVP, the peripapillary region in SVP, and the whole FOV in SVP and DVP, and finally 5 VLD features were obtained, including macular SVP-VLD, macular DVP-VLD, peripapillary SVP-VLD, whole FOV SVP-VLD, and whole FOV DVP-VLD. The FV in CC was determined by thresholding the areas lacking flow information (Spaide, 2016). FV variables, including FV area ratio (FVAR), the number of FV areas larger than 1,000 um^2 (FV1000), and the average size of the FV (FVAS), were calculated separately for the macular region and the peripheral region in CC, so altogether six FV features were extracted, which were macular CC-FVAR, macular CC-FV1000, macular CC-FVAS, peripheral CC-FVAR, peripheral CC-FV1000, and peripheral CC-FVAS. In brief, 20 WSS-OCTA features were extracted, including 2 FAZ features and 18 vascular features. A detailed description of the image processing including removing artifacts and extraction of OCTA parameters was given in our previous work (Ye et al., 2021). In addition, each feature was standardized for eliminating the effects of different feature magnitudes and accelerating convergence.

2.3 Feature selection and classification

To classify VKH disease accurately and objectively using as few parameters as possible, we adopted a feature selection and classification method combining EO and SVM (Figure 2), called

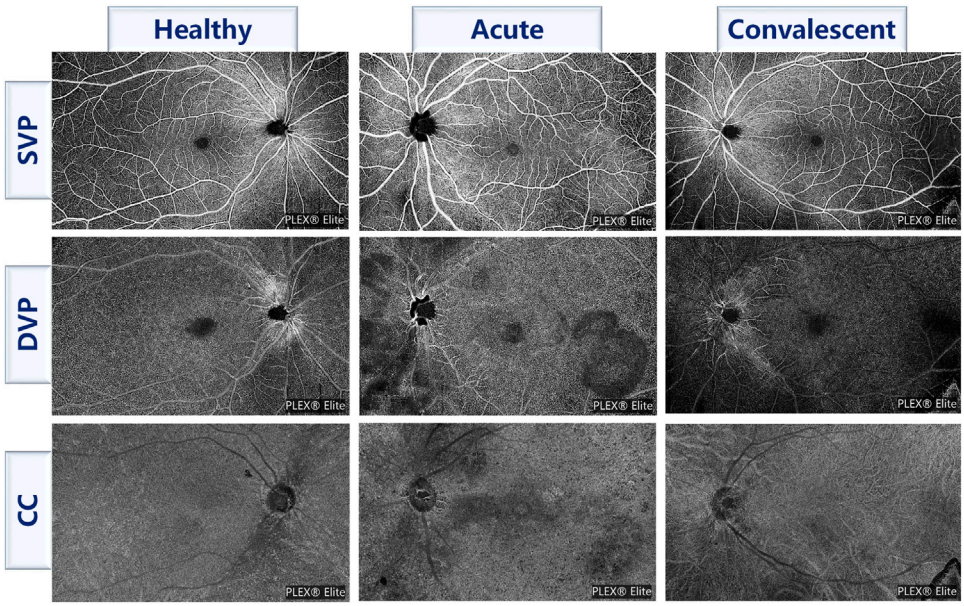

FIGURE 1
Examples of three slabs for three classes of participants. SVP, superficial vascular plexus; DVP, deep vascular plexus; CC, choriocapillaris.

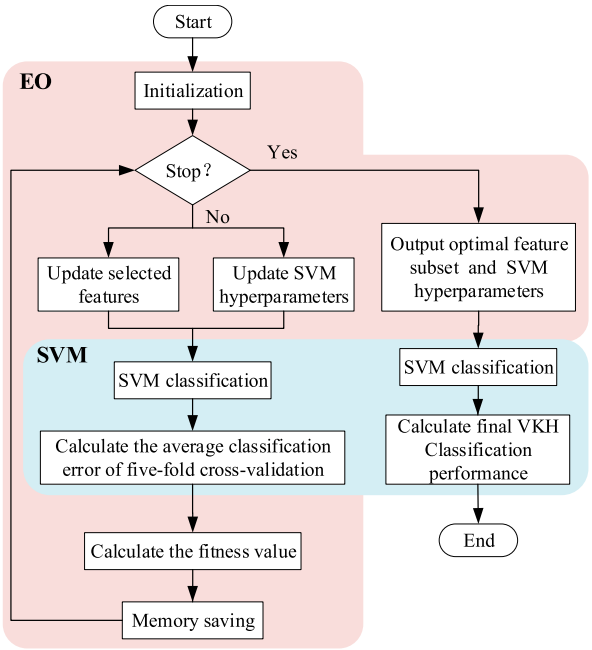

FIGURE 2
Flow chart of the feature selection and classification method combining EO and SVM. EO, equilibrium optimizer; SVM, support vector machine; VKH, vogt-koyanagi-harada.

SVM-EO, to achieve feature selection, SVM hyperparameter optimization, and classification simultaneously, which were implemented in MATLAB 2020b (MathWorks Inc., Natick, MA, United States). EO was used to update the feature subset and SVM hyperparameters, and SVM was applied to classification and construct the fitness function for EO.

2.3.1 Equilibrium optimizer

Faramarzi et al. (2020) proposed EO inspired by the control volume mass balance model used to estimate the dynamic and equilibrium states. The mass balance equation is generally described using a first-order differential equation, and is calculated as:

$$C = C_{eq} + \left(C_0 - C_{eq}\right)F + \frac{G}{\gamma V}\left(1 - F\right) \quad (1)$$

where V is the control volume, C is the concentration inside the control volume, C_{eq} is the concentration at equilibrium, G is the mass generation rate inside the control volume, F is the exponential term coefficient, γ is the flow rate, and C_0 is the initial concentration of the control volume.

The EO is mainly based on Eq. 1 for iterative optimization searching, where C represents the newly generated current solution, C_0 represents the solution obtained in the previous iteration, and C_{eq} represents the best solution currently found by the algorithm. The implementation process of EO is briefly described as follows. First, each variable requiring optimization is initialized randomly based on the upper and lower bounds. Then EO enters the main iteration process to update the solution and memory saving. Specifically, the equilibrium state pool $\boldsymbol{C_{eq}}$ consisting of five candidate solutions is constructed to improve the global search capability of the algorithm and avoid getting trapped in low-quality local optimal solutions. The coefficient $\boldsymbol{F}$ is updated for better balancing the global search and local search and the mass generation rate $\boldsymbol{G}$ is calculated to enhance the local search capability, see Eqs 2, 3. Thus, the current solution $\boldsymbol{C}$ is updated based on Eq. 4. Next, the fitness value of each member of the current solution is compared with that of the previous iteration

and covered if it has a better fitness value to achieve memory saving. The above iterative process is repeated until the iteration ends and all optimal variables are output.

$$\begin{cases} \boldsymbol{F} = a_1 sign(\boldsymbol{r} - 0.5)\left[e^{-\gamma t} - 1\right] \\ t = \left(1 - \dfrac{Ite}{Ite_{max}}\right)^{a_2 \frac{Ite}{Ite_{max}}} \end{cases} \tag{2}$$

$$\boldsymbol{G} = \begin{cases} 0.5\gamma_1 (\boldsymbol{C_{eq}} - \boldsymbol{\gamma C})\boldsymbol{F}, \gamma_2 \geq GP \\ 0, \gamma_2 < GP \end{cases} \tag{3}$$

$$\boldsymbol{C} = \boldsymbol{C_{eq}} + (\boldsymbol{C} - \boldsymbol{C_{eq}})\boldsymbol{F} + \frac{\boldsymbol{G}}{\boldsymbol{\gamma V}}(1 - \boldsymbol{F}) \tag{4}$$

where a_1 and a_2 are constant, $\boldsymbol{\gamma}$ is a random vector between [0,1], Ite and Ite_{max} are the number of current iterations and total iterations, γ_1 and γ_2 are random numbers between [0,1], and GP is the generation probability.

2.3.2 Support vector machine

SVM is a binary linear classifier that tries to minimize structural risk (Ma et al., 2019). It classifies two classes of samples by constructing the optimal hyperplane to maximize the sample intervals, which is a convex quadratic programming problem and the final mathematical model is:

$$\begin{cases} \min \dfrac{1}{2}\|\mathrm{W}\|^2 + \alpha\sum_{\mathrm{i}=1}^{\mathrm{M}}\varepsilon_{\mathrm{i}} \\ \mathrm{s.t.lab_i}\left(\mathrm{W^T feat_i} + \mathrm{b}\right) \geq 1 - \varepsilon_{\mathrm{i}} \\ \varepsilon_{\mathrm{i}} \geq 0 \end{cases} \tag{5}$$

where α is the penalty factor, ε is the slack variable, M is the number of training samples, $(\boldsymbol{feat_i}, lab_i)$ is the i th sample, and $(\boldsymbol{W}, b)$ is the hyperplane parameter. To build a three-class VKH classification model, the one-versus-one method was adopted for the SVM to achieve multi-classification. In addition, the radial basis function (RBF) kernel was used to achieve nonlinear classification because it has only one hyperparameter, bandwidth β, and has been shown to perform well (Caramia et al., 2018). Therefore, to establish accurate SVM classification models for diagnosing VKH, the penalty factor α and bandwidth β were simultaneously optimized.

2.3.3 Combined EO and SVM to classify VKH

The combination of EO and SVM maximizes the powerful search capability of EO and the excellent classification performance of SVM to efficiently detect VKH. First, initialize the input constants ($V = 1$; $a_1 = 2$; $a_2 = 1$; $Ite_{max} = 100$,; $GP = 0.5$) and the parameters for optimization as:

$$C_{i,j}^0 = \begin{cases} \alpha_l + \gamma_j(\alpha_u - \alpha_l), j = 1 \\ \beta_l + \gamma_j(\beta_u - \beta_l), j = 2 \\ F_l + \gamma_j(F_u - F_l), j > 2 \end{cases} \tag{6}$$

where $C_{i,j}^0$ represents the initial value of the j th ($j = 1, 2, 3, \ldots, J$) dimension of the i th ($i = 1, 2, 3, \ldots, I$) member of the population, I and J are the number of population members and the sum of the number of features and SVM hyperparameters, γ_j is a random number between [0, 1], and $[\alpha_l, \alpha_u]$, $[\beta_l, \beta_u]$, and $[F_l, F_u]$ represent the upper and lower bounds of α, β, and features and take the values of [0.001,1000], [0.001,1000], and [0,1]. Then, if the number of the current iteration is less than the total number, the main iteration process is performed, whereupon the selected features and two SVM hyperparameters are updated. Notably, for the current feature $C_{i,j}$ ($j > 2$), if the calculated $C_{i,j}$ is greater than 0.5, then $C_{i,j}$ is taken as 0, indicating that this feature is discarded. Conversely, $C_{i,j}$ is 1, meaning that the feature is selected and all features corresponding to $C_{i,j} = 1$ consist of the current feature subset.

Further, VKH classification was performed using SVM with updated hyperparameters based on the current feature subset, whose classification performance was stably evaluated using the five-fold cross-validation method. In detail, each class of samples in this feature subset was randomly divided into 5 folds according to the participants approximately equally, respectively, and then each fold of all classes was combined separately to form a 1-fold data subset containing all classes. Each 4-fold data subset was used to train the SVM model, and the remaining 1-fold was used to test the trained SVM model. And the average classification error $\overline{Error_{row}}$ obtained after 5 iterations was applied to construct the fitness function as:

$$Fitness_i = \varphi\overline{Error_i} + (1 - \varphi)\frac{Num_i}{J - 2} \tag{7}$$

where $Fitness_i$ is the fitness value of the i th member of the population, φ is the coefficient that balances the classification performance and the number of features ($\varphi = 0.98$), and Num_i is the number of the current feature subset. After that, the fitness value of each member of the current solution (population) was compared with that of the previous iteration for memory saving. After the main iteration, the best feature subset and the optimized SVM hyperparameters were output and used for SVM classification. To comprehensively assess the final VKH classification performance, sensitivity, specificity, accuracy, the receiver operating characteristic (ROC) curve and the area under the curve (AUC) were used as evaluation metrics and classification results based on five-fold cross-validation were given in the form of mean ± standard deviation (SD).

2.4 Global and local interpretability of the VKH classification models

Although the optimal feature subset and the best classification performance could be obtained by the SVM-EO method, the corresponding 2-class and 3-class VKH classification models are black-box models and lack interpretability. SHapley Additive exPlanations (SHAP) is a Shapley value-inspired additivity explanatory model based on game theory (Lundberg and Lee, 2017). SHAP assigns an importance value to each feature for a particular prediction, quantifying the magnitude and direction (positive or negative) of the feature's influence on the prediction, so it is possible to interpret the outputs of any machine learning model. And its interpretable performance has been widely proven and applied (Wang et al., 2021; Baptista et al., 2022; Nohara et al., 2022; Onsree et al., 2022). Therefore, we used the SHAP package in Python to achieve global and local interpretability of the best VKH classification models. Specifically, the classification model that achieved the best classification performance in the five-fold cross-validation was interpreted, and we used the kernel explainer in the SHAP package because it is model-independent and works with any model. The SHAP summary plot (Lundberg et al., 2020) was applied

TABLE 2 Average and best two-class VKH classification results obtained by using the proposed SVM-EO method.

Dataset	Sensitivity (%)		Specificity (%)		Accuracy (%)	
	Average	Best	Average	Best	Average	Best
Dataset1	89.30 ± 5.62	94.36 ± 8.24	82.27 ± 7.06	86.67 ± 21.73	86.66 ± 5.40	91.61 ± 12.17
Dataset2	95.60 ± 1.62	98.00 ± 4.47	99.46 ± 2.96	100.0 ± 0.0	97.19 ± 2.09	98.82 ± 2.63
P	<0.001	0.548	<0.001	0.310	<0.001	0.222

for global interpretability, displaying the feature importance of all features. The longer the bar corresponds to each feature, the more important this feature is. The SHAP force plot (Lundberg et al., 2018) was used to achieve local interpretability, showing how the prediction of a single sample was generated. The combined effect of all features pushed the model's predictions from the base value (the average prediction across all samples) to the final model output (f(x), the predicted value in this example). The features that pushed the prediction up and down were shown in red and blue respectively, and the wider the color area, the greater the impact of the feature.

2.5 Comparison and statistical analysis

We compared the classification performance based on pure WSS-OCTA features and based on clinical characteristics and WSS-OCTA features for two- and three-class VKH diagnoses, respectively. We ran the proposed SVM-EO method 30 times and considered the best classification performance as the final VKH classification performance. The statistical analysis was conducted in SPSS 24 (SPSS Inc., Chicago, IL, United States). The Mann-Whitney U test was performed to assess differences in classification performance due to different features and classes. Statistical significance was set at $p \leq 0.05$.

3 Results

3.1 Dataset

In this study, 20 eyes of 13 VKH patients in the acute phase, 30 eyes of 17 VKH patients in the convalescent phase, and 30 eyes of 15 age-matched healthy controls were included and analyzed. Four datasets were formed based on 2 clinical characteristics (IOP and logMAR BCVA) and 20 WSS-OCTA features for building two- and three-class VKH classification models, as follows: Dataset1: a two-class dataset consisting of 20 WSS-OCTA features; Dataset2: a two-class dataset composed of all 22 features; Dataset3: a three-class dataset made up of 20 WSS-OCTA features; Dataset4: a three-class dataset comprising all 22 features.

3.2 Two-class VKH classification results based on Dataset1 and Dataset2

We compared the average and best two-class VKH classification results obtained by the SVM-EO method based on Dataset1 and Dataset2. According to Table 2, the sensitivity, specificity, and accuracy obtained based on Dataset2 were significantly better than those acquired using Dataset1 concerning the average results. In terms of the best results, the sensitivity, specificity, and accuracy obtained based on Dataset2 were also superior to those gained with dataset1, although there was no significant difference, a smaller standard deviation was achieved. The best AUC obtained using Dataset2 was also markedly higher than that achieved by Dataset1 (Figure 3A), although there was no significant difference ($p = 0.421$). There are 7 eyes misidentified in Dataset1 (Figure 3B), while only one eye is misidentified in Dataset2 (Figure 3C). In terms of the features selected, the best feature subset obtained with Dataset1 contained 5 features, which were AFAZ, whole FOV DVP-VLD, macular SVP-VPD, peripheral CC-FVAR, and macular CC-FV1000, while the best feature subset gained from Dataset2 consisted of 4 features, namely, logMAR BCVA, macular DVP-VLD, whole FOV SVP-VPD, and whole FOV CC-VPD.

3.3 Three-class VKH classification results based on Dataset3 and Dataset4

For the average classification performance, the sensitivity and specificity of the HC, acute-phase VKH, and convalescent-phase VKH classes gained from Dataset4 were significantly outperformed by those.

Obtained with Dataset3 ($p < 0.001$, Table 3). The average overall accuracy obtained using Dataset4 was also significantly more favorable than that achieved with Dataset3 ($p < 0.001$). From the best three-classification results, the sensitivity of the HC class and the specificity of the convalescent-phase VKH class based on Dataset4 were significantly greater than those of Dataset3 ($p < 0.05$). Unexpectedly, the.

Best sensitivity of the HC class derived for Dataset3 was poorer than its average sensitivity, which may be since the proposed method used the overall error for constructing the fitness function, and although the sensitivity of this class is lower, the sensitivity of the other two classes is much higher, which phenomenon leads to higher overall accuracy (lower overall error). In addition, the sensitivity and specificity of the other categories from Dataset 4 were excellent compared to those of Dataset3, but not significantly different. Although the best overall accuracy obtained using Dataset4 is not significantly better than that obtained based on Dataset3, the former has a smaller standard deviation. The AUCs of HC, acute-phase VKH, and convalescent-phase VKH classes acquired from Dataset4 (Figure 4B) were clearly outstanding than those expressed from Dataset3

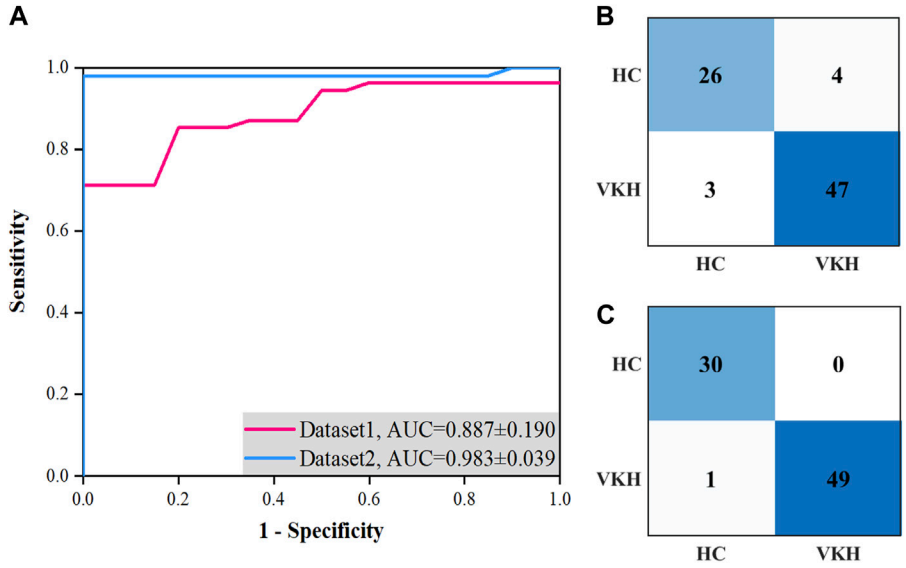

FIGURE 3
Best ROC curves and confusion matrices for two-class VKH classification with the SVM-EO method based on Dataset1 and Dataset2 using the five-fold cross-validation. **(A)** Best ROC curves. **(B)** Confusion matrix based on Dataset1. **(C)** Confusion matrix based on Dataset2.

TABLE 3 Average and best three-class VKH classification results obtained by using the feature selection and classification method.

Dataset	Class	Sensitivity (%)		Specificity (%)		Overall accuracy (%)	
		Average	Best	Average	Best	Average	Best
Dataset3	HC	86.53 ± 4.02	80.29 ± 12.86	80.63 ± 4.66	91.00 ± 10.25	82.79 ± 2.41	86.69 ± 8.30
	Acute-phase VKH	80.41 ± 9.18	96.00 ± 8.94	82.97 ± 2.49	83.41 ± 9.88		
	Convalescent-phase VKH	79.85 ± 5.76	86.95 ± 12.68	84.62 ± 3.57	86.36 ± 8.60		
Dataset4	HC	99.56 ± 1.15	100.0 ± 0.0	90.41 ± 2.31	93.56 ± 9.83	93.88 ± 1.37	96.16 ± 5.88
	Acute-phase VKH	94.55 ± 3.97	100.0 ± 0.0	93.82 ± 1.39	95.00 ± 7.45		
	Convalescent-phase VKH	88.26 ± 2.94	89.33 ± 15.35	97.55 ± 1.61	100.0 ± 0.0		
P	HC	<0.001	0.032	<0.001	0.690	<0.001	0.095
	Acute-phase VKH	<0.001	0.690	<0.001	0.095		
	Convalescent-phase VKH	<0.001	0.841	<0.001	0.032		

(Figure 4A), although they were not significantly different (*p*-values of 0.310, 0.690, 0.310, respectively). As far as detailed misidentifications are concerned, the misidentifications of the classification model obtained with Dataset3 are concentrated between HC and convalescent-phase VKH, and sporadically between acute-phase and convalescent-phase VKH (Figure 4C), while in Dataset4 only three convalescent-phase VKH eyes were misidentified as HC eyes (Figure 4D). Regarding the selected features, the best feature subset obtained with Dataset3 included 13 features, specifically AFAZ, AI, peripapillary SVP-VLD, macular DVP-VLD, macular SVP-VPD, whole FOV SVP-VPD, peripapillary SVP-VPD, whole FOV DVP-VPD, peripheral CC-FVAR, macular CC-FV1000, peripheral CC-FV1000, macular CC-FVAS, and peripheral CC-FVAS, whereas the best feature subset retrieved from Dataset4 contains only 6 features, comprising logMAR BCVA, AFAZ, peripapillary SVP-VLD, macular SVP-VPD, macular DVP-VPD, and whole FOV CC-VPD.

3.4 Comparison of the proposed method with the previous VKH classification methods

The above results revealed that the scheme combining clinical characteristics and WSS-OCTA features could obtain better performance of two- and three-class VKH classification, so we took the performance obtained by this scheme as the final VKH classification performance. Given that this is the first study of VKH

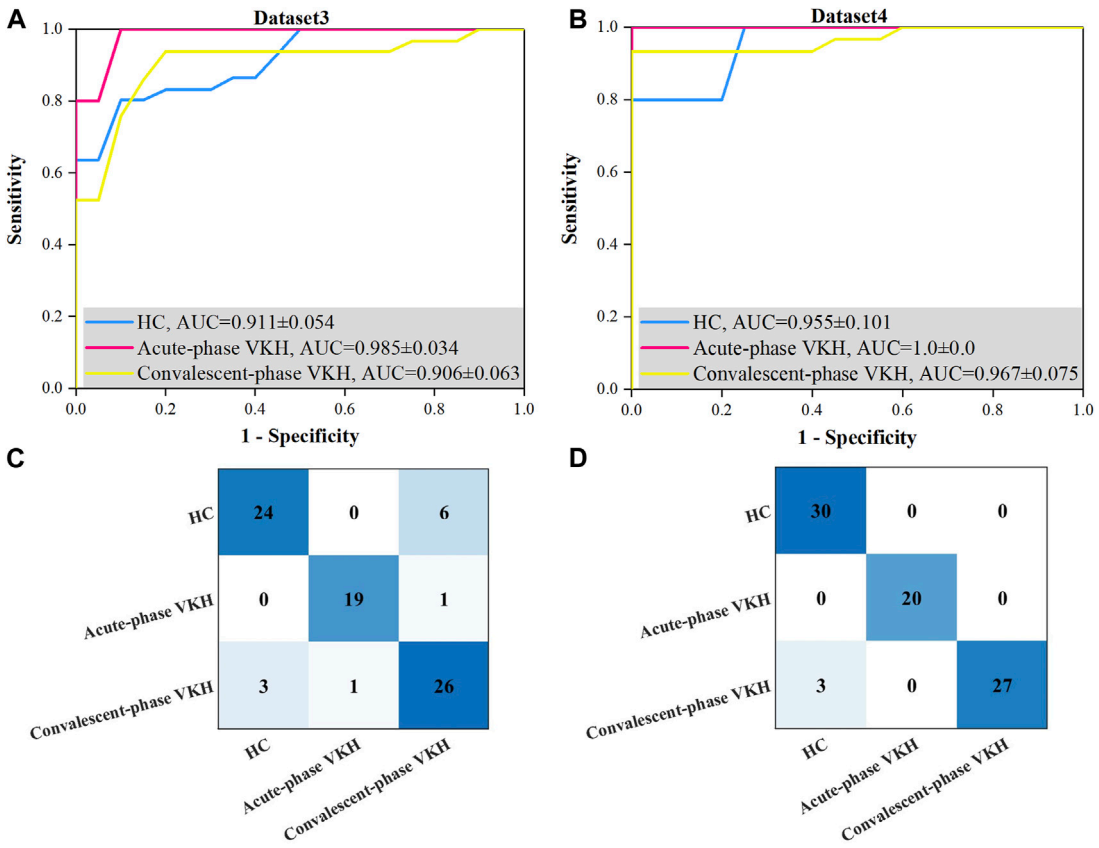

FIGURE 4
Best ROC curves and confusion matrices for three-class VKH classification with the proposed method based on Dataset3 and Dataset4. **(A)** Best ROC curve for Dataset3. **(B)** Best ROC curve for Dataset4. **(C)** Confusion matrix based on Dataset3. **(D)** Confusion matrix based on Dataset4.

TABLE 4 Average and best three-class VKH classification results obtained by using the feature selection and classification method.

Paper	Classification	Sensitivity (%)	Specificity (%)	AUC	Accuracy (%)
Yang et al. (2018)	HC vs. VKH	94.6	92.2	0.934	-
Chen et al. (2020)	HC vs. active VKH	-	-	0.999	-
	HC vs. inactive VKH	-	-	0.902	-
Standardization of Uveitis Nomenclature SUN Working Group (2021a)	Early-stage VKH	-	-	-	92.3
	Late-stage VKH	-	-	-	88
Chang et al. (2021)	HC vs. VKH	-	-	0.808	-
	Active VKH vs. inactive VKH	-	-	0.958	-
This paper	HC vs. VKH	98.00 ± 2.00	100.0 ± 0.0	0.983 ± 0.039	98.82 ± 1.18
	Healthy control	100.0 ± 0.0	93.56 ± 4.39	0.955 ± 0.101	96.16 ± 2.63
	Acute-phase VKH	100.0 ± 0.0	95.00 ± 4.39	1.0 ± 0.0	
	Convalescent-phase VKH	89.33 ± 6.86	100.0 ± 0.0	0.967 ± 0.075	

10.3389/fbioe.2023.1086347

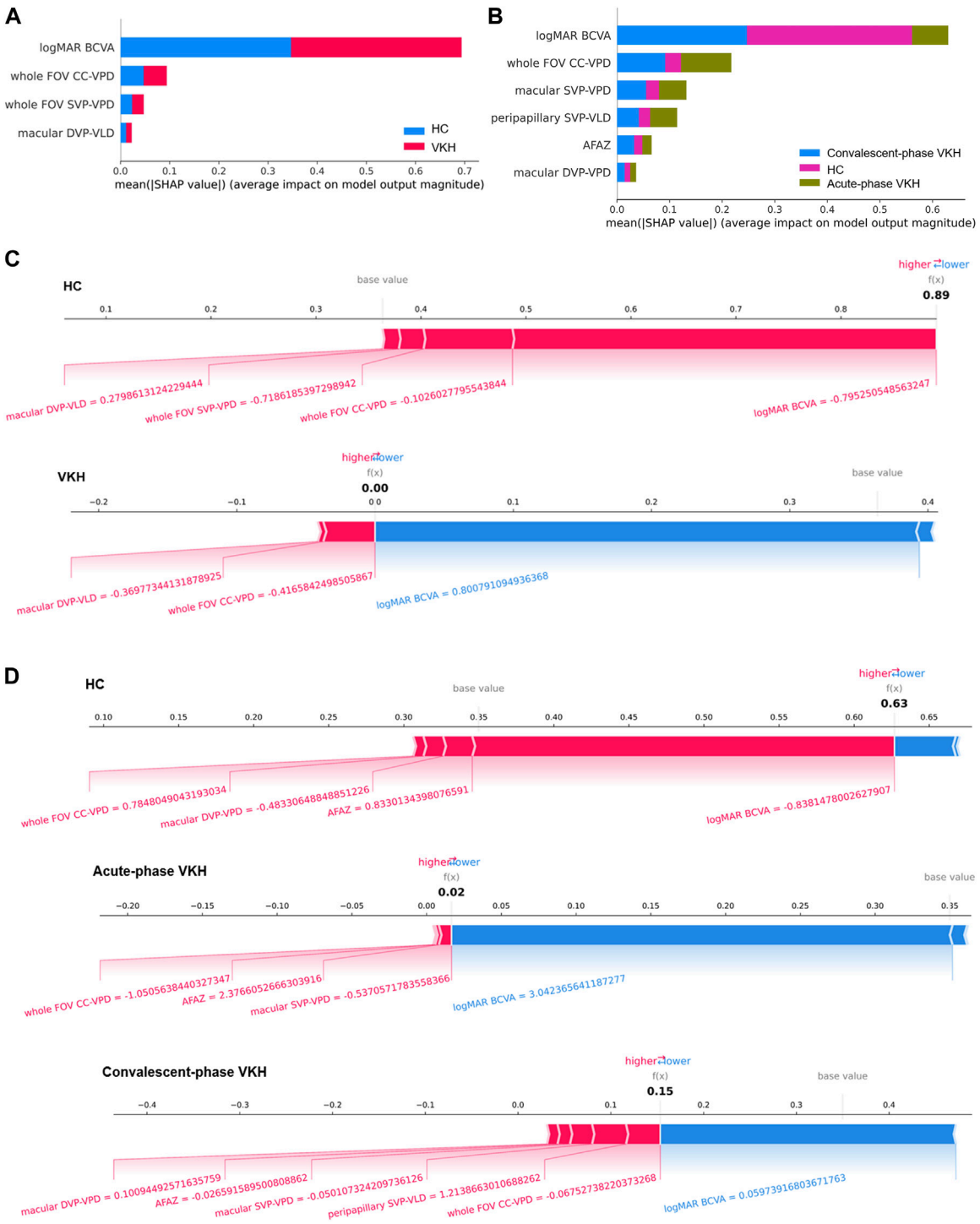

FIGURE 5
Global and local interpretability plots for SHAP-based 2- and 3-class VKH classification models. **(A–B)** Summary plots of feature importance for 2- and 3-class VKH classification models. **(C–D)** Local interpretability force plots for 2- and 3-class VKH classification models (The value of each feature is a standardized value).

classification based on WSS-OCTA features and feature selection using SVM-EO to our knowledge, the classification performance was compared with previous methods for VKH classification based on other imaging features and machine learning. According to Table 4, the most outstanding VKH classification performance was achieved using WSS-OCTA features and the proposed SVM-EO method, both for distinguishing VKH and HC and for identifying acute VKH, convalescent VKH and HC, which demonstrated the effectiveness and superiority of the proposed method.

3.5 Interpretable results for 2- and 3-class VKH classification models

The best features for the 2- and 3-class VKH classification have been given in the foregoing results, and the impact and contribution of these features to the VKH classification are presented here. Figures 5A, B revealed the contributions of each feature to the best 2- and 3-class VKH classification models. Overall, logMAR BCVA and whole FOV CC-VPD were the two most important features for the classification of VKH, whether two or three classifications. And the role of logMAR BCVA was far more important in both the 2-class task and the HC and convalescent-phase VKH categories in the 3- class task. Partially, the importance of each feature in each category may not be consistent with that of the overall classification task. For example, whole FOV CC-VPD was the most important feature for acute-phase VKH, not logMAR BCVA, the most important feature for three-class VKH classification. Figures 5C, D present some examples of the contributions made by each feature for the individual predictions from the best 2-class and 3-class VKH classification models. In the 2-class VKH classification, all features contributed to pushing up the HC class, while only macular DVP-VLD and whole FOV CC-VPD pushed up the VKH class, and logMAR BCVA had the largest effect in both the HC and VKH classes, but in the opposite direction. Similarly, logMAR BCVA had the largest effect in all classes in the 3-class VKH classification, but in the HC class with the acute-phase VKH and convalescent-phase VKH classes in the inverse direction. Whole FOV CC-VPD and AFAZ pushed up the predicted values in all classes, especially whole FOV CC-VPD also pushed up the HC and VKH classes in the 2-class VKH classification. These results confirmed the role of the selected optimal feature combinations in VKH classification, facilitating an interpretable and intelligent classification of VKH consistent with clinical diagnostic logic.

4 Discussion

In the past, many studies have focused on and confirmed microvascular changes in VKH disease based on OCTA (Uji et al., 2017; Karaca et al., 2020; Liang et al., 2020; 2021; Fan et al., 2021; Luo et al., 2021; Qian et al., 2021; Ye et al., 2021), however, no further OCTA-based classification models or criteria for VKH have been developed. In this paper, two two-class (VKH vs. HC) and three-class (HC vs. acute-phase VKH vs. convalescent-phase VKH) VKH datasets were established based on 2 clinical characteristics and 20 WSS-OCTA features including the FAZ, VPD, VLD, and FV features. The SVM-EO method was then used to simultaneously screen for VKH-sensitive features and optimize the hyperparameters of the SVM for effective VKH classification. To the best of our knowledge, this is the first VKH classification study based on WSS-OCTA features and with feature selection and classification by the SVM-EO method for enabling efficient performance. The results demonstrated.

That more efficient and stable classification performance of two- and three-class VKH with the combined clinical characteristics and WSS-OCTA features than with the pure WSS-OCTA features, and outperformed previous VKH classification studies.

Compared with previous studies, our proposed VKH classification method has differences and advantages both in terms of examination method and classification algorithm. In terms of the examination method, the current VKH classification relies on various imaging techniques or metabolomics. Previously, imaging techniques such as FA, ICGA, EDI-OCT, and SS-OCT were used extensively as auxiliary examinations and classifications for VKH (Hedayatfar et al., 2019; Urzua et al., 2020; Li et al., 2021). Based on clinical findings and these auxiliary examinations, several classification criteria for VKH have been proposed, such as RDC, the Classification Criteria for VKH Disease (DCV) (Yang et al., 2018), and the Standardization of Uveitis Nomenclature (SUN) criteria (Standardization of Uveitis Nomenclature SUN Working Group, 2021b). RDC overcomes the shortcomings of the Sugiura (Sugiura, 1978) and AUS criteria (Snyder and Tessler, 1980), and uses FA and ultrasonography findings as useful adjuncts, which is frequently used in clinical practice. The DCV takes into account unique clinical features and ancillary tests (OCT, B-scan ultrasonography, EDI-OCT, ICGA, and FA) and has achieved better AUC, negative predictive value, and sensitivity than RDC (Yang et al., 2018). The SUN criteria for VKH disease (fundus photographs, FA, and OCT) has many factors similar to DCV, but eliminates nonspecific exclusions with regionally relevant ones and does not include EDI-OCT findings (Standardization of Uveitis Nomenclature SUN Working Group, 2021a). In short, these criteria require complex clinical investigations and various imaging examinations, most of which are tedious, difficult to repeat, and invasive (e.g., ICGA and FA). Metabolomics-based analysis methods were also applied for VKH classification. Chen et al. (2020) used plasma metabolomics to identify significant differences in plasma metabolic phenotypes of VKH patients and identified diagnostic biomarkers for VKH disease. Chang et al. (2021) used urine metabolomics to identify predictive urine biomarkers for VKH disease. However, the VKH classification based on metabolomic analysis remains in laboratory research, and it is an expensive and time-consuming examination. Thus, a simplified and precise classification algorithm is needed and will be more conducive to VKH classification (Herbort et al., 2021). Using a simplified, rapid, and non-invasive imaging examination like WSS-OCTA with extracted disease-specific vascular parameters, along with common and easily measurable clinical characteristics (IOP and logMAR BCVA), we aim to develop a repeatable, easy-to-conduct VKH diagnostic method.

In addition, an advanced and efficient feature selection and classification method called SVM-EO was adopted to screen sensitive parameters and accurately classify VKH, which is the second particular advantage of this paper. Either imaging examinations combined with clinical characteristics or metabolomics leads to a large number of features, some of which are irrelevant, redundant and potentially reducing VKH classification performance, and therefore there is a necessity for feature selection of the extracted features. For example, Chang et al. (2021) identified 35 differential metabolites based on projection values obtained by principal component analysis (PCA) and orthogonal projection-discriminant analysis of potential structure (OPLS-DA) and statistical analysis and then modeled the classification of VKH by binary LR classifier. Yang et al. (2018) used latent class analysis (LCA) to screen 21 variables from 37 variables for the development of the best-fitting three-class

VKH classification model. These methods are well-established and commonly used statistical analysis-based feature selection methods in medical practice, not machine learning-based methods, which may result in not great classification performance. Feature selection is essentially a global optimization problem, so metaheuristic algorithms are widely used for feature selection because of their powerful global search capability (Houssein et al., 2021b). The EO is a novel metaheuristic algorithm proven to outperform many classical optimization algorithms, and recent methods combining EO and machine learning algorithms such as KNN and SVM have been effectively applied to public datasets (Ouadfel and Abd Elaziz, 2022) and practical problems such as stock market prediction (Houssein et al., 2021a) and bearing fault identification (Tan et al., 2021). The classification performance of machine learning algorithms depends not only on the selected features but also on the optimality of their hyperparameters. However, the aforementioned studies either focus on feature selection or hyperparameter optimization of machine learning algorithms. In this paper, instead of feature selection or hyperparameter optimization alone, we integrated an EO and an SVM to simultaneously screen for the optimal features and hyperparameters to achieve the best VKH classification performance with the fewest features.

The classification results also demonstrate the feasibility and superiority of the proposed SVM-EO method. First, good VKH classification performance was achieved based on pure WSS-OCTA features, and the number of features was effectively reduced (5 and 13 features for 2- and 3-class VKH classification). Surprisingly, based on the combination of clinical characteristics and WSS-OCTA features, not only was the best combination of features with a smaller number of features (4 and 6 features for 2- and 3-class VKH) obtained, but also the significantly better average VKH classification performance and the best VKH classification performance with smaller standard deviations were obtained, both in terms of sensitivity, specificity, AUC, and accuracy (Tables 2, 3). Therefore, the combination of clinical characteristics and WSS-OCTA features was considered to be the optimal solution. Finally, the comparison with previous VKH classification studies found that the state-of-the-art VKH classification performance was accomplished based on this scheme and the SVM-EO method (Table 4). Notably, although Chen et al. (2020) achieved a higher AUC between HC and active VKH classes (0.999) than HC class (0.955), this paper achieved an AUC of 1 for the acute-phase VKH class in the 3-class VKH classification (Table 4) and no misidentification between the acute-phase VKH class and the HC class (Figure 4), indicating that this paper achieved better VKH classification performance.

In terms of the features screened, except for the AFAZ parameter ($p = 0.055$), the selected features were all parameters that proved to be significantly different between groups (Ye et al., 2021), indicating that the method of selecting sensitive parameters in this paper is reliable and valid. This also explains why FV parameters were not chosen for both 2- and 3-class VKH classification, as we previously found no significant differences in FV parameters between HC and convalescent-phase VKH (Ye et al., 2021). The VPD parameters accounted for half of the number of features screened for VKH classification, which also supported VPD as a sensitive indicator of VKH (Liang et al., 2020; Fan et al., 2021). Interestingly, only two of the screened features in the 2- and 3-class VKH classification (logMAR BCVA and whole FOV CC-VPD) were identical, the others were not. The reason for this phenomenon may be that some features, although easily distinguishable between HC and VKH, are difficult to distinguish between acute-phase VKH and convalescent-phase VKH, and *vice versa*. In addition, as the SVM classification model is a black box model (Chen and Gao, 2020), the global and local interpretability of the best 2- and 3-class classification models based on SHAP was investigated to discover the contribution of the selected features toward the VKH classification (Figure 5). Unlike previous studies that highlighted the correlation between OCTA features and logMAR BCVA (Liang et al., 2020; 2021; Qian et al., 2021; Ye et al., 2021), here Figure 5 exposes that the logMAR BCVA is the most important feature for VKH classification, which in turn justifies the impairment of visual acuity due to the onset and progression of VKH. However, the only logMAR BCVA is not sufficient for the classification of VKH, as it is not disease-specific, and many ophthalmic conditions such as diabetic retinopathy, retinal vein occlusion, and glaucoma can also cause visual changes and are correlated with the OCTA features of these diseases (Liang et al., 2021). The key contribution of WSS-OCTA features to VKH classification in the model is irreplaceable. On the one hand, these features are disease-specific. Both high 2- and 3-class VKH classifications were achieved based on WSS-OCTA features along with an accuracy of 91.62% and 86.69%. On the other hand, combining these features with logMAR BCVA not only enabled disease-specific classification but also achieved the best classification performance (98.82% and 96.16%), significantly outperforming them alone. In conclusion, WSS-OCTA features and clinical characteristics are compatible with each other and jointly contribute to highly specific and sensitive VKH classification.

There are some limitations in this paper. Firstly, the number of VKH patients and HC recruited was relatively low due to the strict subject inclusion and exclusion criteria, which resulted in a relatively small sample size. More VKH subjects will be recruited in our future work to increase the sample size. Moreover, including patients with other VKH stages will work for establishing a comprehensive diagnostic model for accurate grading of VKH phases. Secondly, although various WSS-OCTA features were screened, manually segmenting OCTA images and computing WSS-OCTA features were time-consuming and subjective, so automatically segmenting OCTA images and extracting WSS-OCTA features based on deep learning and image processing techniques will be carried out. Finally, conducting a multicenter prospective study of VKH intelligent classification will be helpful to validate and test the generalization and real-world classification performance of the VKH classification model established in this paper.

5 Conclusion

To establish a simplified and feasible VKH classification model, we carried out a VKH intelligent classification study based on WSS-OCTA images and clinical characteristics, and adopted a new feature selection and classification method named SVM-EO to improve the classification performance. The results showed that outstanding 2- and 3-class VKH classification performance was achieved. In addition, we investigated the interpretability of the VKH

classification model based on SHAP, giving the importance ranking of the selected features and examples of the contribution of each feature to the prediction of a single sample, thus achieving VKH intelligent classification in accordance with clinical diagnostic logic. However, the modest sample size and artificially calculated WSS-OCTA features limit the clinical validation and application of this classification model. In the future, we will expand the sample size and adopt deep learning methods to achieve automatic segmentation and feature extraction of OCTA images for real-world applications of VKH intelligent classification.

Data availability statement

The original contributions presented in the study are included in the article/supplementary material, further inquiries can be directed to the corresponding authors.

Ethics statement

The studies involving human participants were reviewed and approved by The Ethics Committee of the Zhongshan Ophthalmic Center. The patients/participants provided their written informed consent to participate in this study.

Author contributions

PX: conceptualization, methodology, writing—original draft, and supervision. KM: conceptualization, methodology, software, and writing—original draft. WC, XY, and XH: investigation and data collection and writing—review and editing. GW, ZD, YH, and ZL: methodology and writing—review and editing. JY: conceptualization, writing—review and editing, and supervision. All authors read and approved the final manuscript.

Funding

This work was supported by the National Natural Science Foundation of China (Nos. 82230033 and 82271133), the Department of Science and Technology of Guangdong Province (Nos. 2021TX06Y127 and 2021TQ06Y137), the Basic and Applied Basic Research Foundation of Guangdong Province (No. 2022A1515011486), and the Guangzhou Science and Technology Plan Project (No.202103010001).

Conflict of interest

The authors declare that the research was conducted in the absence of any commercial or financial relationships that could be construed as a potential conflict of interest.

Publisher's note

All claims expressed in this article are solely those of the authors and do not necessarily represent those of their affiliated organizations, or those of the publisher, the editors and the reviewers. Any product that may be evaluated in this article, or claim that may be made by its manufacturer, is not guaranteed or endorsed by the publisher.

References

Agarwal, M., Radosavljevic, A., Patnaik, G., Rishi, E., and Pichi, F. (2020). Diagnostic value of optical coherence tomography in the early diagnosis of macular complications in chronic vogt-koyanagi-harada disease. *Ocul. Immunol. Inflamm.* 30, 801–808. doi:10.1080/09273948.2020.1833225

Baptista, M. L., Goebel, K., and Henriques, E. M. P. (2022). Relation between prognostics predictor evaluation metrics and local interpretability SHAP values. *Artif. Intell.* 306, 103667. doi:10.1016/j.artint.2022.103667

Caramia, C., Torricelli, D., Schmid, M., Munoz-Gonzalez, A., Gonzalez-Vargas, J., Grandas, F., et al. (2018). IMU-based classification of Parkinson's disease from gait: A sensitivity analysis on sensor location and feature selection. *IEEE J. Biomed. Health Inf.* 22, 1765–1774. doi:10.1109/JBHI.2018.2865218

Chang, R., Zhu, Y., Xu, J., Chen, L., Su, G., Kijlstra, A., et al. (2021). Identification of urine metabolic biomarkers for vogt-koyanagi-harada disease. *Front. Cell Dev. Biol.* 9, 637489. doi:10.3389/fcell.2021.637489

Chee, S.-P., Chan, S.-W. N., and Jap, A. (2017). Comparison of enhanced depth imaging and swept source optical coherence tomography in assessment of choroidal thickness in vogt–koyanagi–harada disease. *Ocul. Immunol. Inflamm.* 25, 528–532. doi:10.3109/09273948.2016.1151896

Chen, L., Chang, R., Pan, S., Xu, J., Cao, Q., Su, G., et al. (2020). Plasma metabolomics study of Vogt-Koyanagi-Harada disease identifies potential diagnostic biomarkers. *Exp. Eye Res.* 196, 108070. doi:10.1016/j.exer.2020.108070

Chen, S., and Gao, C. (2020). Linear priors mined and integrated for transparency of blast furnace black-box SVM model. *IEEE Trans. Ind. Inf.* 16, 3862–3870. doi:10.1109/TII.2019.2940475

EiOo, EiLin, Chee, S. P., and Wong, K. K. Y. (2020). Vogt-koyanagi-harada disease managed with immunomodulatory therapy within 3 Months of disease onset. *Am. J. Ophthalmol.* 220, 37–44. doi:10.1016/j.ajo.2020.07.036

Fan, S., Lin, D., Hu, J., Cao, J., Wu, K., Li, Y., et al. (2021). Evaluation of microvasculature alterations in convalescent Vogt-Koyanagi-Harada disease using optical coherence tomography angiography. *Eye* 35, 1993–1998. doi:10.1038/s41433-020-01210-5

Faramarzi, A., Heidarinejad, M., Stephens, B., and Mirjalili, S. (2020). Equilibrium optimizer: A novel optimization algorithm. *Knowl.-Based Syst.* 191, 105190. doi:10.1016/j.knosys.2019.105190

Hedayatfar, A., Khochtali, S., Khairallah, M., Takeuchi, M., El Asrar, A. A., and Herbort, C. P. (2019). Revised diagnostic criteria" for Vogt-Koyanagi-Harada disease fail to improve disease management. *J. Curr. Ophthalmol.* 31, 1–7. doi:10.1016/j.joco.2018.10.011

Herber, R., Pillunat, L. E., and Raiskup, F. (2021). Development of a classification system based on corneal biomechanical properties using artificial intelligence predicting keratoconus severity. *Eye Vis.* 8, 21. doi:10.1186/s40662-021-00244-4

Herbort, C. P., Tugal-Tutkun, I., Abu-El-Asrar, A., Gupta, A., Takeuchi, M., Fardeau, C., et al. (2021). Precise, simplified diagnostic criteria and optimised management of initial-onset vogt–koyanagi–harada disease: An updated review. *Eye* 36, 29–43. doi:10.1038/s41433-021-01573-3

Houssein, E. H., Dirar, M., Abualigah, L., and Mohamed, W. M. (2021a). An efficient equilibrium optimizer with support vector regression for stock market prediction. *Neural comput. Appl.* 34, 3165–3200. doi:10.1007/s00521-021-06580-9

Houssein, E. H., Ibrahim, I. E., Neggaz, N., Hassaballah, M., and Wazery, Y. M. (2021b). An efficient ECG arrhythmia classification method based on Manta ray foraging optimization. *Expert Syst. Appl.* 181, 115131. doi:10.1016/j.eswa.2021.115131

Karaca, I., Yılmaz, S. G., Afrashi, F., and Nalçacı, S. (2020). Assessment of macular capillary perfusion in patients with inactive vogt-koyanagi-harada disease: An optical coherence tomography angiography study. *Graefes Arch. Clin. Exp. Ophthalmol.* 258, 1181–1190. doi:10.1007/s00417-020-04676-x

Li, Y., Su, G., Huang, F., Zhu, Y., Luo, X., Kijlstra, A., et al. (2021). Identification of differently expressed mRNAs by peripheral blood mononuclear cells in Vogt-Koyanagi-Harada disease. *Genes Dis.* 9, 1378–1388. doi:10.1016/j.gendis.2021.06.002

Liang, A., Jia, S., Gao, F., Han, X., Pei, M., Qu, Y., et al. (2021). Decrease of choriocapillary vascular density measured by optical coherence tomography angiography in Vogt-Koyanagi-Harada disease. *Graefes Arch. Clin. Exp. Ophthalmol.* 259, 3395–3404. doi:10.1007/s00417-021-05238-5

Liang, A., Zhao, C., Jia, S., Gao, F., Han, X., Pei, M., et al. (2020). Retinal microcirculation defects on OCTA correlate with active inflammation and vision in vogt–koyanagi–harada disease. *Ocul. Immunol. Inflamm.* 29, 1417–1423. doi:10.1080/09273948.2020.1751212

Lin, D., Chen, J., Lin, Z., Li, X., Zhang, K., Wu, X., et al. (2020). A practical model for the identification of congenital cataracts using machine learning. *EBioMedicine* 51, 102621. doi:10.1016/j.ebiom.2019.102621

Lundberg, S. M., Erion, G., Chen, H., DeGrave, A., Prutkin, J. M., Nair, B., et al. (2020). From local explanations to global understanding with explainable AI for trees. *Nat. Mach. Intell.* 2, 56–67. doi:10.1038/s42256-019-0138-9

Lundberg, S. M., and Lee, S.-I. (2017). A unified approach to interpreting model predictions. https://arxiv.org/abs/1705.07874.10

Lundberg, S. M., Nair, B., Vavilala, M. S., Horibe, M., Eisses, M. J., Adams, T., et al. (2018). Explainable machine-learning predictions for the prevention of hypoxaemia during surgery. *Nat. Biomed. Eng.* 2, 749–760. doi:10.1038/s41551-018-0304-0

Luo, K., Cai, H., Hu, Y., Jin, C., Gan, X., Deng, Y., et al. (2021). Distinguishing microvasculature features of vogt-koyanagi-harada in patients in acute and convalescent phases using optical coherence tomography angiography. *Ocul. Immunol. Inflamm.* 29, 465–471. doi:10.1080/09273948.2019.1695856

Ma, K., Chen, Y., Zhang, X., Zheng, H., Yu, S., Cai, S., et al. (2019). sEMG-based trunk compensation detection in rehabilitation training. *Front. Neurosci.* 13, 1250. doi:10.3389/fnins.2019.01250

Nohara, Y., Matsumoto, K., Soejima, H., and Nakashima, N. (2022). Explanation of machine learning models using shapley additive explanation and application for real data in hospital. *Comput. Methods Programs Biomed.* 214, 106584. doi:10.1016/j.cmpb.2021.106584

O'Keefe, G. A. D., and Rao, N. A. (2017). Vogt-Koyanagi-Harada disease. *Surv. Ophthalmol.* 62, 1–25. doi:10.1016/j.survophthal.2016.05.002

Onsree, T., Tippayawong, N., Phithakkitnukoon, S., and Lauterbach, J. (2022). Interpretable machine-learning model with a collaborative game approach to predict yields and higher heating value of torrefied biomass. *Energy* 249, 123676. doi:10.1016/j.energy.2022.123676

Ouadfel, S., and Abd Elaziz, M. (2022). Efficient high-dimension feature selection based on enhanced equilibrium optimizer. *Expert Syst. Appl.* 187, 115882. doi:10.1016/j.eswa.2021.115882

Qian, Y., Yang, J., Liang, A., Zhao, C., Gao, F., and Zhang, M. (2021). Widefield swept-source optical coherence tomography angiography assessment of choroidal changes in vogt-koyanagi-harada disease. *Front. Med.* 8, 698644. doi:10.3389/fmed.2021.698644

Read, R. W., Holland, G. N., Rao, N. A., Tabbara, K. F., Ohno, S., Arellanes-Garcia, L., et al. (2001). Revised diagnostic criteria for vogt-koyanagi-harada disease: Report of an international committee on nomenclature. *Am. J. Ophthalmol.* 131, 647–652. doi:10.1016/s0002-9394(01)00925-4

Shilaskar, S., and Ghatol, A. (2013). Feature selection for medical diagnosis: Evaluation for cardiovascular diseases. *Expert Syst. Appl.* 40, 4146–4153. doi:10.1016/j.eswa.2013.01.032

Snyder, D. A., and Tessler, H. H. (1980). Vogt–koyanagi–harada syndrome. *Am. J. Ophthalmol.* 90, 69–75. doi:10.1016/S0002-9394(14)75078-0

Spaide, R. F. (2016). Choriocapillaris flow features follow a power law distribution: Implications for characterization and mechanisms of disease progression. *Am. J. Ophthalmol.* 170, 58–67. doi:10.1016/j.ajo.2016.07.023

Standardization of Uveitis Nomenclature (Sun) Working Group (2021a). Classification criteria for vogt-koyanagi-harada disease. *Am. J. Ophthalmol.* 228, 205–211. doi:10.1016/j.ajo.2021.03.036

Standardization of Uveitis Nomenclature (Sun) Working Group (2021b). Development of classification criteria for the uveitides. *Am. J. Ophthalmol.* 228, 96–105. doi:10.1016/j.ajo.2021.03.061

Sugiura, S. (1978). Vogt-Koyanagi-Harada disease. *Jpn. J. Ophthalmol.* 22, 9–35.

Tan, H., Xie, S., Liu, R., and Ma, W. (2021). Bearing fault identification based on stacking modified composite multiscale dispersion entropy and optimised support vector machine. *Measurement* 186, 110180. doi:10.1016/j.measurement.2021.110180

Tang, T., Yu, Z., Xu, Q., Peng, Z., Fan, Y., Wang, K., et al. (2020). A machine learning-based algorithm used to estimate the physiological elongation of ocular axial length in myopic children. *Eye Vis.* 7, 50. doi:10.1186/s40662-020-00214-2

Ting, D. S. J., Foo, V. H., Yang, L. W. Y., Sia, J. T., Ang, M., Lin, H., et al. (2021). Artificial intelligence for anterior segment diseases: Emerging applications in ophthalmology. *Br. J. Ophthalmol.* 105, 158–168. doi:10.1136/bjophthalmol-2019-315651

Triolo, G., Rabiolo, A., Shemonski, N. D., Fard, A., Di Matteo, F., Sacconi, R., et al. (2017). Optical coherence tomography angiography macular and peripapillary vessel perfusion density in healthy subjects, glaucoma suspects, and glaucoma patients. *Investig. Opthalmology Vis. Sci.* 58, 5713. doi:10.1167/iovs.17-22865

Uji, A., Balasubramanian, S., Lei, J., Baghdasaryan, E., Al-Sheikh, M., and Sadda, S. R. (2017). Impact of multiple en face image averaging on quantitative assessment from optical coherence tomography angiography images. *Ophthalmology* 124, 944–952. doi:10.1016/j.ophtha.2017.02.006

Urzua, C. A., Herbort, C., Valenzuela, R. A., Abu El-Asrar, A. M., Arellanes-Garcia, L., Schlaen, A., et al. (2020). Initial-onset acute and chronic recurrent stages are two distinctive courses of Vogt-Koyanagi-Harada disease. *J. Ophthalmic Inflamm. Infect.* 10, 23. doi:10.1186/s12348-020-00214-2

Wang, K., Tian, J., Zheng, C., Yang, H., Ren, J., Liu, Y., et al. (2021). Interpretable prediction of 3-year all-cause mortality in patients with heart failure caused by coronary heart disease based on machine learning and SHAP. *Comput. Biol. Med.* 137, 104813. doi:10.1016/j.compbiomed.2021.104813

Yang, P., Zhong, Y., Du, L., Chi, W., Chen, L., Zhang, R., et al. (2018). Development and evaluation of diagnostic criteria for vogt-koyanagi-harada disease. *JAMA Ophthalmol.* 136, 1025. doi:10.1001/jamaophthalmol.2018.2664

Ye, X., Zhang, H., Xiao, P., Wang, G., Hu, X., Yan, C., et al. (2021). Microvasculature features of vogt-koyanagi-harada disease revealed by widefield swept-source optical coherence tomography angiography. *Front. Med.* 8, 719593. doi:10.3389/fmed.2021.719593

frontiers | Frontiers in Bioengineering and Biotechnology

TYPE Original Research
PUBLISHED 10 May 2023
DOI 10.3389/fbioe.2023.1174419

OPEN ACCESS

EDITED BY
Matthew A. Reilly,
The Ohio State University, United States

REVIEWED BY
Manmohan Singh,
University of Houston, United States
Shi Song Rong,
Harvard Medical School, United States

*CORRESPONDENCE
Yu Cai,
cai_yuu@hotmail.com
Yingzi Pan,
panyingzi99@126.com

RECEIVED 26 February 2023
ACCEPTED 20 April 2023
PUBLISHED 10 May 2023

CITATION
Wei Y, Cai Y, Bao C, Zhu Y and Pan Y (2023), The role of corneal biomechanics in visual field progression of primary open-angle glaucoma with ocular normotension or hypertension: a prospective longitude study. *Front. Bioeng. Biotechnol.* 11:1174419. doi: 10.3389/fbioe.2023.1174419

The role of corneal biomechanics in visual field progression of primary open-angle glaucoma with ocular normotension or hypertension: a prospective longitude study

Yahui Wei, Yu Cai*, Chenying Bao, Yanfei Zhu and Yingzi Pan*

Department of Ophthalmology, Peking University First Hospital, Beijing, China

Introduction: To analyze effects of dynamic corneal response parameters (DCRs) on visual field (VF) progression in normal-tension glaucoma (NTG) and hypertension glaucoma (HTG).

Methods: This was a prospective cohort study. This study included 57 subjects with NTG and 54 with HTG, followed up for 4 years. The subjects were divided into progressive and nonprogressive groups according to VF progression. DCRs were evaluated by corneal visualization Scheimpflug technology. General linear models (GLMs) were used to compare DCRs between two groups, adjusting for age, axial length (AL), mean deviation (MD), etc. VF progression risk factors were evaluated by logistic regression and receiver operating characteristic (ROC) curves.

Results: For NTG, first applanation deflection area (A1Area) was increased in progressive group and constituted an independent risk factor for VF progression. ROC curve of A1Area combined with other relevant factors (age, AL, MD, etc.) for NTG progression had an area under curve (AUC) of 0.813, similar to the ROC curve with A1area alone (AUC = 0.751, p = 0.232). ROC curve with MD had an AUC of 0.638, lower than A1Area-combined ROC curve (p = 0.036). There was no significant difference in DCRs between the two groups in HTG.

Conclusion: Corneas in progressive NTG group were more deformable than nonprogressive group. A1Area may be an independent risk factor for NTG progression. It suggested that the eyes with more deformable corneas may also be less tolerant to pressure and accelerate VF progression. VF progression in HTG group was not related to DCRs. Its specific mechanism needs further studies.

KEYWORDS

open-angle glaucoma, visual field progression, corneal biomechanics, normal tension glaucoma, CorVis ST

Introduction

Glaucoma is a leading cause of irreversible visual impairment and blindness worldwide (Tham YC et al., 2014). It is defined as a progressive optic neuropathy with characteristic changes in the optic nerve head (ONH) and corresponding visual field (VF) defects. Although intraocular pressure (IOP) is the most significant risk factor for glaucoma development and progression (Kass et al., 2002; Leske et al., 2007), reducing IOP to normal or even reducing it by 45% was still not enough to control VF progression clinically in some primary open-angle glaucoma (POAG) patients (Leske et al., 2004). Another group (Susanna et al., 2019) found in a study of 334 glaucoma patients with an average follow-up time of 4.3 years that approximately a quarter of patients with seemingly well-controlled IOP (IOP ≤ 18 mmHg) still had VF progression during follow-up. Although high IOP is considered the most important risk factor for glaucomatous optic nerve (GON) damage, there is still confusion about which other factors, such as hypoperfusion or parapapillary vascularity, are also risk factors for glaucomatous VF progression.

Recently, our study and several other studies showed that the corneas in normal-tension glaucoma (NTG) were softer and easier to deform than that in hypertension glaucoma (HTG) or the normal physiological state (Wei et al., 2021; Wu et al., 2022; Xu et al., 2022). Another study by our group (Li et al., 2017) also found that the corneas were more deformable in the worse eyes of asymmetric NTG patients. This finding provided evidence for the NTG pathophysiology hypothesis that lower tolerance for normal IOP of softer eyeballs causes mechanical damage. The above results have drawn scholars' attention to the role of corneal biomechanics in glaucomatous VF progression.

Some studies have found that the corneal biomechanical characteristics (CBCs) of glaucoma patients were related to VF progression (Li et al., 2018; Jung et al., 2019). Most studies believed that the more corneal deformation ability of the eyeball, the faster the visual field progressed. CBCs may also provide some explanations for the VF progression of some glaucoma patients with seemingly well-controlled IOP. Jung et al. (2019) found that the deformation amplitude (DA) was increased in eyes with progressive POAG, that is, the deformability of the cornea was increased. A prior study of our group (Li et al., 2018) found that the time at the first applanation (A1T) in the progressive NTG group was reduced, while the DA was increased; that is, the progressive eyes were more easily deformed. Recently, the results of a study (Qassim et al., 2021) was contradictory to the conclusions of previous studies. They followed up 228 glaucoma suspect eyes (with glaucomatous optic nerve defects but without visual field damage) for 4.2 years and found that thin (smaller central cornea thickness, CCT) and hard (greater stiffness parameter at the first applanation, SP-A1) corneas were more likely to progress. The contradiction may be due to the following reasons: When comparing the corneal biomechanical index SP-A1, the author merely corrected for CCT and did not correct for age or axial length (AL), which may affect the results to some extent (Liu et al., 2021; Chen et al., 2022). Second, IOP was not used as one of the criteria when the participants were enrolled; thus, it was impossible to distinguish between NTG and HTG in the study, which may have an impact on the results. The relationship between corneal biomechanics and glaucoma progression still needs further study.

In this paper, POAG was divided into NTG and HTG according to 24-h Goldmann applanation tonometry (GAT) measurement when firstly diagnosed, and these subjects were analyzed separately. The purpose of this study is to explore the role of CBCs in VF progression among NTG and HTG patients with well-controlled IOP, to probe the corneal biomechanical risk factors for VF progression, and to provide auxiliary evidence for clinical evaluation of POAG VF progression.

Methods

Subjects

This was a prospective cohort study. The patients were recruited consecutively from the Glaucoma Department of Ophthalmology at Peking University First Hospital diagnosed with POAG from October 2018 to January 2019. The institutional review board approved the study protocol, and the study was conducted in full accordance with the tenets of the Declaration of Helsinki. Informed consent was obtained from all volunteers before the study commenced.

POAG was defined as a glaucomatous optic disc (cup-to-disc ratio greater than 0.6, asymmetry of the cup-to-disc ratio ≥ 0.2 between eyes and the presence of local or diffuse retinal nerve fiber layer defects or neuroretinal rim defects in absence of any other abnormalities that could explain such findings) and/or with a corresponding glaucomatous VF defect with an open angle, with other secondary factors excluded. Patients were assigned to the HTG group or the NTG group based on 24-h IOP measured by GAT when first diagnosed.

The inclusion criteria for POAG patients were as follows: age over 40 years, best-corrected visual acuity (BCVA) of 20/40 or better, and astigmatism less than 3.0 diopters. Patients with any of the following criteria were excluded: corneal scarring, any trauma or a history of previous ocular surgery, inflammatory eye disease, and systemic disease conditions with a known or anticipated effect on dynamic corneal response parameter (DCR) measurement (including diabetes mellitus).

All subjects underwent a thorough ophthalmic evaluation, including slit-lamp biomicroscopy, fundus examination, GAT measurement and gonioscopy. All subjects underwent automated perimetry using a Humphrey Field Analyzer II (Carl Zeiss Meditec, Jena, Germany) with a full threshold 24–2 SITA standard program. Central corneal thickness (CCT) was measured with a Pentacam (Oculus Optikgeräte GmbH, Wetzlar, Germany). AL was measured using an IOL-Master 500 (Carl Zeiss Meditec, Jena, Germany). The duration of prostaglandin (PG) treatment was recorded in all POAG patients.

If both eyes of a POAG patient met the inclusion criteria, the eye with more severe glaucoma [defined as a lower mean deviation (MD) value] was included in the analysis.

Corneal visualization scheimpflug technology measurements

All measurements obtained with the Corneal visualization Scheimpflug technology (CST) were taken by the same experienced technicians and captured automatically to minimize operator dependence. Only CST examinations with a quality score of "OK" were included in the analysis.

The DCRs evaluated in this study were deflection length, amplitude, area and time at the first and second applanation (Vinciguerra et al., 2016; Lopes et al., 2017; Vinciguerra et al., 2017). Briefly, a faster and larger deformation at the first applanation (A1), as well as a slower and smaller deformation at the second applanation (A2), indicated a more deformable cornea. That is, higher deflection amplitude (Amp), deflection length (Length), and deflection area (Area) and shorter time (T) at A1 and opposite parameters at A2 indicated a softer cornea.

Glaucoma follow-up

Follow-up was performed every 3–4 months for 4 years in total. Routine ophthalmologic examination, GAT, VF, stereo fundus photography, and spectral-domain optical coherence tomography (RT-Vue 100, Optovue, Fremont, CA) were performed. NTG and HTG populations with target IOP were included in the final analysis. Target IOP was defined as follows (Group, 1998; Leske et al., 2004; Prum et al., 2016): ① NTG: 24-h mean IOP decreased by at least 30% compared with baseline 24-h mean IOP before treatment; ② HTG: IOP ≤ 21 mmHg, and the average 24-h IOP decreased by at least 20% from the baseline 24-h IOP before treatment. The subjects were divided into the progressive and nonprogressive groups according to their Advanced Glaucoma Intervention Study (AGIS) scores (Group, 1994). Visual field progression was defined as an increase of 4 or more points in the AGIS score compared to baseline on each of the 3 consecutive follow-up visual field examinations (Group, 1994).

Statistical analysis

Statistical analyses were performed using SPSS software (V.18, IBM), Stata 15.1 (StataCorp LLC, TX, United States) and MedCalc 15.2.2 (MedCalc Software bvba, Ostend, Belgium). Categorical variables were compared with the Pearson chi-square test. Before comparing the quantitative variables among different groups, the normality of the variables was verified using the Shapiro-Wilk test. Normally distributed continuous variables were expressed as the mean (standard deviation), while nonnormally distributed variables were recorded as the median (first and third quartiles). The *t*-test and the Mann–Whitney *U* test were used for comparisons between the groups. General linear models (GLMs) correcting for the effects of baseline measures of age, sex, GAT, AL, baseline MD and time on PGs were used to compare DCRs between groups. Risk factors for glaucoma progression were evaluated by logistic regression, and a receiver operating characteristic curve (ROC) was drawn to analyze the area under the curve (AUC). AUC, specificity, and sensitivity were used to reflect the ability of DCRs and risk factors to predict glaucoma progression. A value of $p < 0.05$ was considered statistically significant.

Results

Seventy-three patients were initially enrolled in the NTG group, of whom 9 patients (9/73, 12%) were lost to follow-up. Among the 64 subjects completing the follow-up, 7 patients (7/64, 11%) did not reach the target IOP. In 57 patients who finished the 4-year follow-up and reached the target IOP, visual fields of 17 patients (17/57, 30%) were diagnosed with progression and 40 patients without progression. In the HTG group, 75 patients were initially enrolled, with 11 patients (11/75, 15%) lost to follow up in the process. Ten of 64 patients finishing the follow-up (10/64, 16%) did not reach the target IOP. In 54 patients who finished the follow-up and reached the target IOP, 20 patients (20/54, 37%) were diagnosed with progression, and 34 patients were without progression.

Baseline characteristics for the nonprogressive and progressive groups of NTG and HTG are detailed in Table 1. There were no significant differences in gender, AL, GAT, CCT, MD or duration of PG use (months) between the two groups in either NTG or HTG. Among HTG patients, the nonprogressive group was younger ($p = 0.034$).

The comparison of DCRs between the nonprogressive group and the progressive group in NTG is shown in Table 2. In a single variate comparison, there were differences in three parameters at the first applanation (A1), the horizontal length of deflection (A1Length: $p = 0.013$), vertical amplitude of deflection (A1Amp: $p = 0.010$) and deflection area (A1Area: $p = 0.003$), indicating that the NTG progression group had a longer flattening length and larger deformation depth and area.

After GLM adjustment for age, sex, GAT, CCT, AL, MD, and PG durations, there was still a significant difference between the two groups in the deflection area (A1Area: $p = 0.046$), indicating that the NTG progression group had greater corneal deformation, which further confirmed that the NTG progression group had a more deformable cornea.

We further analyzed risk factors for NTG progression by the logistic regression model. According to the above results, there was a significant difference in A1Area between the progressive group and the nonprogressive group of NTG in the GLM analysis. A1Area and several affecting factors, including age, GAT, CCT, AL, and MD, were included in the logistic regression model. The regression model results are shown in Table 3 and indicated that A1Area was an independent risk factor for NTG VF progression, with an odds ratio (OR) of 1.56/0.1 mm^2. For every 0.1 mm^2 increase in A1Area, the risk of NTG progression increased by 1.56 times. The ROC curve of A1Area combined with the above factors to diagnose NTG progression was obtained (Figure 1), with an AUC of 0.813 (95% confidence interval (CI): 0.681, 0.908), sensitivity of 64% and specificity of 91%. When the ROC curve of the diagnosis of NTG progression was plotted with A1Area and MD alone, the AUCs were 0.751 (0.612, 0.861) and 0.638 (0.612, 0.861), respectively (Figure 1). To evaluate the diagnostic performance of A1Area and MD for NTG VF progression, the individual ROC curves for MD and A1Area were compared to the A1Area-combined diagnostic ROC curve. There was no difference between the A1Area and A1Area-combined ROC curves ($p = 0.232$), while the difference between the MD and A1Area-combined ROC curves was significant ($p = 0.036$). The cutoff value of A1Area was 0.198 mm^2, with a sensitivity and specificity of 76% and 73%, respectively.

For HTG, since there was a significant difference in age between the two groups, the DCRs of the two groups were

TABLE 1 Baseline characteristics of the nonprogressive and progressive groups among NTG and HTG patients.

	NTG			HTG		
	Nonprogressive (N = 40)	Progressive (N = 17)	P	Nonprogressive (N = 34)	Progressive (N = 20)	P
Age [y]	59.5 (14.9)	66.6 (10.6)	0.092	60.0 (11.21)	65.5 (10.4)	**0.034**
Sex [M/F]	25/15	8/9	0.280	24/13	10/10	0.568
AL [mm]	24.58 (1.53)	24.41 (2.20)	0.621	24.17 (23.45, 25.48)	23.95 (23.28, 24.92)	0.243
GAT [mmHg]	13.0 (12.0, 15.0)	13.0 (11.5, 15.5)	0.846	16.0 (14.0, 18.0)	14.5 (13.25, 17.0)	0.291
CCT [μm]	521.4 (30.1)	528.9 (40.7)	0.578	540.5 (33.5)	519.2 (30.2)	0.340
MD [dB]	−5.57 (−8.23, −2.57)	−10.33 (−13.36, −5.09)	0.254	−4.88 (−10.32, −1.70)	−6.76 (−17.32, −3.81)	0.179
PGs [m]	16.0 (0, 73)	36.0 (0, 72.5)	0.978	36.0 (30.9)	31.6 (19.3)	0.664

Data are presented as the mean (standard deviation) or median (Q25, Q75). NTG: normal-tension glaucoma; HTG: hypertension glaucoma; N: number; y: year; M: male; F: female; AL: axial length; GAT: intraocular pressure measured by Goldmann applanation tonometry; CCT: central cornea thickness; MD: mean deviation of the visual field; PGs: prostaglandin duration; m: month. The bold value means $p < 0.05$.

TABLE 2 Comparisons of corneal biomechanics of NTG with and without progression.

		Nonprogressive group (N = 37)	Progressive group (N = 20)	Univariate *p*-value	Multivariate *p*-value
Horizontal length	A1Length [mm]	2.41 (2.31, 2.56)	2.54 (2.42, 2.64)	**0.013**	0.109
	A2Length [mm]	2.97 (2.59, 3.71)	3.89 (2.76, 5.72)	0.056	
Vertical depth	A1Amp [mm]	0.10 (0.10, 0.11)	0.11 (0.10, 0.11)	**0.010**	0.060
	A2Amp [mm]	0.12 (0.11, 0.13)	0.12 (0.10, 0.13)	0.720	
Area	A1Area [mm^2]	0.19 (0.17, 0.20)	0.21 (0.20, 0.22)	**0.003**	**0.046**
	A2Area [mm^2]	0.26 (0.20, 0.28)	0.25 (0.21, 0.28)	0.619	
Time	A1T [ms]	7.40 (0.40)	7.26 (0.32)	0.495	
	A2T [ms]	21.87 (21.43, 22.18)	21.80 (21.56, 22.14)	0.565	

Data are presented as the mean (standard deviation) or median (Q25, Q75). NTG: normal-tension glaucoma; A1: the first applanation; Length: deflection length; A2: the second applanation; AMP: deflection amplitude; Area: deflection area; T: time. The bold value means $p < 0.05$.

TABLE 3 Logistic regression model of NTG progression.

	OR	P	95% CI
A1Area	1.56	0.021	1.07, 2.27
age	1.04	0.252	0.97, 1.12
CCT	1.01	0.488	0.99, 1.03
GAT	0.82	0.163	0.61, 1.09
MD	0.93	0.271	0.81, 1.06
AL	1.02	0.932	0.67, 1.56
$R^2 = 0.24$, $p = 0.015$			

NTG: normal-tension glaucoma; OR: odds ratio; CI: confidence interval; A1Area: deflection length at the first applanation; CCT: central cornea thickness; GAT: intraocular pressure measured by Goldmann applanation tonometry; MD: mean deviation; AL: axial length.

compared by GLM with the affecting factors (age, sex, AL, CCT, MD, and PG durations) adjusted. The results are shown in Table 4. There was no significant difference in DCRs between the two groups.

Discussion

In this study, we found that in NTG subjects, the progressive group had greater A1Amp, A1Area, and A1Length than the

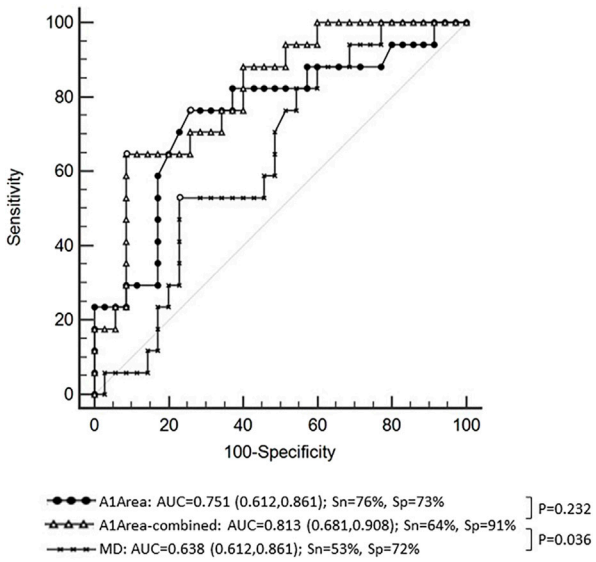

FIGURE 1
The receiver operating characteristic (ROC) curve of A1Area (deflection area at the first applanation) combined with affecting factors with an area under the curve (AUC) of 0.813 and a sensitivity and specificity of 64% and 91%, respectively. The ROC curve of A1Area-combined factors was similar to that of A1Area, with an AUC of 0.751 (p = 0.232), and higher than that of MD (mean deviation of visual field), with an AUC of 0.638 (p = 0.036). Sn: sensitivity; Sp: specificity.

nonprogressive group in univariate analysis. The results indicated that the progressive group had a greater corneal depression depth, displacement area and flattening length at the first applanation than the nonprogressive group, which might indicate that the progressive group had a more deformable cornea. As previous studies (Li et al., 2017; Wei et al., 2021; Wu et al., 2022) indicated that cornea biomechanics were related with age, sex, CCT, AL, IOP, and glaucoma severity, these factors were adjusted in the analysis. In baseline comparisons, MD in the progressive group (−10.33 dB) was lower than that of the nonprogressive group (MD: −5.57 dB), while the difference was not significant (p = 0.254). Although there were no differences in baseline measures between the two NTG groups, we adjusted them in the study. After adjusting the main factors that may affect corneal biomechanics (age, sex, CCT, AL, GAT, MD), the progressive group still had a larger A1area, indicating that the cornea had a larger deflection area at the first applanation. That is, the corneas of the progressive group were more deformable. Previous studies have shown that the cornea, sclera, and lamina cribrosa are continuous collagenous fibrous tissues and are composed of similar extracellular collagen components (Bellezza et al., 2003; Pakravan et al., 2007). Therefore, the deformability of the cornea may reflect the deformability of the posterior sclera and lamina cribrosa to some extent (Susanna et al., 2019). Sayah et al. (2020) found that more deformable eyeballs were more likely to have glaucoma-related optic nerve damage, including thinning of the ganglion cell complex and retinal nerve fiber layer. In this study, we found that the more deformable the cornea, the more visual field progression in NTG. Therefore, we hypothesized that in the eyeballs of NTG patients, whose cornea is more easily deformed, the cribriform plate tissue may also be easily deformed and less resistant to pressure, leading to optic nerve damage and VF progression being more likely to occur.

We found that for HTG, there was no significant difference in DCRs between the groups with or without visual field progression. The results were consistent with previous observations that corneal biomechanical parameters were not significantly different between the HTG and normal groups (Wei et al., 2021). Our results indicated that VF progression in the HTG group with a 30% decrease in IOP compared with the baseline IOP was not related to corneal biomechanics. In HTG, high IOP may be more responsible for GON, and the specific mechanisms need to be further studied.

To the best of our knowledge, this study is the first one separately assessing corneal deformability of NTG and HTG with or without VF progression. Most previous studies did not separate HTG from NTG in POAG. The study was followed up for 4 years. The results of the study were roughly consistent with those of Li et al. (2018) and Jung et al. (2019). A previous study by our group (Li et al., 2018) found that in NTG, the progressive group had a smaller corneal A1T and a larger DA. Jung et al. (2019) found that corneal DA was greater in POAG progression eyes without separating NTG and HTG. Another study that did not distinguish NTG from HTG obtained opposite results in that thin and hard corneas were more likely to progress (Qassim et al., 2021). Considering the differences in pathogenesis between NTG and HTG (Wei et al., 2021), the classification of NTG and HTG in the analysis of POAG corneal

TABLE 4 Comparisons of corneal biomechanics of HTG with and without progression.

		Nonprogressive group (N = 34)	Progressive (N = 20) group	Multivariate p-value
Horizontal length	A1Length [mm]	2.47 (2.34, 2.58)	2.42 (2.35, 2.55)	0.148
	A2Length [mm]	2.86 (2.39, 3.59)	3.02 (2.42, 5.63)	0.728
Vertical depth	A1Amp [mm]	0.11 (0.01)	0.11 (0.01)	0.281
	A2Amp [mm]	0.11 (0.11, 0.11)	0.11 (0.10, 0.11)	0.228
Area	A1Area [mm^2]	0.20 (0.04)	0.19 (0.02)	0.256
	A2Area [mm^2]	0.26 (0.21, 0.29)	0.24 (0.22, 0.30)	0.224
Time	A1T [ms]	7.64 (0.42)	7.71 (0.57)	0.570
	A2T [ms]	21.66 (0.43)	21.45 (0.91)	0.432

Data are presented as the mean (standard deviation) or median (Q25, Q75). HTG: hypertensive glaucoma; A1: first applanation; Length: deflection length; A2: second applanation; AMP: deflection amplitude; Area: deflection area; T: time.

biomechanics is vital. Besides, the parameters used in this study were different and acquired with the whole eye retreat movement eliminated (Wu et al., 2022), which made the results more accurate.

Most scholars believe that glaucomatous optic nerve damage is the result of multiple factors (De Moraes et al., 2011). However, there is still controversy regarding which factors other than IOP are the main risk factors for glaucoma VF progression. Previous studies have found that some factors, such as ocular hypoperfusion (Leske et al., 2004; Dascalu et al., 2021; Fraenkl et al., 2022) and parapapillary vascular factors (Rong et al., 2019; Xu et al., 2022), could affect VF progression. This study suggested that differences in corneal biomechanics may also be one of the reasons for VF progression in NTG patients. The other pathogeneses of NTG remain to be further studied.

Furthermore, this study also analyzed the risk factors for NTG progression and found that the A1Area may be an independent risk factor for NTG progression. The risk of NTG progression increased by 1.56 times for every 0.01 mm^2 increase in A1Area. The area under the ROC curve of A1Area combined with affecting factors for NTG progression was 0.813 [95% CI: (0.681, 0.908)], with a barely satisfactory sensitivity of 64% and a nice specificity of 91%. When A1Area was used to diagnose NTG progression alone, the AUC was 0.751 (0.612, 0.861), with a reasonable sensitivity of 76% and specificity of 73%. Because visual field MD is an important application in the clinical evaluation of VF progression in patients, the diagnostic value of MD was also analyzed. The area under the ROC curve was only 0.638 (0.612, 0.861). We further compared the diagnostic efficacy of A1Area-combined factors with A1Area or MD alone. The results showed that the diagnostic performance of A1Area was similar to that of A1Area-combined factors, while MD had a significantly lower AUC than A1Area-combined factors. The results revealed that A1area was valuable in predicting NTG VF progression, with a greater increase in A1Area indicating a greater likelihood of progression. This suggests that more attention should be paid to the A1Area increase in clinical practice.

This study has some limitations. First, the small sample size of this study may cause bias in the judgment of corneal biomechanical properties. It is necessary to further expand the sample size to fully assess the role of corneal biomechanics in the progression of glaucomatous fields. Second, previous studies have found that PG drugs may have some effects on corneal thickness and corneal biomechanics in glaucoma patients, but there are controversies. Wu et al. (2016) showed that POAG patients who have used PGs for a long time (more than 2 years) were likely to have more corneal deformation than newly diagnosed patients. Another study from the same group (Wu et al., 2020) found that after a mean follow-up of 10.3 months, the corneal deformation ability of glaucoma patients using PGs decreased. Due to the lack of sufficient literature support for the effects of other anti-glaucoma medications on corneal biomechanics, other drugs were not included in the analysis in this paper. In our study, although there was no significant difference in the duration of PGs use between the two groups, the results of this study still need to be treated with caution. In the next step, more newly diagnosed NTG patients will be included to further evaluate the corneal biomechanical properties. In addition, although CST measurement is based on cornea dynamic reflection of the whole process, it is limited by a lack of direct evaluation of corneal strength based on the tissue. Some novel tools provide information about corneal biomechanical properties, such as the Brillouin optical microscopy (Esporcatte et al., 2020). A more comprehensive assessment of corneal biomechanics will be performed with more devices in the future.

Conclusion

NTG patients with VF progression had more deformable corneas than those without progression. It was hypothesized that NTG patients with more deformable corneas may also have more deformable cribriform plate tissue, which could accelerate optic nerve damage and VF progression. The A1Area might be an independent risk factor for NTG progression. Further attention should be paid to A1Area in glaucoma patients' follow-up. There were no significant differences in DCRs between the progressive and nonprogressive groups in HTG. The specific mechanisms underlying this observation need to be further studied.

Data availability statement

The datasets generated and analyzed during the current study are available from the corresponding author on reasonable request.

Ethics statement

The studies involving human participants were reviewed and approved by Peking University First Hospital. The patients/participants provided their written informed consent to participate in this study.

Author contributions

YW collected and analyzed the data, and drafted the manuscript. YC designed the study, and was involved in collecting the data, and also critically revised the manuscript and has given final approval of the version to be published. CB and YZ participated in the collection of the data. YP participated in the design of the study and critically revised the manuscript. All authors read and approved the final manuscript.

Funding

The study was supported by National High Level Hospital Clinical Research Funding (Scientific Research Seed Fund of Peking University First Hospital) (No. 2022SF59) and Natural Science Foundation of Beijing Municipal (No. 7202208).

Conflict of interest

The authors declare that the research was conducted in the absence of any commercial or financial relationships that could be construed as a potential conflict of interest.

Publisher's note

References

Bellezza, A., Rintalan, C., Thompson, H., Downs, J., Hart, R., and Burgoyne, C. (2003). Deformation of the lamina cribrosa and anterior scleral canal wall in early experimental glaucoma. *Investigative Ophthalmol. Vis. Sci.* 44 (2), 623–637. doi:10.1167/iovs.01-1282

Chen, Y., Wang, T., Huang, J., and Su, C. (2022). Relationship of axial length and corneal biomechanical properties with susceptibility to unilateral normal-tension glaucoma. *Graefe's archive Clin. Exp. Ophthalmol.* 260 (1), 255–264. doi:10.1007/s00417-021-05346-2

Dascalu, A., Stana, D., Nicolae, V., Cirstoveanu, C., Vancea, G., Serban, D., et al. (2021). Association between vascular comorbidity and glaucoma progression: A four-year observational study. *Exp. Ther. Med.* 21 (3), 283. doi:10.3892/etm.2021.9714

De Moraes, C., Juthani, V., Liebmann, J., Teng, C., Tello, C., Susanna, R., et al. (2011). Risk factors for visual field progression in treated glaucoma. *Archives Ophthalmol.* 129 (5), 562–568. doi:10.1001/archophthalmol.2011.72

Esporcatte, L. P. G., Salomão, M. Q., Lopes, B. T., Vinciguerra, P., Vinciguerra, R., Roberts, C., et al. (2020). Biomechanical diagnostics of the cornea. *Eye Vis. (Lond)* 5, 9. doi:10.1186/s40662-020-0174-x

Fraenkl, S., Simon, Q., Yucel, Y., Gupta, N., Wittwer, V., Frueh, B., et al. (2022). Impact of cerebral hypoperfusion-reperfusion on optic nerve integrity and visual function in the DBA/2J mouse model of glaucoma. *BMJ open Ophthalmol.* 7 (1), e001078. doi:10.1136/bmjophth-2022-001078

Group (1994). Advanced Glaucoma Intervention Study. 2. Visual field test scoring and reliability. *Ophthalmology* 101 (8), 1445–1455.

Group, C. N.-T. G. S. (1998). The effectiveness of intraocular pressure reduction in the treatment of normal-tension glaucoma. Collaborative Normal-Tension Glaucoma Study Group. *Am. J. Ophthalmol.* 126 (4), 498–505. doi:10.1016/s0002-9394(98)00272-4

Jung, Y., Chun, H., and Moon, J. (2019). Corneal deflection amplitude and visual field progression in primary open-angle glaucoma. *PloS one* 14 (8), e0220655. doi:10.1371/journal.pone.0220655

Kass, M., Heuer, D., Higginbotham, E., Johnson, C., Keltner, J., Miller, J., et al. (2002). The ocular hypertension treatment study: A randomized trial determines that topical ocular hypotensive medication delays or prevents the onset of primary open-angle glaucoma. *Archives Ophthalmol.* 120 (6), 701–713. doi:10.1001/archopht.120.6.701

Leske, M., Heijl, A., Hyman, L., Bengtsson, B., Dong, L., and Yang, Z. (2007). Predictors of long-term progression in the early manifest glaucoma trial. *Ophthalmology* 114 (11), 1965–1972. doi:10.1016/j.ophtha.2007.03.016

Leske, M., Heijl, A., Hyman, L., Bengtsson, B., and Komaroff, E. (2004). Factors for progression and glaucoma treatment: The early manifest glaucoma trial. *Curr. Opin. Ophthalmol.* 15 (2), 102–106. doi:10.1097/00055735-200404000-00008

Li, B., Cai, Y., Pan, Y., Li, M., Fang, Y., Tian, T., et al. (2018). The association between corneal biomechanical parameters and visual field progression in patients with normal tension glaucoma. *Chin. J. Ophthalmol.* 54 (3), 171–176. doi:10.3760/cma.j.issn.0412-4081.2018.03.005

Li, B., Cai, Y., Pan, Y., Li, M., Qiao, R., Fang, Y., et al. (2017). Corneal biomechanical parameters and asymmetric visual field damage in patients with untreated normal tension glaucoma. *Chin. Med. J.* 130 (3), 334–339. doi:10.4103/0366-6999.198920

Liu, G., Rong, H., Zhang, P., Xue, Y., Du, B., Wang, B., et al. (2021). The effect of axial length elongation on corneal biomechanical property. *Front. Bioeng. Biotechnol.* 9, 777239. doi:10.3389/fbioe.2021.777239

Lopes, B., Roberts, C., Elsheikh, A., Vinciguerra, R., Vinciguerra, P., Reisdorf, S., et al. (2017). Repeatability and reproducibility of intraocular pressure and dynamic corneal response parameters assessed by the Corvis ST. *J. Ophthalmol.* 2017, 1–4. doi:10.1155/2017/8515742

Pakravan, M., Parsa, A., Sanagou, M., and Parsa, C. (2007). Central corneal thickness and correlation to optic disc size: A potential link for susceptibility to glaucoma. *Br. J. Ophthalmol.* 91 (1), 26–28. doi:10.1136/bjo.2006.106039

Prum, B. E., Jr, Lim, M. C., Mansberger, S. L., Stein, J. D., Moroi, S. E., Gedde, S. J., et al. (2016). Primary open-angle glaucoma preferred practice Pattern(®) guidelines. *Ophthalmology* 123 (1), 41–111. doi:10.1016/j.ophtha.2015.10.053

Qassim, A., Mullany, S., Abedi, F., Marshall, H., Hassall, M., Kolovos, A., et al. (2021). Corneal stiffness parameters are predictive of structural and functional progression in glaucoma suspect eyes. *Ophthalmology* 128 (7), 993–1004. doi:10.1016/j.ophtha.2020.11.021

Rong, X., Cai, Y., Li, M., Fang, Y., Tian, T., and Pan, Y. (2019). Peripapillary retinal artery in first diagnosed and untreated normal tension glaucoma. *BMC Ophthalmol.* 19 (1), 203. doi:10.1186/s12886-019-1211-1

Sayah, D., Mazzaferri, J., Descovich, D., Costantino, S., and Lesk, M. (2020). The association between ocular rigidity and neuroretinal damage in glaucoma. *Investigative Ophthalmol. Vis. Sci.* 61 (13), 11. doi:10.1167/iovs.61.13.11

Susanna, B., Ogata, N., Jammal, A., Susanna, C., Berchuck, S., and Medeiros, F. (2019). Corneal biomechanics and visual field progression in eyes with seemingly well-controlled intraocular pressure. *Ophthalmology* 126 (12), 1640–1646. doi:10.1016/j.ophtha.2019.07.023

Tham Yc, L. X., Wong, T. Y., Quigley, H. A., Aung, T., and Cheng, C. Y. (2014). Global prevalence of glaucoma and projections of glaucoma burden through 2040: A systematic review and meta-analysis. *Ophthalmology* 121 (11), 2081–2090. doi:10.1016/j.ophtha.2014.05.013

Vinciguerra, R., Elsheikh, A., Roberts, C., Ambrósio, R., Kang, D., Lopes, B., et al. (2016). Influence of pachymetry and intraocular pressure on dynamic corneal response parameters in healthy patients. *J. Refract. Surg.* 32 (8), 550–561. doi:10.3928/1081597x-20160524-01

Vinciguerra, R., Romano, V., Arbabi, E., Brunner, M., Willoughby, C., Batterbury, M., et al. (2017). *In vivo* early corneal biomechanical changes after corneal cross-linking in patients with progressive keratoconus. *J. Refract. Surg.* 33 (12), 840–846. doi:10.3928/1081597x-20170922-02

Wei, Y., Cai, Y., Choy, B., Li, B., Li, R., Xing, C., et al. (2021). Comparison of corneal biomechanics among primary open-angle glaucoma with normal tension or hypertension and controls. *Chin. Med. J.* 134 (9), 1087–1092. doi:10.1097/cm9.0000000000001399

Wu, N., Chen, Y., and Sun, X. (2022). Association between ocular biomechanics measured with Corvis ST and glaucoma severity in patients with untreated primary open angle glaucoma. *Transl. Vis. Sci. Technol.* 11 (6), 10. doi:10.1167/tvst.11.6.10

Wu, N., Chen, Y., Yang, Y., and Sun, X. (2020). The changes of corneal biomechanical properties with long-term treatment of prostaglandin analogue measured by Corvis ST. *BMC Ophthalmol.* 20 (1), 422. doi:10.1186/s12886-020-01693-6

Wu, N., Chen, Y., Yu, X., Li, M., Wen, W., and Sun, X. (2016). Changes in corneal biomechanical properties after long-term topical prostaglandin therapy. *PloS one* 11 (5), e0155527. doi:10.1371/journal.pone.0155527

Xu, Y., Ye, Y., Chen, Z., Xu, J., Yang, Y., Fan, Y., et al. (2022). Corneal stiffness and modulus of normal-tension glaucoma in Chinese. *Am. J. Ophthalmol.* 242, 131–138. doi:10.1016/j.ajo.2022.06.014

frontiers | Frontiers in Bioengineering and Biotechnology

TYPE Original Research
PUBLISHED 01 June 2023
DOI 10.3389/fbioe.2023.1163223

OPEN ACCESS

EDITED BY
Matthew A. Reilly,
The Ohio State University, United States

REVIEWED BY
Gilbert Yong San Lim,
SingHealth, Singapore
Manmohan Singh,
University of Houston, United States
Fulvio Ratto,
National Research Council (CNR), Italy
Zhipeng Yan,
Third Hospital of Hebei Medical University, China
Fangjun Bao,
Affiliated Eye Hospital to Wenzhou Medical University, China

*CORRESPONDENCE
Yang Shen,
doctshenyang@163.com
Xingtao Zhou,
doctzhouxingtao@163.com

†These authors have contributed equally to this work and share first authorship

RECEIVED 10 February 2023
ACCEPTED 12 May 2023
PUBLISHED 01 June 2023

CITATION
Xian Y, Zhao Y, Sun L, Zhang X, Ding L, Liu Z, Li Y, Ding Y, Jiang L, Zhou X and Shen Y (2023), Comparison of bilateral differential characteristics of corneal biomechanics between keratoconus and normal eyes.
Front. Bioeng. Biotechnol. 11:1163223.
doi: 10.3389/fbioe.2023.1163223

Comparison of bilateral differential characteristics of corneal biomechanics between keratoconus and normal eyes

Yiyong Xian[1,2,3,4†], Yu Zhao[1,2,3,4†], Ling Sun[1,2,3,4], Xiaoyu Zhang[1,2,3,4], Lan Ding[1,2,3,4], Zesheng Liu[1,2,3,4], Yuan Li[5], Yanlan Ding[1,2,3,4], Lin Jiang[1,2,3,4], Xingtao Zhou[1,2,3,4*] and Yang Shen[1,2,3,4*]

[1]Department of Ophthalmology and Optometry, Eye and ENT Hospital, Fudan University, Shanghai, China, [2]NHC Key Laboratory of Myopia, Key Laboratory of Myopia, Fudan University, Chinese Academy of Medical Sciences, Shanghai, China, [3]Shanghai Research Center of Ophthalmology and Optometry, Shanghai, China, [4]Shanghai Engineering Research Center of Laser and Autostereoscopic 3D for Vision Care (20DZ2255000), Shanghai, China, [5]Shangqiu First People's Hospital, Shangqiu, China

Purpose: To compare bilateral differences in corneal biomechanics between keratoconus and normal eyes.

Methods: In this case-control study, 346 eyes of 173 patients (aged 22.1 ± 6.1 years) with keratoconus (KC group) and 378 eyes of 189 patients (aged 26.7 ± 5.6 years) with ametropia (control group) were enrolled. Corneal tomography and biomechanical properties were examined using Pentacam HR and Corvis ST, respectively. The corneal biomechanical parameters were compared between eyes with forme fruste keratoconus (FFKC) and normal eyes. Bilateral differences in corneal biomechanical parameters were compared between the KC and control groups. Receiver operating characteristic (ROC) analysis was used to assess discriminative efficacies.

Results: The areas under the ROC curves (AUROCs) of stiffness parameter at the first applanation (SP-A1) and Tomographic and Biomechanical Index (TBI) for identifying FFKC were 0.641 and 0.694, respectively. The bilateral differential values of major corneal biomechanical parameters were significantly increased in the KC group (all $p < 0.05$), except for the Corvis Biomechanical Index (CBI). The AUROCs of the bilateral differential values of the deformation amplitude ratio at 2 mm (ΔDAR2), Integrated Radius (ΔIR), SP-A1 (ΔSP-A1), and the maximum inverse concave radius (ΔMax ICR) for discriminating keratoconus were 0.889, 0.884, 0.826, and 0.805, respectively. The Logistic Regression Model-1 (comprising of ΔDAR2, ΔIR, and age) and the Logistic Regression Model-2 (comprising of ΔIR, ΔARTh, ΔBAD-D, and age) had AUROCs of 0.922 and 0.998, respectively, for discriminating keratoconus.

Conclusion: The bilateral asymmetry of corneal biomechanics was significantly increased in keratoconus compared with normal eyes, which may be helpful for the early detection of keratoconus.

KEYWORDS

keratoconus, corneal ectasia, biomechanics, forme fruste keratoconus, topography, tomography

Introduction

Keratoconus (KC) is a primary corneal ectatic disease characterized by progressive thinning and conic protrusion of the cornea and has an incidence rate of approximately 1/2000 (Gomes et al., 2015). The corneal morphology of advanced keratoconus is significantly altered and has an irregular pattern, which results in complex refractive errors that are difficult to correct with spectacles and thus severely affect patients' visual function and quality of life (Kandel et al., 2022) and cause heavy socioeconomic burdens (Rebenitsch et al., 2011).

Currently, it is not a challenge to diagnose clinical and subclinical keratoconus with modern corneal tomographers and assessment of corneal biomechanics (Vinciguerra et al., 2016; Ambrosio et al., 2017). However, the standards of corneal morphology and biomechanics for KC screening before corneal refractive surgeries are more stringent, and ophthalmologists aim to identify early keratoconus or high-risk corneas to avoid or reduce the risk of postoperative corneal ectasia (Xie et al., 2020). However, the corneal tomography of early keratoconus, especially forme fruste keratoconus (FFKC), may have no abnormalities, and the corneal biomechanics may also be normal. The diagnosis can only be made based on the contralateral eye being clinical keratoconus.

Bilateral asymmetry is a key feature of keratoconus (Gomes et al., 2015) and researchers have proven that the onset of keratoconus differed for each eye (Zadnik et al., 2002; Nichols, 2004). It is reasonable to believe that an abnormal increase in the inter-eye asymmetry of corneal morphology or biomechanics occurs before the more severe eye in patients with FFKC reaches the clinical stage. Diagnostic models for keratoconus, such as the Belin/Ambrosio Enhanced Ectasia Display and the total deviation value (BAD-D), the Corvis Biomechanical Index (CBI), and the Tomographic and biomechanical index (TBI), only judge on the examination data of one eye (Vinciguerra et al., 2016; Ambrosio et al., 2017), ignoring the information of bilateral asymmetry. Our previous study adopted a novel algorithm to quantitively compare the bilateral asymmetry of corneal tomography between keratoconus and normal eyes. The area under the receiver operating characteristic curves (AUROC) for screening keratoconus (including FFKC) reached 0.985 (Shen et al., 2021), significantly higher than that of the traditional CBI and TBI models.

Reportedly, the loss of biomechanical stability in keratoconus was considered to happen earlier than morphologic changes and induce a cyclic cascade leading to thinning and bulging of the cornea (Roberts and Dupps, 2014). Therefore, this study aimed to investigate the bilateral asymmetry of corneal biomechanics between keratoconus (including FFKC) and normal eyes and to evaluate the clinical value of bilateral asymmetry of biomechanical parameters for the early detection of keratoconus.

Subjects and methods

This case-control study was conducted in accordance with the principles of the Declaration of Helsinki and was approved by the Ethics Committee of the Eye and ENT Hospital of Fudan University (2022049). Informed consent was obtained from all patients included in the study.

Patients diagnosed with keratoconus, based on the Global Consensus on Keratoconus Diagnosis from 2015 by experienced experts (XTZ and YS), were included and were allocated to the KC group (n = 173, including 108 patients with bilateral clinical keratoconus, 21 patients with clinical keratoconus in one eye and subclinical keratoconus in the contralateral eye, and 44 patients with clinical keratoconus in one eye with forme fruste keratoconus in the contralateral eye). Within the KC group, the FFKC in one eye (n = 44) was diagnosed based on the presence of manifest keratoconus in the contralateral eye when the eye itself was asymptomatic on slit lamp, topographic (paracentral inferior-superior dioptric asymmetry ≤1.4), and tomographic (central anterior and posterior elevations <8 and 13 μm, respectively, with the Best-Fit-Sphere [BFS] as the reference sphere) examinations (Ruiz Hidalgo et al., 2016; Awad et al., 2017). Patients who had undergone corneal refractive surgery for myopia and had stable conditions for 2 years postoperatively were included in the control group (n = 189), and the preoperative examination records of these patients were used in this study.

Before the examinations, the patients were asked to discontinue the use of soft contact lenses or rigid gas-permeable contact lenses for 2 or 4 weeks, respectively. Patients with a history of ophthalmic surgery, trauma, other eye diseases (e.g., glaucoma), systemic diseases (e.g., connective tissue disease), or serious psychological or psychiatric diseases were excluded from the study.

A total of 346 eyes from 173 patients were included in the KC group, with an average age of 22.1 ± 6.1 years, while the control group comprised 378 eyes of 189 patients, with an average age of 26.7 ± 5.6 years ($Z = -2.236$, $p = 0.025$, Mann-Whitney U test). Figure 1 shows the examination results of bilateral corneal tomography and biomechanics from the same patient with keratoconus as an example and significant bilateral differences were displayed.

Examinations

1) Corneal tomography was conducted using the Pentacam HR (Oculus Optikgerate GmbH, Wetzlar, Germany) Scheimpflug-based anterior segment analyzer according to standard operating procedures (Shen et al., 2019). A total of 25 images were captured in 2 s by the Pentacam HR system using a 475 nm monochromatic blue light-emitting diode and a Scheimpflug camera that rotated around the corneal axis (Kreps et al., 2020). Parameters including mean or maximal keratometry of the anterior surface (FKm/FKmax), central corneal thickness (CCT), thinnest corneal thickness (TCT), and the BAD-D (the total deviation value in the Belin/Ambrosio Enhanced Ectasia display [BAD] system) were recorded. 2) The corneal biomechanical characteristics were analyzed using the Corvis ST (Oculus Optikgerate GmbH, Wetzlar, Germany) non-contact Scheimpflug-based tonometer according to the standard operating procedures by automatic release (Shen et al., 2019), and major biomechanical parameters were recorded as described in the next section. One examination was taken per eye by experienced technicians.

Definitions of the main corneal tomographic and biomechanical parameters

The Corvis ST uses a high-speed Scheimpflug camera to capture the deformation process of the cornea at the horizontal meridian after being subjected to an air puff. The time when the camera starts

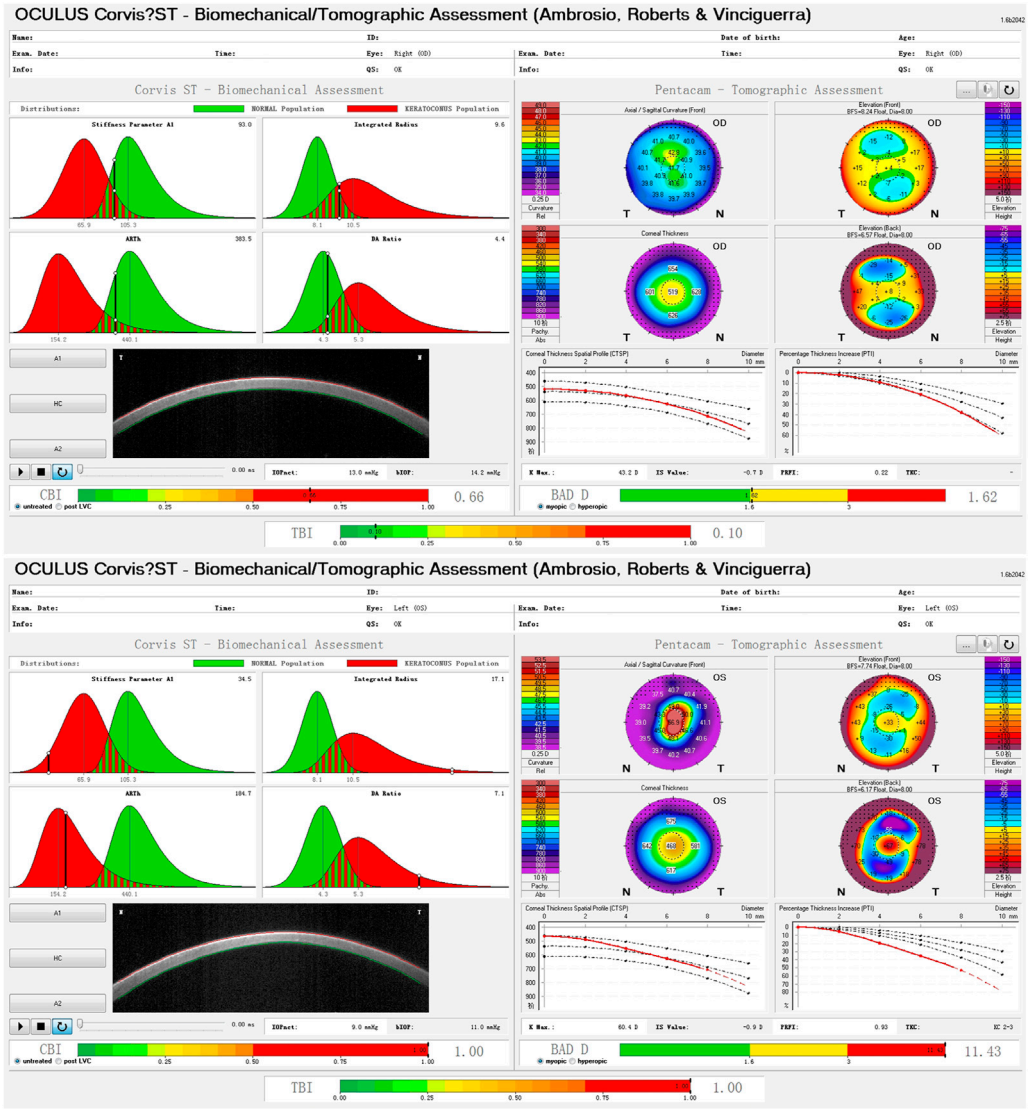

FIGURE 1
Bilateral differences of corneal biomechanics and tomography in a patient with keratoconus.

is set as zero, and the instrument automatically analyzes and obtains three landmark time points during the deformation process: 1) the first applanation (A1): A1 is the moment when the cornea begins to change from a convex shape to a concave shape, and the central cornea is compressed and flattened for the first time; 2) the highest concavity (HC): HC is the moment when the central cornea undergoes the greatest degree of deformation and concavity due to an air puff; and 3) the second applanation (A2): A2 is the second flattening moment of the cornea when it is restored from the highest concavity. (Vellara and Patel, 2015).

As shown in Table 1, major parameters derived from the Corvis ST were included in the study: 1) A1V/A2V: vertical velocity of the corneal apex at A1 or A2; 2) A1DeflA/A2DeflA: vertical deflection amplitude of the corneal apex at A1 or A2; 3) SP-A1: the ratio of the actual pressure on the cornea to the corresponding deflection amplitude at A1; 4) DeflA Max: vertical deflection amplitude of the corneal apex at HC; 5) DAR2/DAR1: the ratio of the deformation amplitude of the central cornea and cornea at paracentral 2mm/1 mm at HC; 6) Max ICR and IR: a curve describing the relationship between time and inverse radius (1/R) of the cornea can be depicted during deformation, through which the maximal inverse concave radius (Max ICR) and the area under the curve (Integrated Radius [IR]) can be calculated; 7) ARTh: the ratio of the thinnest pachymetry at the horizontal meridian to the pachymetric progression index (Vinciguerra et al., 2016); 8) CBI: The Corvis biomechanical index (CBI) is based on logistic regression analysis using the corneal thickness profile and deformation parameters (Vinciguerra et al., 2016); and 9) SSI: The stress-strain index (SSI) reflects the material stiffness of corneas *in vivo,* which would decrease in keratoconus (Eliasy et al., 2019).

The Tomographic and Biomechanical Index (TBI) is a combined tomographic and biomechanical parameter derived from analyzing the data from the Pentacam and Corvis ST and is used for detecting keratoconus (Ambrosio et al., 2017).

TABLE 1 Abbreviations and definitions of major corneal biomechanical and tomographic parameters.

Abbreviations	Definitions
A1V	the velocity at the first applanation
A2V	the velocity at the second applanation
A1DeflA	the deflection amplitude at the first applanation
A2DeflA	the deflection amplitude at the second applanation
DeflA Max	the maximum deflection amplitude
Max ICR	the maximum inverse concave radius
DAR2	the deformation amplitude ratio at 2 mm
DAR1	the deformation amplitude ratio at 1 mm
ARTh	the Ambrosio Relational Thickness horizontal
IR	Integrated Radius
SP-A1	the stiffness parameter at the first applanation
CBI	the Corvis Biomechanical Index
TBI	the Tomographic and Biomechanical Index
SSI	the stress-strain index
BAD-D	the Belin/Ambrosio Enhanced Ectasia Deviation value

Statistical analysis

Statistical analyses were performed using the Statistical Package for the Social Sciences (version 24.0, SPSS, Inc., Chicago, IL, United States) and MedCalc Statistical Software version 20 (MedCalc Software Ltd., Ostend, Belgium).

The right eyes of patients with bilateral clinical keratoconus and the eyes with subclinical/forme fruste keratoconus of patients with very asymmetric keratoconus were selected to form a group to compare with the right eyes of patients in the control group in terms of biomechanical and tomographic properties. For comparison between the FFKC and control eyes, 44 right eyes from the control group were randomly selected.

The bilateral differential parameters were calculated by the absolute differences in binocular parameters and were represented by adding a "Δ" before the name of the corresponding parameters. For example, the bilateral differential parameter "ΔA1V," defined as "binocular asymmetry of A1V," was calculated as the absolute difference between the binocular A1V values.

Continuous variables are described as mean ± standard deviation and 95% confidence intervals (CI), and categorical variables are expressed as frequencies. The Shapiro-Wilk test was used as the normality test. As most parameters were non-normally distributed, the Mann-Whitney *U* test was used to test the difference between the two independent groups. Eyes with greater maximal keratometry of the anterior surface (FKmax) in keratoconus were defined as the "worse eye" and the corresponding FKmax was represented as "FKmax (worse)." Pearson correlation analysis was used to analyze the correlation between FKmax (worse) and the other parameters. Logistic regression analysis was used to construct multivariable models for discriminating keratoconus, and the forward stepwise (conditional) method, a built-in method in the SPSS software, was used for feature selection. The receiver operating characteristic (ROC) analysis was used to evaluate the diagnostic performance of the parameters or models, and the area under the ROC curves (AUROC) and 95% CI were calculated. The optimal cutoff was determined using the maximal Youden index (sensitivity + specificity − 1), and the corresponding sensitivity and specificity were reported. The DeLong test (DeLong et al., 1988) was used to compare the AUROCs between the parameters. All data were examined by a two-tailed test, and $p < 0.05$ was considered statistically significant.

Results

Demographics

In the KC group, the mean keratometry of the anterior surface (FKm) was 47.4 ± 5.2 D, and the TCT was 477 ± 46 μm, while FKm and TCT in the Control group were 43.5 ± 1.3 D and 538 ± 27 μm, respectively (both $p < 0.001$). The BAD-D, CBI, and TBI values were significantly different between the two groups (all $p < 0.001$). The other demographic data are presented in Table 2.

Discriminative efficacies of main biomechanical and tomographic parameters

The efficacies of the main biomechanical and tomographic parameters for discriminating KC are presented in Supplementary Table S1. The TBI, BAD-D, SP-A1, CBI, and ARTh had good discriminative ability for KC, with AUROC of 0.905, 0.900, 0.851, 0.823, and 0.818, respectively (all $p < 0.001$). Supplementary Table S2 shows the differences and discriminative ability of corneal biomechanical parameters between the FFKC and control groups. While other parameters were not significantly different between the two groups, TBI was significantly increased (all $p < 0.01$) and SP-A1 was significantly decreased ($p = 0.023$) in the FFKC group. The AUROCs of TBI and SP-A1 for discriminating FFKC were 0.694 and 0.641, respectively (all $p < 0.05$). The BAD-D was significantly increased in the FFKC group ($p = 0.006$), and the AUROC was 0.670 for identifying FFKC. The ROC curves of the major biomechanical and tomographic parameters for discriminating FFKC are shown in Supplementary Figure S1.

Characteristics of bilateral differences of corneal biomechanical parameters

Table 3 displays the bilateral differences in biomechanical parameters between the two groups. Except for ΔCBI, the other bilateral differential parameters were significantly higher in the KC group than in the control group (all $p < 0.01$). Pearson correlation analysis between FKmax (worse) and bilateral differential parameters (Table 3) showed that FKmax (worse) had the highest positive correlation with ΔDAR2 ($r = 0.606$, $p < 0.001$) (Supplementary Figure S2B) and a mild positive correlation with

TABLE 2 Main demographic data of the keratoconus and control groups.

Parameters	KC group (n = 346)	Control group (n = 378)	Z^a	p^a
	Mean ± SD (95% CI)	Mean ± SD (95% CI)		
FKm (D)	46.5 ± 5.3 (45.7, 47.3)	43.5 ± 1.3 (43.4, 43.7)	−9.191	<0.001
FKmax (D)	52.7 ± 9.8 (51.2, 54.1)	44.7 ± 1.5 (44.5, 44.9)	−10.488	<0.001
CCT (μm)	491 ± 48 (483, 498)	541 ± 27 (537, 545)	−8.962	<0.001
TCT (μm)	484 ± 49 (477, 491)	538 ± 27 (534, 542)	−8.999	<0.001
BAD-D	6.43 ± 5.5 (5.60, 7.26)	1.21 ± 0.5 (1.14, 1.28)	−10.522	<0.001
ARTh	321.7 ± 153.7 (298.7, 344.8)	493.6 ± 92 (480.4, 506.8)	−9.096	<0.001
SP-A1 (mmHg/mm)	79.8 ± 24.3 (76.2, 83.5)	110 ± 15.7 (107.8, 112.3)	−7.983	<0.001
CBI	0.67 ± 0.43 (0.61, 0.74)	0.12 ± 0.22 (0.09, 0.16)	−9.454	<0.001
TBI	0.83 ± 0.31 (0.78, 0.88)	0.23 ± 0.17 (0.20, 0.25)	−10.538	<0.001

Notes: KC, keratoconus; SD, standard deviation; 95% CI, 95% confidence interval for the mean; FKm, mean keratometry of the anterior surface; FKmax, maximum keratometry of the anterior surface; CCT, central corneal thickness; TCT, the thinnest corneal thickness; BAD-D, the Belin/Ambrosio Enhanced Ectasia Deviation value; ARTh, the Ambrosio Relational Thickness horizontal; SP-A1, stiffness parameter at the first applanation; CBI, corvis biomechanical index; TBI, tomographic and biomechanical index; D, diopter; μm, micron; and mmHg/mm, millimeter of mercury per millimeter.

[a]Mann-Whitney *U* test.

TABLE 3 Differences of parameters of bilateral corneal biomechanics and the correlation with FKmax of the worse eye.

Parameters	KC group (n = 173)	Control group (n = 189)	Z^a	P^a	Correlations with FK_{max} (worse)	
	Mean ± SD (95% CI)	Mean ± SD (95% CI)			r	p
ΔA1V (m/s)	0.02 ± 0.02 (0.02, 0.03)	0.01 ± 0.01 (0.01, 0.01)	−7.218	<0.001	0.413	<0.001
ΔA2V (m/s)	0.04 ± 0.03 (0.04, 0.05)	0.02 ± 0.01 (0.02, 0.02)	−8.112	<0.001	0.436	<0.001
ΔA1DeflA (mm)	0.02 ± 0.01 (0.01, 0.02)	0 ± 0 (0, 0.01)	−9.190	<0.001	0.598	<0.001
ΔA2DeflA (mm)	0.02 ± 0.02 (0.02, 0.02)	0.01 ± 0.01 (0.01, 0.01)	−6.927	<0.001	0.439	<0.001
ΔDeflA Max (mm)	0.11 ± 0.09 (0.10, 0.12)	0.04 ± 0.03 (0.04, 0.05)	−8.882	<0.001	0.474	<0.001
ΔMax ICR (mm^{-1})	0.04 ± 0.04 (0.04, 0.05)	0.01 ± 0.02 (0.01, 0.02)	−10.045	<0.001	0.438	<0.001
ΔDAR2	1.28 ± 1.1 (1.12, 1.45)	0.19 ± 0.22 (0.16, 0.22)	−12.784	<0.001	0.606	<0.001
ΔDAR1	0.08 ± 0.07 (0.07, 0.09)	0.02 ± 0.02 (0.02, 0.03)	−9.700	<0.001	0.316	<0.001
ΔARTh	145.93 ± 115.14 (128.65, 163.21)	51.93 ± 49.21 (44.87, 58.99)	−9.214	<0.001	0.007	0.924
ΔMax ICR (mm^{-1})	2.69 ± 2.12 (2.37, 3.00)	0.49 ± 0.35 (0.44, 0.54)	−12.609	<0.001	0.481	<0.001
ΔSP-A1 (mmHg/mm)	21.49 ± 14.75 (19.28, 23.71)	7.36 ± 6.38 (6.44, 8.28)	−10.715	<0.001	0.368	<0.001
ΔCBI	0.3 ± 0.4 (0.24, 0.36)	0.11 ± 0.17 (0.08, 0.13)	−1.037	0.300	−0.230	0.002
ΔTBI	0.16 ± 0.31 (0.11, 0.21)	0.12 ± 0.11 (0.10, 0.13)	−8.359	<0.001	−0.209	0.006
ΔSSI	0.18 ± 0.15 (0.16, 0.20)	0.07 ± 0.06 (0.06, 0.08)	−8.764	<0.001	0.224	0.003
ΔBAD-D	7.53 ± 5.31 (6.73, 8.32)	1.21 ± 0.5 (1.14, 1.28)	−15.055	<0.001	0.574	<0.001

Notes: KC, keratoconus; SD, standard deviation; 95% CI, 95% confidence interval for mean; ΔA1V, asymmetry of velocity at the first applanation; ΔA2V, asymmetry of velocity at the second applanation; ΔA1DeflA, asymmetry of the deflection amplitude at the first applanation; ΔA2DeflA, asymmetry of the deflection amplitude at the second applanation; ΔDeflA Max, asymmetry of the maximum deflection amplitude; ΔMax ICR, asymmetry of the maximum inverse concave radius; ΔDAR2, asymmetry of the deformation amplitude ratio at 2mm; ΔDAR1, asymmetry of the deformation amplitude ratio at 1mm; ΔARTh, asymmetry of the Ambrosio Relational Thickness horizontal; ΔIR, asymmetry of the integrated radius; ΔSP-A1, asymmetry of the stiffness parameter at the first applanation; ΔCBI, asymmetry of the Corvis Biomechanical Index; ΔTBI, asymmetry of the Tomographic and Biomechanical Index; ΔSSI, asymmetry of the stress-strain index; ΔBAD-D, asymmetry of the Belin/Ambrosio Enhanced Ectasia Deviation value; mmHg/mm, millimeter of mercury per millimeter; mm, millimeter; ms, millisecond; and m/s, meter per second.

[a]Mann-Whitney *U* test.

TABLE 4 Receiver operating characteristics analysis for parameters of bilateral corneal biomechanics and tomography.

Parameters	AUROC	Sig.	95% CI	Cut-off	Sensitivity (%)	Specificity (%)
ΔA1V (m/s)	0.719	<0.001	0.666 to 0.773	0.02	53.8	83.6
ΔA2V (m/s)	0.747	<0.001	0.695 to 0.798	0.03	57.2	86.8
ΔA1DeflA (mm)	0.779	<0.001	0.731 to 0.827	0.01	62.4	81.5
ΔA2DeflA (mm)	0.710	<0.001	0.656 to 0.765	0.02	49.7	87.3
ΔDeflA Max (mm)	0.770	<0.001	0.721 to 0.819	0.09	53.2	91.0
ΔMax ICR (mm^{-1})	0.805	<0.001	0.758 to 0.853	0.02	61.5	89.8
ΔDAR2	0.889	<0.001	0.854 to 0.924	0.41	76.9	91.5
ΔDAR1	0.795	<0.001	0.747 to 0.843	0.05	59.1	90.5
ΔARTh	0.780	<0.001	0.732 to 0.829	100.47	57.8	88.9
ΔIR (mm^{-1})	0.884	<0.001	0.845 to 0.922	0.93	80.3	91.5
ΔSP-A1 (mmHg/mm)	0.826	<0.001	0.783 to 0.869	12.90	68.2	82.5
ΔCBI	0.531	0.138	0.468 to 0.595	0.50	30.6	95.8
ΔTBI	0.750	<0.001	0.688 to 0.812	0.01[a]	71.7	94.2
ΔSSI	0.767	<0.001	0.717 to 0.816	0.11	61.8	83.1
ΔBAD-D	0.958	<0.001	0.934 to 0.982	2.12	89.6	97.4
LRM-1	0.922	<0.001	0.893 to 0.952	0.54	78.6	95.8
LRM-2	0.998	<0.001	0.996 to 1.000	0.37	98.8	97.9

Notes: AUROC, area under the curves of receiver operating characteristic; Sig, significance; 95% CI, 95% confidence interval for AUROC; Cut-off, the threshold values; ΔA1V, asymmetry of velocity at the first applanation; ΔA2V, asymmetry of velocity at the second applanation; ΔA1DeflA, asymmetry of the deflection amplitude at the first applanation; ΔA2DeflA, asymmetry of the deflection amplitude at the second applanation; ΔDeflA Max, asymmetry of the maximum deflection amplitude; ΔMax ICR, asymmetry of the maximum inverse concave radius; ΔDAR2, asymmetry of the deformation amplitude ratio at 2 mm; ΔDAR1, asymmetry of the deformation amplitude ratio at 1 mm; ΔARTh, asymmetry of the Ambrosio Relational Thickness horizontal; ΔIR, asymmetry of the integrated radius; ΔSP-A1, asymmetry of the stiffness parameter at the first applanation; ΔCBI, asymmetry of the Corvis Biomechanical Index; ΔTBI, asymmetry of the Tomographic and Biomechanical Index; ΔSSI, asymmetry of the stress-strain index; ΔBAD-D, asymmetry of the Belin/Ambrosio Enhanced Ectasia Deviation value; mmHg/mm, millimeter of mercury per millimeter; mm, millimeter; ms, millisecond; m/s, meter per second; LRM-1, Logistic regression model-1, and LRM-2, Logistic regression model-2.
[a]A smaller value indicates a more positive test.

ΔMax ICR, ΔIR, and ΔBAD-D (r = 0.438, 0.481, and 0.574, respectively; all p < 0.001) (Supplementary Figures S2A, S2E, S2J). Weak but significant correlations were found between FKmax (worse) and ΔDAR1, ΔSP-A1, ΔCBI, ΔTBI, and ΔSSI (all |r| <0.4, p < 0.01) (Supplementary Figures S2C, S2F–I). No significant correlation was found between FKmax (worse) and ΔARTh (r = 0.007, p = 0.924) (Supplementary Figure S2D). The relationship between FKmax (worse) and major bilateral differential parameters is shown in Supplementary Figure S2.

ROC analysis

Table 4 presents the ROC analysis of the bilateral differential biomechanical parameters and Figure 2 shows the ROC curves of the major parameters. The accuracy of the ΔDAR2, ΔIR, ΔSP-A1, and ΔMax ICR was good for discriminating KC, with AUROCs of 0.889, 0.884, 0.826, and 0.805, respectively (all p < 0.001) (Figure 2). When the cutoff was 0.41, the sensitivity and specificity of the ΔDAR2 were 76.9% and 91.5%, respectively. The sensitivity and specificity of ΔIR were 80.3% and 91.5%, respectively, with a cutoff of 0.93 mm^{-1}.

Table 5 displays two multivariable classification models constructed by Logistic regression analysis. The model LRM-1 (Logistic regression model-1), which comprised of ΔDAR2, ΔIR, and age, obtained the AUROC of 0.922 (95% CI: 0.893–0.952, p < 0.001) for identifying keratoconus (including FFKC) (Table 4). Taking ΔBAD-D and ΔARTh into account, another model LRM-2 (Logistic regression model-2), which included ΔIR, Age, ΔARTh, and ΔBAD-D, had the AUROC of 0.998 (95% CI: 0.996–1.000, p < 0.001) for identifying keratoconus (including FFKC) (Table 4), which was significantly higher than that of LRM-1 (z = 5.108, p < 0.001). The corresponding ROC curves are shown in Figure 3.

Discussion

This study compared the characteristics of bilateral differences in corneal biomechanics between the KC and control groups as well as investigated the important role of bilateral biomechanical differences in the early identification of keratoconus and high-risk corneas.

The present study found that most corneal biomechanical parameters, except for CBI, manifested significant bilateral asymmetry in keratoconus when compared with normal eyes, implying that bilateral asymmetry in corneal biomechanics is also a key feature of keratoconus. Moreover, we found that the FFKC

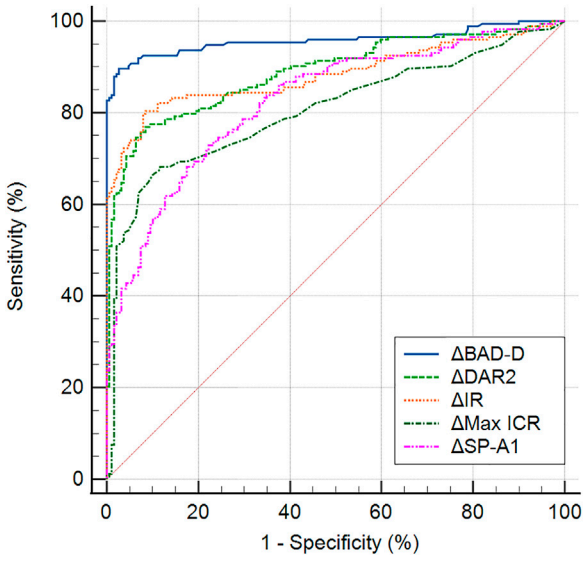

FIGURE 2
Receiver operating characteristic curves of major bilateral differential parameters, ΔDAR2 (asymmetry of the deformation amplitude ratio at 2 mm), ΔIR (asymmetry of Integrated Radius), ΔMax ICR (asymmetry of the maximum inverse concave radius), ΔSP-A1 (asymmetry of the stiffness parameter at the first applanation), and ΔBAD-D (asymmetry of the Belin/Ambrosio Enhanced Ectasia Deviation value), for keratoconus *versus* the control group.

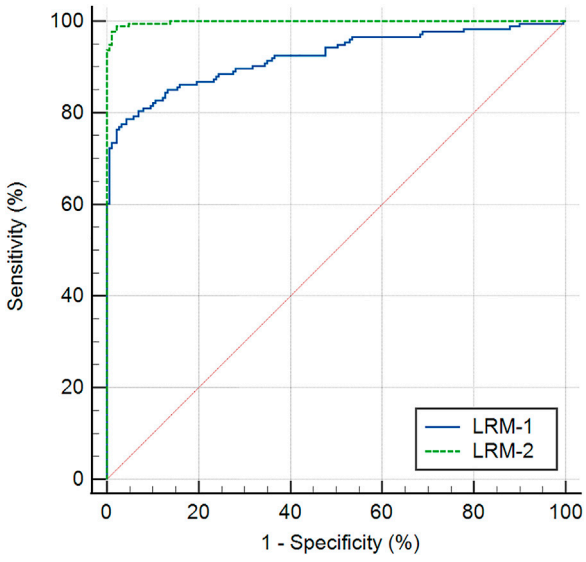

FIGURE 3
Receiver operating characteristic curves of two multivariable classification models, the Logistic regression model-1 (LRM-1), and Logistic regression model-2 (LRM-2) for keratoconus *versus* the control group.

TABLE 5 Logistic regression analysis of bilateral differential parameters in discriminating keratoconus.

	β	S.E.	Wald	df	Sig.	Exp(β)
LRM-1						
ΔDAR2	2.372	0.598	15.706	1	<0.001	10.717
ΔIR	1.863	0.342	29.645	1	<0.001	6.440
Age	−0.109	0.030	13.072	1	<0.001	0.897
Constant	−0.196	0.766	0.065	1	0.798	0.822
LRM-2						
ΔIR	3.723	1.160	10.299	1	0.001	41.385
Age	−0.184	0.078	5.595	1	0.018	0.832
ΔARTh	0.024	0.007	12.630	1	<0.001	1.024
ΔBAD-D	4.798	1.166	16.938	1	<0.001	121.305
Constant	−10.785	3.309	10.623	1	0.001	0.000

Notes: LRM-1, Logistic regression model-1; LRM-2, Logistic regression model-2; ΔDAR2, asymmetry of the deformation amplitude ratio at 2 mm; ΔIR, asymmetry of the integrated radius; ΔARTh, asymmetry of the Ambrosio Relational Thickness horizontal; and ΔBAD-D, asymmetry of the Belin/Ambrosio Enhanced Ectasia Deviation value.

cases had similar patterns in corneal tomography when compared with normal eyes, but their corneal biomechanical stability was significantly lower than that of normal eyes (with significantly decreased SP-A1 and increased TBI; Supplementary Table S2). These findings imply that the compromise in corneal biomechanical properties should occur earlier than the changes in corneal tomography, which is consistent with Asroui's work (Asroui et al., 2022). However, the AUROC of SP-A1 and TBI were too low to meet the requirement of KC screening before corneal refractive surgery. Correlation analysis showed that ΔDAR2 and ΔIR were mildly correlated with FKmax (worse), indicating significant correlations between bilateral asymmetry in biomechanical features and severity of keratoconus. A previous study suggested that the bilateral asymmetry of corneal tomography increases significantly with disease severity (Nichols, 2004; Naderan et al., 2017), which is consistent with the findings of the present study. Herber et al. (2019) revealed that IR and DAR2 showed significant differences among keratoconus groups with different TKC stages. This suggests that the ΔDAR2 and ΔIR may be more sensitive to subtle changes in corneal biomechanics during the development of keratoconus, and would be helpful for the early detection and monitoring of keratoconus.

This study showed that the bilateral differential biomechanical parameters, including ΔDAR2, ΔIR, ΔSP-A1, and ΔMax ICR, had

relatively good discriminative ability for keratoconus (Table 4). Previous studies have confirmed the excellent ability of the abovementioned parameters for detecting clinical keratoconus in monocular analysis, and the AUROC reached 0.95 (Chan et al., 2018; Sedaghat et al., 2018; Herber et al., 2019). However, the accuracy decreases significantly in early keratoconus and the AUROC of SP-A1 was 0.762 in screening subclinical keratoconus (Kataria et al., 2019). In the present study, subclinical and forme fruste keratoconus were included in the KC group; therefore, the discriminative accuracies of these parameters were limited in the monocular analysis (Supplementary Table S1), especially for FFKC (Supplementary Table S2), which were consistent with previous findings (Kataria et al., 2019).

Vinciguerra et al. (2016) developed the CBI model based on pachymetric progression and biomechanical characteristics of the cornea, while Ambrosio et al. (2017) developed the TBI model with combined tomographic and biomechanical characteristics. The accuracy of CBI and TBI for detecting clinical keratoconus was close to 100% (Ambrosio et al., 2017) but dropped to 0.684 and 0.884 for screening subclinical keratoconus, respectively (Asroui et al., 2022). In this study, the AUROCs of CBI and TBI were 0.823 and 0.905, respectively (Supplementary Table S1), similar to those of previous studies. However, CBI was not significantly different between the FFKC and control groups, and the discriminative ability of TBI for FFKC was inadequate, with an AUROC of 0.694 (Supplementary Table S2).

However, it is interesting that in the bilateral differential analysis of the present study, the AUROC of ΔDAR2, ΔIR, and ΔMax ICR increased to 0.889, 0.884, and 0.805, respectively, suggesting that the biomechanical differential parameters had good accuracy in screening keratoconus and may be an effective supplement to current screening models for keratoconus based on monocular analysis. Additionally, the logistic regression model LRM-1 was also able to discriminate keratoconus, with an AUROC of 0.922. After including ΔBAD-D and ΔARTh in the analysis, the logistic regression model LRM-2 showed a significantly enhanced ability to identify keratoconus, with an AUROC of 0.998 (Tables 4, 5).

The LRM-1 in this study was composed of ΔDAR2, ΔIR, and age, which combined the bilateral differential characteristics of corneal biomechanics and obtained a better discriminative accuracy than CBI. Another model LRM-2, which consists of ΔIR, age, ΔARTh, and ΔBAD-D, reflected the bilateral differential characteristics of corneal tomography and biomechanics and had excellent accuracy in identifying keratoconus. Our findings demonstrated that the combination of differential biomechanical parameters can achieve better accuracy for screening keratoconus, while the combination of differential tomographic and biomechanical parameters can further improve the sensitivity and specificity. In the future, evaluation of bilateral asymmetry of keratoconus through large samples, multi-modality, and multi-parameters is expected to develop models with greater discriminative abilities. In the bilateral differential analysis, there were no significant differences in ΔCBI and ΔTBI between the KC and control groups. A possible reason may be that both CBI and TBI values are indices for screening rather than normally distributed variables. In binocular keratoconus cases, the values of CBI and TBI commonly increase to 1.0; thus, ΔCBI and ΔTBI may drop to 0. (Supplementary Figures S2G, S2H). Therefore, the values of ΔCBI and ΔTBI cannot precisely reflect the characteristics of bilateral asymmetry in keratoconus.

Moreover, age was considered an important variable in the regression models and was negatively correlated with the risk of keratoconus (β = −0.109 for LRM-1 and −0.184 for LRM-2, respectively) (Table 5). Previous studies reported that keratoconus has the most significant incidence in the age range of 20–30 years (Gomes et al., 2022) and that age at presentation was the most significant predictor of progression risk (Maile et al., 2022), which indicated that patients with younger age should be given more attention in the screening and monitoring of keratoconus, in accordance with the present study. Therefore, our findings demonstrated that age should also be regarded as an important factor in assessing at-risk corneas prior to refractive surgery.

We also investigated SSI, an index that reflects the material stiffness of the cornea *in vivo* (Eliasy et al., 2019). Our findings showed a relatively low accuracy of SSI and ΔSSI in screening keratoconus, and had AUROCs of 0.718 and 0.767, respectively. A previous study revealed that the SSI was not significantly different between eyes with mild keratoconus and normal eyes, and the AUROC was 0.642 for detecting keratoconus (Herber et al., 2022), which is similar to that in our study (Supplementary Tables S1, S2), suggesting that the SSI alone was not suitable for screening keratoconus. However, the SSI was proven to decrease significantly during the reduction of corneal stiffness in the progression of keratoconus (Padmanabhan et al., 2022) and increased after corneal cross-linking (Nishida et al., 2022), demonstrating that the SSI may be more suitable for monitoring the progression and treatment efficacy in keratoconus, however, its application in screening keratoconus still needs to be further explored.

This study has several limitations. First, the sample size was relatively small, and detailed subgroup analyses were not performed to distinguish the differential biomechanical characteristics among different types of keratoconus. Second, the Corvis ST merely measures the overall biomechanical properties of the cornea in the horizontal meridian, while the cone of keratoconus is often located in the vertical direction. Therefore, there are defects when using the Corvis ST to measure the corneal biomechanics in keratoconus. Further investigations with larger sample sizes and novel instruments, such as Brillouin microscopy (Zhang et al., 2023) and optical coherence elastography (Kirby et al., 2017), are required. Third, while the significantly increased bilateral asymmetry of corneal tomography or biomechanics would be helpful for the early identification of keratoconus, it does not necessarily imply that the increased bilateral asymmetry is keratoconus. The presence of inter-eye asymmetry suggests that ophthalmologists should actively search for potential causes that lead to inter-eye asymmetry, such as history of trauma, oculopathy, or surgeries. Failure to identify a clear cause may suggest abnormal biomechanical attenuation in the worse eye, which could result in a higher risk of corneal ectasia after refractive surgery than in the general population. For such patients, further observations and thorough notifications of surgical risks are absolutely necessary.

In summary, the bilateral differences in corneal biomechanical parameters, including ΔDAR2, ΔIR, ΔSP-A1, and ΔMax ICR, were significantly increased in KC compared with those in the control group and may be helpful for the early screening of keratoconus. The Logistic regression model combining bilateral differential characteristics of

corneal biomechanics and corneal tomography is expected to improve the discriminative efficacy for early keratoconus.

Data availability statement

The raw data supporting the conclusion of this article will be made available by the authors, without undue reservation.

Ethics statement

The studies involving human participants were reviewed and approved by the Ethics Committee of the Fudan University Eye and ENT Hospital Review Board (Shanghai, China) (2022049). The patients/participants provided their written informed consent to participate in this study.

Author contributions

Study concept and design (YX, YZ, XtZ, and YS); data collection (YX, YZ, LS, ZL, YL, YD, LJ, and YS); data analysis and interpretation (YX, YZ, and YS); drafting of the manuscript (YX, YZ, and YS); critical revision of the manuscript (YX, YZ, LS, LD, XtZ, XyZ, and YS); supervision (XtZ and YS). All authors contributed to the article and approved the submitted version.

Funding

National Natural Science Foundation of China (Grant No. 82101183), National Natural Science Foundation of China (Grant No. 82000932), The Joint Research Project of New Frontier Technology in municipal hospitals (SHDC12018103), Project of Shanghai Science and Technology (Grant Nos. 21Y11909800 and 20410710100), Clinical Research Plan of SHDC (SHDC2020CR1043B), Project of Shanghai Xuhui District Science and Technology (XHLHGG202104), Research Project Grant of Shanghai Municipal Commission of Health and Family Planning (20204Y0058), and Shanghai Sailing Program (Grant No. 20YF1405200).

Conflict of interest

The authors declare that the research was conducted in the absence of any commercial or financial relationships that could be construed as a potential conflict of interest.

Publisher's note

All claims expressed in this article are solely those of the authors and do not necessarily represent those of their affiliated organizations, or those of the publisher, the editors and the reviewers. Any product that may be evaluated in this article, or claim that may be made by its manufacturer, is not guaranteed or endorsed by the publisher.

Supplementary material

The Supplementary Material for this article can be found online at: https://www.frontiersin.org/articles/10.3389/fbioe.2023.1163223/full#supplementary-material

References

Ambrosio, R., Lopes, B. T., Faria-Correia, F., Salomao, M. Q., Buhren, J., Roberts, C. J., et al. (2017). Integration of scheimpflug-based corneal tomography and biomechanical assessments for enhancing ectasia detection. *J. Refract Surg.* 33, 434–443. doi:10.3928/1081597X-20170426-02

Asroui, L., Dagher, S. A., Elsheikh, A., Lopes, B. T., Roberts, C. J., Assouad, M., et al. (2022). Biomechanical evaluation of topographically and tomographically normal fellow eyes of patients with keratoconus. *J. Refract Surg.* 38, 318–325. doi:10.3928/1081597X-20220225-01

Awad, E. A., Abou Samra, W. A., Torky, M. A., and El-Kannishy, A. M. (2017). Objective and subjective diagnostic parameters in the fellow eye of unilateral keratoconus. *BMC Ophthalmol.* 17, 186. doi:10.1186/s12886-017-0584-2

Chan, T. C., Wang, Y. M., Yu, M., and Jhanji, V. (2018). Comparison of corneal dynamic parameters and tomographic measurements using Scheimpflug imaging in keratoconus. *Br. J. Ophthalmol.* 102, 42–47. doi:10.1136/bjophthalmol-2017-310355

DeLong, E. R., DeLong, D. M., and Clarke-Pearson, D. L. (1988). Comparing the areas under two or more correlated receiver operating characteristic curves: A nonparametric approach. *Biometrics* 44, 837–845. doi:10.2307/2531595

Eliasy, A., Chen, K.-J., Vinciguerra, R., Lopes, B. T., Abass, A., Vinciguerra, P., et al. (2019). Determination of corneal biomechanical behavior *in-vivo* for healthy eyes using CorVis ST tonometry: Stress-strain index. *Front. Bioeng. Biotechnol.* 7, 105. doi:10.3389/fbioe.2019.00105

Gomes, J. A. P., Rodrigues, P. F., and Lamazales, L. L. (2022). Keratoconus epidemiology: A review. *Saudi J. Ophthalmol.* 36, 3–6. doi:10.4103/sjopt.sjopt_204_21

Gomes, J. A., Tan, D., Rapuano, C. J., Belin, M. W., Ambrosio, R., Guell, J. L., et al. (2015). Global consensus on keratoconus and ectatic diseases. *Cornea* 34, 359–369. doi:10.1097/ICO.0000000000000408

Herber, R., Hasanli, A., Lenk, J., Vinciguerra, R., Terai, N., Pillunat, L. E., et al. (2022). Evaluation of corneal biomechanical indices in distinguishing between normal, very asymmetric, and bilateral keratoconic eyes. *J. Refract Surg.* 38, 364–372. doi:10.3928/1081597X-20220601-01

Herber, R., Ramm, L., Spoerl, E., Raiskup, F., Pillunat, L. E., and Terai, N. (2019). Assessment of corneal biomechanical parameters in healthy and keratoconic eyes using dynamic bidirectional applanation device and dynamic Scheimpflug analyzer. *J. Cataract. Refract Surg.* 45, 778–788. doi:10.1016/j.jcrs.2018.12.015

Kandel, H., Nguyen, V., Piermarocchi, S., Ceklic, L., Teo, K., Arnalich-Montiel, F., et al. (2022). Quality of life impact of eye diseases: A save sight registries study. *Clin. Exp. Ophthalmol.* 50, 386–397. doi:10.1111/ceo.14050

Kataria, P., Padmanabhan, P., Gopalakrishnan, A., Padmanaban, V., Mahadik, S., and Ambrósio, R. (2019). Accuracy of Scheimpflug-derived corneal biomechanical and tomographic indices for detecting subclinical and mild keratectasia in a South Asian population. *J. Cataract. Refract Surg.* 45, 328–336. doi:10.1016/j.jcrs.2018.10.030

Kirby, M. A., Pelivanov, I., Song, S., Ambrozinski, Ł., Yoon, S. J., Gao, L., et al. (2017). Optical coherence elastography in ophthalmology. *J. Biomed. Opt.* 22, 1–28. doi:10.1117/1.JBO.22.12.121720

Kreps, E. O., Jimenez-Garcia, M., Issarti, I., Claerhout, I., Koppen, C., and Rozema, J. J. (2020). Repeatability of the Pentacam HR in various grades of keratoconus. *Am. J. Ophthalmol.* 219, 154–162. doi:10.1016/j.ajo.2020.06.013

Maile, H. P., Li, J.-P. O., Fortune, M. D., Royston, P., Leucci, M. T., Moghul, I., et al. (2022). Personalized model to predict keratoconus progression from demographic, topographic, and genetic data. *Am. J. Ophthalmol.* 240, 321–329. doi:10.1016/j.ajo.2022.04.004

Naderan, M., Rajabi, M. T., and Zarrinbakhsh, P. (2017). Intereye asymmetry in bilateral keratoconus, keratoconus suspect and normal eyes and its relationship with disease severity. *Br. J. Ophthalmol.* 101, 1475–1482. doi:10.1136/bjophthalmol-2016-309841

Nichols, J. J. (2004). The relation between disease asymmetry and severity in keratoconus. *Br. J. Ophthalmol.* 88, 788–791. doi:10.1136/bjo.2003.034520

Nishida, T., Kojima, T., Kataoka, T., Isogai, N., Yoshida, Y., and Nakamura, T. (2022). Evaluation of the relationship between the changes in the corneal biomechanical properties and changes in the anterior segment OCT parameters following customized corneal cross-linking. *Clin. Ophthalmol.* 16, 1909–1923. doi:10.2147/OPTH.S361836

Padmanabhan, P., Lopes, B. T., Eliasy, A., Abass, A., and Elsheikh, A. (2022). *In vivo* biomechanical changes associated with keratoconus progression. *Curr. Eye Res.* 47, 982–986. doi:10.1080/02713683.2022.2058020

Rebenitsch, R. L., Kymes, S. M., Walline, J. J., and Gordon, M. O. (2011). The lifetime economic burden of keratoconus: A decision analysis using a markov model. *Am. J. Ophthalmol.* 151, 768–773.e2. doi:10.1016/j.ajo.2010.10.034

Roberts, C. J., and Dupps, W. J. (2014). Biomechanics of corneal ectasia and biomechanical treatments. *J. Cataract. Refract Surg.* 40, 991–998. doi:10.1016/j.jcrs.2014.04.013

Ruiz Hidalgo, I., Rodriguez, P., Rozema, J. J., Ní Dhubhghaill, S., Zakaria, N., Tassignon, M.-J., et al. (2016). Evaluation of a machine-learning classifier for keratoconus detection based on Scheimpflug tomography. *Cornea* 35, 827–832. doi:10.1097/ICO.0000000000000834

Sedaghat, M.-R., Momeni-Moghaddam, H., Ambrósio, R., Heidari, H.-R., Maddah, N., Danesh, Z., et al. (2018). Diagnostic ability of corneal shape and biomechanical parameters for detecting frank keratoconus. *Cornea* 37, 1025–1034. doi:10.1097/ICO.0000000000001639

Shen, Y., Han, T., Jhanji, V., Shang, J., Zhao, J., Li, M., et al. (2019). Correlation between corneal topographic, densitometry, and biomechanical parameters in keratoconus eyes. *Transl. Vis. Sci. Technol.* 8, 12. doi:10.1167/tvst.8.3.12

Shen, Y., Xian, Y., Han, T., Wang, X., and Zhou, X. (2021). Bilateral differential topography—a novel topographic algorithm for keratoconus and ectatic disease screening. *Front. Bioeng. Biotechnol.* 9, 772982. doi:10.3389/fbioe.2021.772982

Vellara, H. R., and Patel, D. V. (2015). Biomechanical properties of the keratoconic cornea: A review. *Clin. Exp. Optom.* 98, 31–38. doi:10.1111/cxo.12211

Vinciguerra, R., Ambrosio, R., Elsheikh, A., Roberts, C. J., Lopes, B., Morenghi, E., et al. (2016). Detection of keratoconus with a New biomechanical index. *J. Refract Surg.* 32, 803–810. doi:10.3928/1081597X-20160629-01

Xie, Y., Zhao, L., Yang, X., Wu, X., Yang, Y., Huang, X., et al. (2020). Screening candidates for refractive surgery with corneal tomographic-based deep learning. *JAMA Ophthalmol.* 138, 519–526. doi:10.1001/jamaophthalmol.2020.0507

Zadnik, K., Steger-May, K., Fink, B. A., Joslin, C. E., Nichols, J. J., Rosenstiel, C. E., et al. (2002). Between-eye asymmetry in keratoconus. *Cornea* 21, 671–679. doi:10.1097/00003226-200210000-00008

Zhang, H., Asroui, L., Tarib, I., Dupps, W. J., Scarcelli, G., and Randleman, J. B. (2023). Motion tracking Brillouin microscopy evaluation of normal, keratoconic, and post-laser vision correction corneas: Motion tracking Brillouin microscopy in keratoconus and laser vision correction. *Am. J. Ophthalmol.* S0002-9394 (23), 00111. doi:10.1016/j.ajo.2023.03.018

frontiers | Frontiers in Bioengineering and Biotechnology

TYPE Original Research
PUBLISHED 10 July 2023
DOI 10.3389/fbioe.2023.1146828

OPEN ACCESS

EDITED BY
J. Crawford Downs,
University of Alabama at Birmingham,
United States

REVIEWED BY
Hamid Osman,
Taif University, Saudi Arabia
Rui B. Ruben,
Polytechnic Institute of Leiria, Portugal

*CORRESPONDENCE
Ahmed Makarem,
a.makarem@liverpool.ac.uk

RECEIVED 17 January 2023
ACCEPTED 23 June 2023
PUBLISHED 10 July 2023

CITATION
Makarem A, Abass A, Bao F and Elsheikh A (2023), Assessment of age-related change of the ocular support system. *Front. Bioeng. Biotechnol.* 11:1146828. doi: 10.3389/fbioe.2023.1146828

Assessment of age-related change of the ocular support system

Ahmed Makarem[1]*, Ahmed Abass[1,2], Fangjun Bao[3] and Ahmed Elsheikh[1,4,5]

[1]School of Engineering, University of Liverpool, Liverpool, United Kingdom, [2]Faculty of Engineering, Port Said University, Port Fouad, Egypt, [3]School of Optometry and Ophthalmology and Eye Hospital, Wenzhou Medical University, Wenzhou, Zhejiang, China, [4]Beijing Advanced Innovation Center for Biomedical Engineering, Beihang University, Beijing, China, [5]National Institute for Health Research (NIHR), Biomedical Research Centre at Moorfields Eye Hospital NHS Foundation Trust, UCL Institute of Ophthalmology, London, United Kingdom

To estimate the material stiffness of the orbital soft tissue in human orbits using an inverse numerical analysis approach, which could be used in future studies to understand the behaviour under dynamic, non-contact tonometry or simulate various ophthalmological conditions. Clinical data were obtained for the left eye of 185 Chinese participants subjected to a complete ophthalmic examination, including tests by the Corvis ST and Pentacam. 185 numerical models of the eye globes were built with idealised geometry of the sclera while considering the corneal tomography measured by the Pentacam. The models were extended to include representations of the orbital soft tissue (OST), which were given idealised geometry. The movement of the whole eye in response to an air-puff directed at the central cornea was examined and used in an inverse analysis process to estimate the biomechanical stiffness parameters of the OST. The results indicated a weak correlation of E_t with the progression of age, regardless of the stress at which E_t was calculated. However, there was evidence of significant differences in E_t between some of the age groups. There was statistical evidence of significant differences between E_t in the age range $20< years < 43$ relative to E_t in OST with age ranges $43< years < 63$ ($p = 0.022$) and $63< years < 91$ ($p = 0.011$). In contrast, E_t in OST with age ranges $43< years < 63$ and $63< years < 91$ were not significantly different ($p = 0.863$). The optimised mechanical properties of the OST were found to be almost four times stiffer than properties of fatty tissue of previous experimental work. This study consolidated previous findings of the role of extraocular muscles on the ocular suppor system. In addition, the rotation of the globe during corvis loading is suggested to be of posterior components of the globe and shall be further investigated.

KEYWORDS

eye, orbit, cornea, sclera, whole eye moevement

1 Introduction

Eye orbits are bony sockets contained within the skull in which the eyes and the orbital soft tissue (OST) are situated (Bron, 1997). Besides its function to hold the contents of the ocular system, the orientation of the orbit affects the visual field of mammals (Heesy, 2004). The confined space of the bony orbit is mainly filled with the OST, which acts as a shock mitigator in case of sudden or traumatic impacts to the eye or head (Liu et al., 2013). This function and the need to allow the eye globe to move freely upon the contraction and relaxation of the extraocular muscles (EOM) means that the adipose fatty tissue within OST

must possess a relatively low stiffness (Katch et al., 1991; Heesy, 2004; Comley and Fleck, 2012). This low stiffness causes distinctive posterior movement of the eye globe and rotation in the nasal direction when subjected to air-puff tonometry (Boszczyk et al., 2017), and these movements inevitably affect the measurement accuracy of the intraocular pressure (IOP).

The structure of the OST plays a major role in enabling the tissue to act as a shock absorber while allowing the unhindered movement of the intraorbital structures in their respected degrees of freedom (Schoemaker et al., 2006). The OST is composed of EOM, optic nerve, adipose fatty tissue (AFT), and other fibrous connective tissues (Hwang et al., 2019). Bremond et al. identified two parts of the AFT; the outer, extra-conical fat tissue and the central, intra-conical fat (Bremond-Gignac et al., 2004), with this distinction being a consequence of the cone formed by the extra-ocular muscles along with the organisation of the conjunctival tissue. Mesoscopic and histological differences were identified between the two parts with the outer and inner parts constituting thick and thin conjunctival septa, respectively. These differences were thought to be related to the mechanical role of the two parts where the first part acted as a periorbita cushion that enabled globe rotation, while the latter had a major contribution to maintaining the position of the globe, while allowing the movement of the optic nerve in the orbit (Turvey and Golden, 2012; Rootman et al., 2022).

For quite some time, numerical modelling of the OST did not get much attention. Despite the essential findings achieved by previous ocular modelling studies (Stitzel, 2002; Elsheikh et al., 2013; Aboulatta et al., 2021), the effect of the OST was ignored, and the ocular globe was provided with boundary conditions that were assumed to represent the restraints provided by the OST. These boundary conditions commonly restrained the eye's equatorial zone against the movement in the longitudinal direction while permitting it to expand or move laterally (Elsheikh et al., 2013). In doing so, the distributed support provided by the OST was not represented and instead the support was assumed to be concentrated at the equator, leading to an unphysiological concentration of stress at this location. The representation of the OST support in this form also ignored the soft support offered against dynamic loadings of the ocular globe, which could cause inaccuracies in simulating the globe's response. The recent technological advances within numerical solvers allowed a significant increase in computational power, which enabled further studies and more representative, and complex, modelling of OST support (Al-Sukhun et al., 2006; Schoemaker et al., 2006; Schutte et al., 2006; Chen and Weiland, 2011; Boszczyk et al., 2017; Jannesari et al., 2018; Guo et al., 2019; Hwang et al., 2019). These studies included research to evaluate the orbital fat supporting role offered to the globe during its rotation—and represented the effect of shear between the globe and orbital fat (Schoemaker et al., 2006; Schutte et al., 2006). Yet some of these studies included assumptions of high stiffness for the globe and linear behaviour for the orbital fat, possibly affecting the study outcomes (Schutte et al., 2006). The current study builds on these earlier efforts and attempts to offer more representative hyperelastic globe and OST tissue behaviour.

An earlier study (Jannesari et al., 2018) has suggested and demonstrated that the clinical whole eye movement (WEM) and the inverse finite element analysis approach quantify the corneal and fatty tissue biomechanical parameters. The study assumed that the eye is fully supported by the adipose tissue, which is inaccurate (Lockwood, 1885; Lemke and Lucarelli, 2012; Hwang et al., 2019; Banks et al., 2020). Additionally, the cornea and the boundary conditions were oversimplified and assumed to have a symmetrical geometry; (Maloney and Iii, 1993; Kahn and Shaw, 2008); hence a 2D numerical model was used. Therefore, the authors of the current study are confident that it is vital to implicate the geometrical irregularity of the OST to represent the support offered against the dynamic loading applied to the ocular globe within the analyses (Leszczynska et al., 2018) demonstrated that the WEM during tonometry is a quantifiable parameter that could be used to assess tissue behaviour in the orbital space. Thus, within this study, 3D finite element inverse analyses were carried out for 185 ophthalmologically healthy subjects to estimate their OST's material stiffness and investigate the age-related change within the clinical sample. The authors believe this study will widen our understanding of stress-strain behaviour and material stiffness of the orbital soft tissue under dynamic, non-contact tonometry or simulate various ophthalmological conditions. In addition, a comparison of the estimated material stiffness with the experimental will highlight the role of the extraocular muscles in the ocular support system.

TABLE 1 Age groups used in the current study.

Age group	Age range (Years)	Number of samples	Mean age±SD (Years)
Young	20–43	100	29.8 ± 5.4
Middle-aged	> 43–63	50	51.2 ± 6.7
Old	> 63-91	35	72.9 ± 6.0

2 Methods

The study used whole eye movement data recorded for 185 subjects under the dynamic air-puff pressure applied by the Corvis ST tonometer. A numerical model was built for each eye included in the study, simulating its tomography, axial length and IOP, and considering the eye's tissue stiffness as indicated by the Stress-Strain Index (SSI) readings (Eliasy et al., 2019). The eye models were embedded within a medium of orbital soft tissue, whose geometrical boundary surface was provided by Beijing Advanced Innovation Centre for Biomedical Engineering (BAICBE) at Beihang University based on skull MRI scans of a healthy 27-year-old Asian female (Geng et al., 2018).

2.1 Clinical data

A fully anonymised database of 185 Chinese ophthalmologically healthy subjects was retrospectively reviewed, see Table 1. According to the University of Liverpool research ethics policy, approval for this record review using fully anonymised secondary data was ruled unnecessary. Nonetheless, written informed consent was obtained from each participant to use their data in research. The study was

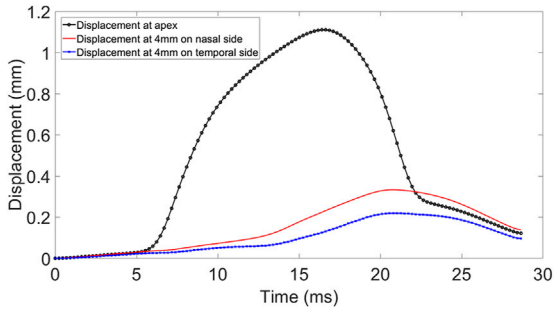

FIGURE 1
Displacement at apex, 4 mm nasal and temporal side of the cornea during Corvis ST procedure.

conducted according to the tenets of the Declaration of Helsinki as set out in 1964 and revised in 2013.

Earlier studies suggest that orbital health conditions, such as thyroid orbitopathy, affect WEM in response to the air pulse produced by Corvis. (Leszczynska et al., 2018; Hwang et al., 2019). Therefore, all participants were subject to a complete ophthalmic examination including tests using the Corvis and Pentacam (OCULUS Optikgeräte GmbH; Wetzlar, Germany). Subjects with a history of use of hypotonic therapies, glaucoma, previous eye disease or ocular surgery were excluded. For consistency, one clinician carried out Corvis examinations for all participants. All exams were individually reviewed by an experienced corneal specialist to ensure that only good-quality scans were included in the study.

The Corvis ST provided a cross-sectional view along the central horizontal meridian of the cornea every 0.23 ms during the air puff application. These cross-sections covered the corneal apex and a 4 mm distance on each of the temporal and nasal sides. Analysis of the cross-sectional views led to the deformation profile at the apex and the 4 mm temporal and nasal points. While the apical deformation included both corneal deflection and the WEM, see Figure 1. the deformations at the temporal and nasal points were mainly caused by the WEM but also included some posterior deformation between these points and the eye's posterior pole (Vinciguerra et al., 2016).

2.2 Finite element modelling

2.2.1 Model generation

The finite element models (FEM) of the eye were constructed using a custom-built MATLAB code described in an earlier study, (Whitford et al., 2015), while a further code was developed herein to build models of the OST. The models were built for analysis by the finite element analysis (FEA) package Abaqus (Abaqus/CAE 6.13-3, Dassault Systèmes Simulia Corp.). Models of the eye globe included 23232 fifteen-noded elements (C3D15H) organised in 1 layer with 16 element rings in the cornea and 72 rings in the sclera. On the other hand, the OST models included 35640 six-noded elements (C3D6H) organised in 5 layers as shown in Figure 2.

The eye models adopted several common attributes reported in earlier studies including the asphericity of both anterior and posterior surfaces of the cornea. The models adopted the corneal profile recorded for each eye by the Corvis ST at no external pressure and assumed rotational symmetry of corneal topography. The models also assumed a spherical shape for the scleral external surface with a radius of 11.5 mm (Whitford et al., 2016). It adopted a variable thickness that changed linearly from 1.2 times the peripheral corneal thickness (PCT) at the posterior pole, to

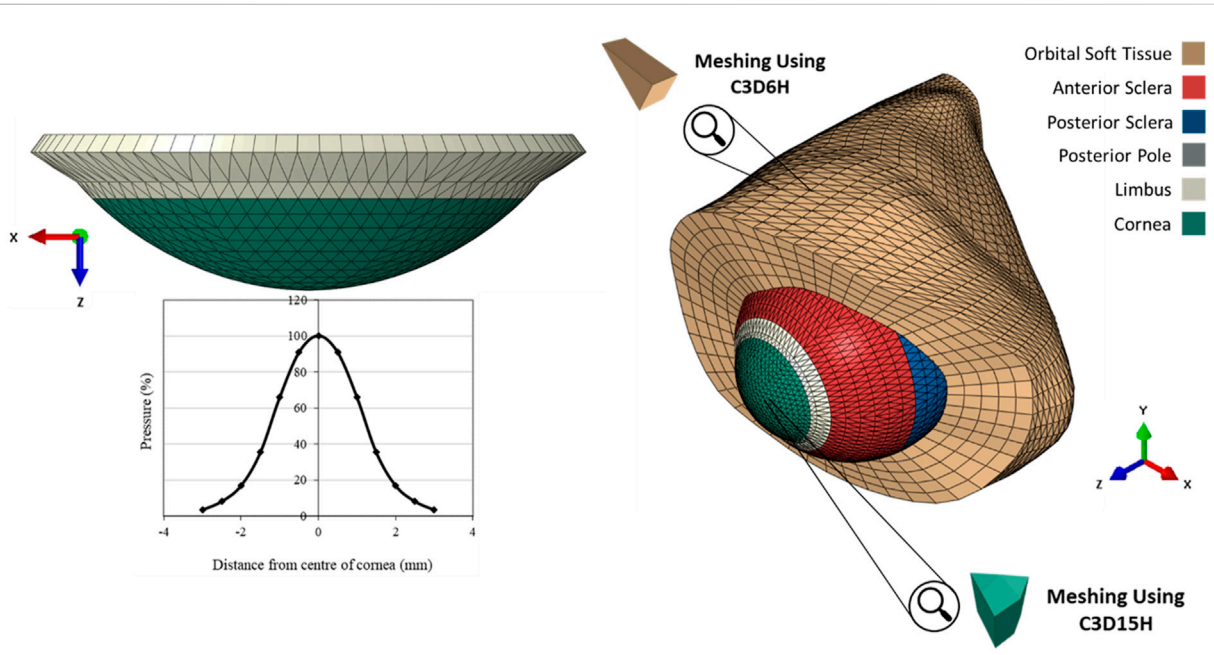

FIGURE 2
The pressure distribution on the cornea during an air puff test, and the Globe-Orbit numerical model that was used for the inverse analysis process.

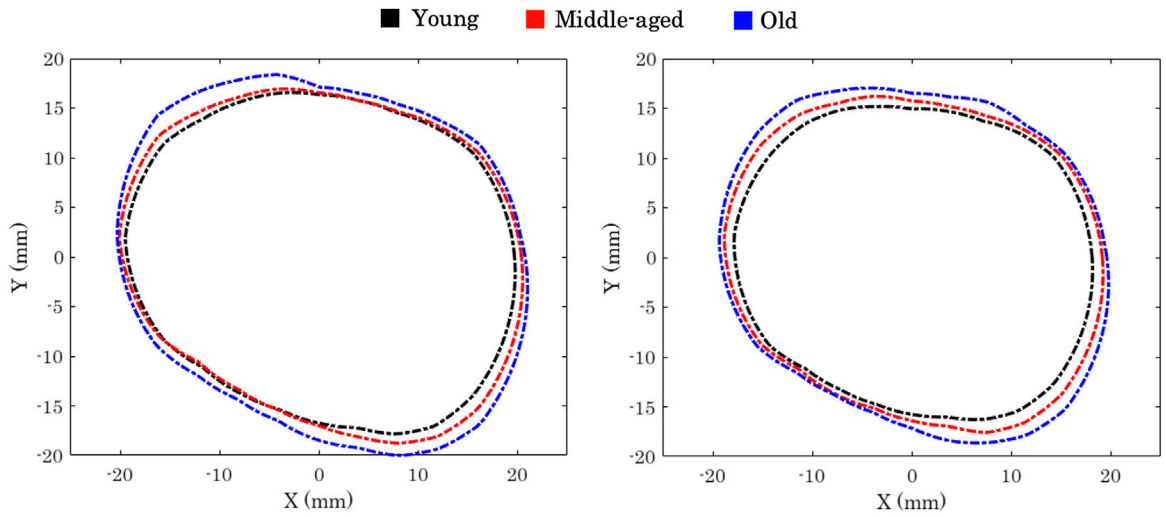

FIGURE 3
Orbital aperture age-related variation in males (left) and females (right) Kahn and Shaw (2008).

0.8 times PCT at the equator and a peripheral corneal thickness (which was greater than CCT by 150 μm) at the limbus (Elsheikh et al., 2013). The models also assumed the corneal stroma had a weak inter-lamellar adhesion (Elsheikh, 2010).

A technique was developed to mesh irregular unsymmetrical shapes, such as the orbital cavity, while ensuring that most elements maintained a consistent shape and size throughout. In this technique, equally spaced points on the longitudinal axis of the combined model were selected, from which radial lines with equal angular spacing were ejected to coincide with the orbital cavity surface. The radial lines were then divided equally to locate intermediate points on each line. These intermediate points, in addition to the orbital surface points and points on the longitudinal axis, formed the nodes between which the elements were formed. This process was used for the whole length of the optic nerve except that within the depth of the eye globe, the radial lines extended from the external surface of the eye model to corresponding points on the orbital surface.

Darcy et al. (2008) carried out a Magnetic Resonance Imaging (MRI) characterisation of orbital changes with age. The outcome of that study suggested a significant increase in the anterior inferior periocular soft-tissue volumes, mainly due to the expansion of fatty tissue in this region. It was also suggested that this trend might be the reason for the lower eyelid prominence, affecting the eye globe's anterior-posterior position within the orbital space. Other studies Fledelius and Stubgaard (1986); Kaye et al. (1992); Pessa et al. (1999); Knudtzon (1949); Lang et al. (1985); Ahmadi et al. (2007), showed changes in exophalmetery value with progression of age, and the most recent study Ahmadi et al. (2007) showed an average reduction of 0.066 *mm/year* in ocular protrusion within both genders. In that study, ocular protrusion was measured from the farthest lateral part of the orbital rim to the corneal apex.

Kahn and Shaw (2008) conducted a three-dimensional computed tomographic study to outline the effect of age on the orbital aperture. The study used a 3D reconstruction of CT scans, followed by measuring orbital aperture width as the distance between the *frontozygomatic suture* and the posterior *lacrimal crest*. This study demonstrated significant changes between age and gender groups in orbital aperture width and area. They also reported that the area increase in the aperture was not uniform across the boundary. In Caucasian males, most of the increase in area was due to a receding boundary at the superior-nasal portion of the rim and a recession of the entire inferior orbital rim, Figure 3.

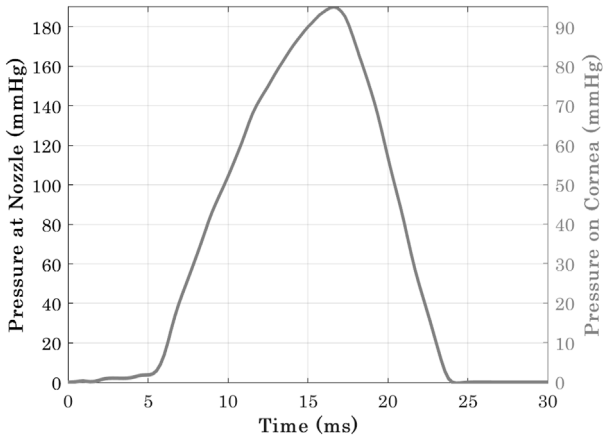

FIGURE 4
Pressure-time distribution at Corvis nozzle and the cornea Eliasy et al. (2019).

2.2.2 Corvis pressure distribution

Corvis applies a jet of pressurised air to the central region of the cornea for a duration of 30 *ms*. A prior experimental study Eliasy et al. (2019) has concluded that air-puff fired from the nozzle has twice the pressure magnitude than the one in contact with the corneal surface, see Figure 4. It was necessary to use an accurate time-pressure distribution. Therefore, 130 pressure profiles of

TABLE 2 Controlling parameters of Ogden constitutive material model in relation to age as obtained from experimental data Elsheikh et al. (2010).

Age (Years)	$\mu(MPa)$				α			
	Cornea	Anterior sclera	Equatorial sclera	Posterior sclera	Cornea	Anterior sclera	Equatorial sclera	Posterior sclera
0	0.104	1.678	0.922	0.433	119.8	31.543	41.521	53.016
25	0.115	1.913	1.081	0.554	119.8	35.303	43.876	53.016
50	0.132	2.224	1.291	0.743	119.8	40.265	46.983	53.016
75	0.157	2.633	1.568	1.096	119.8	46.815	51.084	53.016
100	0.197	3.174	1.934	1.830	119.8	55.458	56.494	53.016

healthy clinical subjects were assessed intervalley throughout the air-puff procedure. It was established that all pressure profiles follow the same trend, where the standard deviation was below 4.3% of maximum applied pressure at the nozzle; hence, only one pressure-time distribution was used in the remainder of the project. In addition, an earlier study obtained the pressure distribution applied on the corneal apex and the spatial reduction in pressure away from the apex and towards the limbus. Joda et al. (2016), see Figure 2. Henceforth, all numerical simulations adopted the mean clinical time-pressure distribution and the spatial-pressure distribution.

2.2.3 Material models

Previous efforts Elsheikh et al. (2009); Geraghty et al. (2012) took place to experimentally quantify stress-strain behaviour of various regions of the globe –the cornea and sclera. Another study Elsheikh et al. (2010) has followed with performing an optimisation analysis to obtain constitutive Ogden material parameters, which provided similar material behaviour for all global regions. In a similar matter, another study (Comley and Fleck, 2012) has carried out an optimisation process to obtain Ogden constitutive material model parameters for the AFT. Therefore, in this study the globe's fifteen-noded and the OST's six-noded numerical models, relied on Ogden Constitutive material model. Abaqus Theory Guide Documentation has provided hyperelastic Ogden strain energy equation, see Eq. 1.

$$U = \sum_{n=1}^{N} \frac{2\mu_i}{\alpha_i}\left(\bar{\lambda}_1^{\alpha_i} + \bar{\lambda}_2^{\alpha_i} + \bar{\lambda}_3^{\alpha_i} - 3\right) + \sum_{n=1}^{N} \frac{1}{D}(J_{el} - 1)^{2i} \qquad (1)$$

Where U is strain energy per unit volume, μ the shear modulus, α the strength hardening exponent, N the function order, $\bar{\lambda}_i$ principal stretch in each of the Cartesian planes, D is compressibility parameter and J_{el} is particle volume. All ocular tissue regions were assumed almost in-compressible with Poisson's ratio of 0.48 Bao et al. (2017); Yu et al. (2013). A number of previous studies have used Ogden material model and proved its ability to represent ocular tissue material behaviour Eliasy et al. (2019); Kotecha (2007); Ogden (1997); Moran et al. (2014). Therefore, this material model required no further investigation during this study and age-related Ogden material parameters were used, Table 2.

2.2.4 Convergence study

A convergence study was carried out in two steps to determine the optimum mesh density of the numerical models used in this study. The first step concentrated on the cornea of the eye globe and involved 12 model representations with the number of elements ranging between 9,408 and 110592. In all 12 models, the OST was represented by the same mesh with 35640 elements, and the focus was on the displacement of the corneal apex under external air pressure. The analysis results of the 12 models allowed the selection of an optimum mesh density in the eye models, which was used in the remainder of the study. The second step then concentrated on the optimum mesh for the OST model. In this work, the optimum eye mesh determined in the first step was adopted, while the OST model had a number of elements ranging between 10692 and 128700 in 12 new models. The displacement of the corneal apex in all models was again used in selecting the optimum density of the OST mesh.

2.2.5 Inverse analysis

A custom-built MATLAB code was constructed to generate a 15 × 5 grid of μ (5×10^{-5} to 5×10^{-3}) and α (0.1–50) values producing 75 combinations of the OST materials parameters. A total of 75 numerical simulations were conducted using each of the α and μ combinations. However, it was found that the root mean square error (RMSE) changed very slightly (below 1%) with changes in α, therefore this parameter was set at a value of 21 in all clinical cases. Within the code, the patient Corvis examination file was read to extract the deformation caused by the air puff test. Analysis of the examination files showed that beyond a 4 mm distance from the corneal apex, there was nearly no corneal deformation (less than 3% of apical deformation). Therefore, it was assumed that the displacement beyond this point was due to the whole eye movement (WEM) inside the orbit space, which was presumed due to the mechanical properties of the OST (Jannesari et al., 2018). Subsequently, two anterior corneal nodes at approximately 4 mm radius on either side (temporal and nasal) of the apex were monitored. In order to eliminate the effect of eye rotation that was observed in both clinical data and numerical predictions (Boszczyk et al., 2017), the mean of the temporal and nasal displacements was considered when assessing the match between the WEM obtained clinically and numerically. The mismatch between the Corvis eye movement results and the models' predictions was calculated for the 15 models using the following objective function:

10.3389/fbioe.2023.1146828

$$RMSE = \sqrt{\frac{\sum_{n=1}^{N} (WEM_{NUMERICAL} - WEM_{CLINICAL})^2}{N}} \quad (2)$$

where RMSE is the root mean square of mismatch between the whole eye movement measured clinically ($WEM_{CLINICAL}$) and predicted numerically ($WEM_{NUMERICAL}$). N is the number of time steps of the simulation (N = 72). Once all 15 simulations were completed, the μ – RMSE results were fitted to a 2nd order polynomial with a local RMSE minimum, from which the μvalues that could give the minimum RMSE were determined.

2.2.6 Statistical analysis

Statistical analyses were carried out using IBM SPSS Statistics 24, IBM, Armonk, New York, U.S. Data were expressed as mean, standard deviation and range. Pearson correlation analysis was performed to study the relationship of the tangent modulus (E_t) in different age groups Table 1 at three stress levels (0.15×10^{-3}, 0.30×10^{-3}, 0.45×10^{-3} MPa). These stress levels covered most of the stress range, to which the OST was subjected in the Corvis ST numerical simulations. In these analyses, p values smaller than 0.05 were indicative of statistical significance.

3 Results

3.1 Convergence study

The eye globe models were analysed under IOP and Corvis ST air pressure with meshes that ranged in the number of elements from 9,408 to 110592. The mesh density study showed a 7.94% change in apical displacement when the number of elements increased from 9,408 to 23232, while a much smaller change in displacement of 0.01% occurred with a further increase in the number of elements from 23232 to 110592 elements. As a result, eye models with 23232 elements were used in the remainder of this study. Models including both the globe and the orbit were also analysed with mesh densities involving numbers of elements between 10692 and 128700 (while fixing the number of elements representing the globe at 23232). The mesh density study showed a 4.34% change in the corneal apical displacement with an increase in the number of elements from 23760 to 35640. A much smaller change in displacement of 1.06% resulted in a further increase from 35640 to 105750 elements. Consequently, a mesh density with 35640 elements, arranged in 13 layers.

3.2 Inverse analysis

Using the "minimum least-squared error" method to determine values of the OST material parameters μ and α that provided the best possible match with the whole eye movement measured clinically resulted in RMSE between 12 and 28 μm (mean ± SD = 24 ± 5) for the 185 eyes considered.

With the μ and α parameters determined, it was possible to plot and compare the stress-strain (σ-ϵ) relationships for individual cornea, Figure 5. To enable these comparisons, the 185 results were split equally across 3 age groups according to ages between

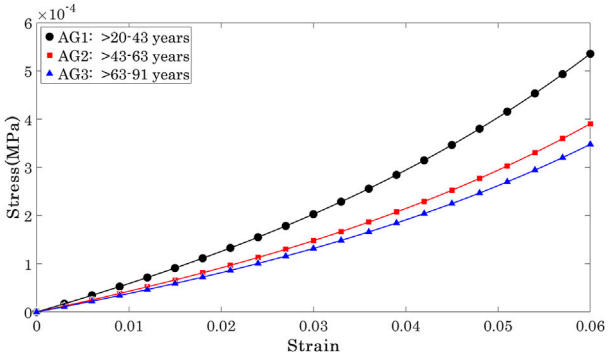

FIGURE 5
Mean Stress-strain behaviour of the OST included in the three age groups.

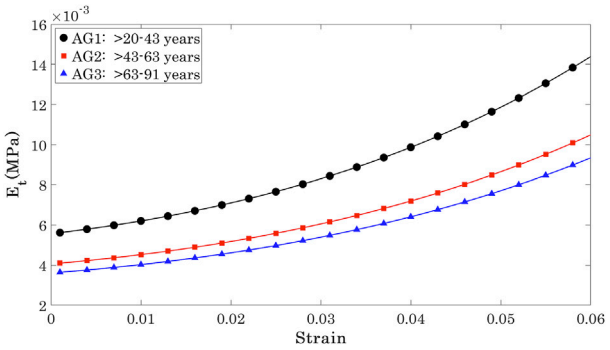

FIGURE 6
Age-related change in the tangent modulus (E_t) calculated for all age groups.

20 and 40 years (mean 29.83 ± 5.4, group AG1, 100 eyes), between 41 and 65 years (mean 51.18 ± 6.7, group AG2, 50 eyes) and between 66 and 91 years (mean 72.91 ± 6.0, group AG2, 35 eyes). The results showed nonlinear behaviour in all 3 groups, with AG3 exhibiting significantly lower stress values at the same strains than AG1 and AG2, while these two later groups demonstrated similar behaviour.

E_t was then determined as the first derivative of stress with respect to strain ($E_t = \partial\sigma/\partial\varepsilon$) Girard et al. (2009); Sigal et al. (2011). E_t showed a significant but weak negative correlation with progression of age at three stress levels (0.15×10^{-3}, 0.30×10^{-3}, 0.45×10^{-3} MPa) that covered most of the stress range to which the OST was subjected in the Corvis ST numerical procedure, Figure 5. At these stress levels, R values remained above 0.20 while p values were ¡0.05 between AG1 and AG2, and AG1 and AG3, although the p-value between AG2 and AG3 was ¿0.05.

The Et values at the three stress levels considered are plotted against age in Figure 6. The results show that while there were large differences between Et at different stress levels, the variation of Et across the age range was slight and limited to −0.27 kPa per decade at $\sigma = 0.15$ kPa, 0.29 kPa per decade at $\sigma = 0.3$ kPa, and −0.29 kPa per decade at $\sigma = 0.45$ kPa.

The results indicated a weak correlation of E_t with the progression of age, regardless of the stress at which E_t was calculated. However, there was evidence of significant differences in E_t between some of the age groups. There was statistical evidence of significant differences between E_t in the age range 20< *years* < 43 relative to E_t in OST with age ranges 43< *years* < 63 ($p = 0.022$) and 63< *years* < 91 ($p = 0.011$). In contrast, E_t in OST with age ranges 43< *years* < 63 and 63< *years* < 91 were not significantly different ($p = 0.863$).

4 Discussion

In this study, 185 numerical models were built while considering corneal tomography in each eye as measured by the Pentacam. The models also included an idealised geometry of the sclera and OST. They were analysed to simulate the performance under intraocular pressure (IOP) and air pressure experienced in Corvis tests. The models then used the corneal deformation profiles recorded by the Corvis under air pressure in an inverse analysis exercise to estimate the material behaviour of the OST. Each subject's model was run 15 times within the inverse analysis with varying material stiffness. Material stiffness producing the most optimum deformation to its corresponding clinical data was saved for this subject along with its age and IOP, ready for further age-related analysis.

Results of the inverse analysis enabled estimation of OST's tangent modulus (E_t) for each of the 185 eyes included in this study. The results indicated a weak correlation of E_t with the progression of age, regardless of the stress at which E_t was calculated. However, there was evidence of significant differences in E_t between some of the age groups. There was statistical evidence of significant differences between E_t in the age range 20< *years* < 43 relative to E_t in OST with age ranges 43< *years* < 63 ($p = 0.022$) and 63< *years* < 91 ($p = 0.011$). In contrast, E_t in OST with age ranges 43< *years* < 63 and 63< *years* < 91 were not significantly different ($p = 0.863$).

Despite efforts to create age-specific numerical models of the eye globe and OST, where some geometrical (and other age-related) variables changed, material optimisation produced 1.6 ± 1 kPa as the mean optimum material stiffness for OST. Prior studiesComley and Fleck (2012); Comley and Fleck (2010) have developed a micro-mechanical model for the soft biological tissue. This proposed model suggested material stiffness of AFT being 0.4 kPa, which is significantly low (4 times softer) compared to the optimised material stiffness estimated in the current study. Hwang et al. (2019) stated that EOMs play a significant role in supporting the eye globe. Nevertheless, the discrepancy between the experimental stiffness of AFT Comley and Fleck (2012) and the optimised stiffness of the current has indirectly quantified the support provided to the eye globe through EOMs and other connective tissues such as Lockwood's ligament. This quantification of mechanical stiffness confirms Hwang's findings Hwang et al. (2019) and provides a comparative scenario of how various OSTs collectively support the globe against an exterior form of frontal loading.

In another study, Jannesari et al. (2018) attempted to estimate biomechanical properties of AFT using a very similar methodology to the current study; by employing an inverse analysis optimisation along with Corvis corneal deformation. However, their numerical set-up involved an idealised two-dimensional axisymmetric geometry of the cornea, while a viscoelastic boundary condition was applied at the limbal conjecture. This study and previous work Hwang et al. (2019); Lemke and Lucarelli (2012); Lockwood (1885); Banks et al. (2020); Comley and Fleck (2012) experimental and numerical findings were produced suggesting that the AFT is not the only form of support provided to the globe. The assumption of an axisymmetric geometry may be suitable for the cornea; however, Corvis corneal deformations show a very prominent occurrence of nasal rotation during retraction of the eye globe. Boszczyk et al. (2017) This nasal rotation drove the need to employ a three-dimensional geometrical set-up in this study, which implements irregularity and asymmetry of the orbital boundary. The orbital soft tissue has been the subject of several anatomical studies focusing on its structure. Sedlmayr (2002); Demer (2002) These studies report that most common eye movements involve sliding within the Tenon's capsule of the OST. Indeed, Schoemaker et al. (2006) have attempted to estimate viscoelastic material properties by assessing the degree of deformation of AFT in eye globe rotation. In this study, a hyper-elastic material model was used to save computational time due to the Corvis pressure loading scenario's simulation. This study differed from Shoemaker's work in the loading conditions, where frontal loading was applied instead of the application of rotations onto the globe. The current study attempted to validate the hyper-elastic material model of OST using Corvis clinical corneal deformations, as suggested by Hwang et al. (2019).

In conclusion, this study utilised inverse finite element analysis with clinical measurements of the WEM under Corvis air pressure to estimate the OST's stiffness and how this changes with age. The OST E_t has shown a weak correlation with age progression at the three different stress levels while showing significant differences between some age groups. With this information, numerical modelling of the eye globe, especially those simulating WEM, can now include models of the OST rather than introducing non-physiologic boundary conditions simulating its effect. Aboulatta et al. (2021); Jannesari et al. (2018) Nevertheless, despite consideration of the orbital geometry's irregularity, numerical simulations did not accurately represent the nasal rotation aspect of clinical retraction of the eye globe. The authors of this study suggest that this rotation may be due to deeper orbital structures, such as EOMs, Lockwood's ligament or other connective tissues. Lockwood (1885); Demer (2002) Thus, it is highly recommended to investigate the rotational response of the globe further, as this will have a considerable effect on future work regarding the simulation of impacts or exterior loading applied to the globe or even the orbital structure as a whole.

This study has consolidated previous findings, which stated the importance of the extraocular muscles in supporting the globe. Despite the age-related geometrical specification of the numerical model used in this study, the model needs improvement and requires the extraocular muscles to be added to it. This athors of this study believe that addition of the extraocular muscles will allow this numerical model to be an accurate representation of the ocular support system.

Data availability statement

The raw data supporting the conclusion of this article will be made available by the authors, without undue reservation.

Ethics statement

According to the University of Liverpool research ethics policy, approval for this record review using fully anonymised secondary data was ruled unnecessary. Nonetheless, written informed consent was obtained from each participant to use their data in research. The study was conducted according to the tenets of the Declaration of Helsinki as set out in 1964 and revised in 2013.

Author contributions

All authors contributed to conception and design of the study. AM and FB organized the database. AM wrote the first draft of the manuscript. AE, AA, and AM wrote sections of the manuscript. All authors contributed to the article and approved the submitted version.

Conflict of interest

The authors declare that the research was conducted in the absence of any commercial or financial relationships that could be construed as a potential conflict of interest.

Publisher's note

All claims expressed in this article are solely those of the authors and do not necessarily represent those of their affiliated organizations, or those of the publisher, the editors and the reviewers. Any product that may be evaluated in this article, or claim that may be made by its manufacturer, is not guaranteed or endorsed by the publisher.

References

Aboulatta, A., Abass, A., Makarem, A., Eliasy, A., Zhou, D., Chen, D., et al. (2021). Experimental evaluation of the viscoelasticity of porcine vitreous. *J. R. Soc. Interface* 18, 20200849. doi:10.1098/rsif.2020.0849

Ahmadi, H., Shams, P., Davies, N., Joshi, N., and Kelly, M. (2007). Age-related changes in the normal sagittal relationship between globe and orbit. *J. plastic, Reconstr. aesthetic Surg.* 60, 246–250. doi:10.1016/j.bjps.2006.07.001

Al-Sukhun, J., Lindqvist, C., and Kontio, R. (2006). Modelling of orbital deformation using finite-element analysis. *J. R. Soc. Interface* 3, 255–262. doi:10.1098/rsif.2005.0084

Banks, C., Husain, Q., and Bleier, B. S. (2020). Endoscopic endonasal intraconal orbit surgery. *World J. Otorhinolaryngology-Head Neck Surg.* 6, 100–105. doi:10.1016/j.wjorl.2019.07.001

Bao, F., Deng, M., Zheng, X., Li, L., Zhao, Y., Cao, S., et al. (2017). Effects of diabetes mellitus on biomechanical properties of the rabbit cornea. *Exp. eye Res.* 161, 82–88. doi:10.1016/j.exer.2017.05.015

Boszczyk, A., Kasprzak, H., and Jóźwik, A. (2017). Eye retraction and rotation during corvis st 'air puff'intraocular pressure measurement and its quantitative analysis. *Ophthalmic Physiological Opt.* 37, 253–262. doi:10.1111/opo.12383

Bremond-Gignac, D., Copin, H., Cussenot, O., Lassau, J.-P., and Henin, D. (2004). Anatomical histological and mesoscopic study of the adipose tissue of the orbit. *Surg. Radiologic Anat.* 26, 297–302. doi:10.1007/s00276-004-0223-5

Bron, A. J., Tripathi, R. C., and Tripathi, B. J. (1997). *Wolff's anatomy of the eye and orbit*. 8th Edn. Chapman & Hall.

Chen, K., and Weiland, J. D. (2011). Mechanical properties of orbital fat and its encapsulating connective tissue. *J. biomechanical Eng.* 133, 064505. doi:10.1115/1.4004289

Comley, K., and Fleck, N. A. (2010). A micromechanical model for the young's modulus of adipose tissue. *Int. J. Solids Struct.* 47, 2982–2990. doi:10.1016/j.ijsolstr.2010.07.001

Comley, K., and Fleck, N. (2012). The compressive response of porcine adipose tissue from low to high strain rate. *Int. J. Impact Eng.* 46, 1–10. doi:10.1016/j.ijimpeng.2011.12.009

Darcy, S. J., Miller, T. A., Goldberg, R. A., Villablanca, J. P., Demer, J. L., and Rudkin, G. H. (2008). Magnetic resonance imaging characterization of orbital changes with age and associated contributions to lower eyelid prominence. *Plastic Reconstr. Surg.* 122, 921–929. doi:10.1097/prs.0b013e3181811ce8

Demer, J. L. (2002). The orbital pulley system: A revolution in concepts of orbital anatomy. *Ann. N. Y. Acad. Sci.* 956, 17–32. doi:10.1111/j.1749-6632.2002.tb02805.x

Eliasy, A., Chen, K.-J., Vinciguerra, R., Lopes, B. T., Abass, A., Vinciguerra, P., et al. (2019). Determination of corneal biomechanical behavior *in-vivo* for healthy eyes using corvis st tonometry: Stress-strain index. *Front. Bioeng. Biotechnol.* 7, 105. doi:10.3389/fbioe.2019.00105

Elsheikh, A. (2010). Finite element modeling of corneal biomechanical behavior. *J. Refract. Surg.* 26, 289–300. doi:10.3928/1081597x-20090710-01

Elsheikh, A., Geraghty, B., Alhasso, D., and Rama, P. (2009). Regional biomechanical behavior of the human sclera and its variation with age. *Investigative Ophthalmol. Vis. Sci.* 50, 3948.

Elsheikh, A., Geraghty, B., Rama, P., Campanelli, M., and Meek, K. M. (2010). Characterization of age-related variation in corneal biomechanical properties. *J. R. Soc. Interface* 7, 1475–1485. doi:10.1098/rsif.2010.0108

Elsheikh, A., Whitford, C., Hamarashid, R., Kassem, W., Joda, A., and Büchler, P. (2013). Stress free configuration of the human eye. *Med. Eng. Phys.* 35, 211–216. doi:10.1016/j.medengphy.2012.09.006

Fledelius, H. C., and Stubgaard, M. (1986). Changes in refraction and corneal curvature during growth and adult life: A cross-sectional study. *Acta Ophthalmol.* 64, 487–491. doi:10.1111/j.1755-3768.1986.tb06959.x

Geng, X., Liu, X., Wei, W., Wang, Y., Wang, L., Chen, K., et al. (2018). Mechanical evaluation of retinal damage associated with blunt craniomaxillofacial trauma: A simulation analysis. *Transl. Vis. Sci. Technol.* 7, 16. doi:10.1167/tvst.7.3.16

Geraghty, B., Jones, S. W., Rama, P., Akhtar, R., and Elsheikh, A. (2012). Age-related variations in the biomechanical properties of human sclera. *J. Mech. Behav. Biomed. Mater.* 16, 181–191. doi:10.1016/j.jmbbm.2012.10.011

Girard, M. J., Suh, J.-K. F., Bottlang, M., Burgoyne, C. F., and Downs, J. C. (2009). Scleral biomechanics in the aging monkey eye. *Investigative Ophthalmol. Vis. Sci.* 50, 5226–5237. doi:10.1167/iovs.08-3363

Guo, H., Gao, Z., Han, B., Zhang, L., Tang, Z., Chen, J., et al. (2019). *In vivo* experimental study on the resistance and stiffness of orbital suspension tissues with/without the extraocular muscles. *Biomed. Eng. OnLine* 18, 68–11. doi:10.1186/s12938-019-0688-4

Heesy, C. P. (2004). On the relationship between orbit orientation and binocular visual field overlap in mammals. *Anatomical Rec. Part A Discov. Mol. Cell. Evol. Biol.* 281, 1104–1110. doi:10.1002/ar.a.20116

Hwang, H. S., Kim, E. C., Kim, M. S., and Yang, S.-W. (2019). A novel method for quantifying the biomechanical parameters of orbital soft tissue using a corneal dynamic scheimpflug analyser: A retrospective study. *BMC Ophthalmol.* 19, 53–59. doi:10.1186/s12886-019-1064-7

Jannesari, M., Kadkhodaei, M., Mosaddegh, P., Kasprzak, H., and Behrouz, M. J. (2018). Assessment of corneal and fatty tissues biomechanical response in dynamic tonometry tests by using inverse models. *Acta Bioeng. biomechanics* 20, 39–48. doi:10.5277/ABB-00969-2017-02

Joda, A. A., Shervin, M. M. S., Kook, D., and Elsheikh, A. (2016). Development and validation of a correction equation for corvis tonometry. *Comput. methods biomechanics Biomed. Eng.* 19, 943–953. doi:10.1080/10255842.2015.1077515

Kahn, D. M., and Shaw, R. B. (2008). Aging of the bony orbit: A three-dimensional computed tomographic study. *Aesthetic Surg. J.* 28, 258–264. doi:10.1016/j.asj.2008.02.007

Katch, V., Becque, M., Marks, C., Moorehead, C., and Rocchini, A. (1991). Gender dimorphism in size, shape and body composition of child-onset obese and nonobese adolescents. *Int. J. Obes.* 15, 267–282.

Kaye, S. B., Green, J. R., Luck, J., and Lowe, K. J. (1992). Dependence of ocular protrusion, asymmetry of protrusion and lateral interorbital width on age. *Acta Ophthalmol.* 70, 762–765. doi:10.1111/j.1755-3768.1992.tb04884.x

Knudtzon, K. (1949). On exophthalmometry: The result of 724 measurements with hertel's exophthalmometer on normal adult individuals. *Acta Psychiatr. Scand.* 24, 523–537. doi:10.1111/j.1600-0447.1949.tb07336.x

Kotecha, A. (2007). What biomechanical properties of the cornea are relevant for the clinician? *Surv. Ophthalmol.* 52, S109–S114. doi:10.1016/j.survophthal.2007.08.004

Lang, J., Schäfer, W., Grafen, W., and Wallner, B. (1985). Side differences in the position of the corneal apex in relation to the lateral orbital margin (measurements with the hertel exophthalmometer). *Klin. Monatsblatter fur Augenheilkd.* 187, 521–524. doi:10.1055/s-2008-1054390

Lemke, B. N., and Lucarelli, M. J. (2012). "Anatomy of the ocular adnexa, orbit, and related facial structures," in *Smith and Nesi's ophthalmic plastic and reconstructive surgery* (New York, NY: Springer), 3–58.

Leszczynska, A., Moehler, K., Spoerl, E., Ramm, L., Herber, R., Pillunat, L. E., et al. (2018). Measurement of orbital biomechanical properties in patients with thyroid orbitopathy using the dynamic scheimpflug analyzer (corvis st). *Curr. eye Res.* 43, 289–292. doi:10.1080/02713683.2017.1405044

Liu, X., Wang, L., Wang, C., Sun, G., Liu, S., and Fan, Y. (2013). Mechanism of traumatic retinal detachment in blunt impact: A finite element study. *J. biomechanics* 46, 1321–1327. doi:10.1016/j.jbiomech.2013.02.006

Lockwood, C. B. (1885). The anatomy of the muscles, ligaments, and fasclae of the orbit, including an account of the capsule of tenon, the check ligaments of the recti, and the suspensory ligaments of the eye. *J. Anat. Physiology* 20, i2–i25.

Maloney, R. K., Bogan, S. J., and Iii, G. O. W. (1993). Determination of corneal image-forming properties from corneal topography. *Am. J. Ophthalmol.* 115, 31–41. doi:10.1016/s0002-9394(14)73521-4

Moran, R., Smith, J. H., and García, J. J. (2014). Fitted hyperelastic parameters for human brain tissue from reported tension, compression, and shear tests. *J. biomechanics* 47, 3762–3766. doi:10.1016/j.jbiomech.2014.09.030

Ogden, R. W. (1997). *Non-linear elastic deformations*. North Chelmsford, MA: Courier Corporation.

Pessa, J. E., Desvigne, L. D., Lambros, V. S., Nimerick, J., Sugunan, B., and Zadoo, V. P. (1999). Changes in ocular globe-to-orbital rim position with age: Implications for aesthetic blepharoplasty of the lower eyelids. *Aesthetic Plast. Surg.* 23, 337–342. doi:10.1007/s002669900295

Rootman, J., Rootman, D. B., Stewart, B., Diniz, S. B., Roelofs, K. A., Cohen, L. M., et al. (2022). Cavernous sinus. *Atlas Orbital Imaging*, 85–89. doi:10.1007/978-3-030-62426-2_6

Schoemaker, I., Hoefnagel, P. P., Mastenbroek, T. J., Kolff, C. F., Schutte, S., van der Helm, F. C., et al. (2006). Elasticity, viscosity, and deformation of orbital fat. *Investigative Ophthalmol. Vis. Sci.* 47, 4819–4826. doi:10.1167/iovs.05-1497

Schutte, S., van den Bedem, S. P., van Keulen, F., van der Helm, F. C., and Simonsz, H. J. (2006). A finite-element analysis model of orbital biomechanics. *Vis. Res.* 46, 1724–1731. doi:10.1016/j.visres.2005.11.022

Sedlmayr, J. C. (2002). *Anatomy, evolution, and functional significance of cephalic vasculature in Archosauria*. Athens, OH: Ohio University.

Sigal, I. A., Yang, H., Roberts, M. D., Grimm, J. L., Burgoyne, C. F., Demirel, S., et al. (2011). Iop-induced lamina cribrosa deformation and scleral canal expansion: Independent or related? *Investigative Ophthalmol. Vis. Sci.* 52, 9023–9032. doi:10.1167/iovs.11-8183

Stitzel, J. D., Duma, S. M., Cormier, J. M., and Herring, I. P. (2002). "A nonlinear finite element model of the eye with experimental validation for the prediction of globe rupture," in SAE Conference Proceedings, May 3, 2002 (Virginia, United States: SAE), 81–102.

Turvey, T. A., and Golden, B. A. (2012). Orbital anatomy for the surgeon. *Oral Maxillofac. Surg. Clin.* 24, 525–536. doi:10.1016/j.coms.2012.08.003

Vinciguerra, R., Elsheikh, A., Roberts, C. J., Ambrósio, R., Jr, Kang, D. S. Y., Lopes, B. T., et al. (2016). Influence of pachymetry and intraocular pressure on dynamic corneal response parameters in healthy patients. *J. Refract. Surg.* 32, 550–561. doi:10.3928/1081597x-20160524-01

Whitford, C., Joda, A., Jones, S., Bao, F., Rama, P., and Elsheikh, A. (2016). *Ex vivo* testing of intact eye globes under inflation conditions to determine regional variation of mechanical stiffness. *Eye Vis.* 3, 21–12. doi:10.1186/s40662-016-0052-8

Whitford, C., Studer, H., Boote, C., Meek, K. M., and Elsheikh, A. (2015). Biomechanical model of the human cornea: Considering shear stiffness and regional variation of collagen anisotropy and density. *J. Mech. Behav. Biomed. Mater.* 42, 76–87. doi:10.1016/j.jmbbm.2014.11.006

Yu, J.-G., Bao, F.-J., Feng, Y.-F., Whitford, C., Ye, T., Huang, Y. B., et al. (2013). Assessment of corneal biomechanical behavior under posterior and anterior pressure. *J. Refract. Surg.* 29, 64–71. doi:10.3928/1081597x-20121228-05

frontiers | Frontiers in Bioengineering and Biotechnology

TYPE Original Research
PUBLISHED 04 August 2023
DOI 10.3389/fbioe.2023.1158299

OPEN ACCESS

EDITED BY
Matthew A. Reilly,
The Ohio State University, United States

REVIEWED BY
Peng Xiao,
Sun Yat-sen University, China
Junjie Wang,
Wenzhou Medical University, China

*CORRESPONDENCE
Yan Wang,
wangyan7143@vip.sina.com

†These authors have contributed equally to this work and share first authorship

RECEIVED 03 February 2023
ACCEPTED 21 July 2023
PUBLISHED 04 August 2023

CITATION
Chen X, Cao H, Huo Y, Song J, Zou H, Li J, Hou J and Wang Y (2023), Screening of sensitive *in vivo* characteristics for early keratoconus diagnosis: a multicenter study.
Front. Bioeng. Biotechnol. 11:1158299.
doi: 10.3389/fbioe.2023.1158299

Screening of sensitive *in vivo* characteristics for early keratoconus diagnosis: a multicenter study

Xuan Chen[1†], Huazheng Cao[1†], Yan Huo[1], Jiaxin Song[2], Haohan Zou[3], Jing Li[4], Jie Hou[5] and Yan Wang[1,2,3,6*]

[1]School of Medicine, Nankai University, Tianjin, China, [2]Clinical College of Ophthalmology, Tianjin Medical University, Tianjin, China, [3]Tianjin Eye Hospital, Tianjin Key Lab of Ophthalmology and Visual Science, Tianjin Eye Institute, Nankai University Affiliated Eye Hospital, Tianjin, China, [4]Shanxi Eye Hospital, Xi'an People's Hospital, Xi'an, Shanxi, China, [5]Jinan Mingshui Eye Hospital, Jinan, Shandong, China, [6]Nankai Eye Institute, Nankai University, Tianjin, China

Purpose: To analyze and compare sensitive *in vivo* characteristics for screening early keratoconus.

Methods: This multicenter, case-control study included 712 eyes, after matching for age and biomechanically corrected intraocular pressure, from three clinics in different cities. The keratoconus (n = 288), early keratoconus (n = 91), and normal cornea (n = 333) groups included eyes diagnosed with bilateral keratoconus, fellow eyes with relatively normal topography with unilateral keratoconus, and normal eyes before refractive surgery, respectively. After adjusting for central corneal thickness, differences *in vivo* characteristics were analyzed among the three groups. The *in vivo* characteristics were measured by Pentacam and Corvis ST. Fifty-four indices were evaluated to screen for a sensitive index for the detection of early keratoconus.

Results: Significant differences were observed in 26 of the 36 corneal biomechanical indeces between the early keratoconus and normal corneas. The area under the receiver operating characteristic curve of tomographic and biomechanical index, Belin/Ambrósio deviation, and Da in differentiating keratoconus from normal cornea was 1.000. Among the top five indeces of the area under the receiver operating characteristic curve for detecting early keratoconus, the corneal biomechanical-related index accounted for 80% (4/5), including A1 dArc length, highest concavity radius, A2 time, and tomographic and biomechanical index, of which the area under the receiver operating characteristic curve of A1 dArc length was 0.901.

Conclusion: A1 dArc length and several corneal biomechanical indices are highly sensitive for the detection of early keratoconus, even in the absence of topographic abnormalities. Ophthalmologists should focus on the clinical application of corneal biomechanics and combine corneal tomography for the timely and accurate detection of early keratoconus.

KEYWORDS

sensitive characteristics, *in vivo*, corneal biomechanics, corneal tomography, early keratoconus

1 Introduction

Corneal refractive surgery decreases corneal stability, which may lead to postoperative ectasia if underlying pre-existing disease occurs, and result in disastrous refractive outcomes (Kim et al., 2019; Jabbour and Bower, 2021). Rigorous preoperative examinations are essential in corneal refractive surgery. Nevertheless, there is a paucity of reported cases in the literature, with a lack of clear risk factors for corneal ectasia (Duffey et al., 2008; Moshirfar et al., 2021). Hence, the preoperative screening of suitable patients remains a challenge for clinicians.

Keratoconus (KC) is one of the most common conditions and comprises a high proportion of patients who are unable to undergo corneal refractive surgery (Al-Amri, 2018). KC is an absolute contraindication for refractive surgery, with a reported incidence of 0.05%–0.23% (Rabinowitz, 1998). It is predominantly characterized by corneal thinning and forward protrusion, resulting in irregular astigmatism and severely reduced visual acuity (Santodomingo-Rubido et al., 2022). KC is one of the blindness diseases worldwide, and there is an urgent need to develop better methods for the accurate clinical diagnosis of early KC (EKC) to avoid corneal ectasia after refractive surgery, which may lead to vision loss that impacts the quality of life.

Currently, corneal topography and tomography are the main tools for diagnosing KC (Santodomingo-Rubido et al., 2022). However, as the morphology of EKC lacks evident abnormalities, relying on corneal tomography alone precludes an early diagnosis. Research on disease pathophysiology suggests that instability of corneal biomechanics changes corneal morphology, leading to corneal ectasia (Andreassen et al., 1980; Roberts and Dupps, 2014). Therefore, extensive efforts have been made to evaluate corneal biomechanical properties to detect keratoconus-like changes as early as possible. Differences in corneal biomechanics between normal corneas and KC have been reported in several studies. Corneal biomechanical changes play an important role in detecting EKC, especially in suspected cases or forme fruste keratoconus (FFKC) (Koh et al., 2020; Asroui et al., 2022). Nevertheless, detecting EKC remains difficult, as the detection ability remains weak in the early disease stage. Early detection of clinical measurements had been studied in previous studies (Shiga et al., 2021; Sedaghat et al., 2018), however, these findings are mixed, the reason for the inconsistent conclusions may be that the effect of age and intraocular pressure was not fully considered. An important feature of the present work is the investigation and analysis of the *in vivo* characteristics of normal corneas with age—and biomechanically corrected intraocular pressure-matched EKC to screen sensitive indices for diagnosing EKC.

2 Materials and methods

2.1 Participant inclusion and exclusion criteria

The study was approved by the ethics committee of Tianjin Eye Hospital (2022032) and performed in accordance with the principles of the Declaration of Helsinki. All participants signed an informed consent form to use their data for the analysis.

Patients enrolled from three clinics (Tianjin Medical University, Tianjin, China; Shanxi Eye Hospital, Shanxi, China; Jinan Mingshui Eye Hospital, Shandong, China) were divided into three groups according to the following criteria: 1) KC group: KC was diagnosed based on the diagnostic criteria of myopia and astigmatism history, corrected distance visual acuity (CDVA) < 20/20, abnormal corneal tomography (any of the following manifestations: asymmetric bow tie type - oblique radial axis, steep central or lower area, and Belin/Ambrósio Deviation (D) ≥ 3), and positive signs on slit lamp biomicroscopy (at least one of Vogt's striae, Fleischer's ring, Munson's sign, or Rizutti's sign) (Rabinowitz, 1998); 2) EKC group: unilateral KC comprising one eye diagnosed with KC and corneal tomography of the fellow eye was relatively normal (no asymmetrical bow tie type—oblique radial axis and no central or lower area steep), I–S of <1.4 D, KISA% index of < 60% (Rabinowitz et al., 1999; Steinberg et al., 2015a; Henriquez et al., 2020); and 3) Normal cornea (NC) group: patients whose refractive outcomes after SMILE have been demonstrated as safe without any complications throughout their at least 2 years of observation, with CDVA ≥ 20/20, normal slit-lamp biomicroscopy, and normal corneal tomography (none of the following manifestations: asymmetric bow tie type—skewed radial axis, steep central or lower area, and D ≥ 3), we select preoperative characteristics for analysis.

The exclusion criteria were ocular diseases other than ametropia and KC, history of other ocular operations, ocular trauma, and systemic diseases. All patients were required to stop wearing contact lenses (soft lenses for at least 2 weeks and hard lenses for at least 4 weeks) before assessment.

2.2 Ophthalmologic examinations

Each patient underwent routine ophthalmic examinations, including uncorrected distance visual acuity, CDVA, non-contact intraocular pressure, objective refraction, manifest refraction, slit lamp biomicroscopy, fundus examination, corneal tomography, and corneal biomechanical examinations. All the examinations were performed by the same technician.

Corneal tomography was examined using a three-dimensional anterior segment analysis system (Pentacam HR, Oculus, Wetzlar, Germany). Multiple images of the anterior segment were captured using a Scheimpflug camera to synthesize three-dimensional images of the anterior segment. All patients underwent measurements in a dark room. Patients were instructed to sit in front of the examination equipment in an upright posture and place their chin and forehead against the chin and forehead trays, respectively. After blinking several times, the patients were instructed to keep their eyes open and gaze at the flashing red dots during the rotation measurement of the equipment to automatically obtain images. Corneal biomechanical examinations were performed using the Corneal Visualization Scheimpflug Technology (Corvis ST, Oculus, Wetzlar, Germany). The ultra-high-speed Scheimpflug technology was scanned at a speed of 4,330 frames/s in the 8 mm horizontal range, and 140 images were acquired within 31 ms under the action of jet pulses. During the measurements, patients were instructed to place their chin and forehead against the chin and forehead trays, respectively, keep their eyes open, and gaze at the blue point after

TABLE 1 Baseline characteristics of the participants.

Parameter	NL (n = 333)	EKC (n = 91)	KC (n = 288)	p-value
Age	22.92 (19–26)	22.93 ± 4.91 (12–34)	22.95 (19.4–26.3)	0.250 [0]
Sex (M/F)	211/122	64/27	179/109	0.360 [0]
IOP (mmHg)	15.71(14.5–17)	14.57(13–16)	13.72(12.5–15)	<0.001 [1]
				<0.001 [2]
				0.007 [3]
bIOP (mmHg)	15.42 (14.35–16.45)	15.39(14.2–16.5)	15.4 (14.3–16.5)	0.658 [0]
CCT (μm)	552.45 ± 24.77 (479–601)	508.55 ± 36.2 (391–586)	467.62 ± 31.96 (375–575)	<0.001 [1]
				<0.001 [2]
				<0.001 [3]
TCT (μm)	548.29 ± 24.94 (473–598)	501.44 ± 36.45 (379–583)	451.13 ± 32.9 (367–551)	<0.001 [1]
				<0.001 [2]
				<0.001 [3]

Mean ± SD (range: minimum to maximum).
Kolmogorov–Smirnov test, One-way analysis of variance, Kruskal–Wallis test, and chi-square test was performed respectively.
[0] p-value (NL, vs. EKC, vs. KC); [1] p-value (NL, vs. EKC); [2] p-value (NL, vs. KC); [3] p-value (KC, vs. EKC).
NL, normal cornea; EKC, early keratoconus; KC, keratoconus; IOP, intraocular pressure; bIOP, biomechanically corrected intraocular pressure; CCT, central corneal thickness; TCT, thinnest corneal thickness.

blinking several times. After the pressure-measuring head was aligned with the cornea, air was automatically ejected to obtain the dynamic response parameters of the cornea. The Pentacam and Corvis ST data were exported to CSV files using the original software of the equipment for analysis. The quality of all inspection results used for analysis was certified by experienced technicians.

2.3 Statistical analysis

Statistical analysis was performed using SPSS software (version 26.0; International Business Machines Corporation, Armonk, NY, United States). Continuous variables are expressed as mean ± standard deviation (minimum to maximum), and categorical variables are expressed as frequencies and percentages. The Kolmogorov–Smirnov test was used to test for normality. One-way analysis of variance was used to compare differences between groups of normally distributed variables, and a non-parametric test (Kruskal–Wallis test) was used to compare differences between groups of non-normally distributed variables. The chi-square test was used to compare differences between groups for categorical variables. Age and intraocular pressure (IOP) have effects on biomechanics, and central corneal thickness (CCT) has little effect on biomechanics (Huseynova et al., 2014; Valbon et al., 2014). Matching for age, biomechanically corrected intraocular pressure (bIOP), and adjusting for CCT using the general linear model, the Bonferroni test was used to analyze the differences *in vivo* characteristics between the two groups. Receiver operating characteristic (ROC) curves were used to evaluate and compare the 54 parameters (Supplementary Table S1). The cutoff value, sensitivity, and specificity were calculated when the differentiating ability was the best. Statistical significance was set at $p < 0.05$.

3 Results

3.1 Demographic and baseline characteristics

A total of 712 eyes were included after matching according to age and bIOP, with an average age of 22.92 ± 5.14 (range: 11–37) years. The KC, EKC, and NC groups comprised 288 eyes diagnosed with KC, 91 contralateral eyes with unilateral KC, and 333 eyes after refractive surgery 2 years, respectively. Details of the baseline characteristics are presented in Table 1.

3.2 Differences in distribution of characteristics

Significant differences were observed in the corneal morphological parameters between the KC and NC groups before and after adjusting for CCT. Nonparametric testing revealed significant differences in 91.7% (33/36) of the corneal biomechanical parameters between the KC and NC groups, and 75% (27/36) were significantly different after adjusting for CCT.

Nonparametric testing revealed significant differences in corneal morphological parameters between the EKC and NC groups, except for Kmax ($p = 0.384$) and IHA ($p = 0.613$). After adjusting for CCT, no significant differences were identified except for Da ($p < 0.001$).

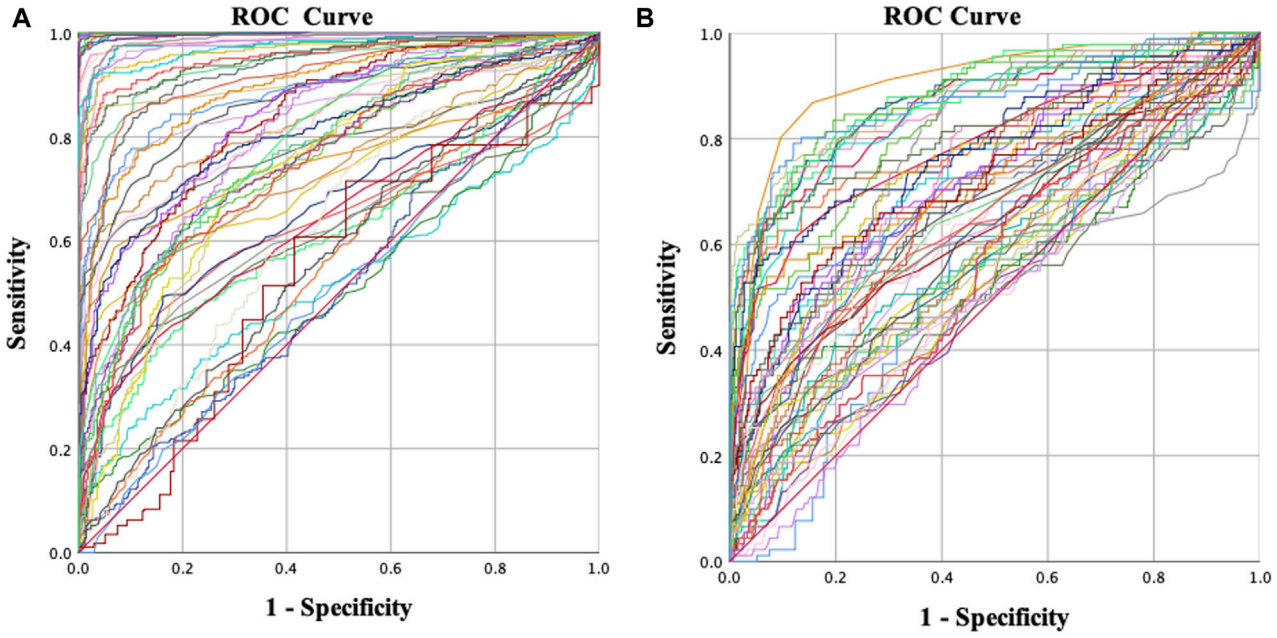

FIGURE 1
Receiver operating characteristic (ROC) curves for different groups. **(A)** Normal vs. keratoconus and **(B)** normal vs. early keratoconus.

Significant differences were observed in 72.2% (26/36) of the biomechanical parameters between the EKC and NC groups.

Analysis before and after adjusting for CCT revealed significant differences in corneal morphological parameters between the KC and EKC groups. Nonparametric testing revealed significant differences in 77.8% (28/36) of the corneal biomechanical parameters between the KC and EKC groups, whereas only 47.2% (17/36) of the parameters were significantly different after adjusting for CCT. Details are presented in Supplementary Table S2.

3.3 Evaluation of diagnostic ability for biomechanics and morphology

The ROC curve analysis included 54 parameters, comprising 36 corneal biomechanical parameters and 18 corneal morphological parameters (Figure 1). When differentiating between KC and NC, the area under the ROC curve (AUROC) of the tomographic and biomechanical index (TBI), D, and Da was 1.000. The AUROC of most parameters was greater than 0.9 and had high sensitivity and specificity (Table 2).

When distinguishing EKC from NC, corneal biomechanical-related parameters accounted for 80% (4/5) of the top five parameters in terms of discrimination ability, including A1 dArc length (AUROC = 0.901), highest concavity radius (AUROC = 0.879), A2 time (AUROC = 0.877), and TBI (AUROC = 0.874).

4 Discussion

To our knowledge, this study aimed to analyze and compare existing *in vivo* characteristics to screen sensitive indices to differentiate EKC and KC from NC. TBI, D, and Da had the best ability to distinguish between KC and NC; however, among the top five indices with the best ability to distinguish EKC from NC, four were related to corneal biomechanics, of which the force index A1 dArc length (AUROC = 0.901) was the best. This indicates the high sensitivity in corneal biomechanics for the diagnosis of EKC.

Detection of early KC, such as FFKC, in clinical practice is extremely difficult (Santodomingo-Rubido et al., 2022). KC is generally already in advanced stages once detected, resulting in irreversible vision loss. Patients with abnormal corneal morphology in both eyes and failure to meet the diagnostic criteria for KC are defined as KC suspect (KCS) (Klyce, 2009). It is challenging for refractive surgeons to diagnose patients with pre-clinical KC or a simple corneal tomography abnormality. TBI and the Corvis biomechanical index (CBI) have been proposed for the diagnosis of typical KC, but reports suggest that their ability to accurately diagnose EKC is relatively insufficient (Steinberg et al., 2015b; Herber et al., 2022). Therefore, this study aimed to identify a more sensitive index for diagnosing EKC.

The most important task was to control for confounding factors as much as possible, and age and bIOP were matched before inclusion of patients in this study because age and IOP had effects on biomechanics, that is, the effect of age and bIOP on the biomechanical properties was not significant difference among the three groups. Previous studies have found that corneal thickness has little influence on these parameters, although Corvis ST parameters correlate with CCT (Huseynova et al., 2014; Valbon et al., 2014). Furthermore, CCT was adjusted using a general linear model prior to analysis. No significant differences were observed in corneal morphological parameters between the EKC and NC groups, except Da ($p < 0.001$), but significant differences ($p < 0.001$) were identified in 26/36 biomechanical parameters. These results suggest that although corneal

TABLE 2 Results of receiver operating characteristic (ROC) curve analysis.

	KC vs. NL					EKC vs. NL				
	Parameter	AUROC	Sensitivity	Specificity	Cut off	Parameter	AUROC	Sensitivity	Specificity	Cut off
1	TBI	1.000	0.993	1.000	0.9375	A1 dArc Length	0.901	0.868	0.844	−0.0175
2	BAD-D	1.000	1.000	1.000	2.825	BAD-D	0.881	0.758	0.892	1.615
3	Da	1.000	0.997	0.997	1.81	HC Radius	0.879	0.835	0.805	6.9205
4	ISV	0.999	0.993	0.982	31.5	A2 Time	0.877	0.835	0.763	22.2025
5	Db	0.999	0.990	1.000	1.745	TBI	0.874	0.791	0.880	0.363
6	Dp	0.999	0.972	0.997	2.96	CBI	0.871	0.736	0.892	0.45
7	IHD	0.998	0.990	0.994	0.0275	Da	0.869	0.736	0.883	1.18
8	Df	0.998	0.972	0.994	2.665	Dt	0.865	0.758	0.856	0.415
9	CBI	0.997	0.979	0.018	0.659	TCT	0.865	0.758	0.856	523.5
10	IVA	0.997	0.969	0.988	0.255	CCT	0.849	0.670	0.907	522.5
11	Kmax	0.992	0.962	0.961	47.425	Max InverseRadius	0.849	0.780	0.799	0.1795
12	Dt	0.990	0.976	0.934	0.73	Dp	0.824	0.791	0.703	1.195
13	TCT	0.990	0.976	0.934	513.5	DA Ratio Max (1 mm)	0.817	0.648	0.931	1.616095
14	KI	0.987	0.958	0.976	1.075	A2 DeflectionVelocity	0.800	0.626	0.910	0.4095
15	Max InverseRadius	0.984	0.931	0.961	0.1945	Integrated Radius	0.790	0.560	0.949	9.4735
16	HC Radius	0.981	0.976	0.925	6.5835	A2 dArc Length	0.786	0.615	0.874	−0.0205
17	CCT	0.979	0.934	0.952	512.5	SSI 2	0.786	0.890	0.592	0.8815
18	Integrated Radius	0.975	0.920	0.973	9.607	A1 Deflection Length	0.747	0.736	0.664	2.2775
19	DA Ratio Max(1 mm)	0.969	0.906	0.964	1.628405	DA Ratio Max (2 mm)	0.732	0.538	0.931	4.820845
20	DA Ratio Max(2 mm)	0.956	0.882	0.952	4.876335	Whole Eye Movement Max [ms]	0.730	0.714	0.706	21.8855
21	SP A1	0.951	0.861	0.946	85.701	Db	0.728	0.538	0.841	0.735
22	K2 F	0.941	0.875	0.895	45.55	A2 Velocity	0.726	0.505	0.910	0.2955
23	SSI 2	0.931	0.837	0.895	0.8015	HC Deflection Length	0.726	0.824	0.562	6.709
24	Km F	0.921	0.840	0.910	44.85	HC Time	0.717	0.648	0.730	17.2035
25	CKI	0.907	0.858	0.955	1.015	A1 Time	0.716	0.780	0.586	7.4
26	SP HC	0.897	0.774	0.886	9.572	SP HC	0.714	0.593	0.805	10.224

ROC, receiver operating characteristic; AUROC, area under the ROC, curve; KC, keratoconus; EKC, early keratoconus; NL, normal cornea.

10.3389/fbioe.2023.1158299

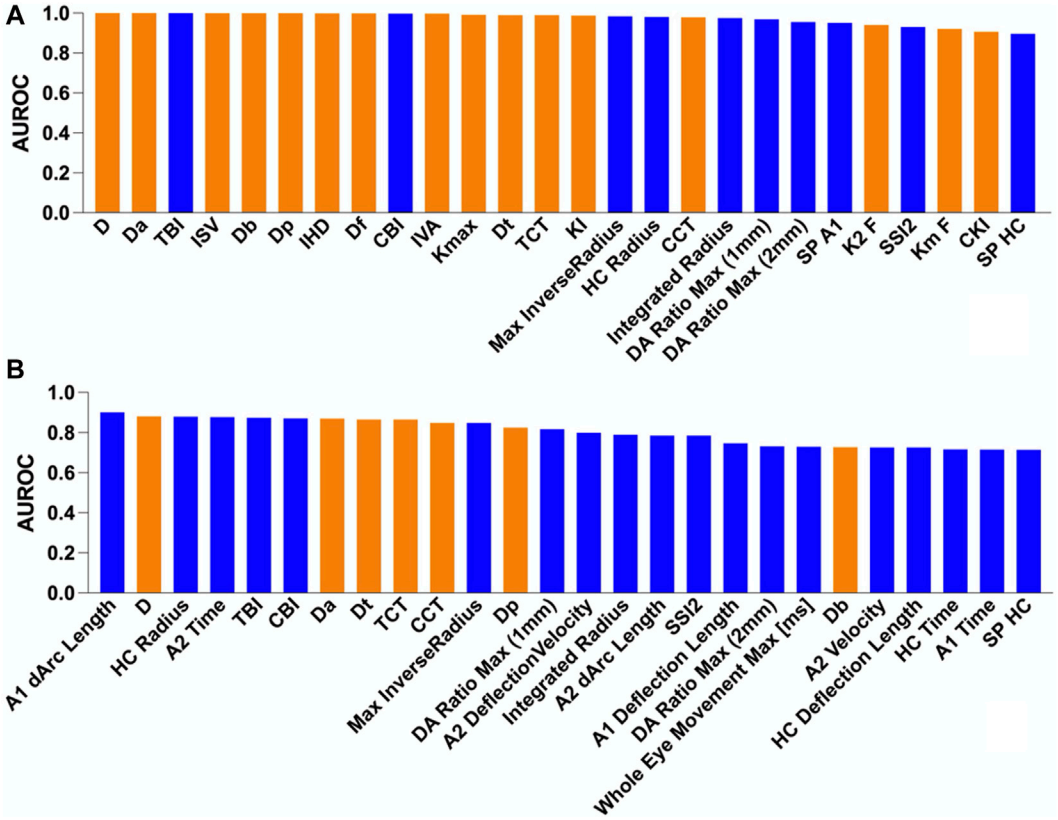

FIGURE 2
Comparison of the area under the receiver operating characteristic (AUROC) curve for different groups. The blue and orange columns indicate corneal biomechanic- and morphology-related parameters, respectively. **(A)** Normal vs. keratoconus and **(B)** normal vs. early keratoconus.

tomography remains relatively normal in EKC, the corneal biomechanics are altered. However, significant differences were observed in less than half of the biomechanical parameters between the KC and EKC groups, indicating that the biomechanical characteristics of EKC tended to be KC. Therefore, corneal biomechanical measurements should be performed routinely during refractive surgery.

According to the previous literature and directly reflecting the disease characteristics, we selected 54 indicators, including 36 biomechanic-related and 18 morphology-related parameters, which were included in the ROC curve analysis. Among the top five parameters that distinguished EKC from NC, corneal biomechanical-related parameters accounted for 80% (4/5), including the A1 dArc length, highest concavity (HC) radius, A2 time, and TBI. Among them, the AUROC of A1 dArc length was 0.901, and this index was the only indicator with excellent discrimination ability, which has not been previously reported. In terms of the safety of refractive surgery, this indicator may help clinicians accurately screen for EKC to avoid corneal ectasia after refractive surgery. Moreover, in terms of the disease itself, this indicator may enable early screening for KC and ensure timely intervention to avoid irreversible vision loss.

A1 dArc length represents the change in arc length of the anterior corneal surface within 3.5 mm on both sides of the corneal apex during the first applanation and the initial state. A softer cornea is associated with a larger deformation amplitude at the center of the anterior surface and a correspondingly larger value. As this indicator may be sensitive to focal changes in the early disease stage, other corneal biomechanical parameters were calculated based on a horizontal range of 8 mm (Lopes et al., 2017). This finding highlights the importance of considering sensitive biomechanical indices. HC radius refers to the radius of curvature of the corneal apex at the highest concavity. A softer cornea is associated with deeper collapse and a smaller radius of curvature. Considering the localization of the early stage of the lesion, this indicator has high sensitivity, and its ability to diagnose occult KC has been previously reported (Elham et al., 2017). The A2 time refers to the time to reach the second applanation, and the sensitivity of diagnosis has also been confirmed (Peris-Martínez et al., 2021). Considering the cumulative effect of this parameter, we avoided its use as a sensitive indicator in preoperative screening for refractive surgery. In accordance with our results, TBI has been reported to accurately detect corneal ectasia compared with other topographic, tomographic, and biomechanical parameters and has a high sensitivity for detecting eyes with normal topography in patients with very asymmetric ectasia (Ambrósio et al., 2017). TBI is based on morphology and biomechanics and reflects the importance of corneal biomechanics.

The ability to distinguish *in vivo* characteristics in the NC, EKC, and KC groups is presented in Figure 2. The orange columns in Figure 2A indicate the absolute advantage of corneal tomography in diagnosing typical KC. Most of the top ten indicators with the ability to distinguish KC from NC were corneal morphological indicators,

with the exception of TBI (AUROC = 1.000) and CBI (AUROC = 0.997). These results suggest that corneal tomography of advanced KC is sufficient to provide reliable diagnostic evidence. TBI was first described by Ambrosio et al. based on corneal morphology and biomechanics (Ambrósio et al., 2017). A new parameter was introduced by cross-validation using the leave-one method to improve the discrimination ability between NC and KC in all other stages. In this study, TBI was the best index to distinguish KC from NC, which is consistent with previous reports (Ferreira-Mendes et al., 2019). CBI was introduced by Vinciguerra et al. by combining corneal dynamic response parameters (DA ratio, Vin, SP A1, and integrated radius) and ARTh using logistic regression (Vinciguerra et al., 2016a). In this study, we observed that CBI could accurately distinguish KC from NC, which is also consistent with previous reports (Langenbucher et al., 2021).

As shown in Figure 2B, the blue columns were more prominent, indicating that the corneal biomechanics were more sensitive in detecting EKC. The discrimination abilities of D, Dt, Da, CCT, and Dp were also good. However, considering that CCT was not matched when patients were included, the difference in distribution between the groups was significant. As D, Dt, Da, and Dp are affected by corneal thickness, the better discrimination ability of these parameters may be affected by corneal thickness. Indeed, in the early stages of the disease, corneal thickness does not decrease significantly, and corneal morphology does not exhibit obvious abnormalities. Therefore, corneal biomechanics is superior to corneal morphology for the detection of EKC. In the clinical screening of occult KC, more attention should be paid to changes in the corneal biomechanics.

Several *in vivo* characteristics (such as A1 dArc length, HC radius, A2 time, and TBI) exhibited good discrimination ability between EKC and NC (Table 2). Therefore, we calculated the corresponding cutoff value for the best discriminating ability and observed low sensitivity and specificity for most indicators. As proposed by Roberts and Dupps, this could be because the initial biomechanical changes in KC are focused rather than a uniform overall change (Roberts and Dupps, 2014). Hence, most corneal parameters have a large overlap between NC and KCS, thus reducing the sensitivity of detecting occult KC or simple corneal tomography abnormalities.

Owing to the complexity of viscoelastic biomechanical behavior and the inability to eliminate confounding factors of age, intraocular pressure and CCT (Huseynova et al., 2014; Valbon et al., 2014; Vinciguerra et al., 2016b), although we matched age and biomechanically intraocular pressure in this study, there are certain challenges in accurately measuring the real biomechanical properties *in vivo* (Huseynova et al., 2014). In addition, existing devices for measuring *in vivo* corneal characteristics are insensitive to spatial position and can only study surface deformation, precluding the characterization of internal corneal biomechanical behavior (De Stefano et al., 2020). Furthermore, selection bias was inevitable. Therefore, before early changes in the disease are identified, it is still necessary to combine corneal biomechanics with corneal tomography for clinical analysis.

In conclusion, this study demonstrated that TBI, D, and Da are the best indicators for diagnosing advanced KC and that corneal tomography is sufficient to provide a reliable diagnostic basis. The high sensitivity of corneal biomechanical index in the diagnosis of EKC, especially sensitive indicators such as A1 dArc length, suggests that ophthalmologists should pay more attention to the biomechanics when diagnosing EKC. The biomechanical properties of EKC are similar those of KC, indicating that corneal biomechanics should be combined with corneal tomography when screening for occult KC.

Data availability statement

The original contributions presented in the study are included in the article/Supplementary Material, further inquiries can be directed to the corresponding author.

Ethics statement

The studies involving human participants were reviewed and approved by the Tianjin Eye Hospital (2022032). Written informed consent to participate in this study was provided by the participants' legal guardian/next of kin.

Author contributions

XC, HC, and YW contributed to the conception and design of the study. XC, YH, JS, JL, and JH organized the database. XC, HC, and YH performed the analysis and interpretation of data. XC wrote the first draft. XC, HC, and YH commented on previous versions of the manuscript. YW provided administrative, technical, or material support, as well as supervision. All authors contributed to the article and approved the submitted version.

Funding

This work was supported by the National Program on Key Research Project of China (2022YFC2404502), the National Natural Science Foundation of China (82271118), the Tianjin Key Medical Discipline (Specialty) Construction Project (TJYXZDXK-016A), and Nankai University Eye Institute (NKYKD202209).

Acknowledgments

The authors would like to thank all the participants of this study and Editage (www.editage.cn) for English language editing assistance.

Conflict of interest

The authors declare that the research was conducted in the absence of any commercial or financial relationships that could be construed as a potential conflict of interest.

Publisher's note

All claims expressed in this article are solely those of the authors and do not necessarily represent those of their affiliated organizations, or those of the publisher, the editors and the reviewers. Any product that may be evaluated in this article, or claim that may be made by its manufacturer, is not guaranteed or endorsed by the publisher.

Supplementary material

The Supplementary Material for this article can be found online at: https://www.frontiersin.org/articles/10.3389/fbioe.2023.1158299/full#supplementary-material

References

Al-Amri, A. M. (2018). Prevalence of keratoconus in A refractive surgery population. *J. Ophthalmol.* 2018, 1–5. doi:10.1155/2018/5983530

Ambrósio, R., Jr., Lopes, B. T., Faria-Correia, F., Salomão, M. Q., Bühren, J., Roberts, C. J., et al. (2017). Integration of scheimpflug-based corneal tomography and biomechanical assessments for enhancing ectasia detection. *J. Refract. Surg.* 33, 434–443. doi:10.3928/1081597X-20170426-02

Andreassen, T. T., Simonsen, A. H., and Oxlund, H. (1980). Biomechanical properties of keratoconus and normal corneas. *Exp. Eye Res.* 31, 435–441. doi:10.1016/S0014-4835(80)80027-3

Asroui, L., Dagher, S. A., Elsheikh, A., Lopes, B. T., Roberts, C. J., Assouad, M., et al. (2022). Biomechanical evaluation of topographically and tomographically normal fellow eyes of patients with keratoconus. *J. Refract. Surg.* 38, 318–325. [Epub 2022 May 1]. PMID: 35536713. doi:10.3928/1081597X-20220225-01

De Stefano, V. S., Ford, M. R., Seven, I., and Dupps, W. J. (2020). Depth-dependent corneal biomechanical properties in normal and keratoconic subjects by optical coherence elastography. *Transl. Vis. Sci. Technol.* 9, 4. doi:10.1167/Tvst.9.7.4

Duffey, R. J., Hardten, D. R., Lindstrom, R. L., Probst, L. E., Schanzlin, D. J., Tate, G. W., et al. (2008). Ectasia after refractive surgery. *Ophthalmology* 115, 1849. Autor Reply 1849–1849; Autor Reply 1850 PMID: 18929166. doi:10.1016/j.ophtha.2008.04.028

Elham, R., Jafarzadehpur, E., Hashemi, H., Amanzadeh, K., Shokrollahzadeh, F., Yekta, A., et al. (2017). Keratoconus diagnosis using Corvis ST measured biomechanical parameters. *J. Curr. Ophthalmol.* 29, 175–181. doi:10.1016/J.Joco.2017.05.002

Ferreira-Mendes, J., Lopes, B. T., Faria-Correia, F., Salomão, M. Q., Rodrigues-Barros, S., and Ambrósio, R. (2019). Enhanced ectasia detection using corneal tomography and biomechanics. *Am. J. Ophthalmol.* 197, 7–16. doi:10.1016/J.Ajo.2018.08.054

Henriquez, M. A., Hadid, M., and Izquierdo, L., Jr. (2020). A systematic review of subclinical keratoconus and forme fruste keratoconus. *J. Refract. Surg.* 36, 270–279. doi:10.3928/1081597X-20200212-03

Herber, R., Hasanli, A., Lenk, J., Vinciguerra, R., Terai, N., Pillunat, L. E., et al. (2022). Evaluation of corneal biomechanical indices in distinguishing between normal, very asymmetric, and bilateral keratoconic eyes. *J. Refract. Surg.* 38, 364–372. doi:10.3928/1081597X-20220601-01

Huseynova, T., Waring, G. O., Roberts, C., Krueger, R. R., and Tomita, M. (2014). Corneal biomechanics as A function of intraocular pressure and pachymetry by dynamic infrared signal and Scheimpflug imaging analysis in normal eyes. *Am. J. Ophthalmol.* 157, 885–893. doi:10.1016/J.Ajo.2013.12.024

Jabbour, S., and Bower, K. S. (2021). Refractive surgery in the US in 2021. *JAMA* 326, 77–78. PMID: 34228079. doi:10.1001/Jama.2020.20245

Kim, T. I., Alió Del Barrio, J. L., Wilkins, M., Cochener, B., and Ang, M. (2019). Refractive surgery. *Lancet* 393, 2085–2098. PMID: 31106754. doi:10.1016/S0140-6736(18)33209-4

Klyce, S. D. (2009). Chasing the suspect: Keratoconus. *Br. J. Ophthalmol.* 93, 845–847. doi:10.1136/Bjo.2008.147371

Koh, S., Inoue, R., Ambrósio, R., Jr., Maeda, N., Miki, A., and Nishida, K. (2020). Correlation between corneal biomechanical indices and the severity of keratoconus. *Cornea* 39, 215–221. doi:10.1097/ICO.0000000000002129

Langenbucher, A., Häfner, L., Eppig, T., Seitz, B., Szentmáry, N., and Flockerzi, E. (2021). Keratoconus detection and classification from parameters of the Corvis®ST: A study based on algorithms of machine learning. *Ophthalmologe* 118, 697–706. doi:10.1007/S00347-020-01231-1

Lopes, B. T., Roberts, C. J., Elsheikh, A., Vinciguerra, R., Vinciguerra, P., Reisdorf, S., et al. (2017). Repeatability and reproducibility of intraocular pressure and dynamic corneal response parameters assessed by the Corvis ST. *J. Ophthalmol.* 2017, 1–4. doi:10.1155/2017/8515742

Moshirfar, M., Tukan, A. N., Bundogji, N., Liu, H. Y., Mccabe, S. E., Ronquillo, Y. C., et al. (2021). Ectasia after corneal refractive surgery: A systematic review. *Ophthalmol. Ther.* 10, 753–776. [Epub 2021 August 20]. PMID: 34417707, PMCID: PMC8589911. doi:10.1007/S40123-021-00383-W

Peris-Martínez, C., Díez-Ajenjo, M. A., García-Domene, M. C., Pinazo-Durán, M. D., Luque-Cobija, M. J., Del Buey-Sayas, M. Á., et al. (2021). Evaluation of intraocular pressure and other biomechanical parameters to distinguish between subclinical keratoconus and healthy corneas. *J. Clin. Med.* 10, 1905. doi:10.3390/Jcm10091905

Rabinowitz, Y. S. (1998). *Keratoconus. Surv. Ophthalmol.* 42, 297–319. doi:10.1016/S0039-6257(97)00119-7

Rabinowitz, Y. S., and Rasheed, K.KISA (1999). KISA% index: A quantitative videokeratography algorithm embodying minimal topographic criteria for diagnosing keratoconus. *J. Cataract. Refract. Surg.* 25, 1327–1335. doi:10.1016/S0886-3350(99)00195-9

Roberts, C. J., and Dupps, W. J., Jr. (2014). Biomechanics of corneal ectasia and biomechanical treatments. *J. Cataract. Refract. Surg.* 40, 991–998. doi:10.1016/J.Jcrs.2014.04.013

Santodomingo-Rubido, J., Carracedo, G., Suzaki, A., Villa-Collar, C., Vincent, S. J., and Wolffsohn, J. S. (2022). Keratoconus: An updated review. *Cont. Lens Anterior Eye.* 45, 101559. [Epub 2022 January 4]. PMID: 34991971. doi:10.1016/J.Clae.2021.101559

Sedaghat, M. R., Momeni-Moghaddam, H., Ambrósio, R., Jr, Heidari, H. R., Maddah, N., Danesh, Z., et al. (2018). Diagnostic ability of corneal shape and biomechanical parameters for detecting frank keratoconus. *Cornea* 37 (8), 1025–1034. doi:10.1097/ICO.0000000000001639

Shiga, S., Kojima, T., Nishida, T., Nakamura, T., and Ichikawa, K. (2021). Evaluation of corvisst biomechanical parameters and anterior segment optical coherence tomography for diagnosing forme fruste keratoconus. *Acta Ophthalmol.* 99, 644–651. doi:10.1111/Aos.14700

Steinberg, J., Aubke-Schultz, S., Frings, A., Hülle, J., Druchkiv, V., Richard, G., et al. (2015a). Correlation of the KISA% index and Scheimpflug tomography in "normal," "subclinical," "keratoconus-suspect" and "clinically manifest" keratoconus eyes. *Acta Ophthalmol.* 93, E199–E207. doi:10.1111/Aos.12590

Steinberg, J., Katz, T., Lücke, K., Frings, A., Druchkiv, V., and Linke, S. J. (2015b). Screening for keratoconus with new dynamic biomechanical *in vivo* Scheimpflug analyses. *Cornea* 34, 1404–1412. doi:10.1097/ICO.0000000000000598

Valbon, B. F., Ambrósio, R., Fontes, B. M., Luz, A., Roberts, C. J., and Alves, M. R. (2014). Ocular biomechanical metrics by Corvis ST in healthy Brazilian patients. *J. Refract. Surg.* 30, 468–473. doi:10.3928/1081597X-20140521-01

Vinciguerra, R., Ambrósio, R., Elsheikh, A., Roberts, C. J., Lopes, B., Morenghi, E., et al. (2016a). Detection of keratoconus with A new biomechanical index. *J. Refract. Surg.* 32, 803–810. doi:10.3928/1081597X-20160629-01

Vinciguerra, R., Elsheikh, A., Roberts, C. J., Ambrósio, R., Kang, D. S., Lopes, B. T., et al. (2016b). Influence of pachymetry and intraocular pressure on dynamic corneal response parameters in healthy patients. *J. Refract. Surg.* 32, 550–561. doi:10.3928/1081597X-20160524-01

frontiers | Frontiers in Bioengineering and Biotechnology

TYPE Brief Research Report
PUBLISHED 18 October 2023
DOI 10.3389/fbioe.2023.1237834

OPEN ACCESS

EDITED BY
Matthew A. Reilly,
The Ohio State University, United States

REVIEWED BY
Hamid Osman,
Taif University, Saudi Arabia
Yilong Zhang,
University of Dundee, United Kingdom

*CORRESPONDENCE
Jie Wu,
wujie@sdfmu.edu.cn

†These authors have contributed equally to this work and share first authorship

RECEIVED 10 June 2023
ACCEPTED 09 October 2023
PUBLISHED 18 October 2023

CITATION
Chu Z, Ren Q, Su W, Cui W and Wu J (2023), Effect of central corneal curvature on corneal material stiffness parameter acquired by dynamic corneal responses. *Front. Bioeng. Biotechnol.* 11:1237834. doi: 10.3389/fbioe.2023.1237834

Effect of central corneal curvature on corneal material stiffness parameter acquired by dynamic corneal responses

Zhe Chu[1,2,3†], Qi Ren[1,2,3†], Wenjie Su[1,2,3], Wei Cui[1,2,3] and Jie Wu[1,2,3*]

[1]Eye Institute of Shandong First Medical University, Qingdao Eye Hospital of Shandong First Medical University, Qingdao, China, [2]State Key Laboratory Cultivation Base, Shandong Provincial Key Laboratory of Ophthalmology, Qingdao, China, [3]School of Ophthalmology, Shandong First Medical University, Qingdao, China

The stress–strain index (SSI) is a measure of corneal material stiffness, which is obtained using the Corvis ST algorithm based on dynamic corneal response parameters. The reduced SSI corresponds to the longer axial length (AL). In a previous study, we found SSI increases as the corneal curvature flattens, whereas a flatter corneal curvature indicates a longer AL (emmetropia or myopia). Therefore, in this cross-sectional study, we aimed to address these contradictory findings. First, we characterized the features of SSI, curvature radius of the anterior corneal surface (CR), and AL and analyzed their correlation with advanced myopia. Next, we compared the relationship between AL and SSI after adjusting for the effect of CR. We found a significant positive correlation between SSI and CR, which contradicts the developmental law of axial myopia. Furthermore, after accounting for the effect of CR, we observed a stronger correlation between SSI and AL than that in the unadjusted model. In conclusion, CR is an independent influencing factor for SSI in addition to AL, which masked the decrease in SSI caused by prolonged AL in axial myopia.

KEYWORDS

corneal material stiffness, dynamic corneal response, stress-strain index, corneal curvature, axial length

1 Introduction

The biomechanical properties of the cornea are often described using parameters such as material modulus and structural stiffness (Kling and Hafezi, 2017). The Corvis ST system measures these properties by evaluating the dynamic corneal response parameters (DCRs) of the air pulse, where the stiffness is influenced by the elastic modulus of the cornea and the size and shape of the air-pulse-depressurized corneal surface. Unlike linear elastic materials, the stress–strain curve of the cornea is nonlinear, similar to most collagen-based soft tissues. This nonlinearity makes it challenging to define the mechanical properties of the cornea using Young's elastic modulus test data alone. The stress–strain index (SSI) is an algorithm predicted by DCRs under air pressure to reflect the entire stress–strain behavior of the corneal material, independent of intraocular pressure and corneal geometry (Eliasy et al., 2019). Previous studies have shown a correlation between reduced corneal stiffness and lower SSI values in myopic eyes (Liu et al., 2021). Myopia is typically associated with elongated eyeballs, but it can also be caused by a highly curved cornea and/or a lens with

increased optical power. Refractive myopia is generally considered unrelated to ocular wall stiffness, whereas axial myopia is influenced by it (Flitcroft et al., 2019). Therefore, in myopic eyes, a higher proportion of axial factors leads to decreased ocular wall stiffness and lower SSI values.

However, our previous study revealed a stronger correlation between SSI and spherical equivalent refractive error (SER) or axial length-to-corneal radius ratio (AL/CR) than between SSI and axial length (AL) alone (Chu et al., 2022; Ren et al., 2023). This suggests that the component of refractive myopia also contributes to reduced SSI. To account for this, we adjusted for the refractive myopia component compensated by CR and analyzed the relationship between SSI and axial growth using the average AL during emmetropization, which is determined with ocular refractive power as a reference point. We observed narrower confidence intervals and steeper slopes than those of SSI and AL. Additionally, SSI was found to be proportional to emmetropic AL determined by ocular refractive power, indicating that SSI increases as CR increases (with decreased corneal refractive power and reduced refractive myopia proportion) (Ren et al., 2023). This suggests that factors associated with refractive myopia gradually mask the effect of AL on SSI as myopia progresses.

Therefore, in this cross-sectional study, our aim was to confirm whether the relationship between SSI and CR depends on the dioptric properties of CR, thereby establishing an indirect relationship between SSI and CR. We first characterized the features of SSI, CR, and AL and analyzed their correlation with advanced myopia. Subsequently, we compared the relationship between AL and SSI after adjusting for the effect of CR.

2 Methods

This cross-sectional comparative study was conducted at the Eye Institute of Shandong First Medical University in Qingdao, China. The study followed the principles outlined in the Declaration of Helsinki and was approved by the Ethics Committee of the Qingdao Eye Hospital of Shandong First Medical University.

Participants included healthy individuals and patients scheduled for refractive surgery at the Qingdao Eye Hospital of Shandong First Medical University between July 2021 and April 2022. To account for the effect of axial myopia on SSI, participants were grouped based on their AL. The study aimed to investigate the relationship between corneal curvature and corneal biomechanics in individuals with myopia; therefore, we excluded participants who met any of the following criteria: 1) astigmatism of 3 diopters (3D) or higher, 2) use of contact lenses, 3) history or suspicion of corneal diseases such as keratoconus, and 4) history of eye surgery. Only data from the right eye of each individual were analyzed due to the high correlation of corneal parameters between the right and left eyes.

To be eligible, participants' medical records needed to include a complete medical history and results of ophthalmic examinations conducted on the same day, including comprehensive optometry results after mydriasis. The mean anterior corneal curvature radius within a 3-mm diameter range of the corneal apex (CR) and AL were measured using the OA 2000 device (Tomey, Japan). The corneal biomechanical parameter, SSI, was determined using the Corvis ST device (Oculus, Wetzlar, Germany). Only measurements with "OK" quality specifications were included in the analysis.

TABLE 1 Characteristics of our study subjects.

Characteristic	N = 267[a]
Gender	
Female	145 (54%)
Male	122 (46%)
Age, year	22 (8)
SSI	0.82 (0.15)
CR, mm	7.78 (0.24)
AL, mm	26.01 (1.48)
AL (categorical)	
<26 mm	135 (51%)
≥26 mm	132 (49%)

Abbreviations: SSI, stress-strain index; CR, curvature radius of the anterior corneal surface; AL, axial length.
[a]n (%); Mean (SD).

Statistical analysis and data visualization were performed using R statistical software (version 4.2.2). The significance level was set at $p < 0.05$. Continuous variables were summarized as mean (standard deviation), while categorical variables were presented as sample size (percentage). Pearson's correlation tests were conducted to examine the relationships between SSI, AL, and CR, and a matrix of plots was created to analyze the correlations between these three variables. Linear regression models were used to examine the associations between the variables: Model 1 treated SSI as the dependent variable and AL as the independent variable, Model 2 included an additional adjustment for CR, and Model 3 further adjusted for the AL×CR interaction term. The Akaike Information Criterion (AIC) (Akaike, 1974) and model likelihood ratio tests (King, 1989) were performed to compare the model performance of these 3 models. The model with the lowest AIC values was chosen as the best-fitting model with the best tradeoff between the goodness of fit and complexity of the model. The AIC can be calculated based on the following equation: AIC = 2k—2log-likelihood, where k represents the number of model parameters and log-likelihood represents the log-likelihood of the model. The model likelihood ratio tests were conducted to assess the statistical significance of the differences in model fit. Finally, a subgroup analysis was conducted by categorizing AL into two groups based on a cutoff score (AL < 26 mm vs. AL ≥ 26 mm). In each group, three linear regression models were used, with and without adjusting for CR, using AL as the predictor variable and SSI as the dependent variable. All models were adjusted for age and sex.

3 Results

3.1 Demographic information and clinical variables on study participants

Table 1 displays the demographic information and clinical variables of our study subjects. A total of 267 participants were included in the present study. As shown in Table 1, continuous

10.3389/fbioe.2023.1237834

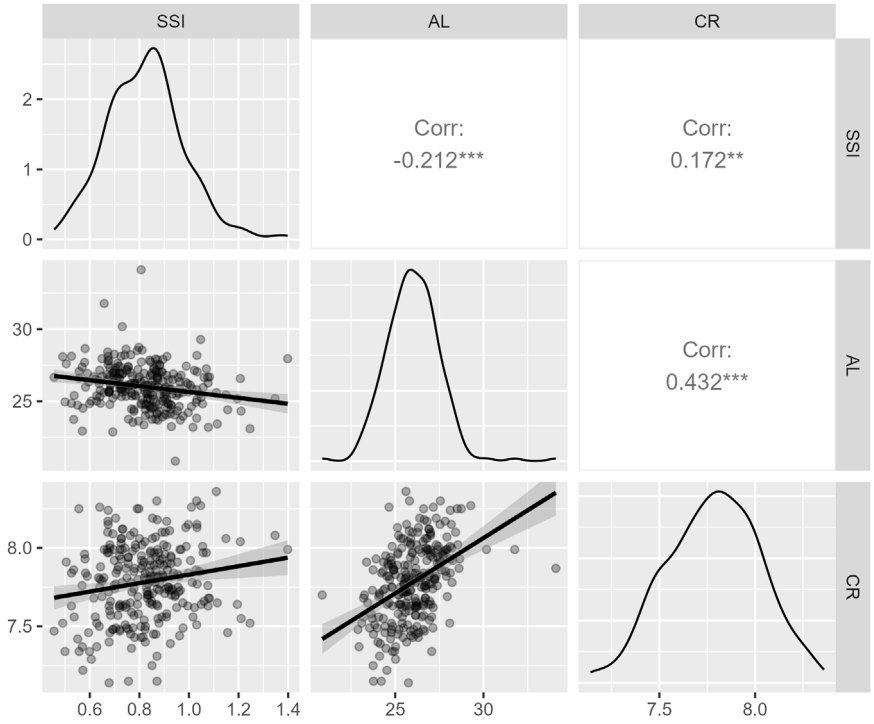

FIGURE 1
A matrix of plots showing the correlations between SSI, AL, and CR. The units of AL and CR are millimeters. Abbreviations: SSI: stress–strain index; CR, curvature radius of the anterior corneal surface; AL: axial length.

TABLE 2 Results of linear regression models.

	Model 1	Model 2	Model 3
(Intercept)	1.41 ***	0.05	−1.75
	[1.08, 1.74]	[-0.54, 0.63]	[-12.55, 9.05]
Age, year	0.00	0.00	0.00
	[-0.00, 0.00]	[-0.00, 0.00]	[-0.00, 0.00]
Male gender	0.01	−0.01	−0.01
	[-0.03, 0.04]	[-0.05, 0.02]	[-0.05, 0.02]
AL, mm	−0.02 ***	−0.04 ***	0.03
	[-0.04, −0.01]	[-0.06, −0.03]	[-0.39, 0.44]
CR, mm		0.23 ***	0.46
		[0.15, 0.32]	[-0.92, 1.85]
AL×CR			−0.01
			[-0.06, 0.04]
N	267	267	267
AIC	−244.8	−271.4	−269.5

Notes: N represents the sample size in each model. The 95% confidence intervals were used to describe the uncertainties of coefficients. All coefficients were reported using unstandardized coefficients. ***$p < 0.001$; **$p < 0.01$; *$p < 0.05$.
Abbreviations: SSI, stress–strain index; AL, axial length; CR, curvature radius of the anterior corneal surface; AIC, akaike information criterion.

TABLE 3 Results of a subgroup analysis.

	Participants with AL < 26		Participants with AL ≥ 26	
	Unadjusted	Adjusted	Unadjusted	Adjusted
(Intercept)	1.49 ***	−0.04	1.12 **	0.12
	[0.71, 2.28]	[-1.00, 0.92]	[0.45, 1.80]	[-0.90, 1.13]
Age, year	−0.00	0.00	0.00 *	0.00 *
	[-0.01, 0.00]	[-0.00, 0.00]	[0.00, 0.01]	[0.00, 0.01]
Male gender	0.04	0.01	−0.03	−0.05
	[-0.02, 0.09]	[-0.04, 0.06]	[-0.08, 0.02]	[-0.10, 0.01]
AL, mm	−0.02	−0.05 **	−0.02	−0.03
	[-0.06, 0.01]	[-0.09, −0.02]	[-0.04, 0.01]	[-0.05, 0.00]
CR, mm		0.28 ***		0.16 *
		[0.17, 0.40]		[0.04, 0.29]
N	135	135	132	132

Notes: N represents the sample size in each model. The 95% confidence intervals were used to describe the uncertainties of coefficients. All coefficients were reported using unstandardized coefficients. The term "Unadjusted" indicates that the models did not include CR, while the term "Adjusted" indicates that the models included CR. ***$p < 0.001$; **$p < 0.01$; *$p < 0.05$. Abbreviations: SSI, stress–strain index; AL, axial length; CR, curvature radius of the anterior corneal surface.

variables are summarized as mean (standard deviation), and categorical variables are summarized as sample size (percentage).

3.2 Correlations between SSI, AL, and CR

To examine the relationships between SSI, AL, and CR, Pearson's correlation tests were performed. As shown in Figure 1, the results suggested a negative correlation between SSI and AL ($r = -0.212$, $p < 0.001$), a positive correlation between SSI and CR ($r = 0.172$, $p = 0.005$), and a positive correlation between AL and CR ($r = 0.432$, $p < 0.001$).

3.3 Results of linear regression models

As stated in the section on Statistical analyses, three linear regression models were performed to study the associations between SSI, AL, and CR. The results of the three regression models were summarized in Table 2. For Model 1, we found that AL was negatively associated with SSI ($\beta = -0.02$, *95% CI* = −0.04 to −0.01, $p < 0.001$) after adjusting for age and gender. For model 2, we found that AL was still negatively associated with SSI ($\beta = -0.04$, *95% CI* = −0.06 to −0.03, $p < 0.001$) after additionally adjusting for CR, while the slope (β) changed from −0.02 (model 1) to −0.04 (model 2). In addition, we further performed a linear regression model with an interaction term (AL×CR) to study whether the relationship between AL and SSI was dependent on CR. In Model 3, CR was treated as a continuous variable, while CR was categorized into three groups based on its mean and standard deviation to facilitate the interpretation of the interaction term (Supplementary Figure S1). As shown in Table 2, the interaction term was not significant ($\beta = -0.01$, *95% CI* = −0.06 to 0.04, $p > 0.05$), indicating that the relationship between AL and SSI was not dependent on CR. The AICs of Model 1, Model 2, and Model 3 were −244.8, −271.4, and −269.5, respectively. The model likelihood ratio tests also suggested that Model 2 was the best-fitting model (Model 2 vs Model 1: F statistics = 29.5, $p < 0.001$; Model 3 vs Model 2: F statistics = 0.1, $p = 0.74$).

Finally, additional four linear regression models with SSI as the dependent variable were performed separately for individuals with AL < 26 and AL ≥ 26. The model results are shown in Table 3. Among participants with AL < 26, the unadjusted model (i.e., the model did not include CR) showed that AL was not associated with SSI ($\beta = -0.02$, *95% CI* = −0.06 to 0.01, $p = 0.13$), while the adjusted model (i.e., the model included CR) showed that AL was negatively associated with SSI ($\beta = -0.05$, *95% CI* = −0.09 to −0.02, $p < 0.01$). However, among participants with AL ≥26, we did not observe a significant association between AL and SSI neither in the unadjusted model ($\beta = -0.02$, *95% CI* = −0.04 to 0.01, $p = 0.25$) or in the adjusted model ($\beta = -0.03$, *95% CI* = −0.05 to 0.00, $p = 0.0591$).

4 Discussion

This study aimed to investigate the correlation between central corneal curvature and corneal biomechanical behavior parameters acquired using DCRs from a dioptric perspective, to address conflicting conclusions reported in previous studies regarding the relationship between SSI and AL in myopic eyes. For this purpose, linear regression models were established to examine the associations between the variables. The comparison of model performance using AIC and model likelihood ratio tests provided valuable insights into the performance of the three models (Table 2). Based on the AIC, Model 2 exhibited the lowest value, indicating the best fit to the data among the three models. Furthermore, the model likelihood ratio tests also supported the superiority of Model 2 over

the other models. Taken together, our findings suggested that Model 2 (including AL and CR as independent variables) captures the data patterns more effectively than Models 1 and 3. Finally, the study found a positive correlation between SSI and CR, contrary to the pattern observed with deepening axial myopia. After adjusting for the effect of CR, the correlation between SSI and AL became more significant, particularly when AL was <26 mm.

DCRs obtained from Corvis ST are influenced by internal structures and scleral stiffness (Kling and Marcos, 2013). SSI has been reported to be associated with reduced biomechanical strength of the cornea related to myopia, and it has been speculated that the correlation between SSI and AL is due to the influence of scleral biomechanics. However, interpreting the relationship between CR and SSI is more complex. First, in axial myopia, the biomechanical strength of the ocular wall including the cornea decreases (Sedaghat et al., 2020), whereas the anterior corneal surface curvature flattens rapidly and eventually stabilizes (Gonzalez Blanco et al., 2008; Jin et al., 2022). In this study, both CR and SSI changed in a unidirectional manner with increasing axial myopia, with CR increasing and SSI decreasing, consistent with theoretical expectations. Second, the absence of a causal relationship between the degree of refractive myopia and the biomechanical strength of the cornea suggests that the correlation between CR and SSI may be indirect, based on the deepening of axial myopia, i.e., a higher CR would correspond to a lower SSI. However, we found the opposite result, indicating that the correlation between CR and SSI was not based on the indirect correlation observed with increasing AL. Third, the linear regression models used in the study demonstrated that the relationship between AL and SSI was not dependent on CR, suggesting that CR is an independent influencing factor for SSI.

The SSI algorithm was developed by using the least squares method based on numerical modeling input and output parameters CCT, bIOP, and stiffness parameter at highest concavity (SP-HC), while corneal curvature was fixed at 7.8 mm (Eliasy et al., 2019). Therefore, after correcting for a wide range of CCT and bIOP values by the least squares method, SSI may still be affected by CR through SP-HC. As a DCR-based stiffness parameter, SP-HC is defined as the final load at corneal pressure divided by the difference between the corneal deflection and the maximum depression value at that time, reflecting the structural properties of the cornea. Differences in corneal curvature can lead to an uneven distribution of air-puff-related stress, resulting in unaccounted strain and variations in SP-HC. While corneal geometry may influence the acquisition of SSI to some extent, the SSI itself should not be correlated with corneal geometry since it is a material index (Eliasy et al., 2019). Considering that the cornea and anterior sclera of normal eyes reach adult levels by the age of 2 and the posterior sclera does not reach adult levels until the age of 13 (Fledelius and Christensen, 1996; Touzeau et al., 2014), we speculate that the following possibility is more likely: At the end of emmetropization, a flatter cornea may correspond to a higher material stiffness. Following emmetropization, as myopia develops, the ocular wall continues to expand, leading to AL growth in the posterior pole of the sclera and CR increasing. In other words, CR reflects the material stiffness of the anterior structure of the eyeball, whereas AL reflects the posterior pole. Our previous study supported the latter (Ren et al., 2023), but the former still requires confirmation through further research.

In addition, the phenomenon of the better correlation of SSI with SER, AL/CR, and astigmatism of the anterior corneal surface, rather than AL (Liu et al., 2021; Chu et al., 2022; Liu et al., 2022) can be explained to some extent, which was due to a deeper degree of SER with steeper corneal curvature. After adjusting for the effect of CR, the relationship between SSI and AL became more significant than that in the unadjusted model. This suggests that flattened corneal curvature masks the decrease in SSI caused by prolonged AL to some extent. The lower significance observed at AL ≥ 26 mm may be attributed to the confounding effect of posterior scleral staphyloma.

From the perspective of dioptric optics, this study analyzed the relationship between SSI and CR and found it to be contrary to the characteristic changes associated with increasing axial myopia. These results suggest that CR is an independent influencing factor for SSI, in addition to AL, indicating that the acquisition of SSI may be influenced, to some extent, by corneal geometry or that corneal flattening may be related to an increase in the material stiffness of the corneal stroma. Furthermore, we confirmed that the effect of CR did not alter the association between AL and the corneal material stiffness parameter obtained through DCRs. Our findings contribute to understanding the influence of corneal curvature on the development of algorithms for the corneal biomechanical behavior parameter acquired by DCRs. However, it is important to note that the average curvature radius of the anterior corneal surface within 3 mm of the apex, as an essential optometry parameter, cannot fully reflect the characteristics of the noncentral corneal region, especially when it is smaller than the applanation length of the air pulse. Therefore, this finding does not represent the effect of global corneal curvature on SSI acquisition. Given the nature of cross-sectional studies, we cannot exclude the possibility that corneal flattening may be related to the increased material stiffness of the corneal stroma, which could lead to the observed positive correlation between CR and SSI. Future studies should focus on examining the relationship between SSI and the best fitting surface of the anterior and posterior corneal surfaces while controlling for myopia-related variables.

5 Conclusion

CR is an independent influencing factor for SSI in addition to AL. CR masks the decrease in SSI caused by prolonged AL in axial myopia.

Data availability statement

The original contributions presented in the study are included in the article/Supplementary Material, further inquiries can be directed to the corresponding author.

Ethics statement

The studies involving humans were approved by the Ethics Committee of the Qingdao Eye Hospital of Shandong First Medical University. The studies were conducted in accordance

with the local legislation and institutional requirements. Written informed consent for participation was not required from the participants or the participants' legal guardians/next of kin in accordance with the national legislation and institutional requirements.

Author contributions

QR and ZC: Study design, data analysis, and manuscript drafting; WS and WC: Data acquisition and data analysis; JW: Manuscript revision. All authors contributed to the article and approved the submitted version.

Acknowledgments

The authors thank Junjie Wang of Wenzhou Medical University for helpful discussions on topics related to this work. The authors also thank Jie Zhang and Wenjun Zhou from Hangzhou Shansier Medical Technologies Ltd. for their statistical advice.

Conflict of interest

The authors declare that the research was conducted in the absence of any commercial or financial relationships that could be construed as a potential conflict of interest.

Publisher's note

All claims expressed in this article are solely those of the authors and do not necessarily represent those of their affiliated organizations, or those of the publisher, the editors and the reviewers. Any product that may be evaluated in this article, or claim that may be made by its manufacturer, is not guaranteed or endorsed by the publisher.

Supplementary material

The Supplementary Material for this article can be found online at: https://www.frontiersin.org/articles/10.3389/fbioe.2023.1237834/full#supplementary-material

References

Akaike, H. (1974). A new look at the statistical model identification. *IEEE Trans. Automatic Control* 19, 716–723. doi:10.1109/TAC.1974.1100705

Chu, Z., Ren, Q., Chen, M., Cheng, L., Cheng, H., Cui, W., et al. (2022). The relationship between axial length/corneal radius of curvature ratio and stress-strain index in myopic eyeballs: using Corvis ST tonometry. *Front. Bioeng. Biotechnol.* 10, 939129. doi:10.3389/fbioe.2022.939129

Eliasy, A., Chen, K. J., Vinciguerra, R., Lopes, B. T., Abass, A., Vinciguerra, P., et al. (2019). Determination of corneal biomechanical behavior in-vivo for healthy eyes using CorVis ST tonometry: stress-strain index. *Front. Bioeng. Biotechnol.* 7, 105. doi:10.3389/fbioe.2019.00105

Fledelius, H. C., and Christensen, A. C. (1996). Reappraisal of the human ocular growth curve in fetal life, infancy, and early childhood. *Br. J. Ophthalmol.* 80, 918–921. doi:10.1136/bjo.80.10.918

Flitcroft, D. I., He, M., Jonas, J. B., Jong, M., Naidoo, K., Ohno-Matsui, K., et al. (2019). IMI - defining and classifying myopia: a proposed set of standards for clinical and epidemiologic studies. *Invest. Ophthalmol. Vis. Sci.* 60, M20–M30. doi:10.1167/iovs.18-25957

Gonzalez Blanco, F., Sanz Fernandez, J. C., and Munoz Sanz, M. A. (2008). Axial length, corneal radius, and age of myopia onset. *Optom. Vis. Sci.* 85, 89–96. doi:10.1097/opx.0b013e3181622602

Jin, G., Liu, Z., Wang, L., Zhu, Y., Luo, L., and Liu, Y. (2022). Corneal biometric features and their association with axial length in high myopia. *Am. J. Ophthalmol.* 238, 45–51. doi:10.1016/j.ajo.2021.11.031

King, G. (1989). *Unifying political methodology: the likelihood theory of statistical inference*. Cambridge University Press.

Kling, S., and Hafezi, F. (2017). Corneal biomechanics - a review. *Ophthalmic Physiol. Opt.* 37, 240–252. doi:10.1111/opo.12345

Kling, S., and Marcos, S. (2013). Contributing factors to corneal deformation in air puff measurements. *Invest. Ophthalmol. Vis. Sci.* 54, 5078–5085. doi:10.1167/iovs.13-12509

Liu, G., Rong, H., Zhang, P., Xue, Y., Du, B., Wang, B., et al. (2021). The effect of axial length elongation on corneal biomechanical property. *Front. Bioeng. Biotechnol.* 9, 777239. doi:10.3389/fbioe.2021.777239

Liu, Y., Pang, C., Ming, S., and Fan, Q. (2022). Effect of myopia and astigmatism deepening on the corneal biomechanical parameter stress-strain index in individuals of Chinese ethnicity. *Front. Bioeng. Biotechnol.* 10, 1018653. doi:10.3389/fbioe.2022.1018653

Ren, Q., Chu, Z., Cui, W., Cheng, L., Su, W., Cheng, H., et al. (2023). Effect of corneal stiffness decrease on axial length elongation in myopia determined based on a mathematical estimation model. *Front. Bioeng. Biotechnol.* 11, 1145032. doi:10.3389/fbioe.2023.1145032

Sedaghat, M. R., Momeni-Moghaddam, H., Azimi, A., Fakhimi, Z., Ziaei, M., Danesh, Z., et al. (2020). Corneal biomechanical properties in varying severities of myopia. *Front. Bioeng. Biotechnol.* 8, 595330. doi:10.3389/fbioe.2020.595330

Touzeau, O., Gaujoux, T., Sandali, O., Allouch, C., Laroche, L., and Borderie, V. (2014). The cornea in high axial myopia. *J. Fr. Ophtalmol.* 37, 449–461. doi:10.1016/j.jfo.2014.01.008

frontiers | Frontiers in Bioengineering and Biotechnology

TYPE Original Research
PUBLISHED 20 October 2023
DOI 10.3389/fbioe.2023.1283293

OPEN ACCESS

EDITED BY
Matthew A. Reilly,
The Ohio State University, United States

REVIEWED BY
Hao Gao,
University of Glasgow, United Kingdom
Zheng Duanmu,
Beijing Information Science and Technology University, China

*CORRESPONDENCE
Nan Qi,
Nan.Qi@sdu.edu.cn

RECEIVED 25 August 2023
ACCEPTED 29 September 2023
PUBLISHED 20 October 2023

CITATION
Han Y and Qi N (2023), Numerical study of critical straight, frown, and chevron incisions in small incision cataract surgery.
Front. Bioeng. Biotechnol. 11:1283293.
doi: 10.3389/fbioe.2023.1283293

Numerical study of critical straight, frown, and chevron incisions in small incision cataract surgery

Yang Han[1,2] and Nan Qi[1,3]*

[1]Research Center for Mathematics and Interdisciplinary Sciences, Shandong University, Qingdao, Shandong, China, [2]Institute of Marine Science and Technology, Shandong University, Qingdao, China, [3]Frontiers Science Center for Nonlinear Expectations, Shandong University, Qingdao, Shandong, China

Introduction: When an intraocular lens (IOL) injector is inserted through a pre-cut corneal incision (e.g., an empirical size of 2.2 mm) during small incision cataract surgery, uncontrollable tearing to the corneal tissue may occur, which is highly associated with the incision shape, size, and location. The goal of this numerical study was to investigate the optimal incision scheme amongst three typical shapes, i.e., straight, frown, and chevron incisions using mechanical modeling and finite element analysis.

Methods: Assuming that the damage is caused by the tissue fracture at the incision tips and is governed by the classical energy release rate (ERR) theory which compares the current ERR value subject to IOL injection and the material's intrinsic parameter, critical ERR G_c.

Results: It was found that for chevron incisions, the incision shape with an angle of 170° was superior which induced minimal ERR value, while for frown incisions, the shape with a central angle of 6° was optimal. Both chevron and frown incisions could allow a larger size of injector to inject through than a straight pre-cut. In particular, the frown incision performed the best due to its lowest corresponding ERR and easy operation.

Discussion: It was also observed that regions where the embedded fibrils are more dispersed and exhibit high isotropy were more favorable. If necessary, the chevron incision was recommended to be more aligned with the direction exhibiting a larger modulus, for example, along the circumferential direction near the limbus. This study provides useful knowledge in operation design and a deep insight into mechanical damage to corneal wounds in small incision cataract surgery.

KEYWORDS

small incision cataract surgery, chevron incision, frown incision, energy release rate, finite element analysis

1 Introduction

Generally in routine cataract surgery, a key step is to insert a (manual or pre-loaded) intraocular lens (IOL) injector into an eye through a pre-cut incision. The goal of this surgery is not only to correct vision loss due to clouding of the lens, but also to create a watertight and stable incision to promote wound healing and reduce astigmatism Sinskey and Stoppel (1994). The length, shape, location of the incision, its relationship to the limbal, and its cross-

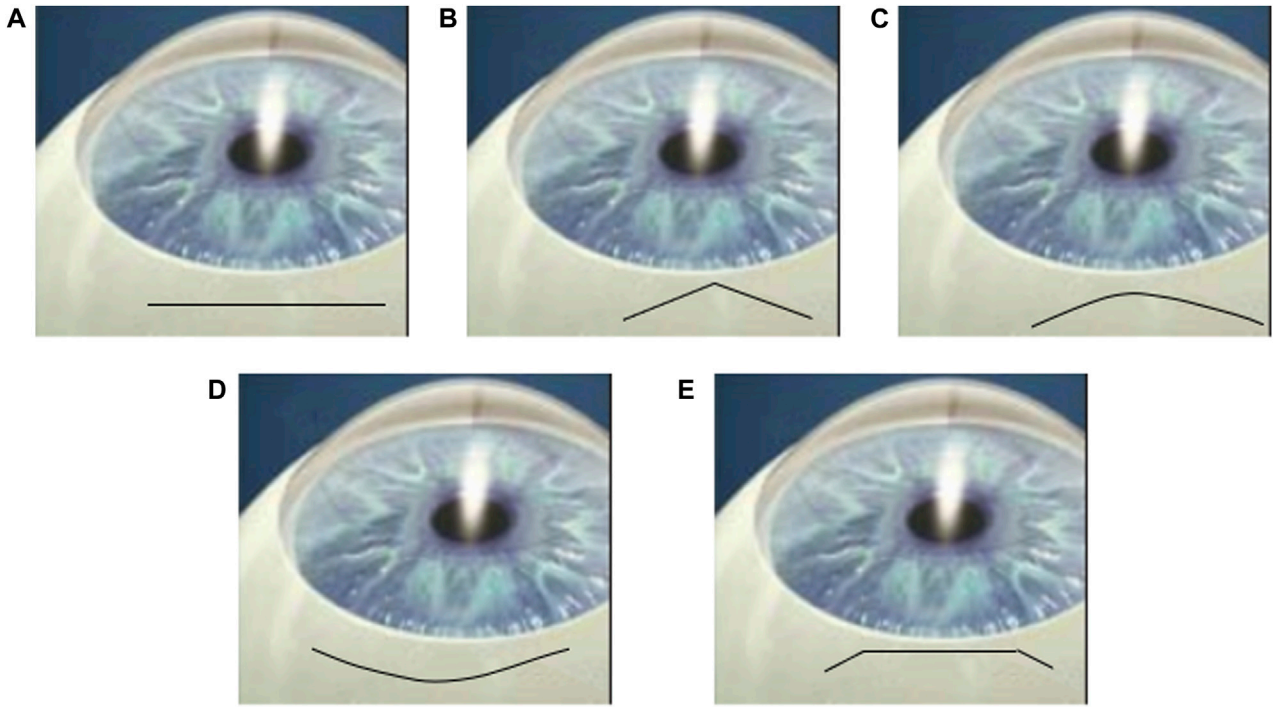

FIGURE 1
Cartoons of **(A)** straight, **(B)** chevron, **(C)** frown, **(D)** smile incisions and **(E)** Blumenthal side cut Haldipurkar et al. (2009).

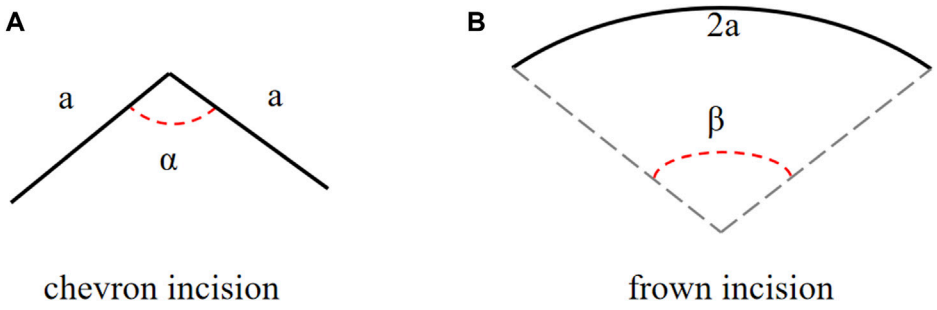

FIGURE 2
The schematic diagrams of **(A)** a chevron and **(B)** frown incisions, angles α and β are adjusted to represent different incision shapes.

sectional profile all contribute to wound healing and the amount of eventual astigmatism after surgery Shaikh et al. (2022), Sinskey and Stoppel (1994).

Over the past two decades, a small incision cataract surgery (SICS), a self-sealing cataract surgery has been widely reported. Due to the sclera-corneal tunnel construction, SICS has less postoperative response, faster and better visual recovery, fewer surgically induced astigmatism, and is easier to correct or control than conventional surgical methods Bernhisel and Pettey (2020), Al Mahmood et al. (2014), Kim et al. (2014). To allow safe insertion and secure incision integrity, this micro corneal incision (usually about 2.2 *mm* long) is carefully treated by surgeons to avoid irregular force-induced tissue damage Nanavaty and Kubrak-Kisza (2017), Kim et al. (2014), He et al. (2021), Zhang et al. (2022). Nanavaty and Kubrak-Kisza (2017) measured the length of the wound before and after IOL implantation to determine whether the wound was stretched.

The shapes of the incision in cataract surgery have attracted enough attention in clinical practice. McFarland first developed a sutureless straight incision in 1990 McFarland (1990), and Pallin described a chevron-shaped incision soon afterward (Pallin 1990; Pallin 1991). During the same period, Singer popularized the frown incision Singer (1991), which was later evidenced to be better than the straight incision in minimizing surgically induced astigmatism Chourasia et al. (2019). Other than these, there are many types of incision for tunnel construction such as smile incision and Blumenthal side cut Haldipurkar et al. (2009). The shapes of all these incisions are presented in Figure 1. Note that smile and frown incisions are both curved but facing the opposite.

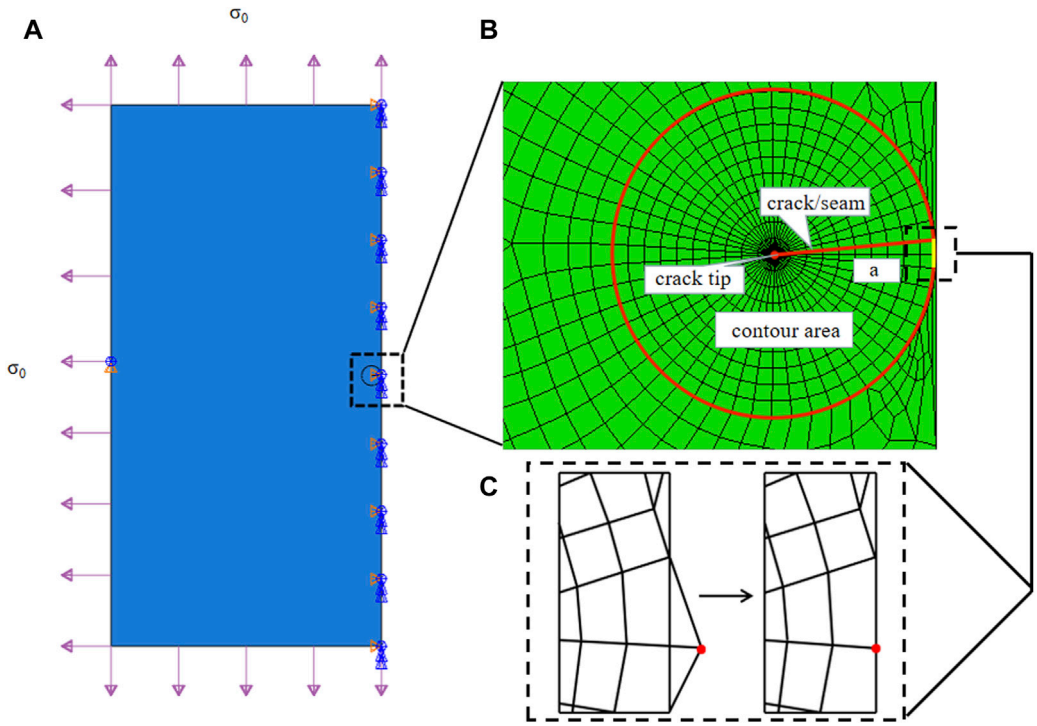

FIGURE 3
(A) Sketch of a two-dimensional plate torn by a typical chevron incision of length $2a$ in the middle under evenly distributed stress σ_0 at each side. Note that in the finite element simulation, only half the problem was modeled. **(B)** The crack tip was surrounded by a spider web-like area for ERR calculation. The configuration of a chevron-shaped incision is defined in Figure 2A. **(C)** Due to the contour design, special treatment was required to pull nodes back onto the symmetrical axis, zooming in at the middle right corner of the designed FE mesh.

In recent years, clinical and experimental studies have compared various incision shapes in the aspect of astigmatism Chourasia et al. (2019), Haldipurkar et al. (2009), Rathi et al. (2022). For example, the prospective study with a sample size of 100 patients concluded that a frown incision is evidently better than a straight incision in minimizing surgically induced astigmatism Chourasia et al. (2019). It was later pointed out that surgically induced astigmatism (SIA) through chevron incisions is the least followed by frown and straight incisions Rathi et al. (2022). However, the effects on wound integrity were scarcely explored and quantified, in particular from a mechanical viewpoint.

The work of Qi et al. (2022) focused on straight incisions in a cataract surgery. By constructing both analytical and numerical models to study the insertion of IOL during surgery, Qi et al. quantified the critical incision lengths according to the material energy release rate (ERR). Contributing factors such as insertion speed and injector size were also considered. However, all incisions were constrained as straight incisions. In this follow-on work, incision shape was the main focus, and a two-dimensional finite element model was constructed to simulate IOL insertion. Critical incision size to avoid wound tearing was quantified and optimal incision shape was selected amongst straight, chevron, and frown incisions.

2 Materials and methods

The finite element (FE) model was set up by considering a large two-dimensional square sample (60 *mm* by 60 *mm*) with a pre-existing chevron/frown incision (shapes shown in Figures 2A, B) in the middle with incision length $2a = 2.2\ mm$, as shown in Figure 3A. The sample size was chosen so that the incision size was relatively small in comparison to the cornea studied. Due to symmetry, only the left half of the model was simulated in the model. The classic mode I boundary condition was applied with a uniform distribution of stress σ_0 at each edge. The central point on the left edge was fixed to avoid rigid body motion. Assuming that the diameter of the IOL tube is d, then the critical opening of the incision is required to be equal to d to guarantee smooth and safe insertion. In the simulation, we examined the IOL size of 1.73 *mm* averaged from six popular company products (Ultrasert, Eyecee, iSert, CT Lucia, iTec and Rayone, respectively) Nanavaty and Kubrak-Kisza (2017), Zhang et al. (2022), so that the amount of stress being applied was adjusted to induce a $d = 1.73\ mm$ maximal displacement in the middle of the incision.

The cornea was assumed as a simple linear material and its surface curvature was ignored. Typical strain-rate dependent stiffness E is chosen as 9.82 *MPa* at a strain rate of $3\ mm \cdot \text{min}^{-1}$ from porcine corneas Tonsomboon et al. (2014). In a chevron incision, the incision of length $2a$ was composed of two straight lines of the same length a, and the angle between these two arms is α, ranging from 120° to 180° Pallin (1991), Biswas et al. (2022)[1], as defined in Figure 2A. A frown incision

1 Note that with $\alpha = 180°$, a chevron incision coincides with a straight incision.

was assumed to be an arc with arclength $2a$ and central angle β, as defined in Figure 2B. The central angle of a frown incision varied from 5° to 50° characterizing its curvature Sinskey and Stoppel (1994); Singer (1991)[2]. As the corneal material is isotropic, a frown (curving down) and a smile incision (curving up) are the same.

In linear fracture mechanics, a 2D fracture occurs when the energy released by crack propagation along an infinitesimal length is greater than the energy required to break all atomic bonds per unit length, i.e., the crack becomes unstable. This idea is known as Griffith's theory, the energy release rate criterion, or the G criterion Griffith (1921), Irwin and Wells (1965). The criterion is based on the calculation of energy release rate (ERR), G, which simply reads as

$$G > G_c. \tag{1}$$

where G_c is a measurable material parameter and its value at a strain rate of $3\ mm \cdot \mathrm{min}^{-1}$ corresponds to stiffness of $E = 9.82\ MPa$ is $5.40\ kJ/m^2$ Tonsomboon et al. (2014). Thus, the key in FE simulation was to obtain the ERR value and compare it with G_c, if $G > G_c$, further tear may occur.

The crack was firstly represented by a partition and created by defining a "seam," where nodes on elements on each side of the crack could be separated. ERR, as a contour energy integral, was calculated for layers of elements in rings, which required a spider web-like mesh generated around the crack tip. A sweeping strategy was selected around the crack tip, so that quadrilateral elements degraded into triangular elements, as seen in Figure 3B. In particular, each ring of elements along the crack corresponded to a contour integral ERR, and an average of 10 contours were selected for ERR convergence and evaluations. Note that for a chevron/frown incision, some special treatments were required to conduct effective sweeping operations and achieve a conforming and feasible mesh. One was to pull nodes back onto the symmetrical axis, these nodes escaped out of the plate due to the sweeping strategy, as depicted in Figure 3C, and the other was to remove coincident or nearly coincident nodes, especially for frown incisions.

The finite element simulations were performed using the commercially available finite element package Abaqus 2013 (Dassault Syste mes®), and was conducted on 11th Gen Intel® Core™ i5-11400@2.60GHz machine with 16.0 GB RAM. Abaqus script was modified to execute special sweeping operations for chevron/frown incisions via Matlab R2022a (The MathWorks, Inc.). In a typical simulation, a total of 17,882 nodes and 6,580 elements (CPS4R: Bilinear elements using simplified integration with hourglass control) were used, which took about 3–5 min. The grid size was chosen according to a grid independence test (simulations were run for increasingly refined grids until results converged).

3 Results

Figure 4 shows a finite element result of a chevron incision with angle $\alpha = 150°$ and incision length of $2a = 2.2\ mm$, subjected to an applied loading of $\sigma_0 = 3.95\ MPa$ to induce a maximal displacement of $d = 1.73\ mm$. The crack opened unsymmetrically, more towards the chevron incision tip, and the von Mises stress was concentrated at the crack tip. The ERR corresponding to each contour of 10 typical contours was output from Abaqus. To avoid unnecessary effects from the crack tip, only contour integrals from the 4th to 10th contours were collected and all converged to a value of ERR of $5.12\ kJ/m^2$, which is less than $G_c = 5.40\ kJ/m^2$ indicating safe insertion.

We then compared the ERR of chevron incisions with the angle α ranging from 120° to 180° and the same length of $2a = 2.2\ mm$ Kim et al. (2014), as plotted in Figure 5. G equaled to the critical $G_c = 5.40 KJ/m^2$ when $\alpha = 160°$, and for $\alpha \leq 160°$, $G \geq G_c$, the

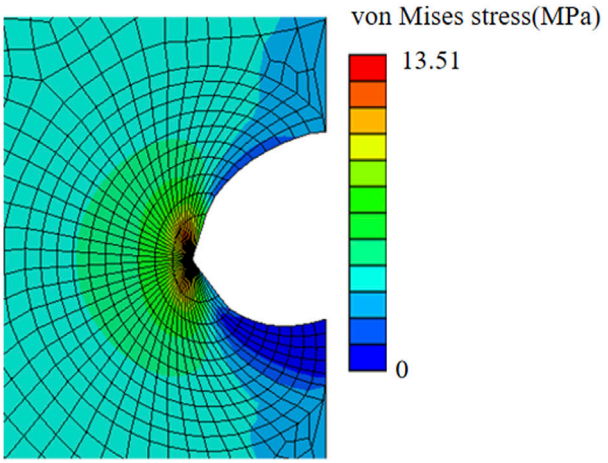

FIGURE 4
von Mises stress distribution of a chevron incision opening with incision length of $2a = 2.2\ mm$ and angle between two arms of 150° subjected to the applied uniform stress of $\sigma_0 = 3.95\ MPa$.

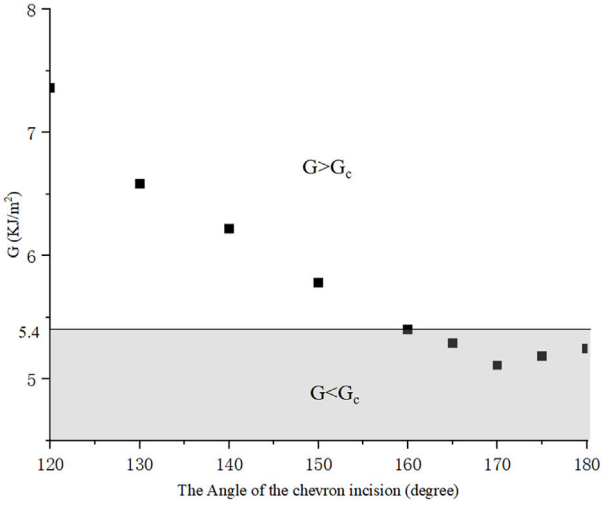

FIGURE 5
With different angles, ERR presents a tendency for chevron incisions with equal length $2a = 2.2\ mm$.

2 Note that with $\beta = 0°$, a frown incision coincides with a straight incision.

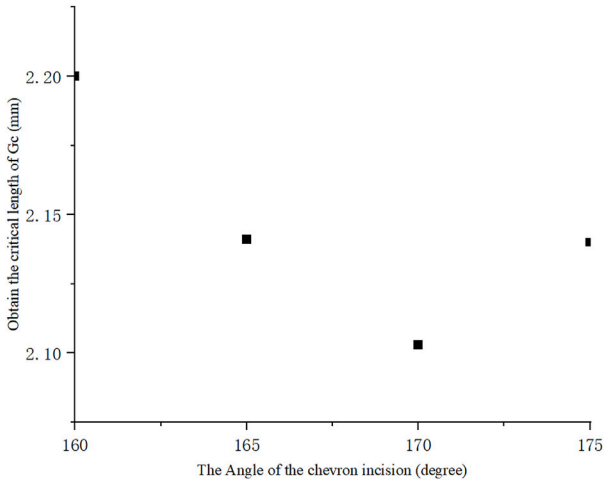

FIGURE 6
Critical incision length for different chevron shapes, the angle between two arms of 170° reached minimum indicating its optimal incision design.

crack further propagated, otherwise, remained stable. It was also found that $G = 5.11 KJ/m^2$ reached the minimum value with $\alpha = 170^{\circ}$, which may indicate an optimal design for chevron-shaped incisions.

To further investigate the critical length for different shapes of incision, four different chevron incisions with angles $\alpha = 160^{\circ}$, 165°, 170°, 175° were selected for numerical simulation, and their critical incision lengths corresponding to $G = G_c$ were shown in Figure 6. It is worth noting that for each shape of chevron incision, the mesh needed to be regenerated as the angle between its two arms changed. It was clearly seen that the critical incision length is the smallest with $\alpha = 170^{\circ}$, i.e., with the least surgically induced damage, which is consistent with the observation that the ERR is minimum with this shape of chevron incision, as plotted in Figure 5. It is again convinced that the design of a chevron incision of angle 170° is optimal in order to maintain a stable corneal configuration.

Furthermore, frown incisions with the same length of $2a = 2.2\ mm$ and different central angle β were simulated. A typical numerical example with $\beta = 35^{\circ}$ was elaborated in Figure 7. Similarly, by adjusting the evenly distributed stress at the boundaries, the value of ERR was taken when the maximum crack opening distance in the middle reached $d = 1.730\ mm$. The crack opened asymmetrically more towards the convex direction and the maximum von Mises stress was concentrated at the crack tip. The contour integral ERR was extracted to converge to a value of $5.40 kJ/m^2$ from the 4^{th} to 10^{th} contours. Figure 8 then plotted the ERRs corresponding to different shapes of frown incisions with the central angle β ranging from 5° to 50°. It could be seen that the minimum ERR value of $G = 4.95\ kJ/m^2$ was obtained when $\beta = 6^{\circ}$. Within a small range of central angle between 5–8°, ERRs kept a small value. The frown design of $\beta = 35^{\circ}$ served as a threshold, for $\beta \leq 35^{\circ}$, then $G \leq G_c$, the 2.2 *mm* incision would not tear further; for $\beta > 35^{\circ}$, the incision became unstable as $G > G_c$. Note again that the mesh had to be regenerated for each shape of the frown incision as the central angle changed.

This numerical model also allows us to incorporate more realistic corneal materials. It was well-known that the cornea has an anisotropy, and X-ray scattering measurements showed that about 66% of the fibrils were located in the 45° sector along the vertical and horizontal directions Pandolfi and Manganiello (2006), as seen in Figure 9A. In specific, the orientation diagram of human corneal fibrils is curved near the corneal limbus to form ring intensification and in the center of the cornea the fibril structure is positively intersected and runs around the rim of the cornea, showing a typical structure of a symmetrical material. as depicted inFigure 9B Meek and Newton (1999), Huang et al. (1996).

In order to study the influence of the material organization on ERRs, an orthotropic material whose moduli satisfied $E_x/E_y = \eta$ was applied, where E_y is the modulus parallel to the symmetric axis of the incision and E_x is the modulus perpendicular to E_y, the othrotropic ratio $\eta = 2, 1.5, 1, 0.75, 0.5$, respectively. Table 1 lists the ERRS under different materials (E_x, E_y) and geometry (α). G is minimal at $\eta = 1$, indicating that the material is isotropic. The less the angle of α, the more effect of η on G.

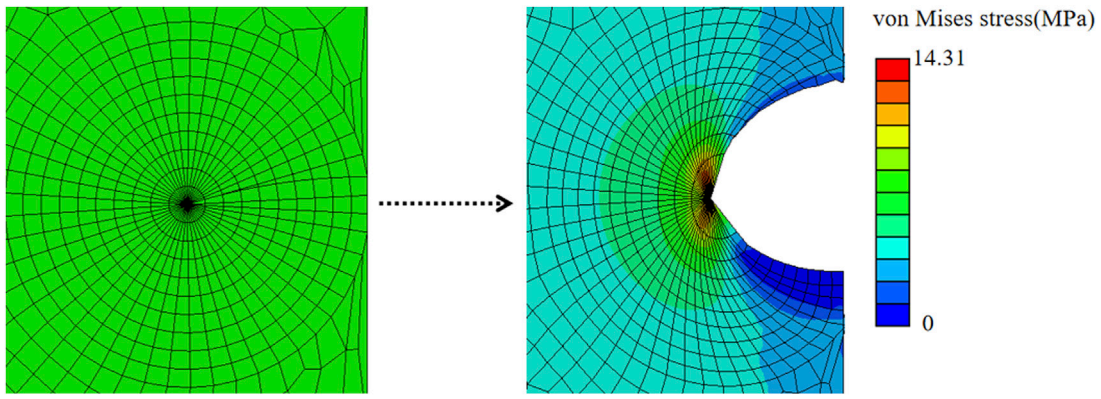

FIGURE 7
Simulation result of a frown incision with $2a = 2.2\ mm$ and central angle of 35°, the incision is highlighted in red.

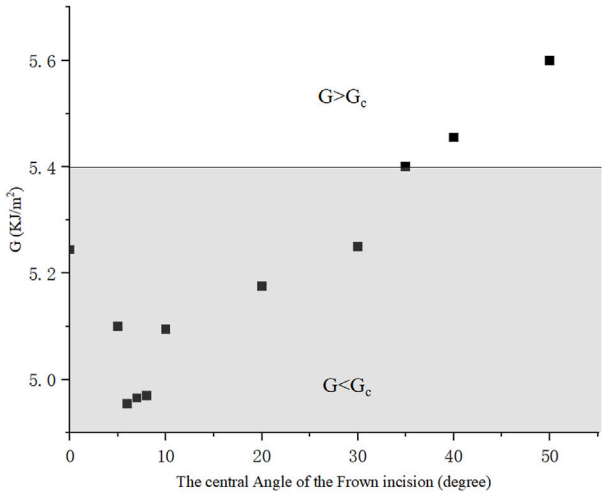

FIGURE 8
ERRs of frown incisions with different central angles, the incision length remained 2.2 *mm*.

4 Discussion

In this work, we observed that with the same incision length of $2a = 2.2$ *mm*, the frown incision shape with central angle $\beta \leq 20^{\circ}$ exhibited at most 5.15% smaller ERR compared to a straight incision and thus better performance to maintain stable corneal configuration, which was consistent with the comment that the tendency for wound edge separation was comparatively less for frown structures Rao et al. (1993). It was also pointed out that frown incisions have the advantage of early wound stability over straight incisions Shaikh et al. (2022). Moreover, a chevron incision with an angle of $170^{\circ} < \alpha < 175^{\circ}$ could achieve a smaller ERR than a straight incision with the same incision length, which was supported by a comparative study by Randeri et al. (2008), Rathi et al. (2022). However, the distinction was not big, only improved by 2.48%. Amongst the three shapes of incision, the frown incision performed significantly superior to the other two for allowing the largest injector through the pre-cut incision in an SICS. Other than this, a frown incision is practically easier to conduct for surgeons than a chevron incision which has a corner in the middle Singer (1991). It was found that the mean SIA value of the frown incision was lower than that of the straight incision, and the UCVA (uncorrected visual acuity) effect of the frown incision group was better than that of the straight incision group Chourasia et al. (2019). In summary, a frown incision is significantly better than a straight incision in reducing surgical astigmatism Chourasia et al. (2019).

The organization of corneal tissue is far more complex than being linear. It could be clearly seen from Table 1 that for chevron incisions, isotropy was favored among all tested angles, indicating practical incision locations were recommended in the dark regions in Figure 9C where the fibrils are most dispersed and exhibit high isotropy. Unlike straight incisions with $\alpha = 180^{\circ}$, E_y is no longer the dominating factor affecting ERR as the incision had both x and y components, the smaller the value of α, the more effect of η on G. If necessary, the chevron incision was recommended to be more aligned with the direction exhibiting a larger modulus, for example, along the circumferential direction near the limbus.

In further studies, finite element models with nonlinear and hyperelastic material descriptions are required based on patient-specific data. It is with no doubt that more complicated material descriptions would change the values in the results, however, the findings in this work are qualitatively representative of the clinical situations, and our simulation results are consistent with many comparative population studies and surgical findings. In addition, frown and smile incisions are required to be distinguished as curving to the rim and center represent differently in anisotropic material characterization. In the meanwhile, the cornea in this study was assumed to be a 2D

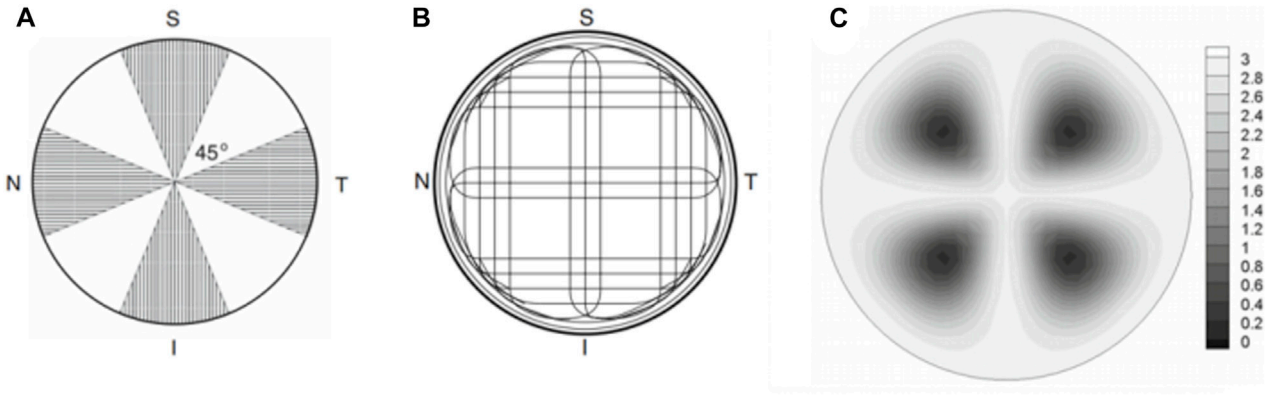

FIGURE 9
(A) Visualization of the corneal sector in which the strong direction of the fibrils is observed Pandolfi and Manganiello (2006); **(B)** Schematic diagram of the direction of human corneal fibers Meek and Newton (1999), Huang et al. (1996); **(C)** A graph of the coefficient defining the anisotropy level of fibrils. Small values correspond to isotropic distribution and large values correspond to significant anisotropy Pandolfi and Manganiello (2006).

TABLE 1 ERRs against the materials orthotropy ratio of chevron incision from different angles.

η	E_x	E_y	G			
			165°	170°	175°	180°
2	19.64	9.82	8.72	8.17	8.25	5.30
1.5	14.73	9.82	7.18	6.75	6.94	5.27
1	9.82	9.82	**5.29**	**5.11**	**5.19**	**5.24**
0.75	9.82	14.73	6.04	5.80	5.84	6.74
0.5	9.82	19.64	6.51	6.30	6.34	8.03

The bold values indicate the minimal ERR associated with each chevron angle at \eta = 1.

plate, however, corneal curvature is an important geometrical parameter for accurate estimation, in particular, in cornea injury and its surgical repair Malik et al. (2012), Juchem et al. (1993), Merriam et al. (2003).

5 Conclusion

In this work, the finite element method was used based on Griffith's energy release rate (ERR) criterion to simulate an optimal incision configuration among straight, frown, and chevron shapes, viewed from the point to maintain stable incision configuration and avoid further uncontrollable tearing in small incision cataract surgery. Chevron and frown incisions with different geometrical parameters including incision length and characteristic angles were considered and compared. It was found that for chevron incisions, the incision shape of angle 170° performed the best with minimal ERR value, while for frown incisions, the shape with a central angle of 6° was favorable. Both chevron and frown incisions could achieve larger sizes of injectors for surgeons to choose from than a straight pre-cut. In particular, frown incision was superior due to its lower corresponding ERR and easy operation. It was also observed that incision locations were recommended to be selected in regions where the embedded fibrils are most dispersed and exhibit high isotropy. If necessary, the chevron incision was recommended to be more aligned with the direction exhibiting a larger modulus, for example, along the circumferential direction near the limbus. This numerical study investigated and quantified the optimal incision shape in small incision cataract surgery from a new aspect, which provides a reference for ophthalmologists to make effective and safe surgical decisions.

Data availability statement

The original contributions presented in the study are included in the article/Supplementary Material, further inquiries can be directed to the corresponding author.

Author contributions

HY: Conceptualization, Formal Analysis, Investigation, Visualization, Writing–original draft. NQ: Conceptualization, Formal Analysis, Investigation, Methodology, Visualization, Writing–original draft.

Funding

The authors declare financial support was received for the research, authorship, and/or publication of this article. We gratefully acknowledge the financial support from the National Natural Science Foundation of China (No. 11902181).

Conflict of interest

The authors declare that the research was conducted in the absence of any commercial or financial relationships that could be construed as a potential conflict of interest.

Publisher's note

References

Al Mahmood, A. M., Al-Swailem, S. A., and Behrens, A. (2014). Clear corneal incision in cataract surgery. *Middle East Afr. J. Ophthalmol.* 21, 25–31. doi:10.4103/0974-9233.124084

Bernhisel, A., and Pettey, J. (2020). Manual small incision cataract surgery. *Curr. Opin. Ophthalmol.* 31, 74–79. doi:10.1097/icu.0000000000000624

Biswas, S. K., Islam, Q., Husain, R., Sultana, S., and Anjum, N. (2022). Astigmatic change in manual small incision cataract surgery (msics) with chevron type of incision. *Int. J. Innovative Sci. Res. Technol.* 7, 794–799. doi:10.5281/zenodo.6535997

Chourasia, P., Kumar, G., and Kumar, S. (2019). Comparison of surgically induced astigmatism in manual small incision cataract surgery following straight versus frown incision. *Int. J. Res. Rev.* 6, 328–336.

Griffith, A. A. (1921). Vi. the phenomena of rupture and flow in solids. *Philosophical Trans. R. Soc. Lond. Ser. A, Contain. Pap. a Math. or Phys. Character* 221, 163–198.

Haldipurkar, S., Shikari, H. T., and Gokhale, V. (2009). Wound construction in manual small incision cataract surgery. *Indian J. Ophthalmol.* 57, 9–13. doi:10.4103/0301-4738.44491

He, Q., Huang, J., He, X., Yu, W., Yap, M., and Han, W. (2021). Effect of corneal incision features on anterior and posterior corneal astigmatism and higher-order aberrations after cataract surgery. *Acta Ophthalmol.* 99, e1027–e1040. doi:10.1111/aos.14778

Huang, Y., Tuft, S. J., and Meek, K. M. (1996). A histochemical and x-ray diffraction study of keratoconus epikeratoplasty: report of two cases. *Cornea* 15, 320–328. doi:10.1097/00003226-199605000-00016

Irwin, G., and Wells, A. (1965). A continuum-mechanics view of crack propagation. *Metall. Rev.* 10, 223–270. doi:10.1179/mtlr.1965.10.1.223

Juchem, M., Skorpik, F., and Crammer, A. (1993). "Clear cornea incision – frown incision: induzierter astigmatismus 1 monat und 3 monate postoperativ," in 7. Kongreß der Deutschsprachigen Gesellschaft für Intraokularlinsen Implantation, Zürich, 4. bis 6. März 1993, 104–108.

Kim, Y.-K., Kim, Y. W., Woo, S. J., and Park, K. H. (2014). Comparison of surgically-induced astigmatism after combined phacoemulsification and 23-gauge vitrectomy: 2.2-mm vs. 2.75-mm cataract surgery. *Korean J. Ophthalmol.* 28, 130–137. doi:10.3341/kjo.2014.28.2.130

Malik, V., Kumar, S., Kamboj, R., Jain, C., and Jain, K. (2012). Comparison of astigmatism following manual small incision cataract surgery: superior versus temporal approach. *Nepal. J. Ophthalmol.* 4, 54–58. doi:10.3126/nepjoph.v4i1.5851

McFarland, M. (1990). Surgeon undertakes phaco, foldable iol series sans sutures. *Ocul. Surg. News* 1, 15.

Meek, K. M., and Newton, R. H. (1999). Organization of collagen fibrils in the corneal stroma in relation to mechanical properties and surgical practice. *J. Refract. Surg.* 15, 695–699. doi:10.3928/1081-597x-19991101-18

Merriam, J. C., Zheng, L., Merriam, J. E., Zaider, M., and Lindström, B. (2003). The effect of incisions for cataract on corneal curvature. *Ophthalmology* 110, 1807–1813. doi:10.1016/s0161-6420(03)00537-2

Nanavaty, M. A., and Kubrak-Kisza, M. (2017). Evaluation of preloaded intraocular lens injection systems: *ex vivo* study. *J. Cataract Refract. Surg.* 43, 558–563. doi:10.1016/j.jcrs.2017.02.019

Pallin, S. L. (1990). Chevron incision for cataract surgery. *J. Cataract Refract. Surg.* 16, 779–781. doi:10.1016/s0886-3350(13)81032-2

Pallin, S. L. (1991). Chevron sutureless closure: a preliminary report. *J. Cataract Refract. Surg.* 17, 706–709. doi:10.1016/s0886-3350(13)80687-6

Pandolfi, A., and Manganiello, F. (2006). A model for the human cornea: constitutive formulation and numerical analysis. *Biomechanics Model. Mechanobiol.* 5, 237–246. doi:10.1007/s10237-005-0014-x

Qi, N., Lockington, D., Wang, L., Ramaesh, K., and Luo, X. (2022). Estimations of critical clear corneal incisions required for lens insertion in cataract surgery: a mathematical aspect. *Front. Physiology* 13, 834214. doi:10.3389/fphys.2022.834214

Randeri, J. K., Desai, R. J., Mehta, F. S., Billore, O., Gupta, A., Kukadia, G., et al. (2008). "Incision induced astigmatism-a comparative study of chevron incision and frown incision in sics," in AIOS Proceedings, Bangalore.

Rao, G., Basti, S., Vasavada, A., Thomas, R., Braganza, A., Challa, J., et al. (1993). Extracapsular cataract extraction: surgical techniques. *Indian J. Ophthalmol.* 41, 195–210.

Rathi, M., Dabas, R., Verma, R., Rustagi, I. M., Mathur, S., and Dhania, S. (2022). Comparison of surgically induced astigmatism in chevron, straight, and frown incisions in manual small-incision cataract surgery. *Indian J. Ophthalmol.* 70, 3865–3868. doi:10.4103/ijo.ijo_1589_22

Shaikh, R., Avanthi, S., and Misquith, S. C. (2022). Comparison of postoperative astigmatism in small incision cataract surgery based on size and shape of the incision. *IP Int. J. Ocular Oncol. Oculoplasty* 7, 391–393. doi:10.18231/j.ijooo.2021.082

Singer, J. A. (1991). Frown incision for minimizing induced astigmatism after small incision cataract surgery with rigid optic intraocular lens implantation. *J. Cataract Refract. Surg.* 17, 677–688. doi:10.1016/s0886-3350(13)80683-9

Sinskey, R. M., and Stoppel, J. O. (1994). Induced astigmatism in a 6.0 mm no-stitch frown incision. *J. Cataract Refract. Surg.* 20, 406–409. doi:10.1016/s0886-3350(13)80175-7

Tonsomboon, K., Koh, C. T., and Oyen, M. L. (2014). Time-dependent fracture toughness of cornea. *J. Mech. Behav. Biomed. Mater.* 34, 116–123. doi:10.1016/j.jmbbm.2014.01.015

Zhang, L., Schickhardt, S., Fang, H., Auerbach, F., Cagampang, P., III, Merz, P. R., et al. (2022). Comparison of a new iol injector system against 3 standard iol injector systems with different incision sizes: miyake-apple view experimental laboratory study. *J. Cataract Refract. Surg.* 48, 230–237. doi:10.1097/j.jcrs.0000000000000736

frontiers | Frontiers in Bioengineering and Biotechnology

TYPE Original Research
PUBLISHED 08 November 2023
DOI 10.3389/fbioe.2023.1277970

OPEN ACCESS

EDITED BY
Matthew A. Reilly,
The Ohio State University, United States

REVIEWED BY
Nan Qi,
Shandong University, China
Junjie Wang,
Wenzhou Medical University, China

*CORRESPONDENCE
Osama M. Maklad,
o.maklad@gre.ac.uk

RECEIVED 15 August 2023
ACCEPTED 23 October 2023
PUBLISHED 08 November 2023

CITATION
Desouky NA, Saafan MM, Mansour MH and Maklad OM (2023), Patient-specific air puff-induced loading using machine learning.
Front. Bioeng. Biotechnol. 11:1277970.
doi: 10.3389/fbioe.2023.1277970

Patient-specific air puff-induced loading using machine learning

Nada A. Desouky[1], Mahmoud M. Saafan[2], Mohamed H. Mansour[1] and Osama M. Maklad[1,3]*

[1]Mechanical Power Engineering Department, Faculty of Engineering, Mansoura University, Mansoura, Egypt, [2]Computers and Control Systems Engineering Department, Faculty of Engineering, Mansoura University, Mansoura, Egypt, [3]School of Engineering, Centre for Advanced Manufacturing and Materials, University of Greenwich, London, United Kingdom

Introduction: The air puff test is a contactless tonometry test used to measure the intraocular pressure and the cornea's biomechanical properties. Limitations that most challenge the accuracy of the estimation of the corneal material and the intraocular pressure are the strong intercorrelation between the intraocular pressure and the corneal parameters, either the material properties that can change from one person to another because of age or the geometry parameters like central corneal thickness. This influence produces inaccuracies in the corneal deformation parameters while extracting the IOP parametric equation, which can be reduced through the consideration of the patient-specific air puff pressure distribution taking into account the changes in corneal parameters. This air puff pressure loading distribution can be determined precisely from the fluid-structure interaction (FSI) coupling between the air puff and the eye model. However, the computational fluid dynamics simulation of the air puff in the coupling algorithm is a time-consuming model that is impractical to use in clinical practice and large parametric studies.

Methods: By using a supervised machine learning algorithm, we predict the time-dependent air puff pressure distribution for different corneal parameters via a parametric study of the corneal deformations and the gradient boosting algorithm.

Results: The results confirmed that the algorithm gives the time-dependent air puff pressure distribution with an MAE of 0.0258, an RMSE of 0.0673, and an execution time of 93 s, which is then applied to the finite element model of the eye generating the corresponding corneal deformations taking into account the FSI influence. Using corneal deformations, the response parameters can be extracted and used to produce more accurate algorithms of the intraocular pressure and corneal material stress-strain index (SSI).

Discussion: Estimating the distribution of air pressure on the cornea is essential to increase the accuracy of intraocular pressure (IOP) measurements, which serve as valuable indicator of corneal disease. We find that the air puff pressure loading is largely influenced by complex changes in corneal parameters unique to each patient case. With our innovative algorithm, we can preserve the same accuracy developed by the CFD-based FSI model, while reducing the computational time from approximately 101000 s (28 h) to 720 s (12 min), which is about 99.2%

reduction in time. This huge improvement in computational cost will lead to significant improvement in the parametric equations for IOP and the Stress-Strain Index (SSI).

KEYWORDS

air puff pressure, intraocular pressure (IOP), ocular biomechanics, fluid-structure interaction (FSI), reduced order modelling, machine learning (ML), Gradient Boosting Regressor (GBR)

1 Introduction

Ophthalmology clinical practice utilizes the non-contact air puff tonometry test to measure the human cornea's biomechanical properties and the Intraocular Pressure (IOP). Precise IOP is an essential aspect in the evaluation of patients at risk for eye diseases such as glaucoma which involves an increase in IOP above normal levels leading to optic nerve damage. Glaucoma is one of the leading asymptomatic causes of permanent blindness in the developed world. A common reason for the IOP increase is the aqueous humuor not draining properly due to blockage of the trabecular meshwork (Stevens et al., 2013). The Ocular Response Analyzer (ORA) (Luce, 2005) was the first tonometry device that used an air puff to determine the ocular biomechanical properties, using a dynamic infrared signal analysis. Then, a new development for better visualisation of the cornea's deformation was conducted with the aid of the ultra-high-speed Scheimpflug camera using the Corvis-St tonometer (Koprowski, 2014). Corvis-St tonometer applies a concentrated air puff into the centre of the cornea, causing deformation in the cornea's geometry, which regains its original configuration due to its elasticity. By using image processing, the corneal deformation is recorded to estimate the corneal biomechanical properties and the IOP using a programmed parametric equation.

Another degenerative eye disease of the cornea is keratoconus, where the cornea progressively thins over time, making the shape of the thinned cornea a cone with protrusion (Bao et al., 2016). This is the result of major changes in the thickness, shape, and biomechanical properties (Read and Collins, 2011), which usually produce irregular astigmatism with blurry vision. The tonometry measurements of IOP in patients with keratoconus tend to be lower due to the strong correlation between the IOP measurements and the altered biomechanical properties, particularly the Central corneal thickness (CCT) (Patel and McLaughlin, 1999), (Brooks et al., 1984). Moreover, understanding the biomechanical characteristics and structure of the cornea in keratoconic eyes can also help to clarify the pathophysiology and aetiology of this disorder, which can aid in its treatment (Ambekar et al., 2011).

Therefore, accurate measurements of both the IOP and corneal biomechanical parameters *in vivo* are of utmost importance; however, the challenge is the mutual dependence between the two making it hard to separate the effect of IOP from the biomechanical parameters like thickness and material stiffness on the corneal response parameters (Liu and Roberts, 2005). The solution to the challenge is to solve an inverse problem to assess a more accurate measurement of the corneal material behaviour based on an improved value of the IOP (Maklad et al., 2020a), (Eliasy et al., 2019).

This demonstrates the necessity to study the fluid-structure interaction between the air puff and the cornea (Maklad et al., 2021). So, in order to reduce the association between the IOP and the corneal parameters and consequently increase the IOP estimation's accuracy, the air puff pressure distribution profiles on the cornea should be taken into account when measuring the corneal deformation (Maklad et al., 2020a). This pressure load exerted on the cornea exhibits dynamically significant changes as a response to the shape of the corneal deformation, which can change clinical interpretations (Yousefi et al., 2022). This effect was called the effect of corneal load alteration with surface shape (CLASS) by Yousefi et al. (Yousefi et al., 2022). As a result, the air puff pressure value and distribution should be obtained based on the patient's corneal parameters (Maklad et al., 2020b; Maklad et al., 2021; Yousefi et al., 2022).

While the co-simulation of the Fluid-Structure Interaction (FSI) helped to get accurate values of the pressure distribution and the corneal deformation (Simonini and Pandolfi, 2016; Ariza-Gracia et al., 2018; Maklad et al., 2018), the evolution of considering the FSI approach led to a precise estimation of the changing value and distribution of the air jet pressure with the corneal characteristics which led to the biomechanically corrected equations for estimating the accurate IOP and the corneal material stress-strain index (Maklad et al., 2020a), (Maklad et al., 2020b), (Maklad et al., 2018). However, the correct prediction of the air puff pressure in the CFD model for the FSI approach was a time-consuming model, which took too long to get the accurate air puff pressure for each patient-specific geometry.

Our primary goal in this study is to investigate how the corneal characteristics, separately, affect the air puff pressure measurements and produce a new algorithm that uses machine learning to reduce the computational cost. Despite the fact that numerical models of fluid flow have been of significant research interest in many physical and mechanical phenomena, especially when the physical process experiences FSI (Maklad et al., 2020b), (Maklad et al., 2018), (Ariza-Gracia et al., 2015), some recent works (Kutz, 2017; Brunton et al., 2020; Usman et al., 2021) indicated that machine learning (ML) have the potential to be used as a replacement for some of the time-consuming numerical solvers providing reduced-order models, improved optimization performance, and reduced computational cost. Thus, we have established a supervised regression ML algorithm using the Gradient Boosting Regressor (GBR) to estimate the time-dependent air puff corneal pressure distribution profiles to be used as a replacement for the CFD model in the FSI co-simulation of Maklad et al. (Maklad et al., 2020b) to reduce the computational cost and hence update a new version of the algorithms of the IOP and the corneal material estimation. The primary contribution of the current study is to examine the effect of changing the corneal parameters: the IOP, CCT, and material stiffness coefficient (μ) on the air puff pressure profiles, propose a GBR machine learning algorithm for estimating patient-specific air puff pressure loading, and apply the predicted

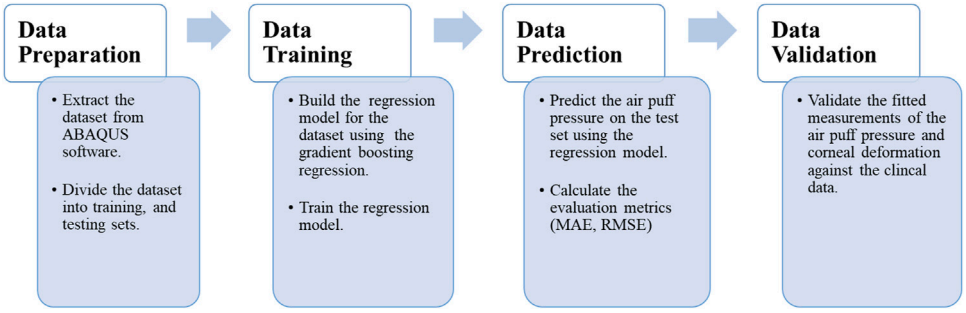

FIGURE 1
Flowchart of the data processing in the current study.

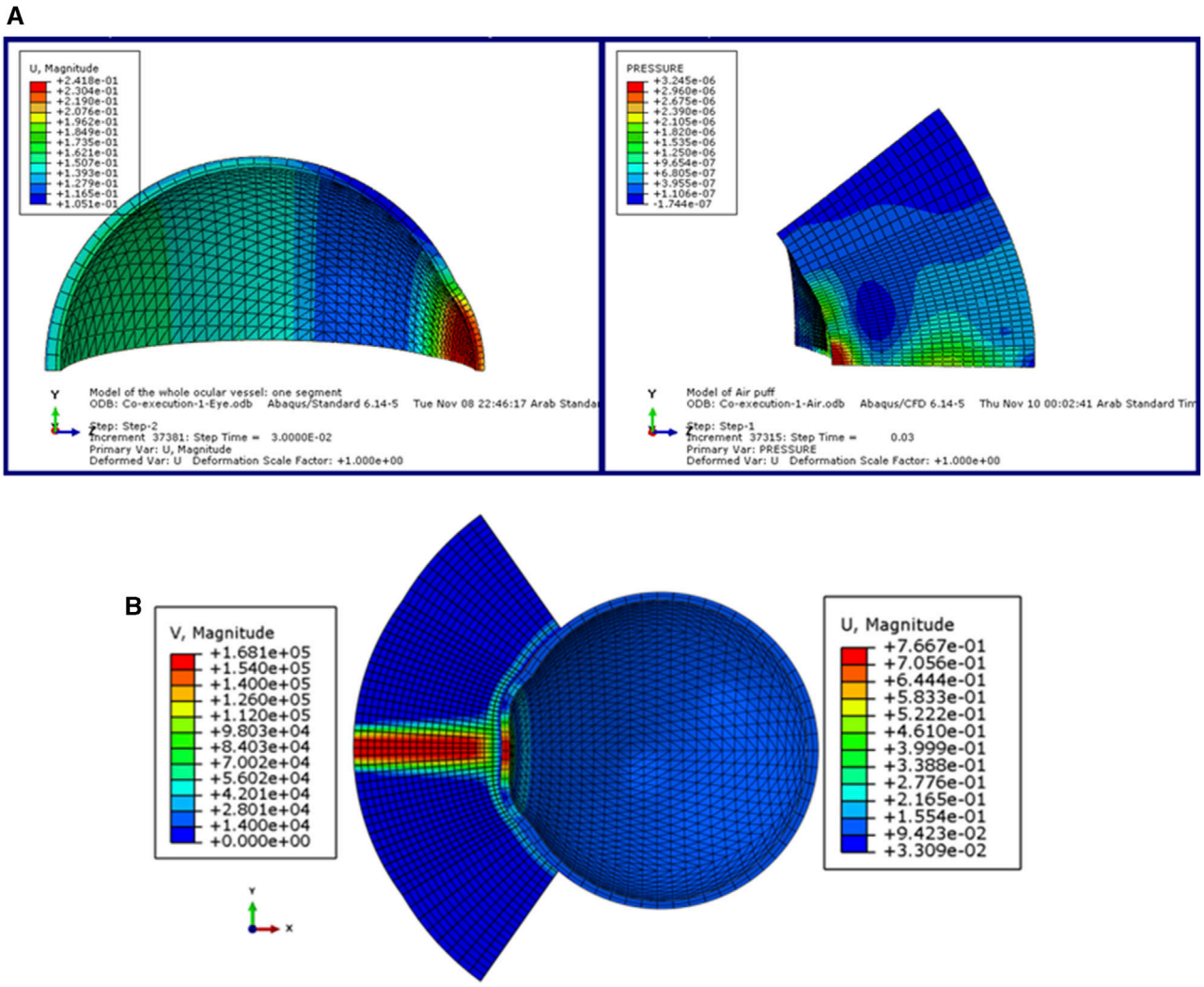

FIGURE 2
(A) The model of the eye and the air puff with the deformation and pressure values respectively, and **(B)** The FSI coupled model of the air puff test in ABAQUS software (Maklad, 2019).

pressure loading to the FE model of the eye in the ABAQUS software to produce the corneal deformation without the need for the CFD time-consuming model.

The organization of the paper is as follows. In Section 2, the processing of the input dataset with the proposed regression algorithm and methods of its evaluation are introduced. Section

TABLE 1 The values of the corneal parameters used to test our regression model.

IOP (mmHg)	10	13	15	17	20	22	24	25
CCT (μm)	445	495	545	595	645			
μ	0.0328	0.0541	0.0683	0.0811	0.1082			

3 presents the results of the GBR fitted algorithm, investigating the effect of each corneal parameter on the estimation of the air puff corneal pressure load, with a graphical user interface of the GBR algorithm. Moreover, the predicted corneal deformation based on the predicted air puff pressure, with a full validation of the algorithm with the clinical data is presented. Section 4 concludes the paper and introduces our future work.

2 Materials and methods

The current section begins by presenting the data set used in our approach and the algorithm used in the learning and predicting process. Then, we introduce the evaluation matrices used to evaluate our model's performance, and the section ends by constructing a validation study between the clinical data extracted from patients' cases and our current algorithm. Figure 1 depicts the data processing steps in our algorithm, which will be described in detail in the following sub-sections.

2.1 Data collection and processing

In this section, we explain the input dataset of our algorithm of the fully coupled FSI simulation of the air jet CFD model and the FE model of the eye obtained from the model of (Maklad et al., 2020b). Figure 2 shows the coupled FSI model from the ABAQUS 6.14 software. Due to the rotational symmetry of the results of the parametric study of (Maklad et al., 2020b) in both domains, a quarter of the two domains were simulated to save running time as shown in Figure 2A, while Figure 2B shows the deformation values of the whole ocular vessel with the air puff's velocity values shown in (mm/s) on the left, while the eye model's deformation values are shown in (mm) on the right.

The parameters included in the study are the IOP, the CCT, and the material stiffness coefficient (μ). The selection of the six values of the material stiffness coefficient is based on the relation with age as obtained by (Elsheikh et al., 2010) with μ = 0.0328 representing age = 30 years and μ = 0.1082 representing age = 100 years. The influence of each parameter on the estimation of the pressure distribution on the cornea is studied while the other parameters are fixed. First, the pressure distribution on the cornea is estimated using the range of the IOP values from 10 to 25 mmHg at CCT of 445 μm, and material stiffness coefficient of 0.0541. Then, at IOP = 15 mmHg and material stiffness coefficient = 0.0541, the influence of different values of the CCT in the range from 445 to 645 μm is tested on the calculation of the pressure on the cornea. Likewise, the pressure distribution on the cornea is estimated against the variations of the material stiffness coefficient in the range from 0.0328 to 0.1082 at the same IOP of 15 mmHg and the CCT of 545 μm. Finally, to estimate and evaluate the pressure distribution on the cornea for different corneal parameters, a complete simulation of 17 different new cases of the FSI model of Maklad et al. (Maklad et al., 2020b) in the ABAQUS 6–14 software has been performed. Table 1 summarises the corneal parameters that have been included in the study.

2.2 The Gradient Boosting Regressor (GBR) algorithm

GBM or Gradient Boosting Machine is a popular machine learning algorithm used for both regression and classification tasks. Using the GBM algorithms to solve regression problems is called the Gradient Boosting Regressor (GBR) technique, which is based mainly on the loss function, the base learner, and the additive model (Friedman, 2001). GBR ensemble model contains a series of tree models arranged sequentially, allowing each subsequent model to learn from the errors of its predecessor, and the predictions are generated by boosting the weak models, typically decision trees, to create a more powerful and robust predictive model (Friedman et al., 2000). To implement the GBR algorithm, it is necessary to specify the hyperparameters, which are an integral part of the learning algorithm and significantly affect its performance and accuracy. The parameters used in our algorithm are the squared-loss function, a learning rate of 0.3, 2,700 boosting stages, max_depth of 6, and the min_samples_split of 5. In gradient descent, the loss function is optimized for model generalization and the default option is the squared error that defines the calculated error as the residual.

Another crucial parameter is the learning rate, which indicates the rate at which the contribution of each tree shrinks. Careful selection of the learning rate is vital; a lower choice results in a slower learning process but increases the reliability and efficiency of the model. The number of estimators' parameters represents the number of boosting stages to execute, and the higher the number, the better the performance. Then, there is the max-depth parameter, which constrains the nodes in each tree, and the final parameter is the minimum number of samples needed to split an internal node (sklearn.ensemble.GradientBoostingRegressor, 2020). In each subsequent run of the algorithm, the dataset was randomly split into 70% for training and 20% for testing, with the remaining data allocated for validation. Simulations were performed on an Intel Core i7 8550U processor with 8 GB RAM. A detailed discussion of the mathematical formulation of GBR models will follow.

For an additive model with a given input x_i and prediction $\hat{y}_i$, the form of the model of GBR is of the following form (sklearn.ensemble.GradientBoostingRegressor, 2020):

$$\hat{y}_i = F_M(x_i) = \sum_{m=1}^{M} \vartheta h_m(x_i) \quad (1)$$

The constant M denotes the n_estimators parameter, ϑ is the learning rate parameter, and h_m is the basic function that is known as the weak learner's estimator. As is known, the GBR algorithm is built

TABLE 2 The corneal parameters of the four clinical cases used in the validation.

Corneal parameter/Case id	Case 1 (Age = 73)	Case 2 (Age = 54)	Case 3 (Age = 63)	Case 4 (Age = 40)
IOP (mmHg)	17.5	18	15	24
CCT (μm)	560	579	548	582
μ	0.061	0.054	0.057	0.051

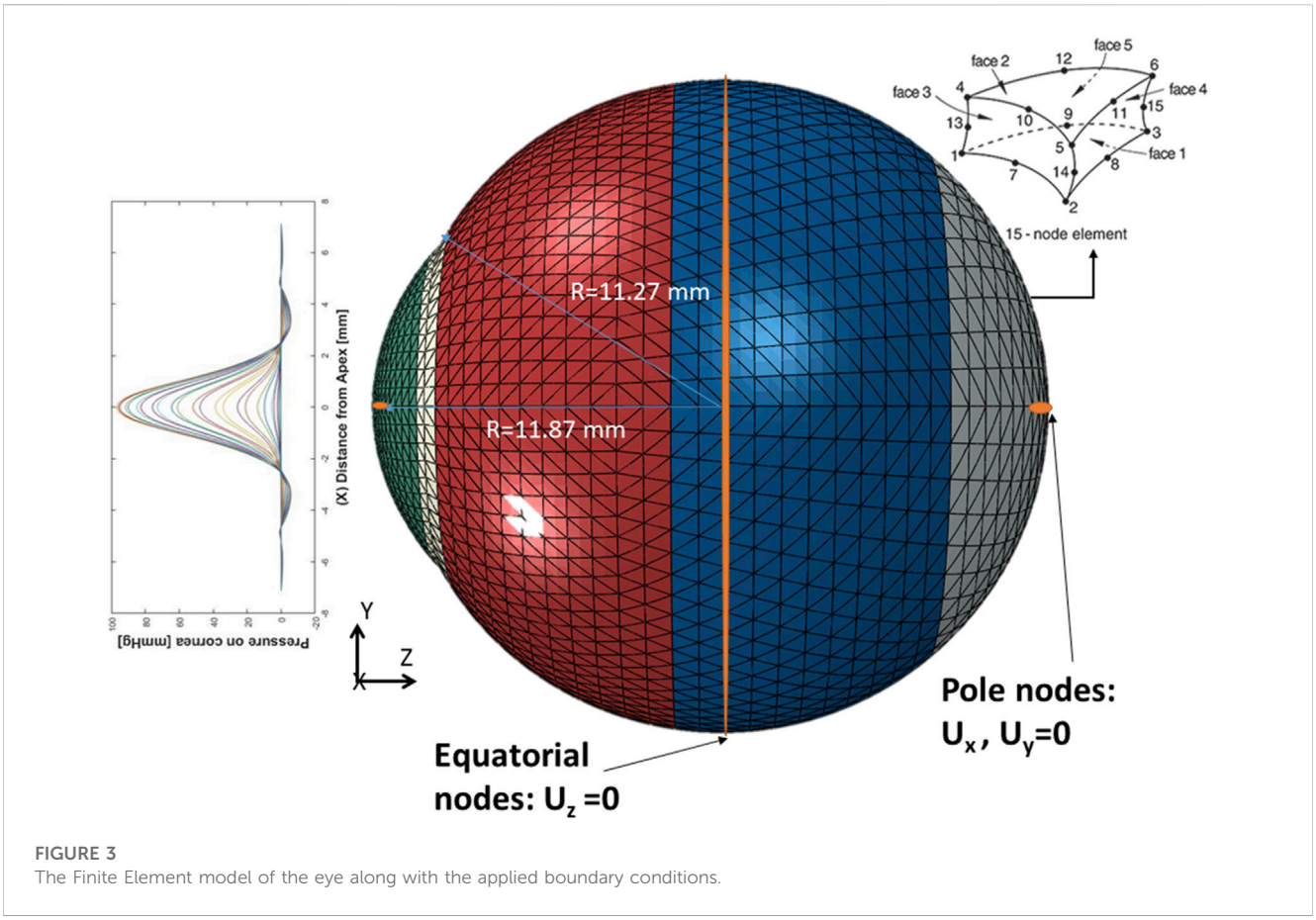

FIGURE 3
The Finite Element model of the eye along with the applied boundary conditions.

in a greedy fashion (sklearn.ensemble.GradientBoostingRegressor, 2020):

$$F_m(x) = F_{m-1}(x) + \vartheta h_m(x) \tag{2}$$

The newly inserted tree h_m is fitted at each iteration to reduce a sum of losses L_m, given the previous ensemble F_{m-1}:

$$h_m = \arg\min_h L_m = \arg\min_h \sum_{i=1}^{n} l(y_i, F_{m-1}(x_i) + h(x_i)) \tag{3}$$

As a result, with the loss parameter $l(y_i, F(x_i))$, the model formula is now:

$$F_m(x) = F_{m-1}(x) + \vartheta \arg\min_h \sum_{i=1}^{n} l(y_i, F_{m-1}(x_i) + h(x_i)) \tag{4}$$

By default, for the least-squares loss, the initial model F_0 is selected as the mean of the target values, which is the constant that minimizes the loss. So, with a first-order Taylor approximation, the value of l can be approximated as follows (sklearn.ensemble.GradientBoostingRegressor, 2020):

$$l(y_i, F_{m-1}(x_i) + h(x_i)) \approx l(y_i, F_{m-1}(x_i)) + h(x_i)\left[\frac{\partial l(y_i, F(x_i))}{\partial F(x_i)}\right]_{F=F_{m-1}} \tag{5}$$

The quantity $-\left[\frac{\partial l(y_i, F(x_i))}{\partial F(x_i)}\right]_{F=F_{m-1}}$ represents the negative gradient $-g_i$, which is calculated using a gradient descent method, and by removing the constant terms, it approximately results in:

$$h_m \approx \arg\min_h \sum_{i=1}^{n} h(x_i) g_i \tag{6}$$

The gradients are updated at each iteration until convergence is achieved and this can be considered some kind of gradient descent in

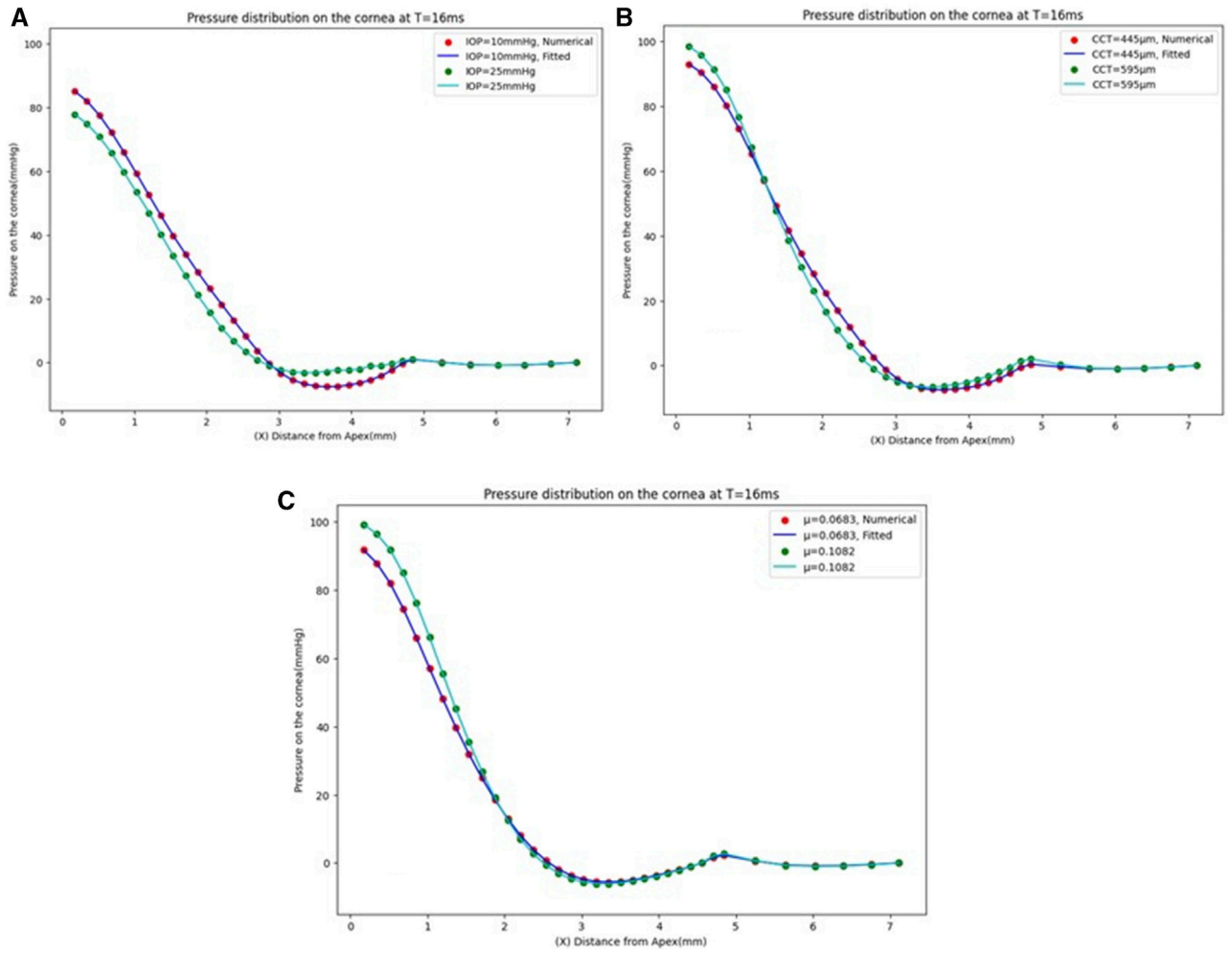

FIGURE 4
Pressure distribution on the cornea at T = 16 m. **(A)** At CCT = 445 μm and μ = 0.0541, **(B)** At IOP = 15 mmHg and μ = 0.0541, and **(C)** At IOP = 15 mmHg and CCT = 545 μm.

a functional space (sklearn.ensemble.GradientBoostingRegressor, 2020).

To assess the effectiveness of the GBR algorithm, it is essential to quantify the model error. We used the Mean Absolute Error (MAE) and Root Mean Square Error (RMSE) criteria to measure the error in our approach. The MAE provides insight into the difference between observed and actual data, calculated mathematically as follows:

$$\mathrm{MAE} = \sum_{i=1}^{n} \frac{|\mathrm{Predicted} - \mathrm{Actual}|}{n} \tag{7}$$

By calculating the standard deviation of the prediction errors, the RMSE can be estimated, which is represented as:

$$\mathrm{RMSE} = \sqrt{\sum_{i=1}^{n} \frac{(\mathrm{Predicted} - \mathrm{Actual})^2}{n}} \tag{8}$$

Additionally, as the computational cost is our research concern, another significant consideration is the computational time which represents the time the model has taken to learn and produce predictions from the input data.

2.3 Validation of the GBR algorithm

To validate our algorithm against the literature, the normalised air puff pressure was compared to the studies by Kling et al. (Kling et al., 2014) and Muench et al. (Muench et al., 2019) at two different time steps at T = 10 and 16 m. Then, to clinically validate our algorithm, a set of clinical data with a wide range of corneal parameters for four healthy patients provided by Vincieye Clinic in Milan, Italy, and Rio de Janeiro Corneal Tomography and Biomechanics Study Group, Brazil, was selected to be the input data for our GBR algorithm to predict their air puff loading and compare the corneal deformations. The ethical standards set out in the 1964 Declaration of Helsinki and their revision in 2013 were observed and all patients provided written informed consent before

TABLE 3 The RMSE estimated the pressure load by changing each corneal parameter separately.

Corneal parameter		RMSE
IOP (mmHg)	10	0.0186
	13	0.0453
	15	0.0511
	17	0.0530
	20	0.0769
	25	0.0894
CCT (μm)	445	0.0322
	495	0.1021
	545	0.0467
	595	0.0458
	645	0.0759
μ	0.0328	0.0201
	0.0541	0.0340
	0.0683	0.0119
	0.0811	0.0362
	0.1082	0.0533

using their de-identified data in research. The selected clinical cases are summarised in Table 2.

After predicting the air puff pressure loading with the GBR algorithm, we applied it to the FE model of the eye in ABAQUS 6–14. The three-dimensional eye FE model consisted of 10,000 fifteen-nodded continuum elements (C3D15H) with nine integration points, arranged in two layers, and distributed along 15 rings in the cornea and 35 rings in the sclera. The rigid body motion of the FE model of the eye was prevented in the Z-direction at the equatorial nodes, while the motions in the *X* and *Y* directions of the posterior and anterior pole nodes were restricted with free movement in the Z-direction, as shown in Figure 3, which is the same as applied in (Maklad et al., 2020a), (Eliasy et al., 2019), (Maklad, 2019).

3 Results and discussion

After building the GBR model, we used it to obtain the pressure distribution on the cornea at different time steps of the test for the corresponding patent-specific corneal parameters: IOP, CCT, and material stiffness coefficient (μ). A graphical user interface of the GBR algorithm was built in MATLAB to make it easier to change the corneal parameters and generate new predictions of the air puff pressure distribution.

3.1 Effect of the corneal parameters (IOP, CCT, and μ)

The GBR model has been analysed to see the effect of changing the IOP on the pressure distribution estimation. The pressure distribution on the cornea is obtained at the corneal surface for eight different values of the IOP (10, 13, 15, 17, 20, 22, 24, and 25 mmHg), while the other parameters are the same at a CCT of 445 μm and a material stiffness coefficient of 0.0541. The results of the comparison between the fitted GBR algorithm and the numerical values obtained from the FSI model show a good agreement with MAE = 0.0212, RMSE = 0.0682, and an execution time of 12 s. Then, we demonstrated the influence of different values of the CCT in the range (445, 495, 545, 595, and 645 μm) on the pressure distribution on the cornea at an IOP of 15 mmHg and a material stiffness coefficient of 0.0541, and the fitted algorithm shows high

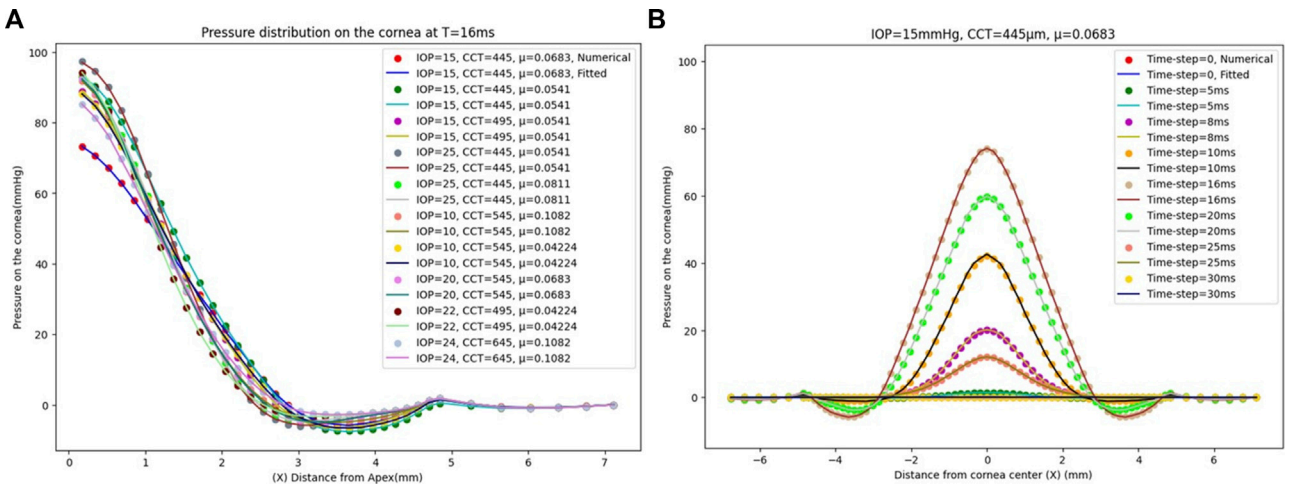

FIGURE 5
(A) The comparison between the numerical ABAQUS model and the fitted GBR algorithm of the pressure distribution on the cornea at T = 16 m with a different corneal parameter of IOP, CCT, and μ. **(B)** The pressure distribution on the cornea at different time steps for IOP = 15 mmHg, CCT = 445 μm, and μ = 0.0683.

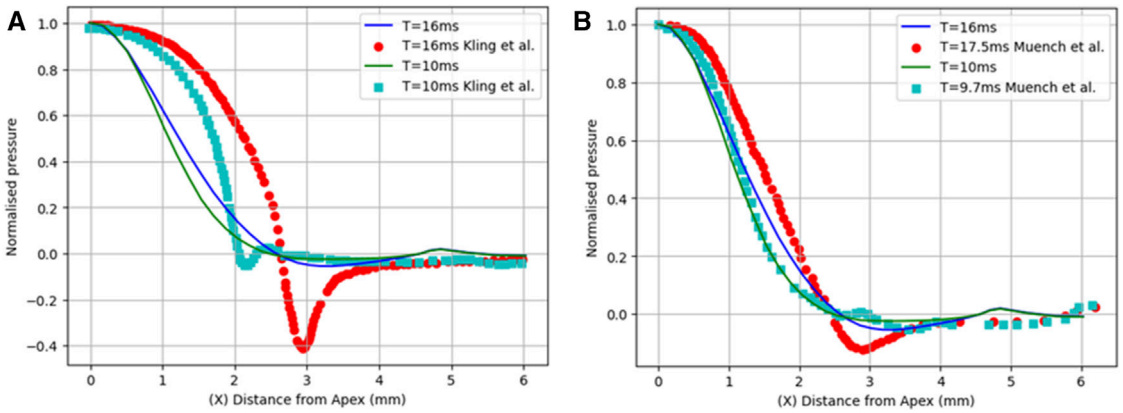

FIGURE 6
Comparison of the normalized pressure distribution with two studies from previous literature: **(A)** Kling et al. (Kling et al., 2014) and **(B)** Muench et al. (Muench et al., 2019).

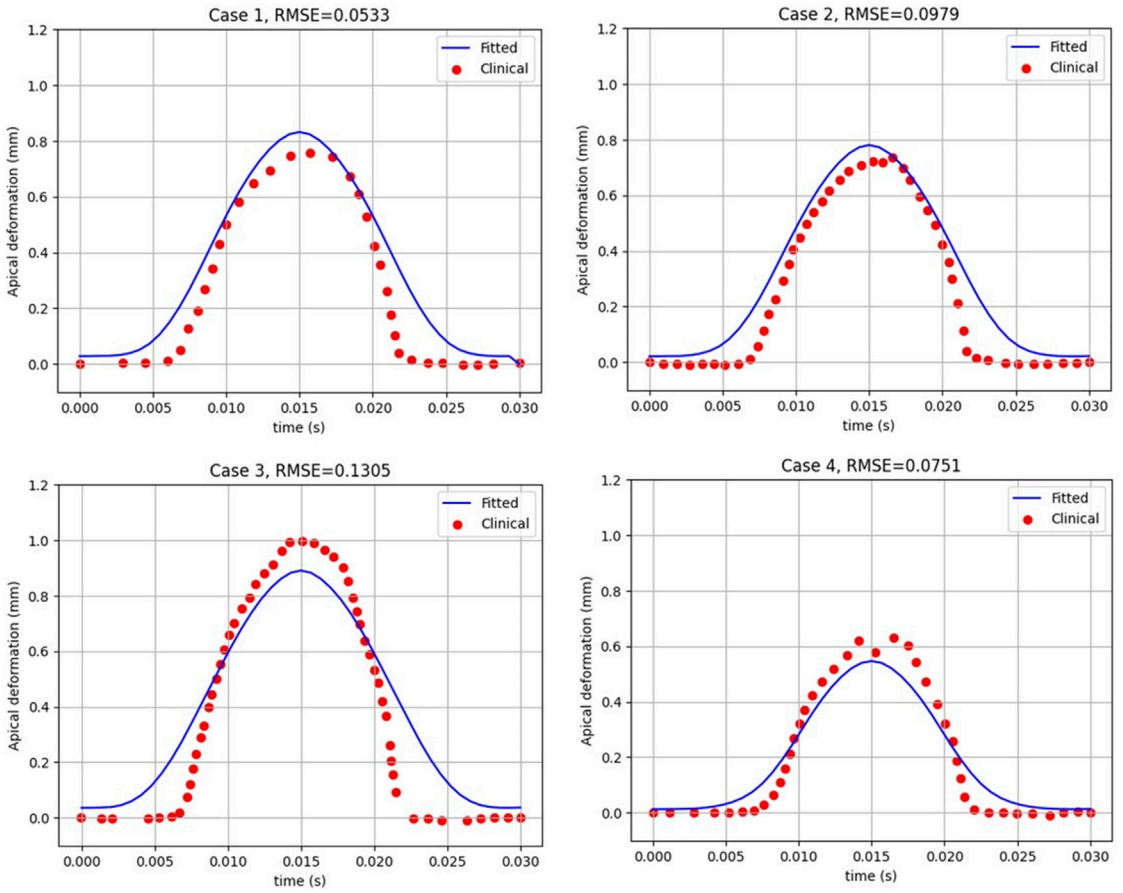

FIGURE 7
The apical deformation resulting from the GBR + FE algorithm compared against its clinical data reference for four clinical cases.

agreement with the numerical ABAQUS model with MAE = 0.0171, RMSE = 0.0578, and an execution time of 10 s. Finally, the variations of the material stiffness coefficient in the range (0.0328, 0.0541, 0.0683, 0.0811, and 0.1082) to represent the age effect are tested at IOP of 15 mmHg and CCT of 545 μm, and the fitted pressure distribution agrees well with the numerical ABAQUS model with an MAE of 0.0113, an RMSE of 0.0491, and an execution time of 12 s. Figure 4 shows the effect of changing each corneal parameter

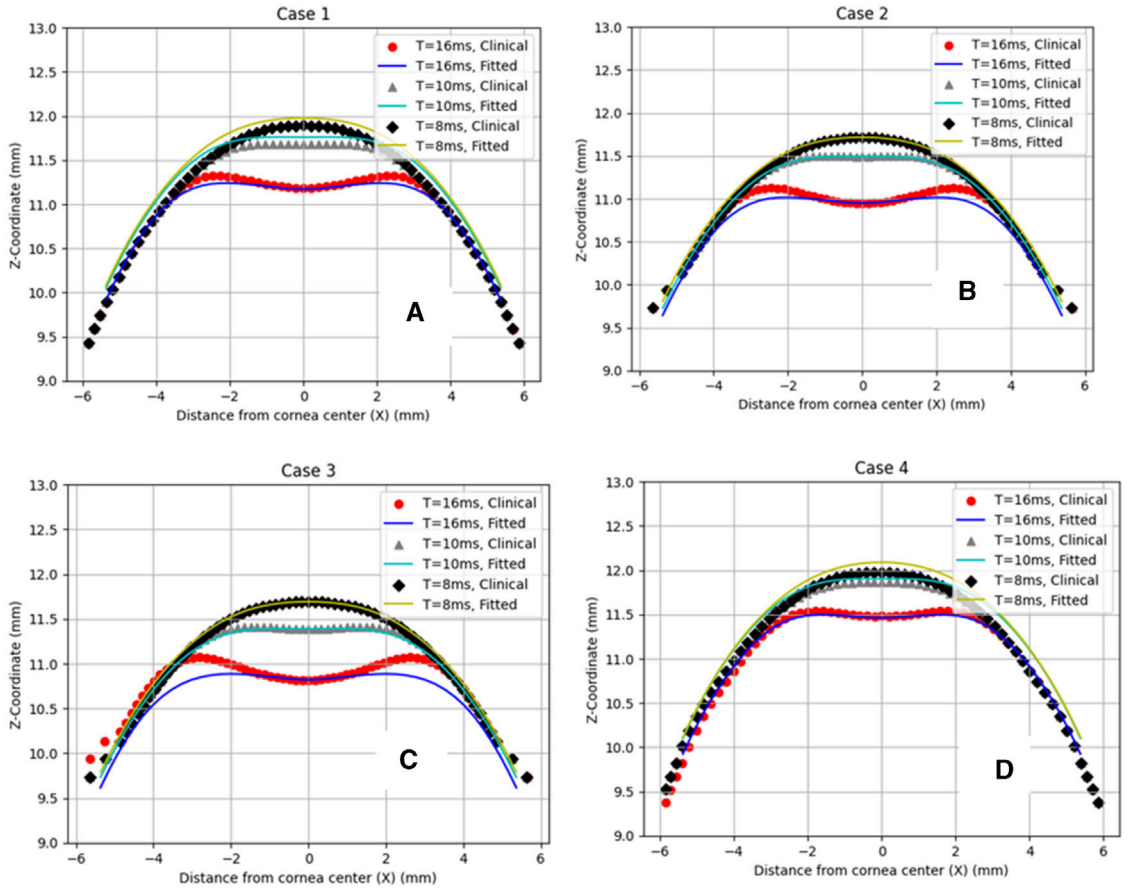

FIGURE 8
Comparison of the corneal deformation results from the fitted algorithm with the four clinical cases. **(A)** Case 1: IOP = 17.5 mmHg, CCT = 560 μm, μ = 0.061, **(B)** Case 2: IOP = 18 mmHg, CCT = 579 μm, μ = 0.054, **(C)** Case 3: IOP = 15 mmHg, CCT = 548 μm, μ = 0.057, **(D)** Case 4: IOP = 24 mmHg, CCT = 582 μm, μ = 0.051.

TABLE 4 The RMSE estimated between the clinical cases with the GBR + FE model and the numerical FE model only for the apical deformation (Maklad, 2019).

Clinical case	RMSE (GBR + FE model vs. clinical)	RMSE (FE model only vs. clinical)
Case 1	0.0533	0.6393
Case 2	0.0979	0.3655
Case 3	0.1305	0.4263
Case 4	0.0751	0.4403

separately on the fitted pressure load at T = 16 m. The plots for minimum and maximum values for the parameters are shown to feel the influence of changing the corneal parameters on the predicted pressure load. They show how the algorithm predictions agreed very much with the numerical values obtained from the FSI model from the ABAQUS software, and Table 3 shows the RMSE estimated between them for all cases at T = 16 m. It is clear from the comparison how the maximum value for the pressure at the apex is different between the two models. Moreover, the difference is not only in the maximum value of the pressure at the apex but also is in the pressure distribution, and this is what we want the ML algorithm to learn and apply to the different models with patient-specific corneal parameters.

3.2 Estimation of the air pressure distribution on the cornea

We analysed the effect of considering all the previous corneal parameters combined on the pressure loading and tested it with the numerical data model to evaluate its effectiveness. To build our model, 17 new different cases were simulated on ABAQUS 6–14 to get their results as the input dataset to our algorithm. The results of the pressure profile in Figure 5A show that changing one parameter of the corneal parameters can change the whole pressure profile and Figure 5B shows the pressure distribution on the cornea at the different time steps. The fitted algorithm with the numerical data model shows a good agreement with an MAE

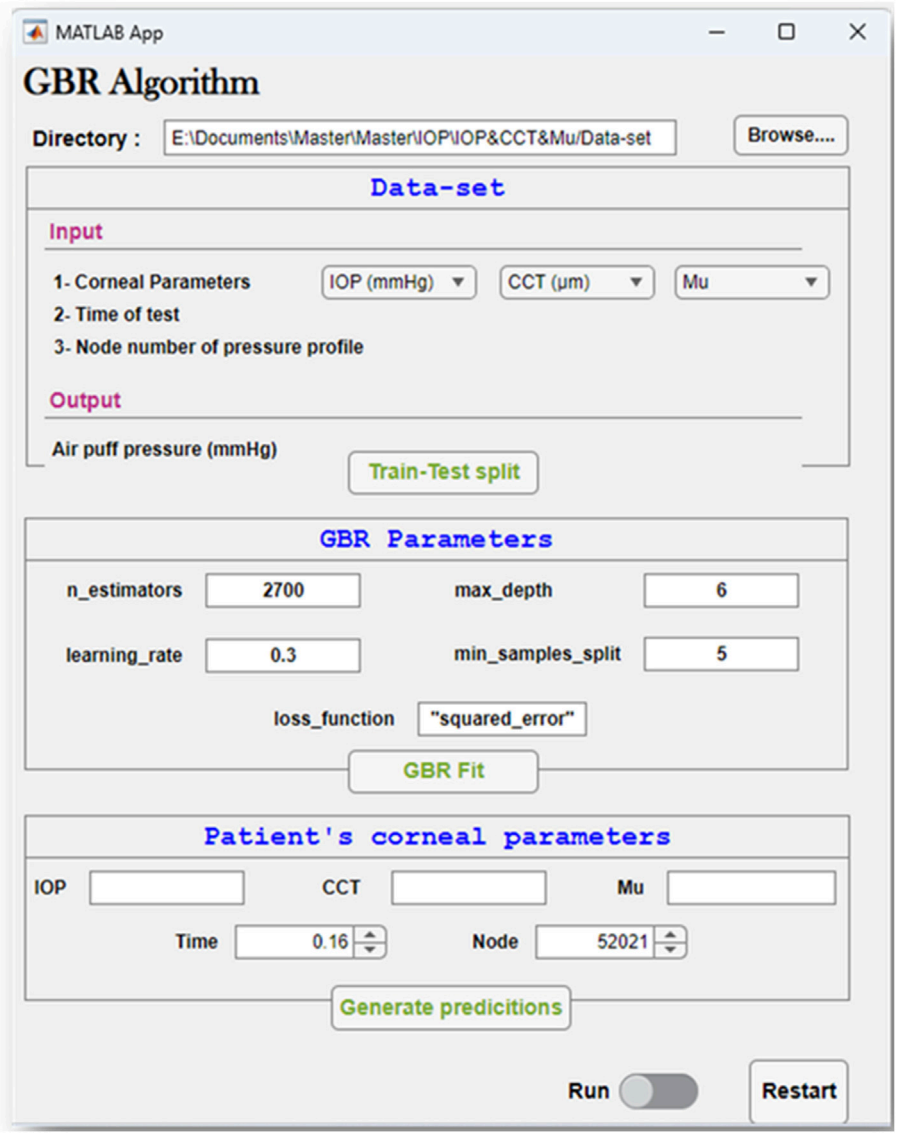

FIGURE 9
Graphical user interface of the GBR algorithm to estimate the air puff pressure.

of 0.0258, an RMSE of 0.0673, and an execution time of 93 s, and the RMSE estimated between them for each case is calculated and provided in Supplementary Table S1 in the Supplementary Material. The findings show that there is no systematic relationship between changing the air puff pressure loading with each parameter separately because the pressure distribution on the cornea is affected by the other parameters, all of which must be considered to obtain an accurate air puff pressure.

3.3 Validation of the GBR algorithm

First, the normalised air puff pressure was compared to that in the studies by Kling et al. (Kling et al., 2014) and Muench et al. (Muench et al., 2019) at two different time steps at T = 10 and 16 m with an acceptable agreement as shown in Figure 6. From this comparison, we believe that the distribution reported by Muench et al. (Muench et al., 2019) is closer to reality since it takes the fluid-structure interaction into account. However, the distribution reported by Kling et al. (Kling et al., 2014) is based on a completely rigid cornea which does not take the FSI influence into account as we have proven that the air puff pressure distribution is significantly affected by the corneal biomechanical parameters.

Then, to clinically validate our algorithm, a set of clinical data with a wide range of corneal parameters for four healthy patients was selected. After predicting the air puff pressure loading with the GBR algorithm, we applied it to the FE model of the eye in ABAQUS 6–14. The FE model took 10 min to finish and generate the corneal deformation from the predicted air puff pressure loading, and these deformations were then compared with the clinical deformation to complete the full validation of our algorithm and be used as an

alternative approach to the CFD model to reduce its computational time within minutes (720 s = 12 min) instead of waiting many hours in the FSI model (101,000 s = 28 h), which is approximately 99.2% reduction in time. Figure 7 shows the comparison of the temporal profile of the apical deformation with the clinical cases and Figure 8 presents the comparison of the spatial corneal deformation based on the predicted air puff pressure loading with their clinical data, and this comparison shows that this algorithm can produce a good and close behaviour to the real corneal behaviour. Additionally, to show the improvement caused by using the GBR algorithm with the FE model instead of using the FE model only to predict the apical deformation, the RMSE calculated for both cases was compared and presented in Table 4.

There is a hysteresis effect that causes some delay for the cornea to return back to the original geometry due to the visco-elastic material behaviour of the cornea in clinical cases. This effect is not considered in the material model of the eye in the ABAQUS co-simulation data set, which can cause some changes in the comparison between the clinical and fitted data after the air puff hits the cornea. Moreover, the fatty tissue surrounding the eye and the shooting angle of the air puff have an influence on the induced loading which was not applied in our model.

3.4 The graphical user interface of the GBR algorithm

To easily manage the interaction between the steps of the GBR algorithm to conduct our study effectively, a graphical user interface was built. Figure 9 depicts the GBR algorithm's main sections, which are summarized as follows: The input file is imported from its directory, which contains the input data and their labelled outputs. The input data set includes the corneal parameters: the IOP, CCT, and μ, with the time of the test, and the node number of the air puff pressure profile. Their labelled output, which is our desired outcome, is the air puff pressure load. This data set is divided into training and testing sets with a test size of 0.25 and a random state of 50. The hyper-parameters used in our model are shown in Figure 9, which are then used to fit our algorithm by improving the weak learner. Then, the patient-specific corneal parameters are inserted to generate their predictions within up to 2 min.

4 Conclusion

Estimating the distribution of air pressure on the cornea is essential to increasing the accuracy of intraocular pressure (IOP) measurements, which serve as valuable indicators of corneal disease. The accuracy of these measurements directly affects the accuracy of the evaluation of the corneal material. While the Fluid-Structure Interaction (FSI) method has successfully provided accurate corneal compressive load predictions based on corneal deformation, it is a time-consuming model that takes too many hours (nearly 28 h) to produce results. In this study, we developed a supervised regression ML algorithm aimed at estimating corneal pressure distribution from corneal parameters while optimizing both accuracy and computational time. The primary result of our research is the creation of a more practical algorithm, namely, the Gradient Boosting Regressor (GBR) model, capable of predicting corneal pressure load considering the influence of the corneal parameters; IOP, central corneal thickness (CCT), material coefficient (representing patient's age), and the test time step. Our findings show that the air puff pressure loading is largely influenced by complex changes in corneal parameters unique to each patient case. Moreover, this innovative algorithm significantly reduces the computational time compared to the CFD-based FSI approach from approximately 101,000 s (28 h) to 720 s (12 min), which is approximately 99.2% reduction in time, while preserving the same accuracy developed by the FSI algorithm. This huge improvement in computational cost will lead to significant improvement in the parametric equation for IOP and the Stress-Strain Index (SSI) by considering a larger number of full-eye patient-specific models with dynamic topography, which is our plan for further research. These algorithms hold great promise for clinical tonometry measurements due to their accuracy and efficiency.

Data availability statement

The original contributions presented in the study are included in the article/Supplementary Material, further inquiries can be directed to the corresponding author.

Ethics statement

The studies involving humans were approved by the University of Liverpool Institutional review board. The studies were conducted in accordance with the local legislation and institutional requirements. Written informed consent for participation was not required from the participants or the participants' legal guardians/next of kin in accordance with the national legislation and institutional requirements.

Author contributions

ND: Data curation, Formal Analysis, Investigation, Software, Validation, Visualization, Writing–original draft, Writing–review and editing. MS: Investigation, Methodology, Project administration, Resources, Software, Supervision, Writing–review and editing. MM: Funding acquisition, Investigation, Project administration, Resources, Supervision, Writing–review and editing. OM: Conceptualization, Investigation, Methodology, Project administration, Supervision, Validation, Visualization, Writing–review and editing.

Funding

The author(s) declare that no financial support was received for the research, authorship, and/or publication of this article.

Acknowledgments

The authors would like to thank the associate editor and the reviewers for their useful feedback that helped improve this paper.

Conflict of interest

The authors declare that the research was conducted in the absence of any commercial or financial relationships that could be construed as a potential conflict of interest.

Publisher's note

All claims expressed in this article are solely those of the authors and do not necessarily represent those of their affiliated organizations, or those of the publisher, the editors and the reviewers. Any product that may be evaluated in this article, or claim that may be made by its manufacturer, is not guaranteed or endorsed by the publisher.

Supplementary material

The Supplementary Material for this article can be found online at: https://www.frontiersin.org/articles/10.3389/fbioe.2023.1277970/full#supplementary-material

References

Ambekar, R., Toussaint, K. C., and Wagoner Johnson, A. (2011). The effect of keratoconus on the structural, mechanical, and optical properties of the cornea. *J. Mech. Behav. Biomed. Mater.* 4 (3), 223–236. doi:10.1016/j.jmbbm.2010.09.014

Ariza-Gracia, M., Zurita, J. F., Piñero, D. P., Rodriguez-Matas, J. F., and Calvo, B. (2015). Coupled biomechanical response of the cornea assessed by non-contact tonometry. A simulation study. *PLoS One* 10(3), e0121486. doi:10.1371/journal.pone.0121486

Ariza-Gracia, M. Á., Wu, W., Calvo, B., Malvè, M., Büchler, P., and Rodriguez Matas, J. F. (2018). Fluid–structure simulation of a general non-contact tonometry. A required complexity? *Comput. Methods Appl. Mech. Eng.* 340, 202–215. doi:10.1016/j.cma.2018.05.031

Bao, F. J., Geraghty, B., Wang, Q. M., and Elsheikh, A. (2016). Consideration of corneal biomechanics in the diagnosis and management of keratoconus: is it important? *Eye Vis.* 3 (1), 18–21. doi:10.1186/s40662-016-0048-4

Brooks, A. M. V., Robertson, I. F., and Mahoney, A. M. (1984). Ocular rigidity and intraocular pressure in keratoconus. *Aust. J. Opthalmology* 12 (4), 317–324. doi:10.1111/j.1442-9071.1984.tb01175.x

Brunton, S. L., Noack, B. R., and Koumoutsakos, P. (2020). Machine learning for fluid mechanics. *Annu. Rev. Fluid Mech.* 52, 477–508. doi:10.1146/annurev-fluid-010719-060214

Eliasy, A., Chen, K. J., Vinciguerra, R., Lopes, B. T., Abass, A., Vinciguerra, P., et al. (2019). Determination of corneal biomechanical behavior *in-vivo* for healthy eyes using CorVis ST tonometry: stress-strain index. *Front. Bioeng. Biotechnol.* 7, 105. doi:10.3389/fbioe.2019.00105

Elsheikh, A., Geraghty, B., Rama, P., Campanelli, M., and Meek, K. M. (2010). Characterization of age-related variation in corneal biomechanical properties. *J. R. Soc. Interface* 7 (51), 1475–1485. doi:10.1098/rsif.2010.0108

Friedman, J., Tibshirani, R., and Hastie, T. (2000). Additive logistic regression: a statistical view of boosting (With discussion and a rejoinder by the authors). *Ann. Statistics* 28 (2), 337–407. doi:10.1214/aos/1016218223

Friedman, J. H. (2001). *Greedy function approximation: a gradient boosting machine*.

Kling, S., Bekesi, N., Dorronsoro, C., Pascual, D., and Marcos, S., "Corneal viscoelastic properties from finite-element analysis of *in vivo* air-puff deformation," *PLoS One*, vol. 9, no. e104904, 8, . 2014, doi:10.1371/journal.pone.0104904

Koprowski, R. (2014). Automatic method of analysis and measurement of additional parameters of corneal deformation in the Corvis tonometer. *Biomed. Eng. Online* 13 (1), 150. doi:10.1186/1475-925X-13-150

Kutz, J. N. (2017). Deep learning in fluid dynamics. *J. Fluid Mech.* 814, 1–4. doi:10.1017/jfm.2016.803

Liu, J., and Roberts, C. J. (2005). Influence of corneal biomechanical properties on intraocular pressure measurement: quantitative analysis. *J. Cataract. Refract Surg.* 31 (1), 146–155. doi:10.1016/j.jcrs.2004.09.031

Luce, D. (2005). Air–jet temporal and spatial pressure properties of the reichert ocular response analyzer (ORA). *Investig. Ophthalmol. Vis. Sci.* 46 (13), 5009.

Maklad, O. (2019). *Influence of fluid structure interaction on human eye biomechanics under air puff non-contact tonometry*. Ph. D. Thesis, no. uk.bl.ethos.778526, Available at: https://ethos.bl.uk/OrderDetails.do?uin=uk.bl.ethos.778526.

Maklad, O., Eliasy, A., Chen, K. J., Theofilis, V., and Elsheikh, A. (2020b). Simulation of air puff tonometry test using arbitrary Lagrangian–eulerian (ALE) deforming mesh for corneal material characterisation. *Int. J. Environ. Res. Public Health* 17 (1), 54. doi:10.3390/ijerph17010054

Maklad, O., Eliasy, A., Chen, K. J., Wang, J., Abass, A., Lopes, B. T., et al. (2020a). Fluid-structure interaction based algorithms for IOP and corneal material behavior. *Front. Bioeng. Biotechnol.* 8 (Aug), 970. doi:10.3389/fbioe.2020.00970

Maklad, O., Theofilis, V., and Elsheikh, A. (2018). "Fluid structure interaction (FSI) simulation of the human eye under the air puff tonometry using computational fluid dynamics (CFD)," in *10th international conference on computational fluid dynamics, ICCFD 2018 - proceedings*. Available at: https://www.iccfd.org/iccfd10/papers/ICCFD10-017-Paper.pdf.

Maklad, O., Theofilis, V., and Elsheikh, A. (2021). *Role of impinging jets in the biomechanical correction of the intraocular pressure (IOP) measurement*.

Muench, S., Roellig, M., Spoerl, E., and Balzani, D. (2019). Numerical and experimental study of the spatial stress distribution on the cornea surface during a non-contact tonometry examination. *Exp. Mech.* 59 (9), 1285–1297. doi:10.1007/s11340-018-00449-0

Patel, S., and McLaughlin, J. M. (1999). Effects of central corneal thickness on measurement of intra-ocular pressure in keratoconus and post-keratoplasty. *Ophthalmic Physiological Opt.* 19 (3), 236–241. doi:10.1046/j.1475-1313.1999.00420.x

Read, S. A., and Collins, M. J. (2011). Intraocular pressure in keratoconus. *Acta Ophthalmol.* 89 (4), 358–364. doi:10.1111/j.1755-3768.2009.01690.x

Simonini, I., and Pandolfi, A. (2016). The influence of intraocular pressure and air jet pressure on corneal contactless tonometry tests. *J. Mech. Behav. Biomed. Mater* 58, 75–89. doi:10.1016/j.jmbbm.2015.07.030

sklearn.ensemble.GradientBoostingRegressor (2020). *Gradient tree boosting*. Available at: https://scikitlearn.org/stable/modules/generated/sklearn.ensemble.GradientBoostingRegressor.html.

Stevens, G. A., White, R. A., Flaxman, S. R., Price, H., Jonas, J. B., Keeffe, J., et al. (2013). Global prevalence of vision impairment and blindness: magnitude and temporal trends, 1990-2010. *Ophthalmology* 120 (12), 2377–2384. doi:10.1016/j.ophtha.2013.05.025

Usman, A., Rafiq, M., Saeed, M., Nauman, A., Almqvist, A., and Liwicki, M. (2021). "Machine learning computational fluid dynamics," in *33rd workshop of the Swedish artificial intelligence society* (SAIS), 2021. doi:10.1109/SAIS53221.2021.9483997

Yousefi, A., Roberts, C. J., and Reilly, M. A., "The shape of corneal deformation alters air puff–induced loading," *Front. Bioeng. Biotechnol.*, vol. 10, 848060, . 2022, doi:10.3389/fbioe.2022.848060

10.3389/fbioe.2023.1277970

Nomenclature

IOP	Intraocular Pressure
CCT	Central Corneal Thickness
FE	Finite Element
CFD	Computational Fluid Dynamics
FSI	Fluid-Structure Interaction
ORA	Ocular Response Analyser
CorVis-ST	Corneal Visualisation Scheimpflug Technology
ALE	Arbitrary Lagrangian-Eulerian
ML	Machine Learning
GBM	Gradient Boosting Machines
GBR	Gradient Boosting Regressor

frontiers | Frontiers in Bioengineering and Biotechnology

TYPE Original Research
PUBLISHED 06 December 2023
DOI 10.3389/fbioe.2023.1273500

OPEN ACCESS

EDITED BY
Matthew A. Reilly,
The Ohio State University, United States

REVIEWED BY
Yingxue Zhang,
Wayne State University, United States
Fulvio Ratto,
National Research Council (CNR), Italy
Junjie Wang,
Wenzhou Medical University, China

*CORRESPONDENCE
Kaili Yang,
kelly1992abc@163.com

RECEIVED 06 August 2023
ACCEPTED 15 November 2023
PUBLISHED 06 December 2023

CITATION
Ren S, Yang K, Xu L, Fan Q, Gu Y, Pang C and Zhao D (2023), Machine learning analysis with the comprehensive index of corneal tomographic and biomechanical parameters in detecting pediatric subclinical keratoconus.
Front. Bioeng. Biotechnol. 11:1273500.
doi: 10.3389/fbioe.2023.1273500

Machine learning analysis with the comprehensive index of corneal tomographic and biomechanical parameters in detecting pediatric subclinical keratoconus

Shengwei Ren, Kaili Yang*, Liyan Xu, Qi Fan, Yuwei Gu, Chenjiu Pang and Dongqing Zhao

Henan Provincial People's Hospital, Henan Eye Hospital, Henan Eye Institute, People's Hospital of Zhengzhou University, Henan University People's Hospital, Zhengzhou, China

Background: Keratoconus (KC) occurs at puberty but diagnosis is focused on adults. The early diagnosis of pediatric KC can prevent its progression and improve the quality of life of patients. This study aimed to evaluate the ability of corneal tomographic and biomechanical variables through machine learning analysis to detect subclinical keratoconus (SKC) in a pediatric population.

Methods: Fifty-two KC, 52 SKC, and 52 control pediatric eyes matched by age and gender were recruited in a case-control study. The corneal tomographic and biomechanical parameters were measured by professionals. A linear mixed-effects test was used to compare the differences among the three groups and a least significant difference analysis was used to conduct pairwise comparisons. The receiver operating characteristic (ROC) curve and the Delong test were used to evaluate diagnostic ability. Variables were used in a multivariate logistic regression in the machine learning analysis, using a stepwise variable selection to decrease overfitting, and comprehensive indices for detecting pediatric SKC eyes were produced in each step.

Results: PE, BAD-D, and TBI had the highest area under the curve (AUC) values in identifying pediatric KC eyes, and the corresponding cutoff values were 12 μm, 2.48, and 0.6, respectively. For discriminating SKC eyes, the highest AUC (95% CI) was found in SP A1 with a value of 0.84 (0.765, 0.915), and BAD-D was the best parameter among the corneal tomographic parameters with an AUC (95% CI) value of 0.817 (0.729, 0.886). Three models were generated in the machine learning analysis, and Model 3 (y = 0.400*PE + 1.982* DA ratio max [2 mm]−0.072 * SP A1−3.245) had the highest AUC (95% CI) value, with 90.4% sensitivity and 76.9% specificity, and the cutoff value providing the best Youden index was 0.19.

Abbreviations: KC, Keratoconus; SKC, Subclinical keratoconus; ROC, Receiver operating characteristic; BAD-D, Belin Ambrosio enhanced ectasia total deviation index; CDVA, Corrected distance visual acuity; K1 F, Flat keratometry; K2 F, Steep keratometry; Ka, Corneal keratometric astigmatism; Kmax F, The maximum keratometry; Kmean F, Mean keratometry; ACT, Corneal thickness at the pachy apex; PCT, Corneal thickness at the pupil's center; TCT, Corneal thickness at the thinnest point of the cornea; FE, Anterior evaluation; PE, Posterior elevation; IOP, Intraocular pressure; bIOP, Biomechanical corrected intraocular pressure; ARTh, Ambrósio's relational thickness horizontal; SP A1, Stiffness parameter at the first applanation; CBI, Corvis biomechanical index; SSI, Stress-strain index; TBI, Tomographic and biomechanical index; LSD, Least significant difference; AUC, Area under the receiver operating characteristic curve; CI, Confidence interval.

Conclusion: The criteria of parameters for diagnosing pediatric KC and SKC eyes were inconsistent with the adult population. Combined corneal tomographic and biomechanical parameters could enhance the early diagnosis of young patients and improve the inadequate representation of pediatric KC research.

KEYWORDS

pediatric keratoconus, subclinical keratoconus, corneal tomographic parameters, corneal biomechanical parameters, machine learning, diagnosis ability

1 Introduction

Keratoconus (KC) is a corneal disorder characterized by an anterior protrusion of the cornea and corneal thinning. (Gomes et al., 2015). It affects all ethnic groups, with the highest prevalence reported in China (0.9%, approximately 12.5 million), India (2.3%, approximately 30 million), and Iran (4% of the rural population, approximately 3.4 million). (Hashemi et al., 2020; Rafat et al., 2022). KC is the leading indication for corneal transplantation, accompanied by serious vision deterioration and irregular astigmatism, and the social and financial burden is remarkable. (Rebenitsch et al., 2011; Rafat et al., 2022).

As a progressive disease, KC typically occurs at puberty and continues to progress until the third or fourth decade of life. (Mukhtar and Ambati, 2018). In addition, several studies have reported that KC is more frequently presented at an advanced stage in young patients than in adults, and pediatric patients with limited cognitive ability are less aware of unilateral visual loss. (Leoni-Mesplie et al., 2012; Ferdi et al., 2019). The persistent underrepresentation of children in KC research has resulted in an inadequate evidence base; therefore, increasing attention to pediatric KC patients is of great value in evaluating the occurrence and development of KC.

Moderate or severe stages of KC are easily diagnosed according to slit lamp findings and topography signs, whereas the detection of abnormal corneas in very early stages or subclinical forms is still a challenge for clinicians. (Mas Tur et al., 2017; Cao et al., 2021; Zhang et al., 2022). Epidemiological studies have revealed that corneal topographic, tomographic, and biomechanical parameters can accurately distinguish a KC or subclinical KC (SKC) eye from a normal eye. (Vinciguerra et al., 2016; Sedaghat et al., 2018; Kataria et al., 2019; Koh et al., 2019). However, the above study mostly focused on adults, who received examinations before refractive surgery mainly to avoid postoperative ectasia. As the clinical manifestation of KC in children is somewhat different from adults, the diagnosis results obtained in adults may not apply to pediatric patients. (Mukhtar and Ambati, 2018; Anitha et al., 2021). However, the diagnosis of pediatric KC is still limited. (Leoni-Mesplie et al., 2012; Wajnsztajn et al., 2021). A retrospective observational study conducted in Egypt reported the eight most useful Pentacam indices in identifying 48 eyes of pediatric KC and SKC. (Hashem et al., 2022). Furthermore, the corneal biomechanics, which are thought to be the initiators of the disease even before notable changes in corneal morphology, were not evaluated in the above study. (Scarcelli et al., 2014; Vinciguerra et al., 2016). A prospective study conducted in Atlanta showed that pediatric KC patients with trisomy 21 had thinner corneas and lower corneal resistance factors than control patients, which were inconsistent with the results in adults. (Neustein and Lenhart, 2022). The above corneal biomechanics were measured by ORA, which has a limited examination area on the cornea and a worse discriminative ability in KC eyes than Corvis ST. (Esporcatte et al., 2023). As an ultra-high speed Scheimpflug camera, Corvis ST can produce various corneal biomechanical parameters and its discriminative ability has been demonstrated to be high in adults. Additionally, studies in pediatric KC patients have been limited. (Vinciguerra et al., 2016; Kataria et al., 2019).

With the advancement of technology, machine learning methods can improve diagnostic ability by incorporating a large amount of data. (Angraal et al., 2020). Several studies have reported the application of machine learning techniques in the field of KC and refractive surgery screening; however, their application has been limited in pediatric KC patients. (Ruiz Hidalgo et al., 2016; Malyugin et al., 2021). Thus, the current study aimed to evaluate the clinical characteristics of KC and SKC eyes in pediatric patients, and explore the diagnostic ability of corneal tomographic and biomechanical parameters in discriminating pediatric SKC eyes, to provide references for the early diagnosis and management of pediatric patients.

2 Materials and methods

2.1 Study participants

This case-control study enrolled 52 control eyes, 52 SKC eyes, and 52 KC eyes of individuals aged <18 years between January 2019 and January 2022 in the Henan Eye Hospital. KC was included as per previous criteria: (Yang et al., 2022): an asymmetric bowtie pattern with or without skewed axes, a Belin Ambrosio enhanced ectasia total deviation index (BAD-D) value > 2.6 by corneal topography, and a positive slit-lamp sign (localized stromal thinning, Vogt's striae, Fleischer's ring, conical protrusion, or anterior stromal scar). The SKC eye in the current study was defined as no clear evidence of KC in one eye, with the contralateral eye meeting the above KC diagnostic criteria. (Ren et al., 2021). The detailed criteria of SKC eye are as follows: without an asymmetric bowtie pattern, a BAD-D value ≤ 2.6 by corneal topography, and no positive slit-lamp sign. Volunteers with a spherical equivalent <8.00 diopters (D), astigmatism <2.00 D, corrected distance visual acuity (CDVA) ≥0.8, and normal corneal topography were recruited in the control group. Eyes with an anterior stromal scar, acute corneal hydrops, soft contact lens wear within the last 2 weeks, rigid contact lens wear within the last 4 weeks, ocular trauma history, ocular surgery history, and other ocular disease history were excluded in the current analysis. Finally,

52 KC eyes, 52 SKC eyes, and 52 control eyes (52 subjects) in pediatric patients matched with age (less than 3 years) and gender were recruited in the analysis.

This study was conducted according to the Declaration of Helsinki guidelines and approved by the Institutional Review Board of the Henan Eye Hospital [ethical approval number: HNEECKY-2019 (5)]. Informed consent was obtained from the legal guardians of pediatric patients.

2.2 Examinations

The clinical examinations were conducted when the patients were first referred to the center. All measurements (slit-lamp examination, CDVA in the logarithm of the minimum angle of resolution (logMAR) unit, corneal tomographic, and biomechanical measurements) were obtained by experienced operators between 9:00 and 17:00.

The Pentacam HR (Oculus, Wetzlar, Germany, software number: 1.21r41) is a corneal topography system that uses a rotating high-resolution camera to analyze the anterior segment of the eye. (de Luis Eguileor et al., 2018). The finding with a high-quality factor was recorded for each eye, and the following parameters were analyzed: the central 3.0 mm of the anterior corneal surface in terms of flat keratometry (K1 F), steep keratometry (K2 F), corneal keratometry astigmatism (Ka, the value of K2 minus K1), maximum keratometry (Kmax F), and mean keratometry (Kmean F), the corneal thickness at the pachy apex (ACT), the pupil's center (PCT), the thinnest point of the cornea (TCT), the thinnest corneal point (front (FE) and posterior elevation values (PE)), and BAD-D values. The Corvis ST (Oculus, Wetzlar, Germany, software number: 1.6b2224) collects parameters during the first applanation, highest concavity, and second applanation phases. (Vinciguerra et al., 2016). The intraocular pressure (IOP), biomechanical corrected intraocular pressure (bIOP), maximum value of the ratio between the deformation amplitude at the apex 1 mm and 2 mm from the central cornea (DA ratio max [1 mm] and DA ratio max [2 mm]), maximum inverse radius, integrated radius, Ambrósio's relational thickness horizontal (ARTh), stiffness parameter at the first applanation (SP A1), Corvis biomechanical index (CBI), and stress-strain index (SSI) were recorded. In addition, the tomographic and biomechanical index (TBI) was obtained by combining Pentacam HR and Corvis ST measurements.

2.3 Analytical Tools and methods

The median and interquartile ranges (P25 and P75) were applied to describe qualitative data. A linear mixed-effects test was used to compare the differences among the three groups and a least significant difference (LSD) analysis was used to conduct pairwise comparisons. The comparisons of corneal biomechanical parameters among different groups have been corrected to adjust for corneal thickness and IOP. (Ren et al., 2021). The receiver operating characteristic (ROC) curve and the Delong test were used to evaluate the diagnostic ability of distinguishing SKC and KC eyes from control eyes. Among that, cutoff (the classification effect is best), sensitivity (the ability of the model to detect patients), specificity (the ability of the model to identify non-patients), Youden index (the sum of sensitivity and specificity minus 1), and area under the ROC curve (AUC, a higher value reflects a better accuracy rate) values and 95% confidence interval (CI) were recorded. (Mandrekar, 2010). The machine learning analysis was conducted through multivariate logistic regression using SPSS 23.0, and the logistic regression was used with forward stepwise selection to choose variables with statistically significant results ($p < 0.05$) in a likelihood ratio test to decrease overfitting. (Angraal et al., 2020). Three steps were generated in the analysis and each step formed a model in the analysis, and the ability of the model to detect pediatric SKC eyes was evaluated through ROC analysis using MedCalc software. $p < 0.05$ (two-tailed) was considered as a statistically significant difference.

3 Results

3.1 Characteristics of the general parameters

In the present study, the male and female ratio was 42:10 and the median age was 16 years (12.25, 17) and 15.5 years (14, 16.75) for the control and KC patients, respectively ($p = 0.320$). SKC eyes and control eyes had higher CDVA (LogMAR) values than KC eyes ($p < 0.05$), and no significant difference was found in the two groups ($p = 1.000$, Table 1).

3.2 Comparisons of the parameters in pediatric control, SKC and KC eyes

Significant differences in corneal tomographic and corneal biomechanical parameters were found among control, SKC and KC eyes in pediatric subjects ($p < 0.05$, Supplementary Tables S1, S2). Pairwise analyses found that SKC eyes of pediatric patients had lower ACT, PCT, and TCT values and higher PE and BAD-D values than control eyes (all $p < 0.05$, Figure 1). Furthermore, KC and SKC eyes had higher TBI values and lower SP A1 values than control eyes after adjusting for IOP and corneal thickness ($p < 0.05$, Figure 2).

3.3 Diagnostic ability of corneal tomographic and biomechanical parameters

Supplementary Table S3 shows the ability of corneal parameters to identify pediatric KC eyes. For corneal tomographic parameters, PE and BAD-D had the highest diagnostic values (AUC = 1), and the corresponding cutoff values were 12 μm and 2.48, respectively. For corneal biomechanical parameters, CBI and SP A1 were excellent, with AUC values of 0.990 (cutoff value: 0.53) and 0.985 (cutoff value: 96.69), respectively. Combined parameters of TBI also had the highest diagnostic values (AUC = 1) at a cutoff value of 0.60 (Figure 3A).

Additionally, the AUC values of corneal parameters in identifying pediatric SKC eyes are shown in Figure 3B. BAD-D was the best parameter among the corneal tomographic parameters, with an AUC (95% CI) value of 0.817 (0.729, 0.886), and the cutoff value providing the best Youden index was 1.14. For corneal biomechanical parameters, the highest AUC (95% CI) was found in SP A1 with 0.840 (0.765, 0.915), and the cutoff value providing the best Youden index was 108.33 mmHg/mm. This was followed by

TABLE 1 Comparisons of general parameters among control, SKC and KC eyes in pediatric subjects.

Parameters	Control (N = 52)	SKC (N = 52)	KC (N = 52)	*P**	$P^{\#1}$	$P^{\#2}$	$P^{\#3}$
Gender, n (%)				1.000	-	-	-
Male	42 (80.16)	42 (80.16)	42 (80.16)				
Female	10 (19.23)	10 (19.23)	10 (19.23)				
Age, M (P25, P75)	16.00 (12.25, 17.00)	15.50 (14.00, 16.75)	15.50 (14.00, 16.75)	0.320	-	-	-
CDVA (LogMAR), M (P25, P75)	0 (0, 0)	0 (0, 0)	0.30 (0.15, 0.52)	<0.001	1.000	<0.001	<0.001

*Kruskal–Wallis test; #1 control vs. SKC; #2 control vs. KC; #3 SKC vs. KC.
SKC, subclinical keratoconus; KC, keratoconus; CDVA, corrected distance visual acuity.

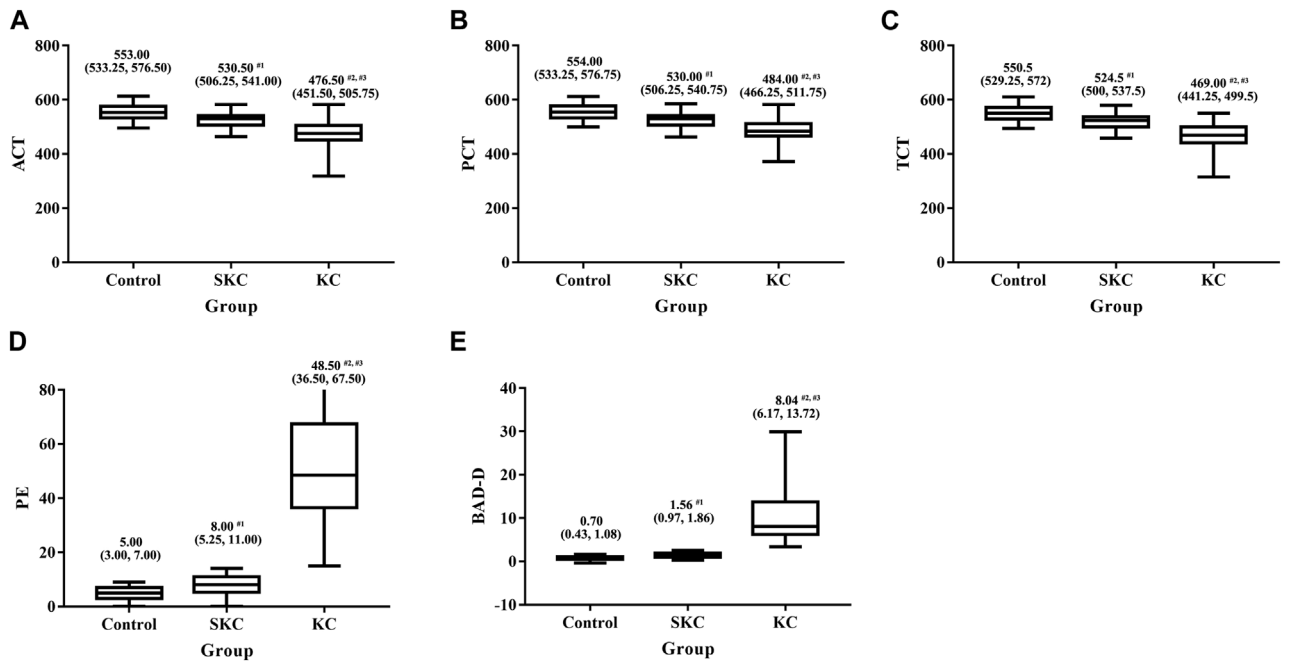

FIGURE 1
Box plot for significantly different corneal tomographic parameters among control, SKC, and KC eyes in pediatric subjects. **(A)** ACT: the corneal thickness at the pachy apex. **(B)** PCT: the corneal thickness at the pupil's center. **(C)** TCT: corneal thickness at the thinnest point of the cornea. **(D)** PE: the posterior thinnest corneal point. **(E)** BAD-D: Belin Ambrosio enhanced ectasia total deviation index. Bars represent the median (P25, P75). $p < 0.001$ for all three groups. $^{\#1}p<0.05$ for SKC vs. control; $^{\#2}p<0.05$ for KC vs. control; $^{\#3}p<0.05$ for KC vs. SKC.

integrated radius and DA ratio max [2 mm], which had AUC values of 0.811 (cutoff value: 8.89) and 0.810 (the cutoff value: 4.37), respectively. The AUC (95% CI) of TBI was 0.784 (0.692, 0.859) and the cutoff value providing the best Youden index was 0.35. The diagnostic abilities of other parameters are shown in Supplementary Table S4.

3.4 Diagnostic ability of comprehensive parameters to detect SKC eye

Three models were separately generated from each step of the multivariate logistic regression in the machine learning analysis (Supplementary Table S5). The ability of comprehensive indices in detecting pediatric SKC eyes is shown in Table 2 and Figure 4. Model 3 (y = 0.400*PE +1.982* DA ratio max [2 mm]−0.072*SP A1−3.245) had the highest AUC (95% CI) value, with a sensitivity of 90.4% and a specificity of 76.9%, and the cutoff value providing the best Youden index was 0.19. Further pairwise comparisons indicated that the AUC value of Model 3 was higher than BAD, CBI, TBI, and Model 1($p<0.05$), and no significant difference was found compared with Model 2 (y = 0.314*PE−0.097*SP A1+8.590, $p > 0.05$, Supplementary Table S6).

4 Discussion

As KC in young patients is reported to be more likely to progress than in adults, the sensitivity index and cutoff values of parameters in pediatric patients is different than in adult patients. (Hashem et al., 2022; Neustein and Lenhart, 2022). The machine learning analysis, analyzing a large number of variables, found that the

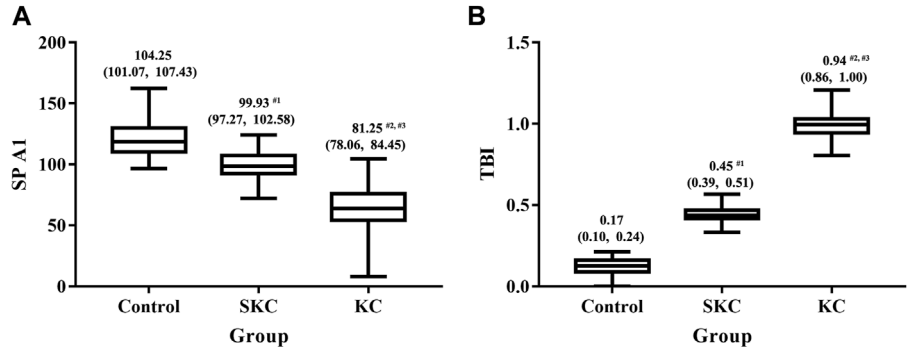

FIGURE 2
Box plot for SPA1 and TBI among control, SKC, and KC eyes in pediatric subjects. **(A)** SP A1: stiffness parameter at the first applanation. **(B)** TBI: tomographic and biomechanical index. Bars represent the median (P25, P75). $p < 0.001$ for all three groups. $^{\#1}p<0.05$ for SKC vs. control; $^{\#2}p<0.05$ for KC vs. control; $^{\#3}p<0.05$ for KC vs. SKC.

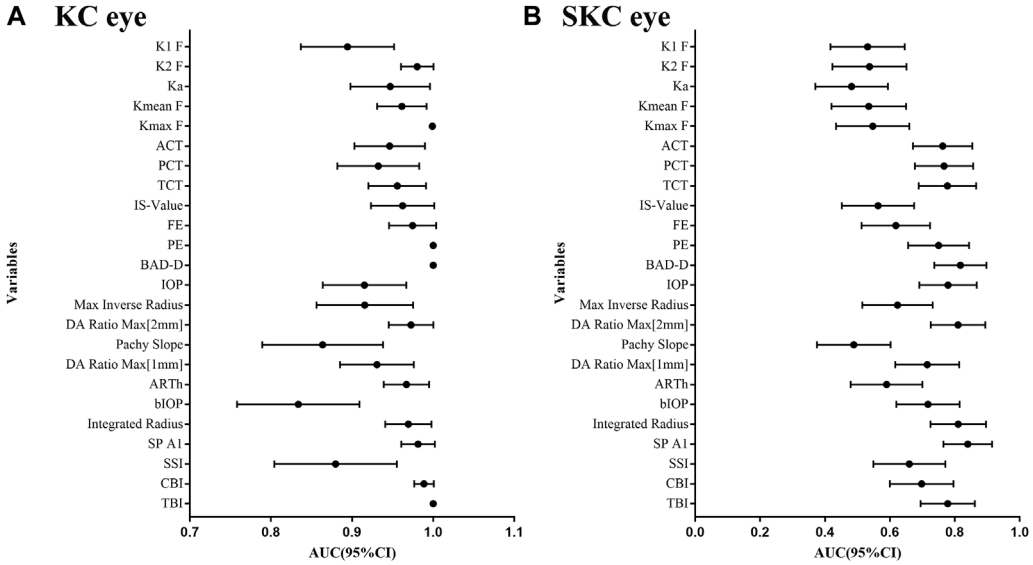

FIGURE 3
AUC values for corneal tomographic and biomechanical variables in diagnosing pediatric SKC and KC eyes. **(A)** Pediatric KC eyes. **(B)** pediatric SKC eyes.

comprehensive index, containing PE, DA ratio max [2 mm], and SP A1, improved the diagnostic capability to differentiate pediatric SKC eyes.

Pentacam is one of the most common techniques in clinical application, as the uniqueness of this device is that it includes tomographic data, topometric data, pachymetry, elevation data, and combined data. (Motlagh et al., 2019). In the present study, BAD-D and PE were highly capable of differentiating pediatric KC and SKC eyes, which was consistent with previous findings in adult patients with similar criteria. BAD-D is a multivariate index that considers several separate indices, and its AUC value in diagnosing adult KC was 0.990, and the cutoff value providing the best Youden index was 2.38 in the study by Hashemi et al., 2016. In the study by Ambrosio et al. (2013) the AUC value in detecting adult SKC eyes was 0.975 and the cutoff value providing the best Youden index was 1.22. PE represents the maximum evaluation of the corneal posterior in a zone above the standardized reference shape, and this variable is widely regarded as the earliest indicator of ecstatic change. (Saad and Gatinel, 2010; Motlagh et al., 2019). The AUC value of PE in diagnosing adult KC was 0.991, and the cutoff value providing the best Youden index was 12 μm in the study by Ambrosio et al., 2013. The AUC value in detecting SKC was 0.882 and the cutoff value providing the best Youden index was 7.5 μm in the study by Du XL et al. (Du et al., 2015), which were both higher than in pediatric patients at the same cutoff values in the current study. In general, the diagnostic efficacy of corneal tomographic variables in pediatric patients was higher than in adult patients at a similar cutoff value, which suggested that

TABLE 2 Ability of comprehensive indices in distinguishing pediatric SKC eyes from control eyes.

Parameters	Cutoff	Specificity	Sensitivity	Youden index	AUC (95% CI)
BAD	1.14	0.827	0.673	0.500	0.817 (0.729, 0.886)
CBI	0.02	0.789	0.615	0.404	0.698 (0.600, 0.784)
TBI	0.35	0.942	0.519	0.462	0.784 (0.692, 0.859)
Model 1	>0.01	0.846	0.692	0.539	0.840 (0.755, 0.904)
Model 2	>0.53	0.923	0.692	0.615	0.879 (0.801, 0.935)
Model 3	>0.19	0.904	0.769	0.673	0.909 (0.837, 0.957)

AUC, area of receiver operating characteristic curve; CI, confidence interval; BAD-D, belin ambrosio enhanced ectasia total deviation index; CBI, corvis biomechanical index; TBI, tomographic and biomechanical index.
Model 1 y = −0.105*SP A1+11.405.
Model 2 y = 0.314*PE−0.097*SP A1+8.590.
Model 3 y = 0.400*PE +1.982* DA ratio max [2 mm]−0.072*SP A1−3.245.

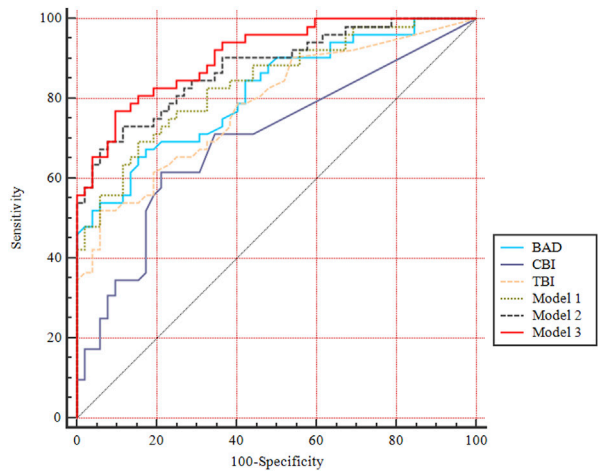

FIGURE 4
ROC curves of comprehensive indices for diagnosing pediatric SKC eyes. BAD-D, Belin Ambrosio enhanced ectasia total deviation index; CBI, Corvis biomechanical index; TBI, tomographic and biomechanical index. Model 1, y =−0.105*SP A1+11.405; Model 2, y = 0.314*PE−0.097*SP A1+8.590; Model 3, y = 0.400*PE +1.982* DA ratio max [2 mm]−0.072*SP A1−3.245.

caution is warranted when using these parameters in different age groups. (Hashem et al., 2022).

The diagnostic criteria of corneal tomographic parameters in pediatric KC are still limited. (Motlagh et al., 2019; Hashem et al., 2022). A prospective study reported that pediatric KC with trisomy 21 has a thinner cornea, with a lower TCT and higher values of Kmax and K2 than normal children, which was consistent with the current results. (Neustein and Lenhart, 2022). In addition, the current study found that the CCT and K1 were significantly different between KC and the control, whereas no significant difference was found in the study by Neustein and Lenhart, 2022 These discrepancies may be attributed to the sample size, ethnicity, and characters of the subjects. In addition, Hashem et al., 2022 reported that relational thickness and other OCULUS values analyzed for the 8-mm zone (CAIRO 8) were the most effective for KC detection in pediatric eyes, which is inconsistent with the present study. On one hand, the parameters included in the analyses were not completely consistent, e.g., BAD-D, which has been widely demonstrated to be one of the best indices for identifying KC and SKC eyes, was not mentioned in the study by Hashem AO et al., and CAIRO 8 was not analyzed in the present study. (Hashemi et al., 2016; Hashem et al., 2022). On the other hand, Hashem et al., 2022 included 40 KC and 8 SKC eyes as a whole case group, despite the inconsistency between SKC and KC eyes, and the KC and SKC eyes were analyzed separately in the current study. The limited sample of pediatric SKC eyes would result in a lack of research evidence of the diagnosis criteria of pediatric SKC eyes. In addition, our previous study reported that pediatric unilateral patients account for 7.82% of all KC patients (86/1,100), (Yang et al., 2022), which might be related to the fact that the minimum age approved for corneal refractive surgery is 18 years and corneal tomography and biomechanics are not commonly examined in children. (Ortega-Usobiaga et al., 2022). Thus, more attention should be paid to children with sight loss, and deep studies are needed to further verify the ability of corneal topographic parameters in pediatric patients.

With the increasing understanding that the changes in corneal biomechanics precede tomography, more attention has been focused on corneal biomechanics in the early diagnosis of KC. (Vinciguerra et al., 2016; Moshirfar et al., 2019; Herber et al., 2022). Corvis ST has been increasingly evaluated in the detection of early adult KC. Evidence of Corvis ST parameters in pediatric KC and SKC is still lacking. (Li et al., 2023). SP A1 is a novel stiffness parameter that is defined as resultant pressure divided by deflection at the first applanation, and the KC eye tends to have a smaller value that represents a weaker cornea. (Vinciguerra et al., 2016; Yang et al., 2020). The present study found that SP A1 in pediatric SKC eyes was lower than that in control eyes after adjusting for IOP and corneal thickness, which indicated that the cornea of the pediatric SKC eye weakened. In addition, the abilities of CBI, SP A1, and DA ratio max (2 mm) in diagnosing pediatric KC eyes were high, which was consistent with previous studies of adult KC. (Kataria et al., 2019; Moshirfar et al., 2019; Ren et al., 2021). DA ratio max [2 mm] is the deformation amplitude measured 2 mm from the corneal center, and a higher value represents a softer cornea or one that is less resistant to cornea deformation. (Yang et al., 2019). CBI, a parameter of the logistic regression analysis, was useful in discriminating KC when the value was higher than 0.5.

(Vinciguerra et al., 2016). The AUCs of SP A1 and integrated radius in the present study were higher than those in a previous study of adult SKC patients, which further indicated that the corneal tests for the evaluation of adults might not be reliable at identifying pediatric patients. (Neustein and Lenhart, 2022). Integrated radius is the integrated area under the curve of the inverse radius, and the KC eye has a higher value than the normal eye. (Ren et al., 2021). In addition, the accuracy of CBI in detecting adult SKC is excellent and relatively higher than that in pediatric SKC eyes in the present study. (Kataria et al., 2019; Ren et al., 2021). The results suggested that the criteria and cutoff values of corneal biomechanics in adult KC and SKC may not suitable for pediatric patients, which should be paid more attention to in clinical application and more comparative studies are needed in the future.

TBI is combined data that are synergistically integrated and has been widely demonstrated to be useful in detecting corneal ectasia. (Koh et al., 2019; Moshirfar et al., 2019). The present study found that TBI was the best variable in detecting pediatric KC eyes. As for diagnosing pediatric SKC eyes, the AUC of TBI in the present study was lower than that in adult SKC eyes. (Ambrosio et al., 2017; Koc et al., 2019). In addition, the ability of TBI was weaker than the combined model obtained through machine analysis. The comprehensive index of PE, DA ratio max [2 mm], and SP A1 could effectively discriminate pediatric SKC eyes from control eyes, providing a reference for exploring the early detection of pediatric patients. The current diagnosis criteria included corneal tomographic and corneal biomechanical parameters, and the accuracy of diagnosing pediatric SKC eye was significantly higher than CBI, DA ratio max [2 mm], SP A1, PE, and integrated radius. Several dynamic corneal response (DCR) parameters of insufficient diagnostic ability could improve the diagnostic ability but cannot currently be considered standalone parameters for screening purposes. (Ali et al., 2014). The accuracy of other DCR variables in detecting SKC eyes was limited reported, and the combined diagnostic mechanism of these parameters needs further evaluation in engineering mechanics.

At present, insufficient attention is being paid to vision loss in children, which has a higher progressive rate than adult patients. Early diagnosis of pediatric KC and further effective early treatments can prevent the need for corneal transplantation and improve the quality of life of patients. (Neustein and Lenhart, 2022). Several limitations must be acknowledged. First, the sample of pediatric SKC eyes included in current study was not large enough, although the population was drawn from a relatively large KC population. Second, the study was conducted in a single center, with strict grouping criteria and matched with age and gender to control bias. Therefore, the results still need to be further validated at other centers. Third, the machine learning methods improved the prediction ability of pediatric SKC eyes, but the validation for the machine learning analysis result was lacking. Including a large number of subjects in the validation analysis is necessary and the study is ongoing and continuing to collect unilateral pediatric KC patients for further validation. Thus, a multicenter pediatric study with a large sample size is needed in the future. Finally, the present machine learning method assumed the input variables and outcomes were probably linear, and non-linear was not considered. Therefore, the possibility of assessing alternative classifiers based on algorithms other than a linear model should be conducted in the future.

In conclusion, the ability of corneal tomographic and biomechanical variables and their cutoff values in detecting pediatric KC and SKC eyes was inconsistent in adult patients, and combined parameters had better discriminative efficacy than single instrument variables in detecting SKC eyes. Relative findings will provide sensitive indices for the follow-up management of unilateral pediatric KC and a reference for the early diagnosis of children suspected to have KC.

Data availability statement

The original contributions presented in the study are included in the article/Supplementary Material, further inquiries can be directed to the corresponding author.

Ethics statement

This study was conducted according to the Declaration of Helsinki guidelines and approved by the Institutional Review Board of Henan Eye Hospital [ethical approval number: HNEECKY-2019 (5)]. Informed consent was obtained from the legal guardians of pediatric patients. The studies were conducted in accordance with the local legislation and institutional requirements. Written informed consent for participation in this study was provided by the participants' legal guardians/next of kin.

Author contributions

SR: Conceptualization, Funding acquisition, Writing–original draft, Writing–review and editing. KY: Conceptualization, Funding acquisition, Methodology, Software, Writing–original draft, Writing–review and editing. LX: Data curation, Methodology, Software, Writing–review and editing. QF: Data curation, Investigation, Validation, Writing–review and editing. YG: Data curation, Formal Analysis, Methodology, Supervision, Writing–review and editing. CP: Data curation, Investigation, Project administration, Supervision, Visualization, Writing–review and editing. DZ: Data curation, Investigation, Methodology, Resources, Validation, Visualization, Writing–review and editing.

Funding

The author(s) declare financial support was received for the research, authorship, and/or publication of this article. This research was supported by the General Project of the Natural Science Foundation of Henan Province (222300420536), Henan Provincial Medical Science Building Key Program (SBGJ202002028, SBGJ202102051, and SBGJ202303043), Henan

Provincial Medical Science and Technology Joint Program (LHGJ20210080), Henan Young Health Science and Technology Innovation Outstanding Program (YXKC2020023), Henan Provincial Science and Technology Research Project (222102310599 and 222102310307), Special Program for Basic Research of Henan Eye Hospital (20JCZD003), and Youth Special Program for Basic Research of Henan Eye Hospital (21JCQN006 and 21JCQN008). The funders had no role in the design and conduct of the study; collection, management, analysis, and interpretation of the data; preparation, review, or approval of the manuscript; and decision to submit the manuscript for publication.

Acknowledgments

All relevant data are included in the paper and its Supporting Information files. Contact KY (kelly1992abc@163.com) for additional information. The authors would like to thank all the participants of this study and Editage (www.editage.cn) for English language editing assistance.

Conflict of interest

The authors declare that the research was conducted in the absence of any commercial or financial relationships that could be construed as a potential conflict of interest.

Publisher's note

Supplementary material

The Supplementary Material for this article can be found online at: https://www.frontiersin.org/articles/10.3389/fbioe.2023.1273500/full#supplementary-material

References

Ali, N. Q., Patel, D. V., and McGhee, C. N. (2014). Biomechanical responses of healthy and keratoconic corneas measured using a noncontact scheimpflug-based tonometer. *Investigative Ophthalmol. Vis. Sci.* 55, 3651–3659. doi:10.1167/iovs.13-13715

Ambrosio, R., Jr., Lopes, B. T., Faria-Correia, F., Salomão, M. Q., Bühren, J., Roberts, C. J., et al. (2017). Integration of scheimpflug-based corneal tomography and biomechanical assessments for enhancing ectasia detection. *J. Refract. Surg. (Thorofare, N. J. 1995)* 33, 434–443. doi:10.3928/1081597x-20170426-02

Ambrosio, R., Jr., Valbon, B. F., Faria-Correia, F., Ramos, I., and Luz, A. (2013). Scheimpflug imaging for laser refractive surgery. *Curr. Opin. Ophthalmol.* 24, 310–320. doi:10.1097/icu.0b013e3283622a94

Angraal, S., Mortazavi, B. J., Gupta, A., Khera, R., Ahmad, T., Desai, N. R., et al. (2020). Machine learning prediction of mortality and hospitalization in heart failure with preserved ejection fraction. *JACC Heart Fail.* 8, 12–21. doi:10.1016/j.jchf.2019.06.013

Anitha, V., Vanathi, M., Raghavan, A., Rajaraman, R., Ravindran, M., and Tandon, R. (2021). Pediatric keratoconus - current perspectives and clinical challenges. *Indian J. Ophthalmol.* 69, 214–225. doi:10.4103/ijo.ijo_1263_20

Cao, K., Verspoor, K., Chan, E., Daniell, M., Sahebjada, S., and Baird, P. N. (2021). Machine learning with a reduced dimensionality representation of comprehensive Pentacam tomography parameters to identify subclinical keratoconus. *Comput. Biol. Med.* 138, 104884. doi:10.1016/j.compbiomed.2021.104884

de Luis Eguileor, B., Escudero Argaluza, J., Pijoan Zubizarreta, J. I., Santamaria Carro, A., and Etxebarria Ecenarro, J. (2018). Evaluation of the reliability and repeatability of scheimpflug system measurement in keratoconus. *Cornea* 37, 177–181. doi:10.1097/ico.0000000000001373

Du, X. L., Chen, M., and Xie, L. X. (2015). Correlation of basic indicators with stages of keratoconus assessed by Pentacam tomography. *Int. J. Ophthalmol.* 8, 1136–1140. doi:10.3980/j.issn.2222-3959.2015.06.10

Esporcatte, L. P. G., Salomao, M. Q., Lopes, B. T., Sena, N., Ferreira, É., Filho, J. B. R. F., et al. (2023). Biomechanics in keratoconus diagnosis. *Curr. eye Res.* 48, 130–136. doi:10.1080/02713683.2022.2041042

Ferdi, A. C., Nguyen, V., Gore, D. M., Allan, B. D., Rozema, J. J., and Watson, S. L. (2019). Keratoconus natural progression: a systematic review and meta-analysis of 11 529 eyes. *Ophthalmology* 126, 935–945. doi:10.1016/j.ophtha.2019.02.029

Gomes, J. A., Tan, D., Rapuano, C. J., Belin, M. W., Ambrósio, R., Guell, J. L., et al. (2015). Global consensus on keratoconus and ectatic diseases. *Cornea* 34, 359–369. doi:10.1097/ico.0000000000000408

Hashem, A. O., Aziz, B. F., Wahba, S. S., Roshdy, M. M., and Elawamry, A. I. (2022). *Diagnostic accuracy of different keratoconus detection indices of pentacam in paediatric eyes*. London, England: Eye.

Hashemi, H., Beiranvand, A., Yekta, A., Maleki, A., Yazdani, N., and Khabazkhoob, M. (2016). Pentacam top indices for diagnosing subclinical and definite keratoconus. *J. Curr. Ophthalmol.* 28, 21–26. doi:10.1016/j.joco.2016.01.009

Hashemi, H., Heydarian, S., Hooshmand, E., Saatchi, M., Yekta, A., Aghamirsalim, M., et al. (2020). The prevalence and risk factors for keratoconus: a systematic review and meta-analysis. *Cornea* 39, 263–270. doi:10.1097/ico.0000000000002150

Herber, R., Hasanli, A., Lenk, J., Vinciguerra, R., Terai, N., Pillunat, L. E., et al. (2022). Evaluation of corneal biomechanical indices in distinguishing between normal, very asymmetric, and bilateral keratoconic eyes. *J. Refract. Surg. (Thorofare, N. J. 1995)* 38, 364–372. doi:10.3928/1081597x-20220601-01

Kataria, P., Padmanabhan, P., Gopalakrishnan, A., Padmanaban, V., Mahadik, S., and Ambrósio, R., Jr. (2019). Accuracy of Scheimpflug-derived corneal biomechanical and tomographic indices for detecting subclinical and mild keratectasia in a South Asian population. *J. cataract Refract. Surg.* 45, 328–336. doi:10.1016/j.jcrs.2018.10.030

Koc, M., Aydemir, E., Tekin, K., Inanc, M., Kosekahya, P., and Kiziltoprak, H. (2019). Biomechanical analysis of subclinical keratoconus with normal topographic, topometric, and tomographic findings. *J. Refract. Surg. (Thorofare, N. J. 1995)* 35, 247–252. doi:10.3928/1081597x-20190226-01

Koh, S., Ambrósio, R., Jr., Inoue, R., Maeda, N., Miki, A., and Nishida, K. (2019). Detection of subclinical corneal ectasia using corneal tomographic and biomechanical assessments in a Japanese population. *J. Refract. Surg. (Thorofare, N. J. 1995)* 35, 383–390. doi:10.3928/1081597x-20190417-01

Leoni-Mesplie, S., Mortemousque, B., Touboul, D., Malet, F., Praud, D., Mesplié, N., et al. (2012). Scalability and severity of keratoconus in children. *Am. J. Ophthalmol.* 154, 56–62.e1. doi:10.1016/j.ajo.2012.01.025

Li, X., Luo, S., Wang, Z., Miao, Y., Zhu, M., Zheng, X., et al. (2023). Dynamic topography analysis of the cornea and its application to the diagnosis of keratoconus. *Comput. Biol. Med.* 158, 106800. doi:10.1016/j.compbiomed.2023.106800

Malyugin, B., Sakhnov, S., Izmailova, S., et al. (2021). *Keratoconus diagnostic and treatment algorithms based on machine-learning methods*, 11. Basel, Switzerland: Diagnostics.

Mandrekar, J. N. (2010). Receiver operating characteristic curve in diagnostic test assessment. *J. Thorac. Oncol. official Publ. Int. Assoc. Study Lung Cancer* 5, 1315–1316. doi:10.1097/jto.0b013e3181ec173d

Mas Tur, V., MacGregor, C., Jayaswal, R., O'Brart, D., and Maycock, N. (2017). A review of keratoconus: diagnosis, pathophysiology, and genetics. *Surv. Ophthalmol.* 62, 770–783. doi:10.1016/j.survophthal.2017.06.009

Moshirfar, M., Motlagh, M. N., Murri, M. S., Momeni-Moghaddam, H., Ronquillo, Y. C., and Hoopes, P. C. (2019). Advances in biomechanical parameters for screening of refractive surgery candidates: a review of the literature, Part III. *Med. hypothesis, Discov. innovation Ophthalmol. J.* 8, 219–240.

Motlagh, M. N., Moshirfar, M., Murri, M. S., Skanchy, D. F., Momeni-Moghaddam, H., Ronquillo, Y. C., et al. (2019). Pentacam® corneal tomography for screening of refractive surgery candidates: a review of the literature, Part I. *Med. hypothesis, Discov. innovation Ophthalmol. J.* 8, 177–203.

Mukhtar, S., and Ambati, B. K. (2018). Pediatric keratoconus: a review of the literature. *Int. Ophthalmol.* 38, 2257–2266. doi:10.1007/s10792-017-0699-8

Neustein, R. F., and Lenhart, P. D. (2022). Detecting keratoconus: feasibility and findings in three pediatric risk groups. *J. Pediatr. Ophthalmol. strabismus* 59, 94–101. doi:10.3928/01913913-20210802-01

Ortega-Usobiaga, J., Rocha-de-Lossada, C., Llovet-Rausell, A., and Llovet-Osuna, F. (2022). Update on contraindications in laser corneal refractive surgery. *Arch. Soc. Esp. Oftalmol. Engl. Ed.* 98, 105–111. doi:10.1016/j.oftale.2022.07.003

Rafat, M., Jabbarvand, M., Sharma, N., Xeroudaki, M., Tabe, S., Omrani, R., et al. (2022). Bioengineered corneal tissue for minimally invasive vision restoration in advanced keratoconus in two clinical cohorts. *Nat. Biotechnol.* 41, 70–81. doi:10.1038/s41587-022-01408-w

Rebenitsch, R. L., Kymes, S. M., Walline, J. J., and Gordon, M. O. (2011). The lifetime economic burden of keratoconus: a decision analysis using a markov model. *Am. J. Ophthalmol.* 151, 768–773.e2. doi:10.1016/j.ajo.2010.10.034

Ren, S., Xu, L., Fan, Q., Gu, Y., and Yang, K. (2021). Accuracy of new Corvis ST parameters for detecting subclinical and clinical keratoconus eyes in a Chinese population. *Sci. Rep.* 11, 4962. doi:10.1038/s41598-021-84370-y

Ruiz Hidalgo, I., Rodriguez, P., Rozema, J. J., Ní Dhubhghaill, S., Zakaria, N., Tassignon, M. J., et al. (2016). Evaluation of a machine-learning classifier for keratoconus detection based on scheimpflug tomography. *Cornea* 35, 827–832. doi:10.1097/ico.0000000000000834

Saad, A., and Gatinel, D. (2010). Topographic and tomographic properties of forme fruste keratoconus corneas. *Investigative Ophthalmol. Vis. Sci.* 51, 5546–5555. doi:10.1167/iovs.10-5369

Scarcelli, G., Besner, S., Pineda, R., and Yun, S. H. (2014). Biomechanical characterization of keratoconus corneas *ex vivo* with Brillouin microscopy. *Investigative Ophthalmol. Vis. Sci.* 55, 4490–4495. doi:10.1167/iovs.14-14450

Sedaghat, M. R., Momeni-Moghaddam, H., Ambrosio, R., Jr., Heidari, H. R., Maddah, N., Danesh, Z., et al. (2018). Diagnostic ability of corneal shape and biomechanical parameters for detecting frank keratoconus. *J. Ophthalmol.* 37, 1025–1034. doi:10.1097/ico.0000000000001639

Vinciguerra, R., Ambrosio, R., Jr., Elsheikh, A., Roberts, C. J., Lopes, B., Morenghi, E., et al. (2016). Detection of keratoconus with a new biomechanical index. *J. Refract. Surg. (Thorofare, N. J. 1995)* 32, 803–810. doi:10.3928/1081597x-20160629-01

Wajnsztajn, D., Hopkinson, C. L., and Larkin, D. F. P. (2021). Keratoplasty for keratoconus in young patients: demographics, clinical features, and post-transplant outcomes. *Eur. J. Ophthalmol.* 226, 68–75. doi:10.1016/j.ajo.2021.02.003

Yang, K., Gu, Y., Xu, L., Fan, Q., Zhu, M., Wang, Q., et al. (2022). Distribution of pediatric keratoconus by different age and gender groups. *Front. Pediatr.* 10, 937246. doi:10.3389/fped.2022.937246

Yang, K., Xu, L., Fan, Q., and Ren, S. (2020). Association between corneal stiffness parameter at the first applanation and keratoconus severity. *J. Ophthalmol.* 2020, 1–8. doi:10.1155/2020/6667507

Yang, K., Xu, L., Fan, Q., Zhao, D., and Ren, S. (2019). Repeatability and comparison of new Corvis ST parameters in normal and keratoconus eyes. *Sci. Rep.* 9, 15379. doi:10.1038/s41598-019-51502-4

Zhang, H., Zhang, X., Hua, L., Li, L., Tian, L., et al. (2022). An exploratory analysis of forme fruste keratoconus sensitivity diagnostic parameters. *Int. Ophthalmol.* 42, 2473–2481. doi:10.1007/s10792-022-02246-0

frontiers | Frontiers in Bioengineering and Biotechnology

TYPE Original Research
PUBLISHED 07 December 2023
DOI 10.3389/fbioe.2023.1242166

OPEN ACCESS

EDITED BY
Matthew A. Reilly,
The Ohio State University, United States

REVIEWED BY
Joel Palko,
West Virginia State University, United States
Jun Liu,
The Ohio State University, United States

*CORRESPONDENCE
András M. Komáromy,
komaromy@msu.edu

RECEIVED 18 June 2023
ACCEPTED 27 November 2023
PUBLISHED 07 December 2023

CITATION
Raphtis VA, Sharma D, Wang S, Kim JY, Jacobson AL, Harman CD and Komáromy AM (2023), Ocular pulse amplitude (OPA) in canine *ADAMTS10*-open-angle glaucoma (*ADAMTS10*-OAG).
Front. Bioeng. Biotechnol. 11:1242166.
doi: 10.3389/fbioe.2023.1242166

Ocular pulse amplitude (OPA) in canine *ADAMTS10*-open-angle glaucoma (*ADAMTS10*-OAG)

Vanessa A. Raphtis[1], Dhruv Sharma[2], Sichao Wang[2], Jae Y. Kim[1], Amanda L. Jacobson[1], Christine D. Harman[1] and András M. Komáromy[1]*

[1]Department of Small Animal Clinical Sciences, College of Veterinary Medicine, Michigan State University, East Lansing, MI, United States, [2]Center for Statistical Training and Consulting, Michigan State University, East Lansing, MI, United States

Introduction: The role of ocular rigidity and biomechanics remains incompletely understood in glaucoma, including assessing an individual's sensitivity to intraocular pressure (IOP). In this regard, the clinical assessment of ocular biomechanics represents an important need. The purpose of this study was to determine a possible relationship between the G661R missense mutation in the *ADAMTS10* gene and the ocular pulse amplitude (OPA), the difference between diastolic and systolic intraocular pressure (IOP), in a well-established canine model of open-angle glaucoma (OAG).

Methods: Animals studied included 39 *ADAMTS10*-mutant dogs with different stages of OAG and 14 unaffected control male and female dogs between 6 months and 12 years (median: 3.2 years). Dogs were sedated intravenously with butorphanol tartrate and midazolam HCl, and their IOPs were measured with the Icare® Tonovet rebound tonometer. The Reichert Model 30™ Pneumotonometer was used to measure OPA. Central corneal thickness (CCT) was measured via Accutome® PachPen, and A-scan biometry was assessed with DGH Technology Scanmate. All outcome measures of left and right eyes were averaged for each dog. Data analysis was conducted with ANOVA, ANCOVA, and regression models.

Results: *ADAMTS10*-OAG-affected dogs displayed a greater IOP of 23.0 ± 7.0 mmHg (mean ± SD) compared to 15.3 ± 3.6 mmHg in normal dogs ($p < 0.0001$). Mutant dogs had a significantly lower OPA of 4.1 ± 2.0 mmHg compared to 6.5 ± 2.8 mmHg of normal dogs ($p < 0.01$). There was no significant age effect, but OPA was correlated with IOP in *ADAMTS10*-mutant dogs.

Abbreviations: *ADAMTS10*, A disintegrin and metalloproteinase with thrombospondin motifs 10; ANCOVA, analysis of covariance; ANOVA, analysis of variance; AXL, axial length; CCT, central corneal thickness; CD, corneal diameter; cumIOP, cumulative IOP; IOP, intraocular pressure; NTG, normal tension glaucoma; OAG, open-angle glaucoma; OHT, ocular hypertension; OPA, ocular pulse amplitude; ORA, Ocular Response Analyzer®; POAG, primary open-angle glaucoma; POBF, pulsatile ocular blood flow; PP, perfusion pressure; PPS, peripapillary sclera; VPA, vascular pulse amplitude.

Conclusion: The lower OPA in *ADAMTS10*-mutant dogs corresponds to the previously documented weaker and biochemically distinct posterior sclera, but a direct relationship remains to be confirmed. The OPA may be a valuable clinical tool to assess ocular stiffness and an individual's susceptibility to IOP elevation.

KEYWORDS

***ADAMTS10*, dog, glaucoma, intraocular pressure (IOP), ocular pulse amplitude (OPA), ocular rigidity**

Introduction

Glaucoma is a common, incurable neurodegenerative disease and the leading cause of irreversible blindness worldwide, affecting over 70 million people (Quigley and Broman, 2006). Open-angle glaucoma (OAG) and angle-closure glaucoma are the two primary disease types, depending on the particular abnormalities of the aqueous humor outflow pathways within the iridocorneal angle that increase intraocular pressure (IOP) (Weinreb et al., 2014; Jonas et al., 2017). The pathogenic mechanisms of glaucomatous optic neuropathy leading to retinal ganglion cell (RGC) death and vision loss remain only partly understood. The three primary risk factors are advancing age, genetics, and IOP-related biomechanical stress on the optic nerve head (ONH) (Weinreb et al., 2016; Jonas et al., 2017). Current glaucoma treatment is limited to lowering IOP by medical and surgical means (Weinreb et al., 2014; Jonas et al., 2017).

Even though the prevalence of glaucoma increases with IOP elevation, glaucomatous ONH damage can develop at any IOP level based on significant interindividual variabilities in susceptibility (Sommer et al., 1991; Weinreb et al., 2016). At diagnosis, approximately half of primary OAG (POAG) patients have normal IOP between 10–20 mmHg (Collaborative Normal-Tension Glaucoma Study Group, 1998a; Koz et al., 2009; Weinreb et al., 2016). Nevertheless, IOP-related biomechanical stress is important in these normal tension glaucoma (NTG) patients because a 30% IOP reduction significantly slowed disease progression (Collaborative Normal-Tension Glaucoma Study Group, 1998b). In contrast, individuals with ocular hypertension (OHT) can tolerate increased IOP >21 mmHg without ONH damage (Weinreb et al., 2016). Susceptibility to IOP may be based on connective tissue properties of the fibrous tunic of the globe consisting of cornea, sclera, and lamina cribrosa of the ONH (Bellezza et al., 2000; Burgoyne et al., 2005; Downs et al., 2009; Burgoyne, 2011; Park and Komaromy, 2021).

The biomechanical properties of the eye have been studied in great detail in the laboratory setting using human cadaver eyes and animal models (Coudrillier et al., 2016; Hopkins et al., 2020; Park and Komaromy, 2021; Safa et al., 2022). Clinical measurements of connective tissue properties in human glaucoma eyes are limited to the cornea and include central corneal thickness (CTT) and corneal hysteresis by use of Ocular Response Analyzer® (ORA) (Gordon et al., 2002; Medeiros et al., 2013; Ayyalasomayajula et al., 2016; Weinreb et al., 2016). These measurements exclude the posterior pole of the globe, including the peripapillary sclera (**PPS**) and the lamina cribrosa, whose biomechanical factors likely impact the ONH's IOP susceptibility (Downs et al., 2009; Burgoyne, 2011; Safa et al., 2022). There is a critical need for additional clinical tools to measure ocular biomechanics that are not limited to the cornea to evaluate susceptibility to IOP in patients.

In this study, we tested the hypothesis that the measurement of ocular pulse amplitude (OPA) may allow the comparison of biomechanical properties of the entire fibrous tunic *in vivo*. The OPA is defined as the IOP difference between systole and diastole of the pulsatile choroidal blood flow, and appears to be correlated with ocular rigidity based on observations in glaucoma patients (Tonjum, 1972; Dastiridou et al., 2009). We took advantage of a well-defined, clinically relevant canine glaucoma model, the OAG-affected Beagle, with a G661R missense mutation in the *ADAMTS10* gene (Kuchtey et al., 2011). Differences in IOP susceptibilities are well recognized by veterinary ophthalmologists when comparing glaucoma-affected dog breeds (Park and Komaromy, 2021). For example, Beagles with *ADAMTS10*-OAG tolerate elevated IOP much better, with slower progression of vision loss, than other glaucoma-affected breeds with comparable IOPs (Kuchtey et al., 2011; Park and Komaromy, 2021). Compared to normal dogs, the posterior scleral of *ADAMTS10*-mutant Beagles is biochemically distinct and weaker with a lower normalized ocular rigidity (Palko et al., 2013; Boote et al., 2016; Palko et al., 2016). This study shows a significantly smaller OPA in *ADAMTS10*-mutants whose sclera is softer than the normal, supporting the potential clinical value of OPA as a measure of glaucoma susceptibility.

Materials and methods

Animals

A total of 101 eyes of 53 purpose-bred dogs (both eyes of 48 dogs and one eye of 5 dogs each), 39 at different stages of *ADAMTS10*-OAG, and 14 normal, glaucoma-unaffected dogs were used. Twenty-six males and 27 females were included between the ages of 6 months and 12 years (median: 3.2 years) (Figure 1). In addition, a separate independent experiment was performed to determine the repeatability of OPA measurements in dogs: A total of 34 eyes of 18 purpose-bred dogs (both eyes of 16 dogs and one eye of 2 dogs each), 14 at different stages of *ADAMTS10*-OAG, and 4 normal, glaucoma-unaffected dogs were used. Ten males and 8 females were included between the ages of 1–8 years (median: 2.8 years).

Genotypes were confirmed based on the *ADAMTS10* gene sequence: glaucomatous dogs were homozygous for the G661R missense mutation, which is responsible for OAG in Beagles, while the normal dogs were either carriers of the mutation or homozygous for the wildtype allele (Kuchtey et al., 2011). Glaucomatous dogs that received pressure-lowering medication were excluded from this study. The dogs were group-housed in the same environment at the Michigan State University College of Veterinary Medicine with a 12 h/12 h light/dark cycle and fed the same diet.

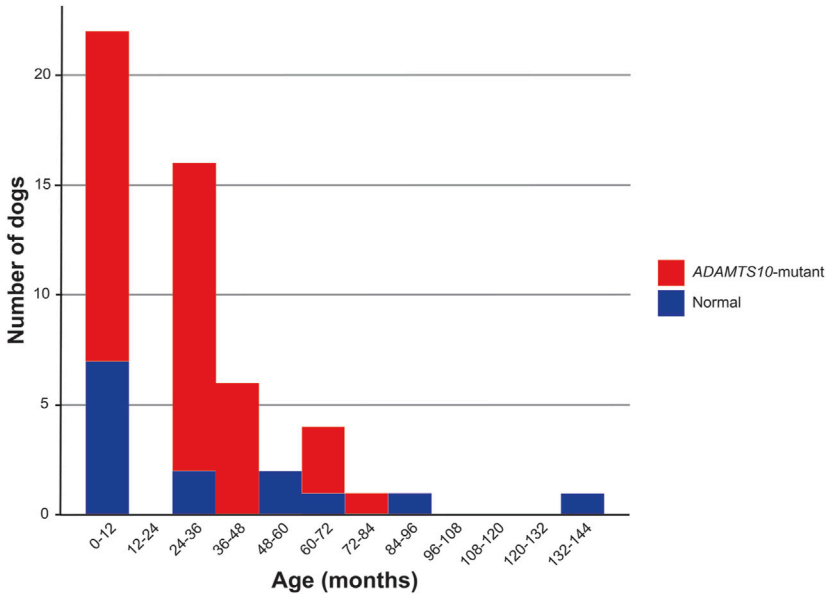

FIGURE 1
Age distribution. This histogram compares the age distribution for normal and *ADAMTS10*-mutant dogs enrolled in the study.

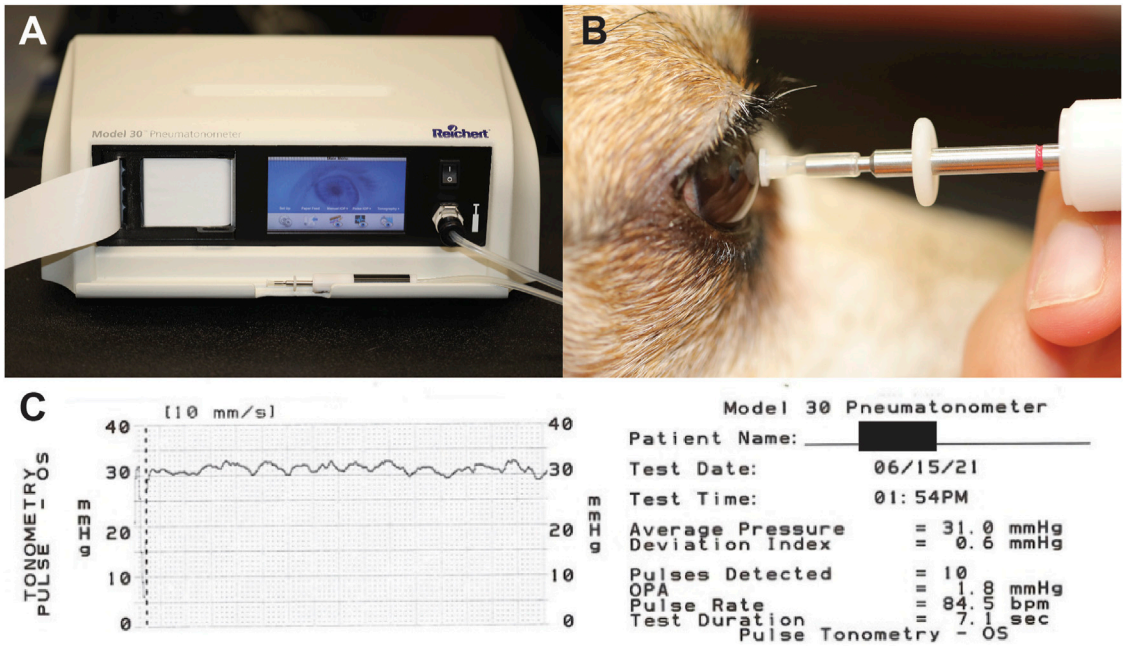

FIGURE 2
Equipment and setup for OPA measurements. **(A)** The Reichert Model 30™ Pneumotonometer. **(B)** Placement of pneumotonometer probe on central corneal. **(C)** Chart produced by Reichert Model 30™ Pneumotonometer documenting measurements recorded.

Study design

Dogs were sedated intravenously with a combination of 0.3 mg/kg butorphanol tartrate (Bayer Healthcare LLC, Animal Health Division, Shawnee Mission, KS, United States) and 0.3 mg/kg midazolam HCl (Avet Pharmaceuticals Inc., East Brunswick, NJ, United States). Dogs were placed in a lateral recumbent position for blood pressure measurements. Systolic, diastolic, and mean arterial blood pressures were measured with Mindray Passport® 12 Patient Monitor and blood pressure cuff (Mindray, Shenzhen Mindray Bio-Medical Electronics Co., Ltd., Nanshan, Shenzhen, Guangdong Province, China) placed over the left or right dorsal pedal artery. Intraocular pressure was measured manually via iCare TonoVet® rebound tonometer (Icare Finland Oy, Vantaa, Finland) while dogs were in a seated position.

Mean perfusion pressure (PP) was calculated as the difference between mean arterial blood pressure and IOP, and vascular pulse amplitude (VPA) as the difference between systolic and diastolic blood pressure.

The left or right eye was randomly selected for every dog to begin measurements for OPA. Dogs were placed in sternal position for pneumotonometer measurements. Ocular surface anesthesia was achieved by administering one drop of proparacaine HCl 0.5% ophthalmic solution (Akorn, Inc., Lake Forest, IL, United States). The Reichert Model 30™ Pneumotonometer (Reichert, Inc., Depew, NY, United States) was used to measure OPA as well as provide additional measurements of IOP, a deviation index, and pulsation rate (Figure 2A). Measurements were recorded by placing the pneumotonometer probe tip on the central cornea following manufacturer guidelines (Figure 2B). The probe tip contains a small (5-mm diameter) fenestrated membrane that permits air to flow through vents in the tip until it conforms to the shape of the cornea. Once the force of pressure being applied to the cornea is equal to the force of pressure in the anterior chamber, the pneumatic sensor charts and records both IOP and an ocular pulse waveform (Figure 2C). Each dog went through this measurement process twice, once to become acclimated to the probe and noise of the machine and a second time for data collection. The data were recorded and printed via the pneumotonometer's integrated chart strip printout.

Lastly, dogs received one drop of OptixCare® Plus Eye Lube (CLC MEDICA, Ontario, Canada) and were placed in a seated position for central corneal thickness (**CCT**) measurements taken via PachPen® handheld pachymeter (Accutome, Inc., Malvern, PA, USA). Dogs were also in a seated position while the axial length (**AXL**) of the eye was measured via Scanmate A DGH 6000 A-scan (DGH Technology, Inc., Exton, PA, United States).

Archival corneal diameter (CD) was available for 34/101 eyes (34/53 dogs). Measurements occurred using Jameson calipers (Integra Miltex, York, PA, United States). Estimated cumulative IOP (cumIOP) data were available for 81/101 eyes (43/53 dogs): Daily averages of archival diurnal IOPs measured with the iCare TonoVet® rebound tonometer were plotted as a function of time in days. Areas under the curve were calculated to obtain estimates of cumIOPs (mmHg x days). Since IOP measurements were not performed continuously, the cumIOP data are considered estimates.

Repeatability

A separate experiment was performed to determine the repeatability of OPA measurements in dogs. The same experimental setup was used as described for the main experiment. The left or right eye was randomly selected for every dog to begin measurements for OPA. Each of the 18 dogs went through the measurement process twice. The median interval between the first and second measurements was 19 min (range: 6–22 min).

Statistical analyses

All outcome measures of left and right eyes were averaged for each dog. Data were analyzed by descriptive statistics, analysis of variance (ANOVA), regression analysis, and mixed effects models using R. ANOVA models were used to assess the effect of mutation on OPA and the effect of mutation by age on OPA. A linear model was applied to determine the impact of age on OPA. An analysis of covariance (ANCOVA) was used to analyze the effect of mutation by age on OPA with the following control variables: IOP, PP, AXL, CCT, VPA, CD, and cumIOP. These analyses were performed for all dogs combined as well as by excluding young adult dogs <12 months of age. Possible relationships between variables were evaluated by bivariate correlation analysis for all dogs combined but also separately for normal and *ADAMTS10*-mutant dogs. Pearson correlation coefficient was calculated between age and AXL for the normal and *ADAMTS10*-mutant groups. A Bland-Altman analysis was used to interpret the repeatability data.

Intraocular pressure measured by iCare TonoVet® rebound tonometer was used for all the analyses. Even though not the primary purpose of this study, IOPs measured by iCare TonoVet® and Reichert Model 30™ Pneumotonometer were compared with Bland-Altman plots and by regression analysis without averaging left and right eyes (Prism 9; GraphPad Software, Boston, MA).

Results

Effect of *ADAMTS10* mutation on OPA

Ocular pulse amplitude could be easily measured in lightly sedated dogs. Because there was a significant correlation between left and right eyes on OPA (r = 0.42, 95% CI [0.16, 0.63], $p = 0.003$), outcome measures were averaged for each dog. Testing by ANOVA revealed that OPA was significantly lower in *ADAMTS10*-mutant dogs (4.1 ± 2.0 mmHg; mean ± standard deviation) compared to normal control dogs (6.5 ± 2.8 mmHg; $p < 0.01$; Figure 3A). When controlling for the following variables, the mutation effect became even more significant ($p < 0.001$): age, mutation by age, IOP, cumIOP, PP, AXL, CCT, CD, and gender. With 39 *ADAMTS10*-mutant and 14 normal dogs, a desired 0.05 type I error, and a power of 0.80 the detectable effect size was considered reasonable with 0.89 standard deviations (SD). When excluding the younger dogs <12 months, the same trend remained, although the difference in OPA was no longer significant (mutant vs. normal: 4.9 ± 2.2 mmHg vs. 6.5 ± 3.0 mmHg; $p = 0.05$; Figure 3B). In a separate repeatability study, the Bland-Altman plot showed good agreement between first and second OPA measurements (Figure 4).

As expected, IOPs were significantly higher in mutant vs. normal dogs (23.0 ± 7.0 mmHg vs. 15.3 ± 3.6 mmHg; $p < 0.0001$), but PPs were not significantly different despite being smaller in mutant dogs (75.5 ± 20.9 mmHg vs. 88.6 ± 29.7 mmHg; $p = 0.18$). Axial length was significantly larger in mutant vs. normal dogs (20.9 ± 0.6 mm vs. 19.8 ± 0.8 mm; $p = 0.01$), but there was no significant difference in mean CCT (666.3 ± 52.0 µm vs. 634.1 ± 24.7 µm; $p = 0.74$) between mutant and normal dogs. There was no significant difference in CD, regardless of whether young dogs <12 months were included (mutant vs. normal 15.9 ± 0.9 mm vs. 15.3 ± 0.6 mm) or not (mutant vs. normal 16.1 ± 1.0 vs. 15.3 ± 0.6 mm). The difference in AXL remained when young dogs <12 months were excluded (21.2 ± 0.5 mm vs. 20.1 ± 0.6 mm; $p < 0.001$). We could not detect a significant difference in cumIOP between *ADAMTS10*-mutant and normal dogs (17,058 ± 14,309 mmHg day vs. 14,981 ± 8,280 mmHg day; $p > 0.9$).

10.3389/fbioe.2023.1242166

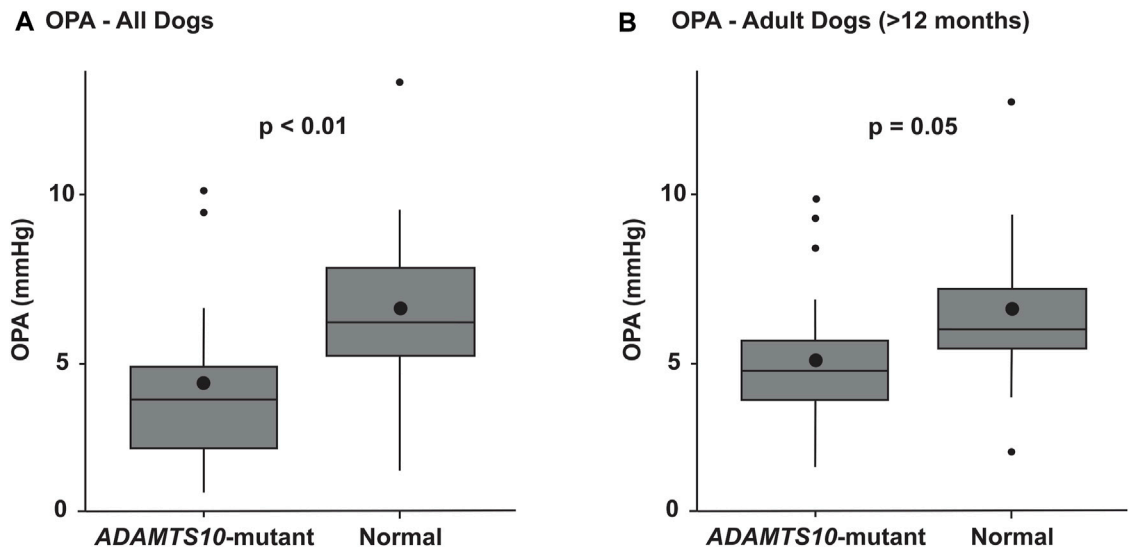

FIGURE 3
Box plots summarizing the OPAs of *ADAMTS10*-mutant and normal dogs. **(A)** The mutant group had a significantly smaller OPA than the normal control group ($p < 0.01$). **(B)** When excluding the younger dogs <12 months, the same trend remained, but the difference was no longer significant ($p = 0.05$). The boxes represent the middle 50% of the data, with the centerline being the median. The bottom and top whiskers show the first and third quartiles, respectively. Outliers are shown as small black dots. The larger black dots inside the boxes represent the means.

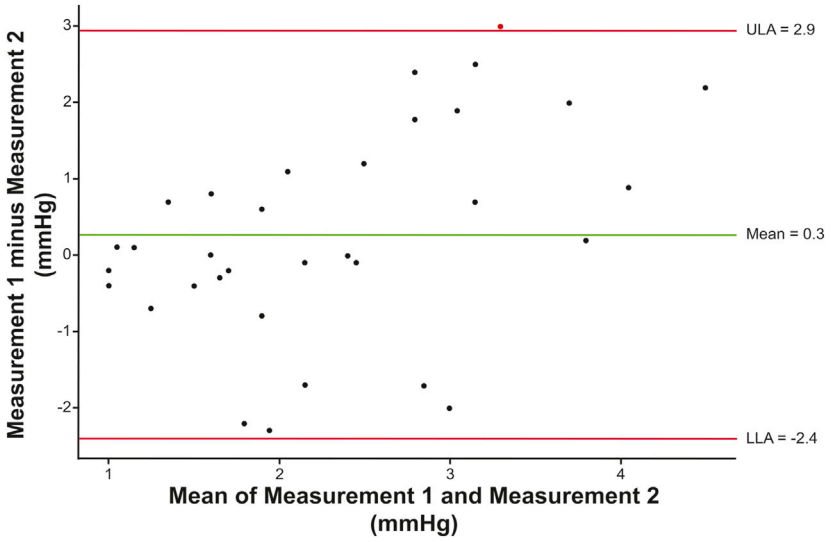

FIGURE 4
Repeatability of canine OPA measurements. The Bland-Altman plot compares first and second measurements in a group of 34 eyes of 18 dogs (median time interval: 19 min, range: 6–22 min). The estimated means of the differences between the two measurements are shown by the green horizontal line. The 95% CI is marked by the red lines representing the upper (ULA) and lower (LLA) limits of agreement (mean ± 1.96 SD). Overall, the OPA measurements did not follow any trends and were mainly located within the 95% CI.

Other parameters affecting OPA

There was no OPA age effect over all the dogs tested (Figure 5). The age range for normal dogs was 11 years (133 months), and the median was 2.5 years (30 months). The age range for *ADAMTS10*-mutant dogs was 6 years (73 months), and the median was 3 years (38 months) (Figure 1). When tested over all dogs, we did not find any significant correlations between OPA and these parameters: IOP ($p = 0.17$), PP ($p = 0.34$), AXL, ($p = 0.62$), CCT ($p = 0.91$), and VPA ($p = 0.34$) (Figure 6). We did find significant correlations between IOP and PP ($r = -0.41$; $p = 0.01$), IOP and AXL ($r = 0.43$; $p = 0.001$), and AXL and CCT ($r = 0.34$; $p = 0.02$). When analyzing *ADAMTS10*-mutant dogs alone, we found a significant positive correlation between OPA and IOP ($r = 0.61$; $p = 0.004$) (Figure 6). Furthermore, mutant dogs showed

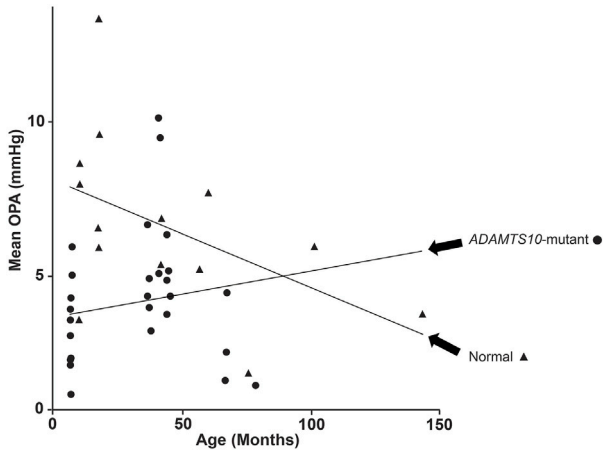

FIGURE 5
Change of OPA with age for *ADAMTS10*-mutant and normal dogs. Despite the trendlines, there was no detectable age effect on OPA.

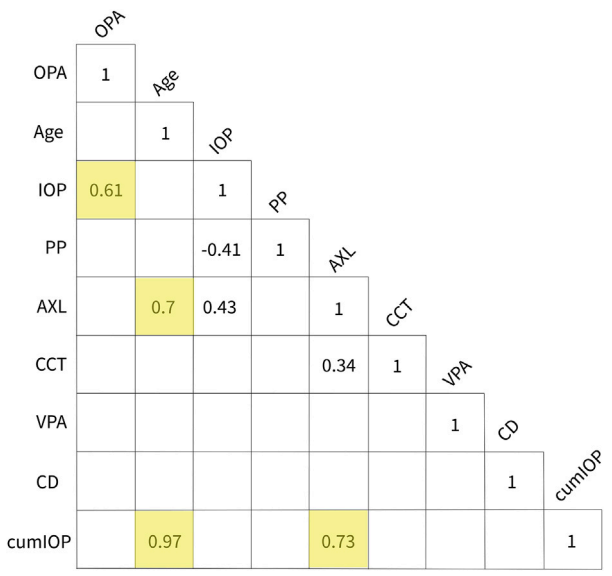

FIGURE 6
Summary of correlations. Unshaded numbers show that OPA was not correlated with any of the other parameters when analyzing all dogs together. Significant correlations were found between IOP and PP, IOP and AXL, and AXL and CCT. No significant correlations were found in the normal dog group. The yellow-shaded numbers show the significant correlations in the *ADAMTS10*-mutant dog group: These were between OPA and IOP, age and AXL, age and cumIOP, and between AXL and cumIOP. Abbreviations: AXL, axial length; CD, corneal diameter; cumIOP, cumulative IOP; IOP, intraocular pressure; OPA, ocular pulse amplitude; CCT, central corneal thickness; PP, perfusion pressure; VPA, vascular pulse amplitude.

significant positive correlations between age and AXL ($r = 0.7$; $p < 0.001$), between age and cumIOP ($r = 0.97$; $p < 0.001$), and between AXL and cumIOP ($r = 0.73$; $p < 0.001$). There were no significant correlations between any of the parameters in the normal control dogs, including age and AXL (Figure 6).

Comparison of tonometers

Because the iCare TonoVet® is the standard tonometer used in our laboratory and widely used in veterinary clinical practice, we used IOP measurements taken with this instrument for our statistical analyses. However, as part of the study design, IOPs were also measured with the Reichert Model 30™ pneumotonometer immediately before OPA assessment; these readings were not used in our analyses. Nevertheless, Bland-Altman plot and linear regression analysis showed good agreement between the two tonometers with the pneumotonometer overestimating most IOPs compared to the TonoVet® (Figure 7).

Discussion

Ocular stiffness may be essential to glaucoma pathophysiology, but the exact role of tissue biomechanics and susceptibility to IOP-related damage is not entirely understood (Park and Komaromy, 2021; Safa et al., 2022). The most commonly used clinical assessments of ocular biomechanics are limited to the cornea and consist of CCT and corneal hysteresis (Gordon et al., 2002; Medeiros et al., 2013; Ayyalasomayajula et al., 2016; Weinreb et al., 2016). Because of their importance in IOP susceptibility, there is a critical need for additional clinical tools that include the biomechanics of the PPS and lamina cribrosa (Downs et al., 2009; Burgoyne, 2011; Safa et al., 2022). Measurement of OPA may be such a tool. The extent of transient IOP fluctuations, such as from saccades, blinking, ocular pulse, or controlled microvolumetric intraocular injections, is related to overall ocular coat stiffness, including corneal and PPS stiffness (Liu and He, 2009; Morris et al., 2013; Beaton et al., 2015; Sturmer and Kniestedt, 2015; Clayson et al., 2017; Sherwood et al., 2019; Turner et al., 2019; Sayah et al., 2020; Ma et al., 2021; Markert et al., 2022). In the current study we demonstrated that compared to normals the OPA is significantly reduced in *ADAMTS10*-mutant Beagles, a well-established, clinically relevant large animal model of OAG with decreased scleral stiffness and normalized ocular rigidity (Palko et al., 2013; Boote et al., 2016; Palko et al., 2016). We suspect that the softer *ADAMTS10*-mutant sclera is in part responsible for an improved IOP tolerance with slower progression of ONH atrophy and vision loss in Beagles with *ADAMTS10*-OAG compared to other glaucoma-affected canine breeds with comparable IOPs (Kuchtey et al., 2011; Park and Komaromy, 2021).

Ocular pulse amplitude is the difference between diastolic and systolic IOP and is created by the pulsatile choroidal blood flow (Dastiridou et al., 2009; Beaton et al., 2015; Sturmer and Kniestedt, 2015). Our conclusions on *ADAMTS10*-mutant dogs are based on observations in human patients that OPA and ocular rigidity are correlated at controlled IOPs of 15–45 mmHg: increased transient IOP fluctuations, such as OPA, are associated with greater rigidity (Dastiridou et al., 2009). However, the relationship between OPA and ocular rigidity may differ for different eyes because many other factors impact OPA. The OPA measurements using a pneumotonograph were well tolerated and easily performed in lightly sedated dogs, supporting the potential routine clinical application. The reasonable repeatability of the canine OPA measurements demonstrated in a separate experiment further supports their potential clinical usefulness.

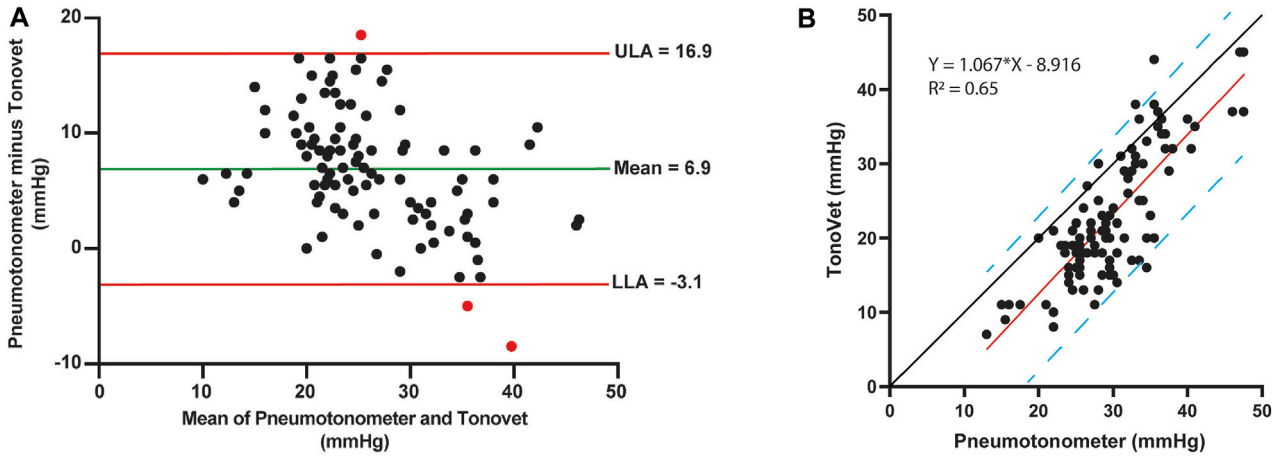

FIGURE 7
Comparison of tonometers. **(A)** Bland-Altman plot comparing Reichert Model 30™ pneumotonometer and iCare TonoVet® rebound tonometer. The estimated means of the differences between the two tonometers are shown by the green horizontal line. The 95% CI is marked by the red lines representing the upper (ULA) and lower (LLA) limits of agreement (mean ± 1.96 SD). Overall, the IOP measurements did not follow any trends and were mainly located within the 95% CI. The estimated means of the differences (±SD) were 6.9 ± 5.1 mmHg. **(B)** IOP regression analyses between tonometers with linear equation and R^2 values. The red line shows strong linear correlation between Reichert Model 30™ pneumotonometer and iCare TonoVet® rebound tonometer with the blue dashed lines marking the 95% prediction intervals. Compared to the black y = x line, the pneumotonometer overestimated most IOPs when compared to the TonoVet® with data points mostly located to the left of the y = x line.

Our canine OPA values (normal: 6.5 ± 2.8 mmHg; *ADAMTS10*-mutant: 4.1 ± 2.0 mmHg) are comparable to the 0.9–7.2-mmHg range in normal and glaucomatous humans; although the mean OPAs in dogs are lower than previously reported in humans (2.2 and 3.0 mmHg, respectively) (Kaufmann et al., 2006; Kac et al., 2011; Sturmer and Kniestedt, 2015). The higher pressure readings by the pneumotonometer could explain this. The obtained data supported our hypothesis that the softer *ADAMTS10*-mutant sclera may be partly responsible for the significantly lower OPA because it provides less resistance to the pulsatile choroidal blood flow. Our finding of lower OPA in *ADAMTS10*-mutant dogs is even more significant, considering that their ocular rigidity and OPA should be higher with higher baseline IOPs (Friedenwald, 1937; Dastiridou et al., 2009; Downs, 2015).

While not widely used in clinical settings, OPA was measured previously in humans with different forms of glaucoma; however, IOP susceptibility was not explicitly studied. In most studies, OPA with chronic POAG was not different from normal individuals (Sturmer and Kniestedt, 2015). Some studies showed reduced or elevated OPA in POAG patients (Trew and Smith, 1991a; Trew and Smith, 1991b; Mittag et al., 1994; Schmidt et al., 1997; Kerr et al., 1998; Schmidt et al., 1998; Khan et al., 2002; Kniestedt et al., 2006; Punjabi et al., 2006; Romppainen et al., 2007; Stalmans et al., 2008; Vulsteke et al., 2008; Asejczyk-Widlicka et al., 2014; Katsimpris et al., 2014; Sturmer and Kniestedt, 2015; Milioti et al., 2017). These variations were based on diverse study populations with various degrees of glaucomatous optic neuropathy, different IOP ranges, and the use of IOP-lowering medications (Sturmer and Kniestedt, 2015). In general, OPA increased with progressing POAG, suggesting increased ocular stiffening (Romppainen et al., 2007; Weizer et al., 2007; Kac et al., 2011; Kynigopoulos et al., 2012; Moghimi et al., 2013; Gross et al., 2014; Sturmer and Kniestedt, 2015). Our OPA data supported this: differences between *ADAMTS10*-mutant and normal dogs became less significant when excluding young dogs before the development of glaucoma. Others have shown increased OPA with decreased glaucoma severity or better IOP control and decreased OPA with progressive ONH atrophy and visual field loss (Agarwal et al., 2003; Weizer et al., 2007; Vulsteke et al., 2008; Sturmer and Kniestedt, 2015).

Controversial results have also been reported when comparing NTG patients to normal: Some found that NTG patients had lower OPA or pulsatile ocular blood flow (**POBF**) than normal controls (Quaranta et al., 1994; Schmidt et al., 1997; Schwenn et al., 2002). Considering that NTG patients are more susceptible to IOP since they develop glaucomatous optic neuropathy and visual field loss without documented IOP elevation, these findings contradict our results with lower OPA in *ADAMTS10*-mutant dogs that are more resistant to IOP elevation. Others did not find OPA differences between NTG patients, normals, or chronic POAG-affected individuals (Khan et al., 2002; Kniestedt et al., 2006; Read et al., 2008; Stalmans et al., 2008; Vulsteke et al., 2008). Another study found significantly lower OPA in NTG than in POAG patients, OHT, and normal controls. A logistic regression model was established to identify OPA as an independent risk factor for NTG (Schwenn et al., 2002). OPA and IOP were significantly higher in NTG patients with central visual field loss compared to NTG patients without visual field loss, with a significant correlation between OPA increase and central visual field loss (Lee et al., 2012). OPA measurement could be helpful in the detection and screening of NTG patients, but additional studies are needed for validation.

In contrast to NTG patients, individuals with OHT are more resistant to IOP elevation without developing ONH damage (Weinreb et al., 2016). Studies of OPA in OHT-affected individuals are variable, with some showing higher ocular rigidity compared to POAG patients and others not showing an OPA

difference between OHT, POAG, and control groups (Schwenn et al., 2002; Wang et al., 2013). In patients with OHT and chronic POAG, increased OPA was a significant risk factor for visual field loss (Gross et al., 2014).

While we did not include dogs treated with glaucoma medications, a weakness of several referenced human clinical studies is the unknown contribution of glaucoma treatments on the OPA. There are only limited data on the effect of topical glaucoma medications: For example, while the prostaglandin analog latanoprost and the carbonic anhydrase inhibitor dorzolamide HCl were associated with increased POBF, the beta-adrenergic blocker timolol maleate did not affect POBF (Claridge and Smith, 1994; Schmidt et al., 1998; Georgopoulos et al., 2002). Another study showed an OPA-lowering effect of the prostaglandin analogs tafluprost and latanoprost in human patients with NTG and POAG (Park et al., 2015).

The measurement of OPA is a reasonably old method and has been performed by several investigators over the past century on humans and various animal species (Thiel, 1928; Susuki, 1962; Bynke and Krakau, 1964; Lawrence and Schlegel, 1966; Lester, 1966; Bynke, 1968). The reliability of ocular pulse pressure waves measured with a pneumatic tonometer has been previously documented in dogs, confirmed with manometric systems, and compared to humans and rabbits (Tonjum, 1972). The pneumotonography used in this study has been well-established in dogs and is routinely used in our laboratory to measure aqueous humor outflow facility (Gelatt et al., 1996). The pneumotonography tonometer was previously compared to other applanation tonometers in dogs (Gelatt and MacKay, 1998). We have shown an excellent linear correlation between the Reichert Model 30™ Pneumotonometer and the iCare TonoVet® rebound tonometer, with the pneumotonometer reading consistently higher than the rebound tonometer. Because the iCare TonoVet® is the standard tonometer used in our laboratory and widely used in veterinary clinical practice, we used IOP measurements taken with this rebound tonometer for our statistical analyses.

As expected, IOPs were significantly higher in mutant vs. normal dogs because the G661R missense mutation in *ADAMTS10* is responsible for OAG (Kuchtey et al., 2011). The IOPs were not high enough to affect PPs significantly, although there was a significant negative correlation between IOP and PP. There were also no significant differences in CCT, but we found a significant correlation between IOP and CCT. In human glaucoma patients, OPA has been previously positively associated with CCT (Weizer et al., 2007). Axial length was significantly larger in our mutant vs. normal dogs, with a significant positive correlation between IOP and AXL, consistent with the chronic IOP increase associated with *ADAMTS10*-OAG and the development of buphthalmos. The significant linear age-AXL correlation in *ADAMTS10*-mutant dogs further supported this. Since there was no such correlation in normal dogs, and all enrolled canine eyes were considered adult-size (Tuntivanich et al., 2007), the increase in AXL with age was likely disease-related.

Despite the extensive age range (normal = 11 years; mutant = 6 years), we could not detect a significant OPA age effect in mutant and normal dogs. The trend lines in Figure 5 are likely affected by the outliers. We have previously reported that age was positively associated with complex modulus and negatively associated with loss tangent, suggesting increased stiffness and decreased mechanical damping with age in *ADAMTS10*-mutant and normal dogs (Palko et al., 2016). This disagreement should be investigated in a future study by comparing OPA and scleral biomechanics in the same canine globes–this was beyond the scope of the current, non-terminal study. We did observe that OPA differences became less significant when excluding young adult dogs <12 months of age.

We found a significant positive correlation between OPA and IOP in *ADAMTS10*-mutant dogs. This finding is consistent with several human studies that found positive correlations between OPA and IOP in healthy individuals and patients with NTG and OHT (Phillips et al., 1992; Kaufmann et al., 2006; Kim et al., 2013; Sturmer and Kniestedt, 2015).

The remodeling of the sclera is likely more affected by cumIOP rather than a single measurement taken on the procedure day. Therefore, we attempted to include cumIOP as a variable. Because the number of archival IOP data varied between dogs and was not collected continuously, the cumIOP numbers in this study should be considered estimates. The numbers were highly variable and surprisingly not significantly different between mutant and normal dogs, possibly because of the more advanced age of some normal dogs. While we did not find any cumIOP-OPA correlation, age and AXL were positively correlated with cumIOP in *ADAMTS10*-mutant dogs.

The lack of a significant correlation between OPA and PP is consistent with results from human studies (Sturmer and Kniestedt, 2015). We also did not find a significant correlation between OPA and AXL and between OPA and CD. Previous studies reported significant negative correlations between OPA and AXL, especially in human eyes with high myopia (Kaufmann et al., 2006; Sturmer and Kniestedt, 2015; Yang and Koh, 2015).

We found no significant correlations between OPA and VPA in our dogs. One study in human NTG patients showed a positive correlation between OPA and blood pressure amplitude (Kim et al., 2013). The OPA and blood pressure variances ratio was a potential diagnostic indicator for early human POAG, but the study included only ten normal and 11 glaucoma patients (Robert et al., 2012).

The significant correlation between the two eyes' OPA justified averaging parameters from the left and right eyes. A previous simulation study showed that using the average of both eyes of the same individual as an analysis unit preserved type I error better than other statistical techniques while maintaining the power (Huang et al., 2018).

In addition to the lack of direct comparison of OPA and scleral biomechanics in the same eyes, our study has several other limitations, including the relatively small sample size compared to most referenced human studies. Because we do not have any clear indication of reduced ocular blood flow in *ADAMTS10*-mutant dogs, the additional measurement of pulsatile blood flow would have strengthened the main conclusions of our study regarding the OPA-scleral biomechanics relationship. Nevertheless, to our knowledge, this is the first study that evaluates OPA as a potential clinical measure for ocular rigidity in a well-established large animal glaucoma model with well-defined scleral biomechanics. Others proposed a relationship between corneal hysteresis and OPA and their heritability in human subjects (Kaufmann et al., 2006; Carbonaro et al., 2008). Future studies will be strengthened by directly comparing

OPA with *ex vivo* corneal and scleral biomechanical measurements in the same eyes. We are aware of the potential limitations of OPA measurement since it is not only influenced by ocular rigidity but also by other factors, such as the amplitude of the pulsatile blood flow. Nevertheless, the expanded clinical testing of ocular rigidity by including OPA has excellent potential in assessing glaucoma risk relative to IOP.

Data availability statement

The raw data supporting the conclusions of this article will be made available by the authors, without undue reservation.

Ethics statement

The animal study was approved by Michigan State University Institutional Animal Care and Use Committee (IACUC). The study was conducted in accordance with the local legislation and institutional requirements.

Author contributions

VR: conceptualization, methodology, and writing manuscript; DS: data analysis; SW: data analysis; JK: conceptualization and methodology; AJ: conceptualization and methodology; CH: conceptualization and methodology; AK: conceptualization, writing manuscript, and supervision. All authors contributed to the article and approved the submitted version.

Funding

This work was supported by the National Institutes of Health (R01-EY025752, T35-OD016477-19, R01-EY032478), the BrightFocus Foundation (G2022007S), and the Ronald and Sharon Loessel Endowment Fund.

Acknowledgments

The authors thank Dr. Simon Petersen-Jones, Janice Querubin, Lydia Kapeller, Ava Cabble, and the Michigan State University Campus Animal Resources staff for their technical support.

Conflict of interest

AK is a consultant and received research funding from Reichert, Inc.

The remaining authors declare that the research was conducted in the absence of any commercial or financial relationships that could be construed as a potential conflict of interest.

Publisher's note

References

Agarwal, H. C., Gupta, V., Sihota, R., and Singh, K. (2003). Pulsatile ocular blood flow among normal subjects and patients with high tension glaucoma. *Indian J. Ophthalmol.* 51, 133–138.

Asejczyk-Widlicka, M., Krzyzanowska-Berkowska, P., Kowalska, M., and Iskander, D. R. (2014). Clinical utility of spectral analysis of intraocular pressure pulse wave. *BMC Ophthalmol.* 14, 30. doi:10.1186/1471-2415-14-30

Ayyalasomayajula, A., Park, R. I., Simon, B. R., and Vande Geest, J. P. (2016). A porohyperelastic finite element model of the eye: the influence of stiffness and permeability on intraocular pressure and optic nerve head biomechanics. *Comput. Methods Biomech. Biomed. Engin* 19, 591–602. doi:10.1080/10255842.2015.1052417

Beaton, L., Mazzaferri, J., Lalonde, F., Hidalgo-Aguirre, M., Descovich, D., Lesk, M. R., et al. (2015). Non-invasive measurement of choroidal volume change and ocular rigidity through automated segmentation of high-speed OCT imaging. *Biomed. Opt. Express* 6, 1694–1706. doi:10.1364/boe.6.001694

Bellezza, A. J., Hart, R. T., and Burgoyne, C. F. (2000). The optic nerve head as a biomechanical structure: initial finite element modeling. *Invest. Ophthalmol. Vis. Sci.* 41, 2991–3000.

Boote, C., Palko, J. R., Sorensen, T., Mohammadvali, A., Elsheikh, A., Komaromy, A. M., et al. (2016). Changes in posterior scleral collagen microstructure in canine eyes with an ADAMTS10 mutation. *Mol. Vis.* 22, 503–517.

Burgoyne, C. F. (2011). A biomechanical paradigm for axonal insult within the optic nerve head in aging and glaucoma. *Exp. Eye Res.* 93, 120–132. doi:10.1016/j.exer.2010.09.005

Burgoyne, C. F., Downs, J. C., Bellezza, A. J., Suh, J. K., and Hart, R. T. (2005). The optic nerve head as a biomechanical structure: a new paradigm for understanding the role of IOP-related stress and strain in the pathophysiology of glaucomatous optic nerve head damage. *Prog. Retin Eye Res.* 24, 39–73. doi:10.1016/j.preteyeres.2004.06.001

Bynke, H. G. (1968). Further estimation of the oculosphygmography as a diagnostic method in carotid occlusive disease. *Acta Ophthalmol. (Copenh)* 46, 792–805. doi:10.1111/j.1755-3768.1968.tb02878.x

Bynke, H. G., and Krakau, C. E. (1964). A handy instrument for oculo-sphygmography with some clinical results. *Ophthalmologica* 148, 367–373. doi:10.1159/000304708

Carbonaro, F., Andrew, T., Mackey, D. A., Spector, T. D., and Hammond, C. J. (2008). The heritability of corneal hysteresis and ocular pulse amplitude: a twin study. *Ophthalmology* 115, 1545–1549. doi:10.1016/j.ophtha.2008.02.011

Claridge, K. G., and Smith, S. E. (1994). Diurnal variation in pulsatile ocular blood flow in normal and glaucomatous eyes. *Surv. Ophthalmol.* 38 (Suppl. l), S198–S205. doi:10.1016/0039-6257(94)90067-1

Clayson, K., Pan, X., Pavlatos, E., Short, R., Morris, H., Hart, R. T., et al. (2017). Corneoscleral stiffening increases IOP spike magnitudes during rapid microvolumetric change in the eye. *Exp. Eye Res.* 165, 29–34. doi:10.1016/j.exer.2017.08.015

COLLABORATIVE NORMAL-TENSION GLAUCOMA STUDY GROUP (1998a). Comparison of glaucomatous progression between untreated patients with normal-tension glaucoma and patients with therapeutically reduced intraocular pressures. Collaborative Normal-Tension Glaucoma Study Group. *Am. J. Ophthalmol.* 126, 487–497. doi:10.1016/s0002-9394(98)00223-2

COLLABORATIVE NORMAL-TENSION GLAUCOMA STUDY GROUP (1998b). The effectiveness of intraocular pressure reduction in the treatment of normal-tension glaucoma. Collaborative Normal-Tension Glaucoma Study Group. *Am. J. Ophthalmol.* 126, 498–505. doi:10.1016/s0002-9394(98)00272-4

Coudrillier, B., Campbell, I. C., Read, A. T., Geraldes, D. M., Vo, N. T., Feola, A., et al. (2016). Effects of peripapillary scleral stiffening on the deformation of the lamina cribrosa. *Invest. Ophthalmol. Vis. Sci.* 57, 2666–2677. doi:10.1167/iovs.15-18193

Dastiridou, A. I., Ginis, H. S., De Brouwere, D., Tsilimbaris, M. K., and Pallikaris, I. G. (2009). Ocular rigidity, ocular pulse amplitude, and pulsatile ocular blood flow: the effect of intraocular pressure. *Invest. Ophthalmol. Vis. Sci.* 50, 5718–5722. doi:10.1167/iovs.09-3760

Downs, J. C. (2015). IOP telemetry in the nonhuman primate. *Exp. Eye Res.* 141, 91–98. doi:10.1016/j.exer.2015.07.015

Downs, J. C., Roberts, M. D., Burgoyne, C. F., and Hart, R. T. (2009). Multiscale finite element modeling of the lamina cribrosa microarchitecture in the eye. *Annu. Int. Conf. IEEE Eng. Med. Biol. Soc.* 2009, 4277–4280. doi:10.1109/IEMBS.2009.5332755

Friedenwald, J. S. (1937). Contribution to the theory and practice of tonometry. *Am. J. Ophthalmol.* 20, 985–1024. doi:10.1016/s0002-9394(37)90425-2

Gelatt, K. N., Gum, G. G., Mackay, E. O., and Gelatt, K. J. (1996). Estimations of aqueous humor outflow facility by pneumatonography in normal, genetic carrier and glaucomatous beagles. *Veterinary & Comp. Ophthalmol.* 6, 148–151.

Gelatt, K. N., and Mackay, E. O. (1998). Distribution of intraocular pressure in dogs. *Vet. Ophthalmol.* 1, 109–114. doi:10.1046/j.1463-5224.1998.00024.x

Georgopoulos, G. T., Diestelhorst, M., Fisher, R., Ruokonen, P., and Krieglstein, G. K. (2002). The short-term effect of latanoprost on intraocular pressure and pulsatile ocular blood flow. *Acta Ophthalmol. Scand.* 80, 54–58. doi:10.1034/j.1600-0420.2002.800111.x

Gordon, M. O., Beiser, J. A., Brandt, J. D., Heuer, D. K., Higginbotham, E. J., Johnson, C. A., et al. (2002). The Ocular Hypertension Treatment Study: baseline factors that predict the onset of primary open-angle glaucoma. *Arch. Ophthalmol.* 120, 714–720. doi:10.1001/archopht.120.6.714

Gross, S., Gugleta, K., Turksever, C., Ledolter, A., Kochkorov, A., Flammer, J., et al. (2014). Analysis of risk factors for long-term glaucomatous damage development. *Klin. Monbl Augenheilkd* 231, 335–339. doi:10.1055/s-0034-1368222

Hopkins, A. A., Murphy, R., Irnaten, M., Wallace, D. M., Quill, B., and O'Brien, C. (2020). The role of lamina cribrosa tissue stiffness and fibrosis as fundamental biomechanical drivers of pathological glaucoma cupping. *Am. J. Physiol. Cell Physiol.* 319, C611–C623. doi:10.1152/ajpcell.00054.2020

Huang, J., Huang, J., Chen, Y., and Ying, G. S. (2018). Evaluation of approaches to analyzing continuous correlated eye data when sample size is small. *Ophthalmic Epidemiol.* 25, 45–54. doi:10.1080/09286586.2017.1339809

Jonas, J. B., Aung, T., Bourne, R. R., Bron, A. M., Ritch, R., and Panda-Jonas, S. (2017). Glaucoma. *Lancet* 390, 2183–2193. doi:10.1016/s0140-6736(17)31469-1

Kac, M. J., Solari, H. P., Velarde, G. C., Brazuna, R., Cardoso, G. P., and Ventura, M. P. (2011). Ocular pulse amplitude in patients with asymmetric primary open-angle glaucoma. *Curr. Eye Res.* 36, 727–732. doi:10.3109/02713683.2011.584652

Katsimpris, J. M., Theoulakis, P. E., Papadopoulos, G. E., Katsimpris, A., Lepidas, J., and Petropoulos, I. K. (2014). Ocular pulse amplitude measurement using pascal dynamic contour tonometer in glaucoma patients. *Klin. Monbl Augenheilkd* 231, 363–367. doi:10.1055/s-0034-1368220

Kaufmann, C., Bachmann, L. M., Robert, Y. C., and Thiel, M. A. (2006). Ocular pulse amplitude in healthy subjects as measured by dynamic contour tonometry. *Arch. Ophthalmol.* 124, 1104–1108. doi:10.1001/archopht.124.8.1104

Kerr, J., Nelson, P., and O'Brien, C. (1998). A comparison of ocular blood flow in untreated primary open-angle glaucoma and ocular hypertension. *Am. J. Ophthalmol.* 126, 42–51. doi:10.1016/s0002-9394(98)00074-9

Khan, J. C., Hughes, E. H., Tom, B. D., and Diamond, J. P. (2002). Pulsatile ocular blood flow: the effect of the Valsalva manoeuvre in open angle and normal tension glaucoma: a case report and prospective study. *Br. J. Ophthalmol.* 86, 1089–1092. doi:10.1136/bjo.86.10.1089

Kim, Y. J., Lee, K. S., Lee, J. R., Na, J. H., Choi, J., Han, S., et al. (2013). Ocular pulse amplitude as a dynamic parameter and its relationship with 24-h intraocular pressure and blood pressure in glaucoma. *Exp. Eye Res.* 115, 65–72. doi:10.1016/j.exer.2013.06.010

Kniestedt, C., Lin, S., Choe, J., Nee, M., Bostrom, A., Sturmer, J., et al. (2006). Correlation between intraocular pressure, central corneal thickness, stage of glaucoma, and demographic patient data: prospective analysis of biophysical parameters in tertiary glaucoma practice populations. *J. Glaucoma* 15, 91–97. doi:10.1097/00061198-200604000-00003

Koz, O. G., Turkcu, M. F., Yarangumeli, A., Koz, C., and Kural, G. (2009). Normotensive glaucoma and risk factors in normotensive eyes with pseudoexfoliation syndrome. *J. Glaucoma* 18, 684–688. doi:10.1097/ijg.0b013e31819c4311

Kuchtey, J., Olson, L. M., Rinkoski, T., Mackay, E. O., Iverson, T. M., Gelatt, K. N., et al. (2011). Mapping of the disease locus and identification of ADAMTS10 as a candidate gene in a canine model of primary open angle glaucoma. *PLoS Genet.* 7, e1001306. doi:10.1371/journal.pgen.1001306

Kynigopoulos, M., Tzamalis, A., Ntampos, K., and Schlote, T. (2012). Decreased ocular pulse amplitude associated with functional and structural damage in open-angle glaucoma. *Eur. J. Ophthalmol.* 22, 111–116. doi:10.5301/ejo.5000043

Lawrence, C., and Schlegel, W. A. (1966). Ophthalmic pulse studies. I. Influence of intraocular pressure. *Invest. Ophthalmol.* 5, 515–525.

Lee, M., Cho, E. H., Lew, H. M., and Ahn, J. (2012). Relationship between ocular pulse amplitude and glaucomatous central visual field defect in normal-tension glaucoma. *J. Glaucoma* 21, 596–600. doi:10.1097/ijg.0b013e31824cfbf7

Lester, H. A. (1966). Ocular oscillometry in cerebrovascular disease. *Arch. Ophthalmol.* 76, 391–398. doi:10.1001/archopht.1966.03850010393018

Liu, J., and He, X. (2009). Corneal stiffness affects IOP elevation during rapid volume change in the eye. *Invest. Ophthalmol. Vis. Sci.* 50, 2224–2229. doi:10.1167/iovs.08-2365

Markert, J. E., Turner, D. C., Jasien, J. V., Nyankerh, C. N. A., Samuels, B. C., and Downs, J. C. (2022). Ocular pulse amplitude correlates with ocular rigidity at native IOP despite the variability in intraocular pulse volume with each heartbeat. *Transl. Vis. Sci. Technol.* 11, 6. doi:10.1167/tvst.11.9.6

Ma, Y., Moroi, S. E., and Roberts, C. J. (2021). Non-invasive clinical measurement of ocular rigidity and comparison to biomechanical and morphological parameters in glaucomatous and healthy subjects. *Front. Med. (Lausanne)* 8, 701997. doi:10.3389/fmed.2021.701997

Medeiros, F. A., Meira-Freitas, D., Lisboa, R., Kuang, T. M., Zangwill, L. M., and Weinreb, R. N. (2013). Corneal hysteresis as a risk factor for glaucoma progression: a prospective longitudinal study. *Ophthalmology* 120, 1533–1540. doi:10.1016/j.ophtha.2013.01.032

Milioti, G., Langenbucher, A., Seitz, B., and Low, U. (2017). Effect of morphological and functional parameters on ocular pulse amplitudes: an analysis in ocular hypertension and different types of glaucoma. *Klin. Monbl Augenheilkd* 234, 223–230. doi:10.1055/s-0042-101350

Mittag, T. W., Serle, J., Schumer, R., Brodie, S., Stegman, D., Schmidt, K. G., et al. (1994). Studies of the ocular pulse in primates. *Surv. Ophthalmol.* 38 (Suppl. l), S183–S190. doi:10.1016/0039-6257(94)90065-5

Moghimi, S., Torabi, H., Fakhraie, G., Nassiri, N., and Mohammadi, M. (2013). Dynamic contour tonometry in primary open angle glaucoma and pseudoexfoliation glaucoma: factors associated with intraocular pressure and ocular pulse amplitude. *Middle East Afr. J. Ophthalmol.* 20, 158–162. doi:10.4103/0974-9233.110606

Morris, H. J., Tang, J., Cruz Perez, B., Pan, X., Hart, R. T., Weber, P. A., et al. (2013). Correlation between biomechanical responses of posterior sclera and IOP elevations during micro intraocular volume change. *Invest. Ophthalmol. Vis. Sci.* 54, 7215–7222. doi:10.1167/iovs.13-12441

Palko, J. R., Iwabe, S., Pan, X., Agarwal, G., Komaromy, A. M., and Liu, J. (2013). Biomechanical properties and correlation with collagen solubility profile in the posterior sclera of canine eyes with an ADAMTS10 mutation. *Invest. Ophthalmol. Vis. Sci.* 54, 2685–2695. doi:10.1167/iovs.12-10621

Palko, J. R., Morris, H. J., Pan, X., Harman, C. D., Koehl, K. L., Gelatt, K. N., et al. (2016). Influence of age on ocular biomechanical properties in a canine glaucoma model with ADAMTS10 mutation. *PLoS One* 11, e0156466. doi:10.1371/journal.pone.0156466

Park, S. A., and Komaromy, A. M. (2021). Biomechanics of the optic nerve head and sclera in canine glaucoma: a brief review. *Vet. Ophthalmol.* 24, 316–325. doi:10.1111/vop.12923

Park, S. H., Yoo, S. H., and Ha, S. J. (2015). Comparison of ocular pulse amplitude-lowering effects of tafluprost and latanoprost by dynamic contour tonometry. *J. Ocul. Pharmacol. Ther.* 31, 617–622. doi:10.1089/jop.2014.0122

Phillips, C. I., Tsukahara, S., Hosaka, O., and Adams, W. (1992). Ocular pulsation correlates with ocular tension: the choroid as piston for an aqueous pump? *Ophthalmic Res.* 24, 338–343. doi:10.1159/000267190

Punjabi, O. S., Ho, H. K., Kniestedt, C., Bostrom, A. G., Stamper, R. L., and Lin, S. C. (2006). Intraocular pressure and ocular pulse amplitude comparisons in different types of glaucoma using dynamic contour tonometry. *Curr. Eye Res.* 31, 851–862. doi:10.1080/02713680600899887

Quaranta, L., Manni, G., Donato, F., and Bucci, M. G. (1994). The effect of increased intraocular pressure on pulsatile ocular blood flow in low tension glaucoma. *Surv. Ophthalmol.* 38, S177–S182. doi:10.1016/0039-6257(94)90064-7

Quigley, H. A., and Broman, A. T. (2006). The number of people with glaucoma worldwide in 2010 and 2020. *Br. J. Ophthalmol.* 90, 262–267. doi:10.1136/bjo.2005.081224

Read, S. A., Collins, M. J., and Iskander, D. R. (2008). Diurnal variation of axial length, intraocular pressure, and anterior eye biometrics. *Invest. Ophthalmol. Vis. Sci.* 49, 2911–2918. doi:10.1167/iovs.08-1833

Robert, Y. C., Wild, A., Kessels, A. G., Backes, W. H., Zollinger, A., and Bachmann, L. M. (2012). Discrimination of healthy and glaucomatous eyes based on the ocular pulse amplitude: a diagnostic case-control study. *Ophthalmic Res.* 48, 1–5. doi:10.1159/000334616

Romppainen, T., Kniestedt, C., Bachmann, L. M., and Sturmer, J. (2007). Ocular pulse amplitude: a new biometrical parameter for the diagnose of glaucoma? *Ophthalmologe* 104, 230–235. doi:10.1007/s00347-006-1467-8

Safa, B. N., Wong, C. A., Ha, J., and Ethier, C. R. (2022). Glaucoma and biomechanics. *Curr. Opin. Ophthalmol.* 33, 80–90. doi:10.1097/icu.0000000000000829

Sayah, D. N., Mazzaferri, J., Ghesquiere, P., Duval, R., Rezende, F., Costantino, S., et al. (2020). Non-invasive *in vivo* measurement of ocular rigidity: clinical validation, repeatability and method improvement. *Exp. Eye Res.* 190, 107831. doi:10.1016/j.exer.2019.107831

Schmidt, K. G., Ruckmann, A. V., Mittag, T. W., Hessemer, V., and Pillunat, L. E. (1997). Reduced ocular pulse amplitude in low tension glaucoma is independent of vasospasm. *Eye (Lond)* 11 (Pt 4), 485–488. doi:10.1038/eye.1997.131

Schmidt, K. G., Von Ruckmann, A., and Pillunat, L. E. (1998). Topical carbonic anhydrase inhibition increases ocular pulse amplitude in high tension primary open angle glaucoma. *Br. J. Ophthalmol.* 82, 758–762. doi:10.1136/bjo.82.7.758

Schwenn, O., Troost, R., Vogel, A., Grus, F., Beck, S., and Pfeiffer, N. (2002). Ocular pulse amplitude in patients with open angle glaucoma, normal tension glaucoma, and ocular hypertension. *Br. J. Ophthalmol.* 86, 981–984. doi:10.1136/bjo.86.9.981

Sherwood, J. M., Boazak, E. M., Feola, A. J., Parker, K., Ethier, C. R., and Overby, D. R. (2019). Measurement of ocular compliance using iPerfusion. *Front. Bioeng. Biotechnol.* 7, 276. doi:10.3389/fbioe.2019.00276

Sommer, A., Tielsch, J. M., Katz, J., Quigley, H. A., Gottsch, J. D., Javitt, J., et al. (1991). Relationship between intraocular pressure and primary open angle glaucoma among white and black Americans. The Baltimore Eye Survey. *Arch. Ophthalmol.* 109, 1090–1095. doi:10.1001/archopht.1991.01080080050026

Stalmans, I., Harris, A., Vanbellinghen, V., Zeyen, T., and Siesky, B. (2008). Ocular pulse amplitude in normal tension and primary open angle glaucoma. *J. Glaucoma* 17, 403–407. doi:10.1097/ijg.0b013e31815c5f2c

Sturmer, J. P., and Kniestedt, C. (2015). Role of ocular pulse amplitude in glaucoma. *Klin. Monbl Augenheilkd* 232, 162–168. doi:10.1055/s-0034-1396232

Susuki, I. (1962). Corneal pulsations and corneal pulse wave. *Jap J. Opthal* 6, 190–194.

Thiel, R. (1928). Hornhautpulsation, Blutdruck und Augendruck. *Ber. Dtsch. Ophthal Ges.* 47, 198–206.

Tonjum, A. M. (1972). Studies on the ocular pulse pressure wave in human, dog, and rabbit eyes with a pneumatic tonometer. *Acta Ophthalmol. (Copenh)* 50, 677–688. doi:10.1111/j.1755-3768.1972.tb06608.x

Trew, D. R., and Smith, S. E. (1991a). Postural studies in pulsatile ocular blood flow: I. Ocular hypertension and normotension. *Br. J. Ophthalmol.* 75, 66–70. doi:10.1136/bjo.75.2.66

Trew, D. R., and Smith, S. E. (1991b). Postural studies in pulsatile ocular blood flow: II. Chronic open angle glaucoma. *Br. J. Ophthalmol.* 75, 71–75. doi:10.1136/bjo.75.2.71

Tuntivanich, N., Petersen-Jones, S. M., Steibel, J. P., Johnson, C., and Forcier, J. Q. (2007). Postnatal development of canine axial globe length measured by B-scan ultrasonography. *Vet. Ophthalmol.* 10, 2–5. doi:10.1111/j.1463-5224.2007.00481.x

Turner, D. C., Edmiston, A. M., Zohner, Y. E., Byrne, K. J., Seigfreid, W. P., Girkin, C. A., et al. (2019). Transient intraocular pressure fluctuations: source, magnitude, frequency, and associated mechanical energy. *Invest. Ophthalmol. Vis. Sci.* 60, 2572–2582. doi:10.1167/iovs.19-26600

Vulsteke, C., Stalmans, I., Fieuws, S., and Zeyen, T. (2008). Correlation between ocular pulse amplitude measured by dynamic contour tonometer and visual field defects. *Graefes Arch. Clin. Exp. Ophthalmol.* 246, 559–565. doi:10.1007/s00417-007-0706-2

Wang, J., Freeman, E. E., Descovich, D., Harasymowycz, P. J., Kamdeu Fansi, A., Li, G., et al. (2013). Estimation of ocular rigidity in glaucoma using ocular pulse amplitude and pulsatile choroidal blood flow. *Invest. Ophthalmol. Vis. Sci.* 54, 1706–1711. doi:10.1167/iovs.12-9841

Weinreb, R. N., Aung, T., and Medeiros, F. A. (2014). The pathophysiology and treatment of glaucoma: a review. *JAMA* 311, 1901–1911. doi:10.1001/jama.2014.3192

Weinreb, R. N., Leung, C. K., Crowston, J. G., Medeiros, F. A., Friedman, D. S., Wiggs, J. L., et al. (2016). Primary open-angle glaucoma. *Nat. Rev. Dis. Prim.* 2, 16067. doi:10.1038/nrdp.2016.67

Weizer, J. S., Asrani, S., Stinnett, S. S., and Herndon, L. W. (2007). The clinical utility of dynamic contour tonometry and ocular pulse amplitude. *J. Glaucoma* 16, 700–703. doi:10.1097/ijg.0b013e31806ab2fe

Yang, Y. S., and Koh, J. W. (2015). Choroidal blood flow change in eyes with high myopia. *Korean J. Ophthalmol.* 29, 309–314. doi:10.3341/kjo.2015.29.5.309

frontiers | Frontiers in Bioengineering and Biotechnology

TYPE Original Research
PUBLISHED 15 December 2023
DOI 10.3389/fbioe.2023.1242440

OPEN ACCESS

EDITED BY
Matthew A. Reilly,
The Ohio State University, United States

REVIEWED BY
Kai Guo,
University of Illinois Chicago, United States
Jinhai Huang,
Fudan University, China

*CORRESPONDENCE
Ruihua Wei,
rwei@tmu.edu.cn

†These authors have contributed equally to this work and share first authorship

RECEIVED 19 June 2023
ACCEPTED 30 November 2023
PUBLISHED 15 December 2023

CITATION
Liu L, Rong H, Wu D, Xu H, He Q, Du B, Zhang X and Wei R (2023), Analysis of morphological and quantitative changes in pathological myopia and perioperative changes in posterior scleral reinforcement using three-dimensional magnet resonance imaging.
Front. Bioeng. Biotechnol. 11:1242440.
doi: 10.3389/fbioe.2023.1242440

Analysis of morphological and quantitative changes in pathological myopia and perioperative changes in posterior scleral reinforcement using three-dimensional magnet resonance imaging

Lin Liu[1†], Hua Rong[1†], Di Wu[1], He Xu[2], Qing He[1], Bei Du[1], Xuejun Zhang[2] and Ruihua Wei[1*]

[1]Tianjin International Joint Research and Development Centre of Ophthalmology and Vision Science, Eye Institute and School of Optometry, Tianjin Medical University Eye Hospital, Tianjin, China, [2]Department of Radiology, Second Hospital of Tianjin Medical University, Tianjin, China

Objective: To compare the morphological and quantitative changes in pathological myopia (PM) and the perioperative changes in posterior scleral reinforcement (PSR) using three-dimensional magnetic resonance images (3D MRI).

Methods: A total of 49 patients with high myopia (HM; 98 eyes), 15 with pathological myopia (PM; 19 eyes), and 10 without high myopia (NORM; 20 eyes) were recruited between September 2019 and July 2021. The patients underwent measurements of refractive error and axial length, as well as 3D MRI of the eyeball. Python was used to analyze the 3D MRI images, calculate the vitreous volume, establish a topography of the height of the eyeball posterior surface, and calculate the rate of change in height (H). For the PM group undergoing PSR, changes in vitreous volume and the highest point of the eyeball posterior surface in four quadrants (temporal, subtemporal, nasal, and subnasal) were compared before and after PSR.

Results: The vitreous volume was smaller in the NORM group compared to the HM and PM groups ($p < 0.01$). The PM group had a larger volume than the HM group ($p < 0.01$). The H for the PM group was higher than that of the NORM and HM groups ($p < 0.01$). After PSR in the PM group, the total vitreous volume, as well as the volume in the subnasal and supratemporal quadrants, decreased ($p < 0.05$). Additionally, the highest point of the eyeball's posterior surface was generally shifted to the upper nasal side. Finally, the shape and position of the scleral band after PSR were plotted.

Conclusion: 3D MRI is capable of a quantitative description of the eyeball morphology in PM and PSR. It allows for precise calculations of changes in vitreous volume and the H of the posterior surface. It also facilitates a meticulous analysis of the specific details of the scleral band following PSR.

KEYWORDS

high myopia, pathological myopia, 3D MRI, posterior staphyloma, posterior scleral reinforcement (PSR)

Highlights

- In clinical practice, it is crucial to evaluate eyeball morphology and posterior staphyloma comprehensively before posterior scleral reinforcement. But the routine ophthalmic clinical examination is difficult to achieve.
- 3D MRI provides detailed and overall information of eyeball images for pathological myopia and posterior staphyloma. It also can explore the changing details of eyeball morphology before and after posterior scleral reinforcement, and simulate the shape and relative position of scleral bands.
- 3D MRI might be an effective method for surgery plan before PSR and surgery evaluation after PSR in the future.

1 Introduction

The prevalence of high myopia (HM) is projected to increase significantly worldwide between 2000 and 2050. By 2050, it is estimated that 10% of the global population will have HM, representing a five-fold increase from 2% in 2000 (Holden et al., 2016). Within the HM population, the prevalence of pathological myopia (PM) is as high as 50%–70% (Ohno-Matsui et al., 2021). HM is characterized by a high degree of myopic refractive error, while PM is characterized by the presence of specific myopic lesions in the posterior fundus, such as myopic maculopathy, retinoschisis, choroidal neovascularization, chorioretinal atrophy, and posterior staphyloma (PS), which can lead to visual impairment and even blindness (Avila et al., 1984; Hayashi et al., 2010; Jong et al., 2021; Ohno-Matsui et al., 2021).

Currently, the assessment of eyeball and fundus morphology is commonly performed using ophthalmoscopy, B-mode ultrasound imaging, and optical coherence tomography (OCT). These methods primarily focus on detailed changes in the retina, choroid, and scleral structures in the posterior eyeball, rather than the overall shape. Studies have shown that even OCT images with a scanning range of 9 mm may not capture the entire extent of the posterior staphyloma in PM (Miyake et al., 2014; Asai et al., 2016; Kuo et al., 2016; Shinohara et al., 2016; Garcia-Ben et al., 2017; Ohno-Matsui and Jonas, 2019). Based on our clinical experience, we have observed that retinal folds after posterior scleral reinforcement (PSR) on OCT images make it challenging to appreciate the complete morphological changes of the retina.

In clinical research, *in vivo* magnetic resonance imaging (MRI) and planar measurements of different eye axis lines have been used to study eyeball morphology (Moriyama et al., 2012; Shinohara et al., 2013; Nagra et al., 2014; Wang et al., 2016). However, further investigation is needed to describe and clinically apply the three-dimensional (3D) MRI morphology of the eyeball (Ohno-Matsui, 2014; Yu et al., 2018). Computer processing of acquired 3D MRI images plays a crucial role in improving the efficiency and accuracy of MRI (Evans, 2016). The vitreous volume of the eyeball, which varies with axial length, can provide a direct and objective assessment of eyeball expansion. It serves as an important 3D indicator for overall observation of PM and PS.

The primary surgical treatment for PM is posterior scleral reinforcement (PSR) (Gerinec and Slezakova, 2001), where biological materials called scleral flaps are used to cover the thinner sclera in the posterior pole and contract and reinforce it. Over time, the scleral flap integrates into the weakened scleral area, exerting compressive force on the eyeball, which helps control axial elongation and inhibits the progression of high myopia (Xue et al., 2014; Shen et al., 2015; Zhu et al., 2016; Hu et al., 2018; Peng et al., 2019). PSR can also prevent retinal detachment and secondary retinoschisis associated with PM (Zhu et al., 2018). However, the success of the surgery depends on the positioning of the scleral band and the applied pressure. Otherwise, it can lead to severe complications such as retinal ciliary artery obstruction and visual field defects (Karabatsas et al., 1997; Wen et al., 2017).

In this study, we investigated the complete shape of the eyeball and adjacent structures using 3D MRI, which provides more detailed and accurate information compared to previous measurement techniques. We utilized Python to process and analyze the 3D MRI images of the eyeball to evaluate the morphological and quantitative changes in PM, as well as the perioperative changes in PSR, including vitreous volume and scleral band information.

2 Materials and methods

This prospective study was conducted at Tianjin Medical University Eye Hospital between September 2019 and July 2021, involving 73 participants selected through consecutive sampling. Exclusion criteria were applied, including individuals who had undergone scleral buckling, had a history of ocular trauma that could affect the shape of the eyeball, experienced claustrophobia, had a pacemaker or intraocular metal foreign body, or had systemic diseases. Informed consent was obtained from all participants, and for those under 16 years of age, consent was provided by their parents or guardians. The study adhered to the principles outlined in the Declaration of Helsinki and was approved by the ethics committee of Tianjin Medical University Eye Hospital (NO. 2020KY-04).

The participants were categorized into three groups based on the degree of myopic refractive error and MRI images (Jong et al., 2021). The NORM group included individuals with a spherical equivalent

refractive error of both eyes ≥ −0.50 D. The HM group consisted of individuals with a spherical equivalent refractive error of both eyes ≤ −6.00 D but without posterior staphyloma (PS). The PM group comprised individuals with a spherical equivalent refractive error of both eyes ≤ −6.00 D and with PS. All participants underwent a comprehensive ophthalmic examination, which included assessments of best-corrected visual acuity (BCVA), slit-lamp and fundus examinations, and measurements of refractive error and intraocular pressure. The subjects in the PM group underwent posterior scleral reinforcement (PSR) as part of their treatment.

2.1 MR imaging

All eligible patients underwent a 3D MRI examination of the eye using the DiscoveryTM MR750 3.0T scanner (GE Healthcare, Milwaukee, WI, United States) equipped with an 8-channel head coil. Axial position images were obtained using a fast-recovery fast spin-echo acceleration sequence (3D FRFSE-XL) with the following imaging parameters: repetition time of 8,000 ms, echo time of 800 ms, field of view of 18 mm^2 × 18 mm^2, matrix size of 256 × 256, echo train length of 70, bandwidth of 62.5 Hz, slice thickness of 1 mm, and flip angle of 90°. The total scan time for each subject was 8 min and 41 s. T2-weighted images were used, allowing visualization of the outer surface of the intraocular fluid on the MRI. Consequently, the acquired images provided information on the vitreous volume in the posterior segment of the eye.

2.2 3D MRI postprocessing

We utilized Python 3.7.9 to process and analyze the MRI DICOM files. The Breadth-First Search algorithm was employed to extract the areas within the vitreous and cornea. Breadth-First Search (BFS) algorithm is a search algorithm used in graphs or tree data structures. It starts from a source node and explores nodes at the current level before moving on to nodes at the next level, and so on, until it reaches the target node or traverses the entire graph. In this study, it referred to starting from any point within the vitreous body and conducting a diffusion search in the surrounding area. Any point whose grayscale value differs within the threshold range from the previous point was included in the vitreous body matrix.

A Cartesian coordinate system was established with the *x* and *y*-axes parallel to the cross-section of the nuclear magnetic scan, with the origin at an arbitrary point. And then we calculated the geometric center coordinates of the vitreous body, denoted as v_c. Nextly, we translated the eye so that the geometric center of the vitreous body became the new origin, and subsequently calculated the coordinates of the geometric center of the cornea, denoted as c_c. This allowed us to obtain the vector v_c-c_c. We then used the Rodrigues' formula to compute a vector that would rotate the vector v_c-c_c to align with the direction of the vector (0, 0, −1), which points vertically downward. With this vector, we constructed a rotation matrix for the entire eyeball, ensuring that the corneal direction of the eye was oriented vertically downward. This procedure ensured that all eyes were aligned in the same direction before proceeding with the subsequent calculation of the vitreous body volume.

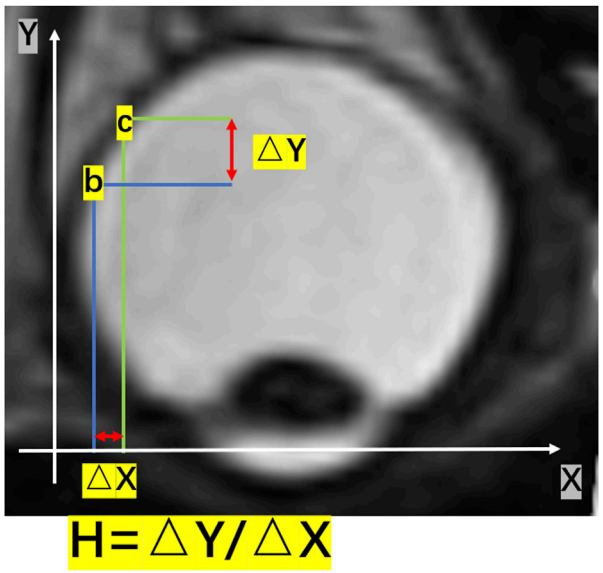

FIGURE 1
A schematic diagram of H in a two-dimensional image. The changing rate of the height of the posterior surface in the horizontal plane was given by H = ΔY/ΔX. ΔY represented the vertical change in height, and ΔX represented the change in distance in the horizontal direction.

We calculated the number of pixels within the vitreous area and converted it into volume. Furthermore, we determined the two points as b and c on the eyeball posterior surface. The point "b" and "c" were two randomed points on the eyeball posterior surface. As Figure 1 shown, It was an example of these two points. ΔX represented the horizontal distance between the two points b and c, and ΔY represented the vertical distance between the two points b and c. The changing rate of the height of the eyeball posterior surface in the horizontal plane was defined as H = ΔY/ΔX (Figure 1).

Based on the height value, we generated a topographic map of the posterior surface of the eyeball (Figure 2). Additionally, we calculated the changing rate of the height for each point on the eyeball posterior surface (H). For eyes undergoing posterior scleral reinforcement (PSR), we used the coronal plane that passing through the geometric center of the vitreous body to divide the eyeball into two parts. The posterior half was further divided into four quadrants using horizontal and sagittal planes: temporal, subtemporal, nasal, and subnasal regions. We individually calculated the volume of each part and analyzed the volume changes in each quadrant before and after surgery.

By combining the volume changes, which provided information on coordinates, with a top-down view of the height map of the posterior surface (Figure 3A, B), we were able to compare the position of the highest point before and after PSR. The height matrices of the posterior surface before and after surgery were used to plot the differences in the height of the eyeball's posterior surface, thereby visualizing the placement and extent of reinforcement of the scleral band (Figure 3C).

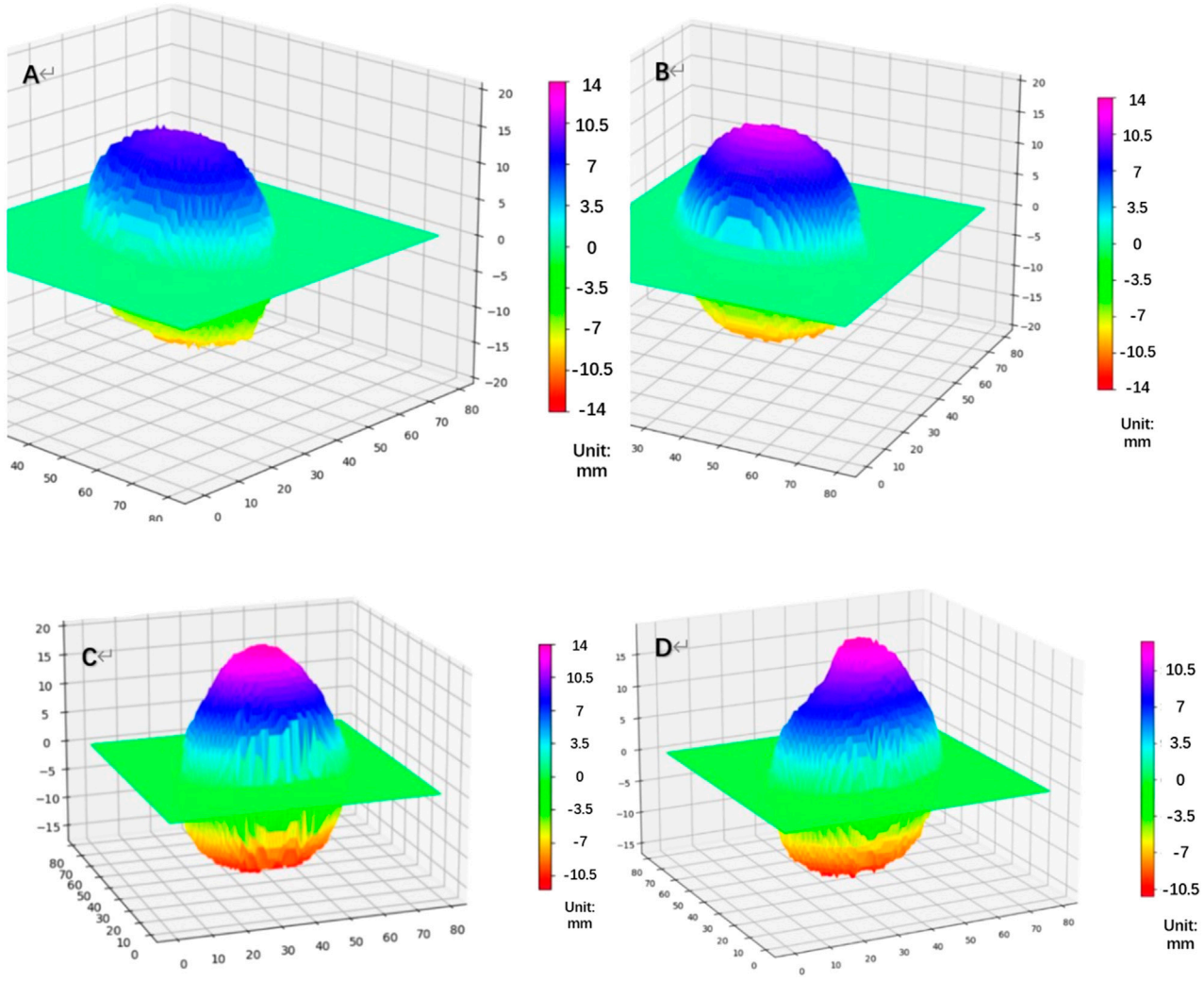

FIGURE 2
Topographic map of the height of the eyeball's posterior surface [**(A)** NORM group, **(B)** HM group, **(C)** PM group: Pre-PSR, **(D)** PM group: Post-PSR] HM, high myopia; PM, pathological myopia; NORM, non-high myopia; PSR, posterior scleral reinforcement.

2.4 AL measurement

Axial length (AL) measurements were obtained using the Lenstar LS-900 (Haag-Streit AG, Berne, Switzerland). During the examination, the participants were instructed to keep their eyes open and focus on a target. To ensure accurate measurements and avoid errors, subjects were allowed to blink between measurements, ensuring an intact tear film. Data analysis was performed using the average of three repeated measurements, where the intrasession differences were no greater than 0.02 mm. This approach ensured the reliability and consistency of the AL measurements.

2.5 PSR procedure

All surgeries were performed by experienced doctors under a microscope to ensure precision and accuracy. Prior to the surgery, all patients provided their informed consent. The surgical strips used were made of homogeneous sclerae that underwent crosslinking and rigorous sterilization using 0.1% genipin, ensuring their safety and suitability for the procedure (Xue et al., 2014).

The surgical procedure was conducted under general anesthesia. Initially, the bulbar conjunctiva was incised at a 210° angle along the corneal limbus, with the inferior temporal aspect of the eye serving as the center point. Traction lines were created for the lateral rectus and inferior rectus muscles. The strips were then carefully inserted inwards and upwards, sequentially passing through the inferior oblique, lateral rectus, and inferior rectus muscles. Non-absorbable 5–0 sutures (Alcon) were used to secure the strips to the equatorial anterior sclera between the inferior and medial recti muscles. The lateral temporal end of the strips was anchored to the equatorial sclera between the superior and lateral recti muscles. Throughout the procedure, thorough checks were

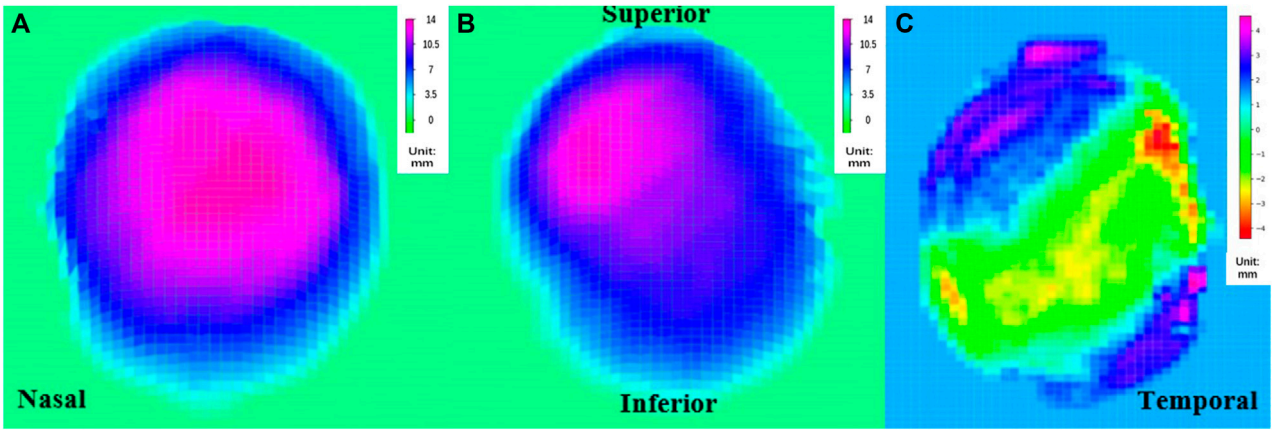

FIGURE 3
Top view of the rear surface height map **(A)** pre-PSR, **(B)** post-PSR, **(C)** the reconstructed image of the scleral band PSR, posterior scleral reinforcement.

performed to ensure that the strips were correctly positioned and oriented before completing the surgery (Zhu et al., 2016).

This standardized surgical approach, along with the use of crosslinked scleral strips and meticulous intraoperative verification, aimed to ensure the effectiveness and success of the posterior scleral reinforcement procedure.

2.6 Statistical analysis

Statistical analyses were performed using SPSS statistical package 25 (SPSS, IBM, Chicago, IL, United States). The Kolmogorov-Smirnov test assessed the data's normal distribution. Considering the inter-eye correlation between individuals, a linear mixed model was used to compared vitreous volumes and H among the NORM, HM, PM groups. Bonferroni *post hoc* analysis was used to compare differences between every two groups. The changes in vitreous volume and the volume in the four quadrants before and after PSR were further examined by Paired *t*-test. A *p*-values less than 0.05 was considered significantly.

3 Results

In total, 135 eyes of 73 patients who met the study inclusion criteria were analyzed. These included 19 eyes of 15 patients in the PM group, 96 eyes of 48 patients in the HM group and 20 eyes of 10 patients in NORM group. The age, spherical equivalence, axial length, and other parameters of the different groups were summarized in Table 1.

3.1 Vitreous volume

Univariate ANOVA revealed the following: the vitreous volume of the NORM group was 5,891 ± 1314 mm^3, which was significantly smaller than that of the HM group at 7,426 ± 451 mm^3 ($p < 0.01$). Meanwhile, the preoperative volume of the PM group was 7,896 ± 757 mm^3, which was significantly larger than that of HM group ($p < 0.01$) (Table 2; Figure 4).

TABLE 1 Patients and initial datas of the eye examinations.

	PM	HM	NORM
No. Patients (eyes) Men Women	15 (19) 6 (8) 9 (11)	48 (96) 22 (44) 26 (52)	10 (20) 4 (8) 6 (12)
Age(y), mean ± SD	55 ± 19.4	49 ± 18.2	43 ± 12.0
SE(D), mean, mean ± SD	−13.5 ± 5.3	−8.22 ± 1.20	−0.14 ± 1.1
AL (mm), mean ± SD	30.03 ± 1.57	27.33 ± 0.47	23.46 ± 0.48
LogMAR, mean ± SD	0.74 ± 0.37	−0.01 ± 0.02	−0.03 ± 0.05

3.2 Altitude change rate

H was 2.89 ± 0.27 and 2.91 ± 0.26 in the NORM and HM groups, respectively. There was no significant difference in H between the two groups ($p = 1.000$). Preoperative H in the PM group was 4.22 ± 0.87, which was significantly higher than that in the NORM and HM groups ($p < 0.01$) (Figure 5).

3.3 Preoperative and postoperative volume changes

Generally, the postoperative vitreous volume in the PM group was 7,254 ± 906 mm^3, indicating an average decrease of 642 mm compared with the preoperative volume ($p < 0.05$). By quadrants, first, the average volume of the upper nasal side of the posterior

TABLE 2 The vitreous volume and H of NORM, HM and PM group.

Parameters	PM	HM	NORM	P (PM-HM)	P (PM-NOR)	P (HM-NOR)
Vitreous volume (mm^3)	7896 ± 757	7426 ± 451	5891 ± 1314	<0.005*	<0.001*	<0.001*
H	4.22 ± 0.87	2.91 ± 0.26	2.89 ± 0.27	<0.001*	<0.001*	1.000

*Means significant differences between two groups using Bonferroni post hoc analysis.

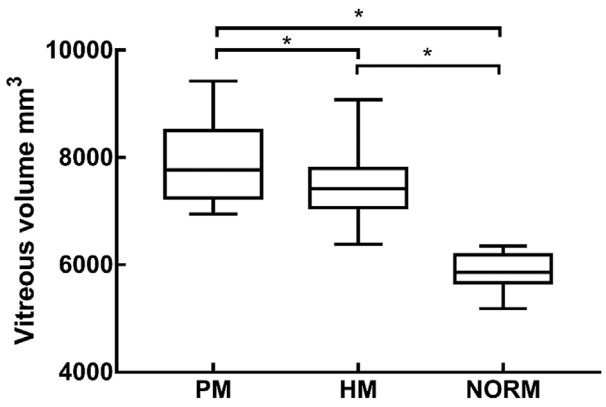

FIGURE 4
The vitreous volume of PM group, HM group, NORM group, * indicated a statistical difference between the two groups HM, high myopia; PM, pathological myopia; NORM, non-high myopia.

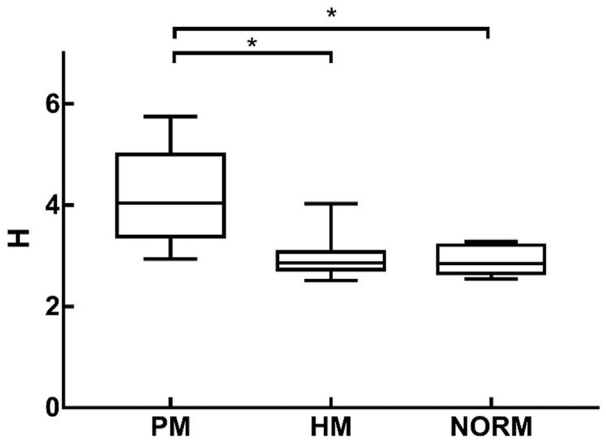

FIGURE 5
H of Pathological Myopia group (PM), High Myopia group (HM), NORM group (NORM), * indicated statistical differences between each of the two groups HM, high myopia; PM, pathological myopia; NORM, non-high myopia.

vitreous body increased by 84 mm^3, although this difference was not significant ($p = 0.177$). Second, the volume of the inferior side of the nose was post-operatively significantly reduced by 104 mm^3 ($p < 0.05$). Third, the volume of the supratemporal side was significantly reduced by 138 mm^3 ($p < 0.05$). Lastly, the average volume of the inferior temporal side was reduced by 1 mm^3, although this difference was not significant ($p = 0.987$) (Table 3).

3.4 Changes in the position of the highest point of the posterior pole before and after PSR

For the PM group, before PSR, the position of the highest point of the posterior pole was as follows: upper side of the nose, five eyes (26.3%); lower side of the nose, four eyes (21.1%); upper temporal side, four eyes (21.1%); and lower temporal side, six eyes (31.6%). After surgery, the position of the highest point of the posterior pole was as follows: upper side of the nose, 13 eyes (68.4%); lower side of the nose, two eyes (10.5%), upper temporal side, three eyes (15.8%); and lower temporal side, one eye (0.05%) (Figure 6).

4 Discussion

The complications arising from pathological myopia (PM) have a significant impact on visual impairment and blindness, particularly in East Asia. Posterior staphyloma (PS) is a distinct change in curvature at the posterior pole of the eyeball and serves as a reliable indicator of PM (Ohno-Matsui, 2014). Traditional methods of observing and analyzing eyeball morphology relied on one-dimensional or two-dimensional measurements, as well as subjective evaluations by clinicians (Jones and Luensmann, 2012; Tatewaki et al., 2019). General ophthalmic examinations may not fully visualize the shape of the staphyloma, further complicating the diagnosis and characterization of PS (Chae et al., 2011; Jo et al., 2012). Therefore, in our study, we employed Python 3.7.9 to process 3D MRI imaging, enabling us to obtain a comprehensive view of eyeball morphology. Volume renderings were utilized to reconstruct, analyze, and describe the data in a three-dimensional manner, presenting a novel approach for clinically studying eyeball morphology in PM.

In our study, we calculated the volume of the vitreous body and analyzed the differences among the NORM, HM, and PM groups. Previous research has indicated a positive correlation between vitreous volume and axial length, as an increase in axial length is primarily attributed to an expansion of the vitreous cavity (Nagra et al., 2014). Similarly, we found that the vitreous volume was larger in the HM and PM groups compared to the NORM group.

To delve deeper into the morphology of the eyeball, we calculated the height (H) and analyzed its variations among the NORM, HM, and PM groups. Our findings revealed that the H of the PM group was significantly greater than that of the NORM and HM groups. The elevated H was attributed to a sudden change in height at the edge of the PS. Interestingly, we observed that the absence of PS, sudden changes in the posterior surface, and a lack of significant H increase were characteristics found in eyes without PM-associated axial elongation. In PM, axial elongation leads to

TABLE 3 Changes in vitreous volume before and after PSR.

Location	Preoperative mm^3	Postoperative mm^3	Post- Pre mm^3	P
Full vitreous	7896 ± 757	7254 ± 906	−642	<0.05*
Superior nasal	1020 ± 184	1105 ± 194	84	0.177
Inferior nasal	966 ± 145	862 ± 139	−104	<0.05*
Superior temporal	976 ± 148	837 ± 137	−138	<0.05*
Inferior temporal	910 ± 119	909 ± 175	−1	0.987

*Means significant differences using Paired t-test.

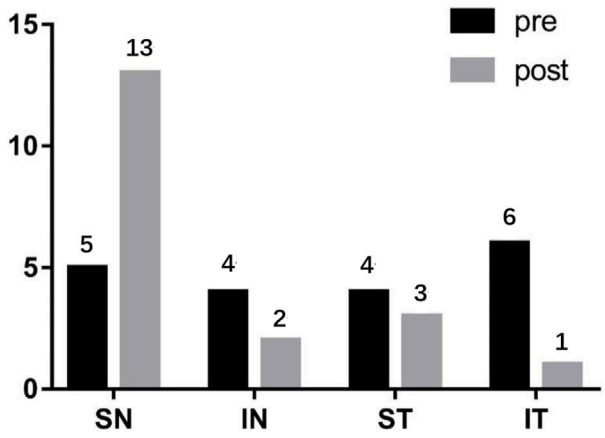

FIGURE 6
The changes of the highest point of the posterior pole before and after PSR SN: Superior nasal; IN: Inferior nasal; ST: Superior temporal; IT: Inferior temporal.

thinning of the posterior pole sclera, reduced biomechanical properties, the development of PS, and retinoschisis. Consequently, patients experience impaired corrected vision and, in severe cases, even blindness, significantly affecting their quality of life (Jones and Luensmann, 2012). posterior scleral reinforcement (PSR) can be employed clinically to strengthen the mechanical integrity of the posterior sclera, control axial elongation, and reattach a detached retina (Shen et al., 2015). However, PSR is associated with potential complications, including local ocular compression protrusion, choroidal atrophy, choroidal neovascularization, post-ciliary retinal artery occlusion, visual field defects, and capillary damage (Wen et al., 2017; Cao et al., 2020). Wen et al. suggested that the shape and positional stability of the allogeneic scleral reinforcement strip are crucial factors affecting the postoperative efficacy of PSR (Wen et al., 2017). Hence, it is imperative to assess the details of the scleral band postoperatively to evaluate the surgical outcomes.

4.1 Perioperative changes in posterior scleral reinforcement

In this study, we conducted a comparative analysis of 3D MRI images before and after posterior scleral reinforcement (PSR) using allogeneic scleral bands. By observing the indentations created by the bands on the sclera, we were able to assess changes in the volume of the vitreous body, height, and position of the posterior pole's highest point.

Our findings revealed a decrease in vitreous volume after surgery, which can be attributed to the compression exerted by the reinforcing bands on the sclera. Specifically, the mean volume of the upper nasal side showed a slight increase of 342 pixels postoperatively compared to the preoperative measurements, although this difference was not statistically significant. On the other hand, the volume of the upper temporal and subnasal sides exhibited significant reductions, while the volume of the subtemporal side did not show a significant change. These volume changes can be explained by the positioning of the reinforcement bands, which passed through the temporal to lower rectus external muscles below the optic nerve and under the inferior rectus muscle. As a result, the upper nasal side appeared to be more prominent, leading to a concentration of the posterior pole's highest point on this side (68.4%) after surgery.

The observed patterns of changes in the distribution of the posterior eyeball's volume among the four quadrants were consistent with the alterations in vitreous volume and the position of the posterior surface's highest point. Thus, 3D MRI imaging provided valuable insights into the shape and position of the allogeneic scleral reinforcement bands.

Overall, this study demonstrated the utility of 3D MRI imaging for evaluating changes in the posterior eyeball's morphology following PSR and provided valuable information on the effects of scleral band placement on vitreous volume, distribution of the highest point, and changes in the quadrants of the posterior surface.

5 Limitations

This article has a few limitations that should be considered. Firstly, the sample size of patients who underwent posterior scleral reinforcement (PSR) was small. This limited sample size may affect the generalizability of the findings. Additionally, compared to other studies, our investigation did not observe any complications or band deviations. It is important to acknowledge that the absence of complications may not be representative of the overall experience with PSR. Furthermore, future studies could benefit from focusing on the localization of extraocular muscles, optic nerves, and fossa veins. By accurately identifying and quantifying the anatomical structures involved, quantitative surgical designs could be developed to enhance the precision and efficacy of PSR procedures.

6 Conclusion

The utilization of computer processing to analyze 3D MRI images of the eyeball offers valuable insights into the topographic height map of the posterior surface and allows for the calculation of vitreous volume. However, the most significant finding of this study lies in the determination of the shape and position of the scleral band following posterior scleral reinforcement (PSR). This technique has the potential to be further developed, enabling 3D MRI images of the eyeball to provide enhanced technical support for surgical design and prognostic evaluation in PSR.

Data availability statement

The raw data supporting the conclusion of this article will be made available by the authors, without undue reservation.

Ethics statement

The studies involving humans were approved by the ethics committee of Tianjin Medical University Eye Hospital. The studies were conducted in accordance with the local legislation and institutional requirements. The participants provided their written informed consent to participate in this study. Written informed consent was obtained from the individual(s) for the publication of any potentially identifiable images or data included in this article.

Author contributions

XZ and RW conceived and supervised the experiment. BD and DW performed the study. QH collected the data, HR designed and implemented Python programs, and analyzed the data. LL and HR wrote the manuscript. All authors contributed to the article and approved the submitted version.

Conflict of interest

The authors declare that the research was conducted in the absence of any commercial or financial relationships that could be construed as a potential conflict of interest.

Publisher's note

References

Asai, T., Ikuno, Y., Akiba, M., Kikawa, T., Usui, S., and Nishida, K. (2016). Analysis of peripapillary geometric characters in high myopia using swept-source optical coherence tomography. *Invest. Ophthalmol. Vis. Sci.* 57 (1), 137–144. doi:10.1167/iovs.15-17510

Avila, M. P., Weiter, J. J., Jalkh, A. E., Trempe, C. L., Pruett, R. C., and Schepens, C. L. (1984). Natural history of choroidal neovascularization in degenerative myopia. *Ophthalmology* 91 (12), 1573–1581. doi:10.1016/s0161-6420(84)34116-1

Cao, K., Wang, J., Zhang, J., Yusufu, M., Jin, S., Zhu, G., et al. (2020). The effectiveness and safety of posterior scleral reinforcement with vitrectomy for myopic foveoschisis treatment: a systematic review and meta-analysis. *Graefes Arch. Clin. Exp. Ophthalmol.* 258 (2), 257–271. doi:10.1007/s00417-019-04550-5

Chae, J. B., Moon, B. G., Yang, S. J., Lee, J. Y., Yoon, Y. H., and Kim, J. G. (2011). Macular gradient measurement in myopic posterior staphyloma using optical coherence tomography. *Korean J. Ophthalmol.* 25 (4), 243–247. doi:10.3341/kjo.2011.25.4.243

Evans, R. S. (2016). Electronic health records: then, now, and in the future. *Yearb. Med. Inf.* 1, S48–S61. doi:10.15265/IYS-2016-s006

Garcia-Ben, A., Kamal-Salah, R., Garcia-Basterra, I., Gonzalez Gómez, A., Morillo Sanchez, M. J., and García-Campos, J. M. (2017). Two- and three-dimensional topographic analysis of pathologically myopic eyes with dome-shaped macula and inferior staphyloma by spectral domain optical coherence tomography. *Graefes Arch. Clin. Exp. Ophthalmol.* 255 (5), 903–912. doi:10.1007/s00417-017-3587-z

Gerinec, A., and Slezakova, G. (2001). Posterior scleroplasty in children with severe myopia. *Bratisl. Lek. Listy* 102 (2), 73–78.

Hayashi, K., Ohno-Matsui, K., Shimada, N., Moriyama, M., Kojima, A., Hayashi, W., et al. (2010). Long-term pattern of progression of myopic maculopathy: a natural history study. *Ophthalmology* 117 (8), 1595–1611.e4. doi:10.1016/j.ophtha.2009.11.003

Holden, B. A., Fricke, T. R., Wilson, D. A., Jong, M., Naidoo, K. S., Sankaridurg, P., et al. (2016). Global prevalence of myopia and high myopia and temporal trends from 2000 through 2050. *Ophthalmology* 123 (5), 1036–1042. doi:10.1016/j.ophtha.2016.01.006

Hu, H., Zhao, G., Wu, R., Zhong, H., Fang, M., and Deng, H. (2018). Axial length/corneal radius of curvature ratio assessment of posterior sclera reinforcement for pathologic myopia. *Ophthalmologica* 239 (2-3), 128–132. doi:10.1159/000484485

Jo, Y., Ikuno, Y., and Nishida, K. (2012). Retinoschisis: a predictive factor in vitrectomy for macular holes without retinal detachment in highly myopic eyes. *Br. J. Ophthalmol.* 96 (2), 197–200. doi:10.1136/bjo.2011.203232

Jones, D., and Luensmann, D. (2012). The prevalence and impact of high myopia. *Eye Contact Lens* 38 (3), 188–196. doi:10.1097/ICL.0b013e31824ccbc3

Jong, M., Jonas, J. B., Wolffsohn, J. S., Berntsen, D. A., Cho, P., Clarkson-Townsend, D., et al. (2021). IMI 2021 yearly digest. *Invest. Ophthalmol. Vis. Sci.* 62 (5), 7. doi:10.1167/iovs.62.5.7

Karabatsas, C. H., Waldock, A., and Potts, M. J. (1997). Cilioretinal artery occlusion following scleral reinforcement surgery. *Acta Ophthalmol. Scand.* 75 (3), 316–318. doi:10.1111/j.1600-0420.1997.tb00784.x

Kuo, A. N., Verkicharla, P. K., Mcnabb, R. P., Cheung, C. Y., Hilal, S., Farsiu, S., et al. (2016). Posterior eye shape measurement with retinal OCT compared to MRI. *Invest. Ophthalmol. Vis. Sci.* 57 (9), 196–203. doi:10.1167/iovs.15-18886

Miyake, M., Yamashiro, K., Akagi-Kurashige, Y., Oishi, A., Tsujikawa, A., Hangai, M., et al. (2014). Analysis of fundus shape in highly myopic eyes by using curvature maps constructed from optical coherence tomography. *PLoS One* 9 (9), e107923. doi:10.1371/journal.pone.0107923

Moriyama, M., Ohno-Matsui, K., Modegi, T., Kondo, J., Takahashi, Y., Tomita, M., et al. (2012). Quantitative analyses of high-resolution 3D MR images of highly myopic eyes to determine their shapes. *Invest. Ophthalmol. Vis. Sci.* 53 (8), 4510–4518. doi:10.1167/iovs.12-9426

Nagra, M., Gilmartin, B., and Logan, N. S. (2014). Estimation of ocular volume from axial length. *Br. J. Ophthalmol.* 98 (12), 1697–1701. doi:10.1136/bjophthalmol-2013-304652

Ohno-Matsui, K. (2014). Proposed classification of posterior staphylomas based on analyses of eye shape by three-dimensional magnetic resonance imaging and wide-field fundus imaging. *Ophthalmology* 121 (9), 1798–1809. doi:10.1016/j.ophtha.2014.03.035

Ohno-Matsui, K., and Jonas, J. B. (2019). Posterior staphyloma in pathologic myopia. *Prog. Retin Eye Res.* 70, 99–109. doi:10.1016/j.preteyeres.2018.12.001

Ohno-Matsui, K., Wu, P.-C., Yamashiro, K., Vutipongsatorn, K., Fang, Y., Cheung, C. M. G., et al. (2021). IMI Pathologic myopia. *Invest. Ophthalmol. Vis. Sci.* 62 (5), 5. doi:10.1167/iovs.62.5.5

Peng, C., Xu, J., Ding, X., Lu, Y., Zhang, J., Wang, F., et al. (2019). Effects of posterior scleral reinforcement in pathological myopia: a 3-year follow-up study. *Graefes Arch. Clin. Exp. Ophthalmol.* 257 (3), 607–617. doi:10.1007/s00417-018-04212-y

Shen, Z. M., Zhang, Z. Y., Zhang, L. Y., Li, Z. G., and Chu, R. Y. (2015). Posterior scleral reinforcement combined with patching therapy for pre-school children with

unilateral high myopia. *Graefes Arch. Clin. Exp. Ophthalmol.* 253 (8), 1391–1395. doi:10.1007/s00417-015-2963-9

Shinohara, K., Moriyama, M., Shimada, N., Nagaoka, N., Ishibashi, T., Tokoro, T., et al. (2013). Analyses of shape of eyes and structure of optic nerves in eyes with tilted disc syndrome by swept-source optical coherence tomography and three-dimensional magnetic resonance imaging. *Eye (Lond)* 27 (11), 1233–1242. doi:10.1038/eye.2013.202

Shinohara, K., Moriyama, M., Shimada, N., Yoshida, T., and Ohno-Matsui, K. (2016). Characteristics of peripapillary staphylomas associated with high myopia determined by swept-source optical coherence tomography. *Am. J. Ophthalmol.* 169, 138–144. doi:10.1016/j.ajo.2016.06.033

Tatewaki, Y., Mutoh, T., Omodaka, K., Thyreau, B., Matsudaira, I., Furukawa, H., et al. (2019). Morphological prediction of glaucoma by quantitative analyses of ocular shape and volume using 3-dimensional T2-weighted MR images. *Sci. Rep.* 9 (1), 15148. doi:10.1038/s41598-019-51611-0

Wang, N. K., Wu, Y. M., Wang, J. P., Liu, L., Yeung, L., Chen, Y. P., et al. (2016). Clinical characteristics of posterior staphylomas in myopic eyes with axial length shorter than 26.5 millimeters. *Am. J. Ophthalmol.* 162, 180–190.e1. doi:10.1016/j.ajo.2015.11.016

Wen, B., Yang, G., Cheng, J., Jin, X., Zhang, H., Wang, F., et al. (2017). Using high-resolution 3D magnetic resonance imaging to quantitatively analyze the shape of eyeballs with high myopia and provide assistance for posterior scleral reinforcement. *Ophthalmologica* 238 (3), 154–162. doi:10.1159/000477466

Xue, A., Bao, F., Zheng, L., Wang, Q., Cheng, L., and Qu, J. (2014). Posterior scleral reinforcement on progressive high myopic young patients. *Optom. Vis. Sci.* 91 (4), 412–418. doi:10.1097/OPX.0000000000000201

Yu, X., Ma, W., Liu, B., Li, Z., Zhao, X., Tanumiharjo, S., et al. (2018). Morphological analysis and quantitative evaluation of myopic maculopathy by three-dimensional magnetic resonance imaging. *Eye (Lond)* 32 (4), 782–787. doi:10.1038/eye.2017.263

Zhu, S. Q., Pan, A. P., Zheng, L. Y., Wu, Y., and Xue, A. Q. (2018). Posterior scleral reinforcement using genipin-cross-linked sclera for macular hole retinal detachment in highly myopic eyes. *Br. J. Ophthalmol.* 102 (12), 1701–1704. doi:10.1136/bjophthalmol-2017-311340

Zhu, S. Q., Zheng, L. Y., Pan, A. P., Yu, A. Y., Wang, Q. M., and Xue, A. Q. (2016). The efficacy and safety of posterior scleral reinforcement using genipin cross-linked sclera for macular detachment and retinoschisis in highly myopic eyes. *Br. J. Ophthalmol.* 100 (11), 1470–1475. doi:10.1136/bjophthalmol-2015-308087

frontiers | Frontiers in Bioengineering and Biotechnology

TYPE Original Research
PUBLISHED 19 January 2024
DOI 10.3389/fbioe.2023.1300830

OPEN ACCESS

EDITED BY
Jonathan Vande Geest,
University of Pittsburgh, United States

REVIEWED BY
Lin Li,
Capital Medical University, China
Zheng Duanmu,
Beijing Information Science and Technology University, China

*CORRESPONDENCE
Ryan M. Pedrigi,
rpedrigi@unl.edu

RECEIVED 23 September 2023
ACCEPTED 26 December 2023
PUBLISHED 19 January 2024

CITATION
Ameku KA, Berggren CC and Pedrigi RM (2024), Implantation of a capsular tension ring during cataract surgery attenuates predicted remodeling of the post-surgical lens capsule along the visual axis.
Front. Bioeng. Biotechnol. 11:1300830.
doi: 10.3389/fbioe.2023.1300830

Implantation of a capsular tension ring during cataract surgery attenuates predicted remodeling of the post-surgical lens capsule along the visual axis

Kurt A. Ameku, Caleb C. Berggren and Ryan M. Pedrigi*

Department of Mechanical and Materials Engineering, University of Nebraska-Lincoln, Lincoln, NE, United States

Introduction: Cataract surgery permanently alters the mechanical environment of the lens capsule by placing a hole in the anterior portion and implanting an intraocular lens (IOL) that has a very different geometry from the native lens. We hypothesized that implant configuration and mechanical interactions with the post-surgical lens capsule play a key role in determining long-term fibrotic remodeling.

Methods: We developed the first finite element-growth and remodeling (FE-G&R) model of the post-surgical lens capsule to evaluate how implantation of an IOL with and without a capsular tension ring (CTR) impacted evolving lens capsule mechanics and associated fibrosis over time after cataract surgery.

Results: Our models predicted that implantation of a CTR with the IOL into the post-surgical lens capsule reduced the mechanical perturbation, thickening, and stiffening along the visual axis in both the remnant anterior and posterior portions compared to implantation of the IOL alone.

Discussion: These findings align with patient studies and suggest that implantation of a CTR with the IOL during routine cataract surgery would attenuate the incidence of visually-debilitating capsule fibrosis. Our work demonstrates that use of such modeling techniques has substantial potential to aid in the design of better surgical strategies and implants.

KEYWORDS

finite element model, growth and remodeling, biomechanics, mechanobiology, intraocular lens, posterior capsule opacification

1 Introduction

Cataracts is the leading cause of blindness worldwide (Wormstone et al., 2021) and the corrective procedure is the most commonly performed eye operation in the world with approximately 20 M procedures annually (Day et al., 2016). Cataract surgery involves placing a hole in the anterior lens capsule, known as a continuous circular capsulorhexis (CCC), breaking up and removing the opacified lens fibers, and implanting an intraocular lens (IOL). An interesting feature of this procedure is that the CCC is permanent. We have previously hypothesized that this permanent mechanical perturbation drives the long-term errant response of the lens epithelial cells after surgery (Pedrigi et al., 2007; Pedrigi et al.,

2009a; Pedrigi and Humphrey, 2011). In particular, lens epithelial cells differentiate into a wound-healing myofibroblast phenotype that causes them to become proliferative, synthetic, contractile, and migratory (Lovicu et al., 2016). These fibrotic behaviors are particularly focused around the CCC edge (which can cause anterior capsule opacification or ACO), the IOL haptics at the equator, and, eventually, the posterior capsule due to cell migration. Here, cell deposition of matrix proteins and contraction of the capsule can lead to the formation of posterior capsule opacification (PCO) which causes the patient to experience particularly severe visual disturbances (Wormstone et al., 2021). An approach that has been successful at mitigating PCO, though not eliminating it, is the use of IOLs with a square-edged optic that physically inhibits epithelial cell migration to the posterior capsule (Wormstone et al., 2021). This demonstrates the importance of the mechanical interaction between the capsule and implant in determining PCO.

Another device that is sometimes implanted during cataract surgery along with the IOL is a capsular tension ring (CTR). This is most often done when patients have experienced trauma or have an underlying condition, such as pseudoexfoliation syndrome, that causes weakness of the zonular fibers that connect the lens to the ciliary muscle and hold it in place within the eye (this connection is also central to the process of accommodation of the native lens). Several studies have concluded that CTRs improve IOL stability within the remnant capsular bag and reduce the incidence of IOL decentration (Li et al., 2016; Miyoshi et al., 2020), capsule contraction (Chen et al., 2021; Yang et al., 2021), and capsule opacification (D'Eliseo et al., 2003; Halili et al., 2014; Zhang et al., 2021). These beneficial effects may at least partially result from an increased magnitude and uniformity of the stress field within the capsule that reduces the mechanical perturbation caused by cataract surgery and implantation of a non-axisymmetric IOL. Indeed, we recently developed a 3-D finite element model of the lens capsule after cataract surgery with an implanted CTR and demonstrated that it induced a nearly uniform stress field in the remnant capsule, albeit with a lower magnitude than homeostatic (Berggren et al., 2021). An important limitation of this model is that it did not consider cell-mediated remodeling of the lens capsule over time after cataract surgery, which is known to dramatically affect its interaction with implants. Although we have previously reported an adaptive model of the lens capsule with a CCC using a growth (changes in mass) and remodeling (changes in microstructure) (G&R) framework, it was an axisymmetric (1-D) model that only included the anterior portion of the capsule without an implanted device (Pedrigi and Humphrey, 2011).

Therefore, herein, we extended our 3-D finite element (FE) model of the post-surgical lens capsule by coupling it to an adapted version of our previously reported G&R framework to assess the impact of implanting a CTR with the IOL on the evolving mechanics over 4 years after cataract surgery. Our FE-G&R models tracked changes to the constituents of the post-surgical capsule at each element, thus allowing for non-axisymmetric adaptations. To our knowledge, this is the first model of the post-surgical lens capsule that can predict implant efficacy over time after cataract surgery. Importantly, efficacy is defined in terms of a key patient outcome: the extent of fibrosis development. We found that implantation of a CTR with the IOL reduced thickening and stiffening of the lens capsule along the visual axis compared to when the IOL was implanted alone. This finding suggests that implantation of CTRs in the lens capsules of normal patients could reduce the incidence of PCO.

2 Materials and methods

2.1 Finite element modeling

All modeling, meshing, and analyses were performed in Abaqus CAE 2019. The lens capsule was meshed with a combination of 3-node shell elements and 4-node reduced integration shell elements (S4R) and the CTR and IOL were meshed with 8-node 3-D continuum elements (C3D8). The final mesh density of each component of the models was determined with a convergence test of the following metrics: for the lens capsule, when the displacement of the capsule pole differed by <1% with an increase in mesh density; for the CTR and IOL, when the displacement of the capsule equator differed by <1%. A description of the salient aspects of each model are given below.

2.1.1 Model of the post-surgical lens capsule with IOL and CTR-IOL

The initial equatorial diameter and thickness profile of the post-surgical lens capsule were the same as used in our previous study (Ameku and Pedrigi, 2022). A 5 mm-diameter CCC was placed in the anterior portion. The unloaded geometry was modeled as a flattened circular membrane with a flat equatorial region and small gap between the anterior and posterior portions. This gap was set as the thickness of the implanted IOL because this is the primary determinant of the post-surgical capsule geometry (along with the zonules attached at the equator) due to contraction in the first weeks after surgery that causes the capsule to be in apposition to the implant. Thus, the initial state of the model represents the capsule ~2 weeks after surgery (Hayashi et al., 2002; Pedrigi et al., 2009a). Two implants were considered, either an IOL alone (IOL model) or the combination of a CTR and IOL (CTR-IOL model). In line with our previous work (Pedrigi and Humphrey, 2011), we assumed the lens capsule was stress free prior to placement of the implanted IOL. The interaction between the post-surgical lens capsule and implanted IOL was modeled with separation allowed after contact, but the post-surgical lens capsule and CTR interaction was modeled with no separation after contact because it provided better stability. All other contact settings for the post-surgical model were set to match those of our previously reported native lens model (Ameku and Pedrigi, 2022). For the IOL simulation, the optic portion of the IOL was centered with respect to the lens capsule and held in place. The haptics were compressed with an applied traction to bring them within the capsule and then released to allow contact with the capsule equator. The lens capsule equator and IOL were restricted to in-plane motion and the lens capsule was not allowed to rotate (Berggren et al., 2021). For the CTR-IOL simulation, the IOL was modeled with the same approach as the simulation with the IOL alone, and the CTR was placed within the capsule similar to the IOL by compressing the loop ends radially and circumferentially with an applied traction and then releasing them to allow contact with the capsule equator. In this simulation, the lens capsule equator and CTR were restricted to in-plane motion, the top portion of the CTR was held to only allow radial motion, and the lens capsule was not allowed to rotate. No interaction between the CTR and IOL was considered because these implants are not

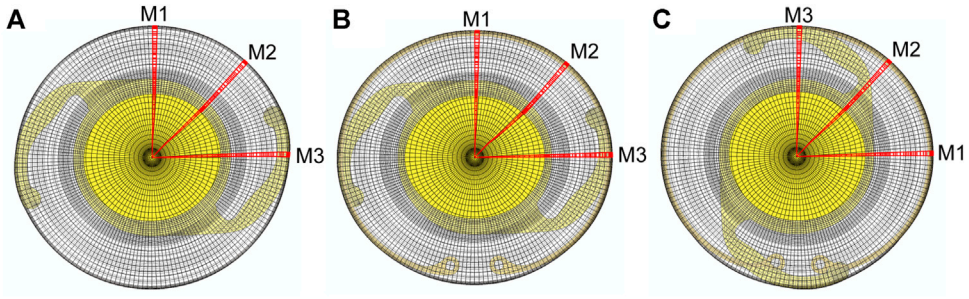

FIGURE 1
Images of the three FE models evaluated in this study showing the orientation of meridians used to report results. The three models are: **(A)** the post-surgical lens capsule with implanted IOL, **(B)** the post-surgical lens capsule with implanted CTR and IOL with the IOL haptics aligned horizontally (CTR-IOL Case 1), and **(C)** the post-surgical lens capsule with implanted CTR and IOL with the IOL haptics aligned vertically (CTR-IOL Case 2). Each model has three distinct meridians highlighted (M1, M2 and M3), with M1 perpendicular to the IOL haptics, M2 at an approximately 45° angle from the haptics, and M3 parallel to the IOL haptics.

designed for coupling within the capsular bag (i.e., they are implanted separately, one above or below the other; for simplicity, we just eliminated the interaction). All boundary conditions regarding the IOL were the same as described for the IOL model. Additionally, to determine whether or not the orientation of the implanted IOL with respect to the CTR affects the results of our model, two cases were considered: CTR-IOL Case 1 considered the IOL haptics aligned perpendicular to the CTR opening (horizontally from the front viewpoint) and CTR-IOL Case 2 considered the IOL haptics aligned with the CTR opening (vertically from the front viewpoint). Videos of each FE simulation are provided in Supplementary Videos S1–S3. Model outputs are provided along three meridians, referred to as M1, M2, and M3, for all models (Figure 1).

2.1.2 Model outputs

For all finite element analyses, the primary readouts were the Cauchy stress tensor and the deformation gradient tensor, $\boldsymbol{F}$, at each increment of the total simulated time. Both metrics were determined with respect to the circumferential and meridional (principal) directions of the lens capsule in all simulations. These were determined to be the principal directions from our previous mechanical (inflation) testing of the lens capsule, wherein shear strain was negligible with respect to these directions (Heistand et al., 2005; Pedrigi et al., 2007).

2.2 Mechanical properties

2.2.1 Lens capsule

We employed the Holzapfel hyperelastic constitutive model that was previously fit to inflation (Pedrigi et al., 2007) and uniaxial (Krag et al., 1997) mechanical testing data for the anterior lens capsule from human donors of comparable age (~65 years) to that being modeled in this study (Berggren et al., 2021; Ameku and Pedrigi, 2022). The constitutive model in terms of Cauchy stress is given by

$$\boldsymbol{\sigma} = \boldsymbol{F}\frac{\partial W_H}{\partial \boldsymbol{F}^T} - p\boldsymbol{I} \quad (1)$$

where $\boldsymbol{F}$ is the deformation gradient tensor, p is the Lagrange multiplier used to enforce incompressibility, $\boldsymbol{I}$ is the identity tensor, and W_H is the Holzapfel strain energy function given by

$$W_H = C_{10}(I_1 - 3) + \frac{k_1}{k_2}\left\{exp\left[k_2(\kappa I_1 + (1-3\kappa)I_4 - 1)^2\right] - 1\right\} \quad (2)$$

where C_{10} is the ground matrix stiffness, k_1 is the stiffness of the fiber families, k_2 is a dimensionless material parameter, κ signifies the in-plane distribution of the fibers, and I_1 and I_4 are the first and fourth invariants of the right Cauchy-Green tensor, respectively (note, I_4 also contains the mean fiber distribution angle, γ). In our previous study (Berggren et al., 2021), we determined the values for these parameters that allowed accurate prediction of the regionally-varying anisotropic mechanical behavior exhibited by the anterior capsule during inflation testing. The final material parameters slightly changed over the meridian of the lens capsule in an element-to-element fashion owing to an increasingly stiffer circumferential direction and more compliant meridional direction from pole to equator. These regional variations in mechanical properties were implemented into the finite element (FE) model using a custom MATLAB script, as previously described (Berggren et al., 2021).

2.2.2 Implanted CTR and IOL

The CTR model was based on a Morcher type 14 capsular tension ring with a maximum undeformed diameter of 12.3 mm and a deformed diameter of 10 mm that is uniform when the loop ends come nearly into contact (Menapace et al., 2000). The CTR was given a thickness of 0.2 mm based on previous models of capsular measuring rings made by our group (Berggren et al., 2021). The IOL model was based on a single-piece Alcon AcrySof monofocal IOL made of hydrophobic acrylic with an overall length of 13 mm, optic diameter of 6 mm, and thickness of 0.2 mm to match the thickness of the CTR (Nejima et al., 2006; Werner et al., 2018). Since both implants undergo small strains (<1%), we used a linear elastic constitutive model, with a Young's modulus of 3.2 GPa and a Poisson's ratio of 0.37 assigned to the CTR, and a Young's modulus of 12 MPa and Poisson's ratio of 0.37 assigned to the IOL (Berggren et al., 2021).

2.3 Growth and remodeling

Our prior growth and remodeling (G&R) work of the lens capsule (Pedrigi and Humphrey, 2011), which was based on studies in vascular mechanics (Baek et al., 2006; Valentin et al., 2013; Latorre and Humphrey, 2018), has demonstrated that a constrained mixture model can effectively capture cell-mediated tissue adaptations driven by altered mechanics. Herein, we used this framework to simulate G&R of the entire lens capsule with the aforementioned implants after cataract surgery in weekly increments over 4 years.

2.3.1 Framework

This framework tracks changes in the deposition and removal of each of the primary load-bearing constituents of the lens capsule, denoted k, and computes the associated strain energy at each G&R time (following a perturbation at time 0) using

$$W_F^k(s) = \frac{M^k(0)}{M(s)} Q^k(s) \hat{W}_F^k\left(\lambda_{n(0)}^k(s)\right) + \int_0^s \frac{m^k(\tau)}{M(s)} q^k(s,\tau) \hat{W}_F^k\left(\lambda_{n(\tau)}^k(s)\right) d\tau, \quad (3)$$

where $M(s)$ is the total mass (note, $M(s) = \sum M^k(s)$) at the current G&R time s, M^k is the mass of constituent k (referred to by a superscript k in all instances), $M^k(0)$ is the mass density in the homeostatic state, $Q^k(s)$ is the fraction of mass produced in the homeostatic state that survives to the current time s, m^k is the rate of mass production at G&R time $\tau \in [0, s]$, q^k is the fraction of mass that was produced at time τ that survives to time s, and W^k is the strain energy of constituent k summed over all cohorts (each cohort deposited at a specific G&R time τ). We employed a Fung-type exponential form of the strain energy function for each constituent given by

$$\hat{W}_F^k\left(\lambda_{n(\tau)}^k(s)\right) = c^k \left\{ exp\left[c_1^k \left(\left(\lambda_{n(\tau)}^k\right)^2 - 1 \right)^2 \right] - 1 \right\}, \quad (4)$$

where c is a measure of overall constituent stiffness, c_1 is a non-dimensional stiffness parameter, and λ_n^k is the stretch experienced by a cohort of constituent k deposited at G&R time τ. This stretch is computed via

$$\lambda_{n(\tau)}^k(s) = G_h^k \frac{\lambda^k(s)}{\lambda^k(\tau)}, \quad (5)$$

where G_h^k denotes the deposition stretch at which the constituent is incorporated within the extant capsule matrix and $\lambda^k(\tau)$ is the stretch of the gross capsule in the direction of constituent k at G&R time τ, given by

$$\lambda^k(\tau) = \sqrt{\left(\lambda_1 \cos(\alpha^k)\right)^2 + \left(\lambda_2 \sin(\alpha^k)\right)^2} \quad (6)$$

where λ_1 and λ_2 are the principal stretches in the circumferential and meridional directions, respectively, and α is the angle of constituent k relative to the circumferential direction.

The primary load-bearing constituent of the native lens capsule is type IV collagen, whereas after cataract surgery non-native fibrillar collagen (types I, III, and V) is also deposited. Thus, our G&R model considered two families of native collagen (type IV) and two families of fibrillar collagen. Rates of mass production and removal of these constituents were determined based on changes in stress from homeostatic using

$$m^k(\tau) = m_o^k\left(1 + K_P^k \Delta\sigma(\tau)\right) \quad (7)$$

and

$$q^k(s,\tau) = exp\left(-q_o^k\left[1 + K_R^k \Delta\sigma(s)\right](s-\tau)\right), \quad (8)$$

respectively, where m_0 is the basal rate of mass production, q_o is the basal rate of mass removal based on an estimate from clinical observations of lens capsule turnover (Pedrigi and Humphrey, 2011), and K_P and K_R are non-dimensional gain-type parameters that amplify changes in the production and removal rates, respectively, based on the magnitude of change in the principal stresses from homeostatic of the gross lens capsule, given by

$$\Delta\sigma = \left| \frac{\sigma_{11} + \sigma_{22}}{(\sigma_{11})_o + (\sigma_{22})_o} - 1 \right| \quad (9)$$

where o denotes original homeostatic, which were obtained from a finite element model of the native lens (Berggren et al., 2021; Ameku and Pedrigi, 2022), and *11* and *22* indicate the circumferential and meridional directions, respectively. These gain parameters were optimized to achieve a desired increase in thickness at the CCC edge based on previously reported anterior capsule opacification (ACO) scores for human cadaver lens capsules that had undergone cataract surgery more than 3 years before the time of death (Maddula et al., 2011). We also calibrated the gain-type parameters of our model to reasonably approximate the increased stiffness reported in our previous study (Pedrigi et al., 2009b; Pedrigi and Humphrey, 2011).

2.3.2 Coupling the G&R framework to the FE model of the post-surgical lens capsule

All simulations used MATLAB as a shell to run both the G&R framework, which is programmed in MATLAB, and the FE models in Abaqus. Because the FE models were non-axisymmetric, mass deposition and removal were tracked at each element over all G&R times after cataract surgery. An FE model of the native lens capsule and fibers was used to determine the homeostatic stress and stretch fields of the capsule (Berggren et al., 2021). The FE models of the post-surgical lens capsule with implanted device (either IOL or CTR-IOL) provided the stress and stretch fields at each G&R time s. The FE models employed the Holzapfel constitutive model, whereas changes in the rates of mass production and removal of both native and fibrillar collagen were accounted for using the Fung-type constitutive model. Parameters for the Fung-type model were obtained at $s < 0$ when the lens capsule was entirely composed of type IV collagen (i.e., before G&R) by using a nonlinear regression to fit biaxial Cauchy stress-stretch data in the circumferential and meridional directions generated from the Holzapfel model via

$$\sigma_{11} = \lambda_1 \frac{\partial W_H}{\partial \lambda_1} - \lambda_3 \frac{\partial W_H}{\partial \lambda_3} \equiv \lambda_1 \sum_{k=1}^{4} \frac{\partial W_F^k}{\partial \lambda_1} \quad (10)$$

$$\sigma_{22} = \lambda_2 \frac{\partial W_H}{\partial \lambda_2} - \lambda_3 \frac{\partial W_H}{\partial \lambda_3} \equiv \lambda_2 \sum_{k=1}^{4} \frac{\partial W_F^k}{\partial \lambda_2}. \quad (11)$$

The material parameters for fibrillar collagen were estimated by assuming that c^k is an order of magnitude larger than that for type IV collagen and the other parameters, $c_1{}^k$ and α^k, were held constant for

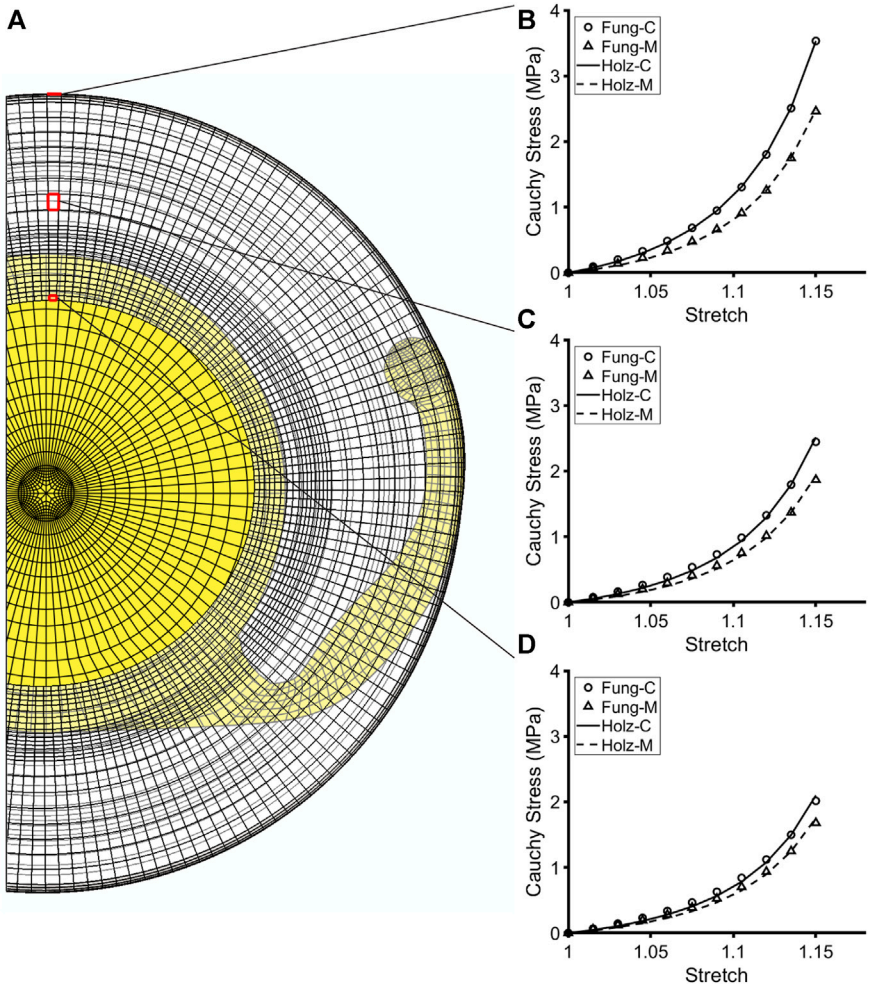

FIGURE 2
Fit of the Holzapfel constitutive model to simulated biaxial mechanical data from the Fung-type model used to compute G&R of the post-surgical capsule immediately after cataract surgery. **(A)** Cut view of the post-surgical FE model with an implanted IOL. **(B–D)** Representative elements highlighted at the CCC edge, anterior midpoint, and equator, showing the anisotropic mechanical behavior of the capsule at each element. Plots illustrate the goodness of fit of the Holzapfel constitutive model (through the parameter k_1) to the biaxial mechanical data generated from the Fung-type model at each respective element, thus validating the approach.

both types of collagen (Pedrigi and Humphrey, 2011). At every G&R time $s \geq 0$, this process was done in reverse, wherein the Fung-type constitutive model was used to generate biaxial Cauchy stress-stretch data that were fit using the Holzapfel model through the stiffness parameter k_1. Because the two constitutive models described the lens capsule mechanical behavior very similarly, resultant fits were excellent (Figure 2). Using this approach, k_1 represented the overall stiffness of the lens capsule constituents, including contributions from both type IV collagen and type I collagen (note that a higher deposition rate of type IV collagen compared to removal only changes the thickness of the capsule, not the stiffness, while that for non-native type I collagen changes both thickness and stiffness). In addition, we did not consider changes in the anisotropy of the capsule over time because the degree of anisotropy in the native lens capsule predicted by the Holzapfel model is modest and there are no data characterizing changes after cataract surgery. As a result, we did not consider changes to the other parameters of the Holzapfel model. Once changes in stiffness (k_1 parameter of the Holzapfel model) and thickness (based on changes in mass) were determined from the G&R framework at each element, they were passed to the FE model of the post-surgical capsule with implant to run the next G&R time step of the loop. Contraction of the capsule equator and CCC were also prescribed in the FE model by incrementally reducing each diameter over the first 6 months of simulation time based on empirical data from patients (Tehrani et al., 2003) (Figure 3).

Finally, as the lens capsule remodels after cataract surgery, the lens epithelial cells migrate to the posterior capsule, which is natively acellular, and over time errant behaviors (e.g., contraction and matrix synthesis) cause the development of posterior capsule opacification. This complication of cataract surgery can take months to years to unfold, depending on the IOL geometry (square versus rounded edge optic). Since a square-edged IOL optic delays the migration of cells to the posterior capsule, we incorporated this feature into the remodeling process using a custom MATLAB program. Specifically, we assumed an

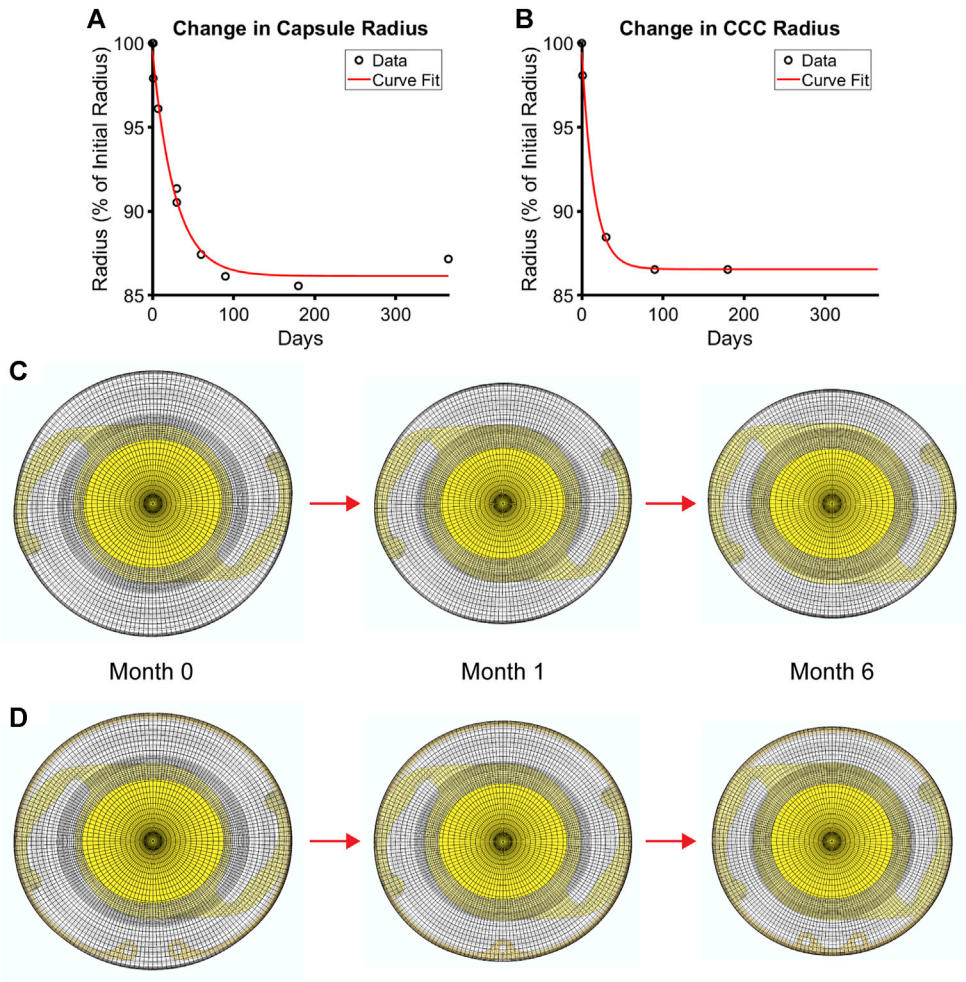

FIGURE 3
Contraction of the post-surgical lens capsule models over time after cataract surgery. Empirical data and the associated fit of changes in **(A)** capsule equatorial radius and **(B)** CCC radius. FE models of the **(C)** post-surgical capsule with implanted IOL and **(D)** post-surgical capsule with implanted CTR and IOL each at the simulated G&R times of 0 (i.e., immediately after surgery), 1, and 6 months after surgery when full contraction is reached.

immediate cellular migration up to the posterior IOL optic edge and then imposed a 1 year delay before allowing migration to the midpoint of the IOL optic (~1.5 mm from the posterior pole) based on previously reported ACO and PCO scores (Maddula et al., 2011). As a result, in the first year of simulation, changes to the constituents only occurred in the remnant anterior capsule and posterior capsule up to the edge of the visual axis; thereafter, we also simulated changes from the edge of the visual axis to 1.5 mm from the posterior pole to consider the development of peripheral PCO (pathology of human cadaver eyes with implanted square-edged IOLs showed ACO and PCO in the peripheral portion of the posterior capsule, but not PCO in the central portion (Maddula et al., 2011), so remodeling in this portion was not considered).

3 Results

Our FE-G&R model predicted cell-mediated changes in constituent mass, which led to changes in thickness and stiffness, of the lens capsule over 4 years after cataract surgery based on changes in stress from homeostatic at each element within each model. We calibrated our growth parameters to achieve predictions of capsule thickening and stiffening based on previously reported empirical data (Pedrigi et al., 2009b; Maddula et al., 2011). Final parameters were $[K_P^{IV}, K_R^{IV}] = [7.5, 1]$ for native (type IV) collagen and $[K_P^{I}, K_R^{I}] = [2, 1]$ for non-native fibrillar (type I) collagen. These growth parameters were then held constant for all models to allow comparisons. All models predicted dramatic increases in the production rates of native and fibrillar collagen (Figure 4; Supplementary Figure S1).

The trends over time were identical between the two constituents (note, there are four constituents in the model, two each of the two types of collagen) and qualitatively similar between the implants with initial spikes in mass production that mostly reduced over time (a few exhibited increases), but remained above pre-surgery homeostatic values. The equatorial regions of the capsule in contact with the implant saw by far the highest rates of mass production (Supplementary Figure S2). Because the CTR contacts the lens capsule over nearly the entire circumference, models with this device exhibited higher mass production over a

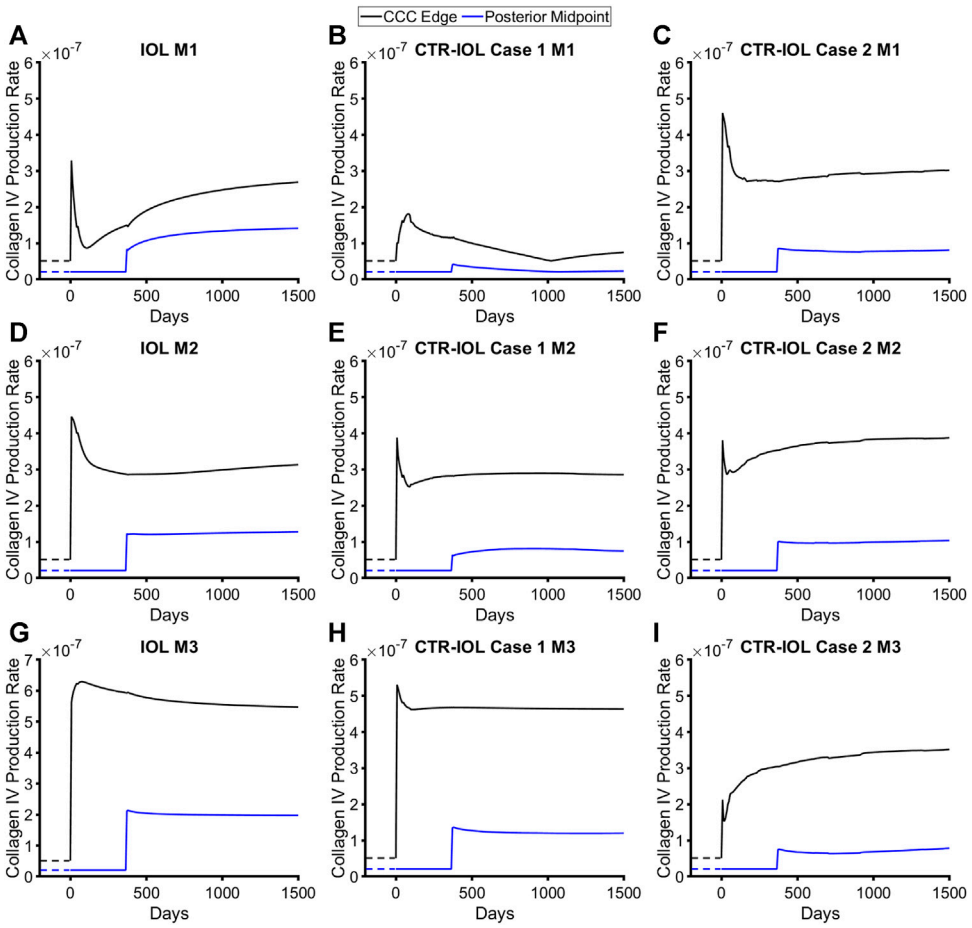

FIGURE 4
Post-surgical lens capsule mass production rates of type IV collagen for the FE-G&R models over time after cataract surgery. The three models are: **(A,D,G)** the post-surgical lens capsule with implanted IOL, **(B,E,H)** the post-surgical lens capsule with implanted CTR and IOL where the IOL haptics are aligned horizontally (Case 1), and **(C,F,I)** the post-surgical lens capsule with implanted CTR and IOL where the IOL haptics are aligned vertically (Case 2). Mass production rates are shown at the CCC edge and posterior midpoint along M1 (top row), M2 (middle row), and M3 (bottom row). Homeostatic values are shown for comparison (dashed lines).

larger area of the equator than models with the IOL alone, where only the region of the capsule contacting the haptics exhibited similar levels of mass production. However, along the visual axis, which we defined as the central region of the post-surgical lens capsule (remnant anterior and posterior) that covered the 6 mm diameter IOL optic, models with the CTR predicted overall lower amounts of mass production than the model with the IOL alone. Specifically, the CTR-IOL Case 1 model showed significantly smaller increases in the rates of mass production compared to the IOL model along M1 (Figures 4A, B) and slightly smaller increases in the direction of M2 (Figures 4D, E) and M3 (Figures 4G, H) in both the anterior and posterior portions of the post-surgical capsule. The CTR-IOL Case 2 model showed an increase in the rates of mass production in the anterior portion of the capsule compared to the IOL model along M1, but decreases along M2 and M3. Similar to the CTR-IOL Case 1 model, mass production in the Case 2 model was uniformly decreased in the posterior capsule (Figures 4C, F, I). This model also exhibited more uniform mass production along all meridians compared to the other models.

In line with predicted rates of mass production, implantation of a CTR led to more uniformly increased thickening around the equator of the post-surgical capsule, but lower thickening along the visual axis compared to implantation of an IOL alone. Specifically, the CTR-IOL Case 1 model predicted a mean anterior thickening along the visual axis at the end of 4 years of 14 μm versus 49 μm in the IOL model in the direction of Meridian 1 (M1) (Figures 5A, B), 57 μm versus 58 μm (M2) (Figures 5D, E), and 83 μm versus 88 μm (M3) (Figures 5G, H). While the CTR-IOL Case 2 model predicted a much more uniform thickening between meridians with mostly higher values compared to the CTR-IOL Case 1 model of 57 μm (M1), 69 μm (M2), and 62 μm (M3) (Figures 5C, F, I). The posterior portion of the post-surgical lens capsule exhibited even more dramatic differences in thickness along the visual axis between both CTR-IOL models versus the IOL model. Here, the CTR-IOL Case 1 model predicted a mean thickening of 1 μm versus 13 μm in the IOL model in the direction of Meridian 1 (M1) (Figures 5A, B), 9 μm versus 12 μm (M2) (Figures 5D, E), and 12 μm versus 18 μm (M3) (Figures 5G, H). The CTR-IOL Case 2 model predicted a mean thickening of 9 μm (M1), 11 μm (M2), and 9 μm (M3) (Figures 5C, F, I).

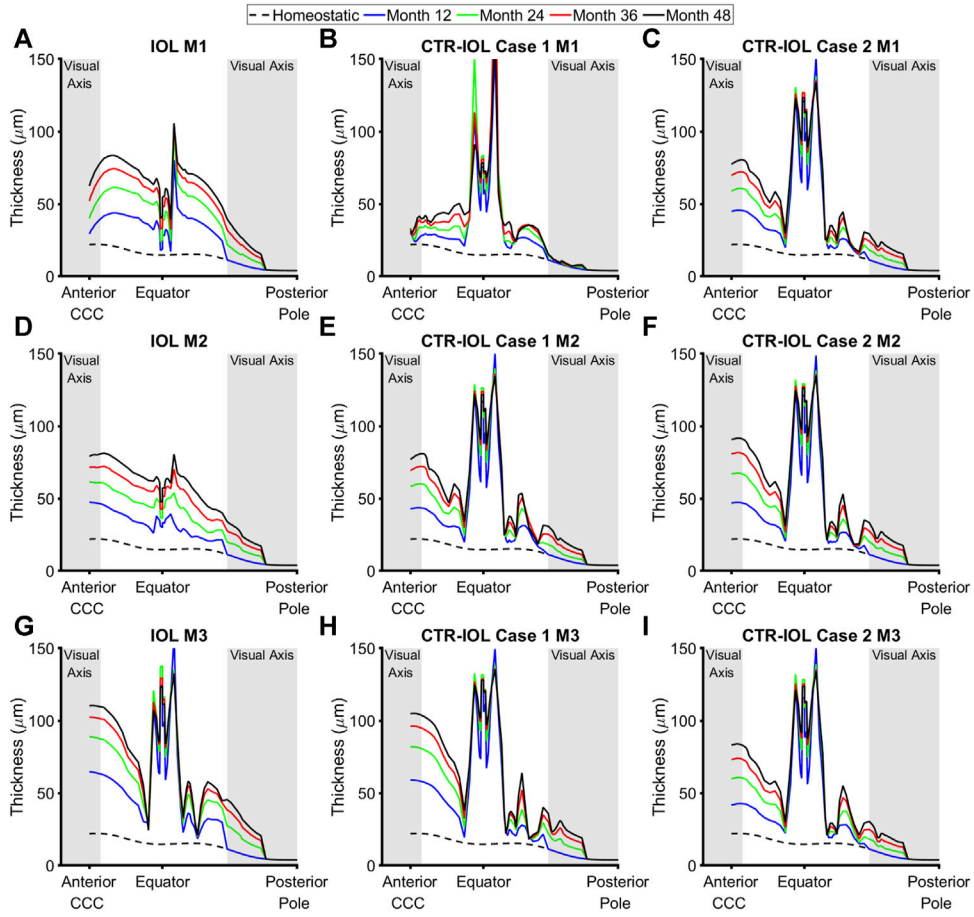

FIGURE 5
Post-surgical lens capsule thickness of the FE-G&R models at select simulation times up to the maximum of 4 years after cataract surgery. The three models are: **(A,D,G)** the post-surgical lens capsule with implanted IOL, **(B,E,H)** the post-surgical lens capsule with implanted CTR and IOL where the IOL haptics are aligned horizontally (Case 1), and **(C,F,I)** the post-surgical lens capsule with implanted CTR and IOL where the IOL haptics are aligned vertically (Case 2). Thickness at each time is shown from the CCC edge to the posterior pole along M1 (top row), M2 (middle row), and M3 (bottom row). The regions of the anterior and posterior visual axes are highlighted in grey. Homeostatic values are shown for comparison (dashed black line).

Stiffness (the k_1 parameter of the Holzapfel model) followed a similar trend as thickness, but with even larger differences between implanted devices. In the anterior visual axis region of the post-surgical lens capsule, the CTR-IOL Case 1 model predicted a mean stiffening at the end of 4 years of 4.78 MPa versus 10.43 MPa in the IOL model in the direction of Meridian 1 (M1) (Figures 6A, B), 10.91 MPa versus 11.10 MPa (M2) (Figures 6D, E), and 15.86 MPa versus 19.81 MPa (M3) (Figures 6G, H). In line with the thickness results, the CTR-IOL Case 2 model also predicted a much more uniform stiffening between meridians with mean values of 10.99 MPa along M1, 11.38 MPa along M2, and 11.14 MPa along M3 (Figures 6C, F, I). In the posterior visual axis region, the CTR-IOL Case 1 model predicted a mean stiffening of 2.21 MPa versus 9.98 MPa in the IOL model in the direction of Meridian 1 (M1) (Figures 6A, B), 7.49 MPa versus 9.50 MPa (M2) (Figures 6D, E), and 8.08 MPa versus 12.36 MPa (M3) (Figures 6G, H). The CTR-IOL Case 2 model predicted a mean stiffening in the posterior visual axis region of 7.36 MPa (M1), 7.97 MPa (M2), and 7.26 MPa (M3) (Figures 6C, F, I).

Since changes in stress ($\Delta\sigma$) drove predicted changes in thickness and stiffness, models with the CTR generally predicted overall lower amounts of change in stress than the model with the IOL alone (Supplementary Figure S3). We also quantified changes in thickness, stiffness, and stress over every meridian of the anterior and posterior visual axis regions of the post-surgical lens capsule, which showed similar trends to results presented for the individual meridians (Supplementary Figure S4).

4 Discussion

In this study, we developed an FE-G&R model to evaluate how implantation of a CTR in combination with an IOL (using two different IOL orientations relative to the CTR) influences mechanical adaptations of the lens capsule over 4 years after cataract surgery compared to when the IOL is implanted alone. All models predicted significantly increased thickening and stiffening at the point of implant contact with the capsule equator, but the models with the CTR predicted these increases more uniformly around the equator due to the increased contact area. However, fibrotic remodeling at the capsule equator would not affect patient vision because it is away from the visual axis, which we defined as the anterior and posterior portions of the capsule that are over the 6 mm-diameter

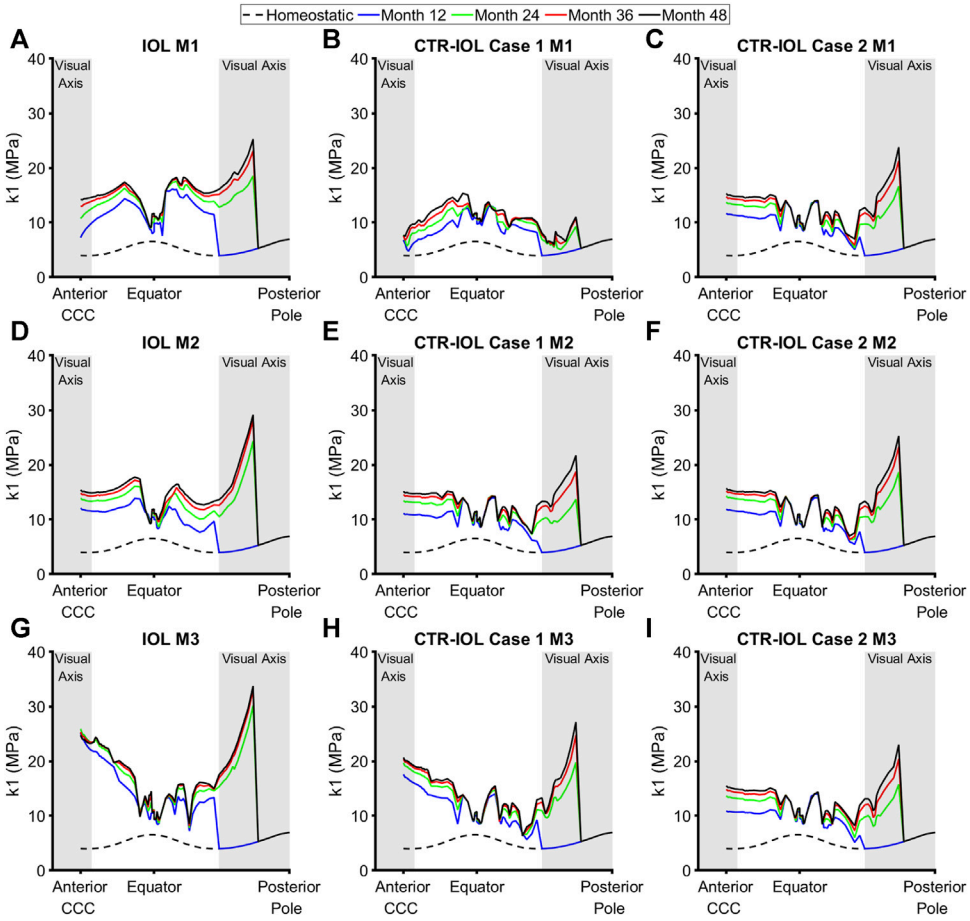

FIGURE 6
Post-surgical lens capsule stiffness (k_1 parameter of the Holzapfel model) of the FE-G&R models at select simulation times up to the maximum of 4 years after cataract surgery. The three models are: **(A,D,G)** the post-surgical lens capsule with implanted IOL, **(B,E,H)** the post-surgical lens capsule with implanted CTR and IOL where the IOL haptics are aligned horizontally (Case 1), and **(C,F,I)** the post-surgical lens capsule with implanted CTR and IOL where the IOL haptics are aligned vertically (Case 2). Stiffness at each time is shown from the CCC edge to the posterior pole along M1 (top row), M2 (middle row), and M3 (bottom row). The regions of the anterior and posterior visual axes are highlighted in grey. Homeostatic values are shown for comparison (dashed black line).

IOL optic. Along the visual axis, models with the CTR predicted a reduced mechanical perturbation of the lens capsule and, in turn, reduced thickening and stiffening compared to the model of the IOL alone. Orientation of the IOL haptics relative to the CTR opening showed only a modest impact on the average results wherein the perpendicular orientation (Case 1) exhibited slightly lower mean values of thickening and stiffening. On the other hand, the parallel orientation (Case 2) exhibited much more uniform remodeling. Overall, these reductions in fibrotic remodeling along the visual axis with implantation of a CTR were particularly noticeable in the posterior portion of the capsule, suggesting that it would lead to better patient outcomes in terms of reduced severity of PCO and associated visual disturbances. This prediction aligns with a recent meta-analysis of eight studies that acquired patient data from 379 eyes implanted with a CTR in combination with an IOL and 333 eyes implanted with an IOL alone (Zhang et al., 2021). They found that eyes implanted with a CTR exhibited a significant reduction in the rate of posterior capsulotomy (a laser-based surgery that serves as the primary treatment for PCO) and PCO score compared to those implanted with the IOL alone (odds ratio of 0.24 and standardized mean difference of −1.40, respectively).

While many studies have modeled the native lens (Burd et al., 2002; Hermans et al., 2006; Reilly, 2014; Burd and Wilde, 2016; David et al., 2017; Cabeza-Gil et al., 2021; Knaus et al., 2021; Knaus et al., 2023), only a few studies have modeled the lens capsule after cataract surgery (Pedrigi and Humphrey, 2011; Berggren et al., 2021; Ameku and Pedrigi, 2022; Cabeza-Gil and Calvo, 2022). Moreover, to our knowledge, this is the first FE-G&R model of the lens capsule in any context. Our G&R framework tracked changes in the deposition and removal of the primary load-bearing constituents of the post-surgical lens capsule, native type IV collagen and non-native (fibrillar) type I collagen, at each element based on changes in the principal stresses relative to homeostatic. To ensure that predicted changes in thickness of the post-surgical capsule were reasonable, we calibrated the type IV collagen growth parameters of the FE-G&R model of the IOL alone to semi-quantitative data reported from a study of fibrosis rates in 157 cadaver eyes from patients previously implanted with three-piece silicone IOLs with square edges that reported maximum thickness increases (at greater than 3 years post-operation) of ~90 μm (Maddula et al., 2011) (which matches our maximum predicted thickening for the

anterior capsule of 90 μm). Similarly, changes in stiffness were calibrated via the type I collagen growth parameters of this model to our previous results from uniaxial mechanical testing of post-surgical capsules demonstrating a ~4-fold increase in stiffness around the CCC edge (Pedrigi et al., 2009b) (compared to the 3.7-fold increase predicted by our model). These growth parameters were then held constant across all models to allow comparisons.

Our G&R framework used a constrained mixture approach that allowed the native and fibrillar collagen constituents to have different mechanical properties and rates of turnover, but also constrained these constituents to move together within the mixture (i.e., the lens capsule at each material point). We assumed that cell-mediated changes in the mass of each constituent were driven by changes in stress within the post-surgical lens capsule for three primary reasons. First, fibrotic lens epithelial cell behaviors appear to last for years after cataract surgery (Marcantonio et al., 2000), which is long after the inflammatory response to the procedure has subsided (~1 month), leaving the permanently altered mechanical environment of the capsule as the most obvious driver. Second, we previously demonstrated that the native anterior lens capsule exhibits a nearly homogeneous stress field that is significantly perturbed during cataract surgery (Pedrigi et al., 2007; Berggren et al., 2021). Third, epithelial cells, including lens epithelial cells, have been shown to be highly mechanosensitive (Kumar et al., 2019; Gao et al., 2022). These points align with numerous studies demonstrating that most cells are mechanosensitive and seek to maintain a homeostatic mechanical environment that, when perturbed, promotes pathologic cell behaviors (Humphrey, 2008; Nims et al., 2022). Many of these mechanobiology studies have focused on the vasculature where the G&R framework used herein was developed and extensively validated through studies of arteries in various applications, including the presence of hypertension (Latorre and Humphrey, 2018), altered blood flow (Karsaj et al., 2010), aneurysms (Baek et al., 2006), and external support (Ramachandra et al., 2020).

The FE-G&R model reported herein leverages years of previous work by us and others. We have previously characterized the mechanics of the native (Heistand et al., 2005; Pedrigi et al., 2007) and post-surgical (Heistand et al., 2006; Pedrigi et al., 2009a; Pedrigi et al., 2009b) lens capsule. We have also previously developed computational models of the lens capsule (Pedrigi et al., 2007; Pedrigi and Humphrey, 2011; David et al., 2017; Berggren et al., 2021; Ameku and Pedrigi, 2022). The current work directly builds on two of these computational studies. First, we previously developed a 1-D G&R model of the anterior portion of the lens capsule with central hole, but no implanted device (Pedrigi and Humphrey, 2011). We demonstrated an ability to calibrate the growth parameters of the model, which were driven by altered stress, to salient mechanical and biological data of the post-surgical lens capsule to predict pathological remodeling over time after surgery. We used an adaptation of this framework herein. Second, we previously developed an FE model of the entire post-surgical lens capsule with implanted IOL and, separately, CTR (Berggren et al., 2021). This model was calibrated to salient mechanical testing (inflation and uniaxial) data and validated. We reported changes to the stress field from homeostatic immediately after surgery, but not over time as there was no growth component to the model. Our study herein combined this FE model with our G&R model to report for the first time: (1) altered mechanics of the entire lens capsule over time after cataract surgery, including changes in thickness, stiffness, and stress; (2) the influence of different implants on predicted evolving lens capsule mechanics and associated fibrosis (ACO and PCO); and (3) implantation of an IOL plus CTR versus IOL alone reduces ACO and PCO. Importantly, this latter prediction qualitatively aligned with patient data showing a similar clinical outcome (Zhang et al., 2021).

There are several limitations of the study to consider. First, we assumed that the stress-free configuration of the capsule was circular due to zonular support, but did not consider the traction imposed by the zonules at the equator of the post-surgical capsule as it contracts and likely comes into tension with the zonules over time. However, this traction would only occur towards the end of the contraction period of the post-surgical capsule (based on previously reported initial diameters for the native lens, ciliary muscle, and post-surgical capsule; see (Strenk et al., 1999; Tehrani et al., 2003; Strenk et al., 2006)), which suggests that it would be small, and, at least in some regions of the capsule, the implant is pushing out against the capsule to disengage the zonules and nullify the traction; thus, it may be insignificant. This zonular traction has also never been measured or estimated. Second, we assumed that the circumferential and meridional directions of the capsule remain principal over remodeling time after cataract surgery. It is possible that the directions of the principal stresses change, which would alter the directions of new fiber deposition. However, the principal directions of a flat orthotropic membrane with a central hole subjected to a *uniform* radial traction are also circumferential and meridional (David and Humphrey, 2004), the non-axisymmetric nature of the loading due to the IOL is localized to only those portions of the capsule in line with the haptics (Berggren et al., 2021), and the degree of material anisotropy of the lens capsule is modest which means that small changes in fiber orientations would not be expected to significantly alter the material symmetry or mechanical behavior. Thus, while adding this complexity is something to consider for future work, we do not expect it to alter model predictions. Third, our model assumed cell migration to the two regions of the posterior capsule where remodeling occurred in two instantaneous steps, one to the IOL optic edge and the next to the mid-periphery of the posterior capsule (with a 1-year delay between them to account for the barrier effect of the sharp-edged IOL optic), thus ignoring continuous migration over time. While this limitation is likely to have only a small effect on predictions of long-term remodeling and little quantitative data exist to better characterize this phenomenon, it is an improvement that can be considered as more data become available. Fourth, there is little data quantifying microstructural changes to the lens capsule over time after surgery. We calibrated our growth parameters to semi-quantitative data from a report that characterized capsule fibrosis in 157 cadaver lenses of patients who had undergone surgery greater than 3 years previously (Maddula et al., 2011), but this study used a categorical scoring system of thickness ranges based on the maximum amount of fibrotic thickening present in the anterior portion of the capsules. There is a need for more detailed histological data that better quantifies capsule thickness and individual constituents spatially (over the capsule) and temporally (after cataract surgery).

5 Conclusion

Our FE-G&R models predicted that implantation of a CTR with the IOL into the lens capsule after cataract surgery reduced

the mechanical perturbation, thickening, and stiffening along the visual axis in both the remnant anterior and posterior portions compared to implantation of an IOL alone. This finding aligns with patient studies and suggests that using this approach during routine cataract surgery would reduce visually debilitating ACO and PCO in all patients, not just those suffering from zonular weakness or dehiscence. To our knowledge, this is the first study to use modeling to demonstrate that the mechanical interactions of the implant and lens capsule play a significant role in determining evolving capsule mechanics and associated fibrosis over time after cataract surgery. It is also the first study to use modeling to predict the efficacy of any implant in terms of the extent of capsule fibrosis (i.e., ACO and PCO) development, which is the most significant complication of cataract surgery. Our work demonstrates that use of such modeling techniques has substantial potential to aid in the design of better surgical strategies and implants.

Data availability statement

The original contributions presented in the study are included in the article/Supplementary Material, further inquiries can be directed to the corresponding author.

Author contributions

KA: Data curation, Formal Analysis, Investigation, Methodology, Software, Validation, Visualization, Writing–original draft, Writing–review and editing. CB: Methodology, Software, Writing–review and editing. RP: Conceptualization, Funding acquisition, Investigation, Project administration, Resources, Supervision, Writing–original draft, Writing–review and editing.

Funding

The author(s) declare financial support was received for the research, authorship, and/or publication of this article. We gratefully acknowledge support for this work from the National Institute of Biomedical Imaging and Bioengineering of the National Institutes of Health under grant R03EB026837.

Acknowledgments

The authors are grateful to Mehrdad Negahban for helpful discussions.

Conflict of interest

The authors declare that the research was conducted in the absence of any commercial or financial relationships that could be construed as a potential conflict of interest.

Publisher's note

Supplementary material

The Supplementary Material for this article can be found online at: https://www.frontiersin.org/articles/10.3389/fbioe.2023.1300830/full#supplementary-material

References

Ameku, K. A., and Pedrigi, R. M. (2022). A biomechanical model for evaluating the performance of accommodative intraocular lenses. *J. Biomech.* 136, 111054. doi:10.1016/j.jbiomech.2022.111054

Baek, S., Rajagopal, K. R., and Humphrey, J. D. (2006). A theoretical model of enlarging intracranial fusiform aneurysms. *J. Biomech. Eng.* 128 (1), 142–149. doi:10.1115/1.2132374

Berggren, C. C., Ameku, K. A., and Pedrigi, R. M. (2021). Altered stress field of the human lens capsule after cataract surgery. *J. Biomech.* 115, 110127. doi:10.1016/j.jbiomech.2020.110127

Burd, H. J., Judge, S. J., and Cross, J. A. (2002). Numerical modelling of the accommodating lens. *Vis. Res.* 42 (18), 2235–2251. doi:10.1016/s0042-6989(02)00094-9

Burd, H. J., and Wilde, G. S. (2016). Finite element modelling of radial lentotomy cuts to improve the accommodation performance of the human lens. *Graefes Arch. Clin. Exp. Ophthalmol.* 254 (4), 727–737. doi:10.1007/s00417-016-3296-z

Cabeza-Gil, I., and Calvo, B. (2022). Predicting the biomechanical stability of IOLs inside the postcataract capsular bag with a finite element model. *Comput. Methods Programs Biomed.* 221, 106868. doi:10.1016/j.cmpb.2022.106868

Cabeza-Gil, I., Grasa, J., and Calvo, B. (2021). A numerical investigation of changes in lens shape during accommodation. *Sci. Rep.* 11 (1), 9639. doi:10.1038/s41598-021-89145-z

Chen, C. X., Wang, J. D., Zhang, J. S., Xiong, Y., Li, J., Chen, S. Y., et al. (2021). Effect of lens capsular tension ring on preventing capsular contraction syndrome in the surgery of retinitis pigmentosa combined with cataract: retrospective case series. *Int. J. Clin. Pract.* 75 (8), e14272. doi:10.1111/ijcp.14272

David, G., and Humphrey, J. D. (2004). Redistribution of stress due to a circular hole in a nonlinear anisotropic membrane. *J. Biomech.* 37 (8), 1197–1203. doi:10.1016/j.jbiomech.2003.12.013

David, G., Pedrigi, R. M., and Humphrey, J. D. (2017). Accommodation of the human lens capsule using a finite element model based on nonlinear regionally anisotropic biomembranes. *Comput. Methods Biomech. Biomed. Engin* 20 (3), 302–307. doi:10.1080/10255842.2016.1228907

Day, A. C., Gore, D. M., Bunce, C., and Evans, J. R. (2016). Laser-assisted cataract surgery versus standard ultrasound phacoemulsification cataract surgery. *Cochrane Database Syst. Rev.* 7 (7), CD010735. doi:10.1002/14651858.cd010735.pub2

D'Eliseo, D., Pastena, B., Longanesi, L., Grisanti, F., and Negrini, V. (2003). Prevention of posterior capsule opacification using capsular tension ring for zonular defects in cataract surgery. *Eur. J. Ophthalmol.* 13 (2), 151–154. doi:10.1177/112067210301300206

Gao, D. D., Huang, J. H., Ding, N., Deng, W. J., Li, P. L., Mai, Y. N., et al. (2022). Mechanosensitive Piezo1 channel in rat epididymal epithelial cells promotes transepithelial K(+) secretion. *Cell Calcium* 104, 102571. doi:10.1016/j.ceca.2022.102571

Halili, I., Mutlu, F. M., Erdurman, F. C., Gundogan, F. C., and Kilic, S. (2014). Influence of capsular tension ring on posterior capsule opacification in myopic eyes. *Indian J. Ophthalmol.* 62 (3), 311–315. doi:10.4103/0301-4738.116469

Hayashi, H., Hayashi, K., Nakao, F., and Hayashi, F. (2002). Elapsed time for capsular apposition to intraocular lens after cataract surgery. *Ophthalmology* 109 (8), 1427–1431. doi:10.1016/s0161-6420(02)01112-0

Heistand, M. R., Pedrigi, R. M., Delange, S. L., Dziezyc, J., and Humphrey, J. D. (2005). Multiaxial mechanical behavior of the porcine anterior lens capsule. *Biomech. Model Mechanobiol.* 4 (2-3), 168–177. doi:10.1007/s10237-005-0073-z

Heistand, M. R., Pedrigi, R. M., Dziezyc, J., and Humphrey, J. D. (2006). Redistribution of strain and curvature in the porcine anterior lens capsule following a continuous circular capsulorhexis. *J. Biomech.* 39 (8), 1537–1542. doi:10.1016/j.jbiomech.2005.04.019

Hermans, E. A., Dubbelman, M., van der Heijde, G. L., and Heethaar, R. M. (2006). Estimating the external force acting on the human eye lens during accommodation by finite element modelling. *Vis. Res.* 46 (21), 3642–3650. doi:10.1016/j.visres.2006.04.012

Humphrey, J. D. (2008). Vascular adaptation and mechanical homeostasis at tissue, cellular, and sub-cellular levels. *Cell Biochem. Biophys.* 50 (2), 53–78. doi:10.1007/s12013-007-9002-3

Karsaj, I., Soric, J., and Humphrey, J. D. (2010). A 3-D framework for arterial growth and remodeling in response to altered hemodynamics. *Int. J. Eng. Sci.* 48 (11), 1357–1372. doi:10.1016/j.ijengsci.2010.06.033

Knaus, K. R., Hipsley, A., and Blemker, S. S. (2021). The action of ciliary muscle contraction on accommodation of the lens explored with a 3D model. *Biomech. Model Mechanobiol.* 20 (3), 879–894. doi:10.1007/s10237-021-01417-9

Knaus, K. R., Hipsley, A., and Blemker, S. S. (2023). A new look at an old problem: 3D modeling of accommodation reveals how age-related biomechanical changes contribute to dysfunction in presbyopia. *Biomech. Model Mechanobiol.* doi:10.1007/s10237-023-01767-6

Krag, S., Olsen, T., and Andreassen, T. T. (1997). Biomechanical characteristics of the human anterior lens capsule in relation to age. *Invest. Ophthalmol. Vis. Sci.* 38 (2), 357–363.

Kumar, B., Chandler, H. L., Plageman, T., and Reilly, M. A. (2019). Lens stretching modulates lens epithelial cell proliferation via YAP regulation. *Invest. Ophthalmol. Vis. Sci.* 60 (12), 3920–3929. doi:10.1167/iovs.19-26893

Latorre, M., and Humphrey, J. D. (2018). Modeling mechano-driven and immuno-mediated aortic maladaptation in hypertension. *Biomech. Model Mechanobiol.* 17 (5), 1497–1511. doi:10.1007/s10237-018-1041-8

Li, B., Wang, Y., Malvankar-Mehta, M. S., and Hutnik, C. M. (2016). Surgical indications, outcomes, and complications with the use of a modified capsular tension ring during cataract surgery. *J. Cataract. Refract Surg.* 42 (11), 1642–1648. doi:10.1016/j.jcrs.2016.10.007

Lovicu, F. J., Shin, E. H., and McAvoy, J. W. (2016). Fibrosis in the lens. Sprouty regulation of TGFβ-signaling prevents lens EMT leading to cataract. *Exp. Eye Res.* 142, 92–101. doi:10.1016/j.exer.2015.02.004

Maddula, S., Werner, L., Ness, P. J., Davis, D., Zaugg, B., Stringham, J., et al. (2011). Pathology of 157 human cadaver eyes with round-edged or modern square-edged silicone intraocular lenses: analyses of capsule bag opacification. *J. Cataract. Refract Surg.* 37 (4), 740–748. doi:10.1016/j.jcrs.2010.10.058

Marcantonio, J. M., Rakic, J. M., Vrensen, G. F., and Duncan, G. (2000). Lens cell populations studied in human donor capsular bags with implanted intraocular lenses. *Invest. Ophthalmol. Vis. Sci.* 41 (5), 1130–1141.

Menapace, R., Findl, O., Georgopoulos, M., Rainer, G., Vass, C., and Schmetterer, K. (2000). The capsular tension ring: designs, applications, and techniques. *J. Cataract. Refract Surg.* 26 (6), 898–912. doi:10.1016/s0886-3350(00)00446-6

Miyoshi, T., Fujie, S., Yoshida, H., Iwamoto, H., Tsukamoto, H., and Oshika, T. (2020). Effects of capsular tension ring on surgical outcomes of premium intraocular lens in patients with suspected zonular weakness. *PLoS One* 15 (2), e0228999. doi:10.1371/journal.pone.0228999

Nejima, R., Miyai, T., Kataoka, Y., Miyata, K., Honbou, M., Tokunaga, T., et al. (2006). Prospective intrapatient comparison of 6.0-millimeter optic single-piece and 3-piece hydrophobic acrylic foldable intraocular lenses. *Ophthalmology* 113 (4), 585–590. doi:10.1016/j.ophtha.2005.10.064

Nims, R. J., Pferdehirt, L., and Guilak, F. (2022). Mechanogenetics: harnessing mechanobiology for cellular engineering. *Curr. Opin. Biotechnol.* 73, 374–379. doi:10.1016/j.copbio.2021.09.011

Pedrigi, R. M., David, G., Dziezyc, J., and Humphrey, J. D. (2007). Regional mechanical properties and stress analysis of the human anterior lens capsule. *Vis. Res.* 47 (13), 1781–1789. doi:10.1016/j.visres.2007.03.014

Pedrigi, R. M., Dziezyc, J., and Humphrey, J. D. (2009b). Altered mechanical behavior and properties of the human anterior lens capsule after cataract surgery. *Exp. Eye Res.* 89 (4), 575–580. doi:10.1016/j.exer.2009.06.001

Pedrigi, R. M., Dziezyc, J., Kalodimos, H. A., and Humphrey, J. D. (2009a). *Ex vivo* quantification of the time course of contractile loading of the porcine lens capsule after cataract-like surgery. *Exp. Eye Res.* 89 (6), 869–875. doi:10.1016/j.exer.2009.07.013

Pedrigi, R. M., and Humphrey, J. D. (2011). Computational model of evolving lens capsule biomechanics following cataract-like surgery. *Ann. Biomed. Eng.* 39 (1), 537–548. doi:10.1007/s10439-010-0133-0

Ramachandra, A. B., Latorre, M., Szafron, J. M., Marsden, A. L., and Humphrey, J. D. (2020). Vascular adaptation in the presence of external support - a modeling study. *J. Mech. Behav. Biomed. Mater* 110, 103943. doi:10.1016/j.jmbbm.2020.103943

Reilly, M. A. (2014). A quantitative geometric mechanics lens model: insights into the mechanisms of accommodation and presbyopia. *Vis. Res.* 103, 20–31. doi:10.1016/j.visres.2014.08.001

Strenk, S. A., Semmlow, J. L., Strenk, L. M., Munoz, P., Gronlund-Jacob, J., and DeMarco, J. K. (1999). Age-related changes in human ciliary muscle and lens: a magnetic resonance imaging study. *Invest. Ophthalmol. Vis. Sci.* 40 (6), 1162–1169.

Strenk, S. A., Strenk, L. M., and Guo, S. (2006). Magnetic resonance imaging of aging, accommodating, phakic, and pseudophakic ciliary muscle diameters. *J. Cataract. Refract Surg.* 32 (11), 1792–1798. doi:10.1016/j.jcrs.2006.05.031

Tehrani, M., Dick, H. B., Krummenauer, F., Pfirrmann, G., Boyle, T., and Stoffelns, B. M. (2003). Capsule measuring ring to predict capsular bag diameter and follow its course after foldable intraocular lens implantation. *J. Cataract. Refract Surg.* 29 (11), 2127–2134. doi:10.1016/s0886-3350(03)00352-3

Valentin, A., Humphrey, J. D., and Holzapfel, G. A. (2013). A finite element-based constrained mixture implementation for arterial growth, remodeling, and adaptation: theory and numerical verification. *Int. J. Numer. Method Biomed. Eng.* 29 (8), 822–849. doi:10.1002/cnm.2555

Werner, L., Ellis, N., Heczko, J. B., Ong, M., Jain, R., Wolfe, P., et al. (2018). *In vivo* evaluation of a new hydrophobic acrylic intraocular lens in the rabbit model. *J. Cataract. Refract Surg.* 44 (12), 1497–1502. doi:10.1016/j.jcrs.2018.07.040

Wormstone, I. M., Wormstone, Y. M., Smith, A. J. O., and Eldred, J. A. (2021). Posterior capsule opacification: what's in the bag? *Prog. Retin Eye Res.* 82, 100905. doi:10.1016/j.preteyeres.2020.100905

Yang, S., Jiang, H., Nie, K., Feng, L., and Fan, W. (2021). Effect of capsular tension ring implantation on capsular stability after phacoemulsification in patients with weak zonules: a randomized controlled trial. CTR implantation in cataract patients with weak zonules. *BMC Ophthalmol.* 21 (1), 19. doi:10.1186/s12886-020-01772-8

Zhang, K., Dong, Y., Zhao, M., Nie, L., Ding, X., and Zhu, C. (2021). The effect of capsule tension ring on posterior capsule opacification: a meta-analysis. *PLoS One* 16 (3), e0246316. doi:10.1371/journal.pone.0246316

frontiers | Frontiers in Bioengineering and Biotechnology

TYPE Original Research
PUBLISHED 15 March 2024
DOI 10.3389/fbioe.2024.1323612

OPEN ACCESS

EDITED BY
J. Crawford Downs,
University of Alabama at Birmingham,
United States

REVIEWED BY
Andri K. Riau,
Singapore Eye Research Institute (SERI),
Singapore
Prema Padmanabhan,
Sankara Nethralaya, India
Lin Li,
Capital Medical University, China

*CORRESPONDENCE
Ahmed Elsheikh,
Ahmed.Elsheikh@liverpool.ac.uk
ShiHao Chen,
csh@eye.ac.cn

†These authors have contributed equally to this work

RECEIVED 18 October 2023
ACCEPTED 30 January 2024
PUBLISHED 15 March 2024

CITATION
Chen W, Bao F, Roberts CJ, Zhang J, Wang C, Li X, Wang J, Abu Said AZM, Mayopa KN, Chen Y, Zheng X, Eliasy A, Elsheikh A and Chen S (2024), Effect of corneal cross-linking on biomechanical changes following transepithelial photorefractive keratectomy and femtosecond laser-assisted LASIK.
Front. Bioeng. Biotechnol. 12:1323612.
doi: 10.3389/fbioe.2024.1323612

Effect of corneal cross-linking on biomechanical changes following transepithelial photorefractive keratectomy and femtosecond laser-assisted LASIK

Wen Chen[1†], FangJun Bao[1,2,3,4†], Cynthia J. Roberts[5], Jia Zhang[1,2,3], Chong Wang[1], XueFei Li[1], JunJie Wang[1,2,3,4], Anas Ziad Masoud Abu Said[1], Kevin Nguelemo Mayopa[1], YaNi Chen[1], XiaoBo Zheng[1,2,3,4], Ashkan Eliasy[6], Ahmed Elsheikh[6,7,8*] and ShiHao Chen[1,2,3,4*]

[1]National Clinical Research Center for Ocular Diseases, Eye Hospital, Wenzhou Medical University, Wenzhou, China, [2]National Engineering Research Center of Ophthalmology and Optometry, Eye Hospital, Wenzhou Medical University, Wenzhou, China, [3]State Key Laboratory of Ophthalmology, Optometry and Vision Sicence, Eye Hospital, Wenzhou Medical University, Wenzhou, China, [4]The Institute of Ocular Biomechanics, WenZhou Medical University, Wenzhou, China, [5]Ophthalmology and Visual Sciences and Biomedical Engineering, The Ohio State University, Columbus, OH, United States, [6]School of Engineering, University of Liverpool, Liverpool, United Kingdom, [7]National Institute for Health Research (NIHR) Biomedical Research Centre for Ophthalmology, Moorfields Eye Hospital NHS Foundation Trust and UCL Institute of Ophthalmology, London, United Kingdom, [8]Beijing Advanced Innovation Center for Biomedical Engineering, Beihang University, Beijing, China

Purpose: To evaluate the change in corneal biomechanics in patients with postoperative ectasia risk when combining two common laser vision correction procedures (tPRK and FS-LASIK) with cross-linking (in tPRK Xtra and FS-LASIK Xtra).

Methods: The study included 143 eyes of 143 myopic, astigmatic patients that were divided into non-cross-linked refractive surgery groups (non-Xtra groups, tPRK and FS-LASIK) and cross-linked groups (Xtra groups, tPRK Xtra and FS-LASIK Xtra) according to an ectasia risk scoring system. The eyes were subjected to measurements including the stress-strain index (SSI), the stiffness parameter at first applanation (SP-A1), the integrated inverse radius (IIR), the deformation amplitude at apex (DA), and the ratio of deformation amplitude between apex and 2 mm from apex (DARatio2mm). The measurements were taken preoperatively and at 1, 3, and 6 months postoperatively (pos1m, pos3m, and pos6m). Posterior demarcation line depth from the endothelium (PDLD) and from the ablation surface (DLA) were recorded at pos1m.

Results: SP-A1 significantly decreased, while IIR, deformation amplitude, and DARatio2mm increased significantly postoperatively in all four groups ($p < 0.01$)—all denoting stiffness decreases. In the FS-LASIK group, the changes in IIR, DA, and DARatio2mm were 32.7 ± 15.1%, 12.9 ± 7.1%, and 27.2 ± 12.0% respectively, which were significantly higher ($p < 0.05$) compared to 20.1 ± 12.8%, 6.4 ± 8.2%, and 19.7 ± 10.4% in the FS-LASIK Xtra group. In the tPRK group, the change in IIR was 27.3 ± 15.5%, significantly larger than 16.9 ± 13.4% in the tPRK Xtra group. The changes of SSI were minimal in the tPRK (–1.5 ± 21.7%, $p = 1.000$), tPRK Xtra (8.4 ± 17.9%, $p = 0.053$), and FS-LASIK Xtra (5.6 ± 12.7%, $p = 0.634$) groups, but was

significant in the FS-LASIK group (–12.1 ± 7.9%, $p < 0.01$). After correcting for baseline biomechanical metrics, preoperative bIOP and the change in central corneal thickness (△CCT) from pre to pos6m, the changes in the IIR in both FS-LASIK and tPRK groups, as well as DA, DARatio2mm and SSI in the FS-LASIK group remained statistically greater than their corresponding Xtra groups (all $p < 0.05$). Most importantly, after correcting for these covariates, the changes in DARatio2mm in the FS-LASIK Xtra became statistically smaller than in the tPRK Xtra ($p = 0.017$).

Conclusion: The statistical analysis results indicate that tPRK Xtra and FS-LASIK Xtra effectively reduced the biomechanical losses caused by refractive surgery (tPRK and FS-LASIK). The decrease in corneal overall stiffness was greater in FS-LASIK than in tPRK, and the biomechanical enhancement of CXL was also higher following LASIK than after tPRK.

KEYWORDS

corneal stiffness, tPRK, FS-LASIK, CXL, Corvis ST

1 Introduction

Due to improvement in vision and high patient satisfaction, laser vision correction (LVC) surgeries have become increasingly popular in recent years. The loss of tissue due to ablation in surface treatments such as tPRK and the separation of a flap or cap in lamellar ablation procedures such as LASIK and SMILE, lead to reductions in corneal stiffness, which have led to some rare cases of corneal instability (Seiler et al., 1998; Malecaze et al., 2006; Randleman et al., 2006; Mattila and Holopainen, 2016). Since Seiler et al. (1998) reported the first iatrogenic keratectasia case after refractive surgery in 1998, which manifested as corneal progressive thinning and shape distortion, there have been more reports of ectasia with associated refractive error increases and loss of visual acuity. The incidence of ectasia after LASIK is between 0.04% and 0.60% (Xu et al., 2017), and much less after PRK (Roszkowska et al., 2017). SMILE, as a relatively new procedure, also has been reported a 0.15% incidence of ectasia post-surgery (Brar et al., 2021). Although rare, iatrogenic ectasia remains an extremely serious complication, which should be avoided.

Corneal cross-linking (CXL) is the most common method used to halt the progression of keratoconus and has been proven effective in stiffening the cornea in both *in vivo* and *ex vivo* testing (Spoerl et al., 1998; Sedaghat et al., 2018). In an attempt to improve the biomechanical integrity of the ablated cornea and reduce the incidence of iatrogenic keratectasia after refractive surgery, Kanellopoulos (2012) was the first to combine prophylactic high irradiance, short exposure CXL with LASIK. This was followed by reports of the clinical efficacy of combining prophylactic CXL with both PRK and SMILE, in procedures termed PRK Xtra and SMILE Xtra (Lee et al., 2017a; Torres-Netto et al., 2020).

Recognition of the importance of corneal biomechanics and the negative effects of LVC surgeries has led to attempts to quantify corneal stiffness *in vivo*, including the deformation parameters of the Corvis ST. These parameters included the deformation amplitude (DA), Stiffness Parameter (SP), and the Integrated Inverse Radius (IIR) (Vinciguerra et al., 2016; Roberts et al., 2017), all of which have been correlated with the cornea's overall stiffness. A more recent development is the Corvis Stress-Strain Index (SSI), designed through finite element modeling to estimate the material stiffness of the cornea–rather than its overall stiffness–and seeks to characterize the non-linear stress-strain behavior and hence the tangent modulus at any intraocular pressure value (Eliasy et al., 2019). This latter point is of particular importance since corneal tissue is known to have non-linear pressure-deformation behavior and stress-strain behavior, and hence the tangent modulus (Et) does not maintain a constant value but increases gradually with load, stress, deformation, and strain (Qin et al., 2019).

In this study, we aimed to use Corvis ST biomechanical parameters, to evaluate corneal biomechanical response to two common LVC procedures, namely tPRK and FS-LASIK, and their variations that combine cross-linking with the tissue ablation procedures; tPRK Xtra and FS-LASIK Xtra.

2 Materials and methods

2.1 Study participants

The study followed the tenets of the Declaration of Helsinki and was approved by the Ethics Committee of the Eye Hospital, WMU. Only the right eye of each patient with no systemic or ocular condition, apart from the refractive error, was selected for analysis. A total of 177 patients who underwent corneal refractive surgery for myopia and astigmatism at the Eye Hospital of Wenzhou Medical University (WMU) were prospectively and consecutively enrolled in this study. Clinical examinations were conducted preoperatively(pre), and at 1 month(pos1m), 3 months(pos3m) and 6 months(pos6m) postoperative, follow-up data at these time points were available for 170, 160, and 143 patients, respectively. Only the 143 patients with complete records were included in the follow-up analysis. Among these patients, 37 received transepithelial PRK (tPRK), 35 underwent tPRK Xtra (tPRK combined with CXL), 35 underwent FS-LASIK, and 36 underwent FS-LASIK Xtra (FS-LASIK combined with CXL). In the Xtra procedures, tPRK and FS-LASIK were combined with accelerated CXL based on the criteria listed in Figure 1, which combined the surgeon's (CSH) personal experience with an ectasia risk scoring system (Randleman et al., 2008; Chan et al., 2018). These patient inclusion criteria were roughly the same as described previously (Zhang et al., 2022), but with slight modifications. The figure shows the criteria used in determining whether to use CXL with FS-LASIK or

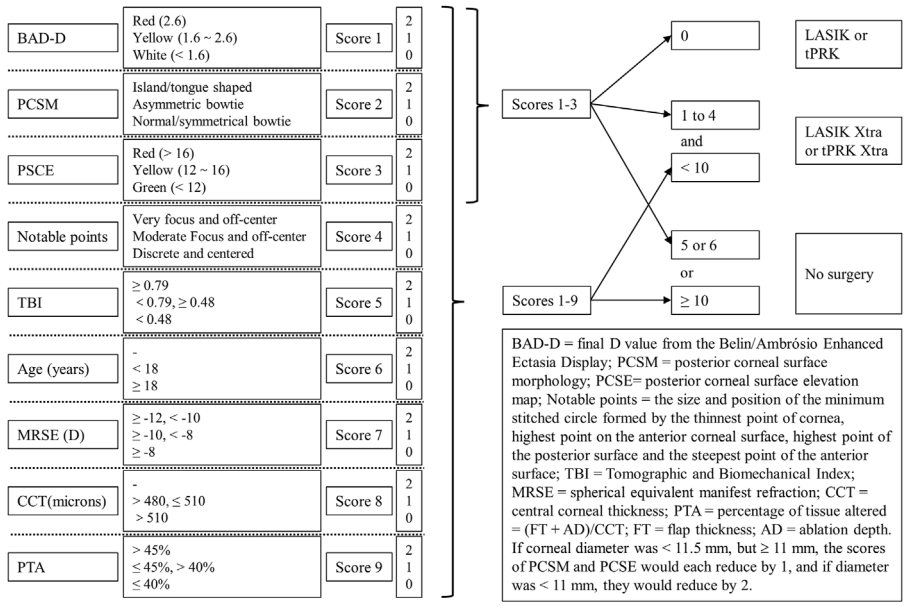

FIGURE 1
Chen ShiHao (CSH) scoring criteria used in preoperative assessment of patients.

tPRK, and the cases in which surgery would not be recommended. In other words, patients with eyes at risk of developing ectasia after LVC underwent either FS-LASIK Xtra or tPRK Xtra to improve the mechanical stability of the cornea postoperatively, while patients without postoperative ectasia risk underwent either FS-LASIK or tPRK. The choice between tPRK and FS-LASIK, or between tPRK Xtra and FS-LASIK Xtra was based on the clinical judgment of the surgeon. Patients' informed and signed consent was received after explaining the advantages and disadvantages of the study. All surgeries were performed by the same experienced surgeon (CSH).

2.2 Surgical techniques

In the tPRK group, ablation of corneal epithelium (ablated depth was set at 50 μm) and stroma was performed in a single step under the aberration-free mode of an Amaris 750 Hz excimer laser (Schwind eye-tech-solutions, Kleinostheim, Germany). In the FS-LASIK procedure, the lamellar flap was separated using FEMTO LDV Crystal Line femtosecond laser (Ziemer Ophthalmic Systems AG, Port, Switzerland). The flaps had a superior hinge, and their thickness ranged from 90 to 110 μm and diameter from 8.5 to 9.0 mm. The remaining specific parameters utilized in both procedures were maintained at a constant level, encompassing a stromal ablation rate of 12 mm/s, an edge-cutting speed of 6 mm/s, a repetition rate of 10 MHz, a pulse duration of 250 fs, and a spot energy of 880 mW. The ablation was then performed using the Amaris 750 Hz excimer laser. Residual stromal bed thickness (RSB) was recorded from surgery planning/treatment printouts. In calculating the RSB, the flap thickness was excluded in the two FS-LASIK groups while the epithelium thickness was not included in the two tPRK groups.

In the Xtra procedures, laser ablation was completed first before treating the residual corneal stroma with isotonic 0.22% riboflavin solution (VibeX Xtra; Avedro, Waltham, MA) for 100–120 s. Excess riboflavin was rinsed off with a saline solution before exposure to UVA in a continuous irradiation protocol at a power of 30 mW/cm^2 and a total dose of 2.1–2.7 J/cm^2. As shown in Table 1, various soaking times of riboflavin and total doses used in CXL procedure were dependent on the sum of the scores in Figure 1. After UVA irradiation, the corneal flap was re-placed to cover the residual corneal stroma in the FS-LASIK Xtra group. This procedure was different from that suggested by Avedro, the CXL machine manufacturer, in which UVA irradiation was to be applied after re-placing the flap on the residual stroma. This change was implemented to ensure that the full stiffening effect of CXL is realized in the residual stroma and not partly consumed in the flap, which ceases to contribute mechanically to the stroma once separated (Kanellopoulos et al., 2015; Randleman et al., 2017). This form of FS-LASIK Xtra was approved by Wenzhou Eye Hospital before using it in practice.

2.3 Data collection

The examinations included measurements by the Corvis ST non-contact tonometer (CVS, Oculus Optikgeräte GmbH, Wetzlar, Germany). Surgical parameters including the optical zone diameter (OZD), manifest refractive error correction (REC) and best-corrected visual acuity (BCVA) were also recorded from surgery planning/treatment printouts. REC was converted into spherical equivalent (SE). The safety index of both procedures, defined as the quotient of the postoperative BCVA divided by the preoperative BCVA, denoted a procedure as safe with values equal to or greater than one. Corneal haze was examined in follow-up by a BQ900 slit lamp (Haag-Streit, Germany), and assessed using the following scoring criteria: 0, normal cornea; 0.5, slight corneal haze; 1, mild

TABLE 1 CXL settings variations with different ectasia risk scores.

Cumulative risk score	Risk classification	Riboflavin soak time(s)	Total dose (J/cm^2)
1 to 3	1	100	2.1
4 to 6	2	110	2.4
7 to 9	3	120	2.7

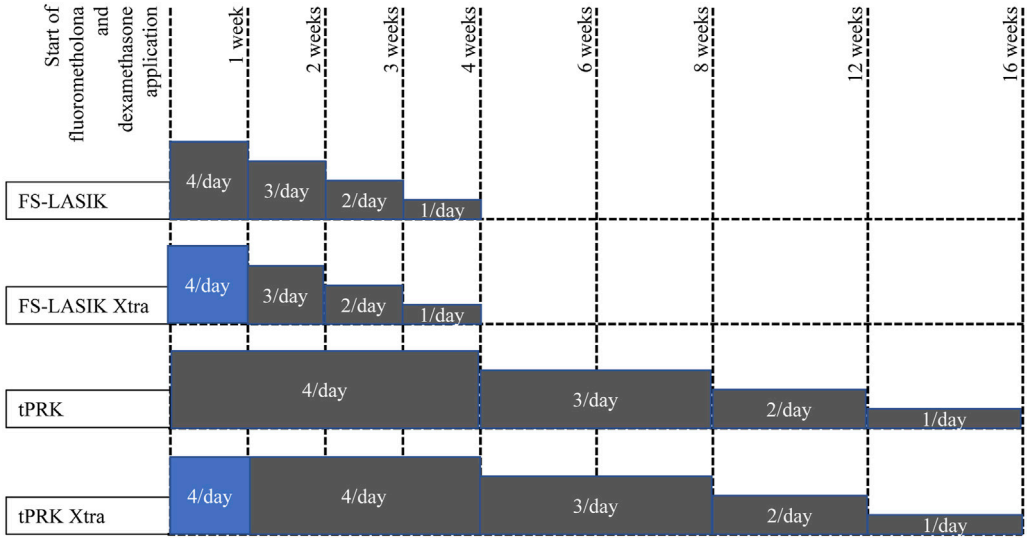

FIGURE 2
Tapering of fluorometholone and dexamethasone application following the four surgeries, grey color means fluorometholone usage while blue color means dexamethasone usage.

haze; 2, moderate opacity or scarring; 3, severe corneal opacity, but clear iris visibility; 4, opaque cornea and corneal ulcer; 5, corneal rupture and necrotizing stromal keratitis (Kim et al., 2006). Central corneal thickness (CCT) and corneal densitometry was measured with a Pentacam (Oculus Optikgerate GmbH). For the two Xtra groups, optical coherence tomography (OCT) (SD-OCT; RTVue-XR; Optovue, Inc., Fremont, CA) scanning was performed to locate the demarcation line within the stroma at 1, 3, 6 months post-surgery. The demarcation line was then used to determine the central thickness of the uncross-linked tissue that included the posterior part of the central stroma and the whole endothelium. This thickness is henceforth called the *posterior* demarcation line depth, or PDLD. This depth was used instead of the commonly used demarcation line depth (DLD), which focuses on the *anterior* part of the corneal thickness in order to avoid the possible confusion that can be created by the flap which had not been cross-linked and would not in any case contribute to the corneal biomechanical behavior. The demarcation line depth from the ablation surface (DLA) was then calculated as RSB—PDLD. The endothelial cell count (ECC) was also obtained using specular microscopy (SP-3000P, Topcon, Tokyo, Japan) at 6 months post-operation. Patients who were unwilling to participate or did not complete the 6 months postoperative follow-up were not included in the study. Ablated stromal depth (ASD) was recorded from surgery planning/treatment printouts. For tPRK, ASD was defined as ablation depth subtracted by central ablated epithelium thickness.

2.4 Postoperative care

The postoperative care was similar for the four procedures. One drop of tobramycin/dexamethasone (Tobradex; Alcon, TX, United States) was instilled at the surgical site. A bandage contact lens (Acuvue Oasys; Johnson & Johnson, FL, United States) was then placed on the cornea and kept for 1 day in the FS-LASIK and FS-LASIK Xtra groups until complete re-epithelization in the tPRK and tPRK Xtra groups–typically between 5 and 7 days. Topical levofloxacin 0.5% (Cravit; Santen, Osaka, Japan) was used until the bandage lens was taken off. This was followed by application of fluorometholone 0.1% (Flumetholon; Santen, Osaka, Japan), topical levofloxacin 0.5% (Cravit; Santen, Osaka, Japan), and dexamethasone (Tobradex; Alcon, Rijksweg, Belgium) whose frequency, duration, and tapering regime varied between the procedures as shown in Figure 2.

2.5 Biomechanical evaluation

All Corvis ST exams were taken three times in a sitting position with undilated pupils by two experienced examiners (WH and HNL) in the same half-day session to minimize diurnal effects. Five biomechanical parameters were chosen for analysis including the SSI, the deformation amplitude at the apex (DA), the ratio of deformation amplitude between the apex and 2 mm from the

TABLE 2 Basic biometric parameters of the four surgery groups.

Parameters	tPRK	tPRK Xtra	FS-LASIK	FS-LASIK Xtra	F	P
Age(years)	25.1 ± 4.1	23.1 ± 5.4	25.3 ± 4.3	24.3 ± 6.4	1.348	0.261
gender ratio	11/26	15/20	18/17	10/26	5.711	0.127
CCT(μm)	542.8 ± 32.0	535.9 ± 33.1	549.3 ± 28.0	546.7 ± 27.4	1.302	0.276
OZD(mm)	6.36 ± 0.39	6.16 ± 0.48	6.39 ± 0.29	6.28 ± 0.45	2.265	0.084
SE(D)	-5.31 ± 1.96	-5.44 ± 2.02	-5.46 ± 1.70	-5.13 ± 1.66	0.231	0.874
ASD(μm)	85.6 ± 22.0	84.2 ± 19.5	82.1 ± 23.1	77.8 ± 18.5	0.957	0.415
bIOP(mmHg)	15.0 ± 1.8	15.4 ± 2.0	14.7 ± 1.8	15.6 ± 2.2	1.462	0.228
Risk classification	-	1.51 ± 0.70	-	1.36 ± 0.59	2.456	0.123

Gender ratio was calculated as Male/Female, CCT, means central corneal thickness; OZD, means optical zone diameter; SE, means spherical equivalent of manifest refractive error correction; ASD, means Ablated stromal depth (ASD), bIOP, means biomechanically corrected intraocular pressure provided by Corvis ST.

apex (DARatio2mm). The fourth parameter was the integrated inverse radius (IIR), which represents the integrated sum of inverse concave radius between the first and the second applanation events. The parameters also included the stiffness parameter at first applanation (SP-A1) calculated as the difference between the adjusted air puff pressure at the first applanation (Adj AP1) and the biomechanically corrected intraocular pressure (bIOP) divided by the defection amplitude at the first applanation (A1 DeflAmp) (Eq. 1, Roberts et al., 2017).

$$SP - A1 = (adjAP1 - bIOP)/(A1DeflAmp) \quad (1)$$

While SSI was developed as a measure of the cornea's material stiffness using finite element analysis, the other four parameters were known to be correlated with the tissue's overall stiffness (Eliasy et al., 2019; Esporcatte et al., 2020) Furthermore, while increases in SSI and SP-A1 indicated stiffness increases, increases in IIR, DA and DARatio2mm pointed at stiffness reductions (Esporcatte et al., 2020).

2.6 Statistical analysis

All analyses were performed using the PASW Statistics 20.0 (SPSS Inc., Chicago, United States). Comparisons by post-op time within each of the four surgery methods were made using the MANOVA of repeated measurements. Comparisons of the biomechanical differences between pre-and post-surgery were carried out using two-way analysis of variance (ANOVA) and, two-way analysis of covariance (ANCOVA) with baseline biomechanical metrics (the biomechanical parameters recorded at the pre-surgery stage), preoperative bIOP and the change in central corneal thickness (△CCT) from pre to each follow-up period (pos1m, pos3m, and pos6m) as covariates. If the data did not fulfill the necessary assumptions of ANCOVA, GLM was used. Analysis of multiple groups was done with one-way ANOVA when the biomechanical comparisons involved the non-Xtra group and non-corresponding Xtra group (e.g., tPRK vs. FS-LASIK Xtra). The frequencies of the categorical variable gender were arranged in a 3 × 2 contingency table and the Chi-square test of independence was used to compare them. A p-value of less than 0.05 was considered statistically significant.

3 Results

The four groups (tPRK, tPRK Xtra, FS-LASIK, and FS-LASIK Xtra) were matched (all $p > 0.05$) in age, gender ratio, CCT, OZD, SE, ASD, and bIOP (Table 2). Further, the tPRK group and the tPRK Xtra group were matched in RSB thickness, while the FS-LASIK group and the FS-LASIK Xtra group were matched in both RSB and flap thickness (all $p > 0.05$). The risk classifications for the tPRK Xtra and FS-LASIK Xtra groups were not significantly different ($p = 0.123$). Table 3 shows the different baselines in Xtra and their corresponding non-Xtra groups, the table also shows the changes in corneal response parameters recorded before and after the four surgeries.

None of patients developed serious complications, and no difference was found in spherical equivalent (SE) among all groups at pos6m. The safety index at pos6m was 1.12 ± 0.11 in tPRK, 1.01 ± 0.06 in tPRK Xtra, 1.06 ± 0.12 in FS-LASIK and 1.03 ± 0.08 in FS-LASIK Xtra. At pos1m, 18.9% (7/37) of eyes in the tPRK group, 65.7% (23/35) in the tPRK Xtra group, and 31.4% (11/35) in the FS-LASIK Xtra group exhibited grade 0.5 haze. Additionally, 20.0% (7/35) of eyes in the tPRK Xtra had grade 1 haze. By the pos3m, haze had persisted only in the Xtra groups, with 60.0% (21/35) of tPRK Xtra eyes and 45.7% (16/35) in FS-LASIK Xtra eyes showing grade 0.5 haze, and 2.9% (1/35) in the FS-LASIK Xtra with grade 1 haze. At pos6m, 25.7% (9/35) of eyes in the tPRK Xtra and 14.3% (5/35) in the FS-LASIK Xtra still had grade 0.5 haze. The residual stromal bed thickness pre-CXL in FS-LASIK Xtra group was significantly lower than in tPRK Xtra group ($p < 0.001$, 374.3 ± 25.7 μm vs. 401.7 ± 40.1 μm). The appearance of a stromal demarcation line was observed in all Xtra eyes in the OCT scans recorded at pos1m (Figure 3). The mean central stromal PDLD was 232.4 ± 50.3 μm (range 128–314 μm), and 269.8 ± 64.6 μm (range 169–393 μm) in FS-LASIK Xtra and tPRK Xtra group, respectively. The differences in PDLD between the two groups were significant ($p = 0.008$). DLA in FS-LASIK Xtra was not different from the tPRK Xtra group ($p = 0.543$, 142.3 ± 52.5 μm vs. 134.9 ± 48.2 μm). In the FS-LASIK Xtra group, the demarcation line was well defined in 86.1% (31/36) of the eyes (Figure 3A), while 13.9% (5/36) had a faint line (Figure 3B). The corresponding ratios in the tPRK Xtra group were 57.1% (20/36) and 42.9% (15/36) (Figures 3C, D). The faint demarcation lines were still observable in 77.1% (27/35) and 60.0%

TABLE 3 Change in corneal biomechanical metrics and CCT after different surgeries of the four surgery groups.

	Stages	tPRK	tPRK Xtra	FS-LASIK	FS-LASIK Xtra	tPRK VS. tPRK Xtra	tPRK VS. LASIK	tPRK Xtra VS. LASIK Xtra	LASIK VS. LASIK Xtra
		Means ± SD				*p*-Value			
SP-A1(mmHg/mm)	Pre	105.97 ± 16.83	107.84 ± 18.6	104.61 ± 14.85	114.1 ± 19.02	1.00	1.00	0.86	0.43
	Pos1m	75.69 ± 13.88	83.78 ± 25.97	76.22 ± 17.84	81.25 ± 15.68	0.42	1.00	1.00	1.00
	Pos3m	77.05 ± 16.70	79.07 ± 16.06	74.66 ± 15.78	83.09 ± 11.62	1.00	1.00	1.00	0.12
	Pos6m	77.75 ± 19.25	80.08 ± 17.50	72.31 ± 16.13	83.27 ± 14.74	1.00	1.00	1.00	0.05*
IIR(mm^{-1})	Pre	8.65 ± 1.21	9.32 ± 0.94	8.25 ± 0.92	9.09 ± 0.94	0.04*	0.38	1.00	<0.01**
	Pos1m	10.52 ± 1.24	10.72 ± 1.27	10.68 ± 0.74	11.22 ± 0.92	1.00	1.00	0.38	0.26
	Pos3m	10.73 ± 1.32	11.1 ± 1.21	10.81 ± 0.97	10.96 ± 1.09	1.00	1.00	1.00	1.00
	Pos6m	10.89 ± 1.13	10.83 ± 1.1	10.84 ± 0.91	10.85 ± 0.82	1.00	1.00	1.00	1.00
DA (mm)	Pre	1.03 ± 0.08	1.07 ± 0.10	1.02 ± 0.07	1.05 ± 0.10	0.34	1.00	1.00	0.42
	Pos1m	1.08 ± 0.08	1.08 ± 0.15	1.10 ± 0.07	1.14 ± 0.09	1.00	1.00	0.16	0.44
	Pos3m	1.10 ± 0.09	1.14 ± 0.14	1.13 ± 0.06	1.12 ± 0.07	0.53	1.00	1.00	1.00
	Pos6m	1.14 ± 0.09	1.14 ± 0.11	1.15 ± 0.07	1.11 ± 0.08	1.00	1.00	0.65	0.51
DARatio2mm	Pre	4.62 ± 0.47	4.54 ± 0.46	4.56 ± 0.44	4.45 ± 0.49	1.00	1.00	1.00	1.00
	Pos1m	5.57 ± 0.60	5.02 ± 0.61	5.87 ± 0.55	5.41 ± 0.53	0.00**	0.17	0.03*	0.01**
	Pos3m	5.42 ± 0.56	5.21 ± 0.45	5.79 ± 0.58	5.30 ± 0.51	0.49	0.01**	1.00	<0.01**
	Pos6m	5.40 ± 0.58	5.20 ± 0.63	5.78 ± 0.52	5.30 ± 0.55	0.86	0.04*	1.00	0.01**
SSI	Pre	0.95 ± 0.14	0.87 ± 0.12	0.98 ± 0.13	0.87 ± 0.12	0.03*	1.00	1.00	0.01**
	Pos1m	0.94 ± 0.13	0.93 ± 0.19	0.91 ± 0.10	0.88 ± 0.13	1.00	1.00	0.13	1.00
	Pos3m	0.93 ± 0.15	0.91 ± 0.20	0.86 ± 0.11	0.91 ± 0.13	0.34	0.02*	1.00	1.00
	Pos6m	0.93 ± 0.20	0.94 ± 0.19	0.85 ± 0.09	0.91 ± 0.12	1.00	0.27	1.00	0.54
CCT (μm)	Pre	554.84 ± 33.62	545.97 ± 34.92	559.52 ± 28.61	555.73 ± 26.54	1.00	1.00	0.43	1.00
	Pos1m	451.70 ± 44.02	437.15 ± 43.94	459.88 ± 35.18	466.64 ± 24.46	0.63	1.00	0.01**	1.00
	Pos3m	450.61 ± 45.43	445.40 ± 44.38	464.60 ± 34.09	469.32 ± 24.98	1.00	0.74	0.06	1.00
	Pos6m	448.08 ± 42.23	450.38 ± 44.35	463.04 ± 35.10	470.65 ± 23.47	1.00	0.55	0.12	1.00

SP-A1, means the stiffness parameter at first applanation; IIR, means integrated inverse radius; DA means the deformation amplitude at the apex, DARatio2mm means the ratio of deformation amplitude between the apex and 2 mm from the apex, SSI, means the stress-strain index; CCT, means central corneal thickness; bIOP, means biomechanically corrected intraocular pressure provided by Corvis ST, * Means $p < 0.05$, ** means $p < 0.01$.

(21/35) in the tPRK Xtra group, at pos3m and pos6m, respectively. In comparison, the FS-LASIK Xtra group demonstrated a lower observable incidence, with 61.1% (22/36) of eyes at pos3m and only 11.1% (4/36) at pos6m exhibiting faint demarcation lines. The ECC in FS-LASIK Xtra remained similar ($p > 0.05$) before (2,857 ± 344 cells/mm^2) and after (2,742 ± 296 cells/mm^2) surgery, and the same finding was true in the tPRK Xtra group (2,786 ± 225 cells/mm^2 vs. 2,790 ± 264 cells/mm^2). At pos1m, the tPRK Xtra group exhibited a significant increase in mean corneal densitometry over the total area compared to preoperative values ($p = 0.015$). In contrast, corneal densitometry remained stable among the tPRK, FS-LASIK, and FS-LASIK Xtra ($p = 0.674$, 0.391 and 1.000, respectively). In contrast, at pos6m and compared to preoperative values, the mean corneal densitometry over the total area in both the tPRK Xtra and FS-LASIK decreased significantly ($p < 0.001$ and 0.026, respectively), while there were no significant differences in the tPRK ($p = 0.218$) and FS-LASIK Xtra ($p = 1.000$). The specific means, standard deviations and *p* values can be found in Supplementary Tables S3, S4.

Figure 4A shows a decrease in SP-A1 at pos1m compared with the pre-surgery stage (pre vs. pos1m, all $p < 0.01$). SP-A1 then remained stable (pos1m vs. pos3m: tPRK, $p = 1.000$; tPRK Xtra, $p = 0.515$; FS-LASIK, $p = 1.000$; FS-LASIK Xtra, $p = 1.000$. pos3m vs. pos6m: tPRK, $p = 1.000$; tPRK Xtra, $p = 1.000$; FS-LASIK, $p = 1.000$; FS-LASIK Xtra, $p = 1.000$. pos1m vs. pos6m: tPRK, $p = 1.000$; tPRK Xtra, $p = 1.000$; FS-LASIK, $p = 0.737$; FS-LASIK Xtra, $p = 1.000$) throughout follow up in all four groups. The specific means ± standard deviations and *p* values can be found in Table 3;

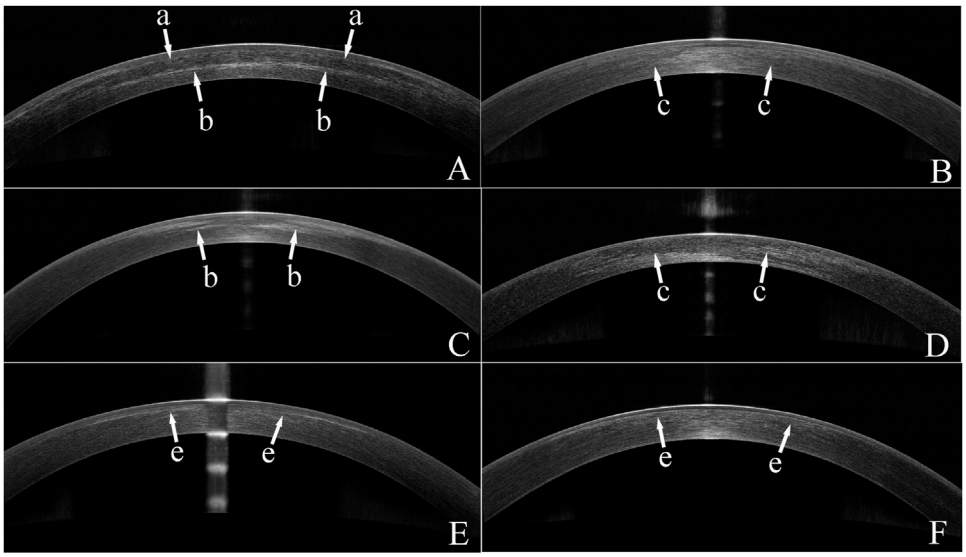

FIGURE 3
Optical coherence tomography (OCT) images of eyes from the two Xtra groups. **(A)** An OCT image of a FS-LASIK Xtra eye with a clear demarcation line at 1 month post surgery(pos1m). The arrows with an "a" indicate the interface between the flap and the residual stroma. Arrows with a "b" indicate the demarcation line. **(B)** An OCT image of a FS-LASIK Xtra eye with a faint demarcation line identified by "c" arrows at pos1m. **(C)** An OCT image of a tPRK Xtra eye showing a clear demarcation line indicated by arrows with a "b" at pos1m. **(D)** An OCT image of a tPRK Xtra eye with a faint demarcation line indicated by "c" arrows at pos1m. **(E)**. An OCT image of a FS-LASIK Xtra eye, recorded at 3 months post-surgery. Arrows with a "e" indicate the haze at the interface. **(F)**. An OCT image of a tPRK Xtra eye, recorded at 6 months post-surgery. Arrows with a "e" indicate the haze in the stroma.

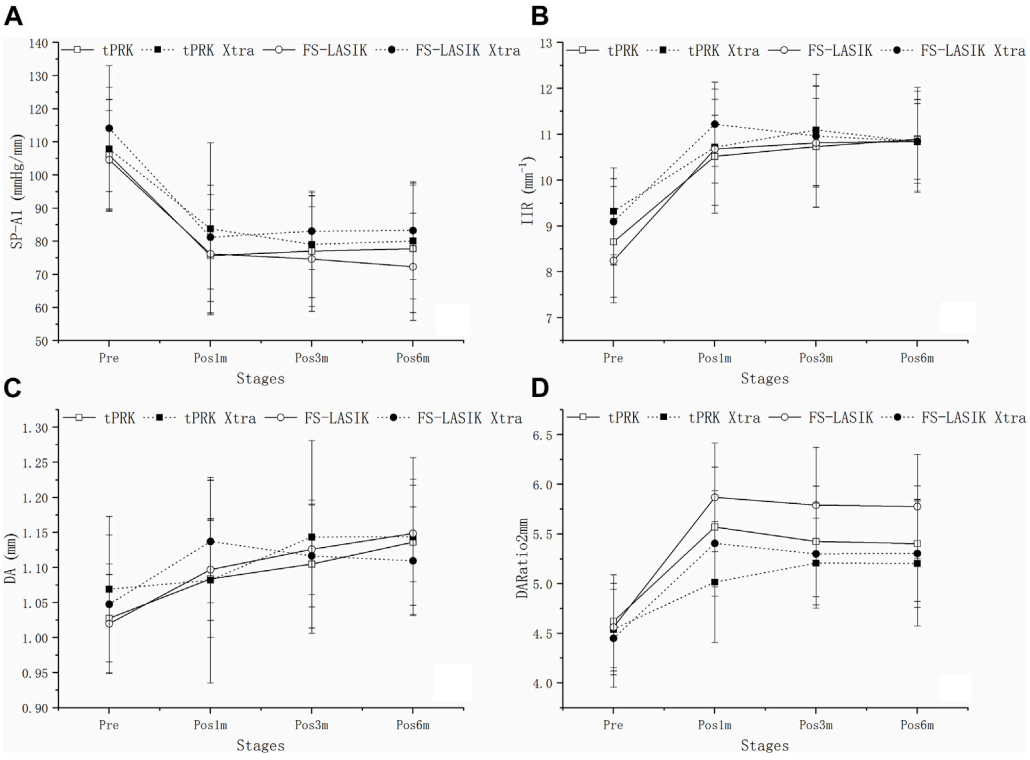

FIGURE 4
Change of SP-A1, IIR, DA and DARatio2mm throughout all follow up stages in the four groups. **(A)**: Change of SP-A1 throughout all follow up stages in the four groups. **(B)**: Change of IIR throughout all follow up stages in the four groups. **(C)**: Change of DA throughout all follow up stages in the four groups. **(D)**: Change of DARatio2mm throughout all follow up stages in the four groups.

TABLE 4 Comparison (*p*-value) of the difference (Δ) of corneal biomechanical metrics between pre and pos6m between the four surgery groups.

	Before baseline correction				After baseline correction			
	tPRK vs. FS-LASIK	tPRK Xtra vs. FS-LASIK Xtra	tPRK vs. tPRK Xtra	FS-LASIK vs. FS-LASIK Xtra	tPRK vs. FS-LASIK	tPRK Xtra vs. FS-LASIK Xtra	tPRK vs. tPRK Xtra	FS-LASIK vs. FS-LASIK Xtra
ΔSP-A1(mmHg/mm)	0.075	0.349	0.888	0.327	0.005**	0.185	0.768	0.235
ΔIIR (mm)	0.095	0.335	0.004**	<0.001**	0.089	0.327	0.003**	<0.001**
ΔDA (mm)	0.106	0.483	0.069	<0.001**	0.098	0.476	0.063	<0.001**
ΔDARatio2mm	<0.001**	0.092	0.288	0.001**	<0.001**	0.017*	0.531	0.002**
ΔSSI	0.008**	0.455	0.009**	<0.001**	0.008**	0.323	0.236	0.007**

Baseline correction means correcting for baseline biomechanical parameter, preoperative bIOP, and the change in central corneal thickness (△CCT) from pre to pos6m of in each group, SP-A1, means the stiffness parameter at first applanation; IIR, means integrated inverse radius, DARatio2mm means the ratio of deformation amplitude between the apex and 2 mm from the apex, SSI, means the stress-strain index, * Means $p < 0.05$, ** means $p < 0.01$.

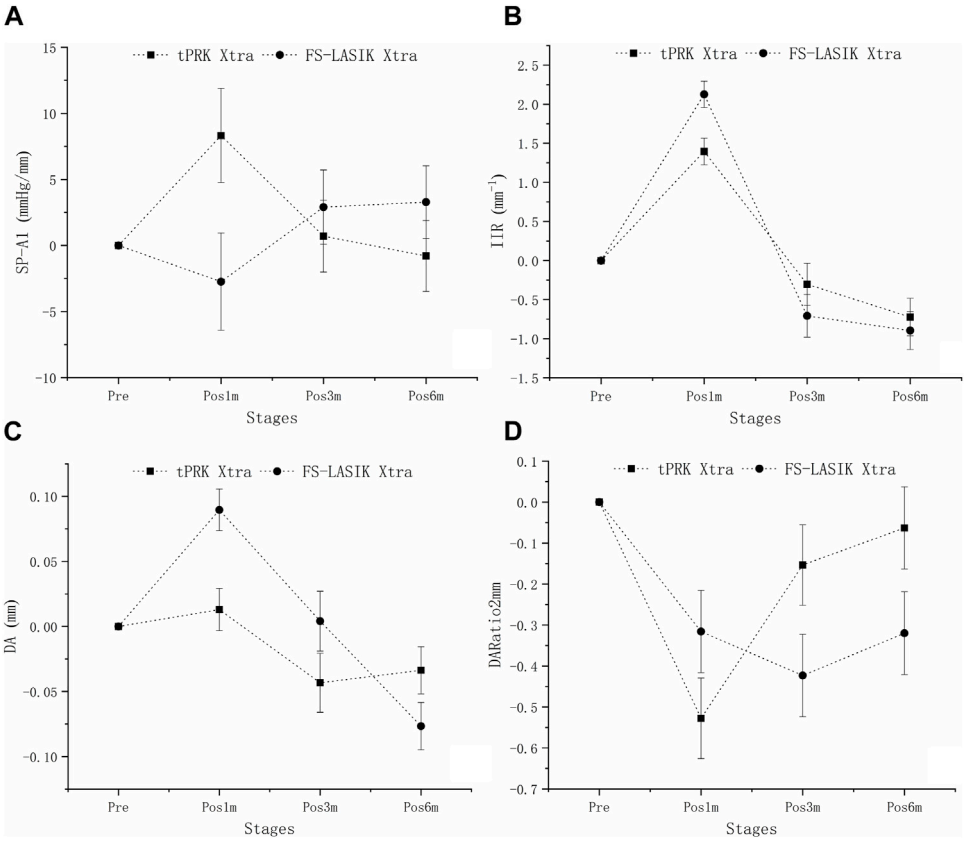

FIGURE 5
Isolating the effects of CXL: the estimated changes in SP-A1, IIR, DA, and DARatio2mm at all follow-up stages across the four groups. These changes are adjusted for preoperative bIOP, baseline biomechanical metrics, and the change in central corneal thickness (△CCT) from baseline to each follow-up stage. **(A)**: Isolating the effects of CXL: the estimated changes in SP-A1 at all follow-up stages across the four groups. **(B)**: Isolating the effects of CXL: the estimated changes in IIR at all follow-up stages across the four groups. **(C)**: Isolating the effects of CXL: the estimated changes in DA at all follow-up stages across the four groups. **(D)**: Isolating the effects of CXL: the estimated changes in DARatio2mm at all follow-up stages across the four groups.

Supplementary Table S2, respectively. Further, Table 4 shows a comparison of the difference in corneal biomechanical metrics between pre and pos6m (Δ, pos6m-pre) for the four surgery groups. There was no significant difference between the four groups in ΔSP-A1 between pre and pos6m (F = 0.911, p = 0.438). After correction for △CCT from pre to pos6m, preoperative bIOP and baseline SP-A1, ΔSP-A1 between pre and pos6m in FS-LASIK group became statistically higher than in the tPRK group (p = 0.005, Table 4), meaning greater reduction in SP-A1 stiffness in FS-LASIK than in tPRK.

Figure 4B shows that IIR exhibited significant increases (denoting stiffness reductions) from pre to pos1m in all surgery groups (all $p < 0.01$). This was followed by significant post-op changes in both the tPRK (pos1m vs. pos6m, $p = 0.033$) and tPRK Xtra (pos1m vs. pos3m, $p = 0.037$) groups, Figure 4B. The specific means ± standard deviations and p values can be found in Table 3; Supplementary Table S2, respectively. In contrast, IIR remained stable in the FS-LASIK and FS-LASIK Xtra groups (all $p > 0.05$, Figure 4B). The change in IIR between pre and pos6m (ΔIIR) was smallest in tPRK Xtra (1.51 ± 1.09 mm^{-1}, or 16.9 ± 13.4%), which was comparable to FS-LASIK Xtra (1.75 ± 0.95 mm^{-1}, or 20.1 ± 12.8%, $p = 1.000$), Figure 4B; Table 4. ΔIIR in tPRK Xtra between pre and pos6m was also significantly lower in tPRK (2.24 ± 1.07 mm^{-1}, or 27.3 ± 15.5%, $p = 0.021$) than in FS-LASIK (2.60 ± 0.97 mm^{-1}, or 32.7 ± 15.1%, $p < 0.001$). The stiffening effect of CXL on IIR was statistically significant in tPRK (tPRK vs. tPRK Xtra, $p = 0.004$) and in FS-LASIK (FS-LASIK vs. FS-LASIK Xtra, $p < 0.001$). Similarly, after correction for △CCT from pre to pos6m, preoperative bIOP and baseline IIR, the stiffening effect of CXL on FS-LASIK (ΔIIR: FS-LASIK vs. FS-LASIK Xtra, $p < 0.001$) and tPRK (ΔIIR: tPRK vs. tPRK Xtra, $p = 0.003$) remained significant, Table 4. This highlights the distinct stiffening effects of corneal cross-linking in different LVC procedures, Figure 5B.

Figure 4C shows that DA increased at pos1m compared with the pre-surgery stage, indicating stiffness reductions in the presence of a stable IOP, in all groups ($p < 0.01$) except tPRK Xtra ($p = 1.000$). DA then continued to increase post-surgery in tPRK (pos1m vs. pos6m, $p = 0.005$), tPRK Xtra (pos1m vs. pos6m, $p = 0.001$) and FS-LASIK (pos1m vs. pos6m, $p = 0.005$), but was stable ($p > 0.05$) in the FS-LASIK Xtra group, Figure 4C; Table 3; Supplementary Table S2. Further, as shown in Figure 4C; Table 4, the change in DA between pre and pos6m (ΔDA) was smallest in FS-LASIK Xtra (0.06 ± 0.08 mm, or 6.4 ± 8.2%), similar to tPRK Xtra (0.07 ± 0.09 mm, or 7.3 ± 8.2%, $p = 1.000$) and tPRK (0.11 ± 0.08 mm, by 10.8 ± 7.6%, $p = 0.069$), while it was significantly higher in FS-LASIK (0.13 ± 0.07 mm, by 12.9 ± 7.1%, $p < 0.001$). Similarly, after correction for △CCT from pre to pos6m, preoperative bIOP and baseline DA, the stiffening effect of CXL on DA remained significant in the FS-LASIK group (FS-LASIK vs. FS-LASIK Xtra, $p < 0.001$), and not in tPRK (tPRK vs. tPRK Xtra, $p = 0.063$), Table 4. The results suggest that CXL may be more effective in enhancing the stiffness in FS-LASIK corneas compared with tPRK, Figure 5C.

There were also significant increases in DARatio2mm between pre and pos1m, indicating stiffness reductions, in all groups (all $p <$ 0.01), and this trend remained valid over the rest of the follow-up period, Figure 4D. The specific means ± standard deviations and p values can be found in Table 3; Supplementary Table S2, respectively. Further, the increases in DARatio2mm between pre and pos6m (ΔDARatio2mm) were highest in FS-LASIK (1.22 ± 0.51), followed by FS-LASIK Xtra (0.85 ± 0.43, $p = 0.008$), and tPRK (0.78 ± 0.48, $p = 0.001$), and was smallest in tPRK Xtra (0.66 ± 0.47, $p < 0.001$), Figure 4D; Table 4. Similarly, after correction for △CCT from pre to pos6m, preoperative bIOP and baseline DARatio2mm, the change in DARatio2mm between pre and pos6m in FS-LASIK was statistically higher than in tPRK (FS-LASIK vs. tPRK $p < 0.001$) and the corresponding Xtra group (FS-LASIK vs. FS-LASIK Xtra, $p = 0.002$), Table 4. Moreover, after these corrections, the changes in DARatio2mm in the FS-LASIK Xtra became statistically smaller than in the tPRK Xtra ($p = 0.017$). The changes of DARatio2mm indicate that FS-LASIK creates greater reductions in corneal stiffness, and benefits from greater biomechanical enhancement in subsequent CXL treatments, compared with tPRK, Figure 5D.

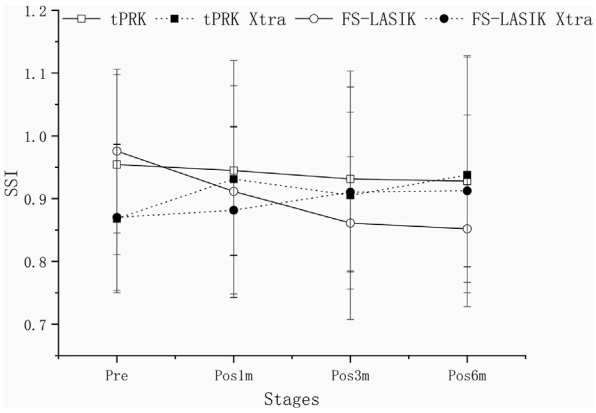

FIGURE 6
Change of SSI throughout all follow up stages in the four groups.

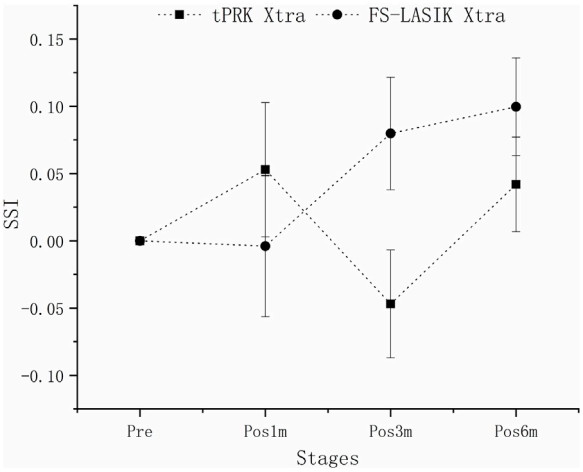

FIGURE 7
Isolating the effects of CXL: the estimated changes in SSI at all follow-up stages across the four groups. These changes are adjusted for preoperative bIOP, baseline biomechanical metrics, and △CCT from baseline to each follow-up stage.

SSI underwent significant decreases in the FS-LASIK group from pre to pos6m ($p < 0.01$), but not in the tPRK ($p = 1.000$), tPRK Xtra ($p = 0.053$) and FS-LASIK Xtra groups ($p = 0.635$), Figure 6. The decrease in SSI from pre to pos6m (ΔSSI) in FS-LASIK (-0.12 ± 0.10, -12.1 ± 7.9%) was statistically higher than in tPRK (-0.03 ± 0.22, or -1.5 ± 21.7%, $p = 0.045$), and was different from the two corresponding Xtra groups (all $p < 0.01$), Figure 6. ΔSSI also showed similar trends ($p = 1.000$) from pre to pos6m in the tPRK Xtra (0.07 ± 0.16, 8.4 ± 17.9%) and the FS-LASIK Xtra groups (0.04 ± 0.11, 5.6 ± 12.7%), while there were no significant differences of SSI in both groups. Meanwhile, the stiffening effect of CXL on SSI from pre to pos6m (ΔSSI) was statistically significant in

FS-LASIK (FS-LASIK vs. FS-LASIK Xtra, $p < 0.001$) and in tPRK (tPRK vs. tPRK Xtra, $p = 0.009$). After correction for ASD, preoperative bIOP and baseline SSI, the change in SSI from pre to pos6m in FS-LASIK remained significantly higher than in tPRK (tPRK vs. FS-LASIK, $p = 0.008$), which indicates a greater reduction in stiffness from the loss of tension in the flap with FS-LASIK. The change in SSI was also higher than in FS-LASIK Xtra (FS-LASIK Xtra vs. FS-LASIK, $p = 0.007$). This indicates a greater reduction in stiffness without CXL in FS-LASIK and thus a positive stiffening effect of CXL. However, ΔSSI from pre to pos6m between tPRK and the corresponding Xtra group was non-significant after correction (tPRK vs. tPRK Xtra, $p = 0.236$), Table 4. ΔSSI results indicate that the stiffening effect of CXL may be less in tPRK than in FS-LASIK, as shown in Figure 7.

4 Discussion

The main objective of this study was to evaluate the corneal biomechanical responses to two of the most commonly used LVC procedures; tPRK and FS-LASIK and their cross-linked variations; tPRK Xtra and FS-LASIK Xtra. The effect of CXL in reducing corneal stiffness deterioration was higher in FS-LASIK than in tPRK which seems to compensate, to some extent, for the larger effect of FS-LASIK on stiffness reduction compared with tPRK.

However, while CXL caused significantly less stiffness reduction after both tPRK-Xtra and FS-LASIK-Xtra which was evident throughout the follow-up period (all $p < 0.01$), the stiffness increases remained much lower than the stiffness losses caused by the LVC procedures (all $p < 0.01$). Despite this large difference in effect, prophylactic CXL remains a useful technique, to counter some of the deleterious biomechanical effects of LVC surgeries and may be effective to reduce the risk of iatrogenic ectasia. This general outcome is compatible with the findings of earlier studies on the subject, and with the growing popularity of Xtra procedures (Kanellopoulos and Asimellis, 2015; Lee et al., 2017a).

Our study relied on five deformation parameters provided by the Corvis ST, three of which correlate with overall corneal stiffness, namely SP-A1, IIR and DARatio2mm, while the SSI, was designed to represent the tissue's material stiffness. In all deformation parameters, there were indications of significant stiffness reductions at the first follow-up point after surgery (pos1m). SP-A1 experienced significant decreases of 27.8 ± 12.7% and 26.4 ± 21.1%, respectively with tPRK and FS-LASIK. The corresponding mean increases in IIR were 22.7 ± 14.4% and 31.5 ± 15.1%, in DA were 5.9 ± 9.4% and 8.9 ± 8.5%, and in DARatio2mm were 20.9 ± 10.8% and 29.6 ± 11.0%. Meanwhile, there were smaller stiffness reductions in Xtra groups compared with the corresponding non-Xtra groups. SP-A1 decreased by 23.1 ± 17.1% and 28.3 ± 11.2%, respectively with tPRK Xtra and FS-LASIK Xtra. There were also corresponding reductions of 15.5 ± 14.0% and 24.2 ± 12.7% in IIR, 1.3 ± 10.7% and 9.2 ± 10.4% in DA, and 10.9 ± 12.4% and 22.0 ± 10.6% in DARatio2mm in tPRK Xtra and FS-LASIK Xtra groups, respectively. Following pos1m and to the end of the follow-up period at pos6m, the differences in these parameters were, in most cases, small and non-significant except for significant increases of DA in tPRK, tPRK Xtra and FS-LASIK Xtra groups and significant increase of IIR in tPRK group.

These trends were generally in agreement with earlier reports except for a few minor differences. The postoperative decrease in SP-A1 in both tPRK and tPRK Xtra groups was similar to the results of a study by Lee et al. (2017a). In another study by Xu et al. (2017), the stiffness increases (indicated by decreases in highest concavity peak distance (PD) and DA) associated with using CXL after LASIK were not significant at all follow-up time points, but this may have been due to the small sample size employed. Further, the lower stiffness reductions noted in our study caused by CXL after both LASIK and tPRK surgeries were similar to the trends observed in two earlier studies, by Lee et al.(2017a, 2017b), Li et al. (2021). However, the non-significant results in DARatio2mm and SP-A1 noted in our study between the tPRK group and its corresponding Xtra group varied from those reported in these two earlier studies (Lee et al., 2017a; Li et al., 2021), which may be due to different crosslinking doses and eyes with risk for developing ectasia after LVC included in our study. These result were similar as our previous animal study (Bao et al., 2021). In the present study, total CXL energy doses varied from 2.1 J/cm^2 to 2.7 J/cm^2, according to the sum of risk scores, whereas both Lee et al. and Li et al. adopted a fixed total dose of 2.7 J/cm^2 which is higher than us. Meanwhile, the previous study by Lee et al. (2017b) involved healthy myopia patients in both the tPRK and tPRK Xtra groups, whereas our study considered patients with high-risk postoperative ectasia for membership of the Xtra groups. This difference in group formation may have contributed to the differences in some of the biomechanical metrics considered in our and earlier studies.

Distinct from the overall stiffness represented by the other four Corvis parameters, the SSI parameter was designed to represent the cornea's material stiffness independent of IOP and corneal geometry (Eliasy et al., 2019). The results showed significant improvement in ΔSSI in FS-LASIK Xtra group over FS-LASIK group, which is compatible with the large body of evidence depicting corneal stiffness increases with CXL (Kanellopoulos et al., 2015; Kling et al., 2017; Torres-Netto et al., 2020). However, notably, SSI was developed using finite element analysis in which tissue separation was not simulated (Eliasy et al., 2019). There are two separate regions in FS-LASIK and FS-LASIK Xtra with different biomechanical environments, the flap without biomechanical contribution and the residual stromal bed, which was not captured in the development of SSI. Thus, the reduction in SSI of FS-LASIK does not fully represent the material properties deterioration. Non-etheless, by the similar flap and RSB thickness adopted, it is still meaningful to compare the SSI changes from pre to pos6m between FS-LASIK and FS-LASIK Xtra. Although there were also different trends observed in two t-PRK groups, the changes were not significant. The SSI changes were also consistent with our previous animal experiments, which showed material stiffness increases caused by CXL after tPRK (Bao et al., 2021). In that study, the increases in SSI between pre-and post-Xtra surgery, were only significant in the tPRK Xtra group with a total CXL energy dose of 2.7 J/cm^2 but not 1.8 J/cm^2 (Bao et al., 2021).

Since the FS-LASIK flap made nearly no biomechanical contribution to the cornea, this procedure led to a smaller effective stromal thickness, and caused a larger reduction in corneal stiffness compared with the surface ablation procedure tPRK (Hashemi et al., 2017; Guo et al., 2019). If the flap is to be ignored biomechanically, the cornea would end up with a smaller effective stromal thickness after FS-LASIK than after tPRK. This effect is exaggerated by the differences in microstructure between the anterior and posterior parts of the stroma. With the anterior stroma

having higher lamellae packing density, more interlacing, and being less hydrated and less easily swollen (Radner et al., 1998; Müller et al., 2001; Bergmanson et al., 2005; Meek and Knupp, 2015; Torres-Netto et al., 2020), the anterior stroma is known to be stiffer than the posterior tissue (Kanellopoulos and Asimellis, 2015). In other words, compared to tPRK, the residual stromal bed in FS-LASIK is thinner and composed of a higher proportion of the softer posterior stroma. Therefore, the combined effect of tissue separation and higher stiffness in the ablated anterior stroma leads to higher stiffness losses caused by FS-LASIK than by tPRK.

Although the results showed a trend for more biomechanical metrics such as DA, DARatio 2 mm and SSI which were significantly different between FS-LASIK Xtra and its corresponding non-Xtra group compared with tPRK Xtra, no statistical difference in these metrics was observed between the two Xtra groups from pre to pos6m. However, it is important to note that DARatio2mm did show a significant statistical difference between tPRK Xtra and FS-LASIK Xtra after correcting for covariates. Meanwhile, FS-LASIK showed greater weakening than tPRK without CXL according to DARatio2mm and SSI. Our results indicate that the stiffening effect after CXL dominates the biomechanical differences between the refractive surgery techniques with a greater impact on the LVC procedure with the greatest weakening. This result was consistent with a previous study, which indicated that the biomechanical weakening of different LVC retreatment options after SMILE seems to be small compared with the enhancement effect of accelerated CXL (9 mW/cm^2, 10 min) (Kling et al., 2017).

If, on the other hand, CXL were applied after re-placing the flap, the expected outcome might have been the opposite. In that case, a large part of the cross-linking would have been consumed in stiffening the flap, leading to a potential risk of flap shrinking and contributing little to post-surgery corneal stiffness (Kanellopoulos and Asimellis, 2015). However, with CXL applied before re-placing the LASIK flap in our study, the fact that FS-LASIK had a smaller residual stromal thickness than tPRK meant that applying the Xtra treatment after the former surgery would stiffen a larger percentage of the posterior stromal thickness (lower PDLD and similar DLA) and lead to more significant biomechanical metric results of CXL. The difference in microstructure of anterior and posterior stroma may induce different stiffening effects in both parts, the increase ratio in posterior part is higher than anterior part after CXL consistent with previous studies (Lombardo et al., 2014; Beshtawi et al., 2016). Several biomechanical metrics were only pronounced in FS-LASIK (demonstrated by DA, DARatio 2 mm and SSI) as explained above. LASIK flap creation significantly reduced stiffness in the anterior stroma (Hashemi et al., 2017; Guo et al., 2019), while CXL may only take effect in the residual stroma under the flap.

Steps were taken to ensure patient safety in FS-LASIK Xtra group, especially with the direct irradiation of the RSB. A higher intensity (30 mW/cm^2) transfer compared to standard CXL protocol was adopted, and the residual stromal thickness was never below 320 μm. As a result of this precaution, the demarcation line was shallower compared with those reported with the Dresden protocol (Aldahlawi et al., 2015; Aldahlawi et al., 2016). All the PDLD (232.4 ± 50.3 μm, range 128–314 μm) in FS-LASIK Xtra were higher than 70 μm, which was considered the safety threshold in a recent study by Hafezi et al. (2021). Further, the endothelial cell count in FS-LASIK Xtra remained similar ($p > 0.05$) before (2,857 ± 344 cells/mm^2) and after (2,742 ± 296 cells/mm^2) surgery. Meanwhile, the safety index was greater than one in the FS-LASIK Xtra group, which also indicates the operation was safe. Ultimately, none of the patients developed serious complications within 6 months of follow-up. Thus, based on the above results, this FS-LASIK Xtra positively affects biomechanical outcomes without endothelial damage or visual acuity threat.

The major limitation of this investigation was that it was a non-randomized study with different baselines between groups. This was addressed by using baseline parameters as co-variates in the statistical analysis. In addition, there were multiple CXL procedures in the XTra groups. Also, the study was limited to data obtained over a follow-up period of 6 months and thus it does not extend to late ectasia. A further study with a larger sample size and longer follow-up would be important to investigate the biomechanical enhancement efficacy of CXL in Xtra surgeries.

In summary, we evaluated the effectiveness of CXL in compensating for the stiffness losses caused in the cornea by two forms of LVC, namely tPRK and FS-LASIK. However, three CXL procedures (2.1, 2.4 and 2.7 J/cm^2) were not sufficient to fully address the reductions caused by the LVC procedures. The biomechanical enhancement of CXL was higher in LASIK than in tPRK, and that phenomenon was useful considering the greater effect of FS-LASIK on corneal biomechanics losses than tPRK. Based on our results, the combined application of CXL with tPRK and FS-LASIK would have a positive effect in reducing the losses in corneal biomechanics and may reduce the risk of developing iatrogenic ectasia.

Data availability statement

The raw data supporting the conclusion of this article will be made available by the authors, without undue reservation.

Ethics statement

The studies involving humans were approved by the Ethics Committee of the Eye Hospital, Wenzhou Medical University. The studies were conducted in accordance with the local legislation and institutional requirements. Written informed consent for participation in this study was provided by the participants'; legal guardians/next of kin.

Author contributions

WC: Data curation, Formal Analysis, Funding acquisition, Writing–original draft, Writing–review and editing. FB: Conceptualization, Data curation, Funding acquisition, Investigation, Methodology, Resources, Writing–original draft, Writing–review and editing. CR: Investigation, Writing–review and editing. JZ: Data curation, Writing–original draft. CW: Data curation, Writing–original draft. XL: Data curation, Writing–original draft. JW: Formal Analysis, Funding acquisition, Writing–review and editing. AA: Data curation, Writing–original draft. KM: Formal Analysis, Writing–original draft. YC: Data curation, Writing–original draft. XZ: Funding acquisition, Methodology, Writing–review and editing. AsE: Investigation, Writing–review and editing. AhE: Supervision, Writing–review

and editing. SC: Funding acquisition, Project administration, Supervision, Writing–review and editing.

Funding

The author(s) declare financial support was received for the research, authorship, and/or publication of this article. This study was supported by XinMiao Talents Program of Zhejiang Province (2020R413086), Zhejiang Provincial Natural Science Foundation of China under Grant (LY18A020008, LY20H120001, LQ20A020008), the National Natural Science Foundation of China (31771020), the Projects of Medical and Health Technology Development Program in Zhejiang Province (2019RC056, 2018KY541, 2016ZHB012), Science and Technology Plan Project of Wenzhou Science and Technology Bureau (Y20180172, Y20170198, Y20170792) and the General Projects of Department of Education of Zhejiang Province (Y201839651).

Conflict of interest

CR is a consultant to Oculus Optikgeräte GmbH and Ziemer Ophthalmic Systems AG. AhE is a consultant to Oculus Optikgeräte GmbH. https://www.oculus.de/.

The remaining authors declare that the research was conducted in the absence of any commercial or financial relationships that could be construed as a potential conflict of interest.

The author(s) declared that they were an editorial board member of Frontiers, at the time of submission. This had no impact on the peer review process and the final decision.

Publisher's note

Supplementary material

The Supplementary Material for this article can be found online at: https://www.frontiersin.org/articles/10.3389/fbioe.2024.1323612/full#supplementary-material

References

Aldahlawi, N. H., Hayes, S., O'Brart, D. P., Akhbanbetova, A., Littlechild, S. L., and Meek, K. M. (2016). Enzymatic resistance of corneas crosslinked using riboflavin in conjunction with low energy, high energy, and pulsed UVA irradiation modes. *Invest. Ophthalmol. Vis. Sci.* 57 (4), 1547–1552. doi:10.1167/iovs.15-18769

Aldahlawi, N. H., Hayes, S., O'Brart, D. P., and Meek, K. M. (2015). Standard versus accelerated riboflavin-ultraviolet corneal collagen crosslinking: resistance against enzymatic digestion. *J. Cataract. Refract Surg.* 41 (9), 1989–1996. doi:10.1016/j.jcrs.2015.10.004

Bao, F., Chen, W., Zheng, X., Miao, Y., Zhu, M., Akiti, S., et al. (2021). Changes in corneal biomechanical properties in PRK followed by two accelerated CXL energy doses in rabbit eyes. *J. Refract Surg.* 37 (12), 853–860. doi:10.3928/1081597x-20210830-03

Bergmanson, J. P., Horne, J., Doughty, M. J., Garcia, M., and Gondo, M. (2005). Assessment of the number of lamellae in the central region of the normal human corneal stroma at the resolution of the transmission electron microscope. *Eye contact lens* 31 (6), 281–287. doi:10.1097/01.icl.0000165280.94927.0d

Beshtawi, I. M., Akhtar, R., Hillarby, M. C., O'Donnell, C., Zhao, X., Brahma, A., et al. (2016). Biomechanical changes of collagen cross-linking on human keratoconic corneas using scanning acoustic microscopy. *Curr. Eye Res.* 41 (5), 609–615. doi:10.3109/02713683.2015.1042545

Brar, S., Roopashree, C. R., and Ganesh, S. (2021). Incidence of ectasia after SMILE from a high-volume refractive surgery center in India. *J. Refract Surg.* 37 (12), 800–808. doi:10.3928/1081597x-20210812-03

Chan, C., Saad, A., Randleman, J. B., Harissi-Dagher, M., Chua, D., Qazi, M., et al. (2018). Analysis of cases and accuracy of 3 risk scoring systems in predicting ectasia after laser *in situ* keratomileusis. *J. Cataract. Refract Surg.* 44 (8), 979–992. doi:10.1016/j.jcrs.2018.05.013

Eliasy, A., Chen, K.-J., Vinciguerra, R., Lopes, B. T., Abass, A., Vinciguerra, P., et al. (2019). Determination of corneal biomechanical behavior *in-vivo* for healthy eyes using CorVis ST tonometry: stress-strain index. *Front. Bioeng. Biotechnol.* 7, 105. doi:10.3389/fbioe.2019.00105

Esporcatte, L. P. G., Salomao, M. Q., Lopes, B. T., Vinciguerra, P., Vinciguerra, R., Roberts, C., et al. (2020). Biomechanical diagnostics of the cornea. *Eye Vis.* 7, 9. doi:10.1186/s40662-020-0174-x

Guo, H., Hosseini-Moghaddam, S. M., and Hodge, W. (2019). Corneal biomechanical properties after SMILE versus FLEX, LASIK, LASEK, or PRK: a systematic review and meta-analysis. *BMC Ophthalmol.* 19 (1), 167. doi:10.1186/s12886-019-1165-3

Hafezi, F., Kling, S., Gilardoni, F., Hafezi, N., Hillen, M., Abrishamchi, R., et al. (2021). Individualized corneal cross-linking with riboflavin and UV-A in ultrathin corneas: the Sub400 protocol. *Am. J. Ophthalmol.* 224, 133–142. doi:10.1016/j.ajo.2020.12.011

Hashemi, H., Asgari, S., Mortazavi, M., and Ghaffari, R. (2017). Evaluation of corneal biomechanics after excimer laser corneal refractive surgery in high myopic patients using dynamic scheimpflug Technology. *Eye Contact Lens* 43 (6), 371–377. doi:10.1097/icl.0000000000000280

Kanellopoulos, A. J. (2012). Long-term safety and efficacy follow-up of prophylactic higher fluence collagen cross-linking in high myopic laser-assisted *in situ* keratomileusis. *Clin. Ophthalmol.* 6, 1125–1130. doi:10.2147/opth.s31256

Kanellopoulos, A. J., and Asimellis, G. (2015). Combined laser *in situ* keratomileusis and prophylactic high-fluence corneal collagen crosslinking for high myopia: two-year safety and efficacy. *J. Cataract. Refract Surg.* 41 (7), 1426–1433. doi:10.1016/j.jcrs.2014.10.045

Kanellopoulos, A. J., Asimellis, G., Salvador-Culla, B., Chodosh, J., and Ciolino, J. B. (2015). High-irradiance CXL combined with myopic LASIK: flap and residual stroma biomechanical properties studied *ex-vivo*. *Br. J. Ophthalmol.* 99 (6), 870–874. doi:10.1136/bjophthalmol-2014-306411

Kim, B., Sarangi, P. P., Lee, Y., Deshpande Kaistha, S., Lee, S., and Rouse, B. T. (2006). Depletion of MCP-1 increases development of herpetic stromal keratitis by innate immune modulation. *J. Leukoc. Biol.* 80 (6), 1405–1415. doi:10.1189/jlb.0406295

Kling, S., Spiru, B., Hafezi, F., and Sekundo, W. (2017). Biomechanical weakening of different Re-treatment options after small incision lenticule extraction (SMILE). *J. Refract Surg.* 33 (3), 193–198. doi:10.3928/1081597x-20161221-01

Lee, H., Roberts, C. J., Ambrosio, R., Jr., Elsheikh, A., Kang, D. S. Y., and Kim, T. I. (2017a). Effect of accelerated corneal crosslinking combined with transepithelial photorefractive keratectomy on dynamic corneal response parameters and biomechanically corrected intraocular pressure measured with a dynamic Scheimpflug analyzer in healthy myopic patients. *J. Cataract. Refract Surg.* 43 (7), 937–945. doi:10.1016/j.jcrs.2017.04.036

Lee, H., Roberts, C. J., Kim, T. I., Ambrósio, R., Jr., Elsheikh, A., and Yong Kang, D. S. (2017b). Changes in biomechanically corrected intraocular pressure and dynamic corneal response parameters before and after transepithelial photorefractive keratectomy and femtosecond laser-assisted laser *in situ* keratomileusis. *J. Cataract. Refract Surg.* 43 (12), 1495–1503. doi:10.1016/j.jcrs.2017.08.019

Li, L., Zhang, B., Hu, Y., Xiong, L., and Wang, Z. (2021). Comparison of safety and efficiency of corneal topography-guided photorefractive keratectomy and combined with crosslinking in myopic correction: an 18-month follow-up. *Med. Baltim.* 100 (2), e23769. doi:10.1097/md.0000000000023769

Lombardo, M., Serrao, S., Rosati, M., Ducoli, P., and Lombardo, G. (2014). Biomechanical changes in the human cornea after transepithelial corneal crosslinking using iontophoresis. *J. Cataract. Refract Surg.* 40 (10), 1706–1715. doi:10.1016/j.jcrs.2014.04.024

Malecaze, F., Coullet, J., Calvas, P., Fournie, P., Arne, J. L., and Brodaty, C. (2006). Corneal ectasia after photorefractive keratectomy for low myopia. *Ophthalmology* 113 (5), 742–746. doi:10.1016/j.ophtha.2005.11.023

Mattila, J. S., and Holopainen, J. M. (2016). Bilateral ectasia after femtosecond laser-assisted small incision lenticule extraction (SMILE). *J. Refract Surg.* 32 (7), 497–500. doi:10.3928/1081597x-20160502-03

Meek, K. M., and Knupp, C. (2015). Corneal structure and transparency. *Prog. Retin Eye Res.* 49, 1–16. doi:10.1016/j.preteyeres.2015.07.001

Müller, L. J., Pels, E., and Vrensen, G. F. (2001). The specific architecture of the anterior stroma accounts for maintenance of corneal curvature. *Br. J. Ophthalmol.* 85 (4), 437–443. doi:10.1136/bjo.85.4.437

Qin, X., Tian, L., Zhang, H., Chen, X., and Li, L. (2019). Evaluation of corneal elastic modulus based on corneal visualization scheimpflug Technology. *Biomed. Eng. Online* 18 (1), 42. doi:10.1186/s12938-019-0662-1

Radner, W., Zehetmayer, M., Aufreiter, R., and Mallinger, R. (1998). Interlacing and cross-angle distribution of collagen lamellae in the human cornea. *Cornea* 17 (5), 537–543. doi:10.1097/00003226-199809000-00012

Randleman, J. B., Caster, A. I., Banning, C. S., and Stulting, R. D. (2006). Corneal ectasia after photorefractive keratectomy. *J. Cataract. Refract Surg.* 32 (8), 1395–1398. doi:10.1016/j.jcrs.2006.02.078

Randleman, J. B., Su, J. P., and Scarcelli, G. (2017). Biomechanical changes after LASIK flap creation combined with rapid cross-linking measured with brillouin microscopy. *J. Refract Surg.* 33 (6), 408–414. doi:10.3928/1081597x-20170421-01

Randleman, J. B., Woodward, M., Lynn, M. J., and Stulting, R. D. (2008). Risk assessment for ectasia after corneal refractive surgery. *Ophthalmology* 115 (1), 37–50.e4. doi:10.1016/j.ophtha.2007.03.073

Roberts, C. J., Mahmoud, A. M., Bons, J. P., Hossain, A., Elsheikh, A., Vinciguerra, R., et al. (2017). Introduction of two novel stiffness parameters and interpretation of air puff-induced biomechanical deformation parameters with a dynamic scheimpflug analyzer. *J. Refract Surg.* 33 (4), 266–273. doi:10.3928/1081597x-20161221-03

Roszkowska, A. M., Sommario, M. S., Urso, M., and Aragona, P. (2017). Post photorefractive keratectomy corneal ectasia. *Int. J. Ophthalmol.* 10 (2), 315–317. doi:10.18240/ijo.2017.02.22

Sedaghat, M. R., Momeni-Moghaddam, H., Ambrosio, R., Jr., Roberts, C. J., Yekta, A. A., Danesh, Z., et al. (2018). Long-term evaluation of corneal biomechanical properties after corneal cross-linking for keratoconus: a 4-year longitudinal study. *J. Refract Surg.* 34 (12), 849–856. doi:10.3928/1081597x-20181012-02

Seiler, T., Koufala, K., and Richter, G. (1998). Iatrogenic keratectasia after laser *in situ* keratomileusis. *J. Refract Surg.* 14 (3), 312–317. doi:10.3928/1081-597x-19980501-15

Spoerl, E., Huhle, M., and Seiler, T. (1998). Induction of cross-links in corneal tissue. *Exp. Eye Res.* 66 (1), 97–103. doi:10.1006/exer.1997.0410

Torres-Netto, E. A., Spiru, B., Kling, S., Gilardoni, F., Lazaridis, A., Sekundo, W., et al. (2020). Similar biomechanical cross-linking effect after SMILE and PRK in human corneas in an *ex vivo* model for postoperative ectasia. *J. Refract Surg.* 36 (1), 49–54. doi:10.3928/1081597x-20191211-01

Vinciguerra, R., Elsheikh, A., Roberts, C. J., Ambrosio, R., Jr., Kang, D. S., Lopes, B. T., et al. (2016). Influence of pachymetry and intraocular pressure on dynamic corneal response parameters in healthy patients. *J. Refract Surg.* 32 (8), 550–561. doi:10.3928/1081597x-20160524-01

Xu, W., Tao, Y., Wang, L., and Huang, Y. (2017). Evaluation of biomechanical changes in myopia patients with unsatisfactory corneas after femto second-laser *in situ* keratomileusis (FS-LASIK) concurrent with accelerated corneal collagen cross-linking using corvis-ST: two-year follow-up results. *Med. Sci. Monit.* 23, 3649–3656. doi:10.12659/msm.905493

Zhang, J., Chen, T., Wang, J., Bao, F., Chen, W., Stojanovic, A., et al. (2022). Laser *in situ* keratomileusis (LASIK) combined with prophylactic corneal cross-linking for correction of myopia: regional analysis of corneal morphology. *Ophthalmol. Ther.* 11 (4), 1423–1439. doi:10.1007/s40123-022-00510-1

frontiers | Frontiers in Bioengineering and Biotechnology

TYPE Original Research
PUBLISHED 04 April 2024
DOI 10.3389/fbioe.2024.1285107

OPEN ACCESS

EDITED BY
Matthew A. Reilly,
The Ohio State University, United States

REVIEWED BY
Greeshma Sharma,
Netaji Subhas University of Technology, India
Vitoantonio Bevilacqua,
Politecnico di Bari, Italy
Josselin Gautier,
University of Rennes 1, France

*CORRESPONDENCE
Mattia Barbieri,
mattia.barbieri@iit.it

†PRESENT ADDRESS
Giulia A. Albanese, ReWing s.r.l., Milano, Italy

RECEIVED 31 August 2023
ACCEPTED 14 March 2024
PUBLISHED 04 April 2024

CITATION
Barbieri M, Albanese GA, Merello A, Crepaldi M, Setti W, Gori M, Canessa A, Sabatini SP, Facchini V and Sandini G (2024), Assessing REALTER simulator: analysis of ocular movements in simulated low-vision conditions with extended reality technology.
Front. Bioeng. Biotechnol. 12:1285107.
doi: 10.3389/fbioe.2024.1285107

Assessing REALTER simulator: analysis of ocular movements in simulated low-vision conditions with extended reality technology

Mattia Barbieri[1,2]*, Giulia A. Albanese[1†], Andrea Merello[3], Marco Crepaldi[3], Walter Setti[4], Monica Gori[4], Andrea Canessa[2], Silvio P. Sabatini[2], Valentina Facchini[5] and Giulio Sandini[1]

[1]Department of Robotics, Brain and Cognitive Sciences, Istituto Italiano di Tecnologia, Genova, Italy, [2]Department of Informatics, Bioengineering, Robotics and Systems Engineering, University of Genoa, Genoa, Italy, [3]Electronic Design Laboratory, Istituto Italiano di Tecnologia, Genova, Italy, [4]Unit for Visually Impaired People, Istituto Italiano di Tecnologia, Genova, Italy, [5]Fondazione David Chiossone per Ciechi e Ipovedenti, Genoa, Italy

Immersive technology, such as extended reality, holds promise as a tool for educating ophthalmologists about the effects of low vision and for enhancing visual rehabilitation protocols. However, immersive simulators have not been evaluated for their ability to induce changes in the oculomotor system, which is crucial for understanding the visual experiences of visually impaired individuals. This study aimed to assess the REALTER (Wearable Egocentric Altered Reality Simulator) system's capacity to induce specific alterations in healthy individuals' oculomotor systems under simulated low-vision conditions. We examined task performance, eye movements, and head movements in healthy participants across various simulated scenarios. Our findings suggest that REALTER can effectively elicit behaviors in healthy individuals resembling those observed in individuals with low vision. Participants with simulated binocular maculopathy demonstrated unstable fixations and a high frequency of wide saccades. Individuals with simulated homonymous hemianopsia showed a tendency to maintain a fixed head position while executing wide saccades to survey their surroundings. Simulation of tubular vision resulted in a significant reduction in saccade amplitudes. REALTER holds promise as both a training tool for ophthalmologists and a research instrument for studying low vision conditions. The simulator has the potential to enhance ophthalmologists' comprehension of the limitations imposed by visual disabilities, thereby facilitating the development of new rehabilitation protocols.

KEYWORDS

extended reality, augmented reality, rehabilitation, visual impairments, eye tracking, immersive technology, gaze-contingency, ocular movements detection

1 Introduction

More than 285 million people worldwide suffer from visual impairments (VIs) (Gori et al., 2016). Among them, 39 million are completely blind, while 10 million experience chronic VIs that affect a partial portion of their field of view (FOV), known as low vision diseases, such as glaucoma, hemianopsia, and age-related macular degeneration (Flaxman

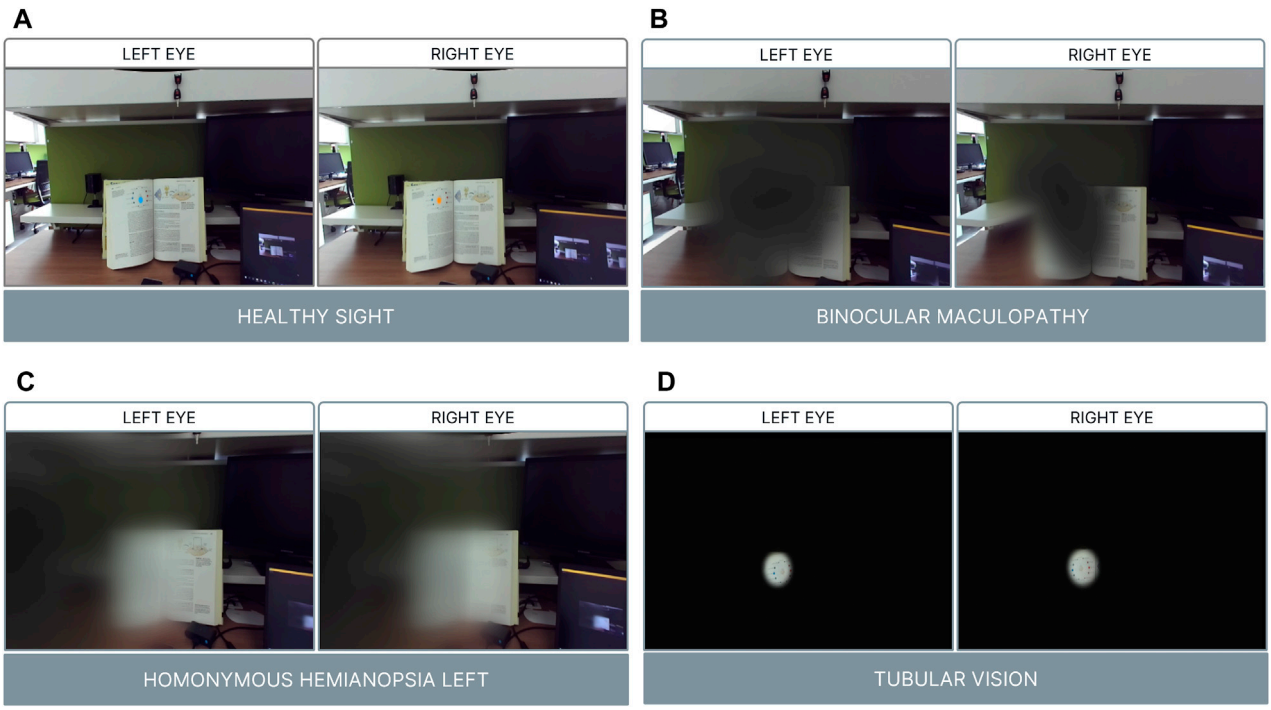

FIGURE 1
Visual conditions. Panel **(A)** Healthy sight with fixations points for each eye; Panel **(B)** Binocular Maculopathy; Panel **(C)** Homonymous Hemianopsia Left; Panel **(D)** Tubular Vision.

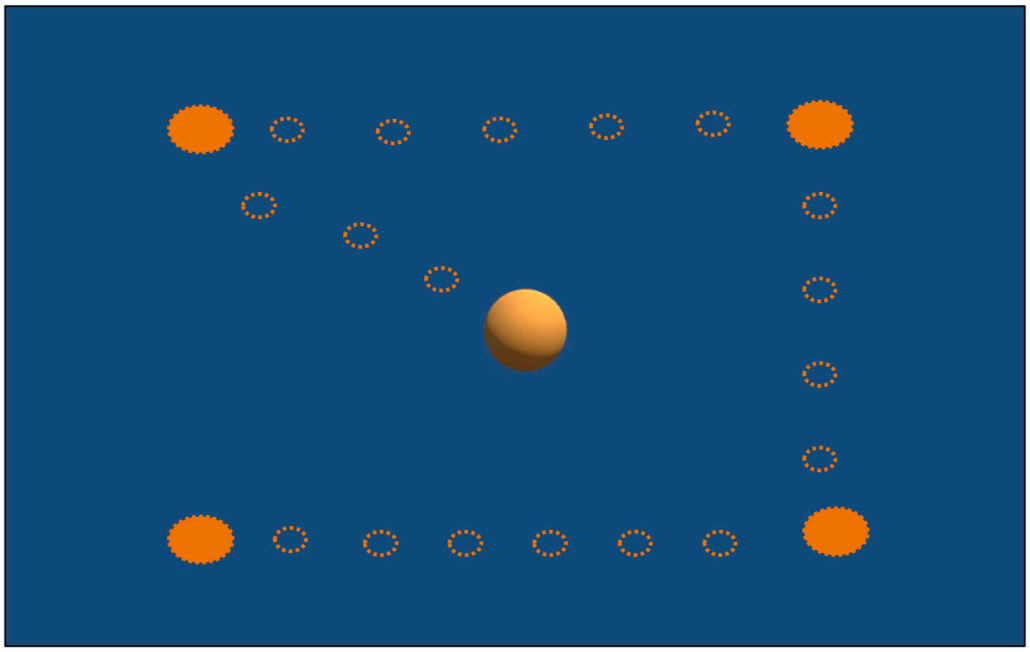

FIGURE 2
Calibration custom task: Subjects should follow with their eyes the sphere's movements: the empty circles show the sphere's path; the full circles show the positions where the sphere remained fixed for 3 s.

et al., 2017). These chronic Vis cannot be corrected with glasses, contact lenses, or surgery and significantly impact daily activities (Leat et al., 1999). Typically, individuals affected by low vision diseases experience a significant loss of their visual field, affecting the central (maculopathy), peripheral (tunnel vision), or half of the vertical visual field (hemianopsias). These conditions impair

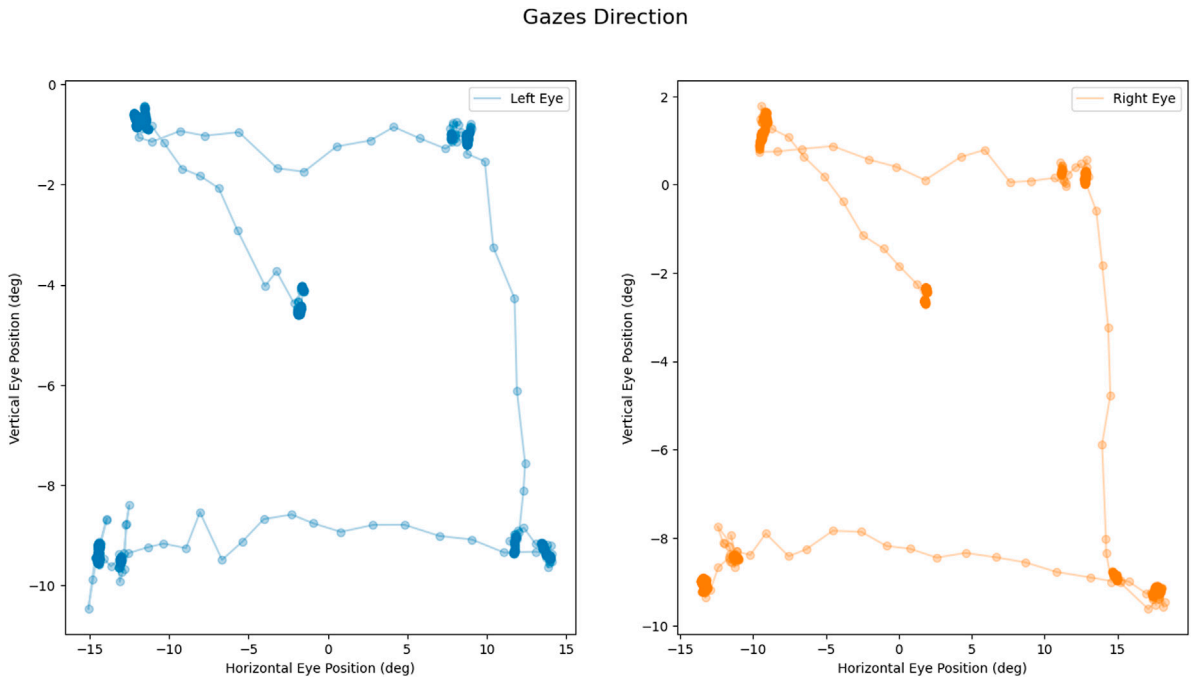

FIGURE 3
Calibration task output: Example of coherent scan paths during the task: left eye movement in blue (on the left); right eye movement in orange (on the right). All measures are expressed in degrees.

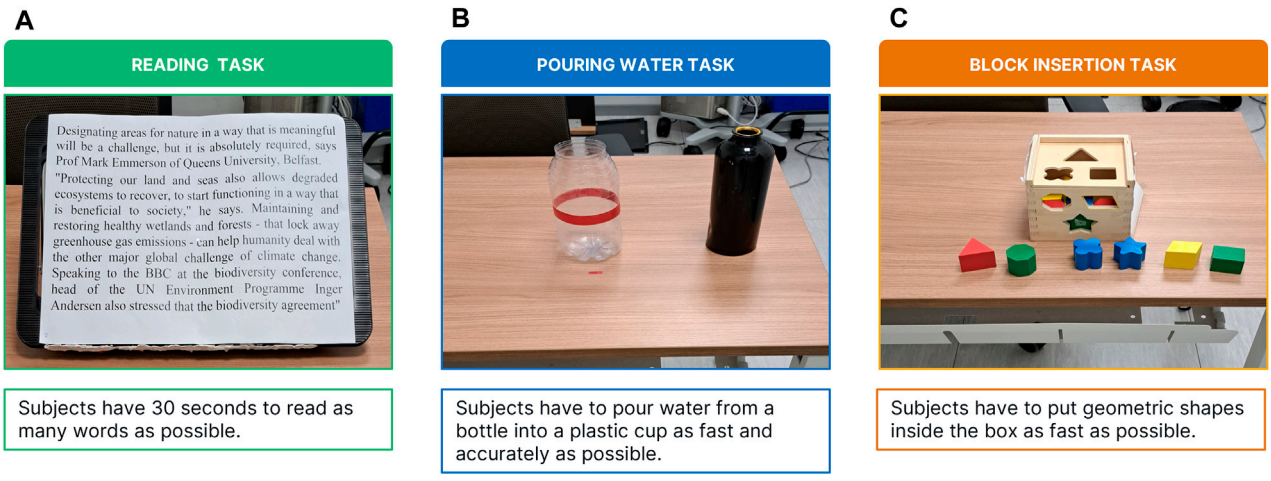

FIGURE 4
Experimental objects: Panel **(A)** A3 paper for the reading task; Panel **(B)** cup and bottle used in the pouring water task; Panel **(C)** the shape-sorting classic cube toy and geometric shapes used in the block insertion task.

activities such as reading (Rubin, 2013), driving, recognizing objects (Cahill et al., 2005), and faces (Taylor et al., 2016). Additionally, visual field distortions significantly compromise the oculomotor system, resulting in eye movement anomalies, especially in saccades (Nuthmann et al., 2022). The form of VIs and their resulting oculomotor instabilities differ according to specific pathologies.

Regarding maculopathies, the National Eye Institute (Rickman et al., 2013) outlined four main stages associated with their symptoms. In the early stage, individuals may exhibit minimal symptoms except for slight blurring of the image in the central visual field. In the intermediate stage, central visual field obstruction by scotoma leads to blurred vision and metamorphopsia, where straight lines appear wavy or crooked start to appear. In the advanced stage, blurred vision and metamorphopsia are compounded by the presence of gray-dark spots. In the most severe cases, scotomas manifest as image distortion and blurred effects overlaid with overlapping gray-dark spots (Hubschman et al., 2009). People with disabilities correlated with binocular

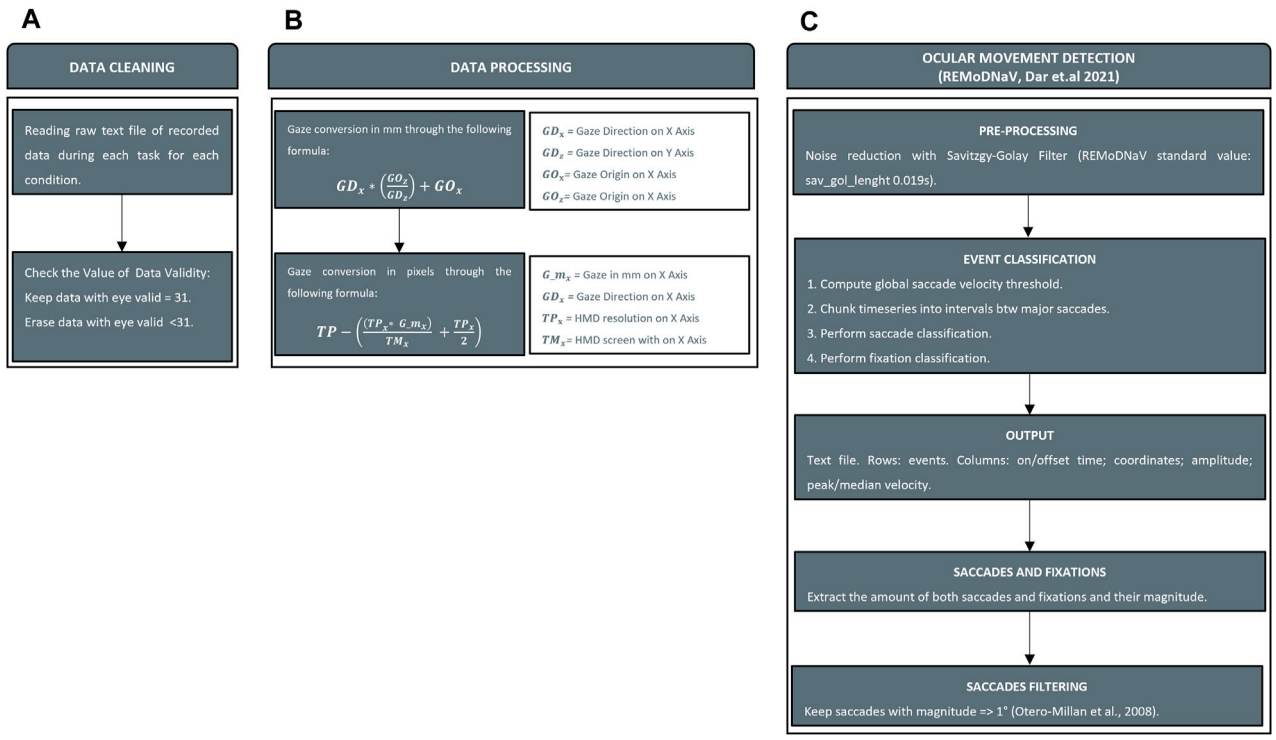

FIGURE 5
Data processing. Panel **(A)** Cleaning invalid value from data recorded. Panel **(B)** Conversion of gaze information from raw data (gaze origin and gaze direction) in mm and pixels. Panel **(C)** Ocular movements detection with REMoDNaV and saccades filtering.

maculopathy, frequently encounter difficulties with tasks requiring a central visual field (Cahill et al., 2005). Maculopathy significantly affects the oculomotor system (Kumar and Chung, 2014). While saccades in healthy individuals are generally horizontally linear in magnitude, maculopathy induces multiple short saccades in various directions (Vullings and Verghese, 2021). Especially during the reading of a text, poor oculomotor control induced by central scotomas leads to abnormalities in interword saccades and an increased number of regressive saccades (Cahill et al., 2005).

The term "hemianopsia" refers to a group of binocular VIs affecting half of the visual field, typically one side of the vertical midline. Impaired hemifields are often obstructed by blurred vision and gray spots in the peripheral areas, rendering those portions of the visual field effectively blind (Wolberg et al., 2022). Hemianopsia can be divided into two main types. First, the heteronymous hemianopsia that encompasses bitemporal and binasal hemianopsia, affecting different areas of the visual field in each eye (Cushing and Brain, 1925; Igersheimer, 1947). Secondly, the homonymous hemianopsia which affects the same vertical midline in both eyes, resulting in the loss of a complete hemifield bilaterally, including half of the macula. Eye movement patterns are disrupted, with more frequent shorter saccades (especially regressive saccades) toward the blind field, and longer fixations in terms of durations (Zihl 1995). The loss of the left half of the vertical visual field affects reading performance, both by causing difficulties in finding the next line in a text (Zihl 1995) and by inducing several errors in the essential information needed to identify a word contained in its initial letters (Grunda et al., 2013).

The last disease under consideration is the loss of peripheral vision (i.e., tubular vision) that leads to a tunnel-like circular visual field. This condition obstructs daily activities, particularly spatial navigation and object recognition (Ophthalmology, 1960). Tubular vision presents initially as a blurred effect in the superior or inferior visual field, progressing to tunnel vision characterized by blurred effects, lack of information, and dark gray peripheral scotomas (Crabb et al., 2013; Gupta et al., 2016). Fixation instabilities and altered saccades are common in individuals with tubular vision, affecting daily tasks such as reading (Nguyen et al., 2014; McDonald et al., 2022).

Many rehabilitation procedures such as prismatic correction (Moss et al., 2014) and compensatory training (Mannan et al., 2010) have been implemented to date. Nonetheless, the World Health Organization reported the need for qualified rehabilitation professionals to apply new user-centered and trans-disciplinary approaches in daily practice (WHO, 2019). The first step of this process would be to train rehabilitators with tools that simulate low-vision diseases to understand how low-vision individuals perceive and interact with the external environment. In particular, by perceiving and navigating the world as low-vision individuals, ophthalmologists and researchers might improve the current scenario of VIs rehabilitation by discovering new rehabilitation techniques.

The question that has emerged in the field is: what is a proper method to exploit the benefit of simulations? Immersive technologies have been demonstrated to represent noteworthy devices to simulate realistic scenarios thanks to their capability to

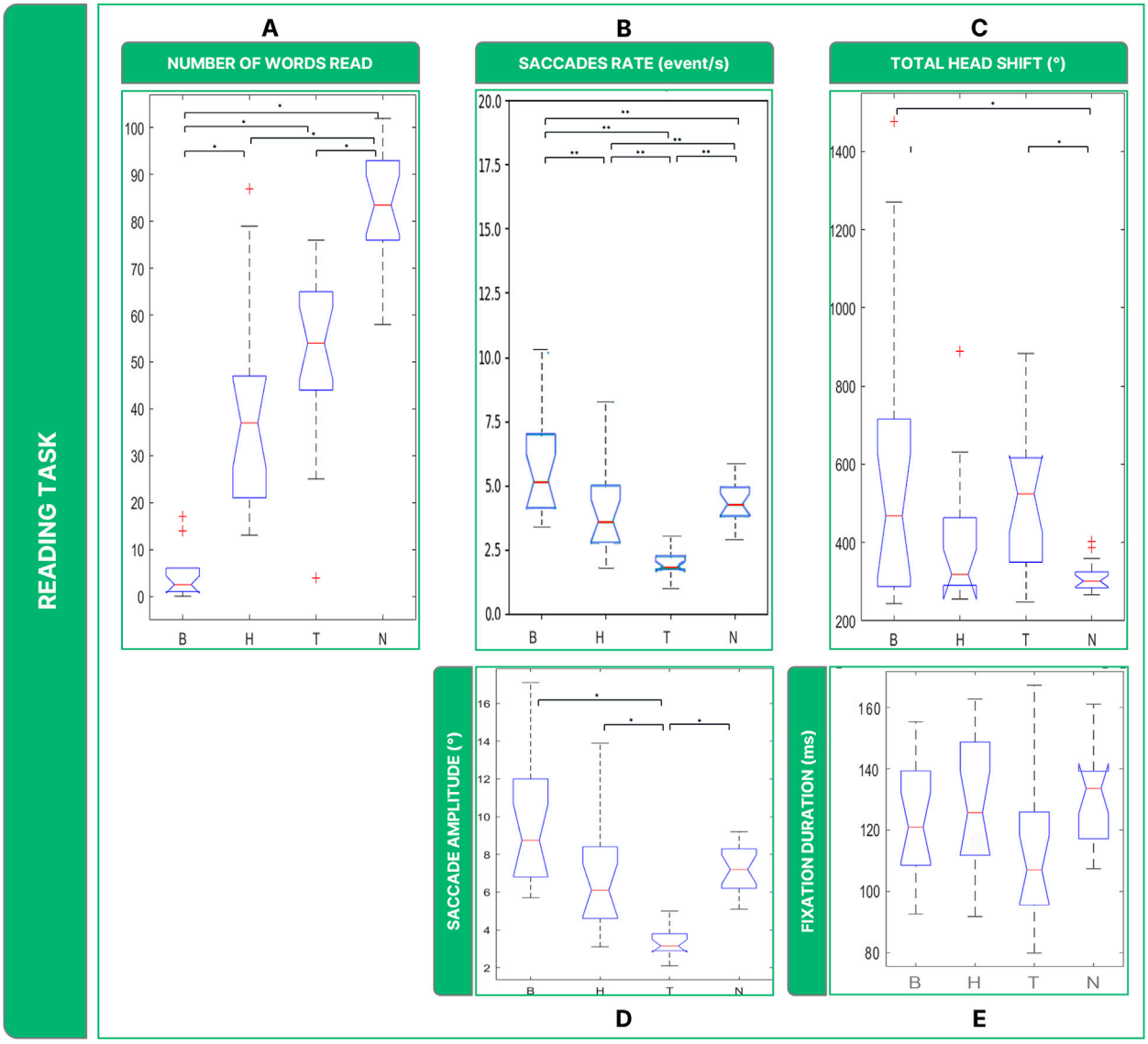

FIGURE 6
Boxplots of the results of the Reading Task: Panel **(A)** number of words read in 30 s; Panel **(B)** saccades rate; Panel **(C)** total head movements. Panel **(D)** saccades magnitude. Panel **(E)** fixations durations. Legend: (*: *p*-value <= 0.050).

elicit a sense of immersion (Suh and Prophet, 2018) and presence (Thornson et al., 2009). Specifically, Soliman et al. (2017) defined immersive technologies as tools that blur the line between the physical and virtual world creating a sense of immersion and enhancing the realism of the virtual experience. Nowadays, the term "immersive technologies" is used to refer to several different technologies, such as virtual reality (VR), augmented reality (AR), spatial audio, and haptic technologies (Handa et al., 2012). It is common to use the term "extended reality" (XR) to indicate a macro category that includes both VR and AR, where VR implies users' immersion entirely in a digital-simulated world (Greengard, 2019), whereas AR combines the digital and physical world, allowing the aligned overlap of 3D digital objects in the real world (Craig, 2013). The peculiarity of exploring the world—real or simulated -, in 3 degrees of freedom (sitting position) or 6 degrees of freedom (standing position) typical of immersive XR, allowed the overcoming of the limitations of static 3D displays. These technologies have already shown their potential in healthcare and rehabilitation for people presenting with attention deficit hyperactivity disorder (Adams et al., 2009), and post-traumatic stress disorder (Kothgassner et al., 2019). Moreover, the use of immersive technologies was demonstrated to enhance learning experiences (T. C. Huang et al., 2016), and foster participation (Fonseca et al., 2014; M. Huang et al., 2010).

A groundbreaking study by Jones et al. (2020), demonstrated the effectiveness of gaze-contingent simulations in both VR and AR through multiple HMDs for accurately simulating VIs in healthy-sighted subjects. Additionally, Chow-Wing-Bom et al. (2020) researched to assess the impact of peripheral vision diseases on daily life activities. Twelve healthy-sighted subjects explored a virtual environment in VR, where the levels of peripheral vision loss were independently manipulated in each eye for each trial. The

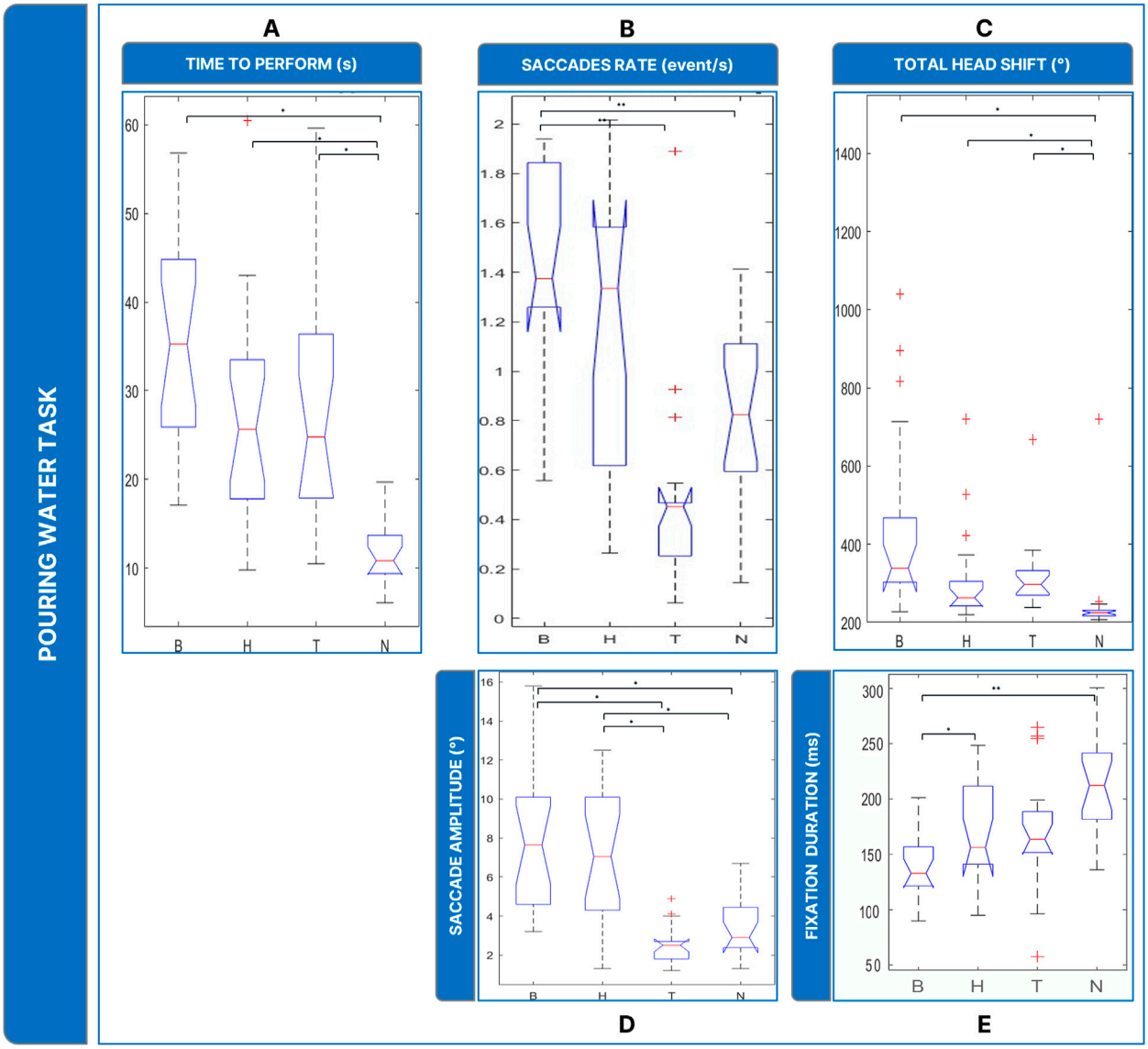

FIGURE 7
Boxplots of the results of the Pouring Water Task: Panel **(A)** time employed for completing the task; Panel **(B)** saccades rate; Panel **(C)** total head movements. Panel **(D)** saccades magnitude. Panel **(E)** fixations durations. Legend: (*: *p*-value ≤0.050).

data revealed that even with significant visual impairment, subjects could successfully complete tasks.

Along this line, we recently introduced the REALTER (wearable egocentric altered reality simulator) project (Barbieri et al., 2023). REALTER is an immersive simulator capable of altering normal sight in real-time to simulate various low-vision conditions using an HMD in a real environment (see Supplementary Video S1 for a demonstration). The Chiossone Foundation for Blind and Low-Vision Individuals in Genoa collaborated on this project, which is part of the European oMERO project (Casiddu et al., 2023), aimed at evaluating the effectiveness of low-vision simulations. REALTER utilizes AR with a video see-through (VST) paradigm, allowing real-world vision mediated by external cameras attached to the HMD. By identifying common diseases requiring rehabilitation, we designed realistic gaze-contingent simulations for various low vision conditions, including loss of central and peripheral vision, hemianopsia, and additional VIs such as achromatopsia, cataracts, and diabetic retinopathy. Considering the peculiarity of the system not to augment, but to alter the reality to recreate low vision individuals' perspective, we used the term *alTered Reality* (TR) instead of AR to define our approach.

The primary goal of the REALTER project is to provide visual rehabilitation centers with a validated tool to assist ophthalmologists in understanding visually impaired individuals' experiences and developing tailored rehabilitation protocols. Our study aimed to validate TR by collecting data from healthy-sighted subjects performing daily actions under simulated low-vision conditions, such as reading, pouring water, and interacting with objects. The realism of the simulations led us to hypothesize that TR could induce alterations in healthy individuals' oculomotor behavior similar to those caused by maculopathy, hemianopsia, and tubular vision. Our experimental protocol considered three different low-vision

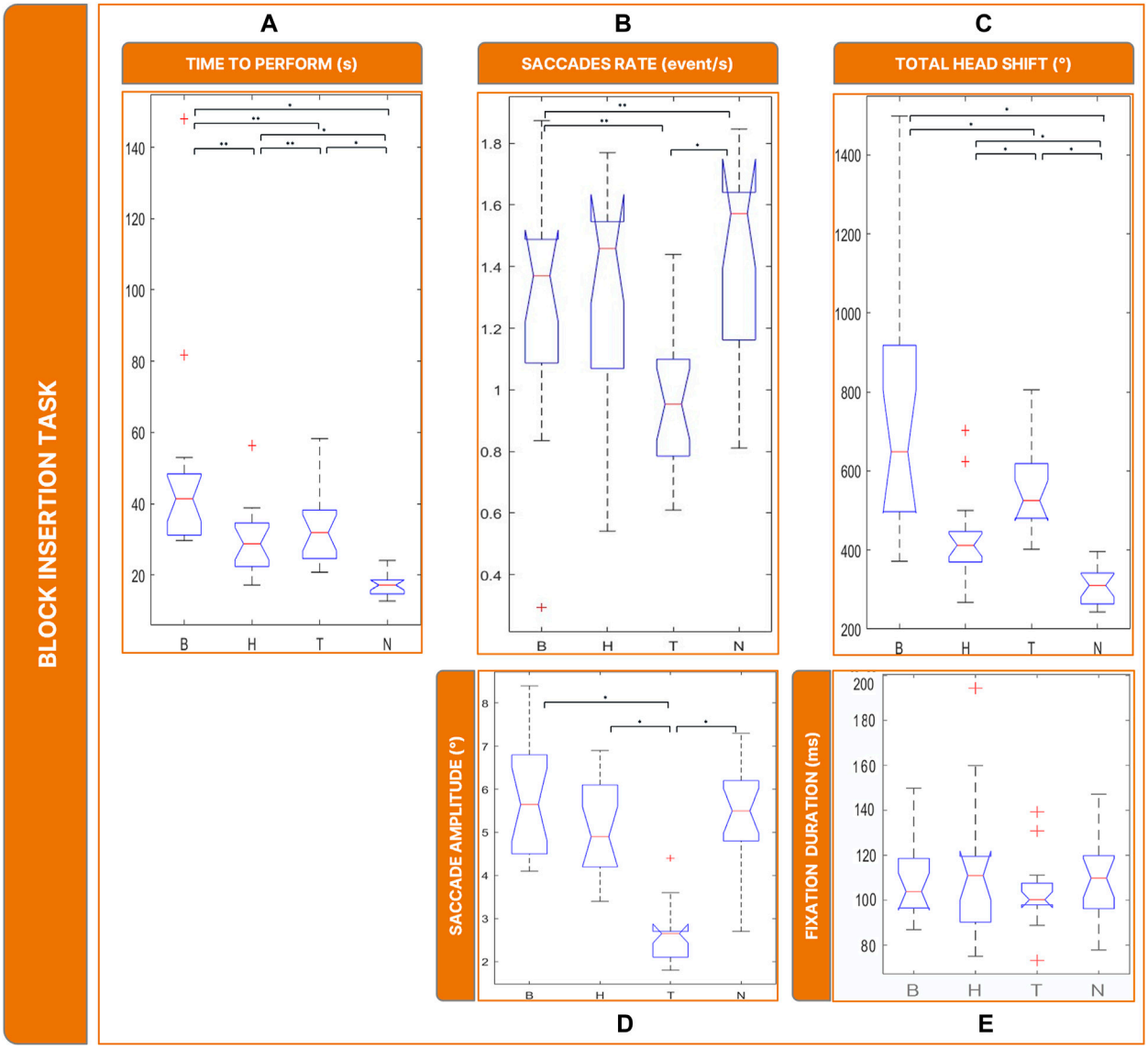

FIGURE 8
Boxplots of the results of the Block Insertion Task: Panel **(A)** time employed for completing the task; Panel **(B)** saccades rate; Panel **(C)** total head movements. Panel **(D)** saccades magnitude. Panel **(E)** fixations durations. Legend: (*: *p*-value <= 0.050).

conditions: advanced binocular maculopathy, homonymous hemianopsia, and tubular vision. The system enabled the analysis of subjects' ocular movements across these conditions, providing insights into compensation strategies for different types of VIs.

Our results indicate that the system is capable of producing distortions in eye movements that vary across the three disabilities and normal vision. Additionally, these distortions resemble the behavior of healthy-sighted individuals and those with low vision in non-simulated conditions (Goodwin, 2014; Nguyen et al., 2014; Verghese et al., 2021; McDonald et al., 2022) suggesting that TR is capable of realistically simulating normal and impaired visual conditions and potentially inducing alterations in ocular movements similar to those observed in individuals with maculopathy, hemianopsia, and tubular vision.

2 Methods and analysis

2.1 Participants

Participants were 18 healthy-sighted adults with a mean age of 28 years, with no experience in low-vision rehabilitation. We defined healthy sight as monocular letter acuity ≤0.3 logMAR. Additionally, subjects have not declared to suffer from VIs. Subjects gave their informed consent to participate in the study. The study was approved by the ethics committee of the local health service (Comitato Etico, ASL 3, Genova, Italy). All experiments were conducted in accordance with the Declaration of PP, (1964). Informed written consent was obtained for all the subjects.

2.2 Immersive system design

The altered reality (TR) is displayed through a VST HMD with an integrated eye tracker (HTC Vive Pro Eye), augmented with external cameras (Stereolabs Zed Mini) able to acquire images from the real world. HTC Vive Pro Eye has a resolution of 2,880 × 1,600 pixels (1,440 × 1,600 per eye), with a 110° FOV and a refresh rate of 90 Hz. It integrates a Tobi eye tracker which detains an accuracy (within FOV 20) of 0.5°–1.1° with a sampling frequency (binocular) of 120 Hz. In addition, the HTC Vive Pro Eye requires two external base stations to trigger `SteamVR` Tracking, a G-sensor, a gyroscope, and a proximity sensor. Stereolabs Zed Mini has been anchored to the headset to enhance pass-through resolution; the camera has a resolution of 720p and a FOV of 90° (horizontal) and 60° (vertical). The device is wired to a backpack PC (HP VR Backpack G2) which is equipped with an Intel Core i7-8850H processor and NVIDIA GeForce RTX 2080 graphic card with 8 GB dedicated GDDR6. The HTC Vive Pro Eye as a tool for measuring saccades in VR was already exploited by Imaoka et al. (2020) with positive results.

The software is written in Unity C# (version 2021.3.3f1). The current version of the software provides an exhaustive portfolio of low vision conditions able to offer different stages of maculopathy, hemianopsias, and tubular vision. Every element of the system is called in the motor engine through multiple software development kits (SDK): `SteamVR v1.14.15` (for VR headset), `ZED SDK v3.7` (for external AR pass-through cameras), and `SRanipal SDK v1.3.6` (for eye tracking). The pass-through camera required the installation of `ZED SDK 3.7.0`, `Cuda 11.6.1`,`SR Runtime`, `SteamVR 2.7.3`.

The integrated eye tracker allows the recording of data about subjects' ocular movements and the design of gaze-contingent simulations. To conduct quantitative analysis, we used both eyes and head data. HTC Vive Pro Eye provides data from both the left and right eye through `SRanipal SDK`: validity of eye data, eyes openness, pupil diameter (mm), pupil position (normalized vector between 0 and 1), gaze origin (mm), and gaze direction (normalized vector between −1 and 1). Data from both eyes were extracted from `VerboseData` in the struct data of `ViveSR.anipal.Eye.EyeDatav2`. Head data were extracted from `Unity.Engine.XR` in the struct data of `InputTracking.GetLocalPosition(XRNode.CenterEye)`. We used time information from `Unity.Engine` in the form of `Time.fixedTime`. Because most low-vision diseases affect the same part of the retina while the eyes are moving, a gaze-contingent paradigm is required to update the position of the disability according to the subject's fixation point. The term gaze indicates the combination between the head and eye movements (Holmqvist et al., 2011a). The gaze-contingent paradigm is an interactive eye tracker application used in computer science to refer to the ability of a computer screen to change in function depending on the viewer's fixation point (Duchowski Theory, 2017). Therefore, the implementation of gaze-contingency required the combination of eyes and head movements. By combining gaze information from `SRanipal` and head movements from `SteamVR`, it was possible to integrate the gaze-contingent paradigm (Figure 1A). Specifically, we used the Unity function `Transform.Direction` to process data related to eye movements in conjunction with information about head movements. The position of the area of impaired vision was regulated by the resulting contingent vector that combined data from both sources to understand the gaze direction.

Low-vision diseases were replicated in TR by overlapping 2D images and 3D Unity's game object rendered with shaders. These simulations were overlaid onto real-world scenes captured by Zed Mini cameras. Different techniques were employed for each visual condition. For simulating binocular maculopathy (Figure 1B), a 2D image of a dark gray spot was used to obscure the central visual field. Additionally, a shader applied to a 3D object implemented a warping effect to mimic the distortion caused by metamorphopsia. This effect was achieved by altering individual pixels with shifted texture samples, introducing non-stationarity through modulation of offset values with a periodic temporal signal, and encoding these offsets in a gaze-contingent deformation map generated by summing a simulated force field. In the case of tunnel vision (Figure 1D) simulation, a 2D black image with a central hole was overlaid, along with a shader producing a dark-blurred effect. This effect allowed the subject to maintain clear vision in the center of the FOV while obstructing the peripheral vision. Lastly, homonymous hemianopsia on the left side (Figure 1C) was simulated using a 3D plane rendered with a shader to create a blurred effect on the left side of the vertical FOV. A dark-blurred effect was applied in both tunnel vision and hemianopsia simulations to reduce visual acuity using Gaussian blur, a multiresolution pyramid approach, and a depth-of-field effect. All three simulations utilized the gaze-contingent paradigm, with experimenters using the PC keyboard to trigger low vision disabilities and control data storage.

Each low vision simulation was qualitatively evaluated by expert ophthalmologists from the Chiossone Foundation in specific evaluation phases to assess their realism.

2.3 Experimental protocol: overview

The goal of the experiment was the validation of REALTER by performing four daily activities: reading, reading, filling a glass of water and interacting with specific objects. Each task was performed under four different simulated visual conditions: binocular maculopathy, tubular vision, homonymous hemianopsia, and healthy sight.

In agreement with the ophthalmologists of the Chiossone Foundation, we focused on the worst case of each family of VIs stored in the simulator portfolio. In particular, the simulator focused on replicating three specific low vision conditions: *i*) an advanced form of maculopathy, corresponding to severe cases of the condition *ii*) homonymous hemianopsia affecting the left hemisphere, which is known to cause difficulties in identifying words based on initial letters in a text *iii*) an advanced stage of glaucoma characterized by VIs in the peripheral field, rendering the acquisition of any information challenging. These conditions were selected based on input from ophthalmologists, who identified them as particularly impactful on the daily lives of affected individuals.

The simulations were presented in a random order to prevent learning effects, with the presentation of normal vision always occurring last. The objective was to evaluate the impact of different low vision conditions on task performance. Performance was assessed based on factors such as execution time, as well as the

number and magnitude of saccadic eye movements, and the duration of fixations. During each task, participants were seated in front of a table. We opted to allow free movement and rotation of the head for two main reasons: firstly, keeping the head fixed would have compromised the realism of the experimental tasks, and secondly, it could have restricted participants in their exploration of compensatory techniques. Each task was carefully selected in collaboration with ophthalmologists from the Chiossone Institute in Genoa. We prioritized tasks that mimic everyday activities, such as reading text or pouring from a bottle, which individuals with low vision often require assistance with. Our aim was to discern differences in eye and head movements among the simulated VIs.

2.4 Experimental protocol: calibration process and familiarization

REALTER required appropriate calibration for each subject. The HTC Vive Pro Eye provided a standard calibration procedure, involving manual adjustment of the head-mounted display (HMD) position to ensure proper interpupillary distance between the eye lenses and calibration of the eye tracker through a 5-point calibration routine. At the outset of the experimental session, a custom saccade detection task was incorporated to verify the accuracy of the eye tracker data. In this task, participants were instructed to track the movement of a sphere within a virtual environment as the sphere changed position four times (see Figure 2). Subsequently, the experimenter conducted a brief analysis by plotting the eye movements' scan path. If the scan path aligned with the movement of the sphere (as depicted in Figure 3), the data were deemed valid. Conversely, if the scan path did not match the sphere's movement, the calibration process had to be restarted from the beginning. To familiarize subjects with the simulated low vision conditions and enhance their comfort, a familiarization session was conducted prior to the tasks. During this phase, participants engaged in simple actions such as scanning the environment and interacting with objects under the three different low-vision conditions.

2.5 Experimental protocol: reading

During the reading task, subjects were asked to read a text written in their native language on an A3 format paper board for a duration of 30 s (see Figure 4A). The font size of the text was 17.5 mm. The paper board was positioned on a stand in front of the subjects, fixed at a distance of 40 cm from their eyes, following the protocol of the MNREAD Acuity Chart test (Legge et al., 1989). Participants were instructed not to interact with the board and to maintain a fixed distance of 40 cm from the stand. They were directed to read as many words as possible within the given time frame. The length of the text ensured that subjects would not finish reading the entire paper page within the allotted time. Different paper pages were used for each visual condition. The outcome measures included the number and magnitude of saccadic eye movements and the number of words read.

2.6 Experimental protocol: pouring water

During the Pouring Water task, participants were required to pour water from a 1-L bottle into an empty cylindrical plastic cup, with dimensions of 7.8 cm in diameter and 24 cm in height. The cup was positioned in front of the subject, 50 cm away (refer to Figure 4B). While executing the task, the subject was allowed to touch the cup but not move it. The full bottle was placed either 15 cm to the right or left of the cup, depending on the subject's dominant hand. Participants were instructed to pour the water with both accuracy and speed, aiming to fill the cup up to a red stripe indicated on its surface. The task concluded when subjects verbally declared that they had reached the red stripe. Outcome measures included the assessment of the number and magnitude of saccadic eye movements and fixations, as well as the duration of the task.

2.7 Experimental protocol: block insertion

The task involved solving a classic shape-sorting cube toy (see Figure 4C). The cube, with dimensions of 14 × 14 × 14 cm, was positioned 50 cm in front of the subjects, who were only permitted to interact with the top and front faces of the cube (the left and right faces were obscured). Participants were tasked with inserting six geometric shapes, located between themselves and the cube, into their respective cavities on the cube's surface. Subjects were given the freedom to select the order in which they inserted the shapes, but they were not allowed to manipulate the cube itself. The task concluded once the subject had successfully inserted all six shapes into their corresponding cavities. To prevent learning effects, the cube was rotated in each condition to present a different face, along with corresponding geometric shapes for insertion. Outcome measures included the assessment of the number and magnitude of saccadic eye movements, as well as the duration of the task.

2.8 Data processing and analysis

Thanks to the embedded sensors and eye-tracking technology, we recorded ocular movements and head kinematics to extract quantitative outcomes for the analysis. To identify the nature of ocular movements, we employed an existing software written in Python language (REMoDNaV) (Dar et al., 2021) able to analyze eye tracking data listed above. REMoDNaV is built on the algorithm by Nystrom and Holmqvist (Nyström and Holmqvist, 2010) that employs an adaptive approach to velocity-based eye-movement event classification (Dar et al., 2021). The software was successfully implemented in multiple studies inherent to the analysts of eye data from XR HMD (Liebers et al., 2021). In its current state, REALTER is designed to measure saccades and fixations. Despite having a sampling frequency of around 120 Hz, the Tobii eye tracker integrated into the HTC Vive Pro eye is defined as low speed. This characteristic leads to several limitations in eye tracking, such as the inability to detect fixational micromovements like microsaccades, drifts, and tremors (Holmqvist et al., 2011b). As a consequence, the eye tracker detected those micromovements as periods of time during which the eyes were kept almost still and the

data analysis by REMoDNaV categorized them as fixations (velocity lower than 2°/s). Nevertheless, low-speed eye trackers (with sampling frequency <250 Hz) are currently employed in research fields to collect data (Gibaldi and Sabatini, 2021). Initially, data were cleaned by removing all data with an eye validity of less than 31 as indicated by Imaoka et al. (2020) (Figure 5A). Secondly, since REMoDNaV required input eye data in pixels, we converted gaze in mm (Eq. 1) and then in pixels (Eq. 2) by considering gaze origin and gaze direction provided by `SRanipal` (Figure 5B). To find the position of the eye on the screen in pixels, Eqs 1, 2 were used. Specifically, Eq. 1 gives the position on the horizontal (x) axis in mm, which is then converted to pixels using Eq. 2. The same procedure was used to find the position on the vertical (y) axis in mm and pixels.

$$\mathrm{G\_m_x} = GD_{x\star}\left(\frac{GO_z}{GD_z}\right) + GO_x \tag{1}$$

GD_x: Normalized Gaze Direction on X-Axis
GD_z: Normalized Gaze Direction on Z-Axis
GO_x: Gaze Origin in mm on X-Axis
GO_z: Gaze Origin in mm on Z-Axis

$$\mathrm{G\_p_x} = TP - \left(\frac{\left(TP_{x\star}\ G\_m_x\right)}{TM_x} + \frac{TP_x}{2}\right) \tag{2}$$

G_m_x: Gaze Direction in mm on X-Axis
GD_x: Normalized Gaze Direction on X-Axis
TP_x: HMD resolution on Horizontal Axis (2,880 pixels)
TM_x: HMD screen width on Horizontal Axis (119 mm)

The second stage involved the interpretation of ocular movements with REMoDNaV (Figure 5C). Although `SRanipal` stored data related to each eye, the analysis of ocular movements was performed on each subject's dominant eye assessed using the hole-in-the-card test (Yang et al., 2010). As output of the analysis, REMoDNaV identified ocular movements. In particular, we focused on the number and amplitude of saccades and the duration of fixations. REMoDNaV detects saccadic eye movements with no distinction between saccades and micro-saccades. In order to clean counting from all putative micro-saccades, we removed all saccades with a magnitude of less than 1° as reported in a study on this topic (Otero-Millan et al., 2008).

Subjects' performance was evaluated in terms of the number of words read in the reading task, and the time to complete the task in the water and shapes tasks. For each task and condition, fixations were evaluated in term of durations (ms), and saccades in terms of amplitude (°) and rate of occurrence (event/s). The latter was calculated by dividing the number of saccades performed by the time taken to perform the task. Head rotations (HR) were evaluated by considering the total rotational shift performed during each task in each condition (Eq. 3). These metrics allow us to compare binocular maculopathy, homonymous hemianopsia, tubular vision, and healthy sight in terms of ocular movements, head movements, and task performance. As the data were not normally distributed, the vision conditions were compared using Friedman's Anova. When significant ($p < 0.050$), post-hoc Tukey-corrected pairwise comparisons were performed to determine which conditions showed significant differences.

$$\mathrm{HR}: \sum_{i=1}^{n-1}\sqrt{(a_i - a_{i+1})^2 + (\beta_i - \beta_{i+1})^2 + (\gamma_i - \gamma_{i+1})^2} \tag{3}$$

a: Rotation about X-Axis;
β: Rotation about Y-Axis;
γ: Rotation about Z-Axis;
i: i-th time sample;
N: Task entire duration.

3 Results

Each task has been evaluated in terms of task performance (words read or time to perform) and ocular movements. In the next sections, low-vision disabilities are abbreviated as B (binocular maculopathy), H (homonymous hemianopsia on left hemifield), and T (tubular vision), while the healthy sight condition is denoted as N (normal vision).

3.1 Ocular movements assessments in healthy sight

First, we evaluated ocular movements performed by subjects wearing the HMD in the healthy sight condition (N): we assessed saccadic eye movements for median magnitude and fixations for median durations.

- reading task: (saccades amplitude: ~7°; fixations duration: ~135 ms);
- water pouring task: (saccades amplitude; fixations duration: ~230 ms);
- block insertion task: (saccades amplitude ~6°; fixations duration: ~160 ms).

3.2 Reading task

Investigating subjects' performance in terms of words read (Figure 6A), Friedman's Anova revealed significant differences between groups ($X^2 = 46.9$, $p < 0.001$). B was the most invalidating low vision condition (on average less than 5 words read), with *post hoc* tests revealing that the number of words read by subjects in B was significantly lower than in the other conditions (B vs. H: $p = 0.001$; B vs. T: $p = 0.001$). Subjects in the healthy sight condition read the highest number of words (~85 words; B vs. N: $p = 0.001$; H vs. N: $p = 0.002$; T vs. N: $p = 0.002$). H and T shared common features, with an average of 38 and 45 words read respectively, and no significant differences were found ($p = 0.315$).

Statistically, the rate of saccades ($X^2 = 37.4$, $p < 0.001$) (Figure 6B) was significantly different between B, H, and T (B vs. H: $p = 0.012$; B vs. T: $p = 0.006$; T vs. H: $p = 0.006$) and they behaved differently than N (B vs. N: $p < 0.036$; T vs. N: $p = 0.006$), with the exception of H which did not show statistical difference (H vs. N: $p < 0.852$).

The analysis of ocular movements showed that all low vision conditions shared comparable results in terms of saccades. Regarding the amplitude in degrees of the ocular movements, there are considerable differences between low vision conditions for saccades (Figure 6D) (X^2 = 37.4, p < 0.001). The amplitude of saccades was particularly low in T (~4°), with *post hoc* tests revealing significantly higher values than in the other two low vision conditions (B vs. T: p < 0.001; H vs. T: p < 0.001) and N (T vs. N: p = 0.001). Although the Friedmann Anova resulted slightly significant (X^2 = 7.087, p < 0.049) (Figure 6E), *post hoc* test did not reveal significant differences in fixation duration among all conditions considered in this study.

It is also possible to highline significant differences between conditions when considering overall rotations performed by the head (X^2 = 13.3, p < 0.004) (Figure 6C). Specifically, the post-hoc test revealed that in the B and T conditions the amount of head rotations performed by the subjects was comparable (B vs. T: p = 1), and both B and T induced them to rotate more than in N (B vs. N: p = 0.004; T vs. N: p = 0.001).

3.3 Pouring water task

Task performance was evaluated by counting the time spent performing the task (Figure 7A). Friedman's Anova revealed significant differences between conditions (X^2 = 33.7, p < 0.001). Post hoc testing revealed that, in terms of time spent to perform the task, low vision conditions required comparable time to perform the task, but there were significant differences from N (B vs. N: p < 0.001; H vs. N: p < 0.001; T vs. N: p = 0 .001).

The analysis of saccades rate (X^2 = 22.7, p < 0.001) (Figure 7B) revealed that B showed a significantly higher rate of saccades than N (p = 0 .001), and T (p = 0 .010).

In addition, the amplitude of saccades (Figure 7D) (X^2 = 28.1, p < 0.001) was larger wider in the low-vision conditions: B and H showed comparable saccades (~3°, B vs. H: p = 1.000) and larger than T and N (~7°, T vs. N: p = 0.313; T vs. B: p < 0.001; H vs. T: p = 0.003; B vs. N: p = 0.005; H vs. N: p = 0.021). In terms of fixation duration (Figure 7E), The Friedmann Anova revealed significant differences between conditions (X^2 = 27.9, p < 0.001). Post hoc tests showed a significatively inferior value of fixation duration of B to N (p = 0.001) and to H (p < 0.010).

Finally, head rotations (Figure 7C) were more present in the low vision conditions (X^2 = 30.9, p < 0.001): post-hoc tests revealed that B, H, and T induced the user to rotate the head more than in N (B vs. N: p < 0.001; T vs. N: p = 0.009, H vs. N: p < 0.001), while the behavior between the low vision conditions was comparable (H vs. B: p = 0.072; H vs. T: p = 1.000; B vs. T: p = 0.360).

3.4 Block insertion task

Given that, as in the previous task, the required focus was on the central FOV, we reasonably found similarities with the water task. Counting the time spent performing the task (Figure 8A), a Friedman's Anova revealed significant differences between conditions (X^2 = 39.8, p < 0.001). Post-hoc tests revealed that all low vision conditions required more time than N to complete the task (B vs. N: p < 0 .001; H vs. N: p = 0.002; T vs. N: p < 0.001). In addition, B required more time to perform the task than H and T (B vs. H: p = 0.002; B vs. T: p = 0.020), while T and H were comparable (T vs. H: p = 0.979).

The rate of saccades (Figure 8B) was significantly different between conditions (X^2 = 22.5, p < 0.001): specifically, T showed a lower rate of saccades (and higher rate of fixations) compared to all the other conditions (T vs. N: p = 0.001; T vs. B: p = 0.024; H vs. T: p = 0.002).

Saccade sizes (Figure 8D) were significantly different between conditions (X^2 = 35.1, p < 0.001). In particular, post-hoc tests revealed that it was smaller in T than in all other conditions ~2°, T vs. B: p = 0.002; T vs. H: p = 0.001; T vs. N: p = < 0.001). There is no significant difference in fixation duration (X^2 = 1.130, p < 0.769) (Figure 8E).

The amount of head rotations (Figure 8C) differed significantly between conditions (X^2 = 43.3, p < 0.001). Post-hoc tests revealed that the total rotation of the head was not significantly different in B and T (T vs. B: p = 0.360) and greater than in H (H vs. B: p < 0.001; H vs. T: p = 0.001). Additionally, all low vision conditions led the subject to move more than in N (B vs. N: p = < 0.001; T vs. N: p = < 0.001; H vs. N: p < 0.001).

4 Discussion

The first significant aspect explored in this study is the occurrence and characteristics of saccades and fixations in healthy-sighted subjects, particularly in relation to our healthy sight condition. Each ocular movement possesses distinct properties. For instance, saccades typically exhibit a specific range of amplitudes (4°–20°), while fixations tend to occur within durations ranging from 200 ms to 400 ms (Holmqvist et al., 2011a). Upon analyzing data obtained from subjects in the healthy sight condition (N), we observed that saccades demonstrated characteristics in terms of magnitude consistent with findings in the literature (Section 2.1). This observation was instrumental in confirming that the immersive system did not disrupt the execution process of saccades under healthy sight conditions, thereby facilitating further examination of data related to simulated low-vision conditions. On the other hand, in both reading and insertion bock tasks, fixation duration appeared to be under the average (Section 2.1).

We assessed the performance and oculomotor behavior of subjects across three different tasks simulating everyday activities (Section 3.1). Data pertaining to subjects' behavior in simulated low-vision conditions, including eye and head movements, also exhibited similarities with alterations previously investigated in various studies (Goodwin, 2014; Nguyen et al., 2014; Verghese et al., 2021; McDonald et al., 2022) involving individuals affected by low-vision conditions (Section 3.2).

4.1 Evaluating subjects' performance

In our evaluation of the reading task, we focused on the number of words read within a specific timeframe. It became evident that binocular maculopathy was the most debilitating low-vision

condition in terms of task performance duration. Compared to homonymous hemianopsia and tunnel vision, the loss of central visual field significantly hindered reading ability. Given the task's requirement for interaction within the central visual field, the presence of central scotomas naturally posed greater obstacles for subjects than in the healthy sight condition. The water pouring and block insertion tasks were assessed based on the time taken to complete them, as these tasks did not impose strict time constraints like the reading task. In both cases, subjects with low vision experienced similar impairments. Unlike the reading task, binocular maculopathy did not prove to be more debilitating than other low-vision conditions. We can speculate that the ability to rely on tactile senses and the occurrence of multisensory integration mitigated the impairments associated with binocular maculopathy. Indeed, Sathian (2000) reported that while sighted individuals primarily rely on vision, those with VIs rely more on tactile senses for pattern recognition. These findings are promising, as they suggest that individuals affected by homonymous hemianopsia and tunnel vision also exhibited slower performance in each task, similar to those who suffer from binocular maculopathy.

4.2 The impact of low-vision conditions on the oculomotor system and head movements

The presence of a central scotoma has been observed to induce instability in the oculomotor system (Nuthmann et al., 2022). Saccadic movements are also affected by the loss of central visual field, often resulting in irregular saccades and the splitting of linear saccades into smaller, irregular ones (Vullings and Verghese, 2021). Subjects affected by central scotomas tend to perform a significantly higher number of saccades with larger amplitudes compared to healthy-sighted subjects (Van der Stigchel et al., 2013). Our study confirmed these observations, particularly regarding the increased number of saccades and their wider amplitude in simulated binocular maculopathy compared to healthy sight conditions. However, unlike previous findings, the saccadic amplitude appeared wider rather than shorter, likely due to subjects' strategy of using wide saccades to move the scotoma towards the peripheral visual field to obtain hidden information.

Subjects affected by homonymous hemianopsia exhibited similar oculomotor control instability as those with binocular maculopathy. Due to the essential information loss, individuals with hemianopsia perform multiple saccades to explore the environment (Grunda et al., 2013). In our study, simulated hemianopsia in the left hemifield resulted in diminished head scanning techniques compared to healthy sight conditions. Keeping the head still while performing saccades was the preferred strategy, aligning with previous findings (Goodwin, 2014).

Similarly, subjects affected by tunnel vision experience alterations in saccadic movements and fixations, with saccades being more numerous, shorter, and slower, and fixations being more unstable compared to healthy-sighted individuals (McDonald et al., 2022). In our study, simulated tunnel vision resulted in a small amount of shorter saccades across all tasks, particularly impacting tasks requiring object recognition, such as water pouring and block insertion.

In summary, subjects in healthy sight condition exhibited distinct behavior compared to those in low-vision conditions across all tasks. In simulated low-vision conditions, the higher rate of saccades indicated that scanning the environment with saccades was a natural technique to achieve task goals. Differences were also observed between binocular maculopathy and tunnel vision in terms of saccades and fixations, with compensatory strategies varying between conditions. The healthy sight condition prompted subjects to keep their heads more fixed compared to low-vision conditions, suggesting increased head movements as a strategy to succeed in tasks, particularly with simulated binocular maculopathy and tunnel vision.

These results suggest that altered reality is capable of inducing alterations in the oculomotor system of healthy-sighted individuals. From a qualitative perspective, we observed similarities in eye and head movements between participants and individuals affected by low vision conditions: multiple nonlinear saccades in binocular maculopathy; minimal head movement in homonymous hemianopsia; and shorter saccades in tubular vision. These findings motivate us to pursue further validation studies aimed at comparing clinical data from low-vision patients with those simulated using REALTER during the execution of our experimental protocol.

4.3 Future works and improvements

Our findings support the use of immersive XR gaze-contingent simulations as a valuable approach to enhance ophthalmologists' training in understanding the effects of low vision conditions. REALTER can be utilized in research centers to investigate how VIs influence sensory perception skills, offering a novel perspective compared to studies involving blindfolded sighted individuals. Specifically, collaborating with professional ophthalmologists in further testing could provide valuable insights into compensatory techniques currently utilized in low-vision rehabilitation and aid in developing new techniques for individuals affected by maculopathy, tunnel vision, and hemianopsia.

In the future, validating the system by measuring the eye movements of low-vision individuals and comparing them with data obtained from healthy-sighted subjects in the simulated condition could aid in demonstrating the effectiveness and clinical relevance of the system.

Further experiments could provide valuable additional insights into understanding the behavioral alterations caused by low-vision conditions. For instance, conducting reading tests using standardized materials such as MNREAD Acuity Charts could offer an opportunity to collect data that could aid low-vision rehabilitators in devising novel rehabilitation techniques. Additionally, investigating the impact of tunnel vision on spatial navigation and visual searching during tasks involving free movement in space could be enlightening.

Given the limited sample size in related studies conducted on healthy individuals in simulated low-vision conditions, future tests should aim to include a larger number of participants. Moreover, due to the variability among healthy subjects in terms of saccadic and fixation properties and task performance, incorporating proper training sessions before experiments to familiarize subjects with simulated diseases could be beneficial. This approach could help

determine subjects' preferred retinal locus and shed light on how training affects task execution techniques.

Regarding the limitations of the immersive system, improvements could be made in terms of hardware, such as replacing the HTC Vive Pro Eye with a standalone HMD equipped with pass-through cameras and a more accurate eye tracker capable of recording ocular movements at a higher sampling frequency. Attention should be given to addressing issues related to gaze position accuracy and the inability to directly set the real-world position of the user's eyes, which can impact the realism and effectiveness of simulations.

Considering the potential of immersive technology to simulate low vision, exploring the possibility of designing altered reality that simulates improvements for individuals with low vision could represent a significant advancement in rehabilitation. Despite challenges such as calibration issues, this perspective holds promise for enhancing low vision rehabilitation through immersive technology.

5 Conclusion

The primary focus of this study was to provide a quantitative assessment of the effectiveness of TR as an immersive low-vision simulator in inducing alterations in the oculomotor system and head movements in healthy-sighted individuals. The results obtained from the experiments demonstrated that: *i*) TR successfully reproduces everyday difficulties encountered by individuals affected by maculopathy, hemianopsia, and tubular vision in healthy-sighted individuals; *ii*) The TR simulator induces oculomotor system alterations in healthy-sighted individuals similar to those observed in the low vision disorders examined in this study.

Our simulator offers a comprehensive portfolio of low vision conditions compared to other studies (Chow-Wing-Bom et al., 2020; Jones et al., 2020), which primarily focused on glaucoma alone. By considering multiple low vision conditions such as maculopathy, hemianopsia, and tubular vision, we provided a more comprehensive analysis of the simulator's capabilities in eliciting everyday difficulties experienced by individuals with various low vision conditions. Additionally, our preliminary analysis of eye and head movements revealed similarities between healthy-sighted subjects in simulated low vision and real individuals affected by VIs. This suggests that TR could be effectively utilized in rehabilitation facilities to train ophthalmologists in low-vision conditions and to study compensatory strategies, facilitating the development of new rehabilitation techniques.

In conclusion, the experiment highlighted significant characteristics unique to each simulated low vision condition. Given its reliability in assessing eye movement data, TR transcends its role as a mere training tool and serves as a valuable resource for advancing understanding of behavioral modifications and compensatory strategies in individuals with low vision. The system is primarily designed to aid ophthalmologists in understanding the limitations faced by patients with low vision, with the goal of developing tailored rehabilitation protocols and providing proper assistance to patients.

While caution should be exercised in interpreting results obtained from healthy subjects regarding VIs, we believe that our findings justify the integration of the simulator into research facilities to study low-vision individuals by conducting studies on healthy-sighted individuals. TR can be utilized in research centers to investigate the effects of low vision on sensory perception through the analysis of eye movements and head behavior.

In summary, TR holds promise for implementation in visual rehabilitation facilities to address the growing need for qualified rehabilitation professionals and to facilitate the development of user-centered and transdisciplinary approaches. Additionally, it serves as a valuable investigation tool for gaining deeper insights into low vision conditions in research institutes.

Data availability statement

The raw data supporting the conclusion of this article will be made available by the authors, without undue reservation.

Ethics statement

The studies involving humans were approved by the ethics committee of the local health service (Comitato Etico, ASL 3, Genova, Italy). All experiments were conducted in accordance with the Declaration of Helsinki (1964). Informed written consent was obtained for all the subjects. The studies were conducted in accordance with the local legislation and institutional requirements. The participants provided their written informed consent to participate in this study. Written informed consent was obtained from the individual(s) for the publication of any potentially identifiable images or data included in this article.

Author contributions

MB: Writing–original draft, Conceptualization, Investigation, Methodology, Software, Data curation. GA: Writing–review and editing, Investigation, Methodology, Formal Analysis. AM: Writing–review and editing, Resources, Software. MC: Writing–review and editing, Resources. WS: Writing–review and editing, Conceptualization, Methodology. MG: Writing–review and editing, Conceptualization. AC: Writing–review and editing, Software, Validation. SS: Writing–review and editing, Conceptualization, Validation, Supervision. VF: Writing–review and editing, Conceptualization. GS: Writing–review and editing, Conceptualization, Supervision, Validation, Resources, Funding acquisition.

Funding

The author(s) declare that financial support was received for the research, authorship, and/or publication of this article. This research was financially supported by the Robotics, Brain, and Cognitive Sciences Unit of the Istituto Italiano di Tecnologia and by Regione Liguria through FILSE SpA in the framework of POR 2014–2020 (Asse 1 "RICERCA E INNOVAZIONE (OT1)"—Azione 1.2.4), and was conducted in collaboration with Chiossone Foundation for Blind and Low Vision Individuals.

Conflict of interest

The authors declare that the research was conducted in the absence of any commercial or financial relationships that could be construed as a potential conflict of interest.

Publisher's note

All claims expressed in this article are solely those of the authors and do not necessarily represent those of their affiliated organizations, or those of the publisher, the editors and the reviewers. Any product that may be evaluated in this article, or claim that may be made by its manufacturer, is not guaranteed or endorsed by the publisher.

Supplementary material

The Supplementary Material for this article can be found online at: https://www.frontiersin.org/articles/10.3389/10.3389/fbioe.2024.1285107/full#supplementary-material

References

Adams, R., Finn, P., Moes, E., Flannery, K., and Rizzo, A. S. (2009). Distractibility in attention/deficit/hyperactivity disorder (ADHD): the virtual reality classroom. *Taylor Francis* 2009, 120–135. doi:10.1080/09297040802169077

Barbieri, M., Canessa, A., Sabatini, S. P., Sandini, G., Albanese, G. A., and Capris, E. (2023). *Realter: an immersive simulator to support low-vision rehabilitation*. Germany: Springer. doi:10.1007/978-3-031-43404-4_27

Cahill, M. T., Banks, A. D., Stinnett, S. S., and Toth, C. A. (2005). Vision-related quality of life in patients with bilateral severe age-related macular degeneration. *Ophthalmology* 112 (1), 152–158. doi:10.1016/j.ophtha.2004.06.036

Casiddu, N., and Porfirione, C. (2023). *HCD methodologies and simulation for visual rehabilitator's education in oMERO project*. China: Books.Google.Com. Available at: https://books.google.com/books?hl=it&lr=&id=inq3EAAAQBAJ&oi=fnd&pg=PA1&dq=oMero+casiddu+&ots=0AMBfV7Cq8&sig=5AY_0NP1yMmDFgP93CETUtFGbtc January 19, 2024).

Chow-Wing-Bom, H., Dekker, T. M., and Jones, P. R. (2020). The worse eye revisited: evaluating the impact of asymmetric peripheral vision loss on everyday function. *Vis. Res.* 169, 49–57. doi:10.1016/J.VISRES.2019.10.012

Crabb, D., Smith, N., Glen, F., and Ophthalmology, R. B.- (2013). *How does glaucoma look? patient perception of visual field loss*. USA: Elsevier. Available at: https://www.sciencedirect.com/science/article/pii/S0161642012011633?casa_token=tAIigZ7qMcgAAAAA:OGJMbrWEIttDchJdSK-YBdjIMBJio8kwKHeTZ9ZU8thajPjquHXzhDyVQ4dWc4etK-S1qYmS Accessed January 23, 2024.

Craig, A. (2013). Understanding augmented reality: concepts and applications. Available at: https://books.google.com/books?hl=it&lr=&id=7_O5LaIC0SwC&oi=fnd&pg=PP1&dq=Craig.

Cushing, H., and Brain, C. W. (1915). Distortions of the visual fields in cases of brain tumour: chiasmal lesions, with especial reference to bitemporal hemianopsia. *Sch. Arch. Org.* 37, 341–400. doi:10.1093/brain/37.3-4.341

Dar, A. H., Wagner, A. S., and Hanke, M. (2021). REMoDNaV: robust eye-movement classification for dynamic stimulation. *Behav. Res. Methods* 53 (1), 399–414. doi:10.3758/s13428-020-01428-x

Duchowski Theory, A. T. (2017). Eye tracking: methodology theory and practice. Available at: https://link.springer.com/content/pdf/10.1007/978-3-319-57883-5.pdf.

Flaxman, S. R., Bourne, R. R. A., Resnikoff, S., Ackland, P., Braithwaite, T., Cicinelli, M. V., et al. (2017). Global causes of blindness and distance vision impairment 1990–2020: a systematic review and meta-analysis. *Lancet Glob. Health* 5 (12), e1221–e1234. doi:10.1016/S2214-109X(17)30393-5

Fonseca, D., Martí, N., Redondo, E., Navarro, I., and Sánchez, A. (2014). Relationship between student profile, tool use, participation, and academic performance with the use of Augmented Reality technology for visualized architecture models. *Comput. Hum. Behav.* 31 (1), 434–445. doi:10.1016/j.chb.2013.03.006

Gibaldi, A., and Sabatini, S. P. (2021). The saccade main sequence revised: a fast and repeatable tool for oculomotor analysis. *Behav. Res. Methods* 53 (1), 167–187. doi:10.3758/s13428-020-01388-2

Goodwin, D. (2014). Homonymous hemianopia: challenges and solutions. *Clin. Ophthalmol.* 8, 1919–1927. doi:10.2147/OPTH.S59452

Gori, M., Cappagli, G., Tonelli, A., Baud-Bovy, G., and Finocchietti, S. (2016). Devices for visually impaired people: high technological devices with low user acceptance and no adaptability for children. *Neurosci. Biobehav. Rev.* 69, 79–88. doi:10.1016/j.neubiorev.2016.06.043

Greengard, S. (2019). Virtual reality. Available at: https://books.google.com/books?hl=it&lr=&id=YU6qDwAAQBAJ&oi=fnd&pg=PR5&dq=Virtual+reality.&ots=XFRS71sZAI&sig=-Og2GkjV-6CevJMIw2zKg3P3FLQ.

Grunda, T., Marsalek, P., and neurobiologiae, P. S.-A. (2013). Homonymous hemianopia and related visual defects: restoration of vision after a stroke. *Eur. Org.* 73, 237–249. doi:10.55782/ane-2013-1933

Gupta, D., and physician, P. C.-A. family (2016). Glaucoma. Amedeolucente.ItD Gupta, PP ChenAmerican family physician, 2016●amedeolucente.It. Available at: https://www.amedeolucente.it/public/Glaucoma(2).pdf.93

Handa, M., Aul, G., and Bajaj, S. (2012). *The state of the VR immersive media ecosystem society for imaging science and technology eric cheng immersive media lead.*

Holmqvist, K., Nyström, M., Andersson, R., and Dewhurst, R. (2011a). Eye tracking: a comprehensive guide to methods and measures. Available at: https://books.google.com/books?hl=it&lr=&id=5rIDPV1EoLUC&oi=fnd&pg=PT23&dq=eye+tracking+holmqvist&ots=_x7EQWsLqI&sig=mgWAa5QxlDl0lAwX7FbamW9BAF8.

Holmqvist, K., Nyström, M., Andersson, R., and Dewhurst, R. (2011b). Eye tracking: a comprehensive guide to methods and measures. Available at: https://books.google.com/books?hl=it&lr=&id=5rIDPV1EoLUC&oi=fnd&pg=PT23&dq=Holmquist.

Huang, H. M., Rauch, U., and Liaw, S. S. (2010). Investigating learners' attitudes toward virtual reality learning environments: based on a constructivist approach. *Comput. Educ.* 55 (3), 1171–1182. doi:10.1016/j.compedu.2010.05.014

Huang, T. C., Chen, C. C., and Chou, Y. W. (2016). Animating eco-education: to see, feel, and discover in an augmented reality-based experiential learning environment. *Comput. Educ.* 96, 72–82. doi:10.1016/j.compedu.2016.02.008

Hubschman, J., Reddy, S., and Ophthalmology, S. S.-C. (2009). Age-related macular degeneration: current treatments. *Taylor FrancisJP Hubschman, S Reddy, S. D. SchwartzClinical Ophthalmol. 2009●Taylor Francis* 3 (1), 155–166. doi:10.2147/opth.s2094

Imaoka, Y., Flury, A., and de Bruin, E. D. (2020). Assessing saccadic eye movements with head-mounted display virtual reality technology. *Front. Psychiatry* 11, 572938. doi:10.3389/fpsyt.2020.572938

Jones, P. R., Somoskeöy, T., Chow-Wing-Bom, H., and Crabb, D. P. (2020). Seeing other perspectives: evaluating the use of virtual and augmented reality to simulate visual impairments (OpenVisSim). *Npj Digit. Med.* 3 (1), 32. doi:10.1038/s41746-020-0242-6

Kothgassner, O. D., Goreis, A., Kafka, J. X., Van Eickels, R. L., Plener, P. L., and Felnhofer, A. (2019). Virtual reality exposure therapy for posttraumatic stress disorder (PTSD): a meta-analysis. *Eur. J. Psychotraumatology* 10 (Issue 1), 1654782. doi:10.1080/20008198.2019.1654782

Kumar, G., and Chung, S. T. L. (2014). Characteristics of fixational eye movements in people with macular disease. *Investigative Ophthalmol. Vis. Sci.* 55 (8), 5125–5133. doi:10.1167/iovs.14-14608

Leat, S., Legge, G., and Science, M. B.-O. (1999). What is low vision? A re-evaluation of definitions. *Journals. Lww. Com.* 76, 198–211. doi:10.1097/00006324-199904000-00023

Legge, G., Luebker, A., and Ross, J. (1989). Psychophysics of reading. VIII. The Minnesota low-vision reading test. *Optom. Vis. Sci.* 66, 843. doi:10.1097/00006324-198912000-00008

Liebers, J., Horn, P., and Burschik, C., (2021). Using gaze behavior and head orientation for implicit identification in virtual reality. *Dl.Acm.OrgJ Liebers, P Horn, C Burschik, U Gruenefeld, S SchneegassProceedings 27th ACM Symposium Virtual Real. Softw. Technol.*, 2021. doi:10.1145/3489849.3489880

Mannan, S. K., Pambakian, A. L. M., and Kennard, C. (2010). Compensatory strategies following visual search training in patients with homonymous hemianopia: an eye movement study. *J. Neurology* 257 (11), 1812–1821. doi:10.1007/s00415-010-5615-3

McDonald, M. A., Stevenson, C. H., Kersten, H. M., and Danesh-Meyer, H. V. (2022). Eye movement abnormalities in glaucoma patients: a review. *Eye Brain* 14, 83–114. doi:10.2147/EB.S361946

Moss, A. M., Harrison, A. R., and Lee, M. S. (2014). Patients with homonymous hemianopia become visually qualified to drive using novel monocular sector prisms. *J. Neuro-Ophthalmology* 34 (1), 53–56. doi:10.1097/WNO.0000000000000060

Nguyen, A. M., van Landingham, S. W., Massof, R. W., Rubin, G. S., and Ramulu, P. Y. (2014). Reading ability and reading engagement in older adults with glaucoma. *Investigative Ophthalmol. Vis. Sci.* 55 (8), 5284–5290. doi:10.1167/iovs.14-14138

Nyström, M., and Holmqvist, K. (2010). An adaptive algorithm for fixation, saccade, and glissade detection in eyetracking data. *Behav. Res. Methods* 42 (1), 188–204.

Nuthmann, A., Thibaut, M., Tran, T. H. C., and Boucart, M. (2022). Impact of neovascular age-related macular degeneration on eye-movement control during scene viewing: viewing biases and guidance by visual salience. *Vis. Res.* 201, 108105. doi:10.1016/j.visres.2022.108105

Ophthalmology, J. L.-A. A. (1960). Results of surgery in patients with tubular fields due to glaucoma. Jamanetwork.Com. Available at: https://jamanetwork.com/journals/jamaophthalmology/article-abstract/626212 (Accessed January 23, 2024).

WHO (2019). WHO global report on traditional and complementary medicine. Available at: https://books.google.com/books?hl=it&lr=&id=WHOyDwAAQBAJ&oi=fnd&pg=PP1&dq=World+Health+Organization.+.

Otero-Millan, J., Troncoso, X. G., Macknik, S. L., Serrano-Pedraza, I., and Martinez-Conde, S. (2008). Saccades and microsaccades during visual fixation, exploration, and search: foundations for a common saccadic generator. *J. Vis.* 8 (14), 21. doi:10.1167/8.14.21

PP, R. (1964). Human experimentation. Code of ethics of the world medical association. *British medical journal*. Declaration of Helsinki 2 (5402), 177–177.

Rickman, C. B., Farsiu, S., Toth, C. A., and Klingeborn, M. (2013). Dry age-related macular degeneration: mechanisms, therapeutic targets, and imaging. *Invest. Ophthalmol. Vis. Sci.* 54 (14). Available at: https://jov.arvojournals.org/article.aspx?articleid=2127428.

Rubin, G. S. (2013). Measuring reading performance. *Vis. Res.* 90, 43–51. doi:10.1016/j.visres.2013.02.015

Sathian, K. (2000). Practice makes perfect: sharper tactile perception in the blind. *Neurology* 54 (12), 2203–2204. doi:10.1212/WNL.54.12.2203

Soliman, M., Peetz, J., and Davydenko, M. (2017). The impact of immersive technology on nature relatedness and pro-environmental behavior. *J. Media Psychol.* 29 (1), 8–17. doi:10.1027/1864-1105/A000213

Suh, A., and Prophet, J. (2018). The state of immersive technology research: a literature analysis. *Comput. Hum. Behav.* 86, 77–90. doi:10.1016/j.chb.2018.04.019

Taylor, D. J., Hobby, A. E., Binns, A. M., and Crabb, D. P. (2016). How does age-related macular degeneration affect real-world visual ability and quality of life? A systematic review. doi:10.1136/bmjopen-2016

Thornson, C. A., Goldiez, B. F., and Le, H. (2009). Predicting presence: constructing the tendency toward presence inventory. *Int. J. Hum. Comput. Stud.* 67 (1), 62–78. doi:10.1016/j.ijhcs.2008.08.006

Van der Stigchel, S., Bethlehem, R. A. I., Klein, B. P., Berendschot, T. T. J. M., Nijboer, T. C. W., and Dumoulin, S. O. (2013). Macular degeneration affects eye movement behavior during visual search. *Front. Psychol.* 4 (SEP), 579. doi:10.3389/fpsyg.2013.00579

Verghese, P., Vullings, C., and Shanidze, N. (2021). Eye movements in macular degeneration. *Annu. Rev. Vis. Sci.* 7, 773–791. doi:10.1146/ANNUREV-VISION-100119-125555

Vullings, C., and Verghese, P. (2021). Mapping the binocular scotoma in macular degeneration. *J. Vis.* 21 (3), 9–12. doi:10.1167/jov.21.3.9

Yang, E., Blake, R., and McDonald, J. E. (2010). A new interocular suppression technique for measuring sensory eye dominance. *Investigative Ophthalmol. Vis. Sci.* 51 (1), 588–593. doi:10.1167/iovs.08-3076

Frontiers in
Bioengineering and Biotechnology

Accelerates the development of therapies, devices, and technologies to improve our lives

A multidisciplinary journal that accelerates the development of biological therapies, devices, processes and technologies to improve our lives by bridging the gap between discoveries and their application.

Discover the latest Research Topics

See more →

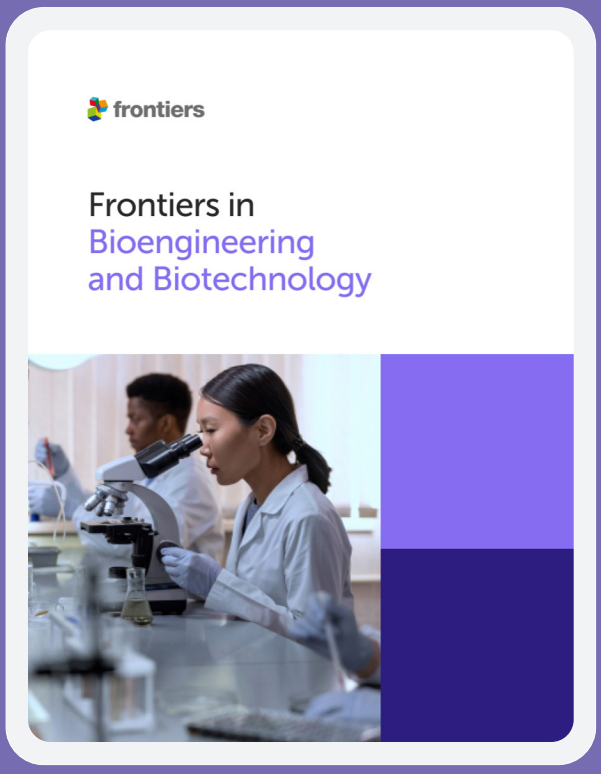

Frontiers

Avenue du Tribunal-Fédéral 34
1005 Lausanne, Switzerland
frontiersin.org

Contact us

+41 (0)21 510 17 00
frontiersin.org/about/contact